

EXPERIMENTAL STUDY ON THE INFLUENCE OF THE GEOMETRY OF SHALLOW RESERVOIRS ON FLOW PATTERNS AND SEDIMENTATION BY SUSPENDED SEDIMENTS

THÈSE N° 4048 (2008)

PRÉSENTÉE LE 25 AVRIL 2008

À LA FACULTÉ DE L'ENVIRONNEMENT NATUREL, ARCHITECTURAL ET CONSTRUIT
LABORATOIRE DE CONSTRUCTIONS HYDRAULIQUES
PROGRAMME DOCTORAL EN ENVIRONNEMENT

ÉCOLE POLYTECHNIQUE FÉDÉRALE DE LAUSANNE

POUR L'OBTENTION DU GRADE DE DOCTEUR ÈS SCIENCES

PAR

Sameh Ahmad KANTOUSH

Master of Engineering in the field of civil engineering, Saga University, Saga, Japon
et de nationalité égyptienne

acceptée sur proposition du jury:

Prof. A. Mermoud, président du jury
Prof. A. Schleiss, directeur de thèse
Prof. H.-E. Minor, rapporteur
Prof. M. Pirotton, rapporteur
Prof. W. Uijtewaal, rapporteur



ÉCOLE POLYTECHNIQUE
FÉDÉRALE DE LAUSANNE

Suisse
2008

I would like to dedicate this thesis to my loving parents, my lovely wife & my lovely country Egypt.....

Water in the Quran

Descriptions in the Quran of seas, rivers and stretches of water suggest no fear of desertification, water shortages or of life in an arid climate. Water is one of God's gifts. As a result, its scarcity can only be a sign of divine wrath, a consequence of man mismanagement of the precious gift or of his ill-conceived projects, since God created all things in due measure, without excess but also without parsimony: "We send down water from the sky in due measure, and let it trickle into the Earth. We are even able to make it disappear. We have produced date groves and vineyards on it for you; from which you have much fruit to eat..." (Quran, sura 23, ayat 18).

The Quran calls for proper governance of water and the equitable sharing of this vital resources when it says: "Announce to them how water must be shared among them; each will have his own special time to drink" (Quran, sura 54, ayat 28).

.....Have not those who disbelieve known that the heavens and the earth were joined together as one united piece, then We parted them? And We have made from water every living thing. Will they not then believe? (Quran, sura 25, ayat 21).

.....He sends down water (rain) from the sky, and the valleys flow according to their measure, but the flood bears away the foam that mounts up to the surface - and (also) from that (ore) which they heat in the fire in order to make ornaments or utensils, rises a foam like unto it, thus does Allâh (by parables) show forth truth and falsehood. Then, as for the foam it passes away as scum upon the banks, while that which is for the good of mankind remains in the earth. Thus Allâh sets forth parables (for the truth and falsehood, i.e. Belief and disbelief)(Quran, sura 14, ayat 13).

.....Were they created by nothing? Or were they themselves the creators? Or did they create the heavens and the earth? Nay, but they have no firm Belief. (Quran, sura 35, ayat 52-53).

Table of Contents

Abstract	XI
Résumé	XV
Zusammenfassung	XIX
Abstract in Arabic	XXIII
List of Symbols	XXVI
1 Introduction	35
1.1 Problematic of sedimentation of shallow reservoirs	35
1.2 Outline of the problem and methodology	36
1.3 Research objectives	38
1.4 Structure of the report	39
2 Literature review and theoretical basis	41
2.1 Flows in shallow reservoirs	41
2.1.1 Definition of shallow flows	41
2.1.2 Hydrodynamics of shallow flows	42
2.1.3 Mixing layers, jet flow and plane turbulent jet	43
2.1.4 Flow separation	45
2.1.5 Stability of symmetric and asymmetric flow	47
2.2 Reservoir sedimentation	50
2.2.1 Definition and functions of reservoirs	51
2.2.1.1 Useful life of reservoirs	52
2.2.2 Problems and measures to mitigate reservoir sedimentation	52
2.2.3 Effects of suspended sediment on reservoir sedimentation	54
2.2.4 Reservoir release and trap efficiency	55

Table of Contents

2.2.4.1	Empirical models for predicting Trap Efficiency (TE)	57
2.2.4.2	Theoretical models for prediction of trap efficiency (TE)	61
2.2.5	Existing methods for reducing siltation by suspended sediment	63
2.2.6	Features of flushing	64
2.2.6.1	Pressure flushing	64
2.2.6.2	Drawdown flushing	64
2.2.6.3	Free flow flushing	65
2.3	Suspended sediment transport and bed form generation	66
2.3.1	Generation of bed forms	68
2.3.2	Interaction between turbulent flow, sediment transport and bed forms	69
2.3.3	Influence of suspended sediment on flow characteristics	71
2.3.3.1	Von Kármán coefficient	71
2.3.3.2	Effect of coarse and fine grains on turbulence	72
2.4	Physical and numerical modeling of flow in shallow reservoirs	72
2.4.1	Experiments dealing with reservoir sedimentation	73
2.4.2	Classification of numerical models associated with reservoir sedimentation	75
2.5	Conclusion	76
3	Experimental facility and measurement techniques	77
3.1	Design of experiments	77
3.2	Description of experimental setups	78
3.3	Configuration and dimension of investigated geometries	79
3.4	Experimental conditions regarding scaling	80
3.4.1	Scaling	84
3.4.2	Hydraulic aspects	86
3.4.3	Sediment aspects	86
3.4.4	Similarity of the beginning of sediment motion	87
3.4.4.1	Choice of sediment material	90
3.5	Measurement techniques	92
3.5.1	Ultrasonic Doppler Velocity Profiler (UVP)	92
3.5.2	Large-Scale Particle Velocimetry (LSPIV)	96
3.5.3	Mini-Echo Sounder (UWS)	99
3.5.3.1	Principles of measuring distances by means of ultrasound	101
3.5.3.2	Characteristics of UltraLab UWS - Echo Sounder	101
3.5.3.3	Parameter setting	102
3.5.4	Suspended sediment concentration (SSC)	104
3.5.4.1	Measuring principle	105

3.5.4.2	Laboratory calibration based on suspensions of known concentration	106
3.5.4.3	Data reliability and errors	107
3.5.4.4	Sensor installation in the upstream and downstream channels	108
3.5.5	Discharge and water level measurements	109
3.6	Experimental procedure	109
3.7	Discussion of the efficiency of the instruments used and the test procedures applied	113
3.8	Characteristics and dimensionless parameters	114
3.8.1	Fluid	114
3.8.2	Flow	115
3.8.3	Geometry	115
3.8.4	Time	116
3.8.5	Sediments	116
3.9	Definition of geometry shape factor SK	117
3.9.1	Validity of empirical formulas and fits	121
3.10	Hydraulic conditions of experiments with clear water	122
3.11	Hydraulic and sediment conditions of experiments with suspended sediment .	125
4	Results and analysis of tests with clear water	127
4.1	Observed flow patterns and features	127
4.1.1	Conclusions regarding features of flow pattern	134
4.2	Flow patterns, streamlines, vorticities for different geometry forms	134
4.2.1	Asymmetric flow (deflected jet) for geometry shape factor $SK > 5.5$ & $h/b = 0.8$, $Fr_{in} = 0.1$, and $Re_{in} = 28000$	135
4.2.2	Symmetric flow (straight jet with spanwise circulation) for geometry shape factor $SK \leq 5.5$ and $h/b = 0.8$, $Fr_{in} = 0.1$, and $Re_{in} = 28000$.	137
4.2.3	Central meandering jet flow for $h/b \leq 0.6$	140
4.3	Influence of hydraulic conditions (Froude and Reynolds numbers) on the flow stability	143
4.4	Observed reattachment lengths and number of gyres	148
4.5	Analysis of velocity profiles: comparison of 3D UVP measurements with LSPIV results	150
4.6	Detailed comparison for cross and longitudinal ratio of velocity profile	155
4.7	Classification of jet flow regimes	159
4.8	Influence of SK on normalized velocity ratio U_{res}/U_{in} along the basin centerline	160
4.9	Influence of SK of the basin on the normalized velocity for each reservoir . .	164
4.10	Influence of SK of the basin on variation of the reattachment lengths $L_{r1} - L_{r2}$	166
4.11	Influence of Fr on the reattachment length $X_r = L_r/B_r$	168

Table of Contents

4.12 Influence of SK on residence time in basin 169

4.13 Influence of SK on ratio of t_{ri}/t_s 169

4.14 Influence of SK on reservoir Sedimentation Index SI 170

4.15 Conclusions regarding clear water experiments 172

5 Results and analysis of tests with sediments 175

5.1 Large coherent structures with and without suspended sediment 175

5.2 Effect of test procedures 177

5.3 Flow field comparison 177

5.4 Comparison of morphological evolution 180

5.5 Long term morphodynamic equilibrium 184

5.5.1 Morphological evolution and corresponding flow field 185

5.5.2 Comparison of deposition depth for different cross sections 187

5.5.3 Suspended sediment concentrations and sediment trap efficiency . . . 192

5.6 Contours of bed deposition and corresponding flow pattern 193

5.6.1 Effect of reservoir width 195

5.6.2 Effect of reservoir length 195

5.6.3 Effect of semi angle of reservoir entrance 197

5.7 Cross and longitudinal sections of deposition thickness 200

5.8 Suspended sediment concentrations 205

5.9 Observed phenomena depending on basin geometry 208

5.10 Classification of bed forms and final bed deposit 216

5.11 Efficiency of flushing 219

5.11.1 Free flow flushing flow and bed morphology 219

5.11.2 Drawdown flushing flow and bed morphology 222

5.12 Influence of reservoir geometry on sedimentation characteristics 227

5.12.1 Influence of aspect ratio of reservoir on storage loss 227

5.12.2 Influence of expansion ratio of reservoir on storage loss 229

5.12.3 Influence of $\sigma = A_{exp}/A_t$ on the silting ratio 230

5.13 Influence of geometry shape factor SK on storage loss SR 231

5.13.1 Time normalized by actual residence time of reservoir 231

5.13.2 Time normalized by initial residence time of reservoir 233

5.14 Effect of SK on mean relative deposited thickness 234

5.15 Discussions and conclusions 236

5.15.1 Influence of sediment feeding test procedure 236

5.15.2 Influence of test duration 237

5.15.3 Influence of basin geometry and bed forms 237

5.15.4 Conclusions regarding phenomena 238

5.15.5 Conclusions regarding flushing 238

6	Trapping and flushing efficiencies	239
6.1	Definition of trap efficiency	239
6.2	Prediction of trap efficiency	240
6.2.1	Influence of Aspect Ratio of reservoir on Trap efficiency	241
6.2.2	Influence of Expansion Ratio of reservoir on trap efficiency	242
6.2.3	Influence of normalized expansion area on trap efficiency	243
6.2.4	Influence of $AR_{exp} = L/\Delta B$ on trap efficiency	244
6.2.5	Influence of geometry shape factor on trap efficiency	245
6.2.6	Influence of relative residence time on trap efficiency	251
6.3	Influence of geometry shape factor SK on reservoir Sedimentation Index SI	252
6.4	Influence of sedimentation index SI on sediment release efficiency RE	253
6.5	Prediction of flushing efficiency	254
6.5.1	Free flow flushing	254
6.5.2	Drawdown flushing	254
6.5.2.1	Characteristics of the channel forming during drawdown flushing	255
7	Numerical simulation	259
7.1	Methodology of numerical study	259
7.2	Preliminary simulations	259
7.2.1	First step: numerical results obtained from simulations with Flow-3D and CCHE2D	260
7.2.1.1	Model description	260
7.2.1.2	Boundary conditions	260
7.2.2	Second step: numerical results obtained by simulations with CCHE2D compared with experiments	262
7.2.2.1	Governing equations	263
7.2.2.2	Morphological processes	265
7.2.2.3	Initial Conditions	265
7.2.2.4	Empirical Formulas	266
7.2.2.5	Turbulence closure	266
7.2.2.6	Results of numerical computations	268
7.2.2.7	Run series A	268
7.2.2.8	Run series B	272
7.2.2.9	Run series C	273
7.2.2.10	Comparison of the different run series along the basin centreline	273
7.2.2.11	Influence of grain size distribution	276
7.2.2.12	Conclusions regarding the simulations with CCHE2D	281

Table of Contents

7.2.3	Third step: numerical simulation with WOLF2D	282
7.2.3.1	Conclusion regarding simulations with WOLF2D	286
7.3	Discussions and conclusions	286
8	Summary, Conclusions, Recommendations and Outlook	289
8.1	Summary and Conclusions	289
8.1.1	Problematic of control silting processes in shallow reservoirs by design of a suitable geometry form	289
8.1.2	Experimental set-up, measurement equipment	290
8.1.3	Geometrical parameters, hydraulic and sediment conditions	290
8.1.4	general phenomena observed with clear water and suspended sediment	291
8.1.5	Results of experiments with clear water flow	292
8.1.6	Empirical approaches for prediction of mean velocity ratio in reservoir, reattachment lengths, relative residence time and sedimentation index	293
8.1.7	Results of experiments with suspended sediment	295
8.1.8	Empirical relationships for prediction of storage losses and relative deposition thickness in a shallow basin	295
8.1.9	Trapping and flushing efficiencies	296
8.1.9.1	Trap efficiency	296
8.1.9.2	Flushing efficiency and flushing channel formation	298
8.1.10	Numerical simulation	300
8.2	Answers to practical questions	301
8.3	Recommendations for design of shallow reservoirs	304
8.4	Outlook and further Research	306
	Acknowledgements	309
	References	313
	List of Figures	333
	List of Tables	347
A	Experimental Test Results for Different Geometries	349
A1	Results of rectangular geometry Test1	351
A1.1	Surface velocity obtained by (LSPIV) measurements	352
A1.2	Two days flushing with clear water over the final bed deposition of the third period (4.5 hours)	360
A1.3	Measurements of bed thickness deposition obtained by Mini Echo Sounder for Test1	362
A1.3.1	Depositions contours	363

	A1.3.2 Bed thickness cross and longitudinal sections	368
A1.4	3D velocity measurements obtained by Ultrasound Velocity Profiler (UVP)	373
	A1.4.1 Results of 3D UVP measurements for the initial state with clear water	374
A2	Results of rectangular geometry Test2	377
	A2.1 Surface velocity obtained by (LSPIV) measurements	378
A3	Results of rectangular geometry Test3	381
	A3.1 Surface velocity obtained by (LSPIV) measurements	382
	A3.2 Measurements of bed thickness deposition obtained by Mini Echo Sounder	385
	A3.2.1 Depositions contours	386
	A3.2.2 Bed thickness cross and longitudinal sections	388
A4	Results of rectangular geometry Test4	391
	A4.1 Surface velocity obtained by (LSPIV) measurements	392
	A4.2 Measurements of suspended sediment concentration obtained by turbiditymeter	396
	A4.3 Measurements of bed thickness deposition obtained by Mini Echo Sounder	400
	A4.3.1 Depositions contours	401
	A4.3.2 Bed thickness cross and longitudinal sections	403
A5	Results of rectangular geometry Test5	408
	A5.1 Surface velocity obtained by (LSPIV) measurements with clear water depth of $h_1 = 0.2m$ for Test5	409
	A5.2 Surface velocity obtained by (LSPIV) measurements with clear water depth of $h_2 = 0.15m$ for Test5	411
	A5.3 Surface velocity obtained by (LSPIV) measurements with clear water depth of $h_3 = 0.10m$ for Test5	413
	A5.4 Surface velocity obtained by (LSPIV) measurements with clear water depth of $h_4 = 0.075m$ for Test5	415
A6	Results of rectangular geometry Test6	417
	A6.1 Surface velocity obtained by (LSPIV) measurements for (Test6) of low discharge	418
A7	Results of rectangular geometry Test7	422
	A7.1 Surface velocity obtained by (LSPIV) measurements	423
A8	Results of rectangular geometry Test8	426
	A8.1 Surface velocity obtained by (LSPIV) measurements	427
	A8.2 Two days flushing with clear water over the final bed deposition of the third period (4.5 hours)	430

Table of Contents

A8.3	Measurements of suspended sediment concentration obtained by turbiditymeter	432
A8.4	Measurements of bed thickness deposition obtained by Mini Echo Sounder	434
A8.4.1	Depositions contours	435
A8.4.2	Bed thickness cross and longitudinal sections	438
A9	Results of rectangular geometry Test9	442
A9.1	Surface velocity obtained by (LSPIV) measurements with clear water for Test9	443
A10	Results of rectangular geometry Test10	445
A10.1	Surface velocity obtained by (LSPIV) measurements with clear water for Test10	446
A11	Results of rectangular geometry Test11	448
A11.1	Surface velocity obtained by (LSPIV) measurements	449
A11.2	Two days flushing with clear water over the final bed deposition of the third period (4.5 hours)	452
A11.3	Measurements of suspended sediment concentration obtained by turbiditymeter	454
A11.4	Measurements of bed thickness deposition obtained by Mini Echo Sounder	456
A11.4.1	Depositions contours	457
A12	Results of rectangular geometry Test12	459
A12.1	Surface velocity obtained by (LSPIV) measurements with clear water for Test12 (Square geometry)	460
A13	Results of rectangular geometry Test13	462
A13.1	Surface velocity obtained by (LSPIV) measurements	463
A13.2	Measurements of suspended sediment concentration obtained by turbiditymeter	466
A13.3	Measurements of bed thickness deposition obtained by Mini Echo Sounder	468
A13.3.1	Depositions contours	469
A14	Results of rectangular geometry Test14	472
A14.1	Surface velocity obtained by (LSPIV) measurements	473
A14.2	Two days flushing with clear water over the final bed deposition of the third period (4.5 hours)	477
A14.3	Measurements of suspended sediment concentration obtained by turbiditymeter	479
A14.4	Measurements of bed thickness deposition obtained by Mini Echo Sounder	483

A14.4.1	Depositions contours	484
A14.4.2	Bed thickness cross and longitudinal sections	490
A15	Results of rectangular geometry Test15	498
A15.1	Surface velocity obtained by (LSPIV) measurements with clear water for Test15 (Square geometry)	499
A16	Results of rectangular geometry Test16	501
A16.1	Surface velocity obtained by (LSPIV) measurements	502
A16.2	Two days flushing with clear water over the final bed deposition of the third period (4.5 hours)	505
A16.3	Measurements of suspended sediment concentration obtained by tur- biditymeter	508
A17	Results of prismatic channel without enlargement zones geometry Test17 . .	518
A17.1	Surface velocity obtained by (LSPIV) measurements with clear water for Test17 (Square geometry)	519
B	Recommendations for LSPIV applications	521
	Curriculum Vitae	525

Abstract

Experimental study on the influence of the geometry of shallow reservoirs on flow patterns and sedimentation by suspended sediments

The worst enemy of sustainable use of reservoirs is sedimentation. Often the main silting process is the result of settling down of suspended sediments. In shallow reservoirs the flow pattern and the sediment deposition processes are strongly influenced by the reservoir geometry.

The trap efficiency of a shallow reservoir depends on the characteristics of the inflowing sediments and the retention time of the water in the reservoir, which in turn are controlled by the reservoir geometry.

With the purpose of controlling the sedimentation in shallow reservoirs, the effects of the geometry on flow pattern and deposition processes were investigated with systematic physical experiments and numerical simulations. This allowed identifying ideal off-stream reservoir geometries, which can minimize or maximize the settlement of suspended sediments. The objective was also to gain deeper insight into the physical processes of sedimentation in shallow reservoirs governed by suspended sediments.

The systematic experimental investigations were carried out in a 6 m long, and 4 m wide and 0.3 m deep shallow basin. The influence of the shallow reservoir geometry was studied for the first time by varying the width, the length, and the expansion angle of the basin in the experiments for clear water and with suspended sediment. In total 11 different reservoir geometries and 4 water depths were analyzed. During the tests several parameters were measured, as $2D$ surface velocities, $3D$ velocity profiles, thickness of deposited sediments, and sediment concentration at the inflow and outflow. Crushed walnut shells with a median grain size, d_{50} , of $50 \mu m$, and a density of $1500 kg/m^3$ were used to simulate the suspended sediments.

After having reached a stable flow pattern with the clear water, velocity measurements were performed. In a second phase, the evolution of the flow and deposition patterns under suspended sediment inflow were investigated. Tests were carried out with durations from 1.5 hours up to 18 hours, in order to follow the morphological evolution. In order to investigate the efficiency of flushing, flushing operations at normal water level as well as with drawdown were examined after the sedimentation tests.

Numerical simulations of the laboratory basin were performed and compared with ex-

perimental results. The purpose was to assess the sensitivity of the results on different flow and sediment parameters and different turbulence closure schemes.

The experimental investigation of the flow and sediment behavior in axi-symmetric geometries with different shapes provides further information on the evolution of the flow pattern and the sediment deposition. Beside the expansion ratio and form ratio of the basin the flow regime was classified by the geometry shape factor SK and inlet Froude number Fr_{in} . The geometry shape factor, defined as a function of wetted perimeter, total reservoir surface area, aspect ratio and expansion density ratio, was used to compare and analyze the experimental results obtained from the different investigated basin geometries.

The clear water experiments investigations revealed under what geometrical conditions the flow changes from symmetrical to asymmetrical behavior. The length of the basin has a strong influence on the change of the flow field. The water depth also significantly affects on the type of jet and vortex structure forming in the basin. On the other, hand the sediment deposition pattern was strongly influenced by the jet type and the flow behavior changed with increasing deposits. The prediction of sediment deposition is linked to the prediction of flow behavior. Furthermore it is very sensitive to the basin geometry and the boundary conditions of inflow and outflow. Some tests were performed until the sediment released at the outlet was equal to the sediments entering at inlet into the basin that means a quasi equilibrium was reached.

Flushing at normal water level allows only a relatively small part of the deposited sediment to be evacuated. As expected, drawdown flushing is much more effective and a significant amount of sediment deposits could be flushed out of the basin.

Regarding the flow pattern in shallow basins empirical relationships for the estimation of the reattachment length of gyres and the normalized residence time as a function of the geometry shape factor, SK, were established. Also empirical equations for the prediction of the jet flow type and velocity magnitude depending on the basin geometry could be formed. Finally empirical equations for the prediction of sedimentation index, silting ratio, trap efficiency and relative deposition thickness, as well as normalized residence time and flushing efficiency could be found.

The numerical simulations revealed that the observed asymmetry in flow and deposition patterns can be explained by the sensitivity of the flow regarding geometry and boundary conditions. The influence of the length and width of the basin on the flow pattern can be predicted in good agreement with experiments by these simulations.

Some recommendations are given for the design procedure of a new shallow reservoir in view of minimizing the sedimentation due to suspended sediment. The deposited sediment volume can be efficiently minimized by an optimal designed reservoir geometry.

Keywords: Shallow flow, geometry shape factor, reservoir geometry, turbulent jet, flow and sediment deposition patterns, suspended sediments, reservoir sedimentation, trap and

flushing efficiencies, silting ratio, empirical models, numerical simulations.

Résumé

Etude expérimentale sur l'influence de la géométrie des réservoirs peu profonds sur l'écoulement et sur le processus d'alluvionnement par sédiments en suspension

Le plus grand ennemi contre l'usage durable des réservoirs est la sédimentation. Ce processus est dû principalement à la décantation des sédiments fin suspendus présent dans l'écoulement. Dans les réservoirs peu profonds, la répartition de vitesse du courant et les processus de la déposition sont fortement influencés par la géométrie de ces réservoirs.

L'efficacité de rétention sédimentaire que présente un réservoir peu profond dépend des caractéristiques des sédiments entrant et de la durée du trajet effectué par l'eau en traversant le réservoir. Cette durée est contrôlée évidemment par la géométrie de ce dernier.

Dans le but de contrôler la sédimentation des réservoirs peu profonds, des expériences physiques systématiques et des simulations numériques ont été faites pour étudier l'influence de la géométrie de ces réservoirs sur la répartition du courant et sur le processus de déposition. Cela a permis d'identifier la géométrie idéale pour minimiser ou maximiser le processus d'envasement. L'objectif était aussi de mieux comprendre les processus physiques de la sédimentation des particules fines suspendues dans ces types de réservoirs.

Des investigations expérimentales systématiques ont été réalisées dans un bassin de 6 m de long, 4.0 m de large et 0.3 m de profondeur. L'influence de la géométrie de réservoir a été étudiée en variant la largeur, la longueur, et l'angle d'expansion des murs du bassin pour un écoulement à eau claire, et puis après, pour un écoulement en mélange avec de sédiments suspendus. Au total, 11 géométries et 4 profondeurs différentes du réservoir ont été analysées. Durant les essais, plusieurs paramètres ont été mesurés, à savoir : la vitesse bidimensionnelle en surface, le profil de vitesse en $3D$, l'épaisseur des sédiments déposés et la concentration sédimentaire à l'entrée et la sortie du bassin. Des coquilles de noix écrasées à un diamètre moyen de grain (d_{50}) égale à $50 \mu m$ et possédant une densité de $1500 kg/m^3$ ont été utilisées pour simuler les sédiments suspendus.

Après avoir atteint un écoulement (ou stationnaire) avec l'eau claire, des mesures de vitesse ont été réalisées. En deuxième phase, des mesures de l'évolution du courant et des dépôts en présence de sédiment suspendu ont été faites. Les essais ont été effectués pendant des durées allant de $1.5heures$ jusqu'à $18heures$ afin de pouvoir suivre l'évolution morphologique du processus. Pour étudier l'efficacité d'évacuation des sédiments du réservoir une

fois ces derniers sont déposés, des essais ont été faits à niveau normal et avec abaissement du plan d'eau.

Des simulations numériques du bassin expérimental du laboratoire ont été réalisées. Les résultats obtenus ont été comparés avec ceux mesurés expérimentalement. Le but était d'étudier la sensibilité de ces résultats sous différentes configurations de courant ainsi que pour différents paramètres de sédiments et schémas de turbulence.

L'analyse de l'essai expérimental effectué sur l'écoulement et sur le comportement des sédiments dans des géométries axi-symétriques possédant des formes variées, a fourni des informations supplémentaires sur l'évolution du schéma du courant et sur le phénomène de déposition des sédiments. En plus de la détermination d'un rapport d'expansion et d'un autre qui dépend de la forme du bassin, un régime de courant a été classé par le moyen d'un facteur de forme géométrique (SK) et du nombre de Froude de l'entrée du bassin, Fr_{in} . Le facteur de forme géométrique défini comme une fonction de périmètre mouillé, la surface totale du bassin, le rapport longueur/largeur et celui d'élargissement, ont été utilisés pour comparer et analyser les résultats expérimentaux obtenus sous les différentes géométries du bassin testées.

D'une part, les essais effectués avec de l'eau claire ont montré les conditions géométriques sous lesquelles l'écoulement change de comportement en passant de symétrique à asymétrique. La longueur du bassin a une grande influence sur le changement du champ d'écoulement. La profondeur de l'eau influence aussi considérablement le type de jet de l'eau et la formation des tourbillons de structure dans le bassin d'essais.

D'autre part, les dépôts de sédiments ont été fortement influencés par le type de jet. Le comportement de courant change avec l'évolution des dépôts. La prédiction de dépôts de sédiments est liée à la prédiction du comportement de l'écoulement. De plus, cette prédiction est très sensible à la géométrie de la cuvette et aux limites amont et aval de l'écoulement. Quelques essais ont été réalisés jusqu'à ce que le débit de sédiments sortant du bassin soit égal au celui entrant. Ceci revient à dire qu'un état d'équilibre quasi-permanent a été atteint.

Lors de la chasse à niveau normal, une proportion relativement faible des sédiments déposés peut être évacuée. Comme attendu, la chasse à nappe libre avec abaissement du plan d'eau est plus efficace donnant ainsi lieu à un volume considérable de dépôts évacués du bassin.

Concernant le champ d'écoulement dans les bassins peu profonds, des relations empiriques pour l'estimation de la longueur de re-attachement des vortex et le temps de résidence normalisé en fonction du facteur de forme géométrique (SK), ont été établies. Des relations empiriques pour la prédiction du type d'écoulement et de la magnitude de la vitesse en fonction de la géométrie du bassin ont été également formulées. Finalement, des relations empiriques pour la prédiction de l'index de sédimentation, du taux d'envasement, de l'efficacité de rétention et de l'épaisseur relative des dépôts, ainsi que le temps de résidence normalisé et l'efficacité de l'évacuation des sédiments ont été établies.

Les simulations numériques ont révélé que l'asymétrie observée dans le champ d'écoulement et dans la disposition des dépôts pourrait être expliquée par la sensibilité du courant à la géométrie et aux conditions limites. L'influence de la longueur et de la largeur du bassin sur le champ d'écoulement peut être évalué avec précision par la simulation numérique, en bon accord avec les résultats des expériences.

Quelques recommandations sont données pour le dimensionnement et la de conception d'un nouveau réservoir peu profond dans l'objectif de minimiser la sédimentation des particules suspendues. Les dépôts de sédiments peuvent être minimisés grâce à une géométrie optimale du bassin.

Mots-clé : Ecoulement peu profond, facteur de forme géométrique, géométrie du réservoir, jet turbulent, champ d'écoulement et disposition et dimensions des dépôts de sédiments, sédiments en suspension, alluvionnement de réservoir, efficacité de rétention et d'évacuation de sédiments, taux d'envasement, modèles empiriques, simulation numérique.

Zusammenfassung

Experimentelle Studie über den Einfluss der Geometrie von Flachwasserspeichern auf Fliessverhalten und Ablagerungsprozesse von Feinsedimenten

Die nachhaltige Nutzung von Speicher wird durch anhaltende Sedimentablagerungen stark beschränkt. Das Absetzen von in Suspension befindlichen Sedimenten ist meistens die Hauptursache der Ablagerungen. Das Fliess- und Absetzverhalten in seichten Speichern wird stark von der Stauseegeometrie beeinflusst.

Das Sedimentrückhaltevermögen eines flachen Speichers hängt von den Sedimentzuflussbedingungen und der Retentionszeit von Wasser im Stausee ab, diese wiederum ist durch die Speichergeometrie gegeben.

Mit dem Ziel, Sedimentablagerungen in flachen Speichern zu kontrollieren, wurden systematische physikalische Versuche und numerische Simulationen durchgeführt, um den Einfluss der Speichergeometrie auf das Fliessverhalten und die Ablagerungsprozesse zu untersuchen. Die Untersuchungen erlauben es, ideale Speichergeometrien im Nebenschluss zur Minimierung oder Maximierung von Sedimentablagerungen zu identifizieren. Ein weiteres Ziel war es, ein besseres Verständnis der physikalischen Ablagerungsprozesse durch Schwebstoffe in Flachwasserspeichern zu erlangen.

In einem 6 m langen, 4 m breiten und 0.3 m tiefen Becken wurden systematische experimentelle Untersuchungen durchgeführt. Der Einfluss der Speichergeometrie wurde zum ersten Mal durch Anpassen der Breite, der Länge und des Expansionswinkels des Beckens mit Reinwasserversuchen sowie mit Schwebstofffracht untersucht. Insgesamt wurden 11 verschiedene Speichergeometrien und 4 Wassertiefen geprüft. Während der Versuche wurden mehrere Parameter gemessen, wie 2D Oberflächengeschwindigkeiten, 3D Geschwindigkeitsprofile, Ablagerungshöhen, sowie Sedimentkonzentrationen bei Zu- und Abfluss. Gemahlene Walnusschalen mit einer mittleren Korngrösse von $d_{50} = 50 \mu m$ und einer Dichte von $\rho = 1500 \text{ kg/m}^3$ wurden zur Nachbildung der Schwebstoffe verwendet.

Sobald jeweils mit Reinwasser ein stationäres Flussbild erreicht worden war, wurden die Geschwindigkeitsmessungen durchgeführt. In einer weiteren Phase wurde die Entwicklung des Flussbildes und der Ablagerungen mit Schwebstoffzufuhr untersucht. Die Untersuchungen dauerten jeweils zwischen 1.5 Stunden und bis zu 18 Stunden um die morphologische Entwicklung verfolgen zu können. Zur Evaluation der Spüleffizienz wurde nach den Ablagerungsversuchen sowohl mit Stauziel als auch mit abgesenktem Wasserspiegel gespült.

Die Resultate der physikalischen Versuche im Laborbecken wurden mit denjenigen der numerischen Simulation verglichen. Ziel war es, die Sensibilität der Resultate auf verschiedene Abfluss- und Sedimentparameter sowie diverse Turbulenzmodelle zu untersuchen.

Die experimentellen Untersuchungen des Abflusses und des Ablagerungsverhaltens in axi-symmetrischer Konfiguration mit verschiedenen geometrischen Formen ergaben weitere Erkenntnisse über die Entwicklung des Flussbildes und der Sedimentablagerungen. Neben dem Expansions- und dem Formfaktor des Beckens, konnte das Flussbild durch den geometrischen Formfaktor SK und die Zuflussfroudzahl klassifiziert werden. Der geometrischen Formfaktor, definiert als Funktion des benetzten Umfangs, der Gesamtbeckenfläche, des Längen/Breitenverhältnisses und der Expansionsdichtezahl, wurde zur Auswertung und Vergleich der Versuchsergebnisse mit verschiedenen Beckengeometrien angewandt.

Die Reinwasserversuche zeigten auf, unter welchen geometrischen Bedingungen das Flussbild von symmetrisch zu asymmetrisch ändert. Die Beckenlänge hat einen grossen Einfluss auf die Änderungen im Flussbild.

Die Wassertiefe beeinflusst ebenfalls signifikant den Strahltyp und die Wirbelstruktur im Becken.

Andererseits wurden die Sedimentablagerungen stark vom Strahltyp beeinflusst und das Flussbild wandelte sich mit zunehmender Ablagerungstiefe. Die Vorhersage der Sedimentablagerungen ist an die Abschätzung des Abflussverhaltens gebunden. Des Weiteren ist sie sehr stark von der Beckengeometrie und den Randbedingungen beim Zufluss und Ausfluss abhängig.

Einige Versuche wurden solange durchgeführt, bis der Sedimentausfluss und -zufluss im Gleichgewicht waren.

Die Spülungen mit Stauziel erlauben nur einen geringen Sedimentaustrag. Wie erwartet ist dieser wesentlich grösser bei abgesenktem Wasserspiegel.

Empirische Beziehungen bezüglich dem Flussbild im flachen Becken für die Abschätzung der Berührungsdistanz der Wirbel und der normalisierten Verweildauer als Funktion des geometrischen Formfaktors, SK, wurden bestimmt. Ebenso wurden empirische Beziehungen für die Voraussage des Strahlabflusstyps und der Geschwindigkeitsgrösse in Abhängigkeit der Beckengeometrie ermittelt. Zum Abschluss konnten noch empirische Beziehungen für die Bestimmung des Sedimentationsindex, der Sedimentationsrate, des Sedimentrückhaltevermögens, und relative Ablagerungstiefe, sowie die normalisierte Verweildauer und Spülfizienz abgeleitet werden.

Die numerischen Simulationen zeigten auf, dass die beobachtete Asymmetrie bezüglich Ablagerungen und Flussbild als sehr starke Abhängigkeit von den Randbedingungen erklärt werden kann. Der Einfluss der Länge und Breite des Beckens auf das Flussbild im Modellversuch kann mit guter Übereinstimmung numerisch simuliert werden.

Einige Empfehlungen für das Dimensionierungsverfahren eines neuen flachen Speichers im Hinblick auf die Minderung der Sedimentablagerungen durch Schwebstoffe können ge-

geben werden. Das Ablagerungsvolumen kann durch eine optimale entworfene Speicher-
geometrie nachhaltig verringert werden.

Stichwörter: Flachwasserabfluss, geometrischer Formfaktor, Speicher-
geometrie, turbulenter Strahl, Fluss- und Sedimentablagerungsbild, Schwebstoffe, Ablagerungen in Speichern, Sedimentrückhalte- und Spülvermögen, Sedimentationsrate, empirische Modelle, numerische Simulationen.

المُلخَص

دراسة معمّلية لتأثير الشكل الهندسي للخزانات الضحلة على نماذج السريان و عملية الترسب برؤاسب دقيقة معلقة

أكبر عائق ضد الاستعمال الدائم للخزانات هو الترسب. السبب الرئيسى لهذه الظاهرة هو تصفية الرؤاسب الدقيقة الموجودة عند التدفق. في الخزانات الضحلة ، توزيع سرعة التيار و عملية الترسب تتأثر تأثيرًا كبيرًا بشكل الخزان. كفاءة الترسب في الخزانات الضحلة تعتمد على كل من خصائص الرؤاسب الداخلة و على مدة سير الماء في الخزان والتي بدورها تخضع لهندسة الخزان. بهدف التحكم في الترسب في الخزانات الضحلة.

تمّ القيام بتجارب فيزيائية منهجية وكذلك صورية لدراسة تأثير هندسة الخزانات على نماذج التدفق و على عملية الترسب. هذا ما سمح بتحديد هندسة مثالية لتقليل أو تقوية عملية الترسب. كان الهدف أيضًا اكتساب فكرة أكبر أو نظر أعمق الى العمليات الفيزيائية لترسبات في هذه الخزانات الضحلة.

التحقيق أ أجري بتجارب منهجية على خزان ضحل طوله ٦ م وعرضه ٤ م وعمقه ٠,٣ م. دراسة تأثير هندسة الخزان تمت أولاً بتغيير العرض ثم الطول ثم بتوسيع زاوية جدران الخزان أولاً لتدفق ماء صافي ثم بعد ذلك بماء مزوج بالرؤاسب. في المجموع ١١ هندسة و٤ أعماق مختلفة لخزان تم دراستها و تحليلها. خلال هذه التجارب عدة متغيرات تم قياسها منها السرعة بعديها في السطح ملامح السرعة على ثلاثة أبعاد سمك الرؤاسب المودعة تركيز الرؤاسب عند مدخل و عند مخرج الخزان. تم تمثيل الرؤاسب في التجربة بمسحوق لقشور الجوز حيث كان متوسط قطر الحبيبات $Q = 50 = 50$ ميكرومتر وكثافتها $1500 \text{ كج} / \text{م}^3$.

بعد الوصول الى تدفق مستمر بالماء الصافي تم اجراء قياسات لسرعة في المرحلة الثانية تم قياس تحرك التيار و الايداعات مع وجود رؤاسب معلقة. مدة التجارب كانت تراوح بين ١,٥ ساعة الى ١٨ ساعة حتى يتم دراسة التطورات المورفولوجية لهذه العملية. لدراسة فعالية التخلص من الرؤاسب بعد ترسيبها، تمت تجارب بمستوى عادى لماء ثم بتخفيض مستوى الماء.

تم اجراء نماذج حسابية لحزان الموجود في المعمل ثم قورنت النتائج بالتى تم قياسها في التجربة بالهدف كان دراسة تأثير هذه النتائج بأحوال مختلفة لتيار و قيم مختلفة لرؤاسب و الاضطرابات في الموائع.

تحليل التجربة المقامة على الحريان و على سلوكالرؤاسب في هندسات ذات تماثل محورى بأشكال مختلفة أعطى معلومات اضافية على حال الحريان وعلى ظاهرة ايداع الرؤاسب،بالأضافة الى تحديد نسبة التوسيع وأخرى تتعلق بشكل الحزان. تم تحديد نظام سريان الماء بواسطة ثابت الشكل الهندسى و بواسطة عدّ فرويد لمدخل الحزان. ثابت الشكل الهندسى معرف كدالة متعلقة بكل من المحيط المبلّ المساحة الكلية لحزان نسبة الطول / العرض نسبة التوسيع تم استعمال هذه الدالة لتحليل نتائج التجارب المجرأة تحت هندسات مختلفة لحزان.

من جهة التجارب التى أجريت بالماء الصافي أظهرت الشروط الهندسية الأزمة التى تحتها التدفق يغير سلوكه من تماثل الى غير تماثل. طول الحزان له تأثير كبير على تغير حقل التدفق. عمق الحزان يثر كذلك على نوع الدفع. سلوك تيار الماء يتغير وفقاً لتغير الرؤاسب. التوقعات المنتظرة لرؤاسب مرتبطة بأشكال و سلوك التدفق المتوقعة. زيادة على ذلك هذه التوقعات تأثر بشكل كبير بهندسة الحزان والشروط الحدية لسريان الداخل و الخارج.

تم اجراء عدة تجارب الى أن صارتركيز الرؤاسب المعلقة الخارجة يساوى تركيز الرؤاسب المعلقة الداخلة فيما يعنى أنه تم الوصول الى حالة اتزان شبه مستقر. عند الأخراج على مستوى عادى يمكن التخلص من نسبة قليلة نوعاً ما من الرؤاسب. و كما كان متوقعا عملية التخلص مع تخفيض مستوى الماء كانت أشد فعالية و تحصل بذلك نسبة عالية من الرؤاسب التى تم التخلص منها خارج الحزان.

فيما يخص حقل التدفق في الخزانات الضحلة تم استنتاج معادلات وضعية من النتائج العملية لتوقع أطوال الدوامات المنفصلة و زمن بقاء الماء الغير بعدى كعلاقة مع ثابت الشكل الهندسى. أثبتت التجارب الصورية أن عدم التماثل الملاحظ فينماذج السريان و الترسيبات من الممكن شرحها بواسطة حساسية السريان لشكل الهندسى لحزان و لشروط الحدية.

تأثير طول و عرض الحزان على حقل التدفق يمكن تحديدها بدقة باجراء التجارب الصورية الحسابية و هى متوافقة بصفة جيدة مع النماذج الحسابية. تم اعطاء بعض التوصيات لتطبيقات الحقيقية الخاصة بوضع منهج تصميمى للخزانات الضحلة الجديدة لكى نقل الترسيبات المرتبطة بالرؤاسب المعلقة. من الممكن تقليل حجم الرؤاسب بكفاءة عالية عن طريق ايجاد الشكل المثالى لحزان.

List of Symbols

Roman Symbols

$(v_{ss})_i$	particle settling velocity for i^{th} size fraction
\acute{p}	porosity of bed material
ΔB	depth of lateral expansion
Δ_i	percentage of the sediment material falling in the i^{th} size fraction of the frequency histogram
δ_m	thickness of the mixing layer
$\partial z_b / \partial t$	total bed deformation rate
σ	normalized expansion area
SSC_{known}	known suspended sediment concentration using the known sediment weight and water volume
A_{exp}	expansion surface area of the basin
A_t	total surface area of the basin
A_{xy}	adjustable coefficient of eddy viscosity parameter
AR	aspect ratio of the basin
B	width of the basin
b	width of the upstream and downstream channels
b_{eff}	width of the flushing channel

List of symbols

c_f	friction coefficient
c_k	concentration of k^{th} size class of sediment
c_{b*k}	equilibrium suspended-load concentration at the interface between the bed-load zone and the suspended-load zone
c_{bk}	average concentration of bed load at the bed-load zone
d	thickness of deposited sediment
d/h	relative deposited
d_s	particle diameter
d_{50}	median grain size
D_{exp}	jet expansion density
ER	lateral expansion ratio
f_{cor}	Coriolis parameter
FE	flushing efficiency
Fr	Froude number
Fr_{in}	Froude number at inlet channel
Fr_{res}	Froude number of reservoir
g	gravitational acceleration
h	flow depth
h	local water depth
h/b	water depth to width of inlet channel ratio
k	turbulent kinetic energy
L	length of the basin
l	length of the upstream and downstream channels
L_c	distance between the center of inlet and outlet channels
L_r	reattachment lengths of reconciliation cells

N	total number of size classes
n_b	bottom roughness
P	wetted perimeter of the length of the side walls
P_{bk}^*	bed material gradation in the subsurface layer when $\partial m/\partial t - \partial z_b/\partial t > 0$
p_{bk}	bed material gradation in the mixing layer
Q	flow discharge
q_{bkx}	component of bed load transport rate in x direction
q_{bky}	component of bed load transport rate in y direction
q_{bk}	bed load transport rate of k^{th} size class
q_{skx}	depth-integrated velocity component in x direction
q_{sly}	depth-integrated velocity component in y direction
R	distance from the edge of channel to the edge of the basin
RE	release efficiency
Re	Reynolds number
Re_{in}	Reynolds number at inlet channel
Re_{res}	Reynolds number of reservoir
SI	sedimentation index
SK	geometry shape factor
SR	silting ratio or storage loss
SSC_{calc} (g/l)	estimated suspended sediment concentration by using the laboratory-derived calibration equation
SSC_{in}	suspended sediment concentration measured at inlet channel
SSC_{out}	suspended sediment concentration measured at outlet channel (released suspended sediment concentration)
t	duration of inflow of suspended sediment
t	time

List of symbols

t^*	dimensionless time
t^{**}	relative time
t_r	actual residence or retention time
t_{ri}	initial residence or retention time
t_s	settling time
t_{ri}/t_s	normalized residence time
TE	sediment trap efficiency
u	depth-integrated velocity component in x direction
U_*	shear velocity
U_{res}	mean reservoir velocity
U_{res}/U_{in}	ratio of time averaged velocities of reservoir and inlet channel
v	depth-integrated velocity component in y directions
v_t	eddy viscosity of flow
V_{dep}	deposited sediment volume after a certain period in the basin
V_{df}	total cumulative deposited volume after a specific period
$V_{flushed}$	volume of flushed sediment with clear water
V_{in}	volume of the entering sediments from the inlet channel
V_{res}	initial reservoir volume (capacity)
V_t	total volume of the basin
w	depth-integrated velocity component in z direction
X_r	normalized reattachment lengths of reconciliation cells
Z	water surface elevation
σ_g	particle size standard deviation
a, b, c	Measured velocity components in the beam axis of UVP
d_a	Arithmetic mean diameter

d_g	Geometric mean diameter
$d_{s,s}$	Settling-velocity weighted mean diameter
d_v	Particle-volume weighted mean diameter
l_e	mixing length or eddy size
q_0	the reference value (total discharge divided by channel width)
q_1	measures the magnitude of the linear variation b
q_1/q_0	minor change in the inflow boundary condition
q_{in}	the actual value specified as inflow boundary condition
U_f	mean downstream velocity at a point
u_{if}	instantaneous deviation from the mean downstream fluid velocity
v_{if}	instantaneous deviation from the vertical fluid velocity
y	distance from the bed

Greek Symbols

α_{bx}	direction cosine of bed load movement
δ	thickness of the bed-load zone
ϵ	dissipation of turbulent energy
ϵ_s	eddy diffusivity of sediment
γ	specific weight of water
γ_o	bulk density of sediment
γ_s	sediment specific weight
λ_d	sediment diameter scale factor
λ_h	vertical length scale factor
λ_l	horizontal length scale factor
λ_n	resistance scale factor

List of symbols

λ_Q	discharge scale factor
λ_s	sediment concentration scale factor
λ_V	velocity scale factor
λ_ω	sediment fall velocity scale factor
λ_{t1}	time scale factor of water flow
$\lambda_{t2}l$	sediment time scale factor
λ_{Vo}	incipient velocity scale factor
ν	kinematic viscosity
ω_{sk}	settling velocity of the k^{th} size class of sediment
ρ	density of water
ρ'_s	dry density
σ_s	turbulent Prandtl-Schmidt number
τ_{bx}	shear stress on the bed surface
τ_{by}	shear stress on the bed surface
τ_{xx}	depth integrated Reynolds stresses
τ_{yx}	depth integrated Reynolds stresses
τ_{yy}	depth integrated Reynolds stresses
θ^*	semi angle of the expansion entrance is measured from the edge of the channel to the edge of the basin
κ	von Kármán constant
ρ	fluid density
θ	Angle of inclination of UVP transducer
ε	kinematic eddy viscosity

Subscripts

c	centerline of the basin
-----	-------------------------

<i>dep</i>	deposits
<i>df</i>	deposits of final volume
<i>eff</i>	effective
<i>exp</i>	expansion
<i>fc</i>	flushing channel
<i>i</i>	initial
<i>in</i>	inlet channel
<i>out</i>	outlet channel
<i>res</i>	reservoir
<i>s</i>	sediment
<i>SSC</i>	suspended sediment concentration
<i>t</i>	total

Introduction

1.1 Problematic of sedimentation of shallow reservoirs

The sustainable use of reservoir for the generation of electricity, irrigation, recreation, as well as domestic and industrial water supply is important issue for the operation of a reservoir systems (Schleiss and Oehy, 2002). Sediment deposition in reservoirs reduces storage capacity and creates risks of blockage of intake structures as well as sediment entrainment in hydraulic schemes. Ponds and lakes face a huge range of problems; many ponds have been very fast by sedimentation.

The planning and design of a sustainable reservoir require the accurate prediction of sediment transport, erosion, and deposition. Numerical simulation of flow and sediment transport in reservoirs is important in order to determine the detailed flow pattern. This typically includes flow separation at the inlet, accompanied by recirculation and stagnation regions where sediment deposits.

Today reservoirs of a run-of-river hydro power plant should also fulfill the purpose of river revitalization, flood protection and the creation of a natural reserve, as well as of upgrading of the landscape. Multipurpose reservoir will therefore allow generation of hydroelectricity at a reasonable price, protect downstream areas against flooding , revitalize the environment and create attractive tourist zones. Designers of modern multipurpose reservoirs of low head hydropower plants, artificial large ponds, and constructed wetland are often faced with the challenge of:

1. understanding the interaction between the flow and deposition pattern in the reservoir.
2. finding equilibrium between flood protection safety, environmental sustainability as well as economical and technical feasibility.
3. fulfilling reservoir storage capacity requirements,
4. estimating sediment trap efficiency and life expectancy of a reservoir

The present research study helps the selection and design of an appropriate reservoir geometries which should minimize sedimentation in artificial constructed shallow ponds and reservoirs, harbors, or maximize sedimentation efficiency in desilting basins, waste water storage chamber and constructed wetland as well.

Moreover, a classification of the flow regimes and the corresponding sediment deposition pattern inside all of these engineering hydraulic applications are given. The study is relevant for the design of new reservoirs as well as to the evaluation of existing ones. The evolution of flow and bed topography in a large water body with suspended sediment is given for various shallow basin geometries. The aim is to understand the behavior and the predication of the flow as well as location and pattern of sediment deposition.

The main purpose of this research is to have a better understanding of the physical processes involved in sedimentation of shallow reservoirs by suspended materials and to investigate the geometry effects on the settlement of suspended sediment and deposition volume. The influence of the reservoir geometry was studied by physical and numerical modeling of the hydrodynamic flow and the suspended sediment transport behavior.

1.2 Outline of the problem and methodology

Today's worldwide annual mean loss of storage capacity due to sedimentation is already higher than the increase of the capacity by construction of new reservoirs (Schleiss and Oehy, 2002). Thus, sustainable use of the reservoirs is not guaranteed on the long term.

Particular attention has to be paid to minimize accumulation of sediment in reservoirs to ensure sustainable use. Such measures can be subdivided into the following categories:

1. Control of the volume of sediments which can flow into a reservoir.
2. Create flow conditions in the reservoirs able to prevent deposition of sediments.
3. Develop techniques to remove deposited sediments from reservoir.

With an innovative arrangement and an optimum operation, a feasible and sustainable solution for multipurpose use of large, shallow reservoirs can be found. The present study will be conducted using three complementary approaches in parallel, as illustrated in Figure. 1.1.

After a review of the state-of the art and theoretical bases, the methodology of the research consists of a first main part devoted to physical model tests. The systematic tests were carried out with different simple shapes of shallow reservoirs. Flow field (velocity, turbulence) and sedimentation rate was measured during the tests. A second part intends to integrate the experimental results into a numerical code for calibration. Based on the analysis of the simulation, general applicable recommendations are given.

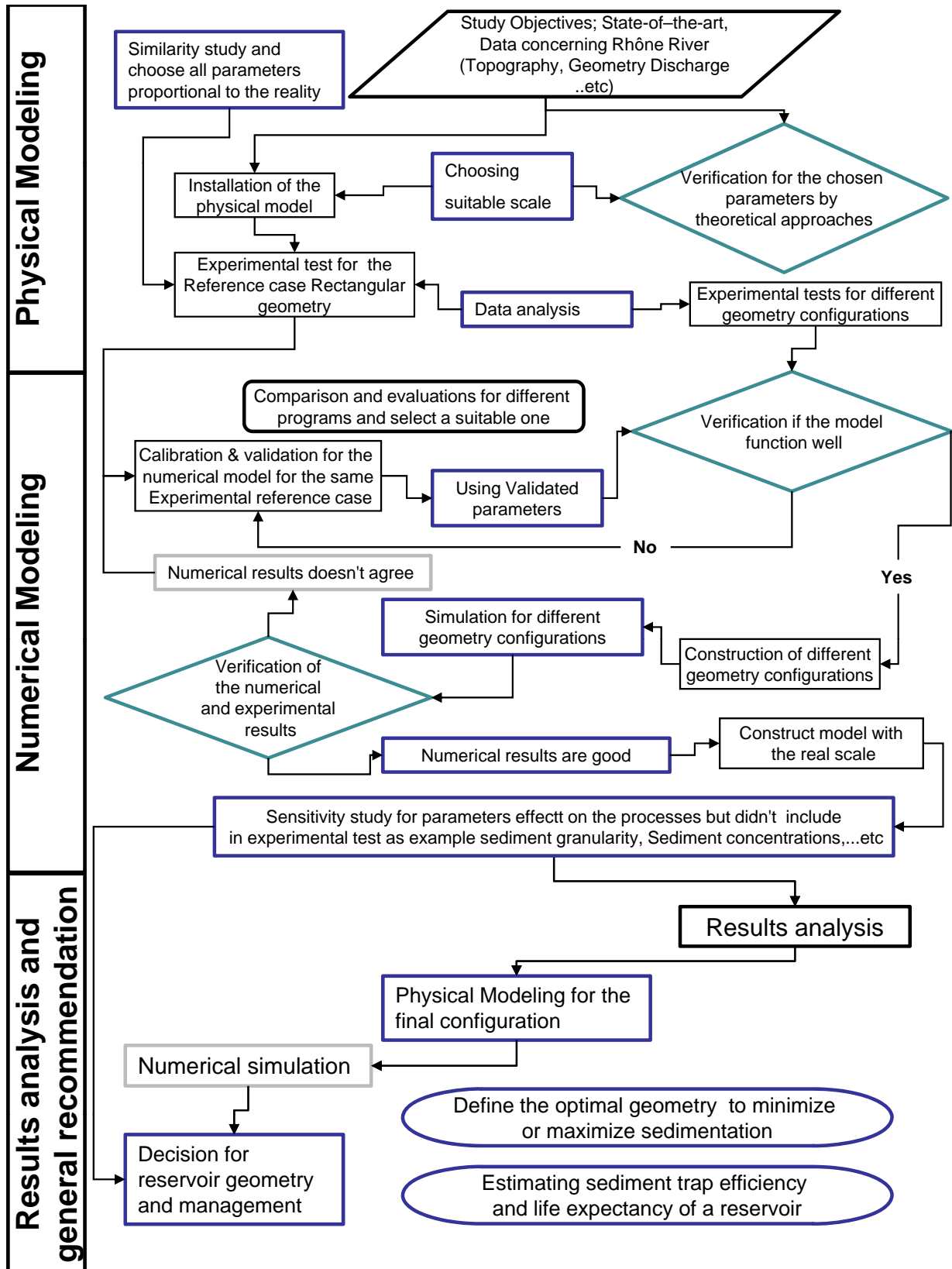


Figure 1.1: Methodology and different phases of the research work

1.3 Research objectives

The study focuses on the sedimentation of shallow reservoirs by suspended sediments and deals with the following questions:

Flow patterns and sedimentation process

1. How functions the processes of flow and sedimentation patterns in shallow reservoirs under suspended load?
2. What is the mechanism governing the sediment exchange process between the jet entering the reservoir and the associated turbulence structures?
3. What is the morphodynamic evolution of the jet flow in the reservoir?
4. Is it possible for a simple reservoir geometry to obtain a long term morphodynamic equilibrium and when it will be reached?

Influence of reservoir geometry

5. What is the influence of the shallow reservoir geometry on the flow and bed deposition behaviors and the main mechanism controlling the morphodynamic evolution?
6. Which geometry of the shallow reservoir has to be chosen in order to minimize or maximize the sedimentation processes?
7. Which flow behavior and hydraulic condition is optimal in view of minimizing sedimentation?
8. What is the relationship between the reservoir geometry and sediment trap efficiency?
9. How the geometry of the reservoir influences the relative deposited thickness?

Operation and flushing

10. How the reservoir has to be operated in order to reduce sedimentation and which mode gives the best flushing efficiency?
11. What is the location, width and depth of the channel which forms during flushing? How influences the geometry shape factor on the flushing efficiency?

Numerical simulation

12. What is the most appropriate numerical model available to simulate the observed flow and sedimentation structures?

1.4 Structure of the report

- *Chapter 2* consists of a literature review. In this chapter relevant domains interfering with reservoir sedimentation are briefly referred to, as shallow flows, suspended sediment transport and trap efficiency. In addition, some examples of problems that exist for reservoir sedimentation are introduced.
- *Chapter 3* describes similitude requirements for the scaled physical model, the physical model setup, the tested parameters, the test procedure and the measurement techniques. The characteristics of measuring instruments are also described and their capabilities are discussed. The instrumentation includes LSPIV setup which was developed to measure surface velocities for the various reservoir geometries.
- *Chapter 4* presents the first phase of the experimental results and analysis with clear water. Moreover, phenomena observed during the clear water tests (asymmetric flow patterns in symmetric geometry), the measurements and results of various reservoir geometries are discussed. A detailed description for the flow mechanism and its processes are given. Influence of the length, width, and angle of the reservoir geometry are clearly analyzed. Classification of jet flow regimes are given according to the geometry and hydraulic flow conditions. The present chapter focuses on the data processing and the analysis of the averaged velocity ratios of U_{res}/U_{in} obtained from LSPIV measurements. Empirical relationships to describe the influence of geometry of reservoir on flow in clear water phase are developed. The empirical formulas refer to the effect of geometry characteristics on the reduction of velocity ratios, reattachment length, sedimentation index and jet classifications.
- *Chapter 5* presents the second phase of the experimental results and analysis with sediment. Suspended sediments concentrations and evolutions of flow and deposition patterns are presented. A detailed description for the flow mechanism and the sediment exchange process. A long period test (18 hour to study the morphological equilibrium in the rectangular reservoir) is discussed. This chapter focuses on the data processing and the analysis of data obtained from the experiments. The analysis and results refer to the effect of geometry characteristics on the flow and sediment behavior. Herein, different dimensionless parameters (Aspect Ratio (AR); Expansion Ratio (ER); and geometry shape factor SK) are analyzed in order to find a relationship with the flow characteristics (relative residence time, relative deposited thickness, and storage loss).
- *Chapter 6* dedicates to the development of a Trap and flushing Efficiencies (TE and FE) empirical model to describe the evolution of deposited and flushed sediments as a function of reservoir geometry shape factor. In addition empirical relationships for direct estimation of TE and FE in large shallow reservoirs are provided. The chapter

closes with a discussion regarding the influence of reservoir geometry on TE, retention time, deposition rate, relative deposit thickness, and silting ratio.

- *Chapter 7* describes the evaluation and comparison of different computer programs (both commercial and academic codes). Then a preliminary verification of the geometry of the designed physical model is done before constructing it in the laboratory, by *2D* and *3D* numerical simulations of the hydrodynamics and of the suspended sediment transport. For further investigation and simulations of the geometry effects on the flow and sediment behavior, CCHE2D, FLOW-3D and WOLF2D programs were used. The comparison between experimental and numerical results of the simulations are given.
- *Chapter 8* summarizes the experimental and numerical results. Recommendations for engineering practices to minimize retention of sediments are given and some concluding remarks on the results of the present study are made. Finally, outlook for future work is provided.

Literature review and theoretical basis

2.1 Flows in shallow reservoirs

2.1.1 Definition of shallow flows

Shallow flows can be defined as predominantly horizontal flows in a fluid domain where the vertical dimension is significantly smaller than the two horizontal dimensions.

Shallow flows are omnipresent in nature, ranging from river, estuarine, and oceanic flows to stratified flows in the atmosphere. Many flows of interest in environmental fluid mechanics, flows in channels, rivers, reservoirs, lakes, estuaries and seas, are shallow turbulent free surface flows (Fig. 2.1 (a, b, & c)). Typically, such estuaries are shallow, except close to the inlets kept deeper by the erosive action of the tidal currents. An important example of such an estuary is the lagoon of Venice (Fig. 2.1(a)).

To obtain a correctly modeled shallow turbulent free surface flow in a laboratory, a sufficiently high Reynolds number and a sufficiently low Froude number are required, which generally leads to a prohibitively large installation.

In the present study, reservoirs with a prototype depth between 5.0 m and 15.0 m are of special interest. Shallow water conditions imply that the length scale of the water body in the vertical direction (H) is much smaller than the smallest length scales in the horizontal directions (L), or $H/L \ll 1$.

By using this assumption, the flow basic equations can be simplified following a normalization procedure (Stoker, 1957). This leads to the shallow water equation (SWE), which is the common point of the various applications. There are several other parameters which may be either large or small, leading to different types of SWE.

In order to see when and where a particular effect is important, it is necessary to derive the SWE with some care, so that the necessary approximations can be defined.

Jirka and Uijtewall (2003) summarized that the shallow flows are largely unidirectional, turbulent shear flows driven by piezometric gradient and occurring in a confined layer depth

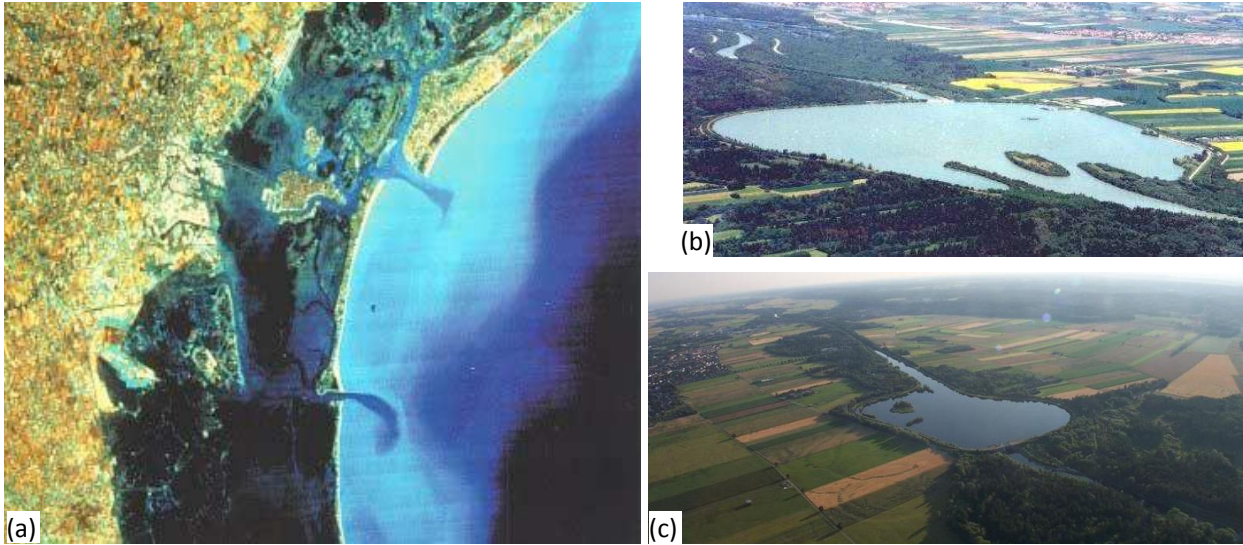


Figure 2.1: (a) Photo of The Lido and Malamocco inlets of the Venice Lagoon and (b, c) Photos of two shallow reservoirs on the Lech River in Germany (<http://www.ballon-team-ammersee.de/>).

H . This confinement leads to a separation of turbulent motions between small scale $3D$ turbulence, $l_{3D} \leq H$, and large scale $2D$ turbulent motions, $l_{2D} \gg H$, with some mutual interaction.

Shallow flows can be considered as two-dimensional or quasi-two-dimensional flows, both regarding their mean velocity field (depth-averaged) as their turbulent fluctuations. In that point of view the three-dimensional features would appear as additional turbulent diffusive and dispersive effects, the latter due to vertical shear profile, on both momentum and mass transport.

A lot of additional features and complexities can perturb or enrich this basic definition of shallow flows. A few examples are :

- a) Non-uniform base flow due to expansion or contractions in external geometry
- b) Flows with curvature giving rise to internal secondary circulations
- c) Internal wave instabilities and mixing at the bounding interfaces in density-stratified shallow flows.

2.1.2 Hydrodynamics of shallow flows

Lakes, reservoirs, bays, estuaries as well as coastal regions often have a very shallow bathymetry (Fig. 2.1). Vertically mixed flows in these systems maybe forced by wind shear, by tidal action, by breakdown of yet larger scale inertial currents, and by river inflows.

Shallow flows are bounded, layered turbulent flows in a domain for which $2D$, namely the flow and the transversal dimensions, greatly exceed the vertical one. By using this assumption, the basic flow equations can be simplified following a normalization procedure (Stoker, 1957). In bounded shear flows, the $3D$ turbulent eddy size is typically limited to the shortest dimension (in case the water depth).

Hence, large-scale, two dimensional coherent turbulent structures with length-scales orders of magnitude greater than the depth are observed in a wide range of shallow shear flows. These structures are important for controlling momentum, constituent transport (Carmer et al. (2002); Rummel et al. (2002)) and appear to result in instabilities of quasi-two-dimensional shear flow (Chen and Jirka (1995, 1997)).

Turbulent shallow flows have been studied experimentally in Chu and Babarutsi (1988), Uijttewaai and Booij (2000), Balachandar et al. (2000); Balachandar and Tachie (2001). The use of scaled laboratory models to investigate shallow flow processes is restricted, mainly because of too low Reynolds numbers and too high Froude numbers at small scales. A compromise has to be made between desired shallowness and model feasibility.

Often the chosen compromise is hardly shallow (e.g. river models with width to depth ratios of 2 to 4, instead of ratios of between 50 and a few hundred as found in real rivers).

Booij (1986, 2003) measured shallow flows in a series of harbours of various forms. The goal was to investigate the dependence of the flow in the harbour entrance on its form, the layout of its entrance and on the shallowness. The measurements show that in a shallow harbour the flow is concentrated along the sides, whereas in a not sufficiently shallow harbour the water rotates as a whole.

Shallowness plays a role in the development of the mixing layer at the harbour, entrance through which momentum is exchanged between river and harbour. Chu and Babarutsi (1988) showed that in shallow flow the development of the mixing layer is suppressed.

2.1.3 Mixing layers, jet flow and plane turbulent jet

Vortex formation in unbounded wakes, jets and mixing layers is assessed by Ho and Huerre (1984), Huerre and Monkewitz (1990), Ortel (1990), and Williamson (1996). Mixing layers have been the topic of turbulence research for many decades. The plane mixing layer has attained great interest, since it is the prototype of an essentially unstable flow where the instabilities lead to the formation of eddy structures.

Apart from the interesting physical phenomena occurring in a mixing layer, it plays an important role in the exchange of mass and momentum in many practical situations where two flows of different velocity get into contact. The velocity difference between both sides of the mixing layer gives rise to instabilities in the fluid motion resulting in the development of the mixing layer. Long living turbulent structures with the vorticity aligned with the mean flow vorticity are continuously fed from the main flow. These large scale structures

which have a length scale of the order of the width of the mixing layer lose energy through the normal energy cascade process to smaller eddies leading to a continuous spectrum of three-dimensional turbulence motions from the large scale structures unto the dissipation range.

A plane mixing layer develops in a self-preserving way with a constant spreading rate, depending only on the relative velocity difference across the mixing layer (Townsend, 1976).

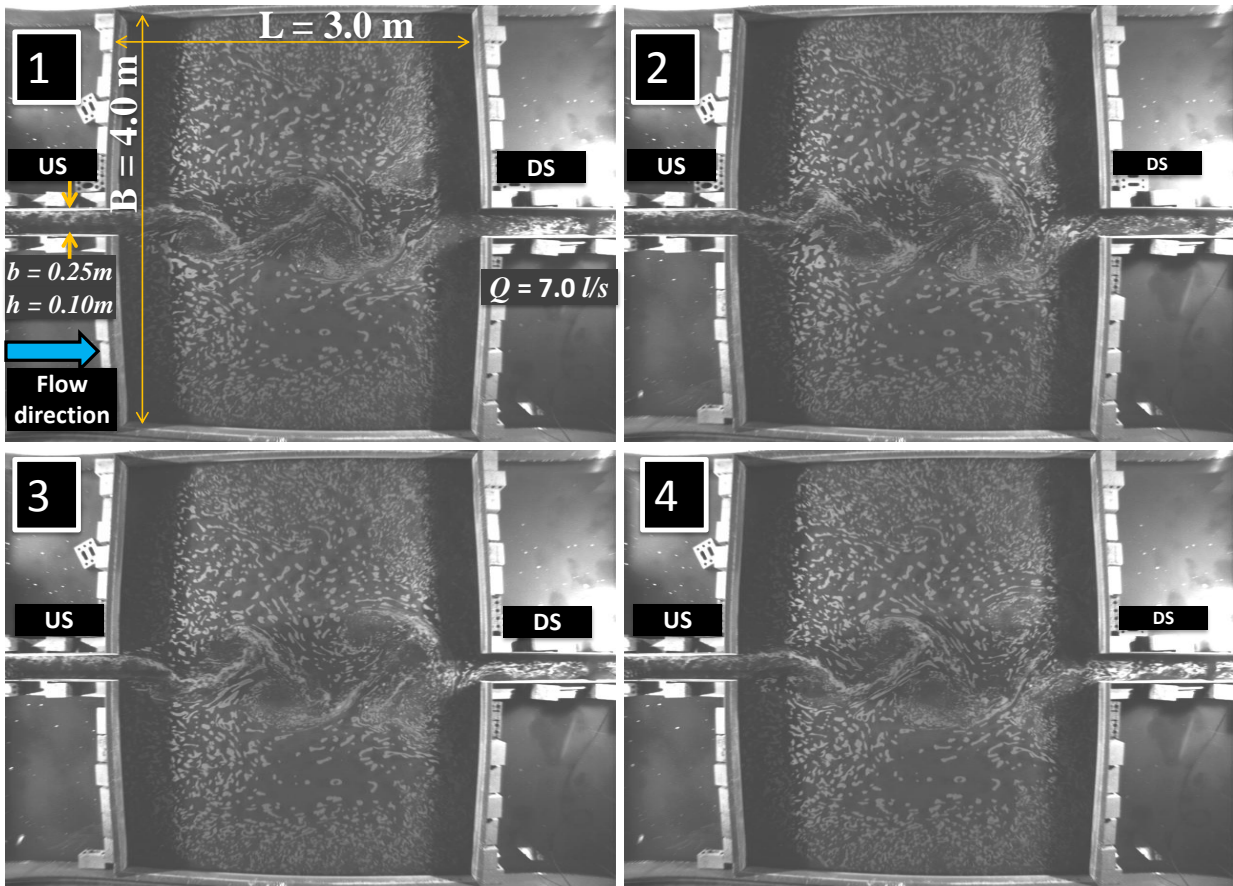


Figure 2.2: 2D coherent structures generation of the mixing layer experiment at LCH. Time interval between photographs is 1 sec.

The occurrence of large-scale instabilities and consequent vortex formation in planar jets was addressed by Giger et al. (1991) and Dracos et al. (1992). They revealed the role of dimensionless water depth on the visualized jet structures and interpreted the turbulence and the entrainment characteristics associated with the jet development.

The geometrical forcing of the mixing layers are shown in Figure 2.2 for shallow rectangular reservoirs having a length to width ratio of 3 : 4. Lateral momentum and mass exchange between the straight flow and the expansion zones is a key element for accurate predictive models for flow and sediment transport. For that visualization of shallow jet for

various rectangular reservoirs Kantoush (2007) has shown the role of the geometry on the visualized jet structure.

The stability of the shear flow generated in a compound channel was addressed by Alavian and Chu (1985) investigating the mean velocity distribution and the turbulent viscosity coefficient. Chen and Jirka (1998) have assessed the linear stability characteristics of shallow flow. Chu and Babarutsi (1988) relate the occurrence of the instability to the critical value of the bed friction number. As shown by Chu et al. (1991), a shallow mixing layer can be generated by spanwise variations of either bed friction or water depth.

For the classical configuration of a shallow mixing layer induced by the merging of high and low speed streams at the trailing-edge of the splitter plate, Uijtewaal and Tukker (1998) performed a comprehensive assessment of turbulence characteristics of the near and far field regions of the mixing layer.

Mixing layers develop for instance at harbour entrances, groyne fields and flood plains, between the main fast flowing stream and a recirculation zone. The horizontal exchange of momentum and mass, including contaminants, sediment and silt, is influenced by the mixing layer. Knowledge of mixing layer development under shallow conditions is of key importance regarding the prediction of shallow flows, sediment transport and erosion as well as the transport of pollutants.

2.1.4 Flow separation

Flow separation and reattachment due to sudden changes in geometry in internal flow occur in many engineering applications as in shallow open channels, sewer systems (storage tank sedimentation), groin fields and shallow reservoirs.

Literature on the experimental investigations of this type of flow can be classified in three groups:

- a) Double-sided expansions (sudden expansion): two dimensional flows with laminar and turbulent separating flow for low and high Reynolds numbers.
- b) One-sided expansion (lateral expansion): shallow and deep large-scale turbulence structures in channels
- c) Flow over a backward-facing step

The location of reattachment zone and the occurring flow structures play an important role for the properties of the recirculation region. The reattachment zone directly forms the initial conditions for the recovery process downstream. The separation zone or the flow downstream of the reattachment can be predicted only if the reattachment length and structure in the reattachment zone are correctly known.

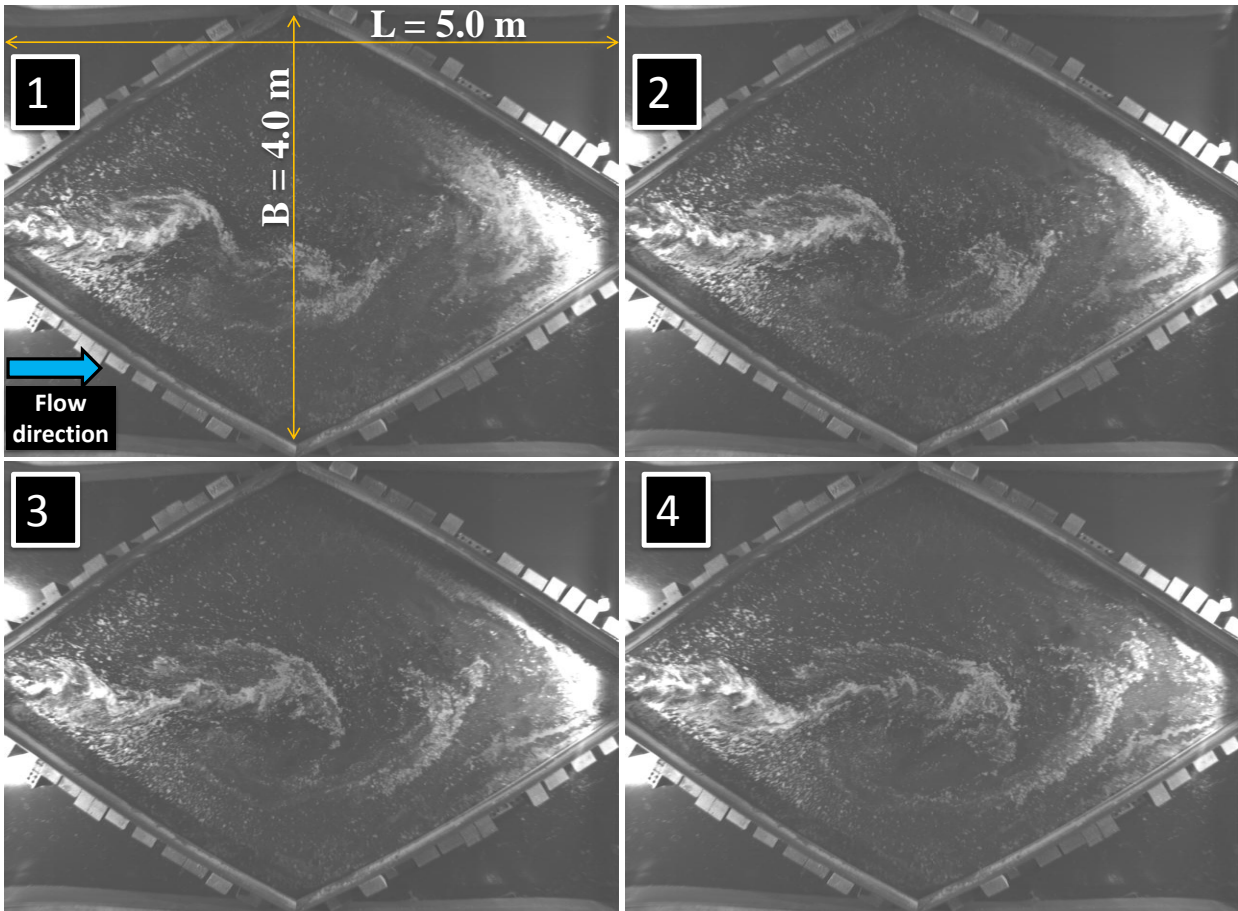


Figure 2.3: Experiment at LCH with shallow jet with 2DCS generation in a lozenge geometry. Time interval between photographs is 1 sec.

Although turbulent recirculating flows with separated shear layer are encountered in many engineering applications, there still remains an incomplete understanding of such separated flow problems. In Figure 2.3 the occurrence of large-scale instabilities and consequent vortex formation in planar jets in a lozenge shape geometry was addressed by Kantoush and Schleiss (2007).

In shallow flow both the limited depth and the bottom friction influence the development of the mixing layer. The limited depth restricts the large structures in the mixing layer to basically 2D horizontal motions. Because of the shallowness the normal energy cascade from large to small eddies is interrupted Chu and Babarutsi (1988).

The bottom friction has a two-fold influence on the large-scale structures. First, the bottom friction is responsible for dissipation of large-scale energy which is transferred directly from the large-scales to the small-scales with interaction of intermediate scales. Second, the bottom friction has a stabilizing influence on the generation of large-scale structures and therefore reduces the growth of the mixing layer.

The effect of friction on the physical process of mixing in the recirculating flow was studied with laboratory experiments by Babarutsi et al. (1989). In an experimental study on groin fields Babarutsi et al. (1989) pointed out a qualitative difference between mixing layer vortex and vortex shedding. The later phenomenon is largest in scale and is associated to the presence of a secondary recirculation cell. The mixing layer vortices are the result of the lateral shear. Talstra et al. (2006) experimentally visualized the behavior of individual coherent structures shed from a separation point in a shallow lateral expansion with a variable inflow width. They observed that the occurrence of large-scale shed vortices is not caused by the flow separation itself but by interaction of initially induced mixing layer vortices with the primary and secondary recirculation areas.

The recent interest in quasi steady or repeatable large coherent eddy structures in free shear flow which co-exist with small scale turbulent phenomena has shown the problem to be more complex (Brown and Roshko, 1974). These eddy structures are now believed to play the major role in the mixing and mass transfer processes in free shear flows (Roshko, 1976).

Although there has been a large number of investigations on coherent structures in plane mixing layer flows (for example Roshko (1976, 1981), very few investigations have been performed of the large eddy structures in reattaching shear layer flows. The investigation by Troutt et al. (1984) strongly supports the importance of large scale organized structures in reattaching separated flow fields.

In the present investigation, a rectangular, triangular and hexagonal cavity type flow is considered with an objective of looking at the physical processes involved, particularly the interaction of the large coherent eddy structures in the separated layer with the recirculating flow.

2.1.5 Stability of symmetric and asymmetric flow

Two-dimensional flow in a symmetric channel with a sudden expansion is a typical example of a flow which is not homogeneous in its flow direction. Traditional stability theories for parallel flows cannot be applied to such a flow because of the inhomogeneity (Kantoush et al., 2007d). So, the stability of the flow has been investigated mainly by numerical methods and experiments. It has been revealed that the transitions and instabilities of the flow include rich phenomena because of the inhomogeneity.

Considerable work has been reported in the past on two dimensional, or nominally two-dimensional flow past planar double-sided expansions, both at low Reynolds numbers where the separating flow is laminar and for moderately high Reynolds numbers where the separating flow is turbulent (Durst et al., 1974). A significant conclusion of these studies has been that while the geometry is symmetric, asymmetric flows develop under certain Reynolds number and geometric conditions.

At low Reynolds numbers the flow remains symmetric with separation regions of equal length on either side of the expanding channel. The length of the separation regions is observed to increase with increasing Reynolds number. At higher Reynolds numbers, however, separation regions of unequal length develop and the asymmetry remains in the flow even up to turbulent flow conditions. The conditions of asymmetry and the value of the transition critical Reynolds number have been reported in the literature both experimentally and numerically (Ouwa et al., 1981).



Figure 2.4: Plan view of the particle streaks and vortex street-like instability of a shallow turbulent wake flow in a rectangular reservoir at LCH. Visualization by introducing particles on the surface.

Experimental investigations of plane sudden-expansion flows have been reported by Durst et al. (1974), Cherdron et al. (1978) and Fearn et al. (1990), who used laser-Doppler anemometry to measure the velocity distributions, including those in close proximity of the recirculation regions, and flow visualization to show the nature of laminar flows. Two recirculation zones were identified in Durst et al. (1974), and a third in Cherdron et al. (1978), which was quantified in terms of detailed velocity measurements Fearn et al. (1990).

Figure 2.4 shows two circulation zones identified in a rectangular geometry by Kantoush et al. (2007d).

The experimental results indicate that the jet produced by the sudden expansion remained symmetric, but became asymmetric with increasing Reynolds number whereby the asymmetric jet attached to one of the walls in the double-sided expansion. The early experiments of Durst et al. (1974) for a channel expansion of 2 : 1 were revisited by Cherdron et al. (1978) with the findings of the latter study.

The two-dimensionality of a water jet in a rectangular channel for low Reynolds numbers was investigated by Ouwa et al. (1981). They observed that the formation of the downstream vortex continued to grow with increasing Reynolds number. Eventually, the flow became unstable destroying the two-dimensionality of the large vortex downstream of the expansion plane, where the vortex became less discernible due to random fluctuations of the flow. Ouwa et al. (1986) used numerical simulations to confirm their experiments, and found both studies to be in agreement. The instability of low Reynolds number expanding planar flows led to several numerical studies that investigated the symmetry-breaking bifurcation using a linear stability approach to locate bifurcation points of the transition between symmetric and asymmetric flows.

One of the original studies for analysis of a flow in symmetric $2D$ channels with smooth expansions was by Sobey and Drazin (1986). Corresponding experiments were performed to verify the numerical simulations but the experiments did not produce the hysteresis effects on the bifurcation as predicted by the numerical simulations. A similar study by Shapira et al. (1990) investigated flows in both smooth and sudden expansion. A linear stability analysis showed that the velocity disturbances were due to the instability of a vortex core along the centerline. Shapira et al. (1990) found good agreement between their results and Sobey (1985) for the critical Reynolds number.

A comparison between the results of Shapira et al. (1990) and the experiments by Cherdron et al. (1978) showed a difference in the value of the Reynolds number at which the flow became unstable. Shapira et al. (1990) suggested the possibility that disturbances were generated by the experiments due to imperfections with the apparatus or slight asymmetries in the geometry.

Another study of particular interest was performed by Fearn et al. (1990) including comparisons of bifurcation calculations with their experiments. Results indicated that as the Reynolds number was increased above a critical value, the symmetric flow lost stability and transitioned to an asymmetric flow forming a pitchfork bifurcation. Fearn et al. (1990) concluded that the transition to non-symmetrical flow was abrupt, which disagreed with claims by Shapira et al. (1990) that the transition is smooth.

Durst et al. (1974) used numerical predictions to confirm previous experimental findings and found that the pitchfork bifurcation had a smooth transition from symmetric to asymmetric flow, confirming the results of Shapira et al. (1990) and contradicting Fearn et al.

(1990).

Two-dimensional asymmetric flow has been extensively investigated but little has been reported on the characteristics of the asymmetry based on three-dimensional effects. A truly two-dimensional flow past a symmetric double-sided expansion is not plausible experimentally. Hence, results are based on a nominally two-dimensional analysis at the center-plane of a ducted test section with a large aspect ratio (step-span to step-height). Given the limitation of experimental verification of the asymmetry, some effort has been spent on looking at the effects of geometry, such as expansion ratio and aspect ratio, on the critical Reynolds number (Sobey, 1985).

These investigations found no systematic dependencies on expansion and aspect ratio. However, they report that in general the value of the critical Reynolds number decreases with increasing expansion ratio and increasing aspect ratio. Recently, Papadopoulos et al. (1999) began investigating the effects of three-dimensionality on low Reynolds number flows past a symmetric sudden expansion in a rectangular channel.

Numerical investigations including those of Fearn et al. (1990), Durst et al. (1993), Battaglia et al. (1997) and Mizushima et al. (1996) made use of conventional time marching finite difference and element integration techniques with simple Navier-Stokes and vorticity-stream function formulations, bifurcation analysis and random vortex methods; with the time-dependent nature of the flow considered in all cases.

They focused on laminar flows. The main conclusion was that the flow through a plane symmetric sudden-expansion becomes unstable as the Reynolds number is increased above a critical value, to yield a stable and asymmetric solutions through a pitchfork (symmetry breaking) bifurcation. There is evidence that transition occurs smoothly and it has been established that the critical Reynolds number decreases with expansion ratio and is affected by the aspect ratio. Foumeny et al. (1996) investigated the critical Reynolds number for a plane symmetric-expansion and for parallel multi-channel cascade systems that are relevant to mixing equipment and found that it was lower for the latter configuration.

2.2 Reservoir sedimentation

In Antiquity, reservoirs for irrigation, water supply and flood protection were built in *Egypt* (the Kosheis reservoir, 2900BC and the Moeris reservoir, 2300BC), in Mesopotamia (700BC) and Persia (500BC), in China (year 600 BC), in Sri Lanka (the Basawakkulam reservoir, 430BC and the Tissa reservoir, 300 BC), in India (the Girnar reservoir, 300BC), as well as in some Asian and European provinces of the Roman Empire (the Cornalbo and Proserpina reservoirs in Spain, 100 AD)(Batuca and Jordaan, 2000).

In the Middle Ages, in spite of the general decline of human creative activities, reservoirs were still built in some Asian provinces of the Byzantine Empire (years 500 – 600), in India

(the Moti Talev and Cuddalore reservoirs, the *XI–th* century) and in Spain (the Almonacid reservoir, the *XI–th*, century) as well. Since 1964, as a result of the construction of the Aswan High Dam (AHD), virtually all of the annual 80 – 110 million tons of sediment load carried by the Nile River has been deposited behind the dam. The main concern has been for the effect of accumulation of these huge sediment deposits on the reservoir’s storage capacity and hydropower production capability.

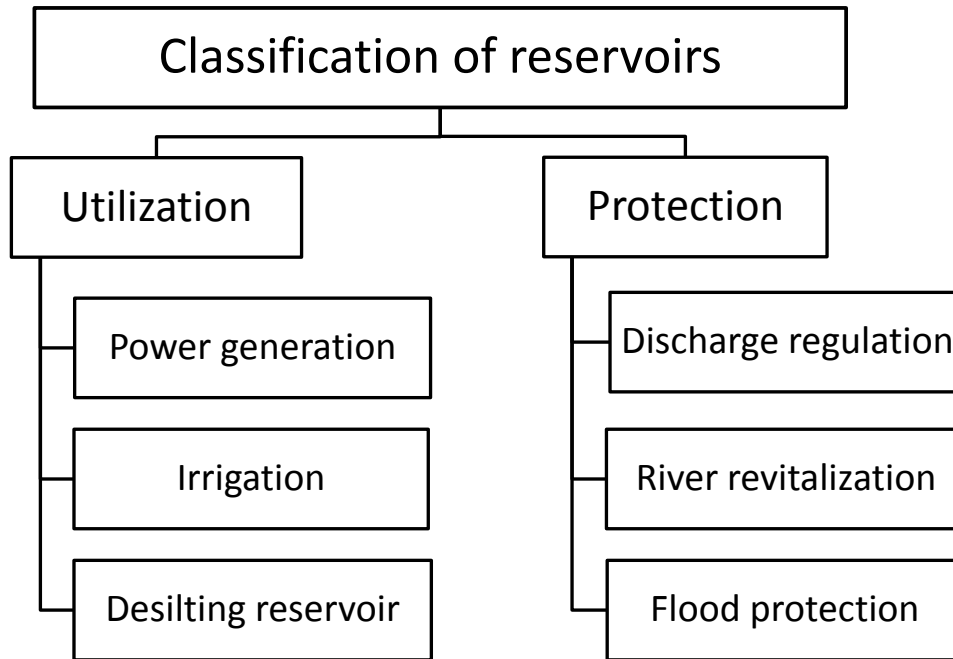


Figure 2.5: Classification of reservoirs.

Large shallow reservoirs of run-of-river power plants on rivers with high suspended sediments are endangered by significant sedimentation. Sediment deposition in reservoirs reduces the storage capacity and generates a risk of blockage of intake structures as well as sediment entrainment in hydropower schemes. Suspended sediment deposition is a complex phenomenon in deep and shallow reservoirs.

2.2.1 Definition and functions of reservoirs

A reservoir is thereby defined as an artificial lake into which water drains and is stored for future use. Sometimes, a reservoir is created by damming of existing natural lakes to improve their capacity.

The behavior of sediments in a shallow reservoir is mainly determined by bed morphology and main 2D water circulation, as well as by the characteristics of the sediment. Reservoirs may be classified into a number of different categories, depending upon several criteria shown in Figure 2.5.

2.2.1.1 Useful life of reservoirs

Reservoir sedimentation has been methodically studied since 1930s (Eakin, 1939), but dam engineering has focused on structural issues, giving relatively little attention to the problem of sediment accumulation (De Cesare and Lafitte, 2007).

The problem confronting the designer is to estimate the rate of deposition and the period of time before the sediment will interfere with the useful functioning of a reservoir.

Several concepts of reservoir life may be defined as its useful, economic, useable, design and full life as adapted from (Murthy, 1977), (Sloff, 1991):

The useful life is the period of time during which the capacity is sufficient to serve designed purposes.

The economic life is the period over which the economic benefits from project operation exceed costs.

The usable life is the period of time during which the reservoir may be operated for either its original or a modified purpose after expiry of its economic life.

The design life is the period of time during which is adopted for the economic analysis of a reservoir.

The full life is the period of time during which the reservoir capacity becomes essentially fully depleted by sedimentation.

The average of full life of man-made storage reservoirs in the world is estimated to be around 22 years (Mahmood, 1987).

2.2.2 Problems and measures to mitigate reservoir sedimentation

It is well accepted that reservoir sedimentation poses a serious threat to available storage. The annual loss of storage in reservoirs is roughly 1% to 2% corresponding to about 50 km^3 world wide (Mahmood, 1987). Some reservoirs have a much higher storage loss, e. g., the Sanmenxia Reservoir in China loses about 1.7% of its capacity per year. On the other hand the gained increase of the reservoir volume due to construction is only about 1% (Schleiss and Oehy, 2002).

In the meantime significant transformations can occur in the catchment area due to the redistribution of sediments and discharges. Sloff (1991) reviewed these phenomena by means of a survey of the scattered literature in order to find the remaining gaps in the applied theory. Theoretical approaches are here desired to estimate the sedimentation threat and even to reconsider the design.

In the past highly empirical models were used for this purpose, but often resulted (sometimes deliberately) in an underestimation of the actual sedimentation rate. This can be ascribed to failing theory as well as to a lack of data. For instance sedimentation rates of the Sefid Rud reservoir in north-west of Iran can be estimated with a 60 years old and highly empirical approach (Tolouie et al., 1993) to be about $35 \cdot 10^6 \text{ m}^3/a$. However, after

construction (in 1962) the measured rate was about $45 \cdot 10^6 \text{ m}^3/a$ causing a storage loss of over 30% in 1980. The original predicted useful reservoir life of one century based on old data, was found to be actually about 30 years (Pazwash, 1982). Flushing operations were started in 1980 which were able to regain about 7% of the lost capacity only.

When dealing with reservoir sedimentation problems, engineers are challenged by difficult questions emerging as how to incorporate reservoir problems in feasibility studies (cost-benefit analysis) including environmental and technical effects, limitations on benefit and possible measures, or what is the impact of sedimentation on the reservoir performance, and what is the impact of the reservoir on stream system morphology. Obviously, a good prediction of the processes, and better understanding of the reservoir behavior are essential to control the sedimentation in reservoir.

Accumulation of sediment in reservoirs has to be limited by measures in order to ensure their sustainable use. Such measures can be subdivided into the following categories (Boillat and Pougatsch, 2000):

- a) Methods to reduce the inflow of sediment into the reservoir, e.g. by erosion control in the catchment or bypassing of sediment-laden flows. This approach is usually very effective, but the dangers already present in the reservoir are not mitigated.
- b) Creating flow conditions within reservoirs which will prevent deposition of sediment, or to induce erosion of accumulated material (sluicing and flushing). The aim of these methods is to reduce the trap efficiency of the reservoir. Flushing methods exercise serious restraints on the reservoir operation and the reservoir yield. Therefore the chief disadvantage of sluicing options is that all require sluicing during the initial period of the high flow season and imply curtailment of power during this period of increasing power demand.
- c) Techniques which can be used to remove sediment that has already been deposited in reservoir. Methods based on hydraulic dredging and mechanical excavation. This is an often used efficient alternative but a very costly one.

Recent books on the state of the art dealing with reservoir sedimentation are presented by Morris and Fan (1998), Batuca and Jordaan (2000) and by the International Committee on Large Dams (1996). A number of case studies for the removal of deposited sediments and compensation of reservoir silting are also described in detail. Methods to mitigate the problems are usually based on reduce the inflow of sediment, the manipulation and control of the processes mentioned above, and the mechanical removal of deposits (e.g., see Fan and Morris, 1992; Sloff, 1997).

Furthermore, large uncertainties in measured and forecasted data of reservoir sedimentation exists. For instance the sediment yield, which is the source of all sedimentation problems can usually not be predicted accurately. Early modeling attempts have often

proved to be unreliable, which forced engineers to put a significant effort in inventing more sophisticated approaches.

In the following sections two specific studies are presented to illustrate the modeling techniques for reservoir-sedimentation management.

2.2.3 Effects of suspended sediment on reservoir sedimentation

Reservoir sedimentation depends on several factors such as sediment production, sediment transportation rate, sediment type, mode of sediment deposition, reservoir operation, reservoir geometry, and stream flow variability. Sediment is transported as suspended and bed load by rivers entering into a reservoir. Due to flow deceleration when a river approaches a reservoir, the sediment transport capacity decreases. The coarse sediments are immediately deposited in a delta, whereas the suspended sediments settle over a large reservoir area.

Furthermore, they are periodically transported by turbidity currents during floods along the reservoir.

The deposited suspended sediments may consolidate by their weight and the weight of overlying water through time. In hydropower developments, sediment particles can damage turbine blades, especially in high-head schemes, and may drastically limit the effective life of the equipment. Predicting the sediment coming into a reservoir, its deposition, and its accumulation throughout the years, after construction of the dam, have been an important issue in hydraulic engineering (De Cesare and Lafitte, 2007).

Despite the advances made in understanding several of the factors involved in reservoir sedimentation, predicting the accumulation of sediment in a reservoir is still a complex problem. Empirical models, based on surveys and field observations, have been developed and applied to estimate annual reservoir sedimentation load (RSL), accumulated reservoir sedimentation load, (ARSL) as well as accumulated reservoir sedimentation volume (ARSV) after a certain period of reservoir operation (Morris and Fan, 1998; Strand and Pemberton, 1982).

Likewise, several mathematical models for predicting reservoir sedimentation have been developed based on the equations of motion and continuity for water and sediment (see, for instance, Chen et al., 1978; Morris and Fan, 1998; Soares et al., 1982). However, empirical methods are still widely used in actual engineering practice (Ruddy, 1987; Shen and Julien, 1993).

The main factors affecting reservoir sedimentation are:

1. *quantity of streamflow;*
2. *quantity of sediment inflow into a reservoir;*
3. *sediment particle size;*

4. *specific weight of the deposits*; and
5. *reservoir size and operation (Bureau of Reclamation, 1987)*.

Reservoir sedimentation volume depends, among other factors, on the quantity of sediment inflow, the percentage of sediment inflow trapped by the reservoir, and the specific weight of the deposited sediment considering the effect of compaction with time. The incoming sediment load and the stream flow discharge are usually measured at hydrometric gauging stations, and a sediment rating curve is constructed.

The sediment rating curve expresses the relationship between the rate of sediment discharge and the rate of stream flow discharge. It is usually represented graphically on logarithmic coordinates. Incoming sediment is generally composed of suspended sediment and bed load. When the bed load cannot be obtained by measurements, it can be estimated by sediment transport formulas (Vanoni, 1975).

2.2.4 Reservoir release and trap efficiency

The sediment Release Efficiency (RE) of a reservoir is the mass ratio of the released sediment to the total sediment inflow over specified time period. Trap Efficiency (TE) is the proportion of the incoming sediment that is deposited, or trapped, in a reservoir:

$$\text{TE} = \frac{S_{in} - S_{out}}{S_{in}} = \frac{S_{settled}}{S_{in}} \quad (2.1)$$

$$\text{RE} = 100 - \text{TE} \quad (2.2)$$

where:

TE: sediment trap efficiency;

RE: sediment release efficiency;

S_{in} : sediment mass entering a reservoir;

S_{out} : sediment mass leaving the reservoir; and

$S_{settled}$: sediment mass deposited within the reservoir.

Churchill (1948) based his empirical relationship on the concept of sediment releasing, whereas Brune (1953) used the concept of sediment trapping which has come into more common use. Several approaches have been undertaken to quantify sediment trap efficiency. Brown (1943) related the ratio of reservoir capacity and watershed area to sediment trap efficiency. Churchill (1948) presented a curve relating the trap efficiency to the ratio between the water retention time and mean velocity in the reservoir.

Based on data from ponded reservoirs in the south-eastern region of the United States of America (USA), Brune (1953) developed an empirical relationship between the sediment

trapped and the ratio of the volume capacity of the reservoir to the mean annual inflow. According to the United States Army Corps of Engineers (1989), the application of Brune’s methodology led researchers to obtain more accurate results than it was possible with the other two approaches Brown (1943). None of these methods, however, included sediment input rates. Extensive published literature is currently available on such topics as reser-

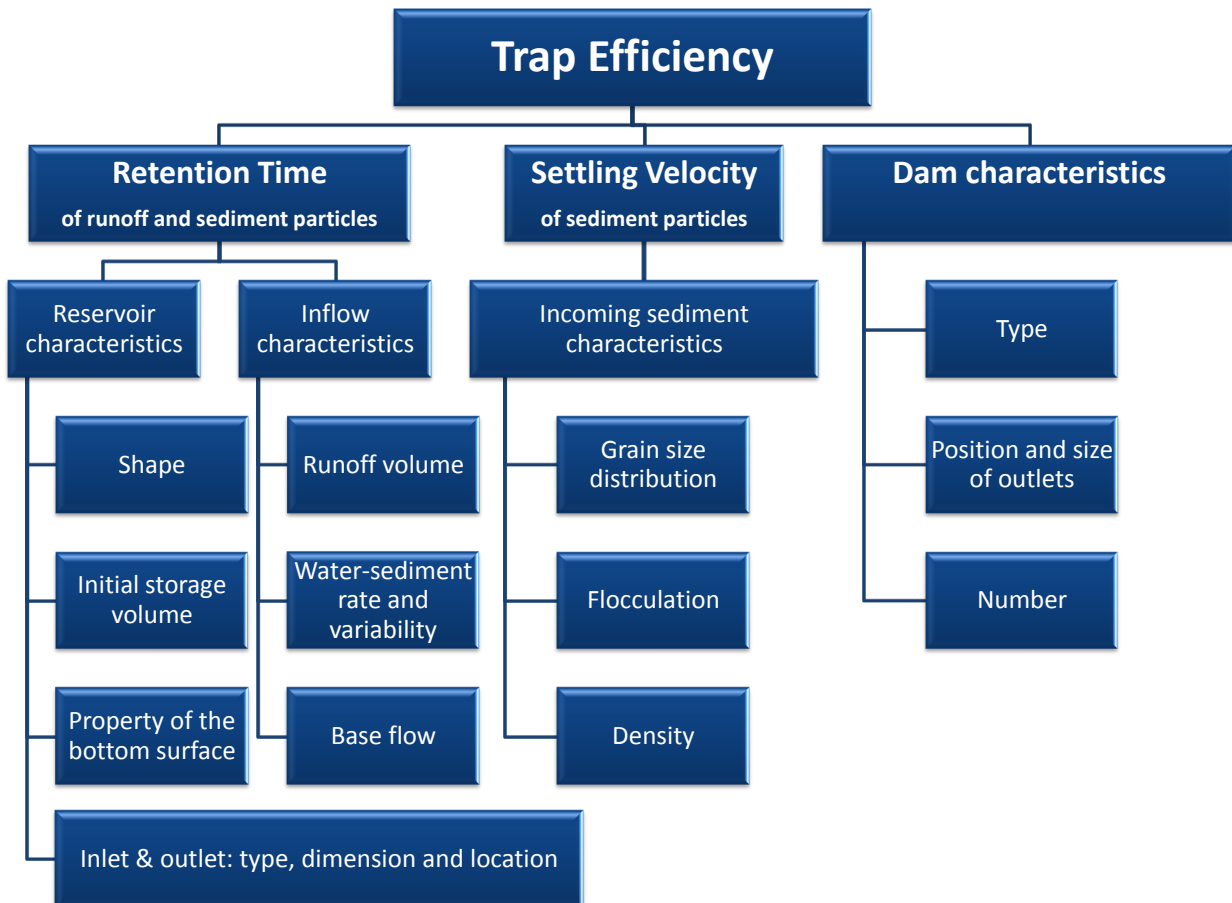


Figure 2.6: Factors influencing the trap efficiency of reservoirs.

voir sedimentation and reservoir engineering (e.g. Annandale, 1987; Fan and Morris, 1992; Vischer and Hager, 1998). As a result of the complexity of the phenomenon involved in sediment deposition in lakes and reservoirs, focused research efforts on numerical and laboratory modeling also have been published. Hotchkiss and Parker (1991) , for example, developed a model that describes delta evolution.

De Cesare et al. (2001) have developed numerical models for deposition due to turbidity currents in reservoirs. Kostic et al. (2002) developed a moving boundary model that captures the co-evolution of topset, foreset and bottom set in lakes. Tarela and Menendez (1999) have presented a two-dimensional numerical model to predict reservoir sedimentation.

The TE of reservoirs depends on several parameters (an overview of the processes taking

place in a reservoir is given by (Heinemann, 1984). Since TE is dependent on the amount of sediment deposited, parameters controlling the sedimentation process are very important (Fig. 2.6).

Therefore, the particle-size distribution of the incoming sediment controls TE in relation to retention time (i.e., the average time the incoming runoff remains in the reservoir). Coarser material will have a higher settling velocity, and less time is required for its deposition. Very fine material, on the other hand, will need long retention times to deposit.

The particle-size distribution of the incoming sediment depends on the type of soils present in the catchment that are being eroded and on the sediment delivery processes. The retention time of a reservoir is related to:

1. the characteristics of the inflow hydrograph and
2. the geometry of the reservoir, including storage capacity, shape and outlet typology.

A small runoff volume will have a larger retention time for a given pond than a very large runoff event, whilst the distance between the inlet and outlet controls the time it takes the runoff water to leave the reservoir or pond. The shape of the reservoir or pond (e.g., expressed as a stage-area curve) can also govern the retention time. Similarly, the location of the principal spillway can also control the retention time. If located at the bottom, the water will flow out directly while, if it is located at the top of the embankment, the runoff water will, first, have the opportunity regulates the discharges) must be taken into account.

Permanent pool storage (in contrast to completely dry reservoirs) also controls the average retention time. Simple models relating TE to a single reservoir parameter are, on the other hand, easy to implement but are far less accurate. One has to distinguish between the TE of a reservoir on a mid to long-term basis and its TE for one single event.

Most of the developed empirical models predict average TE on a mid-term basis because the data used in such models are of a mid-term nature. Theoretical models predict TE for a single event as these are easier to model. These models are tested using data from physical models or data from continuously monitored ponds. However, there is currently little information that could be used to predict the average annual TE of small ponds when using event-based models.

2.2.4.1 Empirical models for predicting Trap Efficiency (TE)

Heinemann (1984) gave an overview of the many empirical models that could be used for predicting TE. Hence in this section we discuss briefly only the most widely used of these models.

TE of a reservoir is not constant in time but, theoretically, will decrease continuously once storage has begun, and it will depend on the variability of the capacity-inflow ratio and of sediment inflow.

Utilizing field measurement data gathered at some small reservoirs in the United States, Gottschalk (1952) has found that the trap efficiency is directly related to the capacity-catchment area ratio:

$$TE = f\left(\frac{C}{A_{catch}}\right) \quad (2.3)$$

where C is the reservoir storage capacity; A_{catch} is the catchment area as shown in Figure 2.7.

One of the first researchers to link empirical data on TE to reservoir characteristics was Brown (1943).

Brown (1958) developed a similar curve based on data from 15 reservoirs as shown in Figure 2.8. Buttling and Shaw (1973) used data from 130 reservoirs to related the annual percentage loss with the C/A_{catch} .

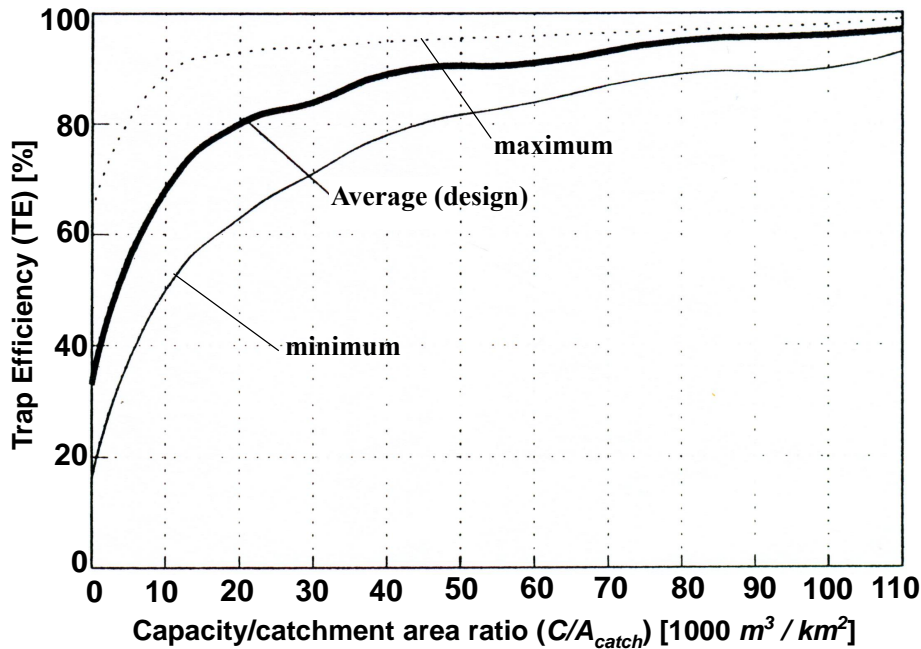


Figure 2.7: Trap efficiency related to capacity-catchment area ratio (after Gottschalk, 1952)

Brune curves. The use of a C/A_{catch} ratio has been discussed by Brune (1953) who stated that reservoirs with the same C/A_{catch} ratio could have completely different TEs if their catchments produced different runoff volumes due to other hydrological characteristics. This explains why there is a high range in TE at lower C/A_{catch} ratios. To overcome this problem, Brune (1953) used a capacity inflow (mean annual runoff) ratio (C/I) to predict TE (Fig. 2.9):

$$TE = f\left(\frac{C}{I}\right) \quad (2.4)$$

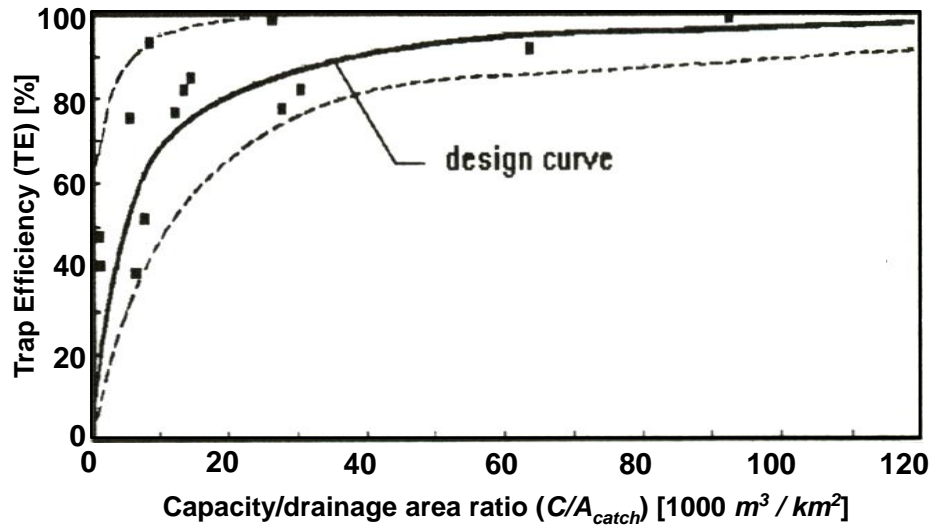


Figure 2.8: Trap efficiency as a function of capacity-catchment area ratio (after Brown, 1958).

where C is the reservoir storage capacity and I is the mean annual inflow. C and I are both expressed in the same units (e.g., m^3/m^3).

Brune (1953) used data from 40 normally ponded reservoirs (i.e., reservoirs which are completely filled by water and have their outlet at the top of the embankment) and 4 other types of reservoirs but the reservoir shape and frequency of drawdown were not considered. The curves produced by Brune (1953) (Fig. 2.9) are the ones most widely used.

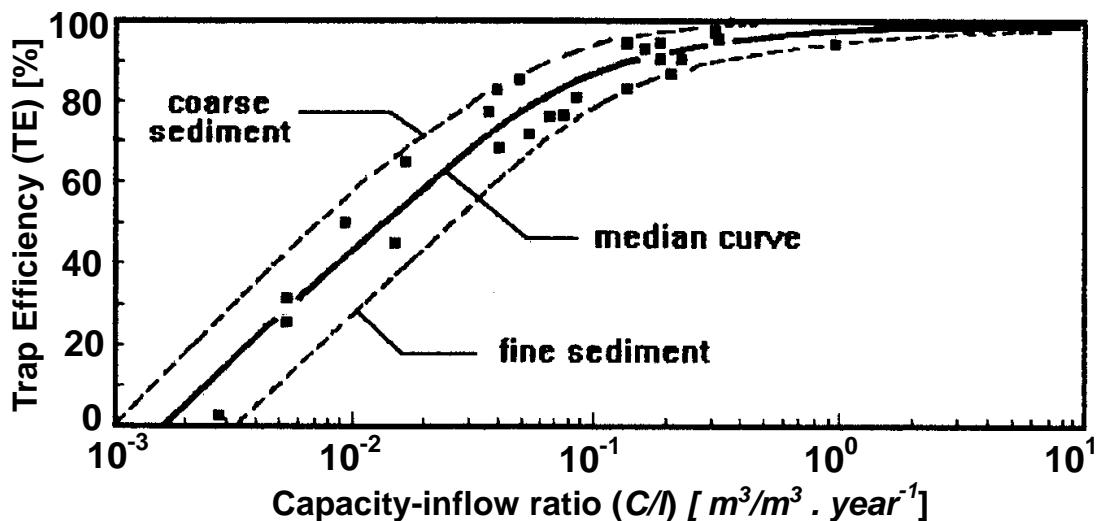


Figure 2.9: Trap efficiency as a function of capacity-catchment area ratio (after Brune, 1953).

A ratio C/I lower than 1 means the reservoir capacity is replaced totally during one year.

A C/I higher than 1 indicates that it is a holdover storage reservoir. The C/I ratio therefore represents the average retention time of the water in the reservoir. The longer the retention time, and hence higher the C/I ratio, the higher the fraction of sediments deposited. Heinemann (1981) has revised and confirmed the Brune curves validity for reservoir catchment areas smaller than 40 km^2 . Pemberton (1978) and Graf (1984) have recommended the curves for practical use.

Churchill curves. Another well-known method to determine the TE of the reservoir was developed by Churchill (1948), assuming that TE depends mainly on the sedimentation index SI (Figs. 2.10 & 2.11):

$$TE = f(SI) \tag{2.5}$$

where SI is the sedimentation index of a reservoir defined as the ratio of retention time to mean flow velocity:

$$SI = \frac{t_D}{U_{mean}} \tag{2.6}$$

with t_D retention time and U_{mean} average flow velocity through the reservoir.

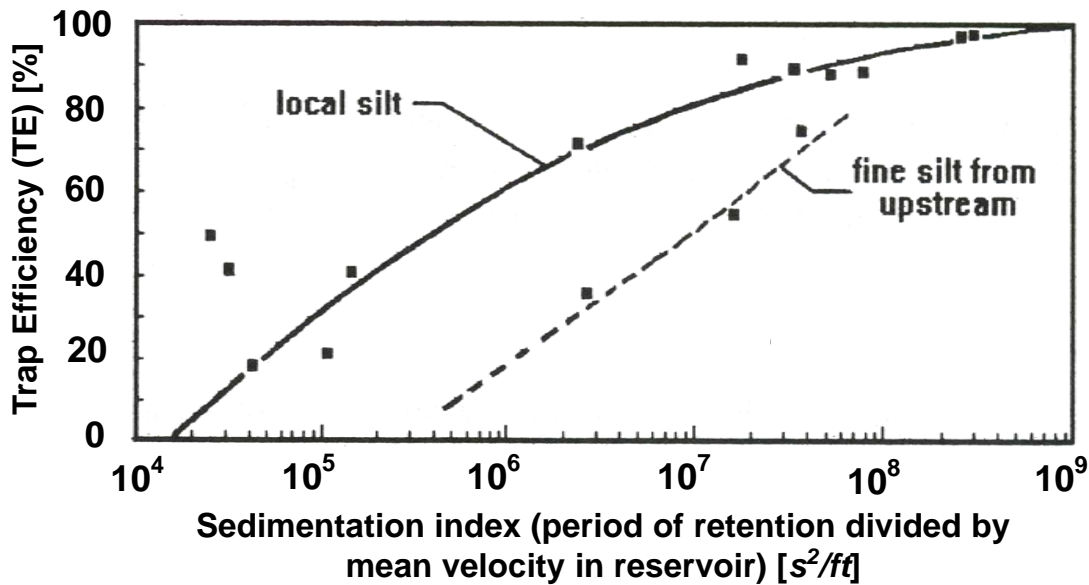


Figure 2.10: Churchill's (1948) curve for local and upstream sediment, relating trap efficiency to a sedimentation index.

Utilizing data from the Tennessee Valley Authority reservoirs, in USA, the following empirical relationship between the percent of sediment passing through a reservoir RE , and its sedimentation index SI (in $s^2/feet$) has been produced as shown in Figure 2.11:

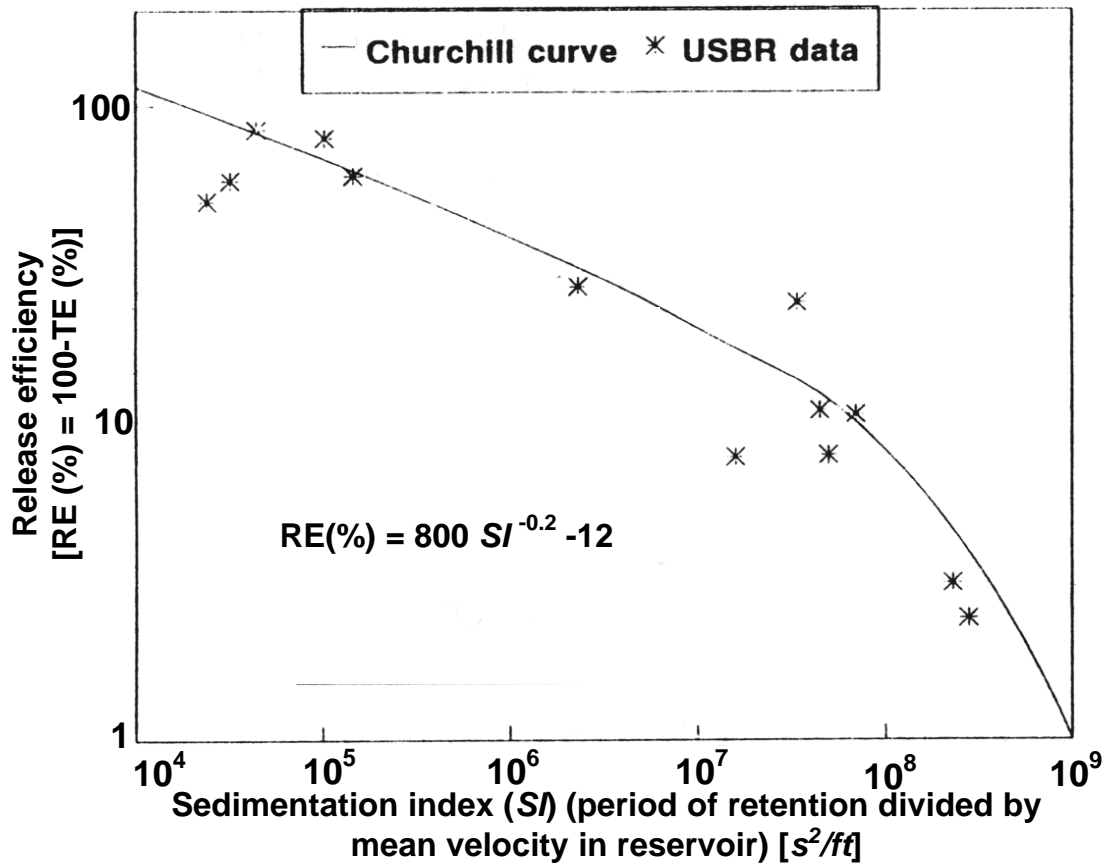


Figure 2.11: Release efficiency RE versus sedimentation index RE .

$$RE = 800SI^{-0.20} - 12 \quad (2.7)$$

The Churchill curve is more suitable for desilting in semi-dry reservoirs than the Brune curves. It cannot be used for durations less than a year (Sloff, 1991). A good comparison of Brune and Churchill methods and curves for computing TE is given in Figure 2.12 (after Bureau of Reclamation, 1987; Murthy, 1977).

2.2.4.2 Theoretical models for prediction of trap efficiency (TE)

Many attempts have been made to model the sediment behavior in ponds and desilting basins. These theoretical models are all based on the principles of particle sedimentation in water.

Differences between the developed models are:

1. whether they are for quiescent flow conditions in a pond or turbulent flow; and
2. whether they are for steady discharge conditions or variable discharge conditions.

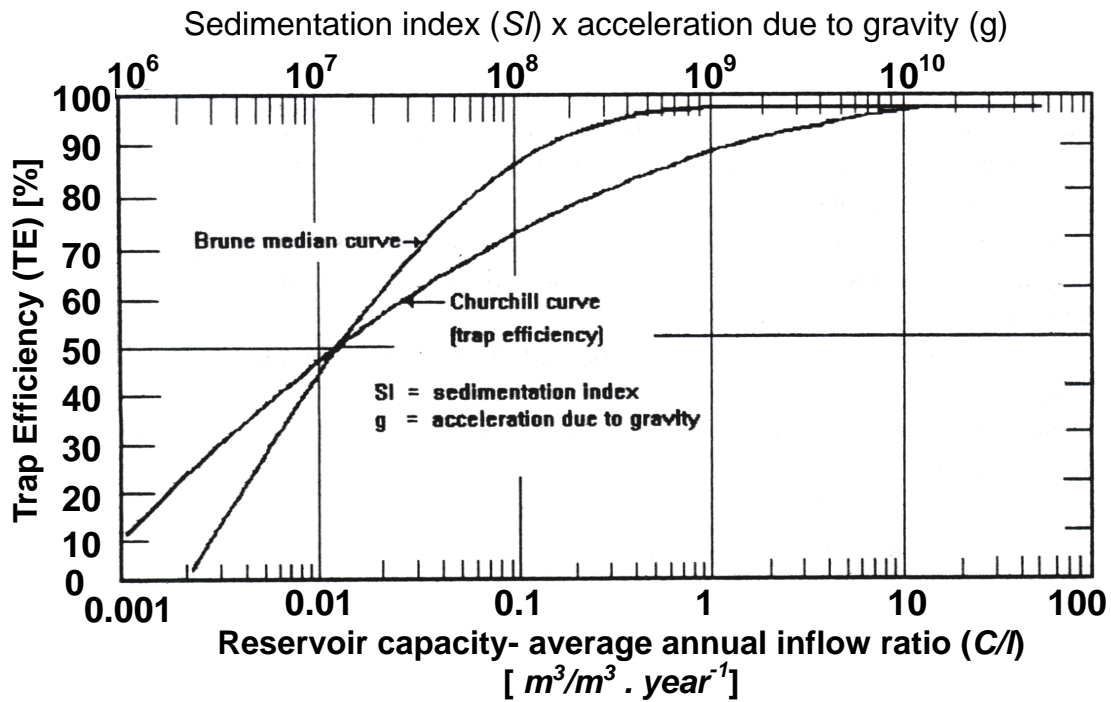


Figure 2.12: The Brune and Churchill trap efficiency curves (Batuca and Jordaan, 2000).

An overview of the theoretically based TE models is provided by Haan et al. (1994). Verstraeten and Poesen (2000) provided an overview of the different methods available to estimate the trap efficiency of reservoirs and ponds. As already mentioned the empirical models predict trap efficiency, mostly of normally ponded large reservoirs using data on a mid to long-term basis. These models relate trap efficiency to a capacity/catchment ratio, a capacity/annual inflow ratio or a sedimentation index.

Today, these empirical models are the most widely used models to predict trap efficiency, even for reservoirs or ponds that have totally different characteristics from the reservoirs used in these models. For small ponds, these models seem to be less appropriate. Furthermore, they also cannot be used for predicting trap efficiency for a single event.

To overcome these restrictions, different theoretical models have been developed based on sedimentation principles. These can be very simple, such as the overflow rate method, but also very complex when runoff and sediment are routed through a pond with incremental time steps. The theoretical-based models are probably more capable of predicting trap efficiency for small ponds with varying geometric characteristics. Some of them also provide data on effluent sediment concentrations and quality.

However, when reconstructing sediment yield values using sedimentation rates over a period of a few months to a few year (the mid-term basis), one needs a trap efficiency value for the whole period, not for one single event. At present only limited research has been done on establishing mid-term trap efficiency models based on theoretical principles. This

is probably the most important gap in trap efficiency research.

2.2.5 Existing methods for reducing siltation by suspended sediment

Sediment management is often in conflict with short-termed water-use management. For example will high water levels, wanted for electricity generation, increase the deposition of sediment. Some times building a new dam may be more economical than reducing sedimentation or removing the deposited material in an existing reservoir (Qian, 1982). In order to control reservoir sedimentation, different approaches such as bypassing, dredging, flushing, sluicing, and upstream sediment trapping have been developed.

Current methods focuses almost exclusively on erosion control. While this is an essential sediment management activity in the catchment area of a reservoir, alone it cannot establish a sediment balance across the impounded reach and preserve long-term capacity (Morris, 1995).

If designers neglect or underestimate the problem of siltation, they may fail to adopt appropriate measures for the eventual release of sediment, such as the installation of adequately sized deep bottom sluices for sediment flushing (Fan and Morris, 1992).

The costly measures required to balance sediment inflows and outflows across the impounded reach of a river have been implemented at only a few reservoirs to date. However, these measures will become increasingly commonplace worldwide as reservoirs age and sediments accumulate to the point that reservoir performance becomes unacceptably impaired (Fan and Morris, 1992). Venting of density currents means that the incoming sediment-laden flow is routed under the stored water and through the low level outlets of the dam.

Bypass tunnels (5 examples in Switzerland as early as 1922, reported in Vischer and Hager (1998) and in Japan already in 1908 reported in SUMI (2005), flushing through outlet gates with partial drawdown (example old Aswan dam completed in 1902 with 180 sluices designed to flush through silt-laden water) and venting of turbidity currents (applied by Nizéry et al. (1953)) are possible measures. Nevertheless, flushing, sluicing, and venting may not be applicable at all sites. Then alternative methods must be used. Dredging is preferable in small reservoirs or in the delta regions of reservoirs. Siphoning uses a small amount of water, but is limited to relatively small reservoirs. With pipes, sediment can be released as they are introduced to the reservoir. This is appreciable for the downstream environment, but a well defined channel which does not move, at the reservoir entrance, is probably needed for good results.

It may be concluded that the combination of both sediment routing and flushing with mechanical methods can be more effective than routing or flushing alone.

2.2.6 Features of flushing

Flushing by complete drawdown of the reservoir is not a new technique. The oldest known practice of flushing was referred to by Drohan (1911), who described the method practised in Spain in the 16th century, where bottom-outlet gates known as the Spanish gates or under sluices were used. The first time a flushing is done, a channel will form in the deposited material in the reservoir. During the next flushing this channel will be maintained by the flushing flows (Morris and Fan, 1998).

Flushing can also be done under pressure. This means that during the water release through the bottom outlets, the water level in the reservoir is kept high. Free-flow (under pressure) flushing means that the reservoir has been emptied and the inflowing water from upstream is routed through the reservoir, resembling natural riverine conditions.

2.2.6.1 Pressure flushing

If flushing takes place under a sustained water level, only a very limited area in the reservoir is cleared (Krumdieck and Chamot, 1979; Mahmood, 1987; Schoklitsch, 1935; Sloff, 1991). During flushing of the Margaritze Reservoir, Austria, first a very stiff and slippery silt and water mixture was squeezed through the bottom outlet followed by a sand-water mixture with certain flow ability (Rienössl and P., 1982).

When flushing the Mangahao hydroelectric scheme, New Zealand, for the first time, nothing happened for one day. The next day silt began to extrude from the dam tunnel and the reservoir emptied, leaving a crater-like depression in the 13m of sediment that had overlain the tunnel entrance (Jowett, 1984). The cleansing under pressure condition occurs by the piping effect produced, which causes part of the sediment to be eroded and the access to the bottom sluices to be cleared (Wu, 1989). If poorly consolidated fine sediments have accumulated above the outlet and when a bottom outlet is opened for the first time, also slope failure can be initiated in the vicinity of the outlet (Morris and Fan, 1998).

2.2.6.2 Drawdown flushing

When low-level outlets are opened, the pool level in a reservoir drops. Consequently, the flow in the reservoir will be favorable for scouring the previous deposits. Thus, the storage capacity of the reservoir can be enlarged. This method is mainly used for small and medium-sized reservoirs.

Brown (1943) stated that drawdown flushing is most effective during the first hours. Nevertheless, Gvelesiani and Shmaltzel (1968) noted that during the process of sediment flushing, the most active erosion occurs in a period of eight to ten hours after the practical erosion begins.

As reported from USSR-reservoirs, the flow reached concentration values up to 400 – 500 g/l,

especially at the initial period of flushing (Gvelesiani and Shmaltzel, 1971). After a certain period of time the value of turbidity becomes stabilized. They suggested that at that time the flushing should be stopped, because the inflowing stream has made its flushing channel and only useful water will be carried out. Ramírez and Rodríguez (1992) divided the flushing of the Cachí Reservoir, Costa Rica, into three phases.

The first phase consists of 25 days of slow water release, lowering the water table one meter per day down to a few meters above minimum level for power generation. The second phase consists of rapid release of the remaining water, i.e. a lowering of about 45 m, during approximately five hours. The third phase consists of free flow of water through the reservoir for two or three days.

As in the Cachí Reservoir, also the flushing of the Gebidem Reservoir, Switzerland, can be divided into these three phases (Rechsteiner, 1996) as well as for the Margaritze Reservoir, Austria (Wagner et al., 1996).

2.2.6.3 Free flow flushing

When all of the stored water in the reservoir has been released, inflowing water to the reservoir acts as an erosive agent and a free-flow phase begins. Stevens (1936) reported that the sluice gate at the Furnish Reservoir, USA, is opened as soon as the storage has been exhausted, permitting the river to flow through the reservoir, cutting a channel through the silt deposits down to the original gravel bed. Brown (1943) argued that the highest rate of sediment removal will be obtained in the first few days or weeks after all stored water has been released.

When the stream has reestablished approximately its original gradient through the reservoir basin, the amount of sediment picked up and transported will greatly decrease. The flow can acquire more load only by the slow process of lateral swinging and broadening of its channel can the flow acquire more load (Brown, 1943). Gvelesiani and Shmaltzel (1968) reported that partial drawdown of the water level of the Zemo-Afchar Reservoir, USSR, was not sufficient to hinder progressive sedimentation. Only after complete drawdown de siltation was successful.

Krumdieck and Chamot (1979) pointed out that free-flow flushing can be efficient even under low-flow conditions. The free-flow condition is used when the sluices are clear of sediment and usually begins when the level of the reservoir is already low (Wu, 1989). If the outlet gates remain open for a period of weeks, scouring and cutting down into deposited sediments over a prolonged period are permitted (Fan and Morris, 1992).

2.3 Suspended sediment transport and bed form generation

The deposition behavior of fine sediment is an important phenomenon in reservoir sedimentation.

Suspended-load transportation in rivers and reservoirs takes place over almost the entire depth of flow, by entrainment of very fine and fine sediment particles (clay, silt and sand). Basically, there are two types of suspensions, namely:

1. Colloidal suspension, which refers to suspension of very small particles due to electromagnetic interaction at molecular scale.
2. Turbulent suspension, which refers to coarser sediment particles maintained in suspension for shorter or longer periods of time, sometimes resuspended, due to flow turbulence and turbulent exchange.

The process of suspension or resuspension of sediment particles is initiated when:

- a) The vertical turbulent component equals the final fall velocity (Bagnold, 1954).
- b) The bed shear velocity is of the same magnitude as the final fall velocity, therefore when one of the following criteria is accomplished:

$$\frac{u_{*cr}}{w_s} = 0.25 \quad (\text{Hinze, 1975}) \quad (2.8)$$

$$\frac{u_{*cr}}{w_s} = 1.0 \quad (\text{Engelund and Hansen, 1967}) \quad (2.9)$$

$$\frac{u_{*cr}}{w_s} = \frac{4}{D_*} \quad \text{For } 1 \leq D_* \leq 10 \quad (\text{Van Rijn, 1984a,b}) \quad (2.10)$$

$$\frac{u_{*cr}}{w_s} = 0.4 \quad \text{For } D_* \geq 10 \quad (\text{Raudkivi, 1997}) \quad (2.11)$$

where u_{*cr} is the critical shear velocity, w_s is the final fall velocity (terminal settling velocity) of suspended particle, D_* is the dimensionless size of sediment particle, defined as:

$$D_* = d_{50} \left[\frac{(s-1)g}{\nu^2} \right]^{1/3} \quad (2.12)$$

where $s = \rho_s/\rho$ =relative sediment-water density

Studies of the mechanics of suspended sediment laden flow have been made with varying

degrees of success. Experimental observations were carried out by Einstein and Chien (1955); Elata and Ippen (1961); Ismail (1951); Vanoni (1946); Vanoni and Nomicos (1960).

From these investigations the following conclusions for open channel flow with suspended sediments have been obtained:

1. The friction factor for the flow decreases as an effect of suspended materials prevails.
2. The von Kármán constant κ , which has been given the value of about 0.4 in a clear water flow, may be smaller in flows with suspended sediment.
3. The mixing length and the scale of turbulence for the flow are reduced because of suspended sediments in the flow.
4. The velocity gradient becomes larger with increasing suspended sediment concentration.
5. Measured velocities in a region near the bottom of the channel appear to be larger compared to values predicted by the velocity defect law.
6. The concentration of suspended sediments near the bottom is generally lower than a value computed from the generally accepted classical equation.

Shear flow over a mobile bed induces sediment transport and the generation of bed forms. The interaction between the flow and the bed usually produces different types of regular patterns characterized by a wide range of sizes and shapes (dunes, ripples, anti-dunes, etc.).

In turn both, sediment transport and bed forms, influence the flow. The importance of studying the presence and evolution of bed forms arises because they can increase the resistance to flow. In particular, experimental results on the influence of suspended sediment on turbulence are still lacking. A mass of sediment grains kept above a bed by the eddies of fluid turbulence is said to be in a state of suspension.

By way of contrast, bed load grains move by rolling and saltation on the bed, with their immersed weight in dynamic equilibrium with a solid transmitted normal stress determined by the action of the fluid shear, on the bed grains (Bagnold, 1966, 1973). Applied to individual grains the concept of suspension is necessarily statistical, because of continuous exchange between bed load and the overlying turbulent flow. However, a steady state exists with respect to a suspended mass in a steady, uniform flow. Thus over a sufficiently long period of time the measured mass will itself be constant whereas the constituent grains that define the mass may continuously be exchanged between bed, bed load and suspended load. A state of dynamic equilibrium thus exists.

2.3.1 Generation of bed forms

Bed deposition features of flows is the mutual interaction between the flow and the erodible bed through sediment transport. This interaction is responsible for the occurrence of a variety of bed forms starting with ripples, dunes, flat bed, anti-dunes, and standing waves with increasing shear stresses or velocities. The form resistance due to these bed forms, caused by local flow separation and recirculation, can be significant. It is dependent on their dimensions as well as on flow and sediment characteristics. Because of the importance of the bed form resistance in determining the overall resistance in sand bed flows, the prediction of bed form geometry is an essential component for estimating flow resistance and water levels during floods in rivers (Karim, 1999).

When an initially flat sand bed is sheared by a fluid, the bed is unstable and gives rise to formation of ripples (Van Rijn, 1984c). This generic sand pattern results from a complex feedback mechanism between the flow and the bed form. At the first stages of the pattern formation, the bed develops a regular pattern of small-amplitude waves which further evolves toward an equilibrium bed form generally of much greater extent.

Despite the huge number of experimental and theoretical studies about ripple formation, this problem is not well understood and even the physical origin of the instability mechanism is questioned. This is essentially due to the fact that there exists no well-established equations describing the coupling between the fluid and the bed form. Several configurations have been investigated depending on the oscillatory or steady nature of the flow. Ripples observed in seas along beaches are an example corresponding to the oscillating case whereas those forming in rivers illustrate the steady configuration.

Another important parameter is the flow depth. In shallow water, deformation of the upper fluid surface couples with the sand bed. This coupling becomes irrelevant when the flow depth is great enough.

A loose flat granular bed subject to a uniform turbulent shear flow may develop an internal periodic non-uniformity such that the time-average streamlines become deformed and interact with the bed surface. In time, the flat bed must deform into an undulating series of periodic bed forms (Yalin and da Silva, 2001).

A range of theories, of varying complexity and completeness, has been proposed to account for the initiation of these bed forms from a plane bed (Engelund and Fredsøe, 1982; Smith, 1970). However, for several decades, approaches to the problem have largely revolved around two separate hypotheses (Raudkivi, 1997). One argument invokes an inherent instability at the sediment water interface owing to the stress imposed by the moving fluid (e.g. Bagnold, 1956; Engelund, 1966; Kennedy, 1963; Reynolds, 1965), whereby the effect of turbulence may be accounted for only indirectly (e.g. Richards, 1980).

The characteristic wavelength and amplitude of the deformed bed is considered to be a function of the bulk flow properties, such as average flow speed or average shear stress.

The classic approach considers the character of a potential channel flow above a fixed bed (Anderson, 1953; Kennedy, 1963). Recent studies by Huang and Song (1993) and Huang and Chiang (2001, 1999) allowed for bed deformation and a lag effect between sediment discharge and flow velocity.

In summary, stability analysis serve to demonstrate the significance of bulk flow parameters, notably the Froude number, in bed form mechanics (Colombini et al., 1987; Engelund and Hansen, 1966; Graf, 1971), but provide no understanding of the detailed physics of bed deformation (Coleman and Fenton, 2000; Gerkema, 2000; Raudkivi, 1997) .

An alternative view predicates that bed forms are initiated from bed defects as a result of turbulent bursting at the boundary and the development of flow separation (e.g. Best, 1992, 1993; Grass, 1970; Raudkivi and Witte, 1990; Yalin and da Silva, 2001). In time, this approach should lead to a better understanding of bed form development (Chanson, 2000; Dinehart, 1999).

However, a general theory for bed form initiation based upon turbulence generation is lacking. In addition, although flow separation plays a significant role in the development of bed forms (Nelson and Drake, 1995), separation is not necessary to induce an initial instability in the granular bed (Coleman and Melville, 1996; Smith, 1970; Yalin and da Silva, 2001). Rather, linear stability theories apply well to the generation of the initial defects (Coleman and Melville, 1994, 1996; Qihua et al., 1999; Smith, 1970).

From the brief argument above, classic approaches to stability theory (Engelund, 1966; Engelund and Hansen, 1966; Kennedy, 1963) should delimit the existence fields in terms of bulk flow parameters for gravel bed forms. However, some bed forms may persist outside, but close to, their respective stability limits, owing to maintenance by turbulence generation, including flow separation. In addition, stability theory does not take into account any effects of the variability in the grain sizes of the bed sediment.

2.3.2 Interaction between turbulent flow, sediment transport and bed forms

The progress towards a generalized bed form theory can only come with detailed knowledge of the interaction between turbulent flow, sediment transport and bed forms gained from experimental studies over real, moving bed forms under controlled conditions. Past studies on the fluidization and resuspension of particles have been mainly empirical experimental and were limited to the study of the bulk process and to the bulk amount of solids involved (Julien, 1995). Analytical studies have been limited and hampered by the fact the processes involve a multitude of particles with very complex interactions.

Several of these studies had to resort to simplifying assumptions on the flow of suspensions and particle interactions (Batchelor, 1977) that place significant restrictions on the applicability of the derived solutions. Numerical studies are capable of modeling the com-

plex hydrodynamic interactions between groups of particles and the interstitial fluid. But only since 1997 computational advancements in algorithms and hardware allow to perform computational studies with a meaningful number of fluidized particles.

Choi and Joseph (2001); Patankar et al. (2001) have used finite element methods and reported results on the resuspension of 300 two-dimensional disks in plane Poiseuille pressure-driven flow at intermediate Reynolds numbers. This type of numerical work has improved the fundamental understanding of particle interactions in a pressure driven shear flow. The Lattice Boltzmann Method (LBM) was developed and adapted to particulate flows (Ladd, 1994). It is ideally suited for the simulation of groups of particles in a viscous fluid as demonstrated by (Ladd, 1996). Qi (2000) has used the method to study various aspects of the complex hydrodynamic interactions between particles and fluids. Feng and Michaelides (2002) used the LBM to study the effect of suspended particles on the lift force exerted on a spherical particle that is attached on the bottom of the flow field in a shear flow.

They concluded that the effect of the suspended particles when they flow close to the bottom increases considerably the transient lift force on the stationary particle. This transient lift is high enough to affect the movement and eventual resuspension of the stationary particle if the latter were free to move. They concluded that direct particle collisions are not necessary for the resuspension process and that hydrodynamic interactions between particles are sufficient for the incipient motion of the stationary particle.

There have been a number of studies where the effect of particle size on the turbulent properties of the carrier fluid have been examined (e.g. Gore and Crowe, 1989; Hetsroni, 1989; Rashidi et al., 1990). Most of these studies dealt with the effect of the particles on the structure of the turbulence in the carrier fluid, through their effect on the coherent structures in the boundary layers.

It was shown that for a certain flow Reynolds number, when the particle Reynolds number was larger than a certain value, they tended to destabilize the coherent structures and cause an increase in the frequency of ejections within a burst. Particles with smaller Reynolds number caused a decrease in the ejection frequency. The bursting frequency remained roughly constant. Other experimental evidence (e.g. Mizukami et al., 1992; Tsuji and Morikawa, 1982; Tsuji et al., 1984) focused on the modulation of the turbulence of the carrier fluid in vertical tubes. Particles with a Reynolds number larger than some critical value cause an increase in the intensity of turbulence, maybe mostly due to vortex shedding. Smaller particles tend to damp the turbulence, maybe by increasing the apparent viscosity.

The particles-turbulence interaction is a highly complex phenomenon, and it depends on the flow Reynolds number, the contents of the admixture, the physical properties, the nature of the flow, the length scales of the turbulence and the particles etc.

2.3.3 Influence of suspended sediment on flow characteristics

The influence of sediment transport on the turbulence characteristics of the carrier fluid has been a subject of great interest for many years. From a practical viewpoint, estimates of transport rates and a better understanding of the processes of bed form generation depend on whether and how the sediment influences the flow characteristics [two-way coupling of Crowe (1993)]. Since the turbulent shear stress within a turbulent boundary layer may be expressed as:

$$\tau = -\rho \overline{u_{if} v_{if}} = \rho l_e^2 \left| \frac{\partial U_f}{\partial y} \right| \left(\frac{\partial U_f}{\partial y} \right) = \rho \varepsilon \frac{\partial U_f}{\partial y} \quad (2.13)$$

there is a relationship between the turbulence intensity (as expressed by the Reynolds stress, $\rho \overline{u_{if} v_{if}}$ where u_{if} and v_{if} and are the instantaneous deviations from the mean downstream and vertical fluid velocities, respectively), fluid density, ρ , mixing length, l_e (or eddy size), kinematic eddy viscosity, ε , and the velocity gradient $\partial U_f / \partial y$, where U_f is the mean downstream velocity at a point and y is distance from the bed. Thus, sediment transport may influence turbulence intensity by affecting:

- a) the density of the fluid-sediment mixture;
- b) mixing length;
- c) eddy viscosity; and
- d) the velocity gradient.

Furthermore, near the boundary, $l = \kappa y$ and $\partial U_f / \partial y = u_* / \kappa y$ (where κ is the von Kármán coefficient and u_* , is shear velocity), and the boundary friction coefficient is proportional to $u_* / \kappa y$. Sediment transport may therefore also influence k and the friction coefficient. In view of this, it is necessary to consider each of these flow parameters when investigating the influence of sediment transport on the flow.

2.3.3.1 Von Kármán coefficient

Einstein and Chien (1955) proposed a graphical relation to predict the von Kármán constant κ based on an energy concept. They also pointed out that the main effect of sediment suspension occurs near the bed. Recently, Muste and Patel (1997) also studied experimentally the effect of sediment suspension on the log law. They concluded that small sediment concentrations have little effect on the log law near the bed. Much debate has arisen concerning the influence of suspended sediment on the von Kármán coefficient, with researchers proposing either a reduction in with increasing sediment suspension Einstein and Chien (e.g. 1955); Nohu (e.g. 1989); Vanoni (e.g. 1946); Vanoni and Nomicos (e.g. 1960) or that remains

constant but that the *law of wake* should be used with appropriate wake coefficient Coleman (1981); Itakura and Kishi (1980); Umeyama and Gerritsen (1992). Recent studies have challenged the assumption that is constant and the outer, wake region is most affected by suspended sediment Lyn (1988, 1991, 1992). Furthermore, Gust and Southard (1983) and Bennett and Bridge (1995) believe that is reduced from its clear water value, even in the case of weak bed load transport with no suspended sediment.

2.3.3.2 Effect of coarse and fine grains on turbulence

Parker and Coleman (1986) found that the turbulent energy expenditure is increased if the suspended sediment is fine grained since less turbulent energy is required to suspended the sediment than is supplied via the work of the downstream component of gravity on the sediment. In contrast, the coarser-grained suspended sediment was reasoned to result in dampening of turbulent energy.

Research work concerning two-phase flows in pipes and wind tunnels has shown that grains may enhance turbulence production when larger than the micro-scale of turbulence or attenuate turbulence when the grains are small enough to be enclosed within the turbulent eddies (Crowe, 1993; Gore and Crowe, 1989; Hetsroni, 1989; Kulick et al., 1994). When large grains are added to a flow, the fluid turbulence may increase Gore and Crowe (e.g., 1989); Hetsroni (e.g., 1989); Mueller (e.g., 1973) or remain relatively unchanged (Lyn, 1992; Rayan, 1980). Other researchers have found that the addition of fine-grained sediment may cause turbulence attenuation (Kulick et al., 1994; Rogers and Eaton, 1991; Xingkui and Ning, 1989).

In addition, factors including the sediment concentration, grain size sorting, and sediment-to-fluid density ratio have also been shown to influence turbulence modulation (Gore and Crowe, 1989; Yarin and Hetsroni, 1994). However, it has also been suggested that the ratio between the response time of a particle within a flow to the scale of the turbulence may influence both turbulence attenuation and enhancement in the carrier fluid (Elghobashi, 1994; Elghobashi and Truesdell, 1993). From the aforementioned research it may be concluded that the understanding of the interaction between turbulence and sediment transport is still far from complete.

2.4 Physical and numerical modeling of flow in shallow reservoirs

The present study focuses on sedimentation of shallow reservoirs with a prototype depth of between 5.0 and 15.0 *m*. A reservoir is thereby defined as an artificial lake into which water drains and is stored for future use. Sometimes, a reservoir is created by damming of existing natural lakes to improve their capacity. The behavior of sediments in a shallow

reservoir is mainly determined by bed morphology and main $2D$ water circulation, as well as by the characteristics of the sediment.

The initiation and evolution of the silting process in reservoirs is basically determined by the water sediment inflow regime (rate and time-space variability, physical properties of mixture). The water sediment inflow mixture brought into reservoirs by the main river and tributaries penetrates and passes through the reservoir as concentrated or spreading biphasic influx jets, which would either further mix or not with the receiving (quiescent) water of the reservoir.

When the penetrating inflow velocity is low, the influx jets will develop as spreading ones. They could then totally or partially mix with the stagnant waters in the basin, and some homogeneous flows towards the dam or spillway would normally occur. This is the usual case with small, narrow and shallow reservoirs, located in low altitude plain regions with gentle slopes.

In the case of medium and large reservoirs, mixing of the spreading biphasic jets with receiving clear water in the reservoir will usually occur in the backwater region of shallow water, up to the water depth where favorable conditions for density and turbidity stratification are met. The silting process in a reservoir generally starts in shallow waters from the upper backwatering reach of the basin and at the junction of the main river and tributaries as well. In these regions, the water sediment flow is drastically decelerated and consequently the bed-load transportation is slowed down or even ceases, while the suspension-carrying capacity of the flow reduces. Thus the settling and the deposition process of sediment begins and continuously progresses as more sediment supplied by the catchment is brought into the reservoir basin by the river system. Various types of sediment deposit could develop within the reservoir basin.

2.4.1 Experiments dealing with reservoir sedimentation

The first attempts to predict sedimentation in reservoirs led to empirical curves relating the reservoir capacity loss with hydrodynamic parameters (Brown, 1958; Brune, 1953; Churchill, 1948). The distribution of sediment deposits was also addressed (Graf, 1983; Heineman, 1961). Schoklitsch (1937) carried out a pioneering laboratory study. In many experiments pronounced delta formations were observed (Graf, 1983). Nowadays, a great amount of field data exists in the technical literature, but a large amount also exists in unpublished reports (Graf, 1983). A typical case is the Lake Mead survey through the Colorado River (Lara and Sanders, 1970).

Experimental investigation on the silting process in reservoirs and lakes was carried out by Mertens (1985) in a square, shallow basin ($5.00 \times 5.00 \times 0.25 \text{ m}$) with a horizontal bottom and an approaching channel 0.25 m wide. Sand (0.25 mm) and plastic granulate material (1.5 mm) were used in two separate runs of constant flow rate (3.00 and 1.35 l/s).

Stovin and Saul (2000) described a series of laboratory experiments in which the sedimentation efficiency of a storage chamber was measured. The model comprised a 2.00 *m*, 0.97 *m* wide and 0.45 *m* deep long chamber. The bottom of the chamber was horizontal. The flow pattern that developed in the tank was asymmetric. The inflow jet veered towards the left wall of the tank, which resulted in a clockwise circulation in the main body of the tank and a smaller, anticlockwise circulation to the left of the inlet. Measurements and simulations for the same model tank have been reported by Stovin (1996) and Stovin and Saul (2000).

Recent laboratory experiments and numerical simulations for a wide flume (Sloff et al., 2004) showed that channel formation in shallow reservoirs is highly dependent on the boundary and the initial flow conditions and the reservoir geometry.

An early experimental study regarding delta formation and its associated stream channel hydraulics has been performed by Chang (1967, 1982) in a large laboratory model basin. Several tests, for various flow rate (5.00 and 6.31 *l/s*), sediment inflow (from 0 to 8.80 *g/s*), and constant or variable hydraulic conditions were carried out.

It was observed that the delta formation started with the deposition of bed load at the channel mouth, while the suspended load was deposited at the whole reservoir surface rather uniformly over the reservoir bottom. Under constant flow conditions, the stream channel had multiple branches and extension of the delta occurred at the mouths of these branches in the form of lobate tongues. Under variable flow conditions, the stream channel adjusted to a single or several distributaries channels, and the delta growth in multiple directions was affected by the channel pattern (alluvial fan).

The delta formation and pattern of sediment deposits in a one-dimensional river-reservoir system were experimentally investigated in a rectangular laboratory flume by Yucel (1977); Yucel and Graf (1973)). A single channel bottom slope of 0.50% was used, with four different flow rates (from 40 to 100.00 *l/s*), three flow depths (from 25.00 to 35.00 *cm*), and two different sizes of natural sand (0.98 and 1.85 *mm*); only qualitative observations were made during the experimental tests. It was observed that the depositing sediment first formed in thin layers which grew into a typical delta of triangular planform shape, and began to advance in the flow direction, maintaining relatively constant delta thickness and rate of movement.

Shieh et al. (2001) investigated the development of alluvial deltas by using movable bed experiments from a flume into a basin. The experimental setup was aimed at the bed-load mode. Results showed that the development of the delta can be divided into three stages. In the first stage, the delta progressed mainly in its length, and a successfully derived equation described the shape factor of the delta in this stage. In the second stage, the delta developed mainly in its width. The length, width, front thickness, and central thickness of the delta were used to scale the geometric similarity. The plane geometry of deltas can be described using Gaussian functions.

2.4.2 Classification of numerical models associated with reservoir sedimentation

Numerical simulation of flow in reservoirs is necessary in order to determine the detailed flow pattern that typically includes separation at the inlet, accompanied by recirculation and stagnation regions. Obviously, information on the flow structure is useful in forecasting retention times and the degree of mixing. The prediction of sediment transport rates is important in river and coastal environmental assessments. Many mathematical models have been developed for simulation of sediment behavior. These models include three major components: water routing, sediment routing, and special function modules.

The first numerical models simulating sediment distribution in reservoirs have been developed in the early 1970's. Chang and Richards (1971) developed a numerical model for silting of rectangular and wide reservoirs. Numerous equations for predicting suspended transport rates are available in the literature, and a good review is given by (Dyer and Soulsby, 1988). They pointed out that one of the principal differences between various suspended transport equations lies in the forms chosen to represent the distribution of eddy viscosity and eddy diffusivity.

However, after examination of a number of representative eddy viscosity expressions, including constant, linear and parabolic depth-dependent distributions, they concluded that all distributions, except the constant distribution, result in similar sediment transport rates.

Computational models generally make use of sediment transport formulas and a one-dimensional *1D* backwater profile calculation (Graf, 1983). Two-dimensional *2D* vertical-averaged models solve the vertical sediment concentration profiles, allowing for more precision in the near-bed particle exchange flux calculation.

However, existing *2D* models do not specifically address the present problem of shallow reservoirs (Lai and Shen, 1996; Van Rijn, 1987). Stovin and Saul (2000) demonstrated the potential that existed to apply Lagrangian particle tracking to the prediction of sediment transport in storage chambers by using *FLUENT* CFD software. Fully *3D* models were developed recently in relation to sedimentation in water intakes (Olsen, 1991; Van Rijn et al., 1990), or estuarine and coastal sedimentation (Lin and Falconer, 1996; Van Rijn et al., 1990). The main disadvantage with *3D* models is the still high computational cost, because they involve very different spatial and time scales.

A comparison of most commercially and academic available computational models can be found in Langendoen (2001), who gives a fairly detailed description of their features to evaluate them. State-of-the-art shows several sediment transport models that may be useful for analyzing sedimentation, issues associated with reservoirs. They can be classified in academic and commercial codes as summarized in Table 2.1 (Kantoush et al., 2005):

Table 2.1: Classification of most commercially and academic available computational models

A- Academic codes	B- Commercial programs
CCHE2D and CCHE3D	DELFT3D
SSIIM	MIKE21
WOLF 1D and 2D	TRIM-2D
MOHID	TELEMAC2D
GSTARS 3.0	FLOW-3D
HEC-6	SMS
BASMENT Software for 2D and 3D	FLUENT CFD

2.5 Conclusion

From the state-of-the-art it may be concluded that existing research on shallow reservoir sedimentation does not consider the influence of the geometry of the reservoir on the sedimentation process by suspension. Therefore, the present research focuses on the influence of the geometry of shallow reservoirs on the settlement of suspended particles in doing systematic physical tests. In addition to engineering applications, the experiments provide a useful database to validate numerical simulation codes at low Reynolds numbers. Furthermore, an interesting separated flow behavior is obtained in order to provide insight on the flow physics.

This study focuses on the sedimentation of shallow reservoirs by suspended sediments and the objective of the experiments is to gain insight into the physical process behind the sedimentation of shallow reservoirs governed by suspended sediment. They are combined with numerical modeling techniques that include the processes as observed.

Until now the effect of the reservoir geometry on the sediment depositions, flow pattern, and trap efficiency was not considered. Therefore, further investigations on the influence of the geometry of a shallow reservoir on the deposition and flow patterns have to be conducted.

Experimental facility and measurement techniques

The present chapter gives the reflections preceding the design and conception of the experimental setup used for this research study.

In addition an overview of the reservoir geometry, the tested parameters as well as the adopted measurement techniques and characteristics of suspended sediments is given.

Experiments program and geometry configuration and the two different testing procedures are described.

In the last sections, characteristics and dimensionless parameters for flow, geometry, time and sediment are presented.

Definition of the geometry shape factor SK and how was it derived, are described.

Finally, experimental conditions are given for experiments with clear water and with sediment water mixture are given.

3.1 Design of experiments

The basic consideration of setting up the experiment is based on several numerical simulations using CCHE2D and FLOW-3D (Kantoush et al., 2005). Preliminary numerical simulations of suspended sediment transport in shallow reservoirs had been used to define the geometrical configurations to be studied experimentally.

The conceptual chart in Figure 3.1 describes the relationship of all factors which influence the selection of the experimental set-up. To determine the best set up for the model design has to be proposed.

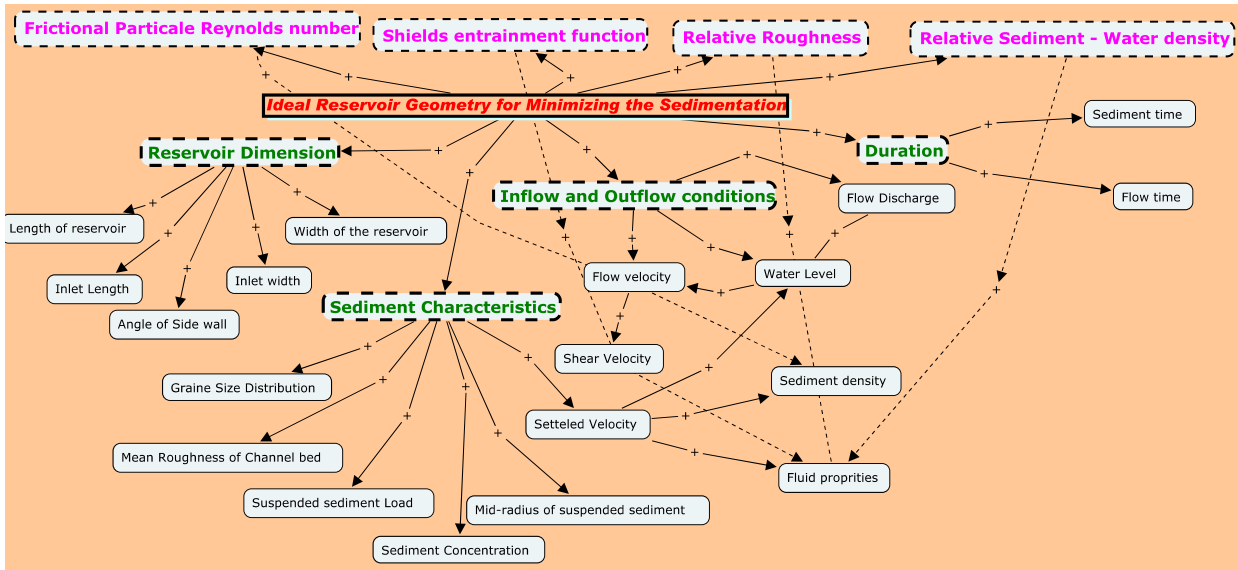


Figure 3.1: Conceptual chart comprising all the possible factors which influence the experimental set-up.

3.2 Description of experimental setups

The experiments were carried out in a new designed test facility at the Laboratory of Hydraulic Constructions (LCH) of the Swiss Federal Institute of Technology (EPFL).

Schematic view of the experimental setup are shown in Figures 3.2 & 3.3. The experimental setup consists of a rectangular inlet channel 0.25 m wide and 1.00 m long, a rectangular shallow basin with inner dimensions of 6.00 m length and 4.00 m width, and a 0.25 m wide and 1.00 m long rectangular outlet channel.

The water level in the basin is controlled by a 0.25 m wide and 0.30 m high flap gate at the end of the outlet. The basin is 0.30 m deep and has a flat bottom. The walls and bottom are hydraulically smooth. Adjacent to the basin, a mixing tank is used to prepare the water-sediment mixture.

A sediment supply tank is mounted above the mixing tank. The mixing tank is equipped with a propeller type mixer to create a homogenous sediment concentration.

To control the sediment concentration, a small gate is installed at the lower end of the sediment supply tank. This tank is attached to a vibrating device with variable speed to control sediment release. The water-sediment mixture is drained by gravity into the water-filled rectangular basin through a flexible pipe with a diameter of 0.10 m.

Along the basin side walls, a 4.00 m long, movable, aluminum frame is mounted, which carries the measurement instruments. A photograph of the final experimental facility and its different parts (mixing tank, inlet and outlet channel,..etc) are illustrated in Figure 3.4.

The main laboratory hydraulic circuit was used for the first four tests (Fig. 3.2) and

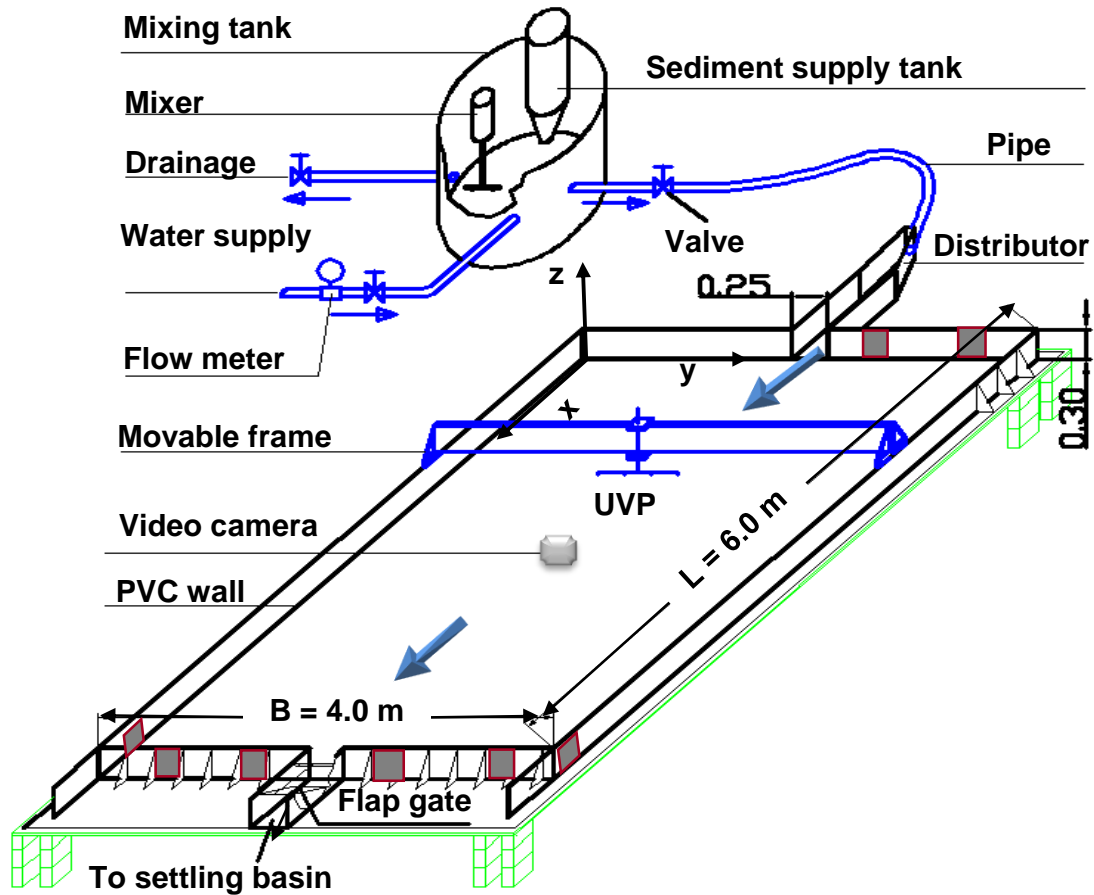


Figure 3.2: Schematic view of the experimental installation for the open circuit tests, looking downstream.

for the rest of the tests a closed circuit was used (Fig. 3.3) to prevent the pollution of the internal laboratory circuit.

3.3 Configuration and dimension of investigated geometries

Ten axi-symmetric basins with different forms were tested to study the geometry shape effect on the flow and deposition pattern. In order to gain insight into the physical process behind the sedimentation of shallow reservoirs governed by suspended sediment; a reference basin geometry with width of $B = 4.0\text{ m}$ and length of $L = 6.0\text{ m}$ was used.

The reference geometry was used for the first six test (from Test1 (T1) to Test6 (T6)), to examine different test procedures and find the optimal one to continue with future test configurations. As a reference case, the rectangular basin geometry was analyzed in detail (Kantoush et al., 2007b).

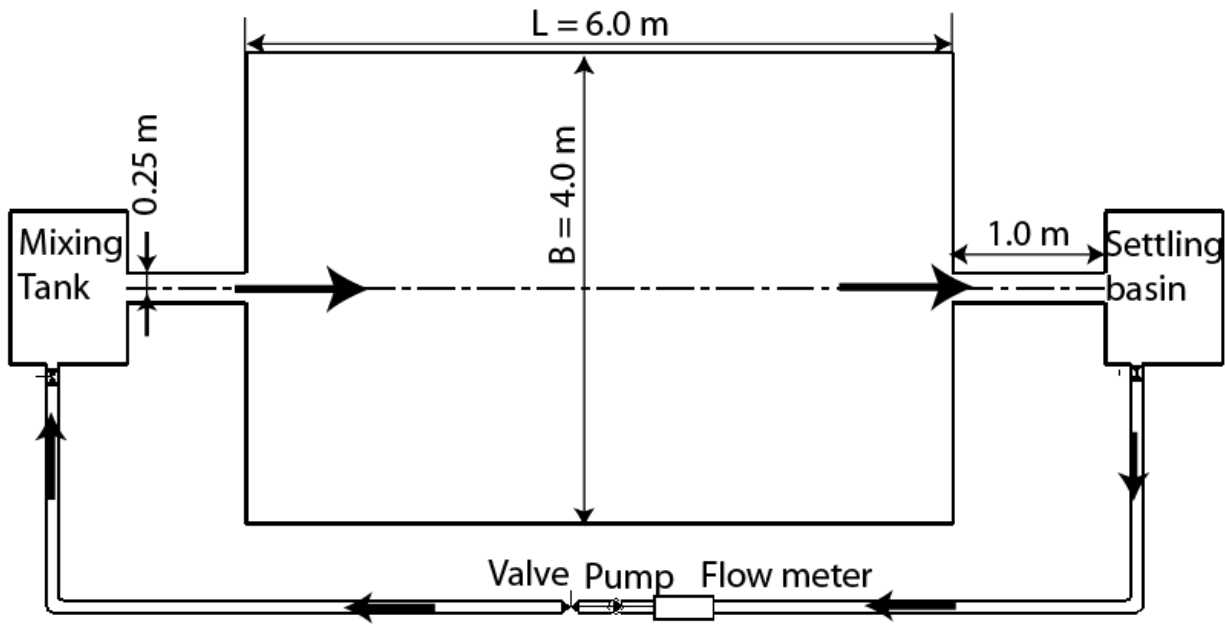


Figure 3.3: Plan view of the experimental installation for the closed circuit tests.

A systematically design for the geometry of the different basins used for the tests can be classified for three groups as shown in Figure 3.5:

1. Reduced width of basin
2. Reduced length of basin
3. Reduced expansion angle of basin

To investigate the effect of the basin width effect on the flow and sedimentation processes in the reservoir the experiments focused on the width achieved in rectangular reservoir 6.0 m long and 3.0, 2.0, 1.0, 0.5 m wide (from T7 to T10), respectively. With a second set of tests the effect of the basin length experimental tests have been conducted in a rectangular shallow basin 4.0 m wide and 5.0, 4.0, and 3.0 m long (from T11 to T13), respectively.

Finally geometries with three expansion angles were tested (from T14 to T16). Figure 3.6 shows pictures of all tested geometry and configurations of the basins obtained from the reference geometry by new walls inside.

3.4 Experimental conditions regarding scaling

To obtain a correctly modeled shallow turbulent free surface flow under laboratory conditions, a sufficiently high Reynolds number, which generally results in a prohibitively large reservoir.



Figure 3.4: Photos of different part of the experimental facilities: (a) general view of the rectangular reservoir; (b) mixing tank with the sediment distributor; (c) inlet channel; (d) outlet channel with the flap gate to control the water level; (e) settling and sediment collecting tank

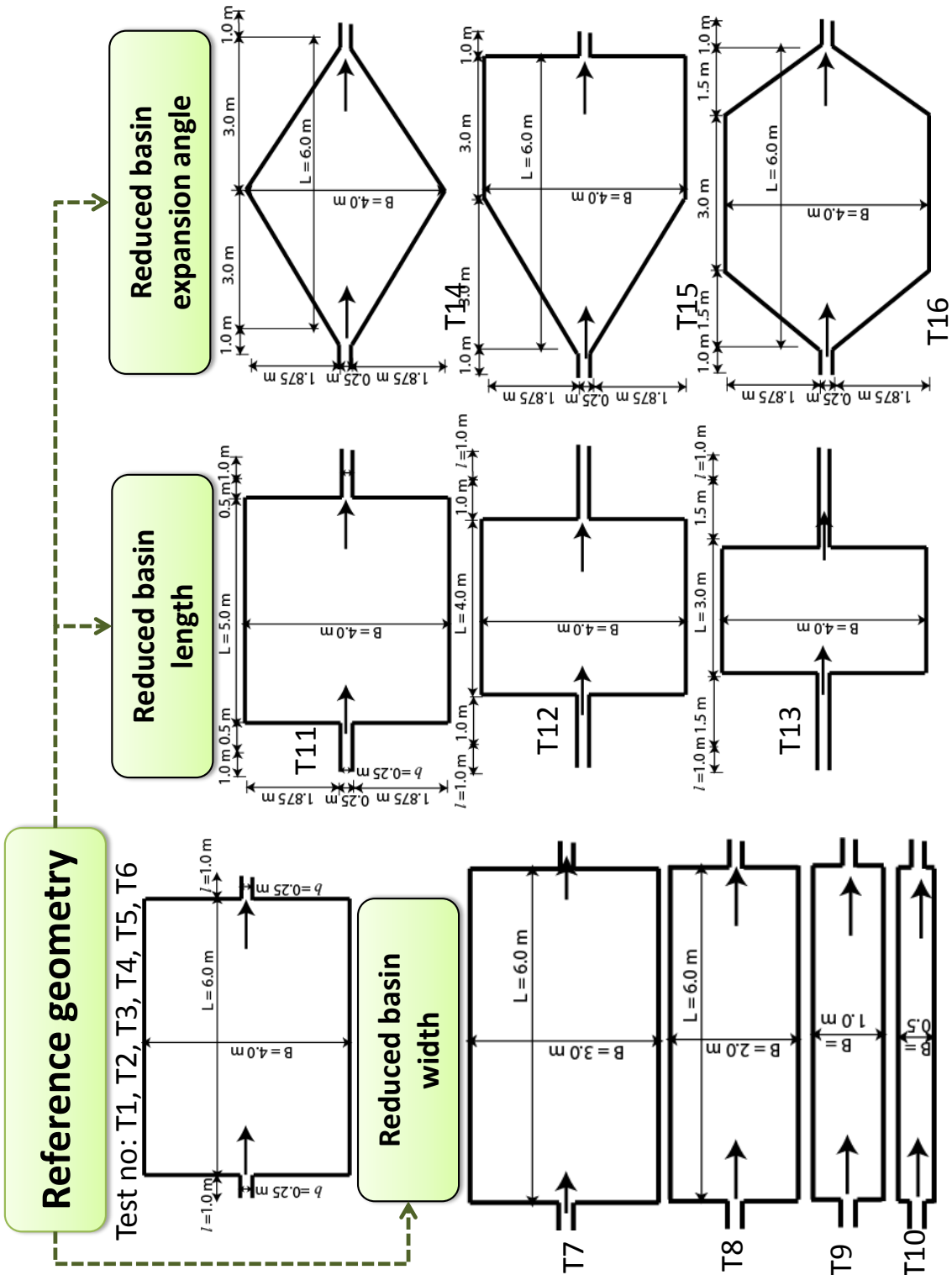


Figure 3.5: Geometry with dimensions of all basins used in the test series.

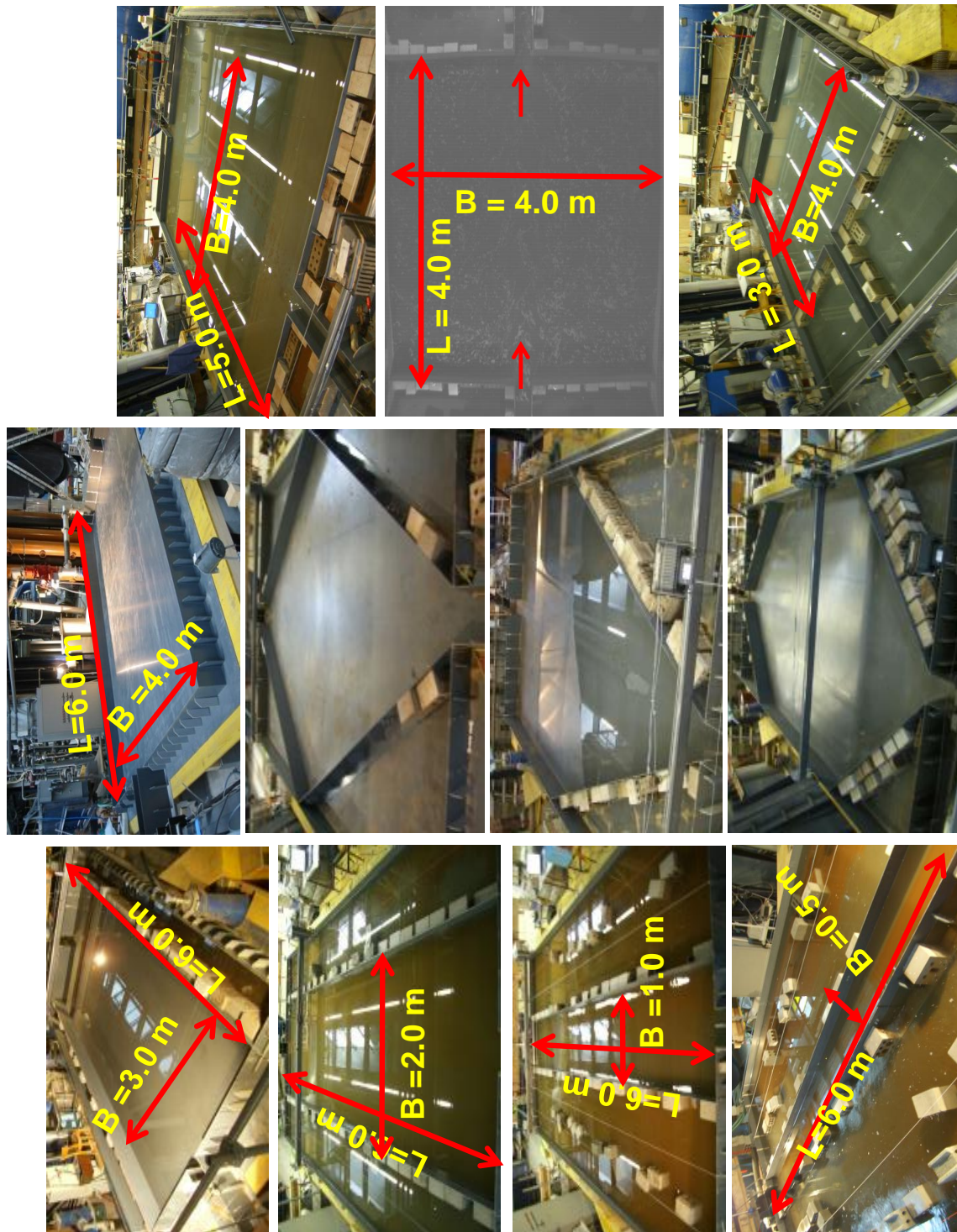


Figure 3.6: Photos of configurations of basins of the test series.

3.4.1 Scaling

The set of characteristic parameters of the two phase phenomenon can be obtained as the sum of those describing the distinct components:

- Fluid. In mechanics a fluid is defined by the numerical values of ρ (kg/m^3), dynamic viscosity μ ($kg/m\ s$), and kinematics viscosity ν (m^2/s)
- Cohesionless granular material, it is clear that a cohesionless granular material is determined by the density and by the absolute size of the grains and by the geometric properties of the granular material (i.e. by the shape of the grain and by the grain size distribution curve). We defined the cohesionless granular material by its density ρ_s (kg/m^3) and absolute size D (m)
- Flow. The characteristic parameters of the flow are, h is the average depth, S is the slope, and g is the force of gravity.

The underlying rationale to physical scale modeling is that it is possible to scale down the geometric, dynamic (force) and kinematic (motion) variables operating in the field and represent them in a realistic laboratory model. Scaled physical models are based on similarity theory, which uses a series of dimensionless parameters that fully characterize the physics. The physical scale modeling described and used here is based on Froude similarity, whereby the key controlling variables in the model are kept within the appropriate range compared to a field prototype. Froude similarity defines the relation between all other variables in the fluvial system (Henderson, 1966) so that some factors are unaltered from prototype to model (e.g. slope), some are linearly scaled (e.g. grain size), whilst others are reduced by a fractional proportion (e.g. flow velocity). The choice of a scaling factor $\lambda = L_p/L_m$, or length scale ratio, to be used in the experiments, is determined by the objectives of the research.

Similitude requirements for movable and fixed bed models have been described in several textbooks (Kobus, 1980; Yalin, 1971). In order to achieve dynamic similarity Yalin (1971) advocates

$$\lambda > (70/Re^*)^{2/3} \quad (3.1)$$

Where Re^* is the grain Reynolds number of the prototype and $Re^* = U_* \cdot d_s / \nu$, where U_* is the shear velocity, ν is the kinematic viscosity, d_s is the characteristic grain size of the bed that represents the roughness, usually taken as d_{90} . There is ongoing debate concerning the critical threshold of Re^* where the flow may be considered to be fully rough and the grains do not lie within the viscous sublayer (see discussion in Moreton et al. (2002)). If it is accepted that this critical threshold value is where $R^* > 25$ (cf. Ashworth et al. (1994)), then calculation of the minimum scaling factor λ in Equation 3.1 uses a number of 25.

The physical model was based on a prototype of a reservoir under investigation along the Rhone River (Bollaert et al., 2000; Heller et al., 2005, 2007). Computation of length scale appropriate for the present experiments using Equation 3.1 (see, Kantoush et al. (2005)) shows that a maximum 1:75 scaling should be used. Given the need to maximize the model Re and Re^* and keep the model grain size as coarse as possible, a 1:50 scaling was selected. Moreover, according to the length of the tested section and the laboratory constrains, the model has been designed with horizontal and vertical scales of $\lambda_l = \lambda_h = 50$. Yang Guowei et al. (1992) used this design method and a suspended load model to define the model sediment characteristics for Danjiangkou reservoir. Moreover, this method is in good agreement with the model-prototype comparison.

All similarity conditions should be fulfilled according the following criteria:

Horizontal length scale

$$\lambda_l = L_p/L_m \quad (3.2)$$

Vertical length scale

$$\lambda_h = h_p/h_m \quad (3.3)$$

Velocity scale (for Froude number)

$$\lambda_V = V_p/V_m = \lambda_h^{1/2} \quad (3.4)$$

Resistance to flow scale

$$\lambda_n = \lambda_h^{2/3}/\lambda_l^{1/2} \quad (3.5)$$

Discharge scale (for water continuity)

$$\lambda_Q = Q_p/Q_m = \lambda_V \lambda_l \lambda_h \quad (3.6)$$

Time scale of water flow

$$\lambda_{t1} = t_p/t_m = \lambda_l/\lambda_V \quad (3.7)$$

Sediment fall velocity scale

$$\lambda_\omega = (\lambda_h/\lambda_l)\lambda_V \quad (3.8)$$

Incipient velocity scale

$$\lambda_{V_o} = \lambda_V = \lambda_h^{1/2} \quad (3.9)$$

Sediment diameter scale

$$\lambda_d = (\lambda_\omega \lambda_V / \lambda_{\gamma_s - \gamma}) \quad (3.10)$$

Sediment concentration scale

$$\lambda_s = \lambda_{\gamma_s} \lambda_{\gamma_s - \gamma}^{-1} \quad (3.11)$$

Sediment time scale

$$\lambda_{t2} = \frac{\lambda_l}{\lambda_V} \cdot \frac{\lambda_{\gamma_s - \gamma}}{\lambda_s} \quad (3.12)$$

where γ_o is the bulk density of sediment; γ_s the sediment specific weight and γ the specific weight of water.

3.4.2 Hydraulic aspects

The hydraulic conditions were chosen to fulfill the sediment transport requirements. Physical scale model are based Froude number ($0.05 \leq Fr \leq 0.43$) is kept the same in model and field, and Reynolds number is relaxed ($14000 \leq Re \leq 28000$), but still kept within the turbulent flow regime ($Re > 2000$) as shown in Table 3.1 for some of experiments. The following hydraulic parameters used for the tests are summarized in Table 3.1:

- Flow depth: h
- Flow discharge: Q
- Depth of flow to width of inlet channel ratio: h/b
- Froude number in the inlet channel: Fr_{in}
- Reynolds number in the inlet channel: Re_{in}

Table 3.1: Hydraulic conditions of experiments

Test No	h [m]	Q [l/s]	h/b [-]	Fr_{in} [-]	Re_{in} [-]
T1	0.200	7.000	0.800	0.100	28000
T2	0.200	7.000	0.800	0.100	28000
T3	0.200	7.000	0.800	0.100	28000
T4	0.200	7.000	0.800	0.100	28000
T5	0.200	7.000	0.800	0.100	28000
T5	0.150	7.000	0.600	0.153	27900
T5	0.100	7.000	0.400	0.283	28000
T5	0.075	7.000	0.300	0.435	27975
T6	0.200	0.035	0.800	0.050	14000
T6	0.200	0.035	0.800	0.050	14000
T7	0.200	7.000	0.800	0.100	28000

3.4.3 Sediment aspects

The sediments have to be in suspension over the entire surface of the experimental basin. Several researchers proposed criteria for the onset of suspension. To ensure that suspension occurs over a large part of the flow depth, a range of velocities for different flow depths was checked against the criteria given by Shieh et al. (2001).

To estimate the sediment transport rates for the different hydraulics conditions the formula of Hancock and Willgoose (2001) and Engelund and Hansen (1967) were compared. Assuming that the flow velocity in the basin corner is approximately 20% of the entrance velocity in the lead channels as observed in the preliminary tests, the sediment transport capacity can be splitted for the two different methods.

As explained before, fluid particle in immediate contact with a solid boundary have zero velocity. Even in turbulent channels, a thin layer of *laminar sublayer* occurs next to the solid boundary, where velocity is low and viscous forces predominate. When the thickness of the laminar sublayer is greater than the height of the surface roughness elements, the boundary is said to be *hydraulically smooth*. However, if the laminar sublayer is thin and surface roughness elements protrude into the zone of turbulent flow, thereby contributing to form drag, the boundary is said to be *hydraulically rough*.

Most of civil engineering problems deal with flows in the fully turbulent range, where the sublayer is very thin compared to the size of roughness element size. In this regime, the frictional resistance is independent of Reynolds number, but is a function of the roughness element size. The shear velocity Reynolds number is defined as:

$$Re_* = \frac{U_* \cdot d_s}{\nu} \quad (3.13)$$

where U_* is the shear velocity, ν is the kinematic viscosity, d_s is the particle diameter.

3.4.4 Similarity of the beginning of sediment motion

The settling velocity of sediment grains is one of the key variables of sediment transport, especially when suspension is the dominant process. It serves to characterize the restoring forces opposing turbulent entraining forces acting on the particle. For example, an error in the estimation of the settling velocity may be amplified by a factor of three or more in the computation of the suspended load transport.

In spite of this importance, it is nearly impossible to obtain its actual value in situ, and in most cases it is obtained from laboratory experiments or predicted by empirical formulas. Often the estimation of the settling velocity of sediment has been done by applying predictive formulas developed for spherical grains only (Gibbs et al., 1971).

However, it is well known that the shape of natural sediment particles is different from a sphere. Consequently, the settling velocity will be lower than that of a sphere with the nominal diameter. Due to the practical implications of this difference, several formulas have been proposed to calculate the settling velocity of natural sediments (for example Ahrens, 2000; Cheng, 1982; Dietrich, 1982; Graf, 1971; Hallermeier, 1981; Van Rijn, 1984b).

All of these have been empirically derived, and in this sense they fit very well the data set employed. However, as new relationships have been proposed, they have not incorporated

Table 3.2: Comparison of different characteristic particle sizes and the corresponding settling velocities of fine crushed walnut shells.

	d [μm]	v_{ss} [mm/s]
Median diameter, size such that 50% is finer d_{50} :	50	0.513
Arithmetic mean diameter, d_a :		
$d_a = (\sum_i d_i \cdot \Delta_i) / (\sum_i \Delta_i)$	62	0.789
Geometric mean diameter, d_g :		
$\log d_g = (\sum_i \log d_i \cdot \Delta_i) / (\sum_i \Delta_i)$	44	0.397
Particle-surface weighted mean diameter, d_s :		
$d_{ss} = \sqrt[2]{\sum_i (d_i^2 \cdot \Delta_i) / (\sum_i \Delta_i)}$	69	0.977
Particle-volume weighted mean diameter, d_v :		
$d_v = \sqrt[3]{\sum_i (d_i^3 \cdot \Delta_i) / (\sum_i \Delta_i)}$	73	1.094

previously published data to check the general accuracy of the respective formulas: In this sense there is considerable uncertainty about which formula is the most accurate.

To estimate the settling velocity of sediment particles, two different approaches can be followed:

1. an idealized one in which the particle is assumed to be a sphere; and
2. a more realistic one in which the natural sediment shape is considered.

In general, the first approach is used extensively (for instance, when the sediment grain size is obtained by using the settling tube, the grain size is calculated by assuming the sediment to be spherical), although some methods take into account the sediment shape.

In Table 3.2 representative diameters are shown, which represent different criteria. Altinakar (1988) proposed that the grain size which has a settling velocity equal to the average settling velocity of the sediment material given by Eq. (3.14) is a representative particle size for the sediment material:

$$v_{ss} = \frac{\sum_i (v_{ss})_i \cdot \Delta_i}{\sum_i \Delta_i} \quad (3.14)$$

where Δ_i represents the percentage of the sediment material falling in the i^{th} size fraction of the frequency histogram and $(v_{ss})_i$ is the settling velocity for that size fraction.

The settling velocity, v_{ss} , can be estimated by means of different methods described in the literature. Considering the small, almost spherical particles and the low Reynolds number, $Re = \frac{d v_{ss}}{\nu} < 0.2$, the Stokes' law has been used. It is expressed as:

$$v_{ss} = g \frac{\rho_s - \rho_w}{\rho_w} \frac{1}{18\nu} d^2 \quad (3.15)$$

With the particle size distribution shown in Figure 3.7 the calculated v_{ss} is 1.0 mm/s . The initial porosity P'_m of the sediment deposits was investigated by two methods:

1. sampling from non-submerged sediments
2. under submerged conditions, representative sampling from submerged deposited sediments after a real test. Hence, the weight of the collected sediment deposits is known and the volume is obtained from the measurement of the bed deposition thickness.

Based on these laboratory investigations, the initial porosity is $P'_m = 0.64$.

The dry density, ρ'_s , was calculated from the porosity $\rho'_s = (1 - P'_m)\rho_s = 550 \text{ kg/m}^3$, the density of wet sediment is $\rho''_s = P'_m \rho + (1 - P'_m)\rho_s = 1180 \text{ kg/m}^3$. The density of the mixture is $\rho_{mix} = C_m + \rho(1 - C_m/\rho_s) = 1001 \text{ kg/m}^3$ where, ρ_{mix} = density of mixture, C_m = sediment concentration by mass in the mixture, ρ = liquid density, ρ_s = sediment density

Due to the low sediment concentrations by volume (C_v) of up to 0.2% , no corrections for the concentration are made on the settling fall velocity and the viscosity of the water. The mixture is considered to be a Newtonian fluid because of $\rho_{mix} - \rho \ll 16 \text{ kg/m}^3$ (Altinakar et al., 1996) and $C_v \ll 1\%$

The inception of sediment motion is related to the shear velocity (or to the bed shear stress). Considering a given channel and bed material, no sediment motion is observed at very low bed shear stress until τ_0 exceeds a critical value. For τ_0 larger than the critical value, bed load motion takes place and the particles will start rolling and sliding in continuous contact with the bed. For increasing values of τ_0 the particles will perform more or less regular jumps which are called saltations.

Considering a particle in suspension, the particle motion in the vertical direction is related to the balance between the particle fall velocity v_{ss} and the turbulent velocity fluctuation in the vertical direction. Turbulence studies (e.g. Hinze, 1975; Schlichting, 1979) suggested that the turbulent velocity fluctuation is of the same order of magnitude as the shear velocity. With this reasoning, a simple criterion for the initiation of suspension (which does not take into account the effect of bed slope) is:

$$\frac{U_*}{v_{ss}} > \text{Critical value} \quad (3.16)$$

Several researchers proposed criterion for the onset of suspension as showed in Section 2.3. In a first approximation, suspended load occurs for:

$$\frac{U_*}{v_{ss}} > 0.25 \text{ to } 2.5 \quad (3.17)$$

For the present study the value of U_*/v_{ss} for walnut shells particles and average hydraulic conditions is 6.

3.4.4.1 Choice of sediment material

There are various materials which can be used to simulate the sediment current in suspension case. The material might be fine grinded grains of Quartz, granular plastic, glass, marble etc.

Several preliminary tests were conducted with four different materials and median diameters. In beginning a very fine sand with a median diameter, d_{50} , of $91 \mu m$ and density $2650 kg/m^3$ was tested. All the fine sand particles were deposited at the inlet channels before the basin and in the mixing tank as well. The second was Kaolin K13, $d_{50} = 4.0 \mu m$, density $2620 kg/m^3$ and the behavior was better than sand. A few material was entering the basin without any homogenous distribution in the entire surface.

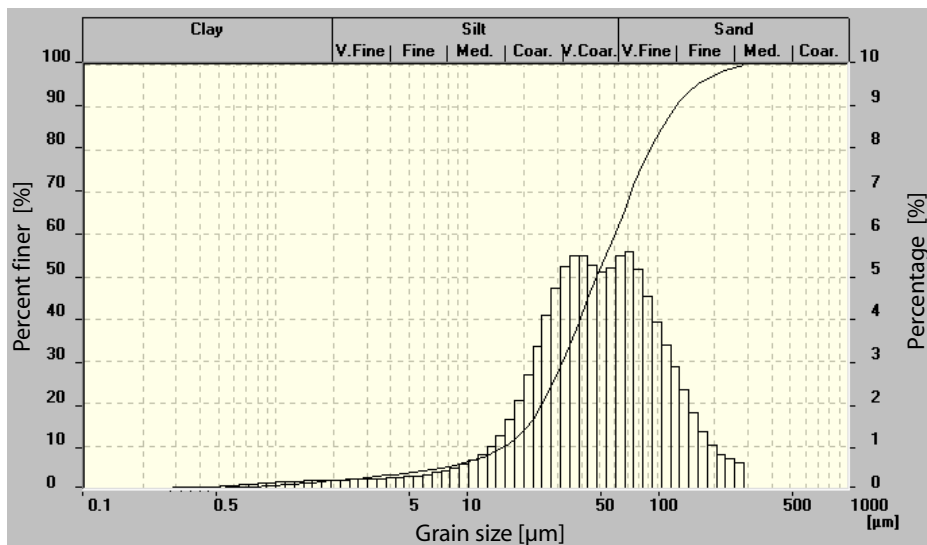


Figure 3.7: Grain size distribution of selected sediment (fine grinded wall nut shells).

Based on the qualitatively experiments of the first two materials obviously, only model materials with smaller density can satisfy the demands of threshold of motion and suspension similarities. Because of that a ground polymer with a density of $1135 kg/m^3$ and d_{50} , of $90 \mu m$, and walnut shells # 80, $d_{50} = 210 \mu m$, density $1500 kg/m^3$ were tested.

Finally walnut shells particle were selected as a material due to several reasons. They are easy to mix and to use in the mixing tank. Furthermore, they produce a complete homogenous distribution in the mixing tank and over the entire surface of the basin.

To ensure a uniform mixture in the mixing tank and reservoir basin, the density of the sediment mixture as well as the clear water were measured before and during the test by means of a turbidity meter.

Walnut shell particles are non cohesive and light grains, which have a well known and relatively narrow particle size distribution, as well as a small settling velocity of $1 mm/s$. The grain size distribution of the sediment material was determined with a Laser-Particle-

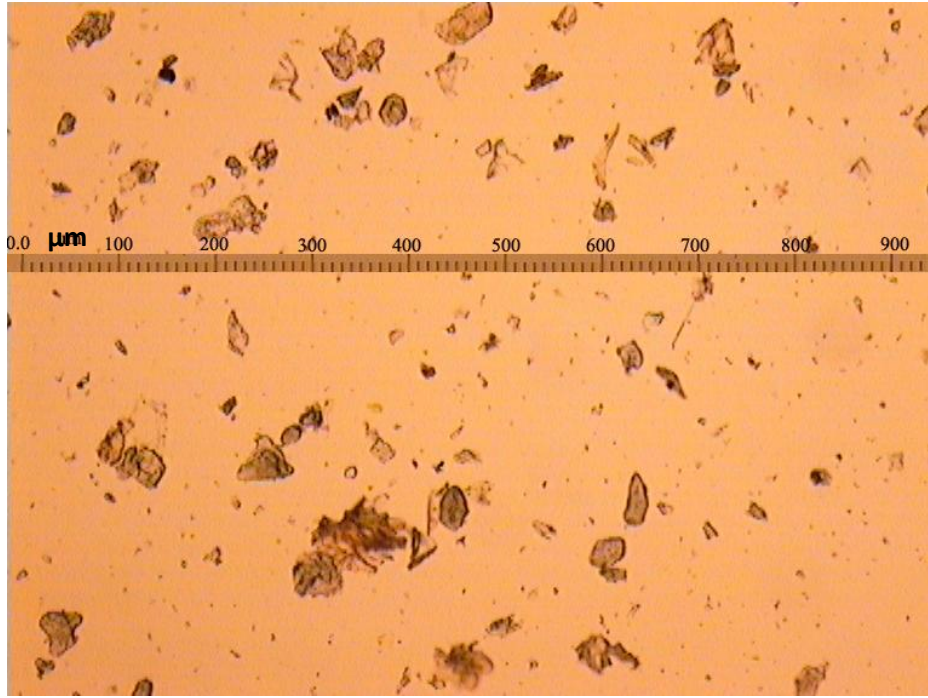


Figure 3.8: Microscopic photograph of the sediment particles used in the experiments (scales are in μm).

Table 3.3: List of parameters describing the physical properties and grain size distribution curve for the sediment material.

ρ_s [kg/m ³]	1500
d_{50} [μm]	50
d_{84} [μm]	115
d_{16} [μm]	22
$\sigma_g = \sqrt{d_{84}/d_{16}}$ [-]	2.4

Sizer instrument (Analysette 22) and is shown in Figure 3.7.

The material has a fairly narrow grain size range, but the frequency histogram is skewed towards large grain sizes, which is typical for ground particles. The particles have a median diameter, d_{50} , of 50 μm . With a standard deviation, σ_g , of 2.4 the grain size distribution cannot be considered being uniform. The uniformity is 0.70, therefore, some grain sorting effects may occur. In Table 3.4.4.1 some of the most commonly used parameters for describing the properties and grain size distribution for the sediment are summarized.

As shown on the microscopic photograph in Figure 3.8 the particles are not perfectly spherical but have slightly angular shapes. Moreover, the particles have heterogeneous nature (mixed component, size, shape) as well. The sediment material absorbs water and thereby changing density as described hereafter in the next Section 3.4.4

3.5 Measurement techniques

Several parameters were measured during every test, namely: 2D surface velocities, 3D velocities, thickness of deposited sediments, concentration of sediment inflow and outflow, water level in the basin, and discharge (see Table 3.4). All techniques have been showed in a series of publications in (Kantoush et al., 2008; Kantoush and Schleiss, 2007; Kantoush et al., 2007e).

Table 3.4: Model parameters and instrumentation used.

Measured parameters	Instrument	Resolution	Dimension
Sediments thickness	MiniEchoSounder UWS	± 1	[mm]
Sediments concentration	Turbidity meter	± 0.001	[g/l]
3D velocity	UVP	± 0.001	[m/s]
2D Surface velocity	LSPIV	± 0.001	[m/s]
Discharge	Flow meter	± 0.1	[l/s]
Water level	Ultrasonic probe	± 1	[mm]

3.5.1 Ultrasonic Doppler Velocity Profiler (UVP)

The velocities were measured by means of an Ultrasonic Doppler Velocity Profiler (Met-Flow, 2005, UVP-DUO), which allows an instantaneous measurement of the 1D velocity profile over the whole flow depth Takeda (1995). The UVP consists of a probe (40mmx13mm) emitting a pulse of ultrasound (US), which travels along the measurement axis, and then switches to a receiving or listening phase. When the US pulse hits a moving particle, part of the ultrasound energy scatters on the particle and echoes back.

The UVP measures the time delay of the echoes to reach the transducer and its Doppler frequency shift, thus, by knowledge of the speed of sound in the medium, UVP determines position and velocity of the particle. This makes UVP able to establish the instantaneous velocity at many separate space points (channels) along the measurement axis, permitting calculation of both time and space-averaged flow variables. It is possible to display the echo signal from the probe by the use of an oscilloscope, which is particularly helpful in recognizing the position of a wall or obstacles in the flow (Met-Flow, 2005). The position, size, and spacing of the measurement locations are dependent on the probe frequency and the maximum velocity setting.

UVP techniques are frequently used in experimental design of hydraulic structures and river training works. Examples of application are small-scale physical models of rivers, mobile beds (Takeda, 1995), side weirs (Rosier et al., 2004b), curved channel flows (Hersberger, 2002), turbidity currents (De Cesare et al., 2001; Oehy, 2003), shallow reservoir sedimentation (Kantoush et al., 2006b). An overview for flow velocity measurements using UVP of 10 years experience in hydraulic modeling applications at LCH is given by De Cesare and Boillat (2006).

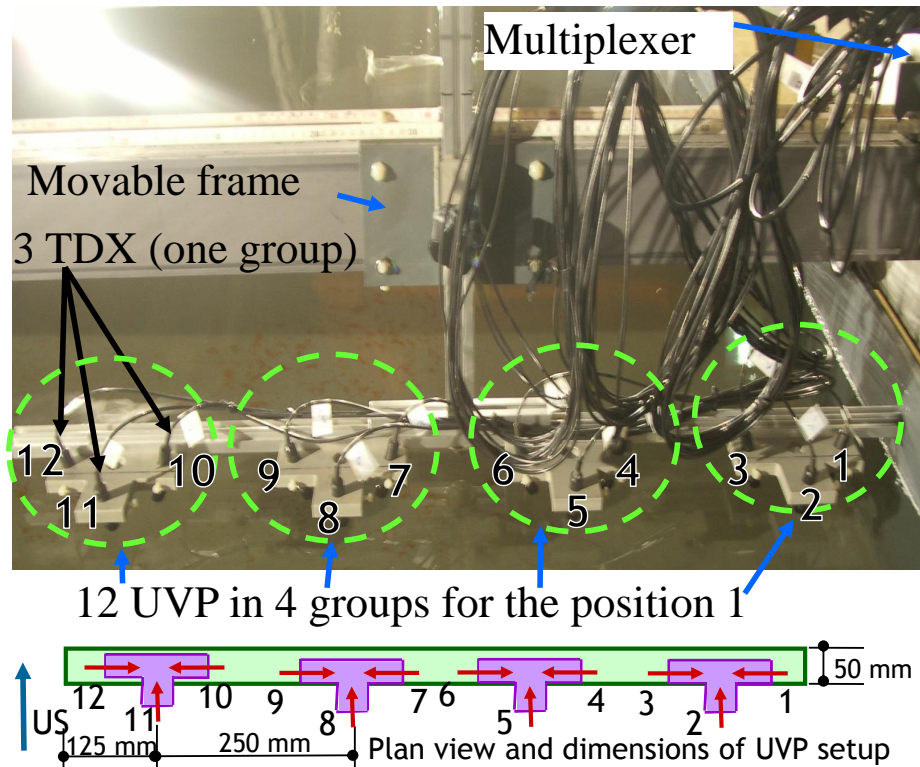


Figure 3.9: Above: Scheme of UVP installations and data acquisition, Below: Plane view and dimensions of UVP.

The measurement probes were fixed on a support in groups of three, allowing the measurement of the 3D flow field (Fig. 3.9). The technical specification of the velocity profiler and the probes can be found in Figure 3.10. Since the number of measurement points was high, four PVC plates were mounted on the measurement frame, allowing to record four groups of three 1D profiles (constituting one 3D profile) to accelerate the data acquisition process (see Figs. 3.9 & 3.10). Measurements are carried out at different time instants. To cover the whole cross section of the basin, 4 positions were chosen along the cross section; each position containing four groups of three probes (see Fig. 3.10).

All twelve probes were installed on a frame which moves in the two horizontal directions. The probes were inclined at 20° to the vertical and had an emitting frequency of $2MHz$ see Figure 3.12. A multiplexer allowed switching between the different transducers (Fig. 3.9).

Velocity profiles were recorded for all points on a 25 cm x 50 cm grid in transversal and in flow direction respectively see Figure 3.10.

For each velocity profile, 24 data points are recorded with time, with a spatial resolution of 256 points over the flow depth. The multiplexer then switches to the next probe to record 24 profiles. Consequently, the measured flow field is not an instantaneous 3D field (see Fig. 3.12). Longer duration samples were carried out to study the effect of the sampling time on the time-averaged velocity. UVP performance and parameter settings have been optimized by preliminary tests.

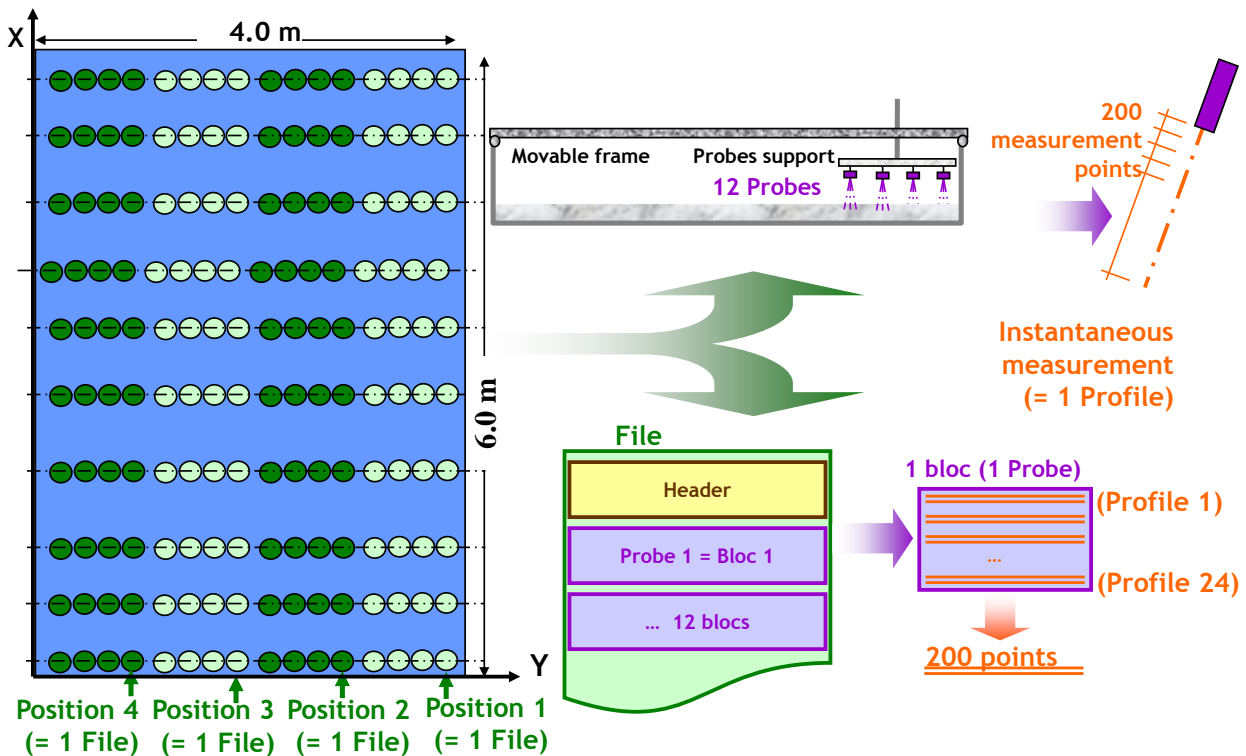


Figure 3.10: Frame positions and file format of velocity raw data acquisition and UVP technical specifications.

Several preliminary tests have been carried out for optimization of UVP parameters specifications. Due to low velocity and shallow flow injection for tracer has to be used. Hydrogen bubbles can be used as fluid tracers for providing echo, i.e., ultrasound reflector. In the performed tests, the bubbles are generating using an array of horizontal stainless steel wires with a diameter of 100 μm with a vertical spacing of 1 cm.

With hydrogen bubble the local obtained echo was sufficient near the transducer but due to the low velocity the bubble did not distribute quickly to the other transducers. Moreover bubbles did not generate in the transducers directions; consequently a fine suspended sediment particle (Walnut crushed shells) has been used to generate US echoes. These

are non cohesive, light weight and homogeneous particles with very low settling velocity to guarantee a completely mixing state in the entire volume. Particle settling velocity is less than 1 *mm/s*. Vertical velocities are approximately 25 times higher than the particles settling velocities. The fine particles with low specific gravity have negligible influence on the vertical velocity measurements.

In order to extract the 3D velocity field in twelve cross sections over the whole reservoir, the acquired binary velocity file needed some treatment. First the twelve 1D records were read from the raw data file, followed by the calculation of the velocity time-averaged measured components (average of 24 profiles).

Then projections of these values to obtain perpendicular velocity components (*u*, *v*, *w*) covering the whole measurement depth. Assuming that the measured velocity components are *a*, *b*, and *c* (Fig. 3.11), the velocity components in the intersection point are given with (see the 3D decomposition vectors in (Fig. 3.11):

$$u = \frac{-2c + a + b}{2 \sin \theta} \quad (3.18)$$

$$v = \frac{a - b}{2 \sin \theta} \quad (3.19)$$

$$w = \frac{a + b}{2 \cos \theta} \quad (3.20)$$

After rearrangement of the velocity profile, the data was exported to a text file for future automatic treatment with Matlab. The pervious procedure for obtaining velocity components is real only at the intersection point of the three probes, because it is the only point which has 3D flow. Due to the inclination of the probes by small angle 20°, small dynamic rang around 6, low velocity and stable structures in the basin, small water volume at every probe channels distort the velocity by 6%, and the probes located near from each other with distance 49 *mm* same calculation methods was used at the whole measurement depth (see the support geometry dimensions Fig. 3.12).

To study the influence of the distance between probes, the same test was repeated with another distance between probes as shown in Figure 3.13. The probes were located more near from each other with distance 24.5 *mm* .

Another configuration has been setup to study the vertical velocity components on shallow reservoir sedimentation patterns. Only one vertical probe was installed at each support as shown in Figure 3.13. Four vertical probes were moved from one position to another to measure the entire cross sections. To study the width of the reservoir geometry on the 3D velocity several experiments have been carried out for four reservoir width configurations (4, 3, 2, and 1 *m*).

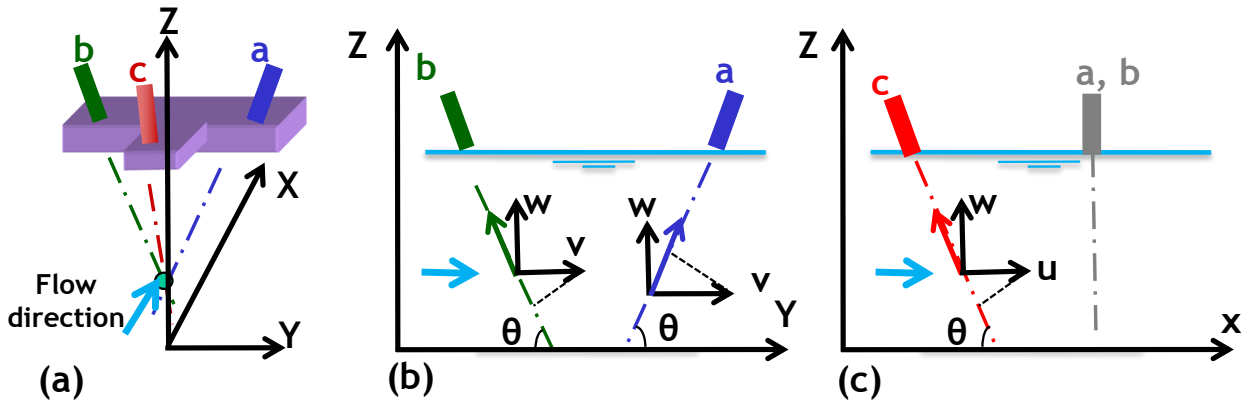


Figure 3.11: (a) 3D velocity vector decomposition, (b) Vector decomposition in plane Y, Z, (c) Vector decomposition in plane X, Z.

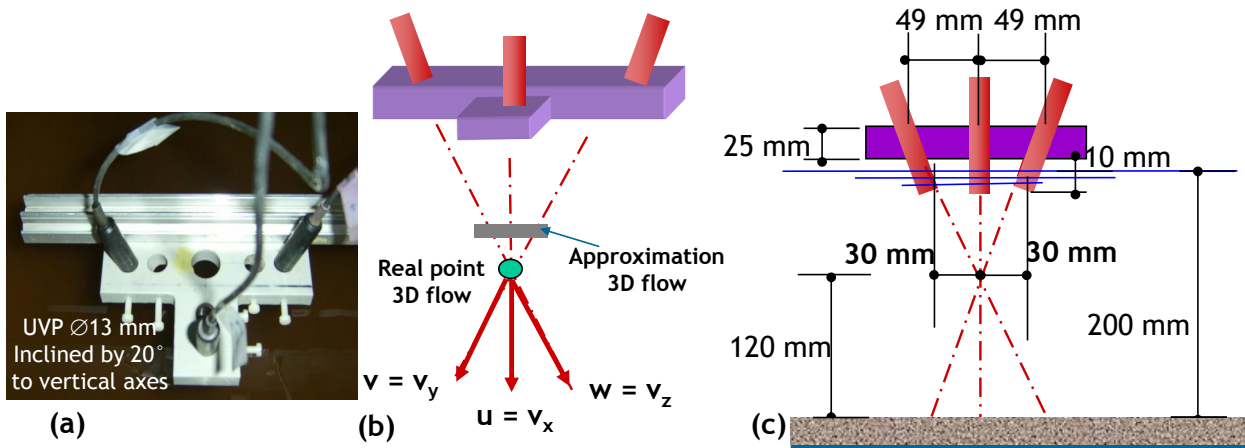


Figure 3.12: (a) Photo of one group of three probes (b) Scheme of 3D treatment, (c) Geometry of the probe support

3.5.2 Large-Scale Particle Velocimetry (LSPIV)

Large-scale particle image velocimetry (LSPIV) is an efficient and powerful technique for measuring river surface velocities. LSPIV is an extension of conventional PIV for velocity measurements in large-scale flows. While the image and data-processing algorithms are similar to those used in conventional PIV, adjustments are required for illumination, seeding, and pre-processing of the recorded images. Surface flow measurements with PIV are described for instance in Adrian (1991).

In hydraulic engineering, this technique has so far mainly been applied for surface velocity measurements of water and ice in very uniform flow fields as well as in groyne field experiments (Emttea et al., 1997; Fujita et al., 1998; Uijttewaal et al., 2001; Weitbrecht

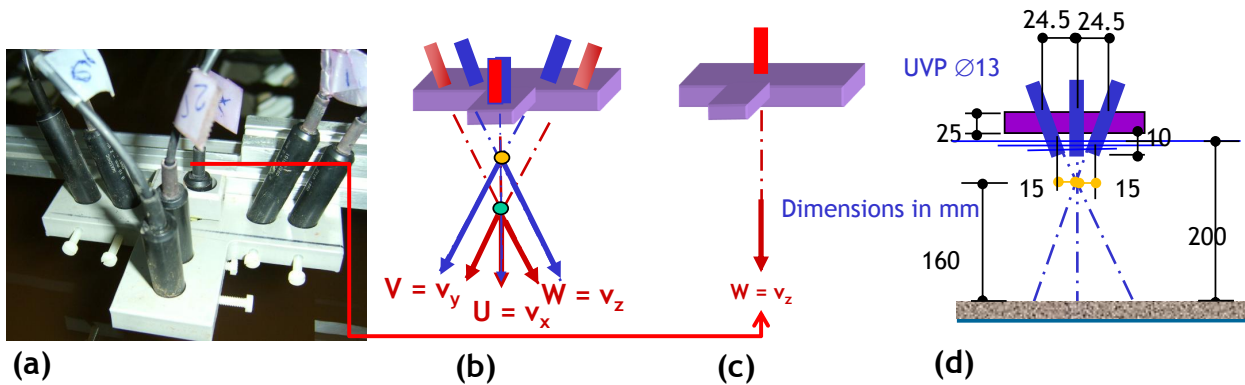


Figure 3.13: Above: Scheme of UVP installations and data acquisition, Below: Plane view and dimensions of UVP

et al., 2002). PIV measurements have not yet been applied to define detailed flow patterns in differently shaped shallow reservoirs on rivers. Kantoush et al. (2007f) investigated surface velocity in shallow reservoirs with ten different geometries.

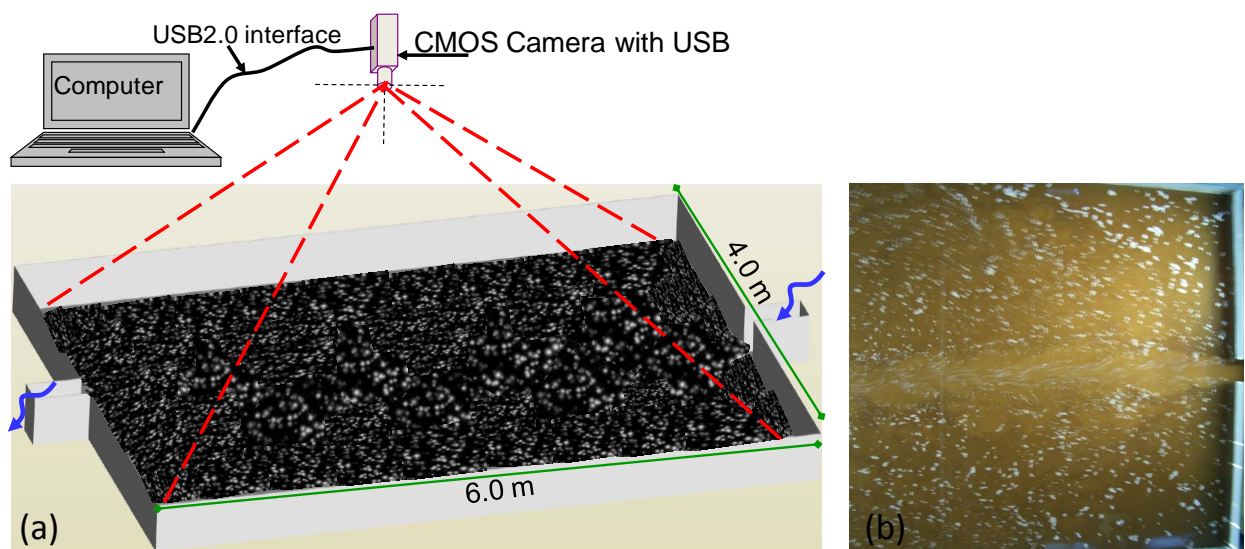


Figure 3.14: (a) Scheme of LSPIV installations and data acquisition (b) Picture from the top during PIV recording.

A digital camera was used to record the images. The camera was fixed above the basin covering an area of 4.0 m by 5.0 m , i.e. a length of 0.5 m was missing at the upstream and downstream ends. The recorded images were systematically transformed to remove perspective distortion from the objective lens using PTLens software and then processed using FlowManager software from (Dantec Dynamics, 2007). Seeding was obtained by means of white plastic particles and reasonable lights as shown in Figure 3.14. The plastic particles

had an average diameter of 3.4 mm and a specific weight of 960 kg/m^3 . The dispersed light allowed recording their positions at two successive instants by means of a video camera .

Conventional PIV determines the velocity of a fluid element indirectly by measuring the velocity of tracer particles within the flow. Rather than finding the displacement of a single seed particle, the PIV technique tracks the movement of a group of particles within a designated area, the so-called interrogation area. Figure shows a typical setup for conventional PIV recording with the different PIV steps, which are briefly explained in the following:

Step 1: A difficult part of the experimental setup is the choice of proper tracer particles. In our case of surface velocity measurements the tracer particles have to float at the water surface so that the material has to be somewhat lighter than water. Particles which are too light can be affected by air flow above the water surface.

The flow is seeded with plastic particles (with average diameter 3.4 mm and specific weight 960 kg/m^3), which are then illuminated. The dispersed light allows their positions to be recorded at two successive instants (Fig. 3.16) by video (SMX-155, monochrome, 1.3 megapixel, CMOS camera with USB2.0 interface and frame rate up to 33 FPS). To capture large measurement planes while the space above the experiment is limited to a maximum of 3.5 m , an f-mount, 15 mm wide angle lens (C-Mount) with small distortion errors was used.

Step 2: The plan view (measurement plan) is divided into several small sub-areas, known as interrogation areas, or IA (see Fig. 3.16).

Step 3: In each IA, the cross-correlation algorithm is applied in order to calculate the shift of the particles, ΔX , in the time between two images, ΔT (Fig. 3.16).

Step 4: A raw vector map is formed from the group of vectors calculated in each IA, showing the velocity field of the measured plane view. This is done for every area, giving a $2D$ map of the instantaneous velocity field at the time of the recording.

Step 5: From the velocity values given by the raw vector map, it is possible to calculate other types of data, such as streamlines, vorticity and vector statistics.

A calibration task required checking the accuracy of the LSPIV system. This task simply entailed comparing PIV velocities with those measured by timing hand released tracers as they moved known distances in the model. As the dimensions of the area of interest and the period between images are preset, velocities follow directly. In actuality, this calibration step is not needed, but it provides additional confirmation of the PIV measurements.

At LCH the technique has been applied by Kantoush et al. (2007a); Kantoush and Schleiss (2007) for surface velocity measurements of different shaped shallow reservoirs. Measurements were also carried out in other applications such as in groyne field experiments, prototype model of river junctions, approach flow in spillways and dams and oil spill with rigid and flexible barriers.

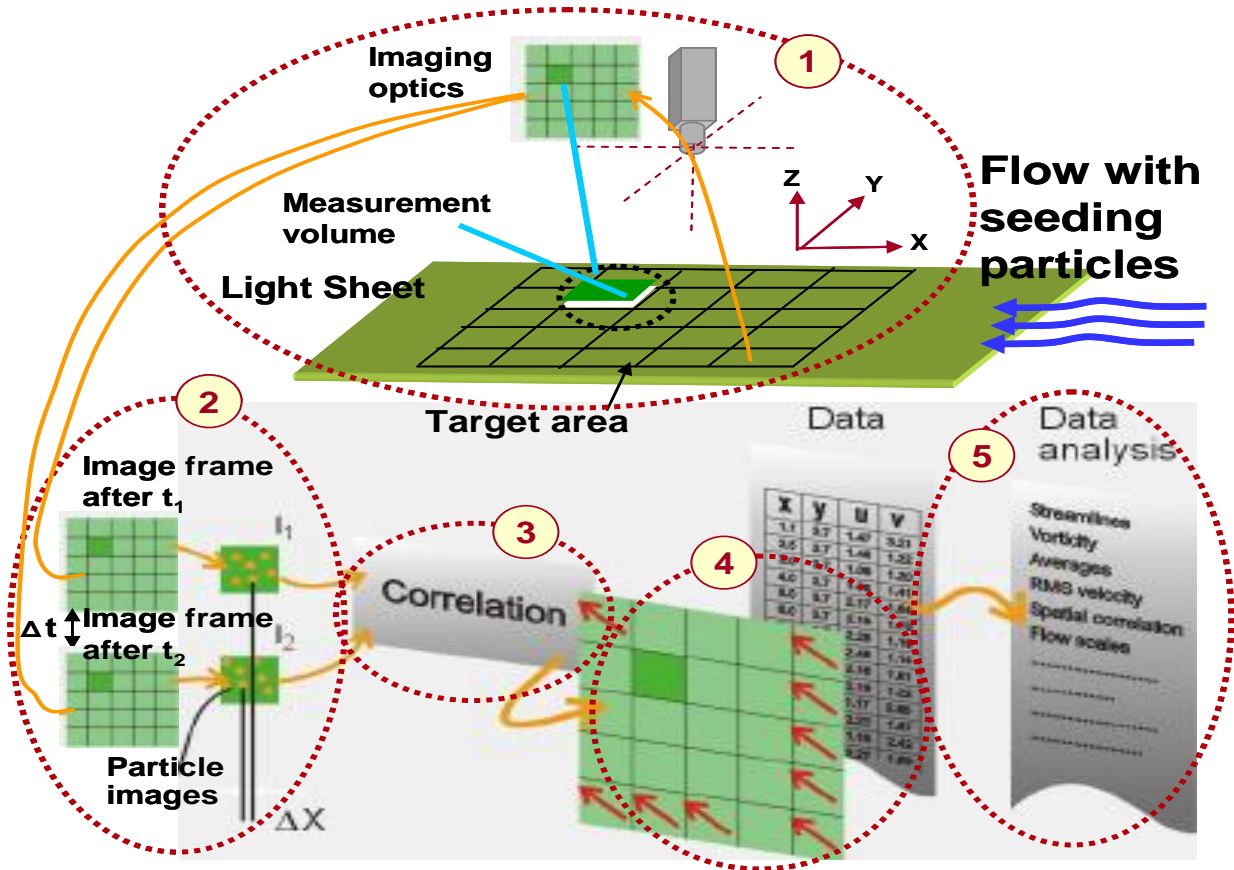


Figure 3.15: Specification steps of LSPIV methodology (Dantec Dynamics, 2007).

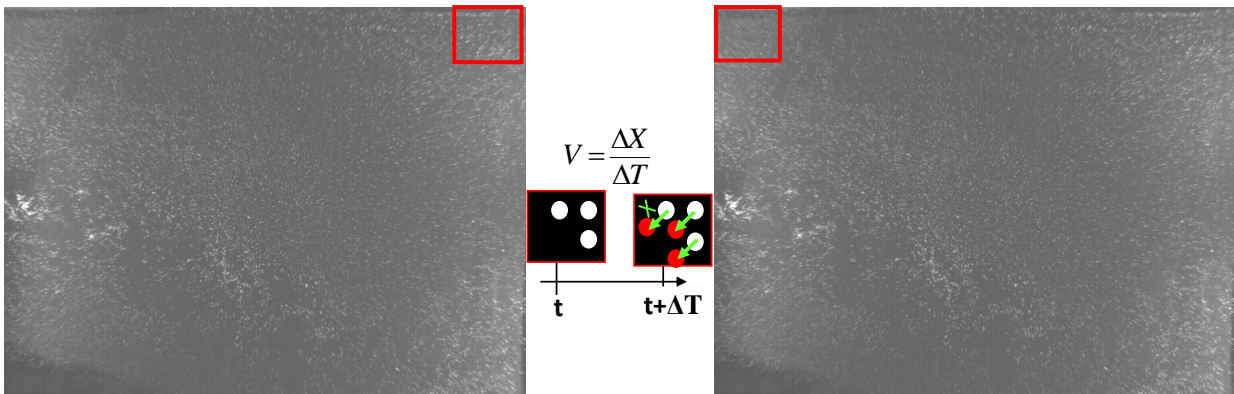


Figure 3.16: Typical PIV image pairs and the basic principle scheme of PIV

3.5.3 Mini-Echo Sounder (UWS)

Measurements of sediment thickness and the total volume of sediment deposited in the basin during the experiments are essential data to assess both quantitatively and qualitatively the siltation problem. The evolution of bed topography in shallow basins with different

geometries was conducted by using UWS.

The Mini-EchoSounder has proved to have a high potential for measuring small bed changes and is believed to be applicable in field tests as well. It is greatly desirable to measure the deposition thickness during physical experiments of sediment transport and depositions. Methods are available for measuring the sediment depth levels in both field experiments and laboratory conditions.

To find the appropriate method suitable for different engineering applications objectives (turbidity currents, wastewater treatment plants and sedimentation tanks, shallow reservoirs, etc) is still a challenge. For field measurements the majority of researchers has employed either acoustic or laser range finding devices (e.g. Irish and White, 1998; Williams and Jackson, 1998).

In the case of laboratory scale studies, the current available techniques include stereo photography (Hancock and Willgoose, 2001), infrared beams (Richards and Robert, 1986), sonic (Dingler et al., 1977), vacuuming (Altinakar et al., 1996; Garcia, 1994) ultrasonic (Best and Ashworth, 1994) depth profilers, and laser 3D-scanning devices (Lague et al., 2003). Continuous measurements of sediment depth have been made in a subaqueous environment by measuring the electrical resistance of particle layer using an array of electrodes in the base of the tank beneath layer (Oehy, 2003; Rooij et al., 1999).

In recent years, pattern matching techniques have been employed by comparing images before and after depositions (e.g. Munro et al., 2004; Rosier et al., 2004a).

In the present study bed deposition measurements of shallow reservoir with different geometries using Echosounder technique have been conducted. For monitoring of in-water sedimentation and erosion processes in laboratories the applied measurement system always plays a key role. Instead of long some draining of the basin in order to measure the current-generated change in bathymetry with laser instruments along the dry bed it is easier and more time saving to use echo sounder to measure the bathymetry during or directly after the test.

Particularly in small-scale experimental set-ups it is imperative to avoid any disturbances that may affect the results of the experiments. Releasing the water might have some influence on the process-generated bathymetry by consolidation. Advanced echo sounders specialized for laboratory purposes are alternative to laser technology.

Due to their drastically narrowed sound beam in combination with high spatial and temporal resolution much lower than one millimeter and their wide range from 2 *cm* up to 15 meters (depending on parameter setting) the accuracy of a millimeter can be guaranteed. The technical achievements like narrow beam pattern in combination with high resolution are the main reason for the use of lab echo sounders as alternative measurement devices

3.5.3.1 Principles of measuring distances by means of ultrasound

The UltraLab UWS - Echosounder is a linear system single beam echo sounder working with an ultrasound frequency of 1MHz and it has to be immersed in water or in contact with a fluid domain. The advantage of the used frequency is not to penetrate into the ground on one hand and to measure with a high accuracy on the other. Equivalent to other single beam systems commonly used for outdoor purposes, the measurement method is based on sound propagation with time. The functionality of common echo sounder is depicted in Figure 3.17.

The transmitted ultrasound impulse is emitted by the sensor's membrane driven by piezo electric crystals, which vibrates with a defined frequency for 1 millisecond. The sound travels through the water with a sound velocity of approximated 1483 m/s (parameter can be set) and hits an object (target), e.g. bottom contour, in a certain distance. Thanks to the achievement to focus the acoustic beam below 3° , the footprint of the sound onto the surface, e.g. model bed, is very narrow, enhancing the spatial resolution.

Such sensor characteristics are rather crucial for precise measurement of object distances and therewith bathymetric contours. These objects or model bed contours serve as acoustic targets for the sound beam which is reflected at their surface as an acoustic echo. During the so called delay time - starting right after the sensor had emitted the acoustic beam - the sensor serves as a receiver. The first echo received by the sensor will be used for distance calculation.

All other echo coming in later will be ignored for processing. The measured travel time of every single acoustic sound impulse (ping) is processed to gain the target distance. This value will be averaged with the results deriving from following pings in respect to temporal resolution. Next to such averaged values a tolerance buffer (range of expectation) can be set.

3.5.3.2 Characteristics of UltraLab UWS - Echo Sounder

The technological design of echo sounders and their physical characteristics determine the possible application for the right measurement tasks. The sound distribution is one main criteria. The membrane's diameter is 20 mm . The Fresnel-Zone ends up in 67.6 mm from the sensor's membrane, where the curves become most narrow. The solid line represents the opening angle of 6 dB which is equivalent to 2.2° . Within the enclosed spatial 3D-volume 75% of the whole sound energy can be found there. Outside the dotted line (20 dB opening angle = 4.6°) only 1% rest energy can be measured.

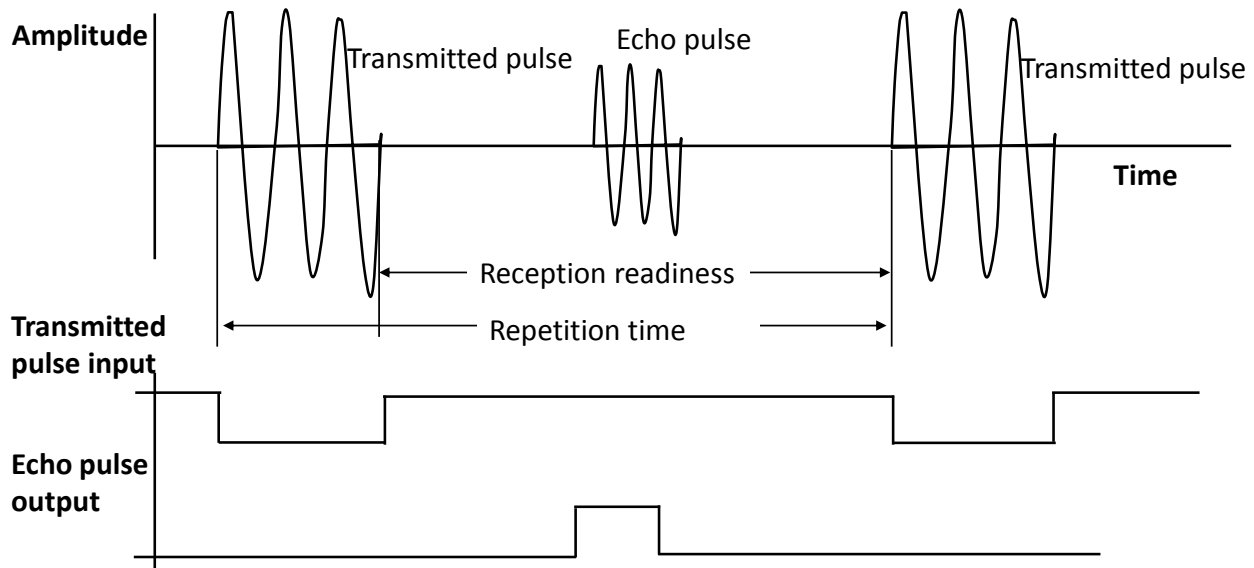


Figure 3.17: Signals at the output of the test-socket seen by an oscilloscope

3.5.3.3 Parameter setting

For calibration purposes the *sound velocity* has to be determined and set in as parameter. For short distances below one meter it is recommendable to decrease the *transmitting power* in order to reduce the acoustic energy within the basin.

Due to particle suspension within the water column the sound can be scattered at a suspension cloud, too. By reducing the *receiver amplification* the sender is not listening to all these slightest scatter echoes but to the real echoes from the surface.

The *delay time* is the moment when the echosounder is not transmitting the sound but receiving the echos before it starts again with another impulse. The smaller the basin is the more acoustic vibration (resonance) stays for a defined time which is due to echos from all the walls.

To be sure that all echos are gone it is better to increase the delay time before starting with the next ping. In case some suspension clouds between the sensor and the bottom contours are disturbing it is recommendable to reduce the *measurement window*. This means that the time of listening for the echos will be shortened to the expected distance. Only those echos within that chosen time slot will be processed. The expected range is recalculated after each measuring cycle and is updated for the current mean value calculation.

For high signal-to-noise ratios, the expected range should be programmed as small as possible. This increases the accuracy of the output data at the most. The mean value is calculated only from those values which fall within the *expected range* (in percent of the actually measured distance values).

The sounder works with an ultrasonic-impulse-run time procedure. UWS first emits an

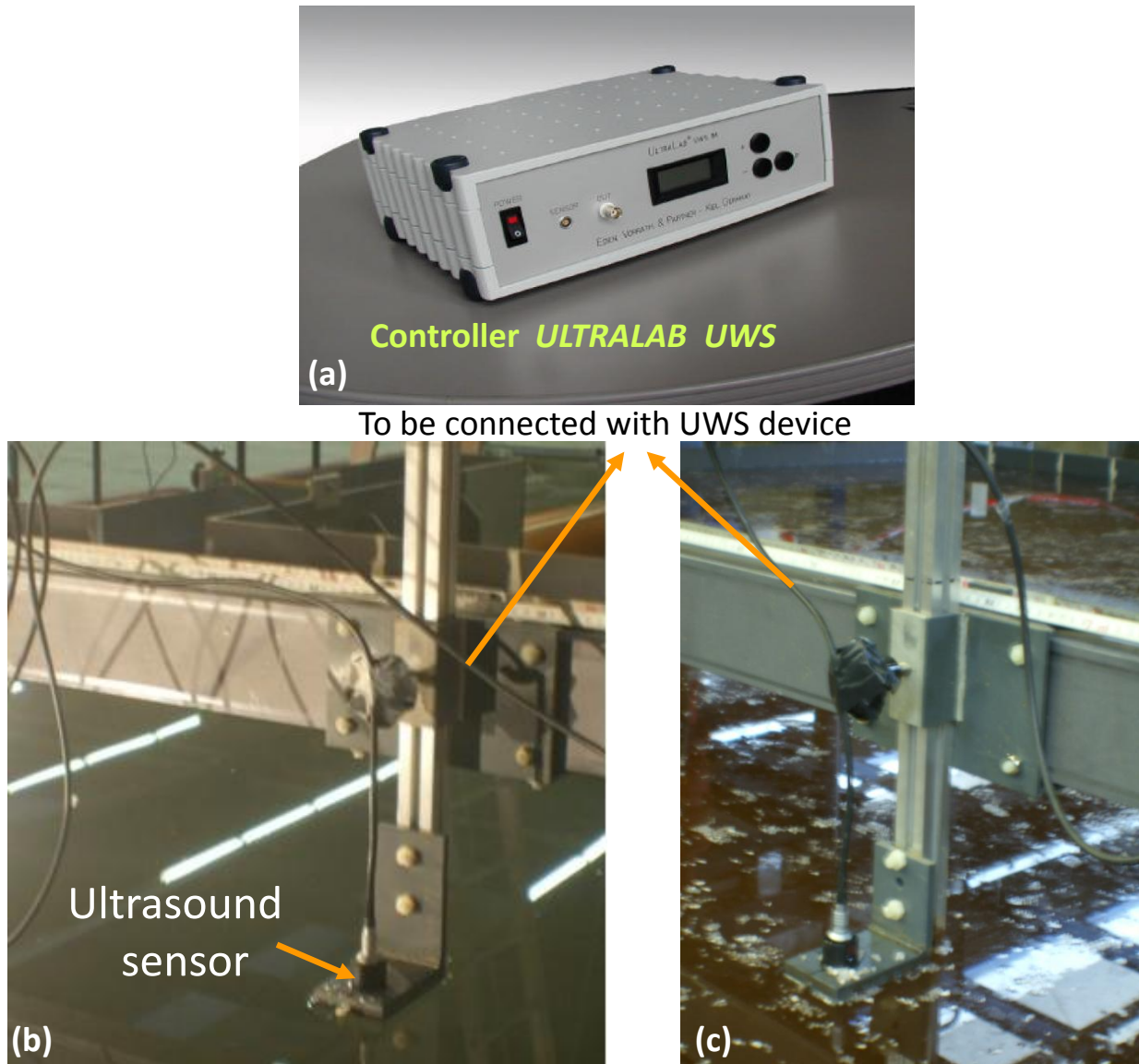


Figure 3.18: (a) Controller unit of Ultrasound sensor (b) Miniature echo sounder mounted on the frame measuring the initial surface with clear water (before sediment deposition) (c) Miniature echo sounder mounted on the frame measuring after sediment deposition

acoustic signal. The transmitted ultrasound impulse is then reflected on any object that serves as a target. This acoustic reflection (echo) propagates in the space and is received by the ultrasound sensor.

To measure the effective distance between target and sensor, at first the run-time which the sound needs from the sensor must be determined and then the run time for the signal from the sensor to the target and back to the sensor again must be determined. Knowing the run time and the sound velocity, the target distance can be computed.

The sounder was mounted on the movable frame (Fig. 3.18) and scanned the surfaces of the entire basin area with clear water (initial state before sediment entrainment) and after sediment depositions. The differences between the two surfaces before and after depositions is the bed thickness (Figs. 3.18 a & b).

Moreover, several reference points were taken manually for calibration comparison with the UWS measurements. It was found that the UWS measures with a high accuracy of ± 1 mm and it's similar for the manual measurements.

Several preliminary tests were conducted for the calibration process for UWS measurements while suspended sediment material crushed walnut shells was used. It was found that UWS able to measure the thickness of a layer of the reference points, independent of the flow conditions or presence of suspended sediment above the layer.

Nevertheless, some anomalous spikes are observed in some points due to suspended sediment clogging. The measured cross sectional profiles were generally 0.05 m apart. In some cases, a 0.025 m spacing was tested, starting and ending at 0.10 m from the basin side walls, i.e. covering a width of 4.0 m. The measured longitudinal profiles were spaced 0.20 m apart. In some cases, a 0.1 m spacing was tested, starting and ending at 0.05 m from the up- and downstream boundaries.

3.5.4 Suspended sediment concentration (SSC)

Accurate determination of suspended sediment concentrations (SSCs) and associated suspended sediment fluxes in rivers is of great importance for many aspects of water resource development and river basin management, including estimation of the useful life of reservoirs. For estimating suspended sediment concentration (SSC) in reservoirs and rivers, turbidity is potentially a much better predictor than water discharge. With sensors calibrated to give a linear response to formazine standards, turbidity and sediment concentration should have a linear correlation close to unity for a given size and composition of suspended particles (Foster et al., 1992; Gippel, 1995).

However, the usefulness of the information obtained depends heavily on the existence of a close relationship between fluctuations in suspended sediment concentration and turbidity and the calibration procedure that relates suspended sediment concentration to the turbidity meter's signal. The detailed turbidity record often contains the signature of sediment inputs to the channel from erosion and mass wasting (Lewis and Eads, 1996).

Two sensors SOLITAX sc were installed at the inlet and outlet channels for online suspended sediments measurements as shown in Figure 3.19. The release suspended sediment concentration is important to determine the trap efficiency of the reservoir. Moreover, a third sensor COSMOS-25 was installed at the outlet channel for comparison between the two measurements.

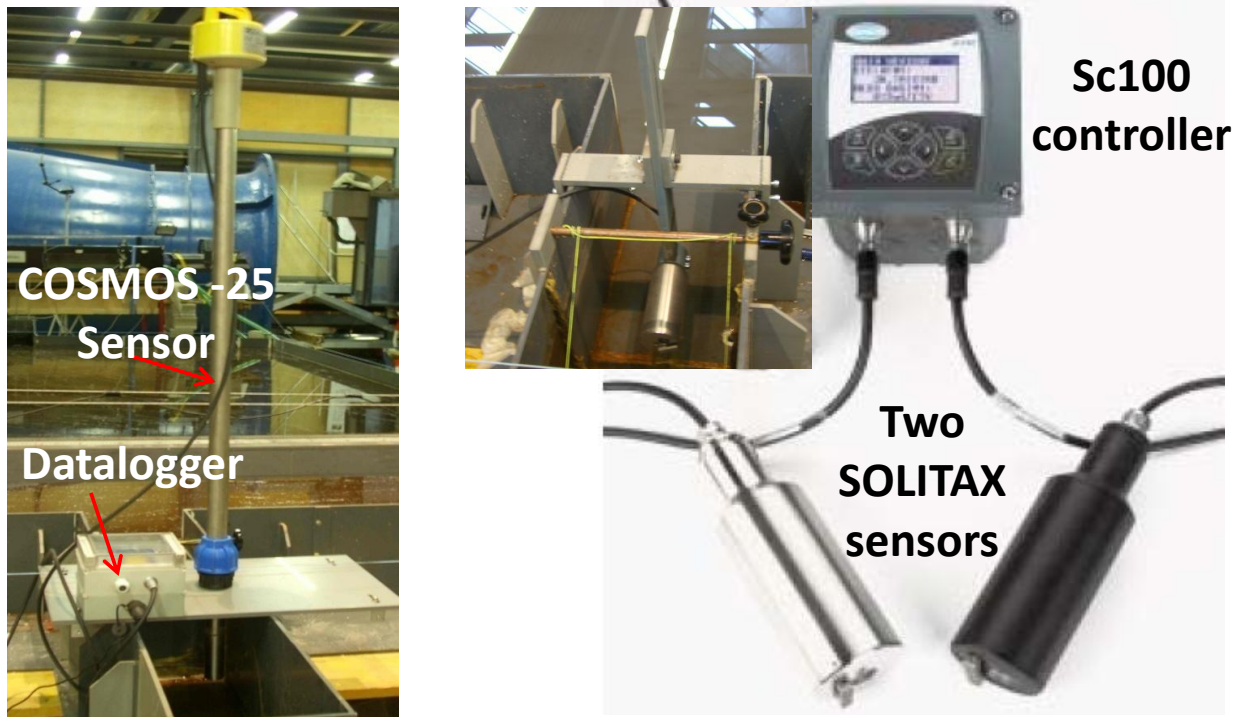


Figure 3.19: (a) COSMOS-25 turbidity and suspended Solids sensor with datalogger from ZÜLLIG company. (b) SOLITAX sc turbidity and suspended solids sensor and controller unit from HACH LANGE company.

3.5.4.1 Measuring principle

Automated measurement of suspended sediments is crucial to the study of sediment transport. The short duration, high-intensity flows that are responsible for a large fraction of sediment movement are best observed by continuous monitoring systems.

The measuring principle is based on a combined infrared absorption scattered light technique that measures the lowest turbidity values in accordance with DIN EN 27027 just as precisely and continuously as high sludge content.

Figure 3.20(a) shows an LED (light-emitting diode) light source in the analyzer's sensor transmits a beam of infrared light into the sample stream at an angle of 45° to the sensor face. A pair of photoreceptors in the sensor face detects light scattered at 90° to the transmitted beam. Reversal point depends on sludge structure and on arrangement of transmitter and receiver. Signal depends on coloration as shown in Figures 3.20(b) and (c). In models that measure suspended solids, a back-scatter photoreceptor positioned at 140° to the transmitted beam detects the light scattered in high-solids sample streams. Turbidity measurements often can be used as a substitute for gravimetric solids measurement.

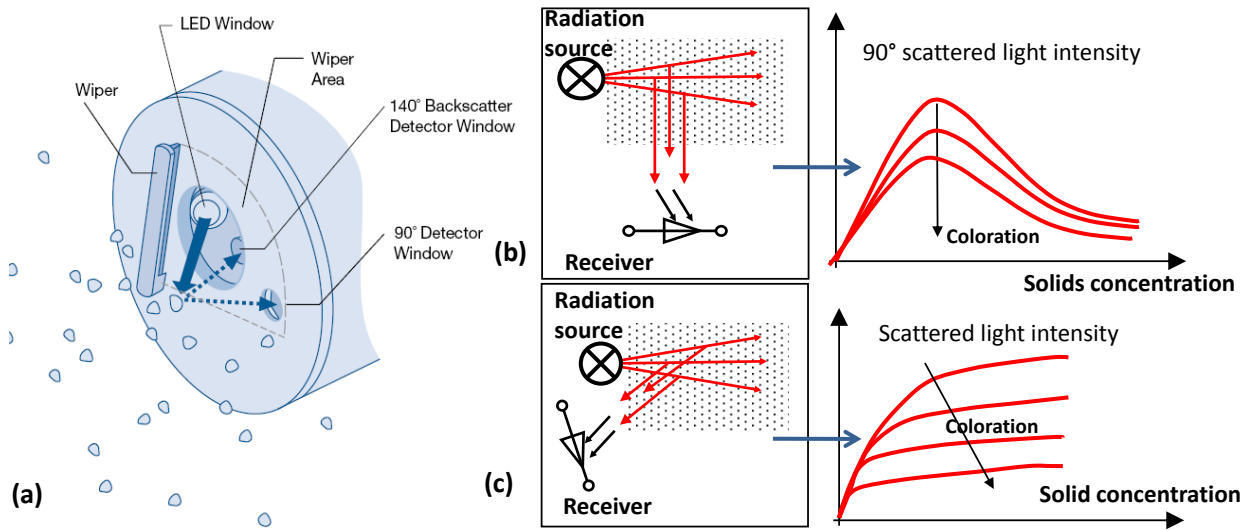


Figure 3.20: (a) Optical measuring principle; (b) The infra red duo scatterd light principle scattered light intensity at 90°; (c) The infra red duo scatterd light principle scattered light intensity at 140° (SOLITAX sc, User Manual, 2005)

3.5.4.2 Laboratory calibration based on suspensions of known concentration

The sediment concentrations of the suspensions material using the crushed walnut shells were regressed against the equivalent values of turbidity associated with the laboratory measurements. Turbidity is an optical measure of the cloudiness of water caused by light scattering from suspended particles.

Two basic steps for calibrating a turbidity meter are commonly involved. The first uses a standardized suspension to test equipment function and to confirm sensor efficiency and stability. This step has been done by the instrument company for documenting instrument drift and other evidence of temporal variability in the probe's response to changes in concentration.

The second step focuses on establishing the precise relationship between SSC and the turbidity signal. Since this calibration relationship will depend on the properties of both the sediment particles and the water, it will be laboratory-specific; therefore, it was established for walnut shells. This relationship was derived in the laboratory by placing the probe in suspensions of crushed walnut shells concentration, representative of the suspended sediment transported in the basin, and covering a range of different sediment concentrations ranging between 0.1 and 10 *g/l*. The obtained calibration relationships of the two different company probes are shown in Figure 3.21.

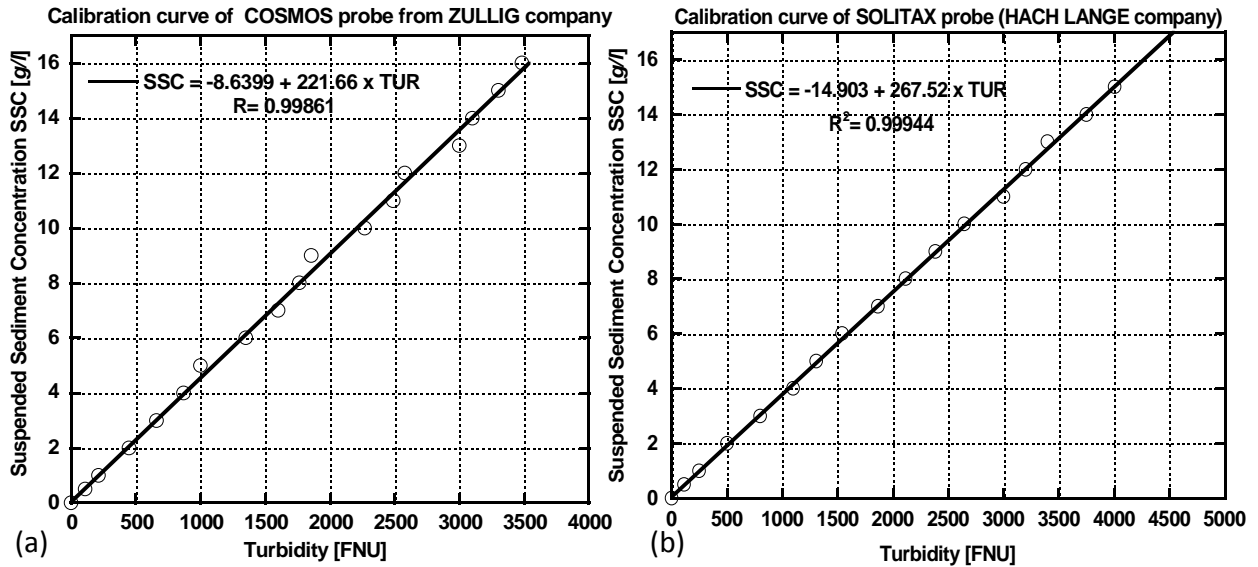


Figure 3.21: (a) The relationships between the suspended sediment concentrations (SSC) and the turbidity (TUR) for SOLITAX probe (b) The relationships between the suspended sediment concentrations (SSC) and the turbidity (TUR) for COSMOS probe.

3.5.4.3 Data reliability and errors

Assuming that there is a close relationship between fluctuations in sediment concentration and turbidity and considering, first, the reliability of the point measurements of SSC provided by a turbidity probe installed at a particular point, errors may stem from several sources, including:

- i) instrument errors associated with the equipment used,
- ii) systematic errors introduced by the calibration procedure employed, and
- iii) methodological errors caused by indirect measurement of the variable under study.

Further uncertainties are introduced if the point measurement of sediment concentration is assumed to be representative of the cross-section, since it is well known that SSCs will vary through the cross-section.

A location towards the edge of the channel may not be representative of the cross-section and, if the position of the probe is fixed, the precise relationship between the concentration at the measuring point and the mean concentration in the cross-section may vary with changing location and discharge.

To determine the error of the concentration measurement, 5 pairs of samples (SSC and TUR) were again used. The turbidity values were substituted into the regression equation

and a set of concentration values was obtained. The average error in SSC associated with the soil method calibration was established, using the following equation:

$$error = \sqrt{\sum \frac{(SSC_{calc} - SSC_{known})^2}{n - 1}} \quad (3.21)$$

where SSC_{calc} (g/l) refers to the estimated SSC using the laboratory-derived calibration equation and SSC_{known} refers to known SSC using the known sediment weight and water volume. The average error associated with the calibration was estimated to be ± 0.125 g/l .

3.5.4.4 Sensor installation in the upstream and downstream channels

Figure 3.22 illustrates the installation overview for two sensors of Solitax sc and one sensor COSMOS-25 for immersion in upstream and downstream leading channels. A procedure using a laboratory turbidity meter has been developed to determine whether an acceptable correlation can be established between turbidity and solids on modeled suspended sediment material walnut shells.

In the preliminary tests several locations were investigated. Due to the homogenous distributions of SSC on the water depth and channel cross section, probes were installed at the middle of the channel width and height on a PVC support fixed on the channel side walls.

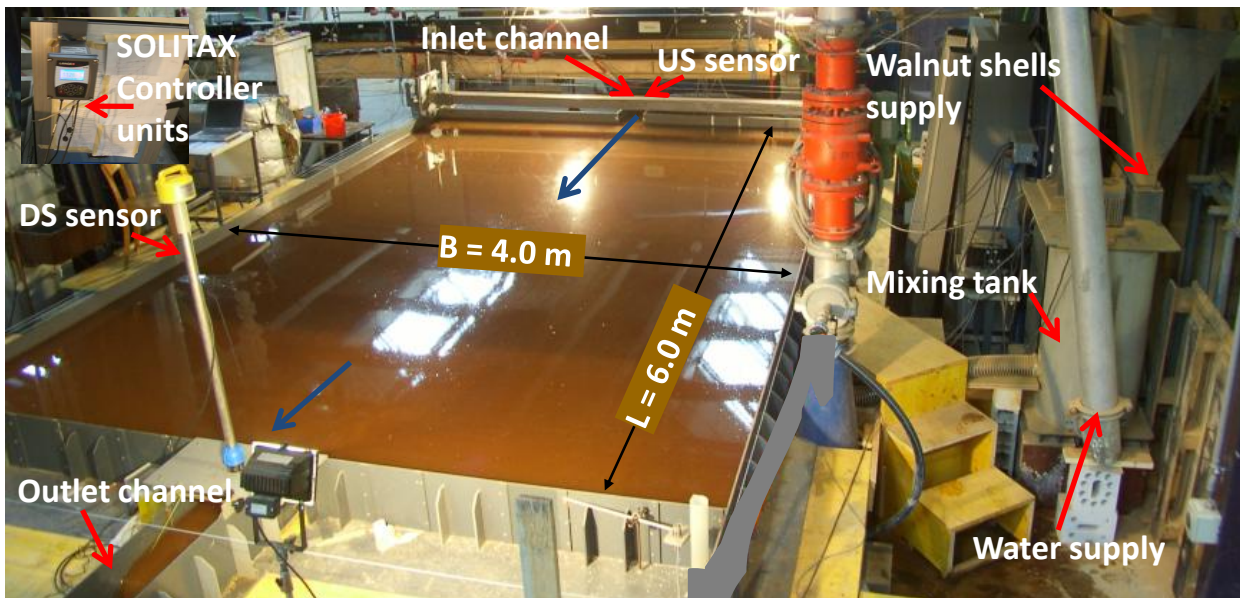


Figure 3.22: Installed turbidity meter in the upstream and downstream leading channel.

3.5.5 Discharge and water level measurements

The flow meter of the inflowing pump was monitored during the experiments which allowed to check the stability of the inflow. During each experiment the location of the water surface at the upstream and downstream channels, and in the reservoir were measured by means of ultrasonic level probes. This allowed a verification that the boundary conditions were constant during the experiments.

3.6 Experimental procedure

Basically the experimental procedure followed the same lines for all experiments as shown in Figure 3.23. Prior to each experiment, the mixing tank and the basin were cleaned. The pump was started and the electromagnetic flow meter and a valve were then used to adjust the desired inflow rate. The downstream flap gate was regulated according to the ultrasound calibration curve to control the water level. Then the basin and mixing tank were filled with clear water. $1D$ vertical velocity profiles as well as local $3D$ velocities were measured with UVP probes. For all sixteen experiments after filling the basin and having reached a stable flow state with the clear water (Phase 1) first LSPIV recording has been performed during 3 min .

Sediment was then added to the sediment supplier tank and the inflow sediment mixture concentration was controlled by the turbidity meter every minutes. The mixer guaranteed a homogenous mixture in the tank. The inflow sediment concentration of 3.0 g/l was kept constant for all experiments. Then in a second phase, the water-sediment mixture was drained by gravity into the water-filled reservoir with different geometries. In the second phase the water sediment mixture is added with two different procedures (Discontinuous and Continuous feeding) as will be explained hereafter in details, see Figure 3.23. The discontinuous feeding with pump interruption was performed with three time steps of 1.5 hrs (total test duration of 4.5 hrs). Without pump interruption a continuous feeding was carried out with one time step of 4.5 hrs . Moreover, a long run time steps were examined with three time steps of $4.5, 4.5, \text{ and } 9.0 \text{ hrs}$ (total duration of test is 18.0 hrs). According to bed deposition patterns and sediment volume evolution it was found that 1.5 hrs is a reasonable time step for the experiments.

The flow circulation pattern with suspended sediment inflow was examined every 30 min using LSPIV over various run time steps as shown in Table 3.5.

Figure 3.24 shows the homogenous suspended sediment mixture. Several pictures show the sediment entering from the upstream inlet channel to the basin. Moreover, the figure shows the mixture arriving at the outlet in a completely mixed state and a certain concentration flowed from the outlet channel.

Every 30 minutes , LSPIV measurements were performed three times and attention was

Table 3.5: Model parameters and instrumentation

Test No	Phase 1		Phase 2: Sediment mixture				No of runs	Total duration [hr]	ISPIV		UVP		UWS Bed level	SOLITAX SSC	Length L [m]	Width B [m]	Area A [m ²]	Jet angle θ [°]	Water depth h [m]	Discharge \dot{Q} [l/s]	Form
	Clear water	1.5hr	3hr	4.5hr	9hr	Run			2D velocity	Phase2 velocity	3D	Bed									
1	☒	☒	☐	☐	☐	3	3x1.5 = 4.5	☒	☒	☒	☒	☐	☐	6.0	4.0	24.0	90	0.20	7.0		
2	☒	☒	☐	☐	☐	3	3x1.5 = 4.5	☒	☒	☒	☒	☐	☐	6.0	4.0	24.0	90	0.20	7.0		
3	☒	☐	☐	☒	☐	3	3x1.5 = 4.5	☒	☒	☒	☒	☐	☐	6.0	4.0	24.0	90	0.20	7.0		
4	☒	☐	☐	☒	☒	3	2x4.5 + 1x9.0 = 18.0	☒	☒	☒	☒	☐	☐	6.0	4.0	24.0	90	0.20	7.0		
5	☐	☐	☐	☐	☐	N/A	N/A	☒	☐	☐	☐	☐	☐	6.0	4.0	24.0	90	0.20, 0.15, 0.10, 0.075	7.0		
6	☐	☐	☐	☐	☐	N/A	N/A	☒	☐	☐	☐	☐	☐	6.0	4.0	24.0	90	0.20	7.0, 3.5		
7	☒	☒	☐	☐	☐	3	3x1.5 = 4.5	☒	☒	☒	☒	☐	☐	6.0	3.0	18.0	90	0.20	7.0		
8	☒	☒	☐	☐	☐	3	3x1.5 = 4.5	☒	☒	☒	☒	☐	☐	6.0	2.0	12.0	90	0.20	7.0		
9	☐	☐	☐	☐	☐	N/A	N/A	☒	☐	☐	☐	☐	☐	6.0	1.0	6.0	90	0.20	7.0		
10	☐	☐	☐	☐	☐	N/A	N/A	☒	☐	☐	☐	☐	☐	6.0	0.5	3.0	90	0.20	7.0		
11	☒	☒	☐	☐	☐	3	3x1.5 = 4.5	☒	☒	☒	☒	☐	☐	5.0	4.0	20.0	90	0.20	7.0		
12	☐	☐	☐	☐	☐	N/A	N/A	☒	☐	☐	☐	☐	☐	4.0	4.0	16.0	90	0.20	7.0		
13	☒	☒	☐	☐	☐	3	3x1.5 = 4.5	☒	☒	☒	☒	☐	☐	3.0	4.0	12.0	90	0.20	7.0		
14	☒	☒	☐	☐	☐	3	3x1.5 + 1x3.0 = 7.5	☒	☒	☒	☒	☐	☐	$L_{max} = 6$	$B_{max} = 4$	12.0	90	0.20	7.0		
15	☐	☐	☐	☐	☐	N/A	N/A	☒	☐	☐	☐	☐	☐	$L_{max} = 6$	$B_{max} = 4$	16.0	90	0.20	7.0		
16	☒	☒	☐	☒	☐	4	3x1.5 + 1x4.5 = 9.0	☒	☒	☒	☒	☐	☐	$L_{max} = 6$	$B_{max} = 4$	12.0	90	0.20	7.0		

N/A: not applicable because there is no sediment entrainment (tests with clear water only)

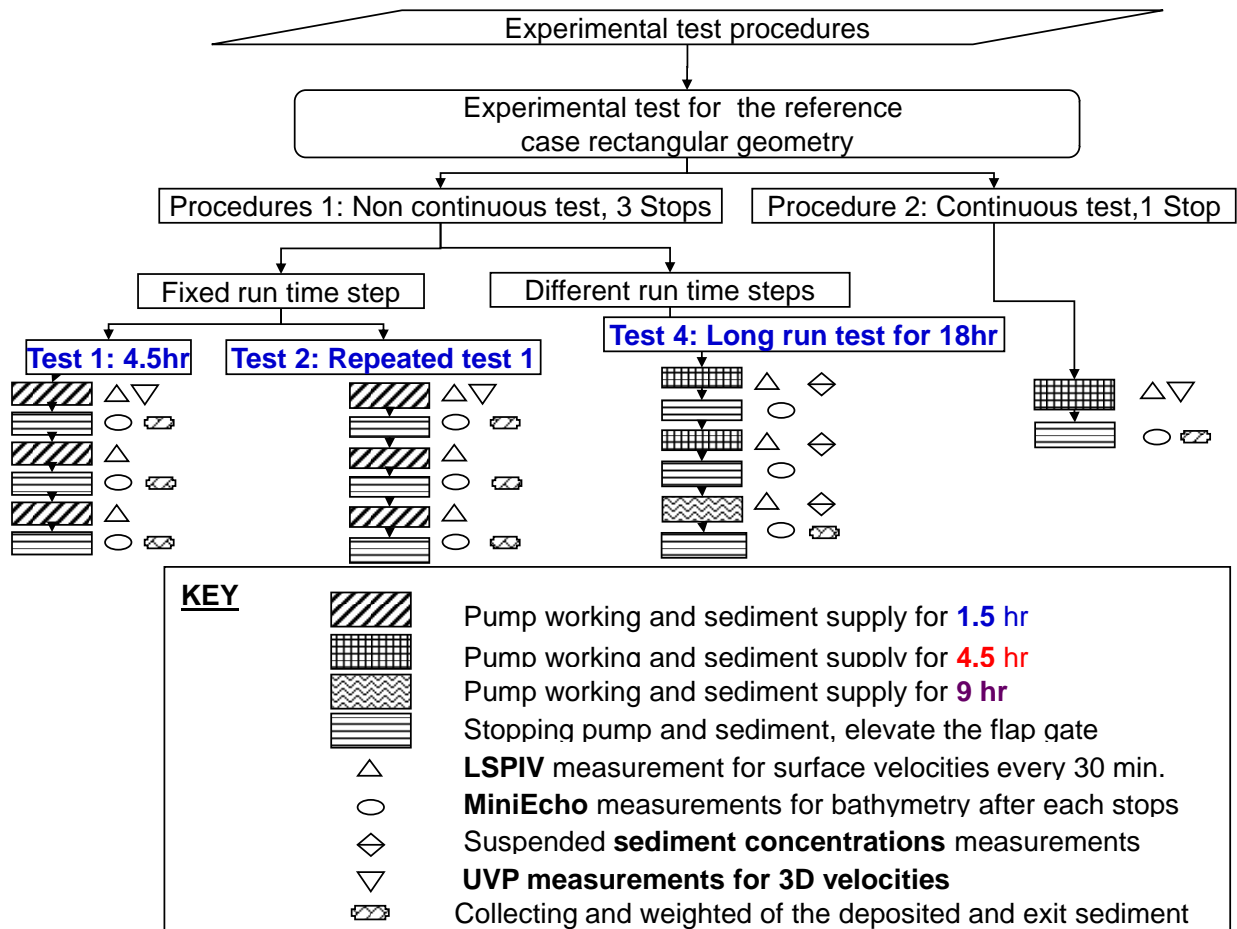


Figure 3.23: Experimental test procedures for the reference rectangular geometry with suspended sediment

paid to the transitional case during the test (decided according to the surface velocity observations). During the experiments for all geometries were repeatedly recorded with a digital video camera for selected durations in order to track the changes in flow patterns, and to determine the propagation of the suspended sediment concentration.

The flap gate was then closed to permit for the suspended sediment to deposit and then start bed level profile measurements by using UWS. Every 1.5 *hrs*, the bed morphology was measured at different cross sections. After each time step the pump was interrupted to allow bed morphology recording. Pictures of the final bed deposition were taken for all experiments. All the previous procedure steps were repeated for each time steps for all geometries.

At the end of each test the sediment at the outlet basin was collected, dried and weighted to calculate the trap efficiency coefficient and sediment volumes as well.

Figure 3.23 shows the different test procedure for the reference rectangular geometry and summarize all the precedent steps in the that schematic figure. Experimental conditions and

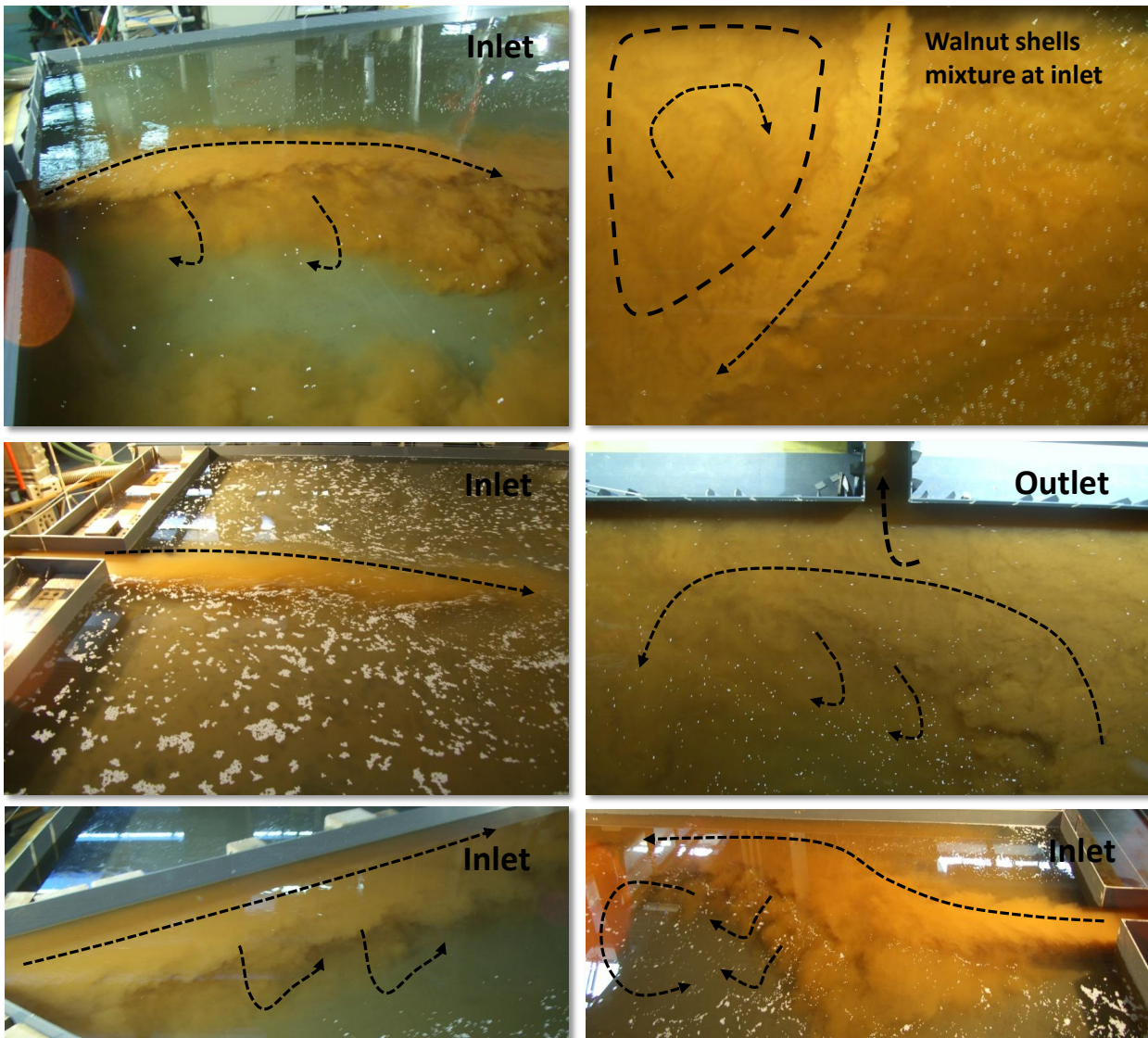


Figure 3.24: Homogenous mixtures of walnut shells at the inlet and outlet of the reservoir with different shapes.

other useful information for the the 16 series of experiments are summarized in Table 3.5.

The following questions of the second phase (with sediment mixture) were investigated by the analysis of the test results of the reference geometry:

1. What is the time step of the test run
2. How many steps are needed for the test
3. Has the test to be interrupted in order to measure the morphological evolution of the bed and how many times
4. Does the interruption have influence on the physics of the flow and deposition patterns

5. Is full morphological equilibrium in the basin reached

Two different experimental procedures were tested in order to find a procedure applying for all test configurations and answer most of these questions. The main differences between alternative procedures can be summarized as following:

1. *Procedure 1*: Discontinuous feeding: after each run of sediment feeding to the water mixture and doing velocity measurements (UVP, PIV& Pictures); close downstream flap gate, open water bypass and stop sediment feeding. After suspended sediment deposits, completion of the bathymetric measurements were done.
2. *Procedure 2*: Continuous feeding: during the whole experiment continuous feeding of the water-sediment mixture and accomplishment of measurements.

The following conclusion was before the long run test has been performed. In the discontinuous feeding procedure, the gradual changes during the transitional state are missing due to the effect of stopping and restarting the flow. For the continuous feeding procedure, it was easy to reach a stable flow and bed form in the basin after 4.5 hours.

A long term test has been performed to investigate the morphodynamic equilibrium and time steps effect with total test period up to 18 *hrs* with different time steps of (4.5 *hrs*, 4.5 *hrs*, and 9 *hrs*). It was found that 4.5 *hrs* is long enough to develop a stable morphology independently on the test procedure. Consequently, most of the experiments were conducted with a total test period of 4.5 *hrs* with three runs each 1.5 *hrs*. For some selected tests a different scenario was selected (see Table 3.5).

3.7 Discussion of the efficiency of the instruments used and the test procedures applied

The influence of the reservoir geometry on sediment transport and deposition was carried out by using six different measurement techniques. Four measurement techniques were used and adapted in order to define detailed flow and deposition patterns throughout the basin, as well as their long-term evolution following progressive bottom deposits (LSPIV, UWS, SOLITAX, and UVP).

The flow structures in a shallow basin could be measured successfully by using LSPIV. It could be demonstrated that LSPIV has potential for measuring low velocities and the sampling rate has to be defined according to the application case. LSPIV has proven to be a reliable, flexible, and economically efficient flow diagnostic tool.

The velocities measured by means of UVP allowed an instantaneous measurement of the 1D and 3D velocity profiles over the whole flow depth. The turbulence large-scale structures and jet expansion in the basin have been determined based on UVP and LSPIV.

- UVP measurements provided precise results of 3D velocity in sediment-water two-phase flow. The obtained results were useful to evaluate the physics of suspended sediment, particularly with the asymmetric curved jet flow structure.

The large horizontal flow pattern in the shallow basin was compared, in detail, to those of LSPIV. It was concluded that despite two different techniques, the flow patterns for different geometrical configurations were in agreement. Comparison between results of measurements with and without suspended sediment confirmed the noticeable influence of sediment on velocity field in shallow basins.

Thickness of bed deposition in shallow basins with different geometries was successfully measured using Mini-Echo Sounder.

Mini-EchoSounder has proved to have a high potential for measuring small bed changes and is believed to be applicable in field tests as well.

Evaluation of two instruments for measuring SSC after calibration relationship relating SSC and turbidity showed that SOLITAX instruments were more suitable for the present research than COSMOS-25. Considering the complex nature of the relationship between SSC and turbidity, reflecting the influence of factors such as particle size and shape and water colour, it is important that the calibration method should adequately represent these naturally occurring variations.

3.8 Characteristics and dimensionless parameters

In this section all characteristic parameters controlling flow and deposition processes in shallow reservoir with different geometry are summarized in order to propose flow, deposition, and geometry formulas. A relationship of generally validity is very difficult to establish since the phenomenon of sedimentation in shallow reservoirs is influenced by a large number of parameters. The set of characteristic parameters of the flow and sediment (two phase flow) in shallow reservoir can be classified into five groups, fluid, flow, geometry, time and sediments. The objective is to derive dimensionless parameters which allows identifying the dominant parameters involved in a physical phenomenon for each group separately. For each group a combination between several characteristic parameters was developed which described in the following.

3.8.1 Fluid

- fluid (ρ , μ and ν (see Section 3.4.1))

3.8.2 Flow

- characteristics parameters of flow: h is the water depth of flow, V_{res} is the initial reservoir volume, Q is the average flow discharge, U_{in} is average water velocity of the inlet and U_{res} is the average water velocity magnitude within the reservoir and it can be define as $U_{res} = \sqrt{u^2 + v^2}$, where u and v are the longitudinal and transversal time averaged velocities within reservoir, respectively. Reattachment length of the recirculation cells is L_r .
- dimensionless parameters of flow: ratio of U_{res}/U_{in} is the normalized velocity along the centerline of the basin and within the basin for each geometry. Froude and Reynolds numbers of the inlet are Fr_{in} and Re_{in} . Froude and Reynolds numbers of the reservoir are Fr_{res} and Re_{res} . Normalized reattachment length is $X_r = L_r/B_r$.

3.8.3 Geometry

All possible characteristics geometrical parameters are depicted in Figure 3.25. Several dimensionless parameters were derived with the objective to find one representative geometrical coefficient combining all different forms of reduced basin width, length, and expansion angle.

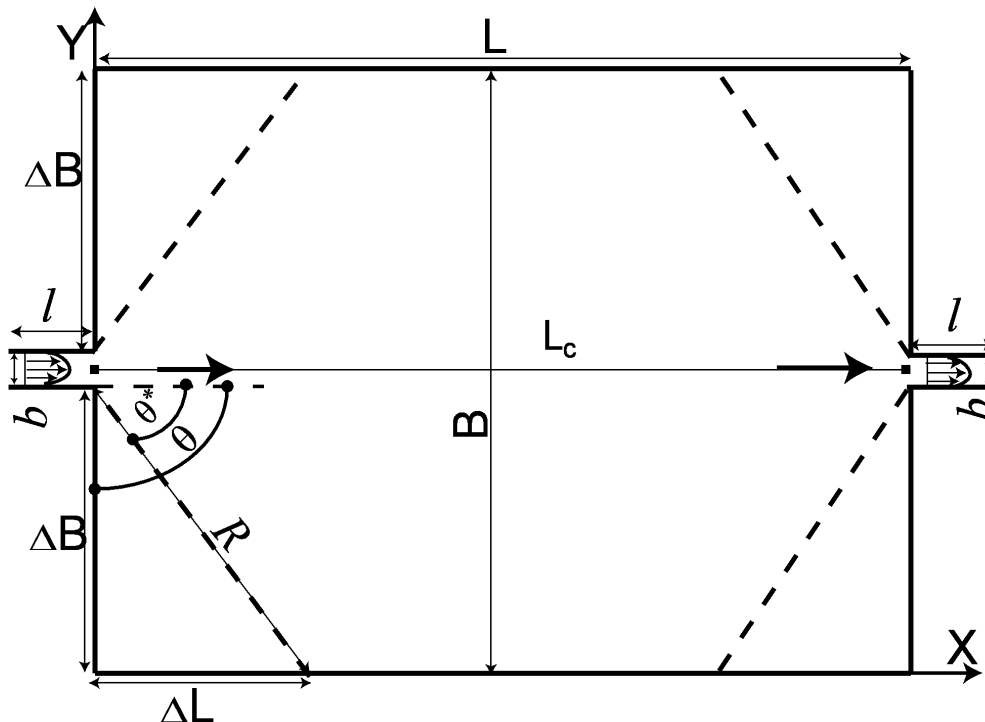


Figure 3.25: Definition of the geometrical parameters of the test configurations

- characteristics parameters of geometry: The geometrical parameters are defined in Figure 3.25 and all tests are summarized in Table 3.6. The geometry is symmet-

ric about the X-Y-Z planes. The following definitions are used and summarized in Table 3.6:

- length and the width of the basin: L & B
- distance between the center of inlet and outlet channels: L_c (for the present study L_c is constant = 6.0 m for all tests)
- length and the width of the upstream and downstream channels which remained constant for all configurations: $l = 1.0$ m , $b = 0.25$ m & $l = 4$ b
- depth of lateral expansion: ΔB
- distance from the edge of channel to the edge of the basin: $R = \Delta B$
- semi angle of the expansion entrance is measured from the edge of the channel to the edge of the basin: θ^*
- total surface area of the basin: A_t
- total volume of reservoir: $A_t \cdot h$
- expansion surface area of the basin: A_{exp}
- total wetted perimeter of the length of the side walls of reservoir: P
- expansion wetted perimeter of the length of the side walls: P_{exp}
- dimensionless parameters of geometry: Several normalized geometrical parameters were derived as example: Expansion ratio and Aspect Ratio of the basin, normalized expansion area, and jet expansion density ratio.
 - expansion Ratio: $ER = B/b$
 - aspect ratio of the basin: $AR = L/B$
 - normalized expansion area: $\sigma = A_{exp}/A_t$
 - jet expansion density can be defined as the ratio $D_{exp} = R/\Delta B$

3.8.4 Time

- characteristics parameters of time: t is the duration of inflow of suspended sediment and it is an important parameter which affects the sediment deposition. Initial residence time of water in reservoir t_{ri} can be define as $t_{ri} = V_{res}/Q$. Settling time is t_s and can be define as $t_s = h / v_{ss}$ where v_{ss} is the particle settling velocity see Section 3.4.4. The actual residence time is $t_r = Q/(V_{res} - V_{df})$ where V_{df} is the volume of final bed dead deposition after duration t .
- dimensionless parameters of time: t^* is dimensionless time $t^* = t / t_r$. Relative time is $t^{**} = t / t_{ri}$ and normalized residence time is t_{ri}/t_s .

3.8.5 Sediments

The characteristics parameters of the sediments can be classified into three groups of sediment particle, concentrations, and depositions.

- characteristics parameters of sediments:
 - sediment particles: grain size distribution and d_{50} is the median grain size diameter, ρ_s is the density of the sediment particles, initial porosity is P'_m , the dry density, ρ'_s , and the density of wet sediment is ρ''_s (see Section 3.4.4).
 - suspended sediment concentrations SSC: C_{in} is the inflow suspended sediment concentration, C_{out} is the released suspended sediment concentration from the outlet,
 - sediment deposition thickness and volume: the evolution of sediment deposition thickness d The deposited volume V_{dep} can be calculated $V_{dep} = d \cdot A_t$, and volume of the inflow suspended sediment at the inlet $V_{in} = W_s d / \rho'_s$ where, $W_s d$ is the total weight of dry sediment.

- dimensionless parameters of sediments: Engineering practice makes use of some technical indicators and parameters to define and characterize quantitatively the silting process of reservoirs, such as the relative deposited thickness d/h , silting ratio (storage loss) $SR = V_{dep}/V_{res}$, Sedimentation Index $SI = g \cdot (t/U_{res})$, and trap efficiency (TE) has two definitions, ratio of difference between suspended sediment concentration at inlet and outlet over suspended sediment concentration at inlet $TE = (C_{in} - C_{out})/C_{in}$, the volume of deposition in reservoir was normalized by volume of the inflow suspended sediment at the inlet V_{in} which gives the second definition for trap efficiency $TE = V_{dep}/V_{in}$ and the sediment release efficiency is $RE) = 100 - TE$.

3.9 Definition of geometry shape factor SK

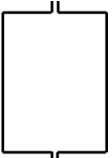










A detailed explanation of all characteristics tested geometrical parameters and configurations are given in Section 3.8.3 and Figure 3.25. In order to represent all geometrical characteristics parameters with flow and deposition results, a geometry shape factor SK was developed.

The main objective is to study the influence of reservoir geometry on flow and sedimentation processes. Thus, there is a need for a dimensionless coefficient representative of different geometry shapes which can be correlated with dimensionless parameters of flow and sediment. Since some geometries with different form has the same Aspect Ratio and Expansion Ratio as shown in Table 3.6.

Several formulas were derived by combination of water depth h , discharge Q , Aspect Ratio AR , Expansion Ratio ER , Wetted perimeter P , total surface area of the basin: A_t , expansion surface area A_{exp} , normalized expansion area $\sigma = A_{exp}/A_t$, depth of lateral expansion ΔB , and distance from the edge of channel to the edge of the basin R .

The following dimensionless geometry shape factors were derived and tested:

Table 3.6: Geometrical properties and configurations of different tests

Test No	B [m]	L [m]	δB [m]	R [m]	θ^* [°]	A_t [m ²]	A_{exp} [m ²]	P [m]	$ER = \frac{P}{b}$ [-]	$AR = \frac{L}{B}$ [-]	$D_{exp} = \frac{R}{\delta B}$ [-]	$\sigma = \frac{A_{exp}}{A_t}$ [-]	$SK = \frac{P}{\sqrt{A_t}} \cdot AR \cdot D_{exp}$ [-]	Form
T1,2,3,4,5,6	4.0	6.0	1.875	1.875	90.00	24.00	11.25	19.50	16.00	1.50	1.00	0.47	5.97	
T7	3.0	6.0	1.375	1.375	90.00	18.00	8.25	17.50	12.00	2.00	1.00	0.46	8.25	
T8	2.0	6.0	0.875	0.875	90.00	12.00	5.25	15.50	8.00	3.00	1.00	0.44	13.42	
T9	1.0	6.0	0.375	0.375	90.00	6.00	2.25	13.50	4.00	6.00	1.00	0.38	33.07	
T10	0.5	6.0	0.125	0.125	90.00	3.00	0.75	12.50	2.00	12.00	1.00	0.25	86.60	
T11	4.0	5.0	1.875	1.875	90.00	20.00	9.25	17.50	16.00	1.25	1.00	0.46	4.89	
T12	4.0	4.0	1.875	1.875	90.00	16.00	7.25	15.50	16.00	1.00	1.00	0.45	3.88	
T13	4.0	3.0	1.875	1.875	90.00	12.00	5.25	13.50	16.00	0.75	1.00	0.44	2.92	
T14	4.0	6.0	1.875	3.537	32.00	12.75	5.63	14.15	16.00	1.50	1.89	0.44	11.2	
T15	4.0	6.0	1.875	3.537	32.00	18.38	8.44	16.83	16.00	1.50	1.89	0.46	11.08	
T16	4.0	6.0	1.875	2.401	51.34	18.38	8.44	15.60	25.60	1.50	1.28	0.46	4.65	

- SK_1 has been identified as a function of the expansion wetted perimeter P_{exp} and the expansion surface area A_{exp} :

$$SK_1 = \frac{P_{exp}^2}{A_{exp}}$$

- SK_2 has been identified as a function of the total surface area A_t , the total wetted perimeter P and reservoir Aspect Ratio AR :

$$SK_2 = \frac{A_t}{P^2} \cdot AR$$

- SK_3 has been identified as a function of the water depth h , and the total wetted perimeter P :

$$SK_3 = \frac{h}{p}$$

- SK_4 has been identified as a function of A_{exp} , h , and P :

$$SK_4 = \frac{A_{exp}}{P \cdot h}$$

- SK_5 has been identified as a function of Expansion ratio ER , and AR :

$$SK_5 = ER \cdot \frac{2 + AR \cdot (ER - 1)}{2ER + AR \cdot (ER - 1)}$$

- SK_6 has been identified as a function of A_t , and P :

$$SK_6 = \frac{A_t}{P^2}$$

- SK_7 has been identified as a function of A_t , and P :

$$SK_7 = \frac{P}{\sqrt{A_t}}$$

- SK_8 has been identified as a function of A_t , P , and ER :

$$SK_8 = \frac{A_t}{P^2} \cdot ER$$

- SK_9 has been identified as a function of A_t , P , AR and ER :

$$SK_9 = \frac{A_t}{P^2} \cdot AR \cdot ER$$

- SK_{10} has been identified as a function of A_t , P , and normalized expansion area σ :

$$SK_{10} = \frac{A_t}{P^2} \cdot \sigma$$

- SK_{11} has been identified as a function of A_t , P , and h :

$$SK_{11} = \sigma \cdot \frac{A_{exp}}{P \cdot h}$$

- SK_{12} has been identified as a function of h , P , the depth of lateral expansion ΔB , and distance from the edge of channel to the edge of the basin R :

$$SK_{12} = \sigma \cdot \frac{h}{P} \cdot \frac{R}{\Delta B} \cdot AR$$

- $SK_{13} = SK$ has been identified as a function of the total surface area A_t , the total wetted perimeter P , reservoir Aspect Ratio AR , the depth of lateral expansion ΔB , distance from the edge of channel to the edge of the basin R , and D_{exp} jet expansion density:

$$SK_{13} = \frac{P}{\sqrt{A_t}} \cdot AR \cdot \frac{R}{\Delta B} = \frac{P}{\sqrt{A_t}} \cdot AR \cdot D_{exp}$$

The correlations between the dimensionless parameters of some selected geometry shape factors which were derived above and normalized velocity in reservoir, and relative deposited thickness are graphically represented in Figure 3.26. Besides a graphical analysis, the Pearson product-moment correlation coefficient R can be used to estimate the correlation of X and Y . It quantifies the extent of a linear relation between two data sets and its square values R^2 ranges between 0 and 1.

In addition to these selected graphical correlations several formula were fitted with dimensionless parameters of flow, time, and sediment which explained in Section 3.8. Moreover, combination between three parameters of flow, sediment, and time was correlated with geometry shape factor.

Combination with all of these dimensional and non-dimensional parameters were combined and the relationship between each combined parameters were investigated. Comparison of the different formula for the shape factor was based on two criteria:

- Separation of experiments according to the jet flow type as will be shown in the following Chapter. For practical reasons, the following purely geometrical parameter is proposed.
- Correlation with flow (velocity in reservoirs, jet flow type) and sediment (relative deposited thickness, trap efficiency) were developed relationship with geometry shape factor as dependent parameter.

$$SK_{13} = SK = \frac{P}{\sqrt{A_t}} \cdot AR \cdot D_{exp} \quad (3.22)$$

The finally selected geometry shape factor is SK in Eq. 3.22, where, A_t is the total surface area of the basin, P is the total wetted perimeter of the length of the side walls, AR is the reservoir aspect ratio, and D_{exp} is the jet expansion density. Therefore all developed relationship with flow and sediment were correlated with geometry shape factor. In the following three chapters only the best fit relationships were presented.

Parameter dimensionless	Ratio of velocity y-axis: U_{res}/U_{in}	Relative deposited thickness: y-axis: d/h
x-axis: SK_1 $SK_1 = \frac{P_{exp}^2}{A_{exp}}$		
x-axis: SK_4 $SK_4 = \frac{A_{exp}}{P \cdot h}$		
x-axis: SK_5 $SK_5 = ER \cdot \frac{2 + AR \cdot (ER - 1)}{2ER + AR \cdot (ER - 1)}$		
x-axis: SK_6 $SK_6 = \frac{A_t}{P^2}$		
x-axis: SK_7 $SK_7 = \frac{P}{\sqrt{A_t}}$		
x-axis: SK_8 $SK_8 = \frac{A_t}{P^2} \cdot ER$		
x-axis: SK_{11} $SK_{11} = \frac{A_{exp}}{P \cdot h} \cdot \sigma$		
x-axis: $SK = SK_{13}$ $SK = SK_{13} = \frac{P}{\sqrt{A_t}} \cdot AR \cdot \frac{R}{\Delta B}$		

Figure 3.26: Graphical analysis of the relation between different dimensionless parameters of geometry SK (x-axis), normalized velocity in reservoir, and relative deposited thickness (y-axis)

3.9.1 Validity of empirical formulas and fits

This subsection concern of the empirical formulas which will be discussed in Chapter 4, 5, and 6. In the following three chapters several empirical formulas of flow and sediments dimensionless parameters which are derived in Section 3.8 will be discussed. At the first stage, basically dimensional and dimensionless parameters have been provided as input variables for Stat10 software for the predication of relative deposited thickness and normalized velocity in reservoir.

The goal of this first stage was to identify how parameters act together. Then, only dimensionless parameters have been used to develop relative deposited thickness and ratio of normalized velocity in reservoir formulas based on the findings of the first stage. The first stage revealed that the dimensionless parameters identified by R^2 method (see Figure 3.26) mainly correspond to the parameters found by Stata10. On the other hand, using dimensional geometrical parameters such as SK_1 , SK_2 , SK_5 , etc. the Stata10 software was not able to reasonably predict the relative deposited thickness and normalized velocity parameters.

At the second stage, the normalized velocity ratio U_{res}/U_{in} , L_c/b have been predicted for the three different jet flow types. Then, formulas for predication of trap efficiency, sedimentation index, etc. were developed. Finally, in order to avoid overfitting, the available data have been randomly separated into a training set (2/3 of the data) and a validation set (1/3).

From the physical point of view all dimensionless parameters have been derived and selected from literature. Therefore, it not only the Froude similarity has to be considered when upscaling the results to prototype scale. If the configurations tested in the laboratory reservoir should be compared to a prototype configuration, Froude and Reynolds similarities have theoretically to be considered simultaneously. Empirical relationships obtained from the experimental data may have limited validity when applied to other scales, since Reynolds number changes significantly.

Precise formulation of geometry shape factor SK should be confirmed based on additional experimental tests with sediment or numerical simulations.

3.10 Hydraulic conditions of experiments with clear water

Various geometrical configurations having different aspect and expansion ratios, and hydraulic conditions have been analyzed for clear water phase are shown in Table 3.7. A reference basin geometry with a constant width of $B = 4.0 \text{ m}$ and length of $L = 6.0 \text{ m}$ is compared to the different test configurations, as summarized in Table 3.7. The first six tests (from T1 to T6) have been conducted for the reference geometry with various objectives:

1. Test 1 (T1) to study the effect of the geometry on the flow patterns and investigate the phenomenon of the asymmetric flow behavior in the symmetric geometry which has been observed during the preliminary tests. Moreover, the discontinuous feeding procedure has been used.
2. Test 2 (T2) repeated test for T1, with the purpose to check the reproducibility and the model sensitivity.

3. Test 3 (T3) the continuous feeding procedure has been used with the same condition as T1 & T2, to examine different test procedures in order to find one approach for all test configurations.
4. Test 4 (T4) long-term test has been performed with durations up to 18 *hours* to account for progressive morphological evolution and to verify the final achievement of dynamic equilibrium. Furthermore, different test durations (1.5 *hrs*, 4.5 *hrs* and 9.0 *hrs*) are examined with the purpose to find the optimal one to continue with additional test configurations. It has to be noticed that these long runs were performed in several time steps 1.5, 4.5, and 9.0 hour, i.e. the facility has been interrupted to allow bed morphology recording.
5. Test 5 (T5) comprising four series was dedicated to investigating the effect of the shallow water depth on the flow pattern and corresponding coherent structures for a fixed geometry aspect ratio $AR = 1.5$ and discharge $Q = 7 \text{ l/s}$ with $Re_{in} = 28000$. To gain further insights to the fundamental aspects of shallow water hydrodynamics, four water depths (20, 15, 10, 7.5 *cm*) have been used. These leads to four different Froude numbers $Fr_{in} = 0.1, 0.154, 0.283, 0.435$ with different ratios of $h/b = 0.8, 0.6, 0.4, 0.3$.
6. Test 6 (T6) was dedicated to investigate the effect of the discharge for a fixed water depth and geometry. Two different discharges $Q = 7.0, 3.5 \text{ l/s}$ with the corresponding $Re_{in} = 28000$ and 14000 and $Fr_{in} = 0.1, 0.05$ for a constant water depth $h = 20 \text{ cm}$, and $h/b = 0.8$

The geometry shape factor SK is used to scale expansion characteristics, such as the reattachment length, for all possible geometries. Moreover, it provides a means to capture the significant role of the geometry in the bifurcation process between asymmetry and symmetry flow.

The different test configurations allowed detailed study of the effect of geometry on the degree of asymmetry of the separated flow in the basin. After filling the basin and reaching a stable flow state with the clear water, LSPIV recordings were performed for 3 *min*. The following hydraulic parameters used for the tests are summarized in Table 3.7:

- Flow depth: h
- Flow discharge: Q
- Reservoir volume (Capacity): $V_{res} = A_t \cdot h$
- Depth to width inlet channel ratio: h/b
- Mean inlet velocity: U_{in}

Table 3.7: Hydraulic conditions for all test configurations

Test No.	h [m]	Q [l/s]	V_{res} [m ³]	h/b [-]	Fr_{in} [-]	Fr_{res} [-]	Re_{in} [-]	Re_{res} [-]	$\frac{U_{res}}{U_{in}}$ [-]	t_r [min]
T1	0.200	7.000	4.800	0.800	0.100	0.045677	28000	12796	0.457	11.429
T2	0.200	7.000	4.800	0.800	0.100	0.045677	28000	12796	0.457	11.429
T3	0.200	7.000	4.800	0.800	0.100	0.045677	28000	12796	0.457	11.429
T4	0.200	7.000	4.800	0.800	0.100	0.045677	28000	12796	0.457	11.429
T5	0.200	7.000	4.800	0.800	0.100	0.045677	28000	12796	0.457	11.429
T5	0.150	7.000	3.600	0.600	0.153	0.052743	27900	9597	0.3439785	8.571
T5	0.100	7.000	2.400	0.400	0.283	0.064597	28000	6398	0.2285	5.714
T5	0.075	7.000	1.800	0.300	0.435	0.07459	27975	4798.5	0.1715282	4.286
T6	0.200	7.000	4.800	0.800	0.1	0.045677	28000	12796	0.46	11.42
T6	0.200	3.5	4.800	0.800	0.050	0.045677	14000	12796	0.914	2285.714
T7	0.200	7.000	3.600	0.800	0.100	0.047476	28000	13300	0.475	8.571
T8	0.200	7.000	2.400	0.800	0.100	0.070664	28000	19796	0.707	5.714
T9	0.200	7.000	1.200	0.800	0.100	0.065667	28000	18396	0.657	2.857
T10	0.200	7.000	0.600	0.800	0.100	0.081958	28000	22960	0.82	1.429
T11	0.200	7.000	4.000	0.800	0.100	0.049975	28000	14000	0.5	9.524
T12	0.200	7.000	3.200	0.800	0.100	0.043578	28000	12208	0.436	7.619
T13	0.200	7.000	2.400	0.800	0.100	0.040979	28000	11480	0.41	5.714
T14	0.200	7.000	2.550	0.800	0.100	0.037981	28000	10640	0.38	6.071
T15	0.200	7.000	3.675	0.800	0.100	0.045577	28000	12768	0.456	8.750
T16	0.200	7.000	3.675	0.800	0.100	0.042478	28000	11900	0.425	8.750

- Mean reservoir velocity: U_{res}
- Ratio of reservoir to inlet velocity: U_{res}/U_{in}
- Froude number in the inlet channel: $Fr_{in} = U_{in}/\sqrt{gh}$
- Froude number in the reservoir: $Fr_{res} = U_{res}/\sqrt{gh}$
- Time averaged velocity magnitude within reservoir: $U_{res} = \sqrt{u^2 + v^2}$, where u , v are longitudinal and transversal velocity within the reservoir, respectively.
- Reynolds number in the inlet channel: $Re_{in} = U_{in}h/\nu$
- Reynolds number in the reservoir: $Re_{res} = U_{res}h/\nu$
- Initial residence or retention time: $t_{ri} = V_{rese}/Q$

3.11 Hydraulic and sediment conditions of experiments with suspended sediment

The experimental parameters and the characteristics of the tested geometries with sediments were presented in Section 3.8.3. Ten shallow reservoir geometry runs with suspended sediment were carried out with the parameters given in Table 3.8.

Each test consists of several runs and each run has several time steps Δt , except for T3 has one run, and the total running time is t .

Two procedures were conducted as shown in Table 3.8. In all geometry, the discharge was kept constant at $Q = 7.0 \text{ l/s}$ and the water level was controlled by a flap gate located in the downstream part of the outlet channel. The downstream water level was kept constant at $h = 0.2 \text{ m}$. The mean inflow suspended sediment concentration was similar for all experiments with $C_{in} = 3.0 \text{ g/l}$.

Table 3.8: Sediment conditions for all tested configurations with suspended sediment.

Test No.	Time steps Δt [min]	Running time t [min]	Test procedure (See Section 3.6)
T1	90	90	1
T1	90	180	1
T1	90	270	1
T2	90	90	1
T2	90	180	1
T2	90	270	1
T3	270	270	2
T4	270	270	2
T4	270	540	2
T4	540	1080	1
T7	90	90	1
T7	90	180	1
T7	90	270	1
T8	90	90	1
T8	90	180	1
T8	90	270	1
T11	90	90	1
T11	90	180	1
T11	90	270	1
T13	90	90	1
T13	90	180	1
T13	90	270	1
T14	90	90	1
T14	90	180	1
T14	90	270	1
T14	180	450	1
T16	90	90	1
T16	90	180	1
T16	90	270	1
T16	270	540	1

Results and analysis of tests with clear water

In this chapter, experimental observations and results are presented and discussed. The main part of the chapter outlines the flow behavior of the experiments with clear water.

In the first section, several geometrical parameters for the test configurations are presented followed by an analysis of the three-dimensional velocity and vertical velocity and of the secondary flow phenomena in the large shallow reservoirs.

Physical interpretation and classification of the flow pattern with clear water results is provided based on geometrical shape factor SK .

The most important aspect of the analysis is to feature the effect of geometry on the flow pattern, reattachment length, Reynolds number (Re), and Froude number (Fr), which has not yet been done before.

Moreover, several empirical relationships to describe the influence of the shape factor SK of the reservoir geometry on flow in clear water phase are developed. Simple empirical relationships between SK and averaged velocity ratios of U_{res}/U_{in} at reservoir centerline are given.

Furthermore, relationships for the whole reservoir surface considering reattachment lengths, ratio of residence and settling time t_r/t_s as well as sedimentation index SI have been derived for the stabilized flow pattern.

The empirically-based relationships for the geometry shape factor were obtained from the experimental data described in the previous chapter. Several formulas have been developed using three different softwares (KaleidaGraph, OriginLab, and Stat10), but only the best formulas are given in the following.

4.1 Observed flow patterns and features

Figures 4.1(a)& 4.2(a) show an overview of the streamlines and behavior of large-scale coherent structures for two shapes with shape factors $SK = (P/\sqrt{A_t}) \cdot AR \cdot D_{exp}$ of 5.97 and 4.89, respectively, (see also Table 3.6).

In order to understand reattachment physics for different reservoir geometries a schematic of the dimensions and geometrical characteristics for all large coherent structures regions are shown in Figures 4.1(b)& 4.2(b). For $SK = 5.97$, a plane jet issues from the narrow leading channel and enters straight into the first half-meter of the much wider basin.

After jet issuance, the main flow tends to curve towards the right hand side over the next two meters, until it stagnates against the right wall as shown in Figure 4.1(a). The main flow separates from the right wall, inducing a zone of flow recirculation (1) (Fig. 4.1(a)). A streamlines of vortices is shed from the stagnation point.

After the jet touches the wall, a separation occurs and generates a large main stable eddy in the center of the basin rotating counterclockwise with size L_{r3} and B_{r3} . When looking from the inflow toward the outflow, two small "triangular" gyres are formed rotating clockwise in the upstream corners of the basin with dimensions L_{r1} and B_{r1} along the right corner and with dimensions L_{r2} and B_{r2} along the left corner.

The deflected jet works as a vortex shedding region between the main eddy in the center and the triangular one in the upstream right corner. Moreover, two mixing layers can be observed between the main flow and both eddies (Fig. 4.1(a)).

The jet seems to be attracted to one side of the basin (in the tests, always to the right side). After the flow has reached the left wall by the counterclockwise large circulation, a separation point forms (Fig. 4.1(b)).

The streamline of the large gyre is shed from the separation point and connects with the core gyre. A second vortex shedding zone in the reverse direction is generated between the main gyre and the small triangular clockwise eddy in the upstream left corner.

The reverse flow jet, which is generated by the inertia of the main gyre, pushes the incoming jet aside and forms a shedding point between four features: *main flow deflected jet, reverse flow jet, large main gyre, right and left triangular corner gyres, Shedding or dynamic eddies*. The jet preference for the right side is weak, since a stable mirror image of the flow pattern can easily be established by slightly disturbing the initial conditions.

The stable asymmetric pattern, with a larger and smaller recirculation zone at the right and left corners, can be explained by a Coanda effect by which any perturbation of the flow field, pushing the main flow to one side of the basin, gives rise to larger velocities. Thus the asymmetry will naturally tend to be accentuated by this Coanda effect.

Since flow asymmetry in symmetric geometry with different shape factors is important, we were motivated to study the effect of SK on the flow asymmetry at $Re_{in} = 28000$.

Figures 4.6& 4.9 present a comparison of streamlines plotted at the symmetry plane in reservoirs with different values of SK . What is now evident is that flow symmetry remains stable when SK is equal to 4.89. As the geometry shape factor of the reservoir SK is increased up to a value of 5.97, flow becomes clearly asymmetrical.

To find a critical geometry shape factor, above which the flow undergoes a transition to asymmetry, the reattachment length for all circulation cells was measured as shown in

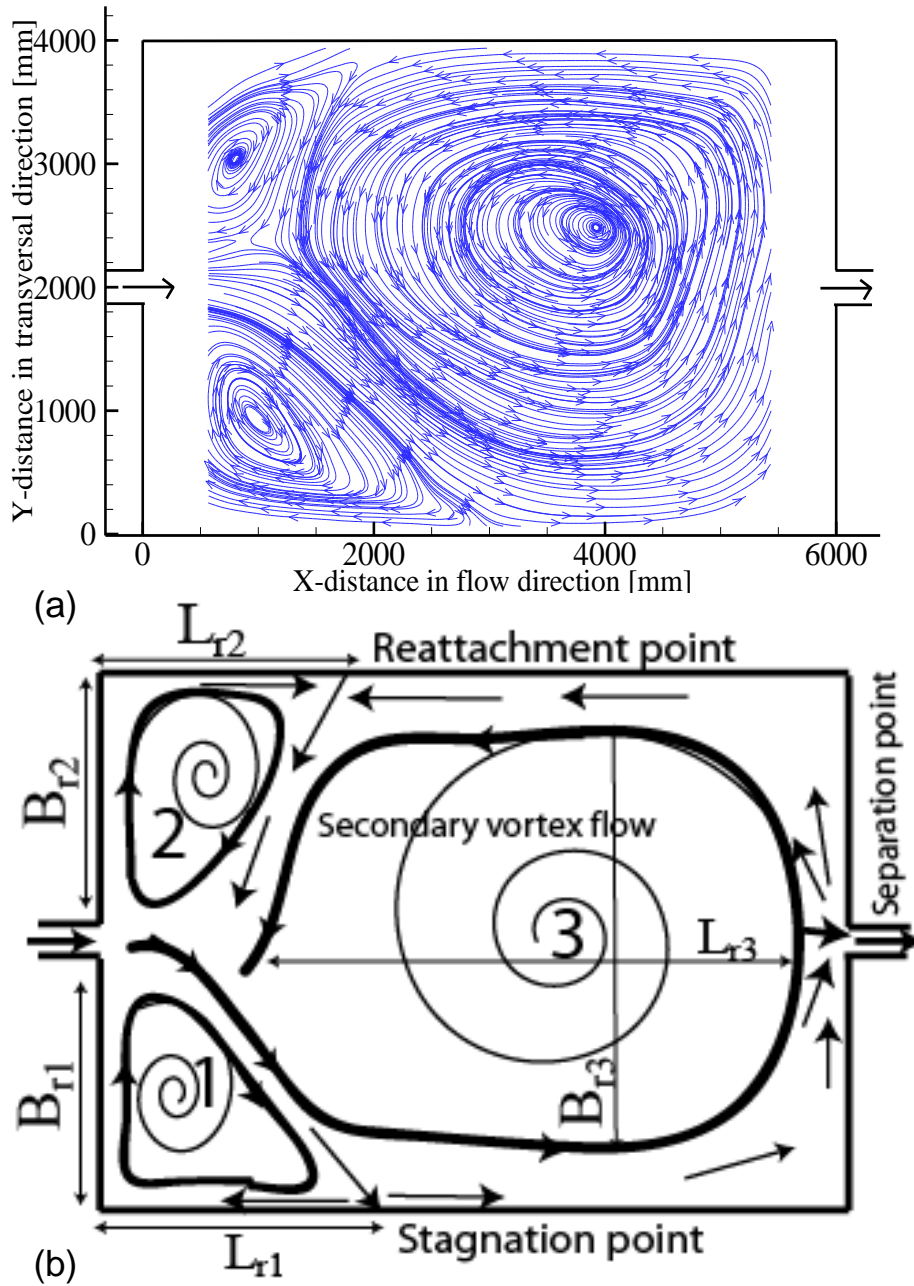


Figure 4.1: (a) Time-averaged streamlines obtained by LSPIV measurements for clear water flow for geometry with shape $SK = 5.9$ (b) Plan view of the rectangular geometry ($L = 6$ m, $B = 4$ m) and the geometrical parameters of the recirculation cells in the basin are L_{r_i} , B_{r_i} for gyres (1, 2, 3).

Figures 4.1(b) & 4.2(b). It is revealed from Figure 4.16 that the critical SK is about 5.5. More details will be explained in Section 4.4.

By decreasing the shape factor $SK < 5.5$, the flow becomes more stable and symmetric, which will be explained in detail hereafter. Figure 4.2 shows the second flow behavior that

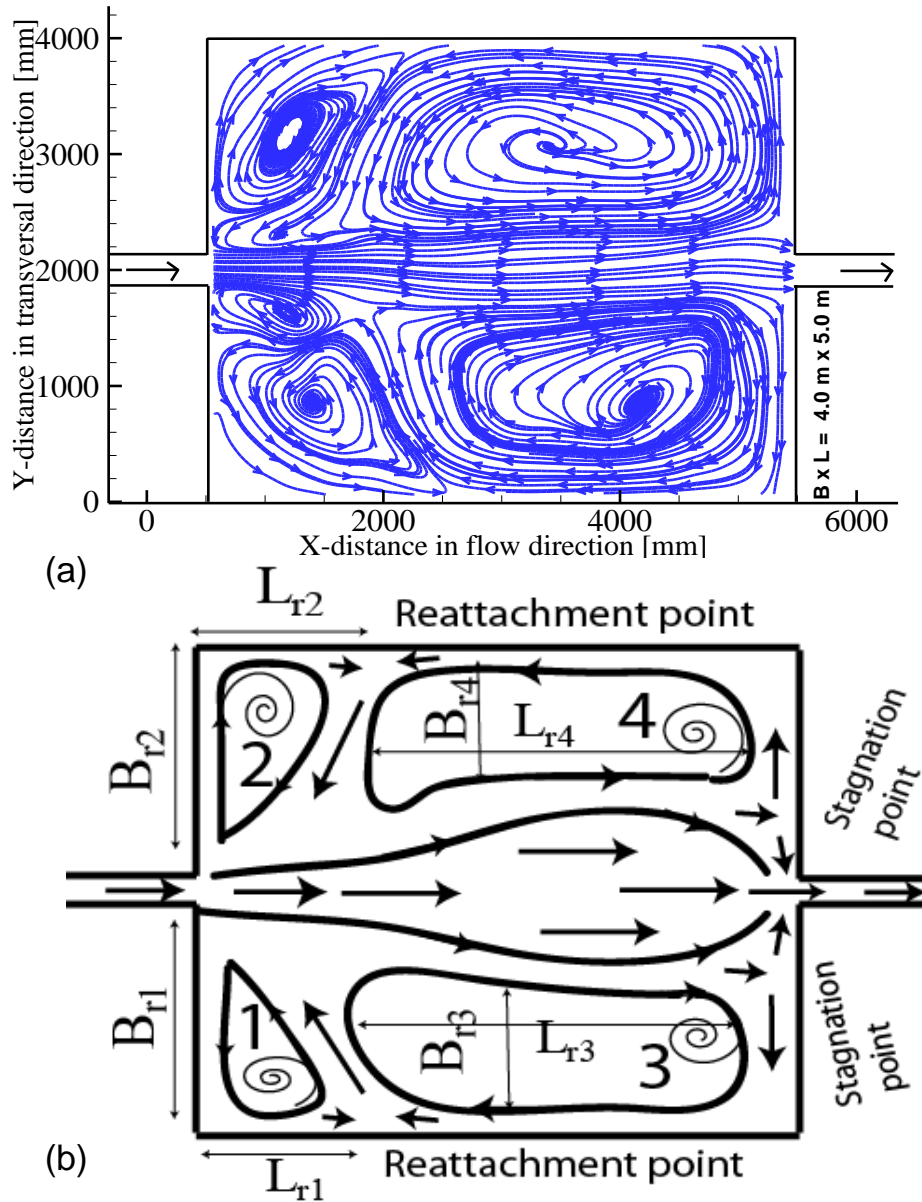


Figure 4.2: (a) Time-averaged streamlines obtained by LSPIV measurements for clear water flow for geometry with shape SK of 4.9 (b) Plan view of the rectangular geometry ($L = 5 \text{ m}$, $B = 4 \text{ m}$) and the geometrical parameters of the recirculation cells in the basin are L_{ri} , B_{ri} for gyres (1, 2, 3, 4).

developed with a shorter geometry length (Tests No 11, 12 & 13) and a hexagonal geometry (Test No 16). In that case, the flow became more stable and symmetric with four large vortices (4 regions in Figure 4.2(b)).

By reducing SK to 2.92, the number of symmetric gyres is reduced to two (coupled) circulation cells along the centerline. The upstream corner vortices disappear completely.

In conclusion, in tested axi-symmetric rectangular configurations, the flow is symmetric

if $SK < 5.5$ and asymmetric if $SK > 5.5$.

One of the primary objectives of these experiments is to examine the impact that variation in the geometry shape parameters, Reynolds and Froude numbers, has on the flow. Consequently, later the ability of the numerical simulations to match the experimental results can be checked. In this regard, flow pattern, vorticity, and number of circulations are important since correct prediction of these feature is a necessary condition for matching the phase averaged flow profiles in the experiment.

In this study, flow pattern and velocity vectors and streamlines results were used to track the horizontal trajectories of the vortex pairs as a function of time to determine the evolution of the vortices. Since the vortex dipole expelled from the jet produces a localized streamwise jet along the centreline, an easy way to track the location of the vortex dipole is to track the local maximum in the velocity on the jet centreline.

In order to explain the mechanisms of the observed jet flow features; time sequence investigations for the jet issuing into stagnant shallow water were conducted for the geometries of $SK = 5.97$ and 4.89 . The flow pattern and streamline evolution of plane jet exhausting into a quiescent water in the rectangular shallow reservoir with geometry shape factor of $SK = 5.97$ are described in the Figures 4.3 and 4.4.

The figures clearly depict the process of transition of the primary vortex pair into a fully developed turbulent jet. The jet penetrates the quiescent water in a nearly straight line, indicating that the surrounding flow is laminar.

In the initial period at $t_1 = 30s$ before the advancing front reaches the outlet flow pattern indicates that near inlet field is dominated by counter-rotating vortex pairs that move downstream by self-induction. The outflow streamlines shown in Figure 4.4 is symmetric.

The figures also show the presence of mostly streamwise secondary vortical structures surrounding the cores of the primary vortex pair. These secondary structures undergo rapid amplification owing to three-dimensional vortex stretching, and cause transition of the primary vortex pair into a well-developed turbulent jet within a short distance from the inlet.

Since the vortex dipole expelled from the jet produces a localized streamwise jet along the centreline it is easy to track the location of the vortex dipole on the jet centreline.

At $t_2 = 60s$ jet spreads along the centerline and velocity increases. Moreover, the growth of velocity magnitudes and the size of the left side gyre is larger than the right one as shown in Figures 4.3 and 4.4.

The jet front reached to the reservoir outlet and the two upstream corners still quiescent. Due to the variation of velocities on left and right sides along the jet there is instability leads to the formation of shear-layer vortices, which subsequently undergo one or more stages of vortex pairing.

The growth of left gyre gives rise to the asymmetric flow fields, as observed at $t_3 = 120s$. As the jet evolves downstream and the velocity increase on one side of the jet leads to a

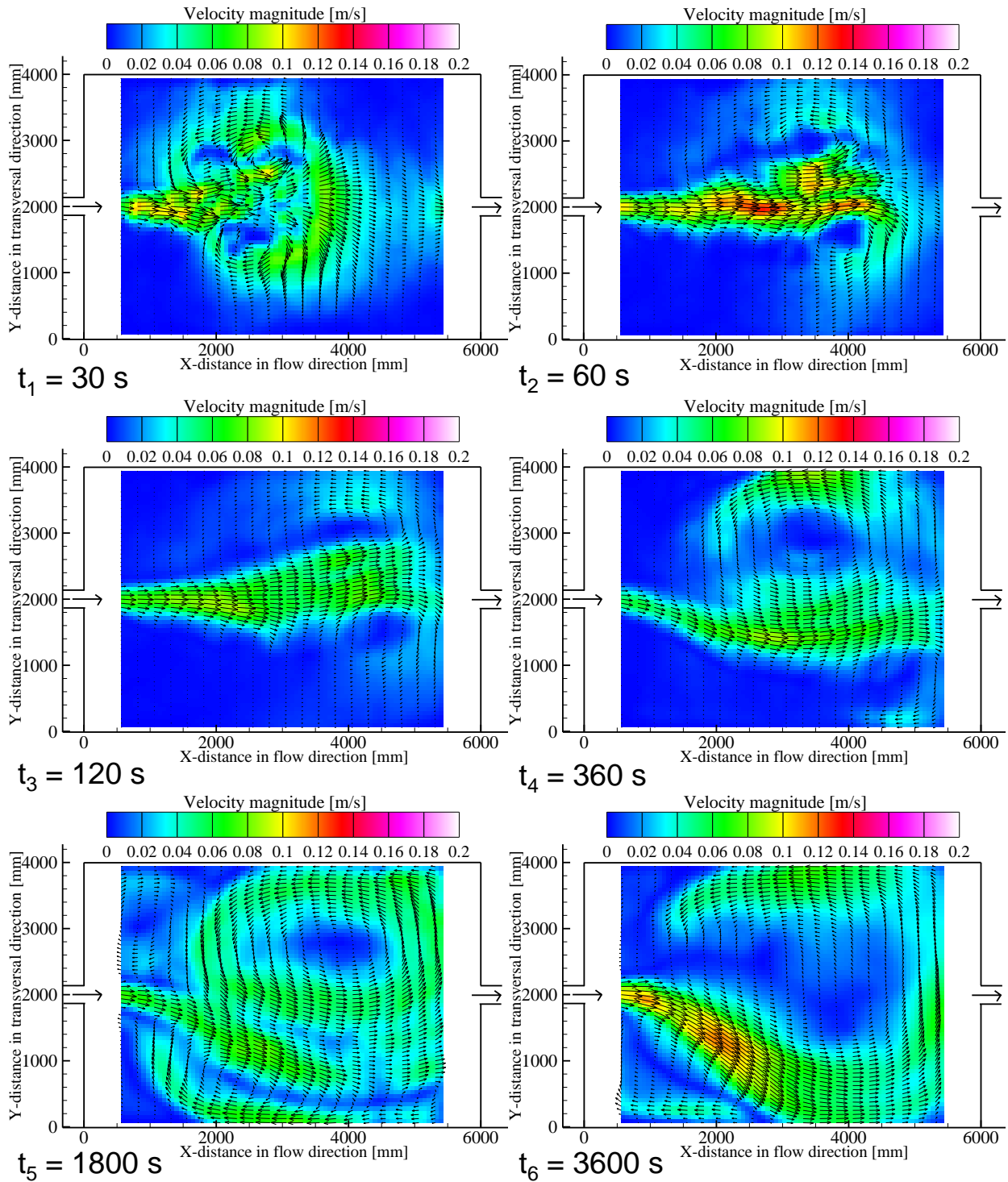


Figure 4.3: Time development of flow vectors and velocity magnitude for geometry with shape SK of 5.97.

local reduced pressure, which in turn tends to amplify the deflection of the flow. Between t_3 and t_4 a transitional phase with the jet deselection from left to right. At $t_5 = 1800$ s, a new

vortex pair at the upstream corners and its size is of the order of the geometry expansion width.

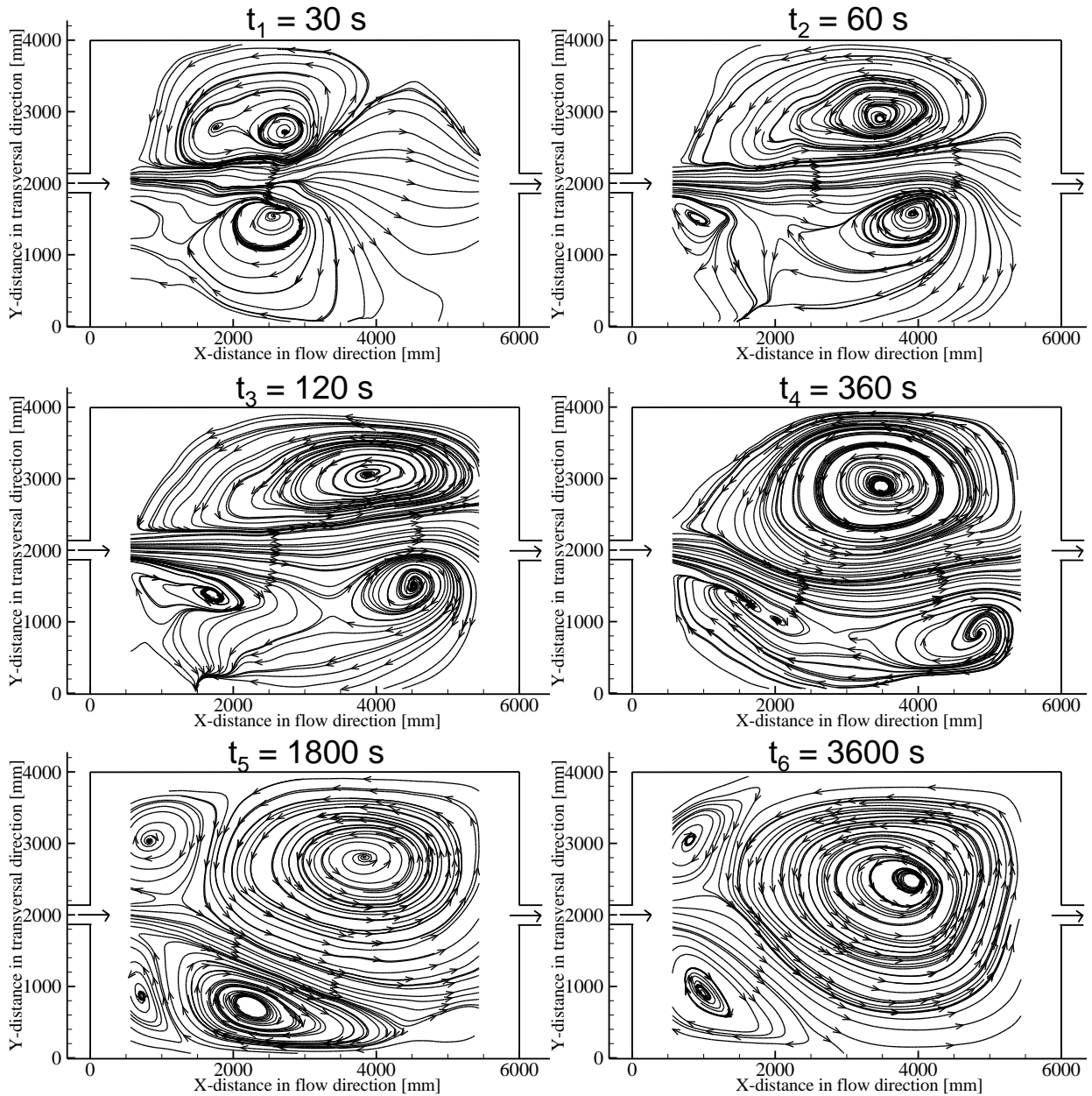


Figure 4.4: Time development of streamlines for geometry with shape SK of 5.97.

In total four gyres are formed at $t_5 = 1800s$. Separation of the shear layer inside the jet entrance is also readily visible in Figures 4.3 and 4.4. When the jet stabilizing process is completed at $t_6 = 3600s$, the core vortex detaches from the exit plane and grows in size with two gyres at the upstream corners.

The streamline plot also shows the presence of corner gyres in the upstream corners the

deflected jet towards the right wall in the converging region and eventually attached to it at the impingement point (stagnation or attachment or reattachment point).

Downstream from the attachment point, in the attachment region, the flow is subjected to the effects of stabilizing curvature. Far downstream from the inlet in the wall jet region, the flow continues to develop to resemble a wall jet flow.

4.1.1 Conclusions regarding features of flow pattern

The above provides a qualitative and quantitative view of the development of spanwise and streamwise vortex structures. However, the flow is highly three-dimensional, and so it is useful to examine the three-dimensional of this flow. The starting jet developed initially in a symmetric flow for all tested geometries.

But the asymmetry phenomenon of the jet is due to an decelerate of the axial velocity about the centerline leads to an increase in the velocity on one side leads to a local reduced pressure on that region which in turns tend to amplify the deflection of the jet (Coanda effect). The Coanda jet is defined as the wall jet along the curved wall.

The flow of fluid with a curved jet is accompanied with the decrease of the pressure behind the curvature jet near the wall corner. The pressure on the wall drops below the surrounding pressure resulting in the attachment of the fluid flow to the wall. The increase of one corner gyre leads to increase its size comparing to the the other side one, both of them controlling the center one.

Once the resulting gyres are established across the basin, flow asymmetry is maintained. Simultaneously, an axial acceleration of the velocity leads to increased the centrifugal forces, which tends to re-establish the symmetry of the flow pattern. A balance between those two effects is reached in the steady state.

4.2 Flow patterns, streamlines, vorticities for different geometry forms

Flow patterns, streamlines, and mean vorticities for all test series are compared in Figures 4.5, 4.6, 4.7, 4.8, 4.9, 4.10, 4.11, 4.12, and 4.13. For all tested geometries, three typical behaviors (flow features) were observed.

The first is a deflected jet (question mark shape jet) with a stable asymmetric flow pattern which has one long and one short separation zone for reduced basin widths B and reduced jet expansion angle θ^* .

The second is a straight jet with a symmetric flow pattern along the centerline with large scale vortices on both the right and left sides for reduced basin lengths and hexagonal geometries.

The third is a central meandering jet flow under periodic perturbation of the meanders amplitude with unstable asymmetric flow pattern for all geometries with specific hydraulic conditions, specially by increasing Froude numbers.

The water level is kept constant for the studied geometries in Sections 4.2.1 and 4.2.2. Tests with variable water depths are discussed in Section 4.2.3.

4.2.1 Asymmetric flow (deflected jet) for geometry shape factor $SK > 5.5$ & $h/b = 0.8$, $Fr_{in} = 0.1$, and $Re_{in} = 28000$

In Figure 4.5(a) - (g) the flow patterns are shown by the velocity vectors and magnitude for various geometries with $SK = 5.97, 8.25, 13.42, 33.07, 86.6, 5.94$ and 5.89 , respectively and a fixed ratio of h/b (water depth to the inlet channel width). Of particular interest is the effect of the geometry on the flow field and the separation zone on both sides.

In Figure 4.5(a), the flow has an asymmetric behavior, leading to a larger gyre size in the right upstream corner side than in the left side. The main gyre size is in accordance with the two corners gyres.

The two corner gyres are depending from each other and alternatively change in size.

Moreover, they control the size and location of the main gyre. By removing the upstream corners, as shown in Figure 4.5(f), the two corner gyres disappeared and only the core gyre is formed.

No changes occurred by removing the downstream corners in the diamond geometry shape.

The observed flow pattern in Figure 4.5(g) did not differ much from what was previously explained for Figure 4.5(f), except for the reduction in size of the center gyre and a downstream shifted separation and reattachment points.

The size and locations of the vortices are clearly visible by streamlines shown in the Figure 4.6 (a), (b), (c), (d), (f) and (g). It is also interesting to plot the mean vorticity maps as given in Figure 4.7.

The vorticity is defined as the curl of the velocity. In accordance with the flow patterns and streamlines, the high vorticity is concentrated at the curved jet entering from the inlet channel and the right side corner.

Figure 4.7(c), exhibits a relatively large area with strong vorticity. It reflects a large portion of flow stabilization due to width reduction.

By reducing the basin width, the flow becomes more homogenous and the transversal vorticity increases. Moreover, no stagnant water is observed in the center of the gyres shown in Figure 4.7(c) & (e).

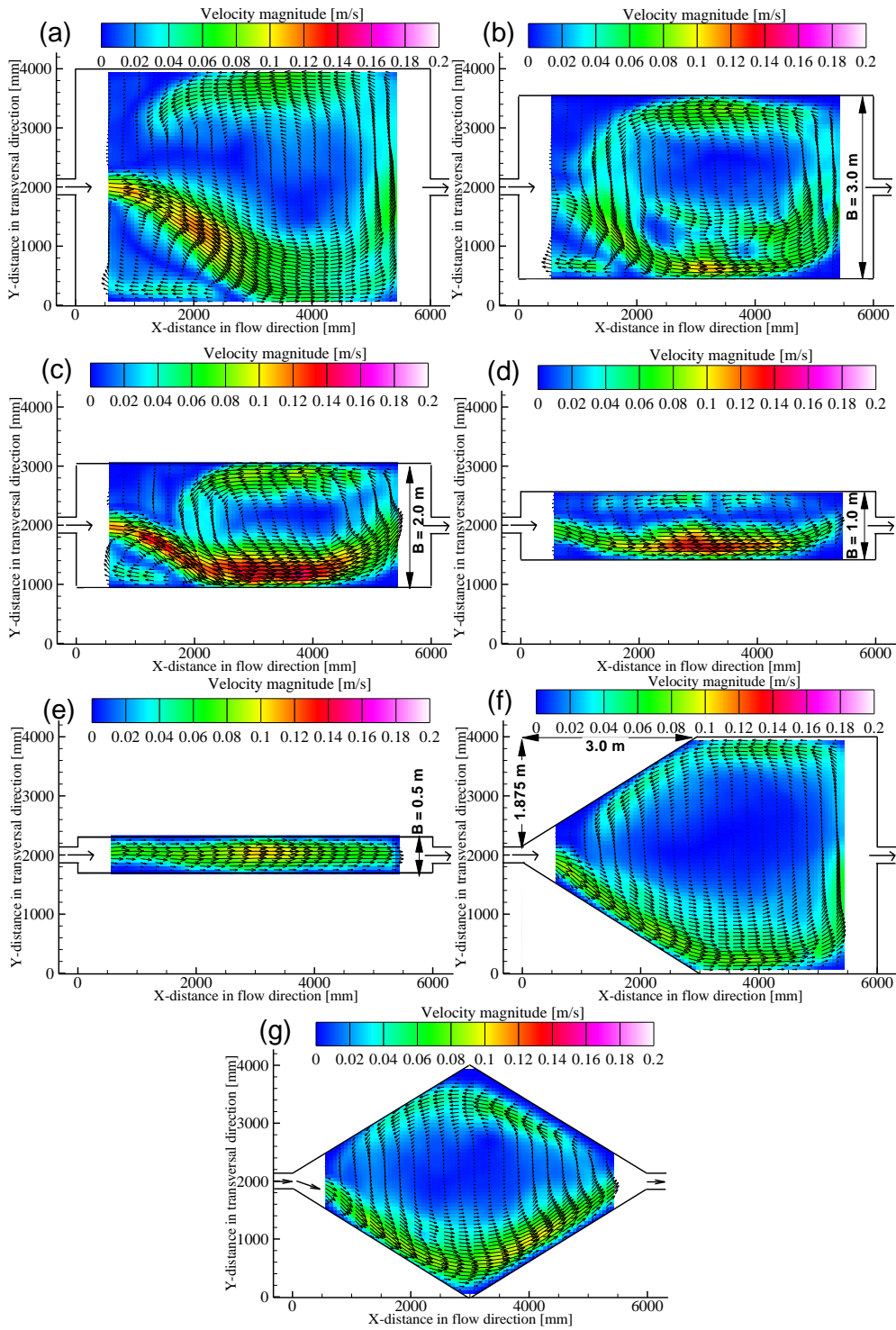


Figure 4.5: Average flow pattern with velocity vectors for seven different geometries with shape factors $SK = 5.97$ (a), 8.25 (b), 13.42 (c), 33.07 (d), 86.60 (e), 5.94 (f), and 5.89 (g).

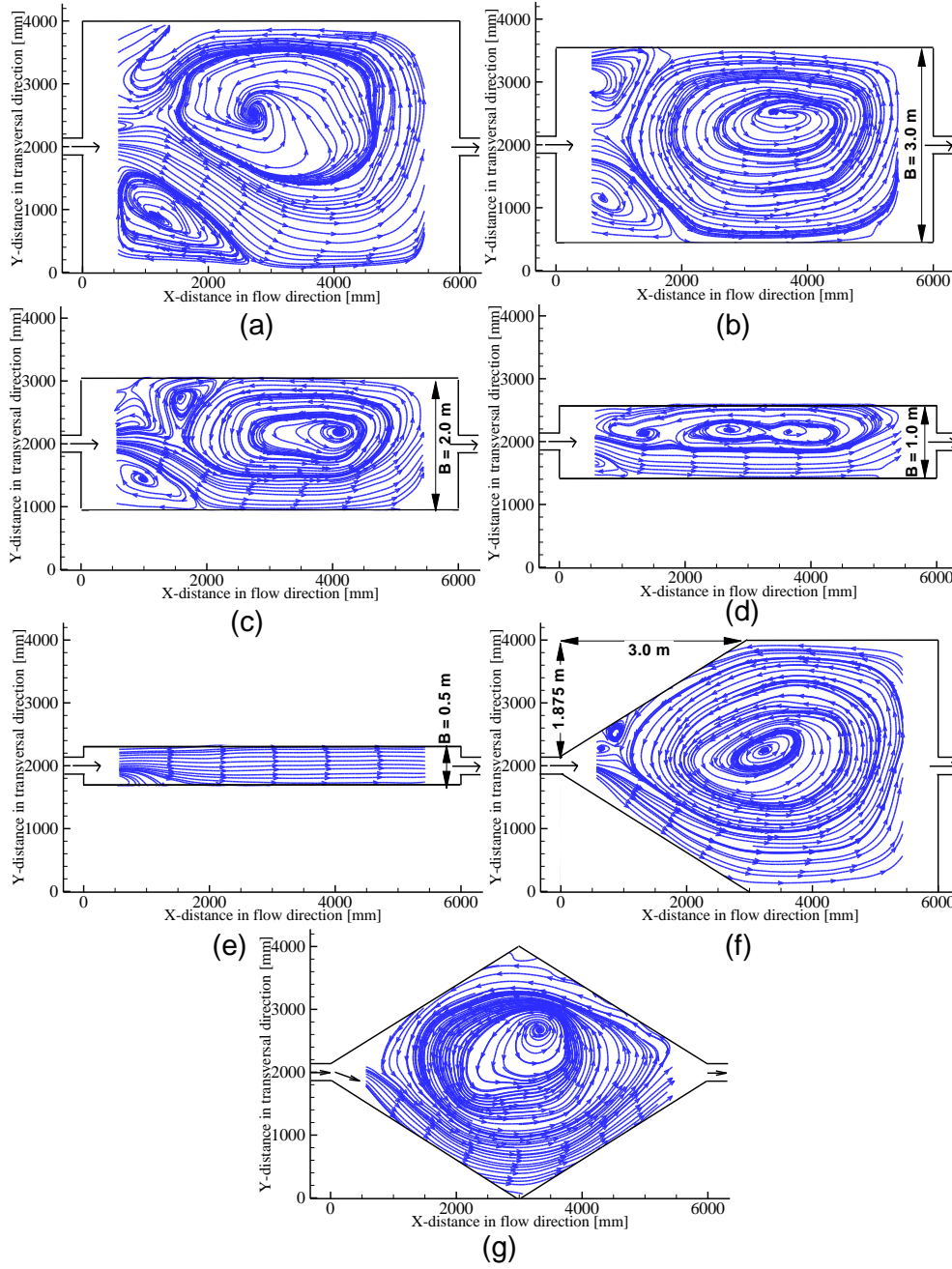


Figure 4.6: Time averaged streamlines for seven different geometries with shape factors $SK = 5.97$ (a), 8.25 (b), 13.42 (c), 33.07 (d), 86.60 (e), 5.94 (f), and 5.89 (g).

4.2.2 Symmetric flow (straight jet with spanwise circulation) for geometry shape factor $SK \leq 5.5$ and $h/b = 0.8$, $Fr_{in} = 0.1$, and $Re_{in} = 28000$

Asymmetry disappears when the geometry shape factor is lower than 5.5, as illustrated by Figures 4.8, 4.9 and 4.10(a), (b), (c) and (d) for LSPIV results for shape factors $SK = 4.89$,

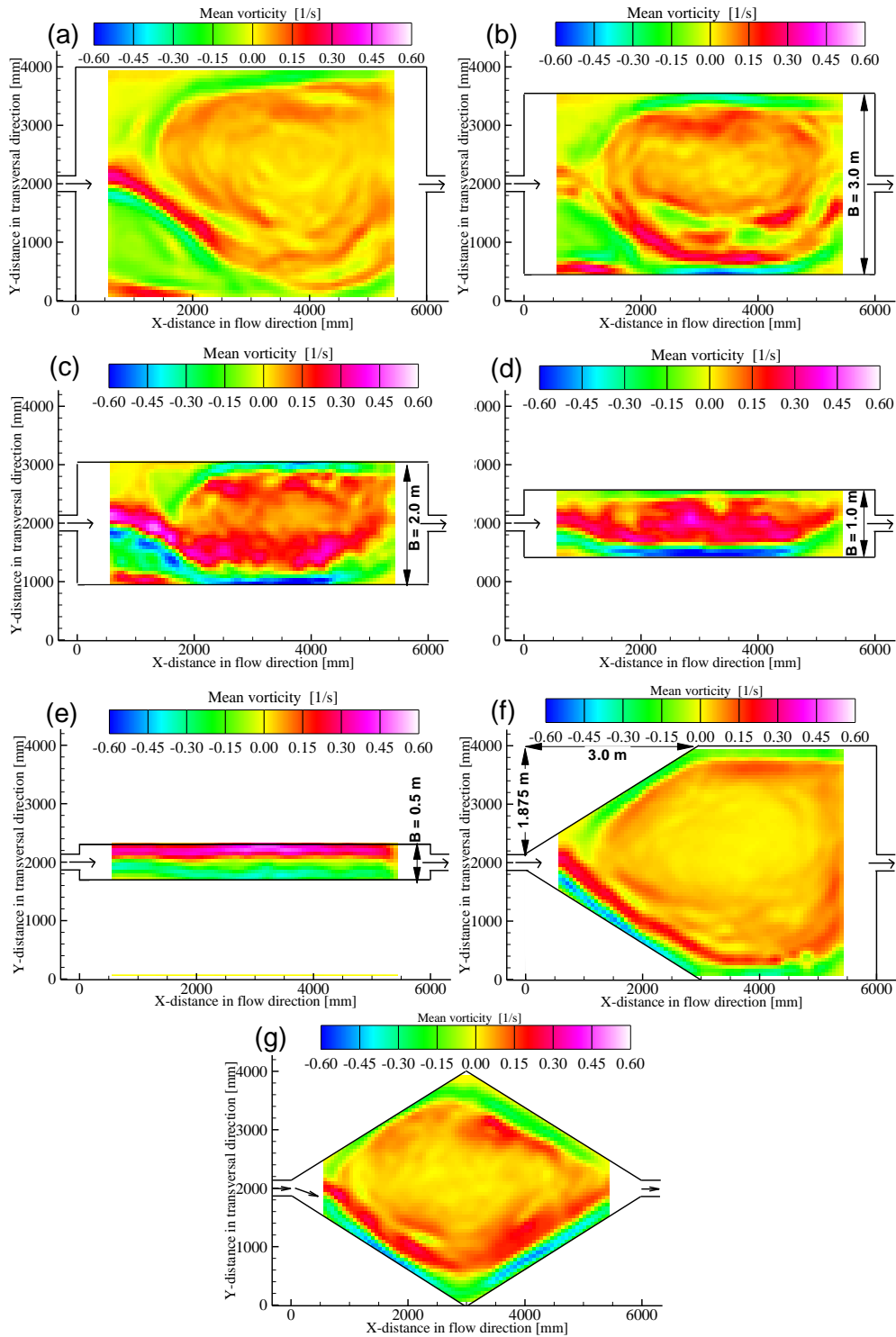


Figure 4.7: Mean vorticity for seven different geometries with shape factors $SK = 5.97$ (a), 8.25 (b), 13.42 (c), 33.07 (d), 86.60 (e), 5.94 (f), and 5.89 (g).

3.88, 2.92 and 3.41 for the same h/b ratio.

By reducing the basin length and consequently decreasing SK ratios, the flow is stabilized with a stable symmetrical pattern.

Four vortices exist in the basin for an SK ratio lower than 5.5 as shown in Figure 4.2. The four gyres interact with the jet, which has some tendency to meander.

By reducing the basin length for $SK = 3.88$, the number of gyres remains constant and the flow pattern becomes rather symmetric with respect to the centerline (Figure 4.9(b)).

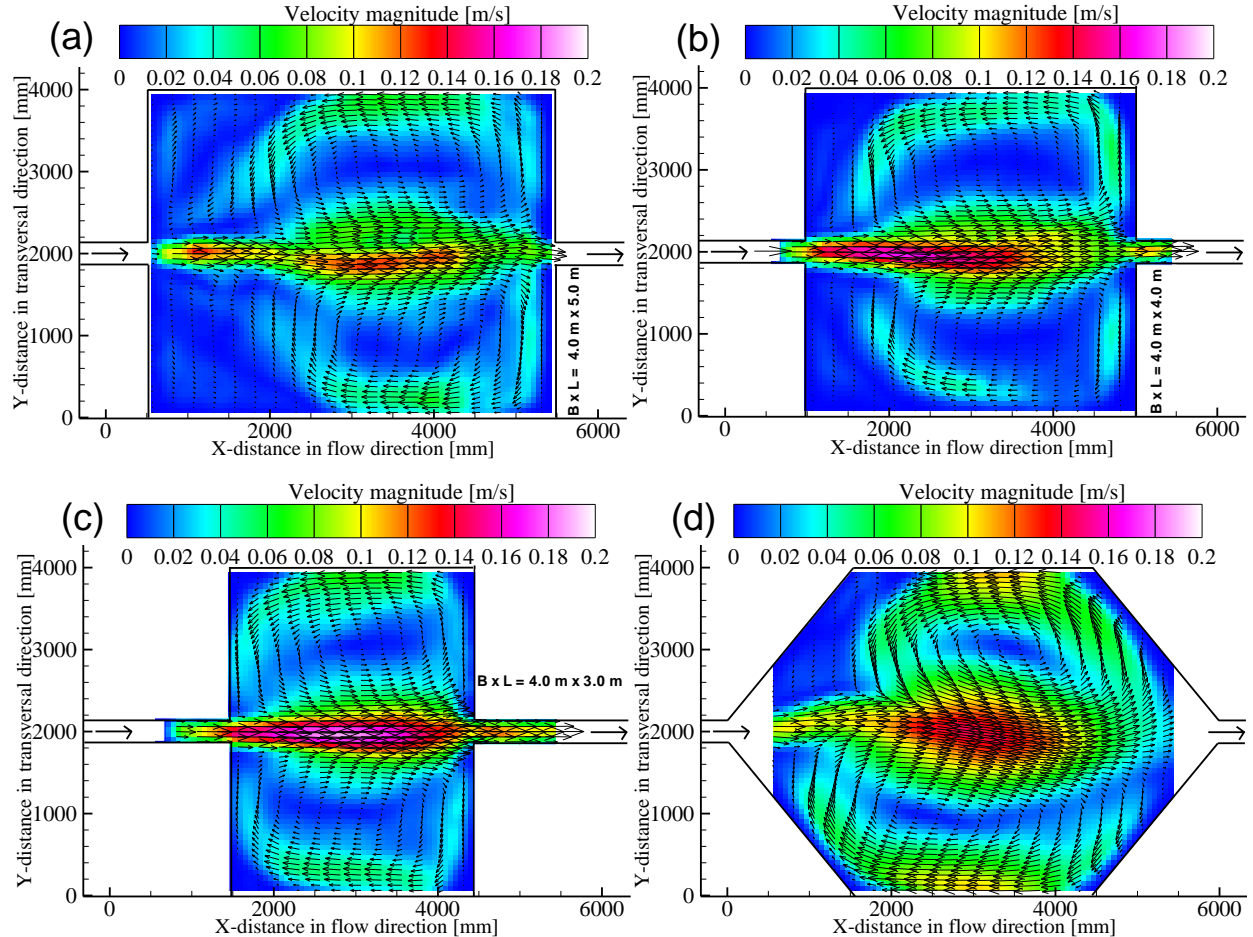


Figure 4.8: Average flow pattern with velocity vectors for five different geometries with shape factors $SK = 4.89$ (a), 3.88 (b), 2.92 (c), and 3.41 (d).

Symmetric streamlines with two vortices can be observed in Figure 4.9(c), for SK ratio of 2.92 and a basin length less than its width. Similar flow patterns and streamlines with two vortices occur by removing the four corners of the reference basin with SK ratio of 5.97 (Figure 4.9(d)).

The predominant change in the flow pattern is an evolution from a four-vortices flow to a distinct two-vortices flow. The corresponding vorticities for these streamlines are shown in Figures 4.10(a), (b), (c) and (d).

By comparing these figures, it can be said that the vorticity values are increasing with decreasing basin lengths.

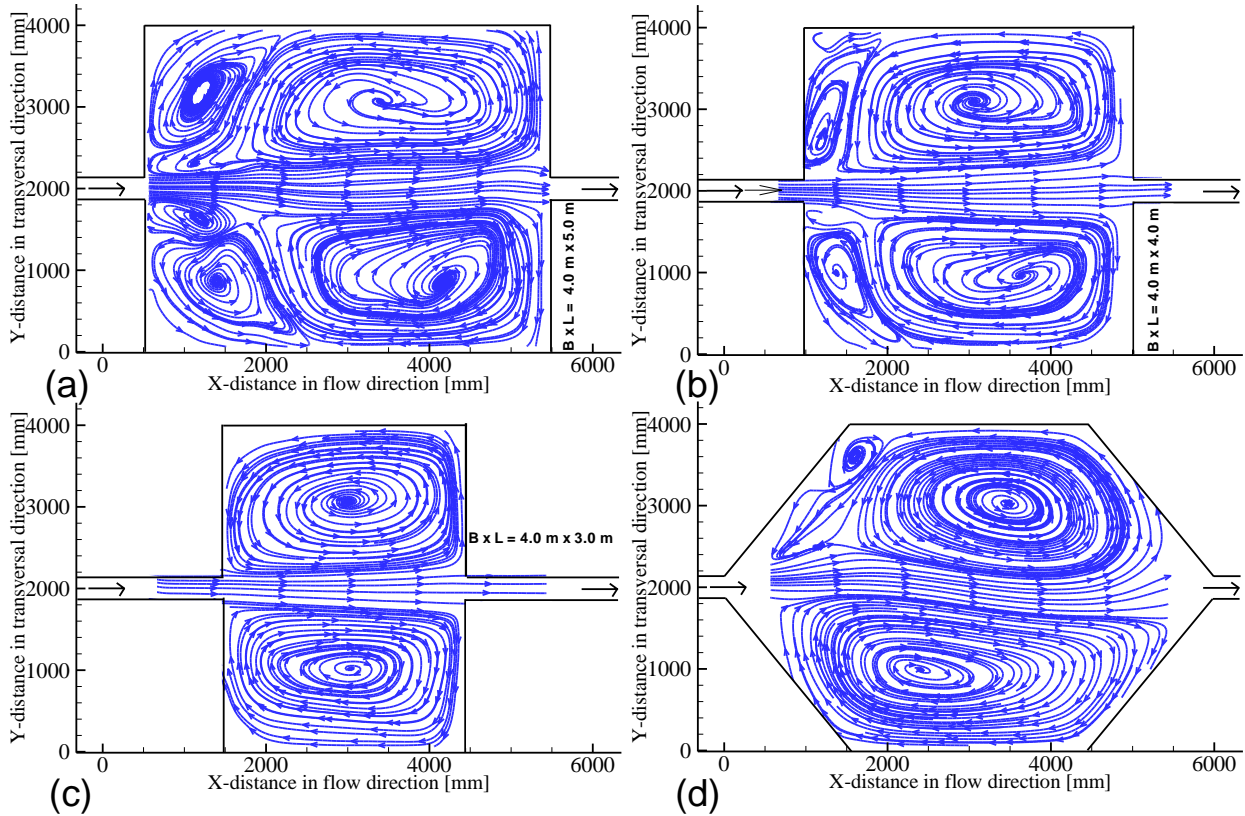


Figure 4.9: Time averaged streamlines for five different geometries with shape factors $SK = 4.89$ (a), 3.88 (b), 2.92 (c), and 3.41 (d).

By comparing all geometries with $SK \leq 5$, it can be concluded that similar symmetric flow patterns occur with small differences regarding the dimensions and strengths of the circulation cells.

4.2.3 Central meandering jet flow for $h/b \leq 0.6$

Meandering jet is the third feature of the jet which has been observed. For the same geometry shape factor $SK = 5.97$, several h/b ratios (water depth to the inlet channel width) have been studied. The depicted results in Figure 4.11(a), (b), and (c) differ only on the ratio of water depth to inlet channel width $h/b = 0.6$, 0.4 , and 0.3 .

In Figure 4.11(a) by reducing h/b from 0.8 to 0.6 , the jet starts meandering around its centerline which accompanied with the appearance of large counter-rotating vortices alternating on both sides of the jet. The size of these structures increase with the downstream direction by pairing.

The apparent onset of the meandering begins with $h/b = 0.6$. An alternating sense of rotation for the meandering jet observed in Figure 4.11(b), of $h/b = 0.4$.

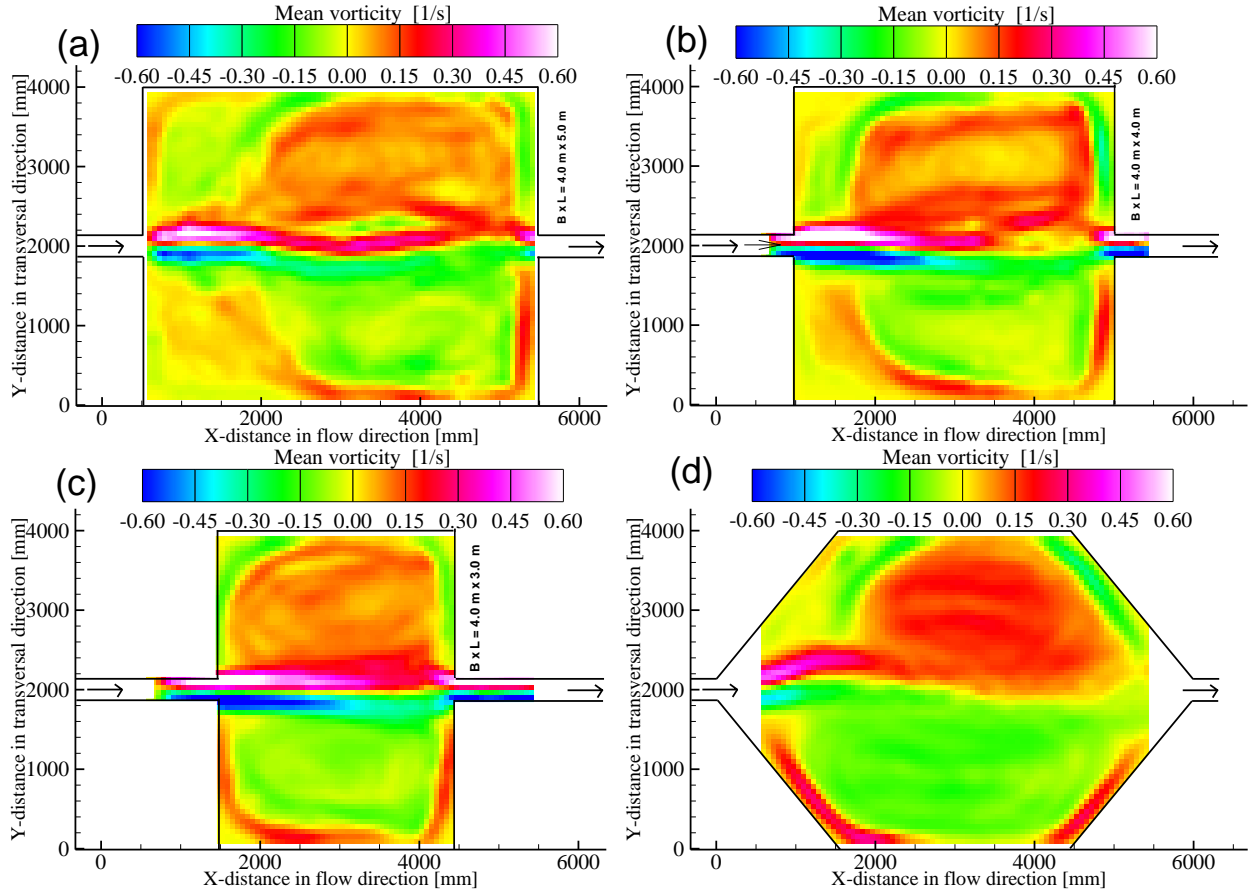


Figure 4.10: Mean vorticity for five different geometries with shape factors $SK = 4.89$ (a), 3.88 (b), 2.92 (c), and 3.41 (d).

Moreover, the reattachment points are moving from left to right wall. Decreasing h/b to 0.3 does not alter the situation described before. Within the range of h/b of our observation, the meandering behavior seems to be preserved for yet different geometry shape factors.

The influenced of the water depth on the development of the jet can also be seen in visual mean streamlines and vorticity observations in Figures 4.12, and 4.13, respectively.

The meandering jet is connected to a series of large two dimensional vortical structures with an alternating sense of rotation which grow at the same rate as the overall growth of the jet.

Figure 4.12(a) shows the streamlines corresponding to the time-averaged velocity field for $h/b = 0.6$. The plot shows a pair of relatively large recirculation regions on either side of the mean jet and its associated separation points.

The centers of these recirculation zones are roughly at a distance of $9b$ perpendicular on the jet flow trajectory at the centers. The right side center at distance of $4b$ from the jet exit but the left one is at $9b$.

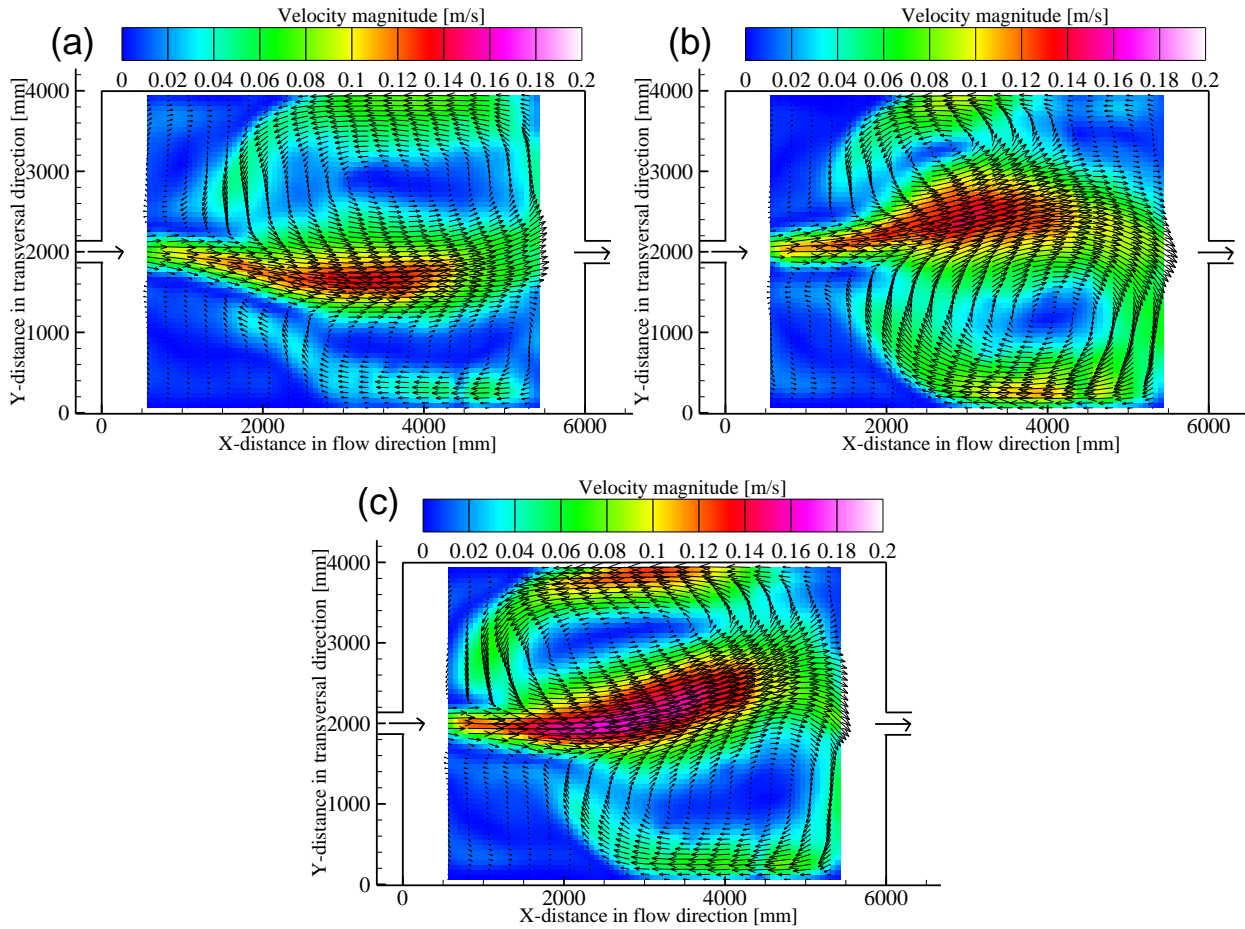


Figure 4.11: Average flow pattern with velocity vectors for the reference geometry with shape factor $SK = 5.97$ and $h/b = 0.6 = 0.6$ (a), 0.4 (b), and 0.3 (c).

It has to be noted that the formation of these recirculation zones is directly connected with the zero-net mass flow characteristic of the jet since the mass flow in the central mean jet has to be balanced by a reverse flow towards the inlet.

By comparing the mean streamlines pattern in Figures 4.12(a), (b), and (c), it can be said that the size of the two upstream corners vortex does not differ by reducing h/b ratios. The mean vorticity contour obtained for $h/b = 0.6$, 0.4, and 0.3 are plotted in Figures 4.13(a), (b), and (c).

The vortex cores are located at a distance of about $6.6b$ from the outlet exit.

The meandering phenomenon is observed with a self-induction of the vorticity field. The meandering flow jet can induce instabilities and enhance mixing in reservoir flow.

4.3. Influence of hydraulic conditions (Froude and Reynolds numbers) on the flow stability

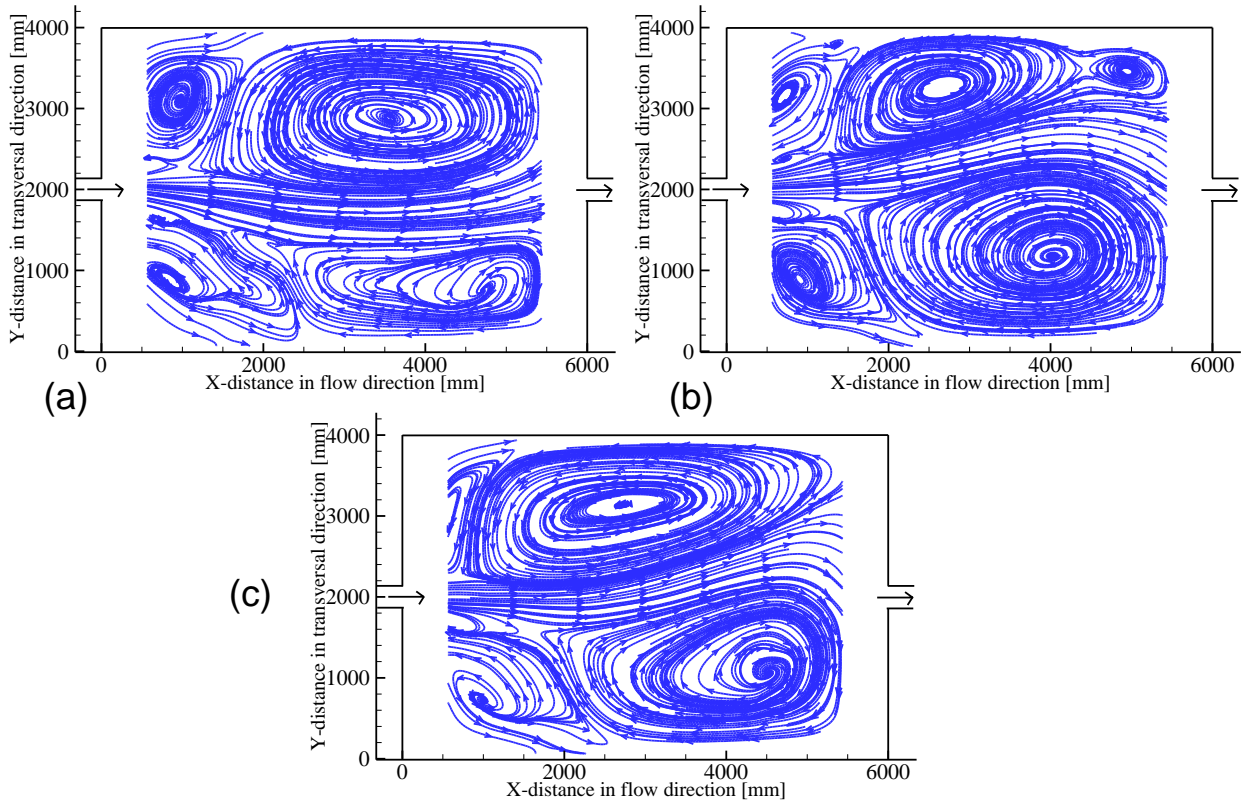


Figure 4.12: Mean streamlines for the reference geometry with shape factor $SK = 5.97$ and $h/b = 0.6 = 0.6$ (a), 0.4 (b), and 0.3 (c).

4.3 Influence of hydraulic conditions (Froude and Reynolds numbers) on the flow stability

The results discussed hereafter concern Tests 5 and 6 and their hydraulic conditions shown in Table 3.7. The herein presented comparison of ratio of U_{res}/U_{in} for a constant reservoir geometry with shape factor $SK = 5.97$ (T5 and T6) and different hydraulic conditions (Table 3.7).

The influence of the hydraulic conditions on the size and shape of the stability of the vortex and flow characteristics have been investigated by varying the inlet Reynolds number Re_{in} between 14000 and 28000 and a variety of the inlet Froude number Fr_{in} ranging from 0.050 to 0.435.

Figures 4.14(a), (b), (c), and (d) show the normalized velocity magnitudes U_{res} of the entire reservoir with the inlet channel velocity U_{in} for a constant Reynolds number $Re_{in} = 28000$ and a variety Fr_{in} 0.100, 0.153, 0.283, 0.435, respectively. The flow is a deviated stable jet with three vortex for $Fr_{in} = 0.100$.

The mean velocity of the deflected jet is about 50% of the inlet mean velocity. After

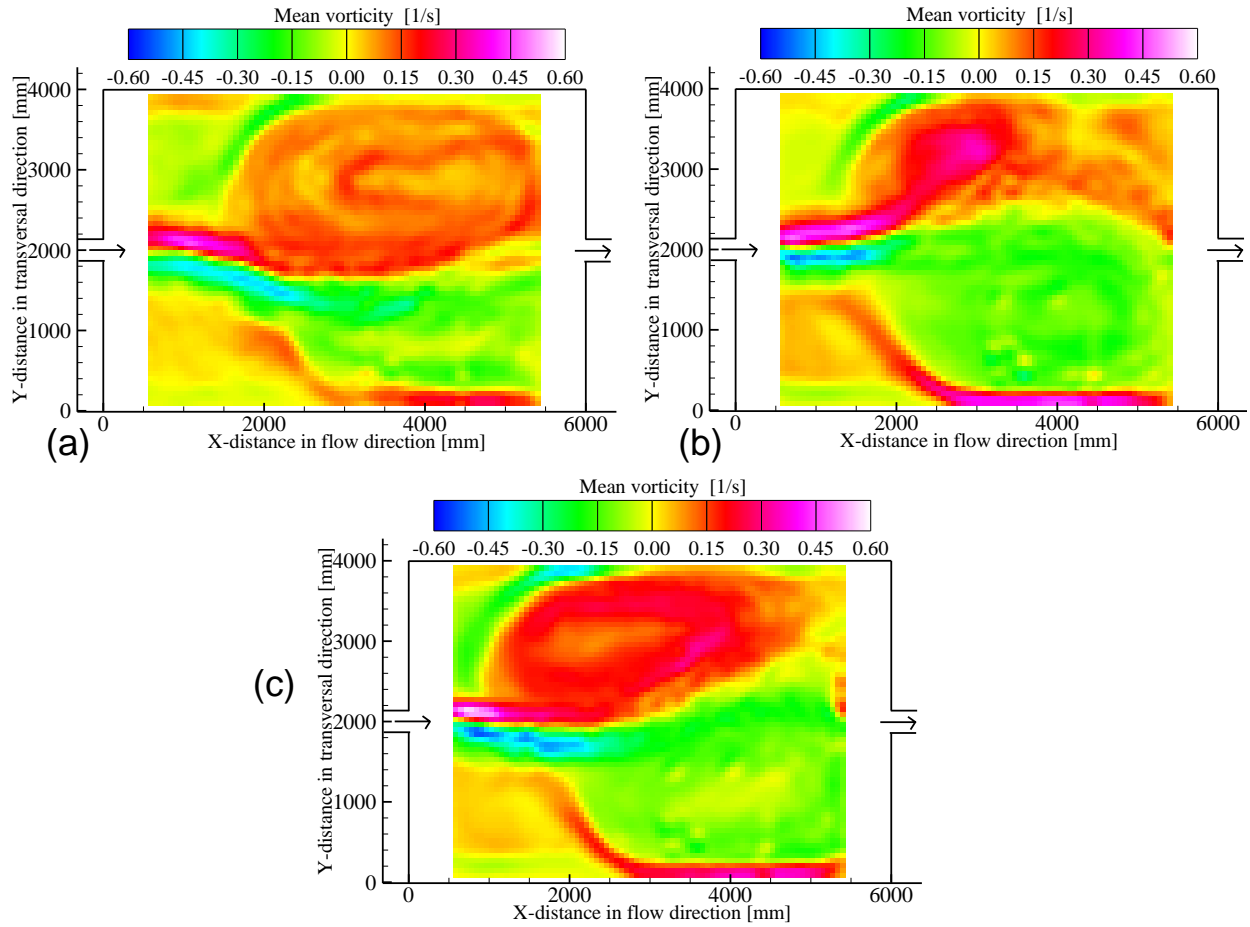


Figure 4.13: Mean vorticity for the reference geometry with shape factor $SK = 5.97$ and $h/b = 0.6 = 0.6$ (a), 0.4 (b), and 0.3 (c).

the impingement point the reattachment length is reduced to 30% on right side jet and the reverse jet towards the inlet as shown in Figure 4.14(a).

In the same figure the flow pattern is characterized by:

- Main gyre that forms in the center part of the reservoir and covers nearly half of its spacing (Figure 4.15(a)); the mean velocity is about 15% of the inlet velocity.
- Right triangular gyre which cover 10% of the entire reservoir surface (Figure 4.15(a)); velocity is about 25% of the inlet velocity.
- Left triangular gyre which cover 5% of the entire reservoir surface (Figure 4.15(a)); velocity is about 15% of the inlet velocity.
- Shedding eddy is regularly due to jet entrainment into a wide reservoir. This eddy moves with the deflected jet and merges with the other gyres, which in turn changing in

4.3. Influence of hydraulic conditions (Froude and Reynolds numbers) on the flow stability

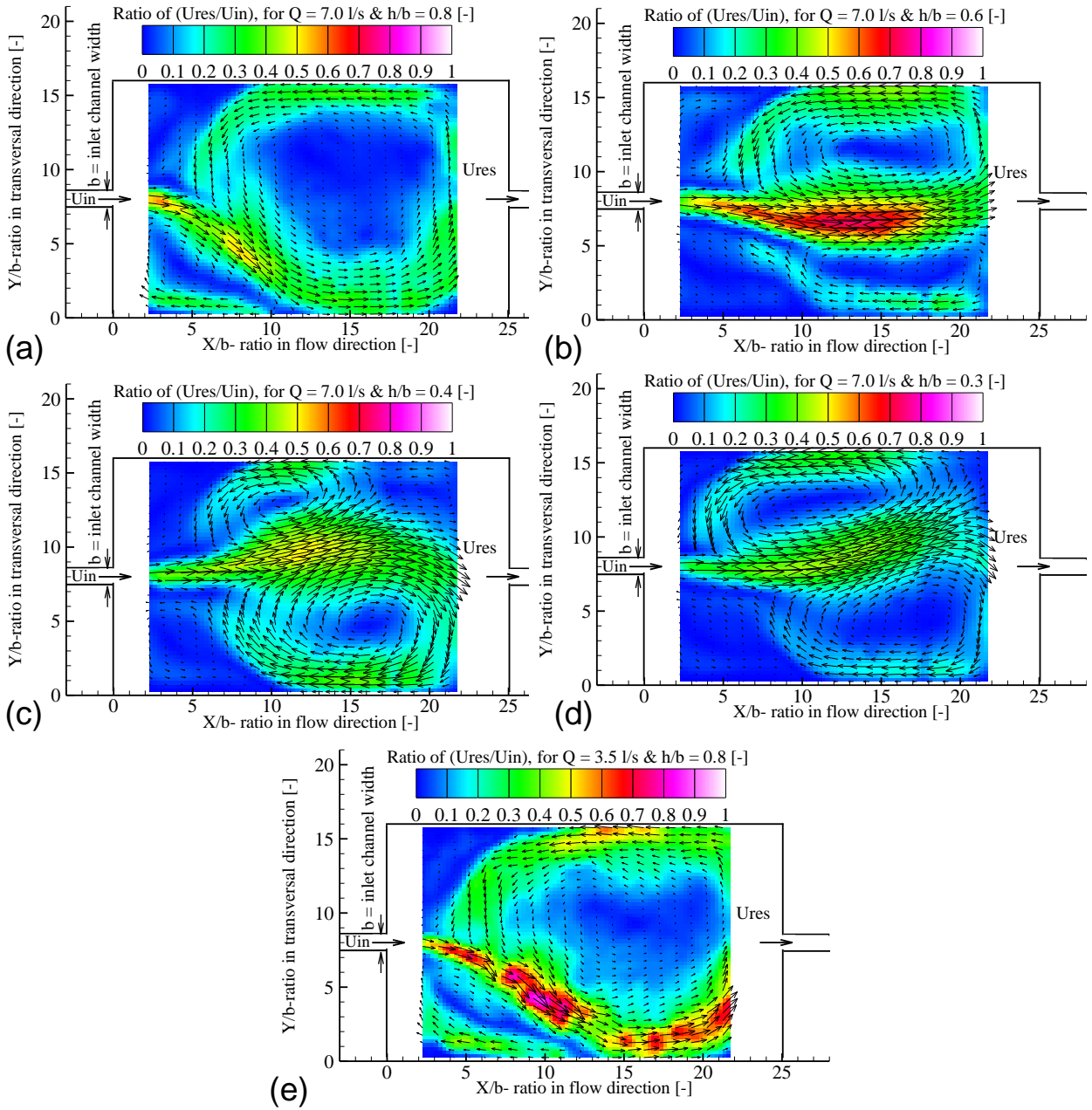


Figure 4.14: Average velocity vectors with ratio of U_{res}/U_{in} for the reference geometry with five different hydraulic conditions: (a) $Re_{in} = 28000$, $Fr_{in} = 0.1$, (b) $Re_{in} = 28000$, $Fr_{in} = 0.153$, (c) $Re_{in} = 28000$, $Fr_{in} = 0.283$, (d) $Re_{in} = 28000$, $Fr_{in} = 0.435$, and (e) $Re_{in} = 14000$, $Fr_{in} = 0.05$.

size due to the interaction with the moving one. After this eddy has been disappeared, another eddy has room to form.

By increasing Fr_{in} to 0.153 (by decreasing water depth) the flow stability and characteristics are completely changed as clearly depicted in Figure 4.14(b). The jet deflection more

or less disappears and a central meandering jet has been formed with pairing circulation as explained in Section 4.2.3.

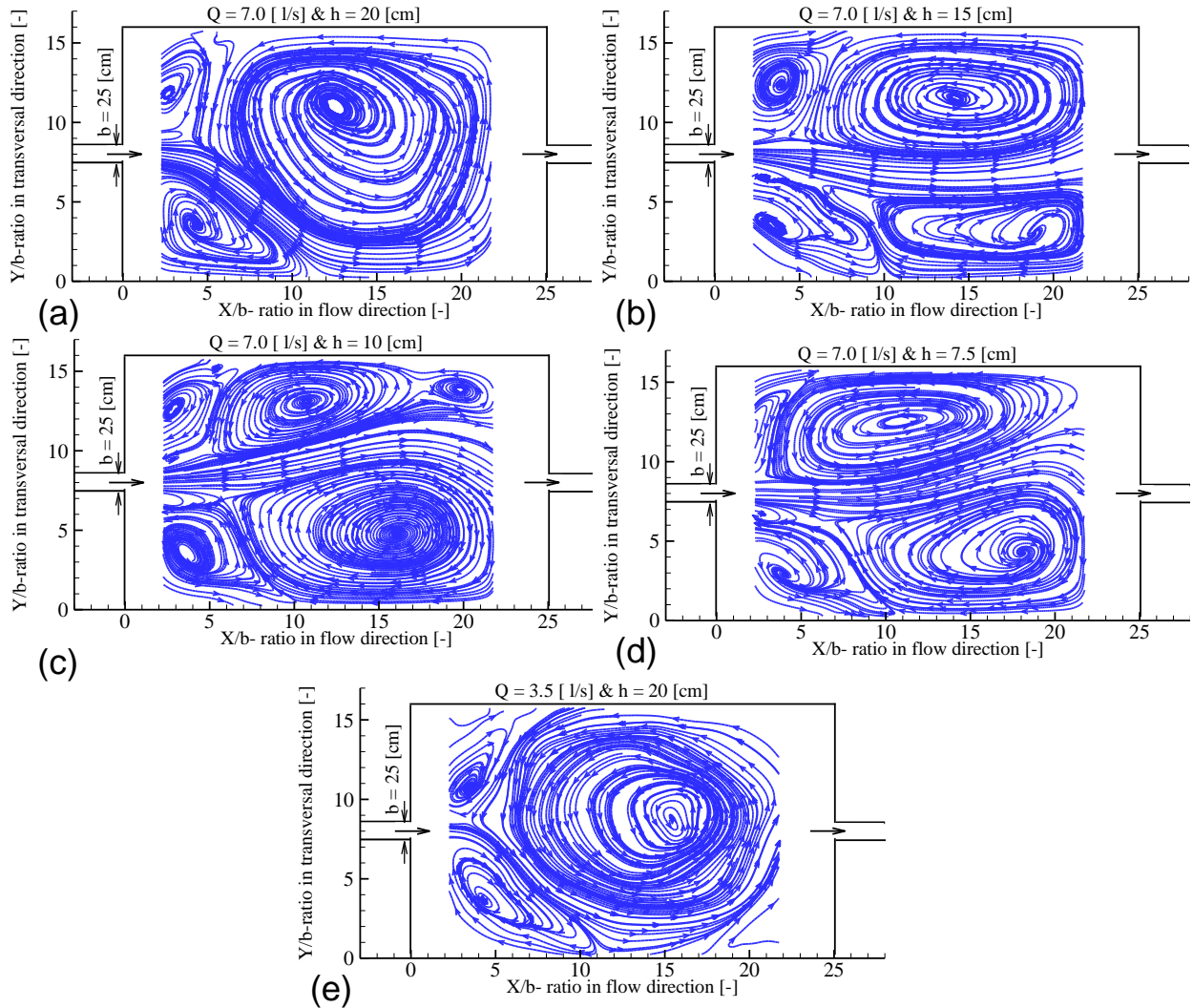


Figure 4.15: Time averaged streamlines for the reference geometry with five different hydraulic conditions:(a) $Re_{in} = 28000, Fr_{in} = 0.1$, (b) $Re_{in} = 28000, Fr_{in} = 0.153$, (c) $Re_{in} = 28000, Fr_{in} = 0.283$, (d) $Re_{in} = 28000, Fr_{in} = 0.435$, and (e) $Re_{in} = 14000, Fr_{in} = 0.05$.

The meandering behavior is forming by increasing the Froude number to $Fr_{in} = 0.283$ and to 0.435. The flow pattern resembles the von Kármán vortex street pattern.

The pairing vortex observed in Figures 4.15(c)&(d), has different shape and size. Moreover, the jet has a sinusoidal shape with different curvatures. By decreasing Fr_{in} to 0.05 the jet still deflected to right side and the mean velocity is about 75% of the inlet mean velocity as depicted in Figure 4.15(e).

Figure 4.15(e) shows the ratio of the reservoir and inlet velocity for a reduced Reynolds

4.3. Influence of hydraulic conditions (Froude and Reynolds numbers) on the flow stability

number $Re_{in} = 14000$. By reducing the Reynolds number the jet still deviated to the right side with three gyres as observed in Figure 4.15(a) for the same geometry with $Re_{in} = 28000$.

By comparing the two figures it can be concluded that similar flow patterns have developed with the same dimensions and strength of the circulation cells but with small differences regarding the mean velocity of the deflected jet as shown in Figure 4.15(e).

In preliminary experiments further two Reynolds numbers ($Re_{in} = 42000$ and 52000) were tested qualitatively. The same deviated flow structure has been observed. As is generally known, with an increasing Reynolds number, the symmetrical flow may become asymmetric in nature, turn to an unsteady state and finally become fully turbulent flow at higher Re .

Finally it can be concluded that water depth has a significant effect on the flow pattern and vortex structure. For $Fr_{in} \leq 0.10$ flow is asymmetric and jet is deflected to one side and by increasing Froude number leads to a central meandering jet.

In the other hand the Reynolds number has a less effect on the flow structure for the studied range of values.

Finally, the influence of the hydraulic conditions (by varying the water depth between 0.075 m and 0.200 m (four different water depth and a fixed discharge), and by varying the discharge between 7.0 l/s and 3.5 l/s (a fixed water depth and two different discharges)) on the stability of the flow in the reference geometry $L = 6\text{ m}$ by $B = 4\text{ m}$, has been analyzed (Table 3.7).

All of the clear water results with different hydraulic conditions were carried out with smooth bed. The relative roughness was increasing by reducing the water depth. Indeed, due to the higher flow velocity, the stabilizing effect of bed friction is amplified when the water depth is reduced.

By reducing the water depth the jet type is completely changed from deselected with three gyres to a meandering jet with four or five gyres. Moreover, several dynamic gyres were formed accompanying with the jet trajectory along the centerline.

As will be shown in the following chapter with sediment, the bed roughness is able to change the deselected jet to the centerline. Furthermore, the jet was stabilized by increasing the depositions and roughness.

From the author's point of view, bottom and wall roughnesses have a relative importance in relation to horizontal turbulent diffusion.

More investigation and analysis for the influence of bed roughness has to be done in future outlook work.

4.4 Observed reattachment lengths and number of gyres

In Section 4.1 a detailed investigation of a symmetric and an asymmetric flow pattern with its associated recirculations have been clearly depicted. The definition and the geometrical dimensions of the formed circulations for two different geometries are shown in Figures 4.1 & 4.2.

The measured evolution of the flow structure with geometry shape factor SK is shown in Figures 4.16(a), (b), and (c) for a Reynolds number of 28000. The flow changes from a symmetric structure at lower SK to an asymmetric one at high SK . At a certain geometry shape factor, flow symmetry is broken, one of the two main recirculation zones becomes shorter than the other, and a third secondary zone of recirculation appears on the center.

The reattachment length plotted in Figure 4.16(a), shows the variation of the lengths of the right and left upstream vortices. One can notice that for low values of SK (less than the critical value beyond which the flow becomes asymmetric) the flow remains symmetric and $L_{r1} = L_{r2}$ and they disappear for SK less than 3.

As SK exceeds the 5.5 bifurcations take place, and the flow characterized by two unequal right and left separation zones of lengths L_{r1} and L_{r2} such that $L_{r1} > L_{r2}$ and a third circulation zone in the center with length of L_{r3} . The two vortices in the corner are in accordance with each other and alternatively change in size.

Moreover, they control the size and location of the main vortex. A further increase in the value of SK leads to reduce the variations between L_{r1} and L_{r2} . Moreover, the third circulation disappear with higher value of SK of 80 where the geometry is very narrow.

This change of structure is summarized in Figure 4.16(b) which shows the variation of the non-dimensional detachment or reattachment length as a function of SK . The right and left corner vortex sizes are defined by their non-dimensional length $X_{r1} = L_{r1}/B_{r1}$ and $X_{r2} = L_{r2}/B_{r2}$ whereas the spanwise gyres by $X_{r3} = L_{r3}/B_{r3}$ and $X_{r4} = L_{r4}/B_{r4}$.

Figure 4.16(b) presents the experimentally measured values of X_{r1} and X_{r2} for all SK of the tested geometries. At low values of SK , the non-dimensional reattachment lengths X_{r1} and X_{r2} are equal indicating symmetric flow. The branching which starts at $SK = 5.5$ indicates the onset of asymmetric flow. For the range SK (6, 30), X_{r1} increases while X_{r2} on the opposite wall decreases when the third recirculation region develops.

The number of vortices associated with the geometry shape factor SK is depicted in Figure 4.16(c). In the absence of the flow bifurcation (symmetric flow) four circulation is deformed in the two upstream corners with X_{r1} and X_{r2} and two along the centerline X_{r3} and X_{r4} .

But in the presence of the flow bifurcation (asymmetric flow) with three circulation zones as showed before. Based on the measured reattachment length for all geometries with and without bifurcations, the following relationships between the non-dimensional reattachment length X_r and the geometry shape factor SK are developed:

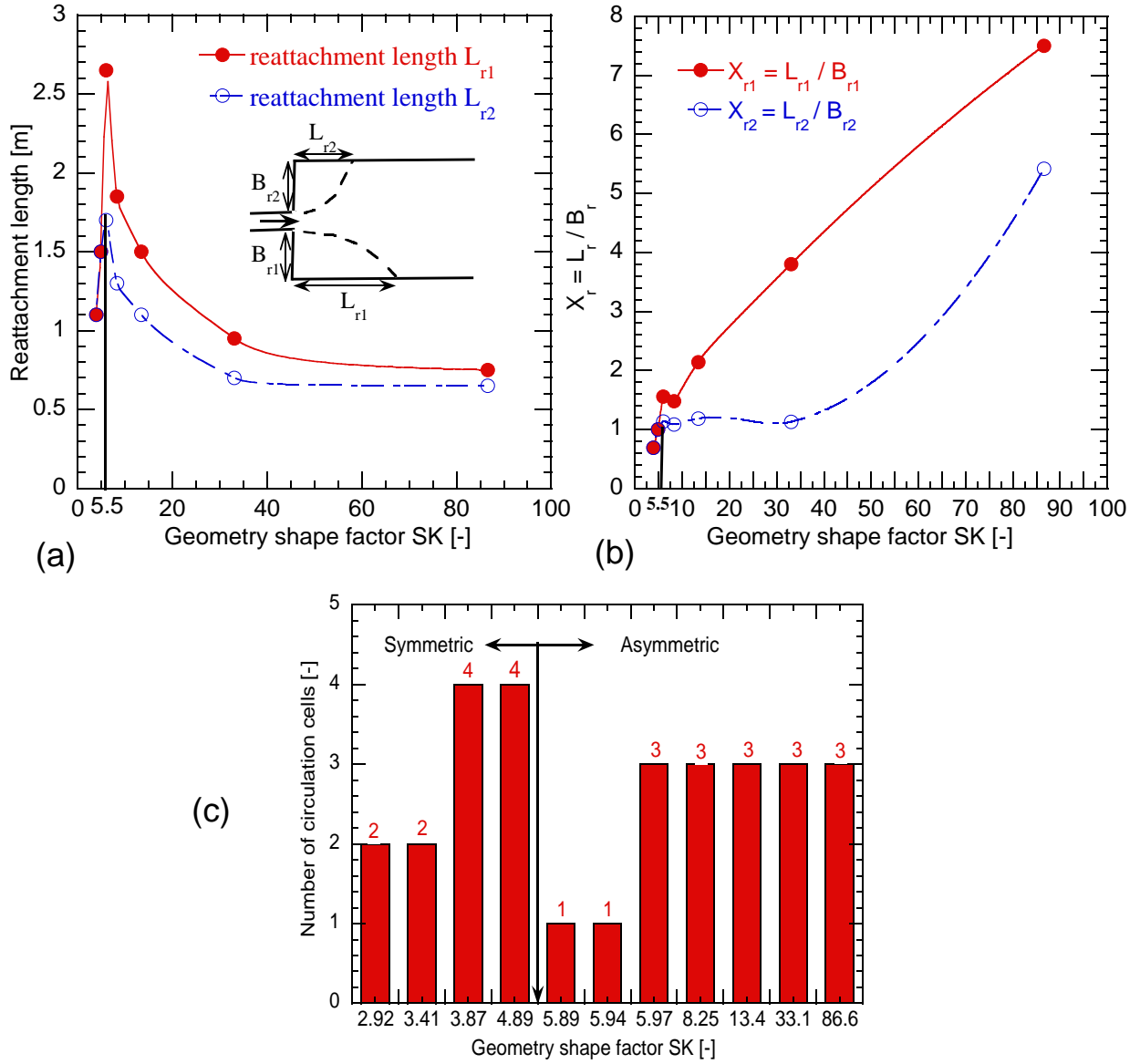


Figure 4.16: Geometry effect at $Re = 28000$ on (a) reattachment length L_r (b) non-dimensional reattachment length X_r (c) circulations number

$$X_{r1} = 0.90 + 0.097SK - 0.00025SK^2 \quad (4.1)$$

$$X_{r2} = 1.2 - 0.027SK + 0.0008SK^2 \quad (4.2)$$

$$X_{r3} = 1.85 - 0.045SK + 0.0008SK^2 \quad (4.3)$$

$$X_{r4} = -2.90 + 2.36SK - 0.25SK^2 \quad (4.4)$$

These relationships help to understand the reattachment and deattachment processes in a shallow rectangular basin with smooth bed and under the mentioned hydraulic conditions.

4.5 Analysis of velocity profiles: comparison of 3D UVP measurements with LSPIV results

Three-dimensional velocity are measured by an Ultrasonic Doppler Velocity Profiler (UVP) as explained in Section 3.5.1. The results are presented here being part of test series prepared to investigate the influence of geometry on flow pattern and velocity behavior.

By investigation of 2D surface velocity fields and profiles of vertical velocity components, a better understanding of the mechanism governing the sediment exchange process between the jet entering the reservoir and the associated turbulence structures is attempted. The turbulence large-scale structures and jet expansion in the basin have been determined based on UVP and LSPIV.

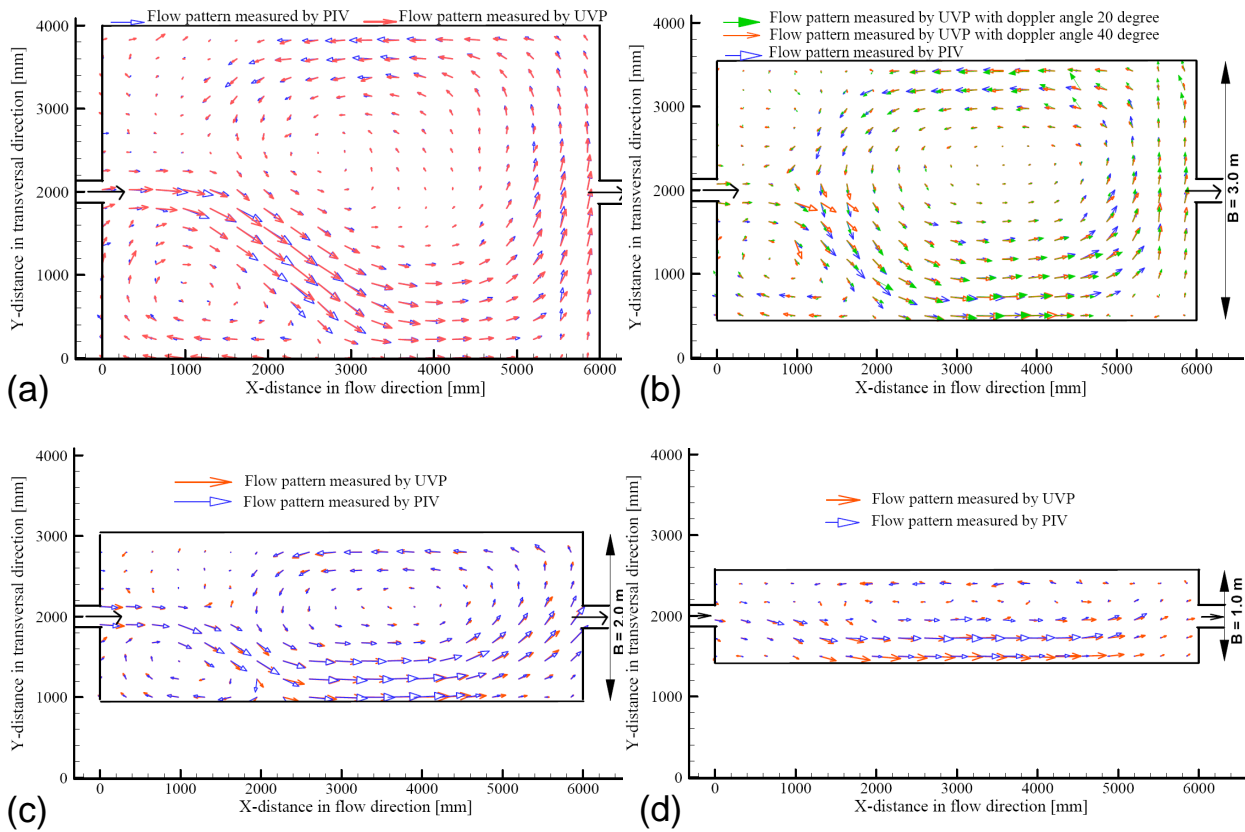


Figure 4.17: Comparison of velocity vectors from UVP and LSPIV for four different geometries with shape factors $SK = 5.97$ (a), 8.25 (b), 13.42 (c), and 33.07 (d)

A comparisons of the 2D-velocity fields obtained by two different techniques (UVP and LSPIV) for four reduced width geometries (Test1, Test7, Test8, and Test9) with SK of 5.97, 8.25, 13.42, and 33.07 are shown in Figures 4.17, (b), (c), and (d), respectively. The central

4.5. Analysis of velocity profiles: comparison of 3D UVP measurements with LSPIV results

stagnation of the three recirculation zone, is observed in the time averaged values measured by UVP probes and LSPIV measurements.

UVP measurements confirm 2D flow map in shallow reservoir and the asymmetric behavior for the reduced basin width (with higher geometry shape factor SK). A small difference is observed in Figures 4.17(c) for the narrow geometry of Test 9. This difference is in accordance with the mean velocity profile.

Figure 4.17(b) shows a comparison between two UVP geometrical setup as showed in Section 3.5.1. The average flow structure of the two setup is very similar to each others which indicates that there is no influence on the UVP results from the geometrical setup. In Figure 4.17 it can be observed that the vector maps obtained by UVP and LSPIV measurements are in good agreement.

The general flow features that develop after the jet is stabilized in the reference reservoir geometry are presented in Figure 4.18 for $Re_{in} = 28000$. The distribution of the vertical velocity in an alluvial river is particularly important to know the transport of suspended sediment.

To investigate the effect of the vertical velocity components on shallow reservoir flow patterns 3D results analysis is shown in Figure 4.18. Vertical velocity distributions were defined to study the vertical velocity effect. For the analysis of the 3D velocities measured by UVP, the vertical velocity contours W with the velocity vectors for Test1 (SK of 5.97) is shown in Figures 4.18(a), (b), and (c).

Vertical velocities are rather small compared to the horizontal ones and confirm the shallow 2D character of the reservoir. Moreover, the eddies with horizontal axis are clearly visible at Figures 4.18(b) and (c). So, together with horizontal circulations, there is a vertical circulation.

Figures 4.18(b) and (c) shows the vertical velocity contours W and the volume streamlines, distributed across the reservoir for four cross sections of every 1.0 m . It can be seen that the higher velocity is shifted to the right hand side and the maximum velocity occurs near the wall; gyres and eddies are clearly shown in Figure 4.18(a).

An overview for the flow features that develop downstream from the sudden expansion are depicted in Figures 4.18(d), (c), and (d). A primary recirculation flow region develops adjacent to the left side and a larger recirculation flow region develops adjacent to the right side. A third recirculation flow region develops on the center and reverse flow region exists close to the downstream left side as can be seen in Figure 4.18(e).

The surface velocity results confirm the asymmetric flow behavior and allow a physical insight into the pertinent fluid flows. The streamlines help to depict the flow structure inferred from three-dimensional UVP data. Figure 4.18(d) plots the streamlines, from which one can clearly observe lines of reattachment on the reservoir surface and bottom. A characteristic feature of streamlines on the surface (roof) and bed (floor) is that they are seemingly invariant with Z , except in regions near the entrance.

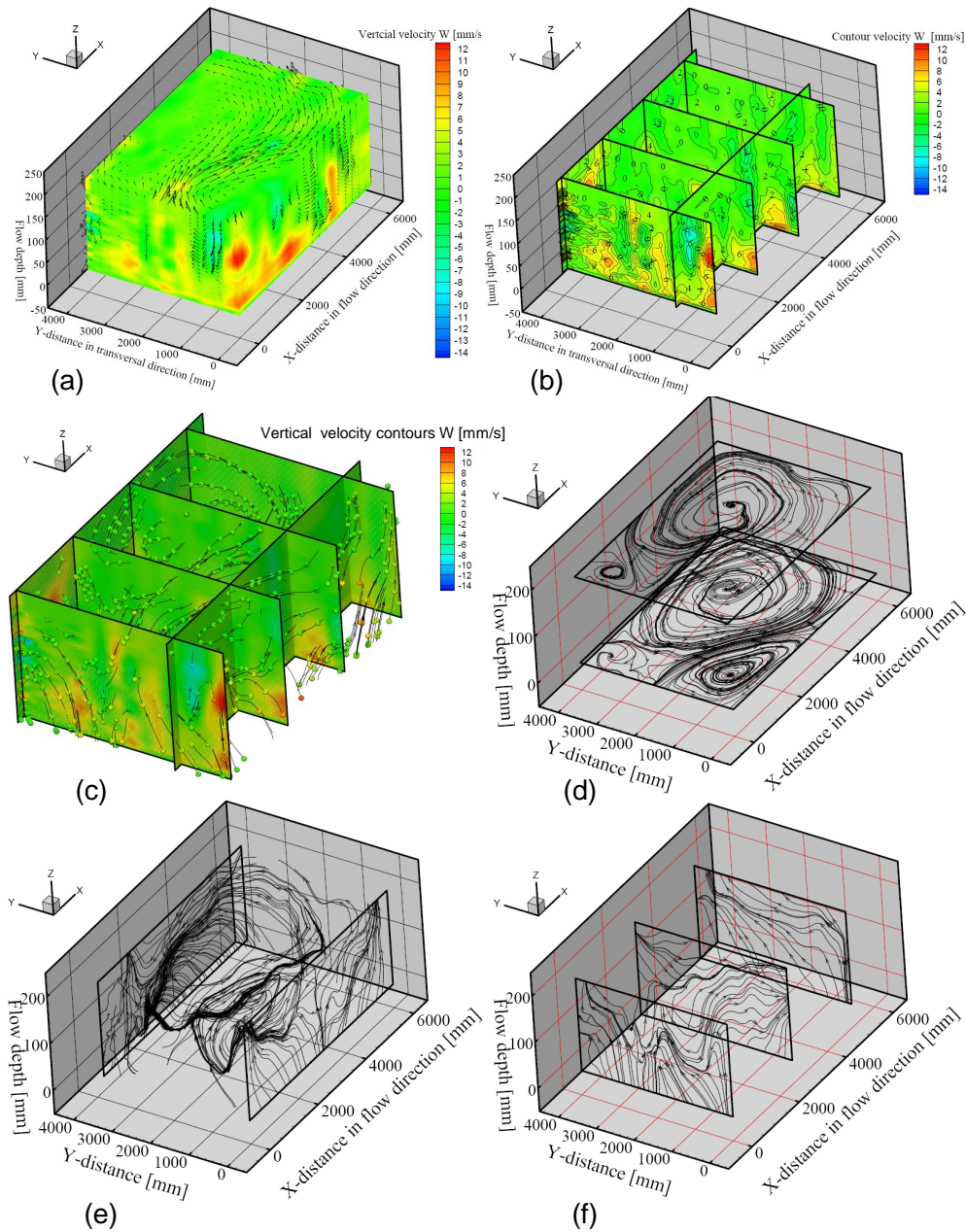


Figure 4.18: (a, b) Three-dimensional plot of vertical velocity contour, and at different streamwise plane, (c) close-up for the vertical velocity contour with the volume streamlines, surface streamlines at (d) roof and floor, streamwise & side walls (e) ,and cross streamwise (f).

It is important to address that there exists a horizontal surface and bottom eddies with asymmetric flow behavior. The reattachment and detachment points are clearly visible. Figures 4.18(e) and (f) also shed some light on the flow complexity at the vertical side walls.

The three-dimensional nature of the flow can be best illustrated by plotting U and W streamlines in planes parallel to the side-wall plane and volume streamlines in between as

4.5. Analysis of velocity profiles: comparison of 3D UVP measurements with LSPIV results

shown in Figure 4.18(e). The resulting secondary flow arises through a complex interaction between the curved flow, as manifested by the presence of primary eddies formed immediately in the upstream corners, and the boundary layer developed over the bed.

Streamlines at different spanwise planes are presented in Figure 4.18(f) to demonstrate the flow behavior near the sidewall. The general flow features that develop near the entrance region is significantly change from the center and exit regions. To show the transversal secondary flow induced by the vertical side-wall, in Figure 4.18(f) streamline plots at selected X-planes are shown. An important feature worth to note in the close-up plot (Fig. 4.18(c)) of vertical contours is the change of sign in the W-velocity components.

Such a nature of the flow gives rise to transversal vortices, as can be clearly seen in Figure 4.18(e). Some of these streamlines flow downstream and later reverse their direction while moving towards the inlet and in that process a reverse flow region develops adjacent to the inlet as can be seen in Figure 4.18(e).

Figures 4.19(a) and (b) presents the 3D vertical velocity contours and U-V streamlines on roof and floor for Test7 of the reduced basin width geometry ($SK = 8.25$). The results confirms the general trends of the above 3D investigations for the reference geometry. For the reduced basin width the asymmetric flow behavior has a very low vertical velocity W as shown in Figure 4.19(a). A characteristic feature of the streamlines on the roof and floor is that they are seemingly invariant with Z, except in regions near the vertical right side-wall as shown in Figure 4.19(b).

Secondary current behavior was observed for the reduced basin width geometry with $SK = 8.25$. The secondary current is more clearly illustrated by V-W velocity vector and U-contour plots shown in Figure 4.20. The flow field in the cross section (spanwise and vertical components combined) shows the evolution of the secondary current at three cross sections plotted at different X planes ($X = 0.75, 2.00, \& 5.00$ m). The bed boundary layer poses shear drag on the primary motion of the fluid particles in the upstream corner and in turn, an increasingly large V-velocity component. It is the non-zero V-velocity component that causes the particle to move in a rotate with respect to the vertical vortical.

In Figure 4.20, at $X = 0.75$ m after the inlet, the flow field does not show a clear secondary current structure. In the same cross section downflow clearly visible while ($V < 0$) and high U-velocity. Streaks of higher mean longitudinal velocity are observed in downflow regions. At the middle section a big secondary cell has developed at the right side-wall and the maximum U-velocity is shifted to the right wall. Asymmetric flow behavior has been confirmed in Figure 4.20.

Moreover, upflow can be seen in the second and the third cross section ($V > 0$). Upflow regions are identified by lower mean longitudinal velocity. The results of UVP measurements have showed patterns of secondary currents in the time average flow structure.

These UVP measurements focus on tracing a complete picture of the large water body movements and developed jet for different reservoir geometries, which was interesting and

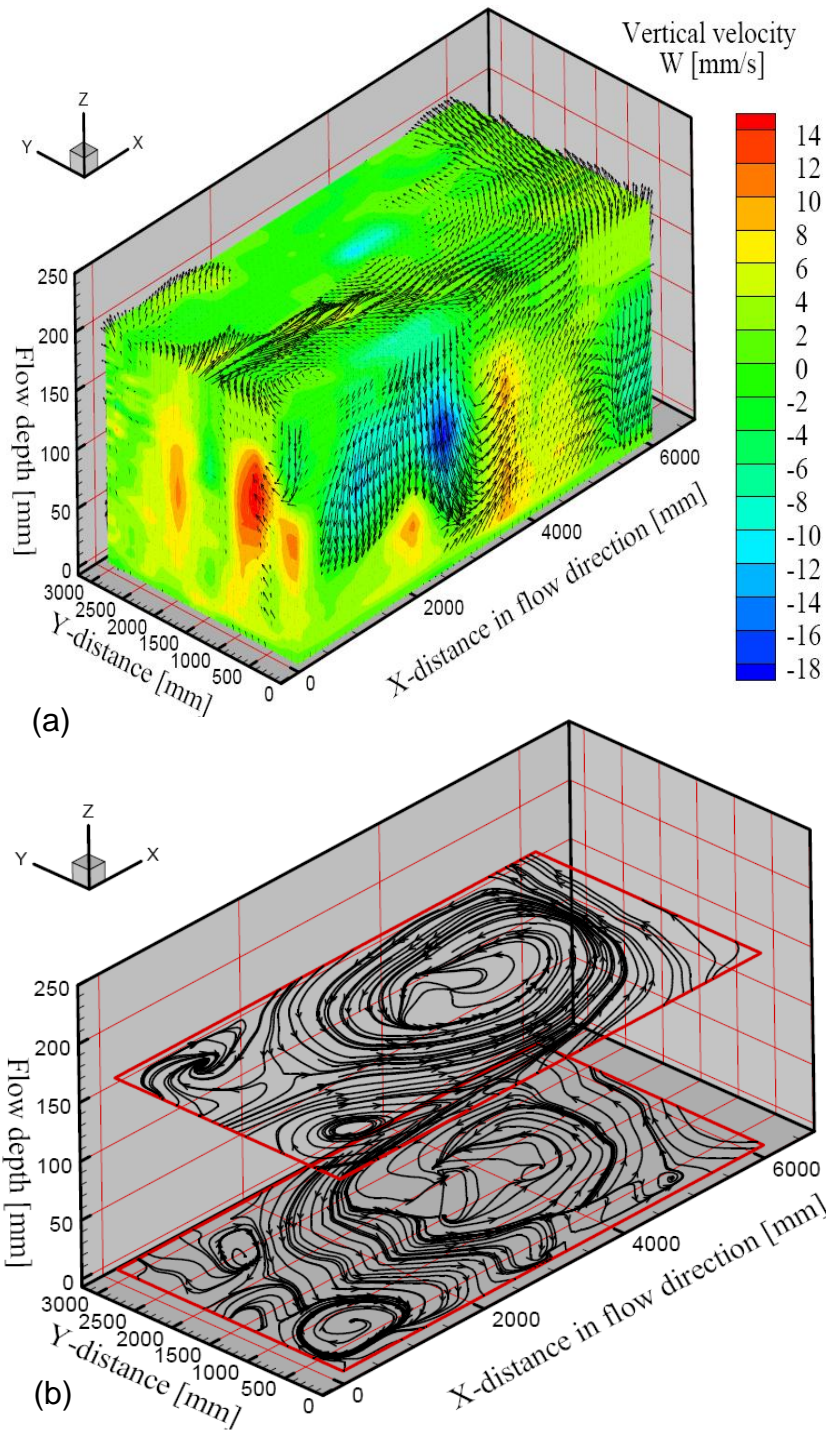


Figure 4.19: Three-dimensional plot of vertical velocity contour and streamlines at different planes of the reservoir geometry with $SK = 8.25$.

complicated to study. Due to the short time measurement and large distances between UVP velocity measured profiles have been chosen. As mentioned before the main objective of UVP measurements is to investigate the effect of the vertical velocity components on the

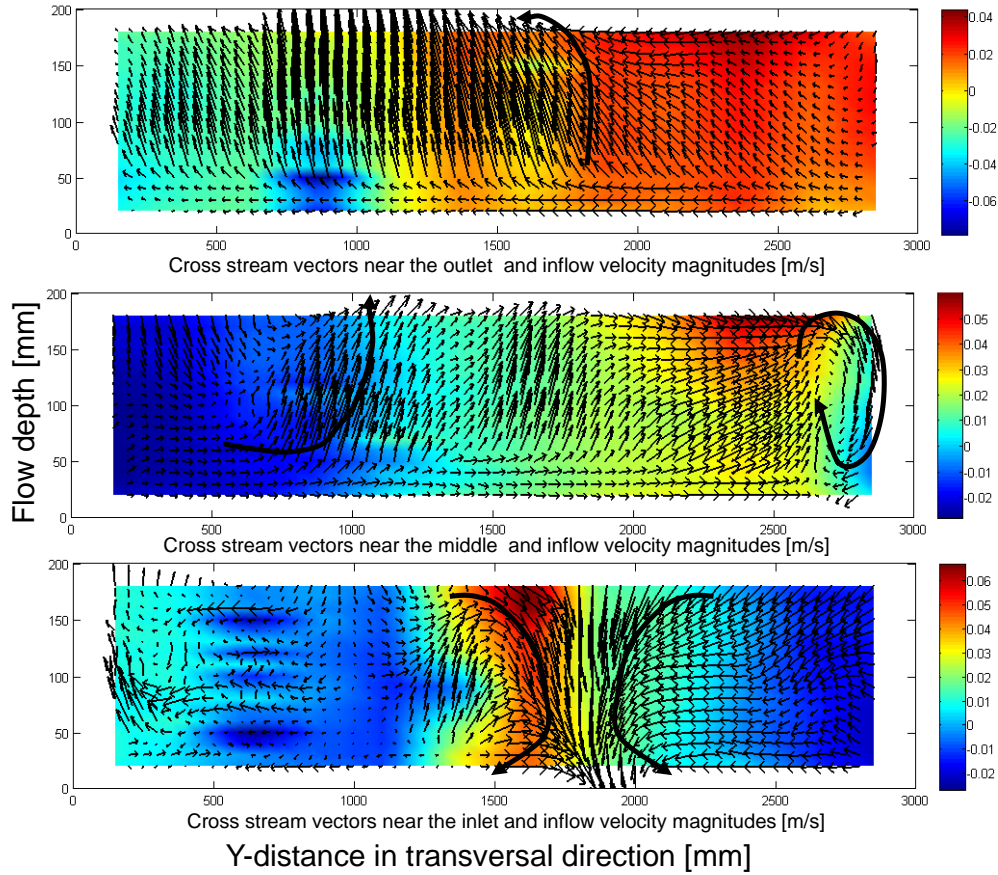


Figure 4.20: V-W velocity vector and U-contour plots for flow $Re = 28000$, at different cross streamwise planes of the reservoir geometry with $SK = 8.25$ at $X = 0.75$, 2.0, and 5.0 m.

shallow reservoir sedimentation patterns.

Furthermore, comparisons of the 2D-velocity fields obtained by two different techniques (UVP and LSPIV). The UVP and LSPIV tests results will be then used for the validation of numerical model. Therefore, the presented secondary currents appreciating should be confirmed by further investigations.

4.6 Detailed comparison for cross and longitudinal ratio of velocity profile

The velocity in the reservoir U_{res} normalized with respect to the inlet flow velocity U_{in} are plotted versus the expansion ratio $ER = B/b$ and L_c/b in Figure 4.21 for $Re_{in} = 28000$ and for different locations at the middle cross section and along the centerline. Figure 4.21 revealing that the flow asymmetry indeed exists in the symmetric reservoir geometry with geometry shape factors $SK > 5.5$ and the flow symmetry for $SK < 5.5$.

The measured velocities are presented in terms of profiles of the mean centerline velocity and normalization by the inlet velocity as shown in Figure 4.21(a). The normalized profiles are asymmetric with two unequal reattachment lengths on the left and right, except for the narrowest one (T9 and T10).

As the flow progress downstream the mean axial velocity show the decelerated in the central core. Upstream of $L_c/b = 6.0$ the mean axial velocity is decreasing by 20 to 60% due to the jet is deviated in that region. The length of the core recirculation is clearly visible in Figure 4.21(a) for all geometries with deviated jet with asymmetric behavior. The core recirculation length is about $15 b$ except for the narrowest geometry. The asymmetry becomes more pronounced as the high-velocity core deflects towards the side.

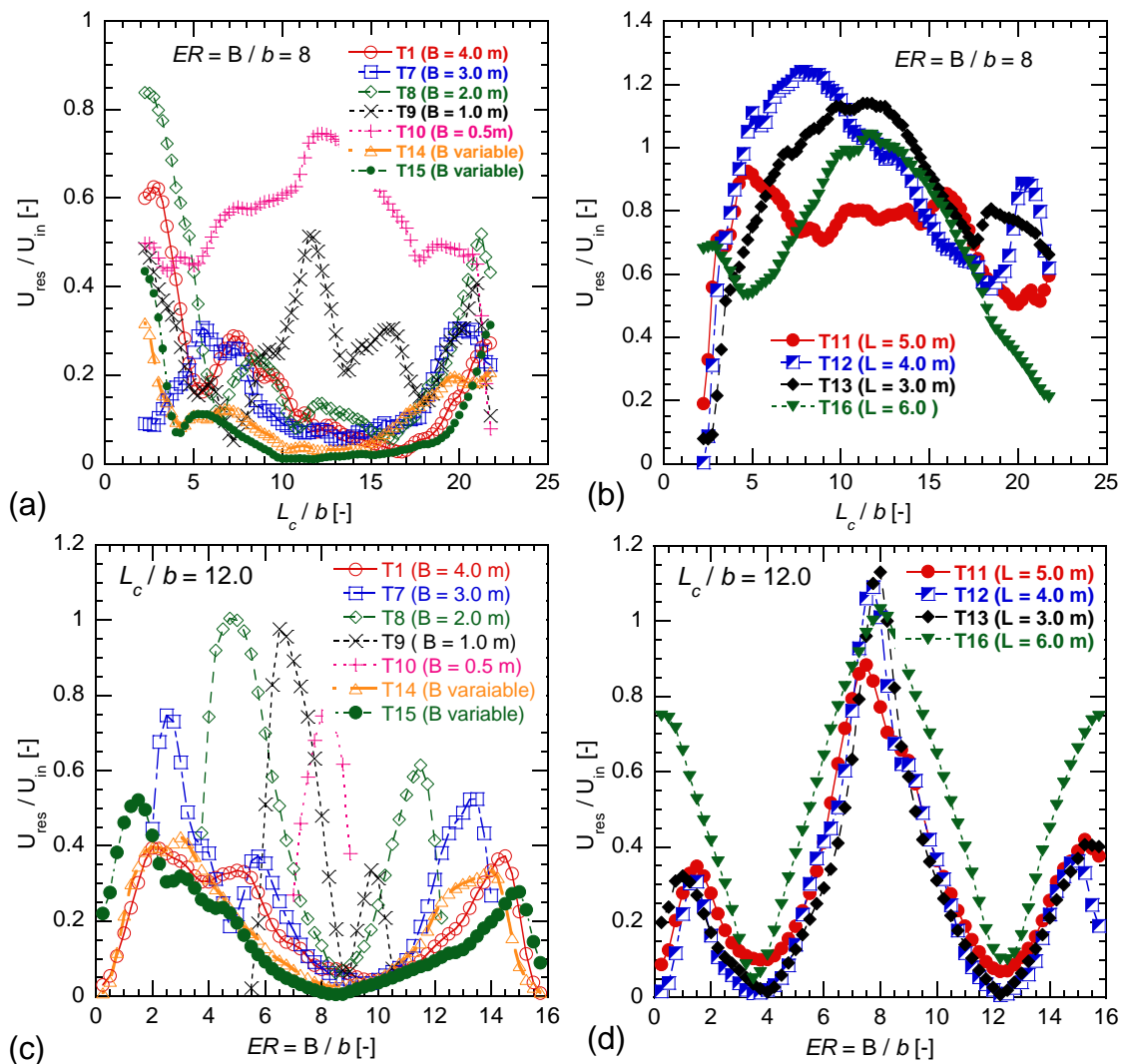


Figure 4.21: Comparison of the mean velocity U_{res}/U_{in} for $Re = 28000$, (a, b) axial distributions of the asymmetric and symmetric jet flow, (c, d) transverse distributions of the asymmetric and symmetric jet flow for tests T1 to T16.

But the asymmetry degree is reduced by reducing the reservoir width for T9 and T10.

On the far side near the outlet mean axial velocity is increasing again and reached to 50% of the inlet velocity. The axial velocity is zero at $L_c/b = 12.0$ for (T14 & T15) as only one center gyre formed into the reservoir. The recirculating velocities of the two upstream corners are higher than the core one. Figure 4.21(b) presents the axial mean velocity for all geometries with straight jet. The centerline velocity is accelerated because of that flow structure is symmetric.

By reducing the reservoir length the number of recirculations is reduced and the flow becomes more symmetric. Velocity distributions in Figure 4.21(b) revealed a symmetric behavior relative to the center width of the basin. Except for the hexagonal geometry (T16) the mean centerline velocity is increasing in the downstream direction till the peak and after that is reducing before the outlet. The peak velocity occurs at different locations on the centerline L_c/b .

Transverse distributions of non-dimensional velocity at middle of basin centerline for geometries of deflected and straight jet are presented in Figures 4.21(c) and (d). These figures illustrate the asymmetric and symmetric behaviors that develop in these distributions inside these symmetric geometries. In Figures 4.21(c) the flow asymmetry is illustrated by showing that flow near the two sides increases in velocity at the expense of the velocity in the vicinity of the reservoir center. As a result of the reducing the reservoir width, fluid flows have higher velocity (Fig. 4.21(c)). Under these circumstances, the asymmetric flow can be maintained stable by the cross-reservoir velocity gradient. In the asymmetric flow region the distribution of streamwise velocity tilts towards the wall that has the smaller reverse flow region.

Figure 4.21(c) is clearly asymmetric, the peak velocity is located away from the centerplane. The flow undergoes a symmetry-breaking bifurcation. The flow immediately is characterized by two primary counter-rotating vortices. As a result of two primary recirculating eddies, the flow near the center is manifested by having large gradients in velocity. The asymmetric behavior which is present in Figure 4.21(c) disappears in the fully developed flow in Figure 4.21(d). Moreover, the velocity profiles coincide quite closely on a common cross sectional curve.

In Figures 4.22(a) and (b), the mean velocity ratio of U_{res}/U_{in} at the basin centerline and transversal sections, respectively are displayed for different Reynolds and Froude numbers. In the interest of clarity the mean centerline velocity curves in Figure 4.22(a) are separated into two sets (1) asymmetric flow for $Fr_{in} \leq 0.1$ (2) meandering flow for $Fr_{in} > 0.1$. Figure 4.22(a) shows the mean velocity (U_{res}/U_{in} profiles for $Re_{in} = 28000$ and $Fr_{in} = 0.43, 0.3, 0.15, 0.1$. The rate of the mean velocity ratios decrease at the centerline plane by decreasing Froude number. The flow is asymmetric and the mean velocity and the size of the center recirculation region are almost identical for $Fr = 0.05$ and 0.1 and $Re_{in} = 14000, 28000$, respectively.

Moreover, the two curves collapse quite closely on a master curve. A slight difference

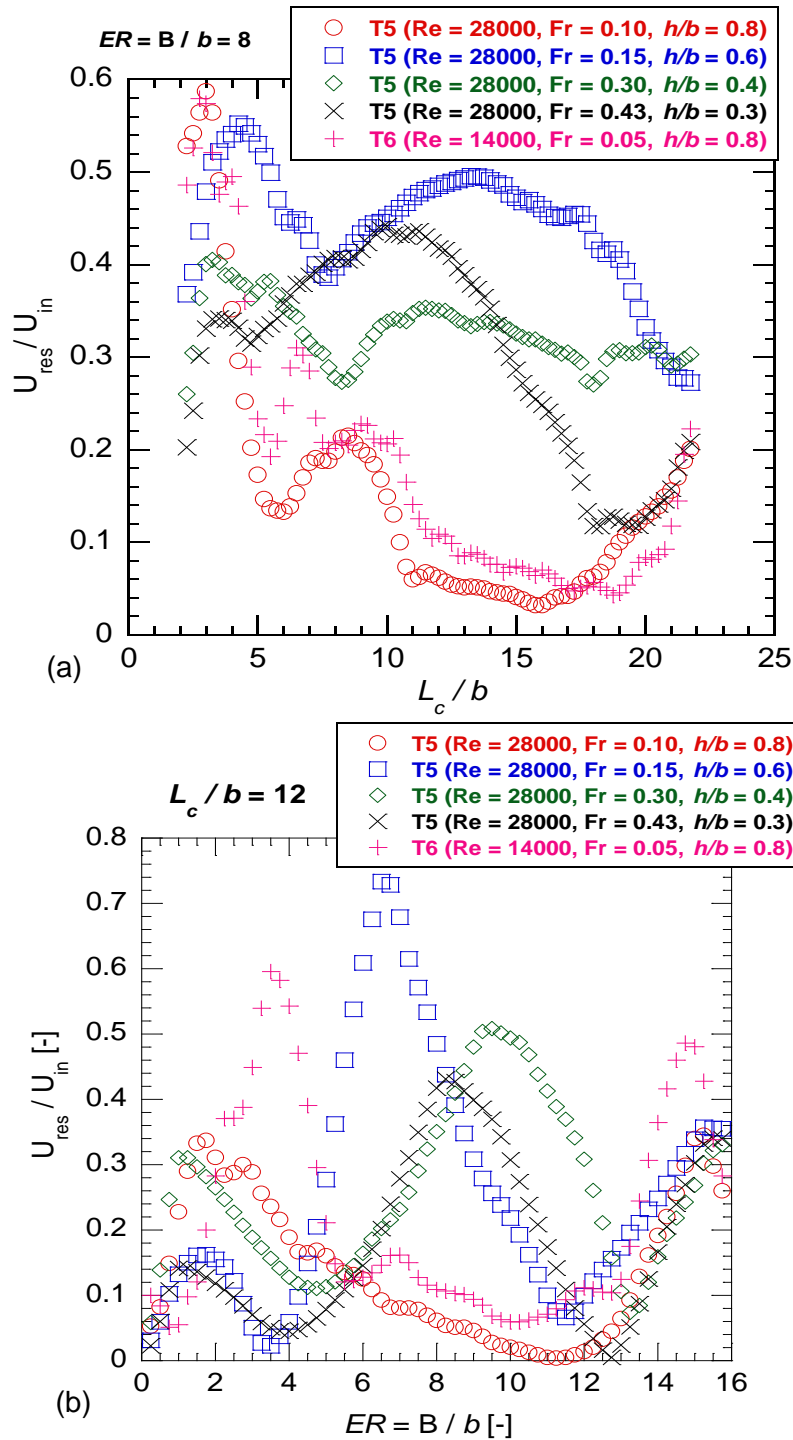


Figure 4.22: Comparison of the mean velocity U_{res}/U_{in} in Test1, (a) axial distributions with various Froude and Reynolds numbers, (b) transverse distributions with various Froude and Reynolds numbers.

in the upstream region between the profiles due to the different length of the jet reattachment. With the high velocity core the asymmetry diminishes as Fr is increased as shown in Figure 4.22(a). A central meandering flow exists with $Fr_{in} = 0.15, 0.30, 0.43$.

The profile with $Fr_{in} = 0.43$ follows a significantly different development with its maximum located at $L_c/b = 10$. Due to the impinging on the wall earlier and resulting in a shorter reattachment length compared to the other two meandering curves. Figure 4.22(b) shows the mean velocity ratio (U_{res}/U_{in} located at the middle cross section of the basin for $Fr_{in} = 0.43, 0.3, 0.15, 0.05, 0.1$.

Again the profile is clearly asymmetric for $Re_{in} = 14000, 28000$. The differences of the maximum velocity across the basin are increasing by increasing of Froude number and accelerating the flow in the basin center.

4.7 Classification of jet flow regimes

Jet flow regimes in a large shallow reservoirs can be classified conveniently by the geometry shape factor SK and inlet Froude number Fr_{in} (see scheme in Fig. 4.23). Three distinct and characteristic flow regimes are observed, namely (i) symmetric (straight jet) and , (ii) asymmetric (deflected jet with a question mark shape) (iii) a central meandering jet, the occurrence of each of which is well-determined within SK and Fr_{in} .

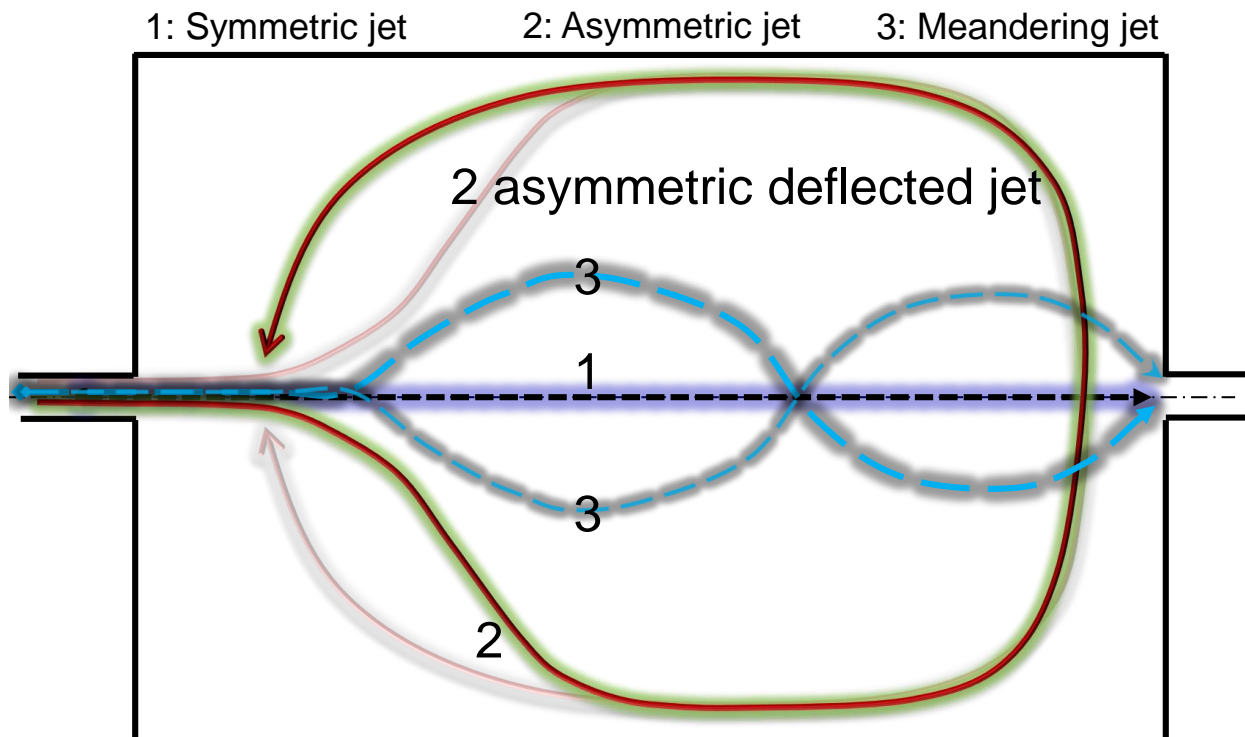


Figure 4.23: Scheme for regime classification of jet flow types: symmetric, asymmetric and meandering.

For the first and second of these flow types (Type 1 and 2, see Fig. 4.23), typically observed for low values of $Fr_{in} < 0.1$. For higher values of $Fr_{in} > 0.15$; the deflected

and straight jet above is modified significantly (see Fig. 4.23), such that, there is significant changing in the reattachment points (Type 3).

For the highest values of $Fr_{in} \geq 0.15$; Type 3 flows are generated in which eddies are formed by flow separation at the walls. In consequence, significant perturbation and flow overturning is observed in the inlet zone.

According to the geometry shape factor SK , symmetric jet flow (Type 1) is developed for low SK values (≤ 5.5) and asymmetric jet flow (Type 2) is developed for higher SK values (> 5.5). The occurrence of each of the above flow Types (1, 2, and 3) clearly depends upon the values of the geometry shape factor and inlet Froude number.

4.8 Influence of geometry shape factor SK on normalized velocity ratio U_{res}/U_{in} along the basin centerline

Based on the systematic clear water phase experiments for various reservoir geometries, several empirical equations for the prediction of the ratio U_{res}/U_{in} of the mean velocity in the reservoir, U_{res} , and in the inlet channel, U_{in} , along the reservoir centerline and average U_{res}/U_{in} ratio over the whole reservoir, for symmetric, meandering and asymmetric jet flow were developed. The equations allow a simple and straightforward estimation of the interaction of the flow with the form of the geometry.

Regarding the mean profiles of the basin centerline, sectional averaged ratios of velocities in reservoir U_{res} and in inlet channel U_{in} at the basin centerline for various geometries with symmetric, meandering and asymmetric flow were used. These profiles represent the overall longitudinal trend of U_{res}/U_{in} without considering the spanwise variation of reservoir. L_c is the distance from the inlet to the outlet channels in the reservoir at center, and b is the inlet and outlet channel width.

According to the centerline velocity ratio the flow jet type can be predicted. As was stated in the results in Section 3.10, jet flow regimes for all tested forms in a large shallow basin can be classified by the geometry shape factor SK ($SK = (P/\sqrt{A_t}) \cdot AR \cdot D_{exp}$) and the inlet Froude number Fr_{in} . Three distinct and characteristic flow regimes are observed, namely:

1. symmetric straight jet for $SK < 5.5$ and $Fr_{in} < 0.1$;
2. asymmetric deflected jet for $SK > 5.5$ and $Fr_{in} < 0.1$;
3. a central meandering jet for $2.5 < SK < 100$ and $Fr_{in} > 0.15$.

The normalized centerline velocity U_{res}/U_{in} for all tests at different axial locations between $L_c = 0$ and $L_c = 6$ m for different geometry forms and flow conditions as a function

of a normalized coordinate L_c/b is plotted in Figure 4.24.

The figure reveals that the jet flow is symmetric for all geometries with geometry shape factors $SK < 5.5$. The centerline velocity ratio is accelerated, since the flow structure is symmetrical. Along the centerline the non-dimensional velocity U_{res}/U_{in} increases significantly by the symmetric jet type which is the most stable type for low Froude numbers $Fr_{in} \leq 0.1$.

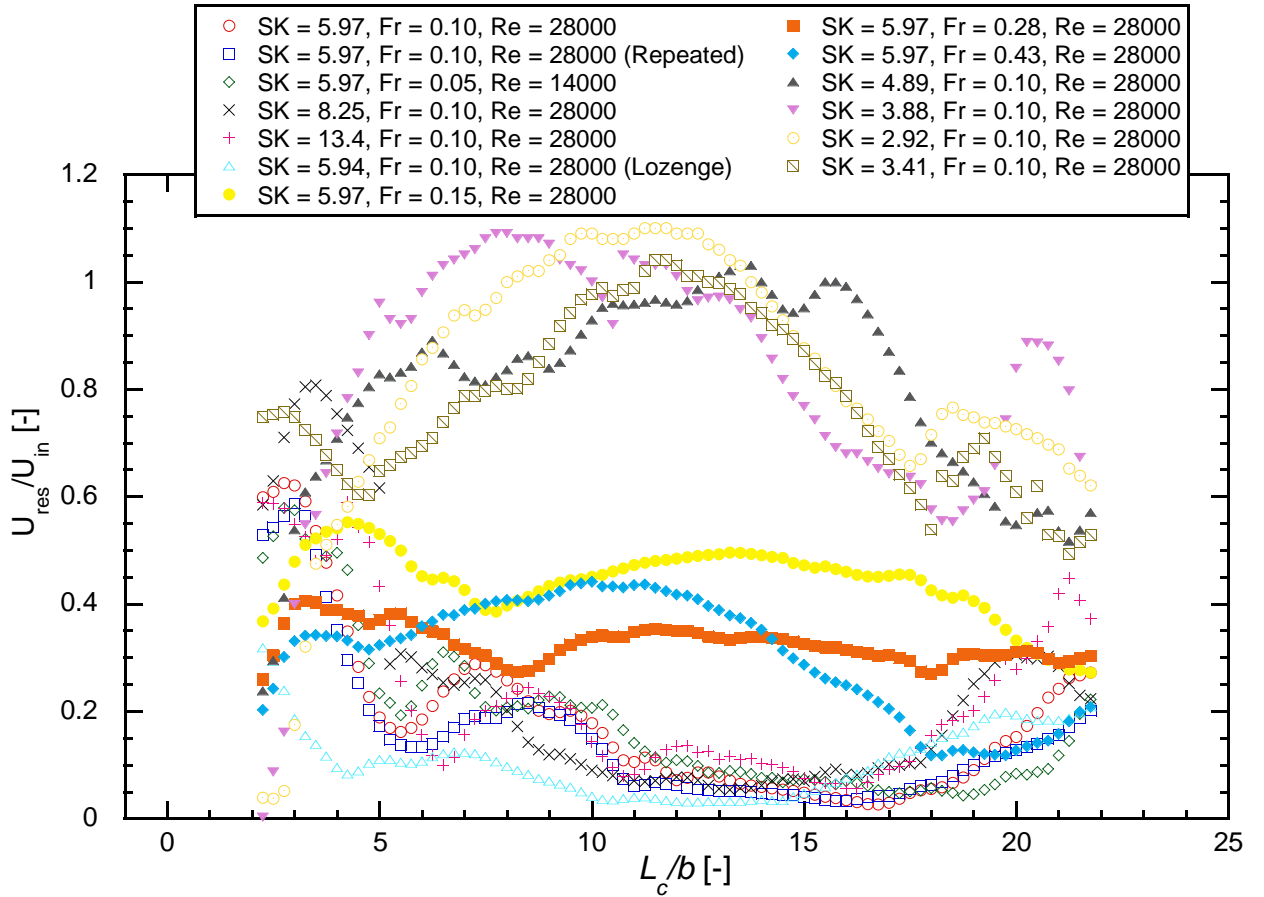


Figure 4.24: Time averaged normalized mean velocity magnitude velocity for symmetric, meandering, and asymmetric jets along the basin centerline as a function of the distance from the inlet channel L_c and the inlet channel width b for various geometry shape factors SK , Froude and Reynolds numbers.

The mean computational velocity has a bell-shape for all tests with $SK < 5.5$ through the basin length with a higher centerline velocity upstream and a smaller velocity further downstream. The maximum velocity was approximately at 40% of the basin length as shown in Figure 4.24.

For increasing the geometry shape factor $SK > 5.5$ and for the same flow conditions, the jet is first rapidly decayed and then deflected to the right with large circulation at the

core which can be determined from Figure 4.24. Along the penetrating distance, the jet centerline velocity is rapidly dropped comparing with the velocity in the symmetric type.

For the highest values of $Fr_{in} = 0.43$, a meandering jet flow is generated in the basins with a geometry shape factor of $2.92 < SK < 86.60$. The jet is meandering around its centerline with an alternating sense of rotations are exist as shown in Figure 4.24.

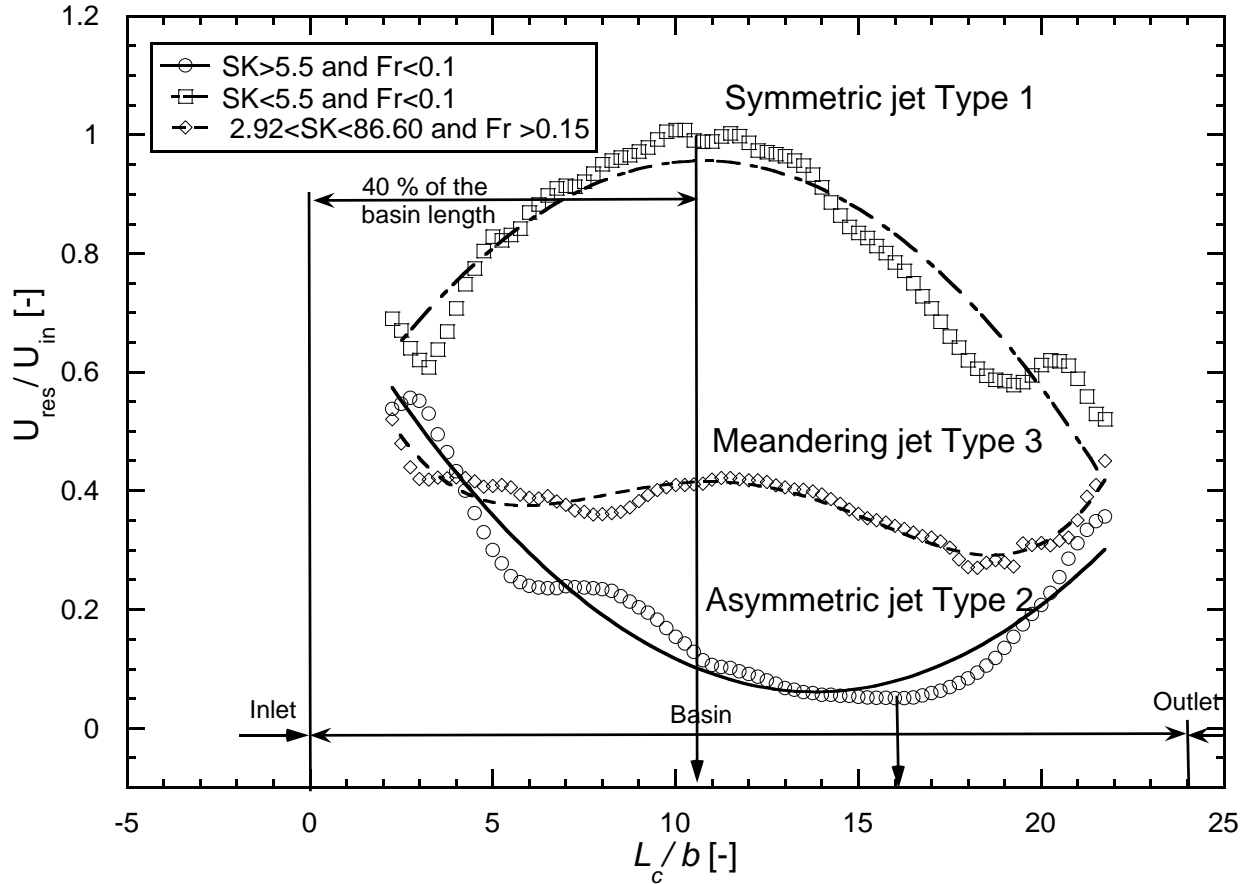


Figure 4.25: Time averaged mean longitudinal velocity for symmetric, asymmetric, and meandering jet at the basin centerline as a function of the distance from the inlet channel L_c and the inlet channel width b .

The profiles have approximately similar behaviors and velocity ratios as well. For the three jet types the average normalized longitudinal velocity at different axial locations as a function of L_c/b is shown in Figure 4.25.

Three empirical relationships for the three jet behaviors could be obtained. Comparison of the measured U_{res}/U_{in} versus the predicted (computed) for symmetric, asymmetric, and meandering jet are shown in Figures 4.26, 4.27 and 4.28, respectively.

The empirical relationships between velocity ratio U_{res}/U_{in} and L_c/b were obtained by trend lines fitted to fractional polynomial functions by using a statistical software (Stata10).

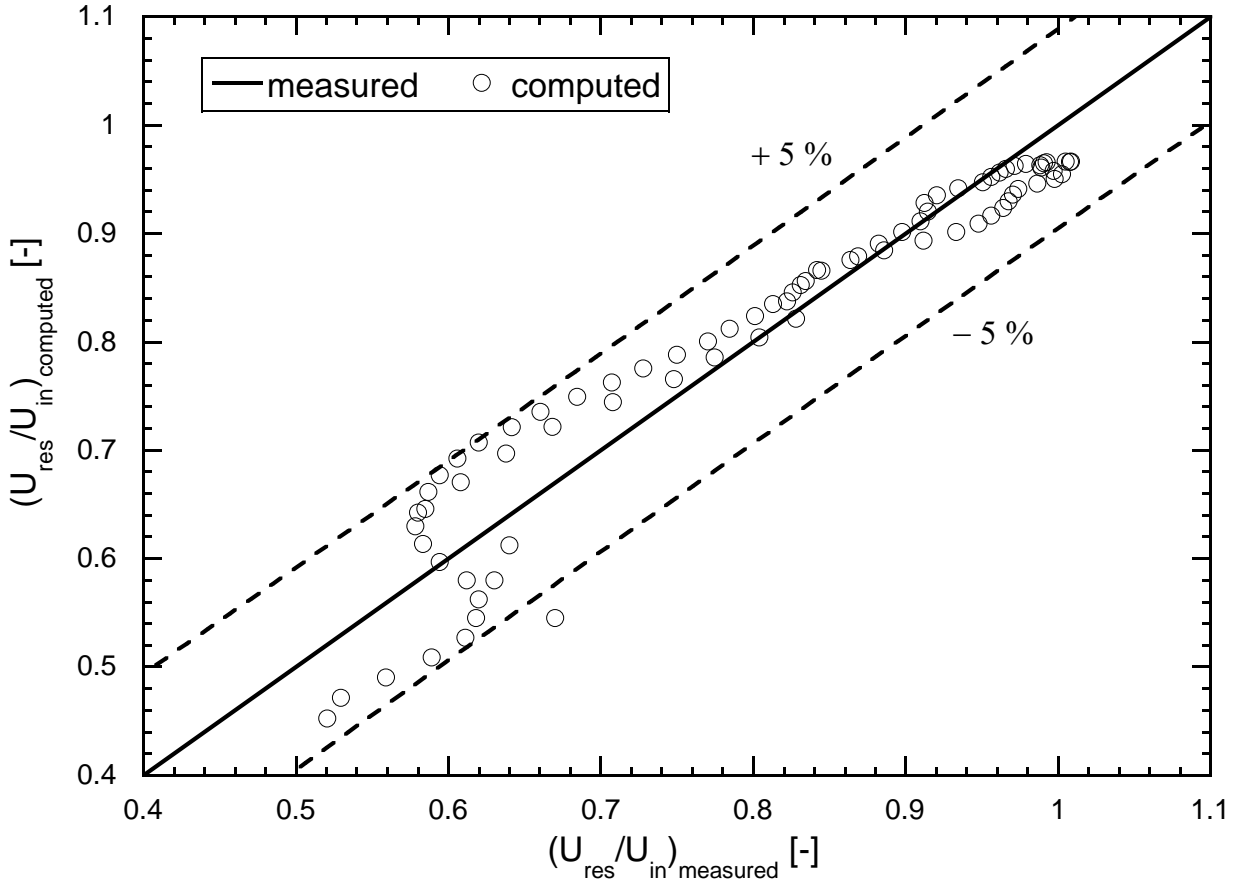


Figure 4.26: Relation for the normalized average velocity of all symmetric jets along the basin centerline (original formula obtained from polynomial curve fitting, Eq. 4.5) and comparison with measured values. The 95 % confidence interval is ± 0.8 .

It can be observed that the peak value is located almost at the middle value of L_c/b .

For a flow regime with a symmetric jet (Type 1), Eq. 4.5 could be found which is applicable for $2.92 < SK < 5.5$ and $0.05 \geq Fr_{in} \leq 0.1$ in the range of $2.25 \leq L_c/b \leq 21.75$:

$$\frac{U_{res}}{U_{in}} = 0.097 \cdot \frac{L_c}{b} \cdot \left(1 - \ln \frac{L_c}{10 \cdot b}\right) \quad R^2 = 0.92 \quad (4.5)$$

where L_c/b ratio of axial distance of the basin and inlet channel width, U_{res}/U_{in} ratio of the velocity magnitude in the reservoir and in the inlet channel along the centerline.

For a flow regime with an asymmetric jet (Type 2), Eq. 4.6 was derived which is applicable for $5.5 < SK < 86.6$ and $0.05 \geq Fr_{in} \leq 0.1$ in the range of $2.25 \leq L_c/b \leq 21.75$:

$$\frac{U_{res}}{U_{in}} = 0.68 - 0.066 \cdot \frac{L_c}{b} + 0.00011 \cdot \left(\frac{L_c}{b}\right)^3 \quad (4.6)$$

For a flow regime with a meandering jet (Type 3), Eq. 4.7 is applicable for $2.92 < SK < 86.60$

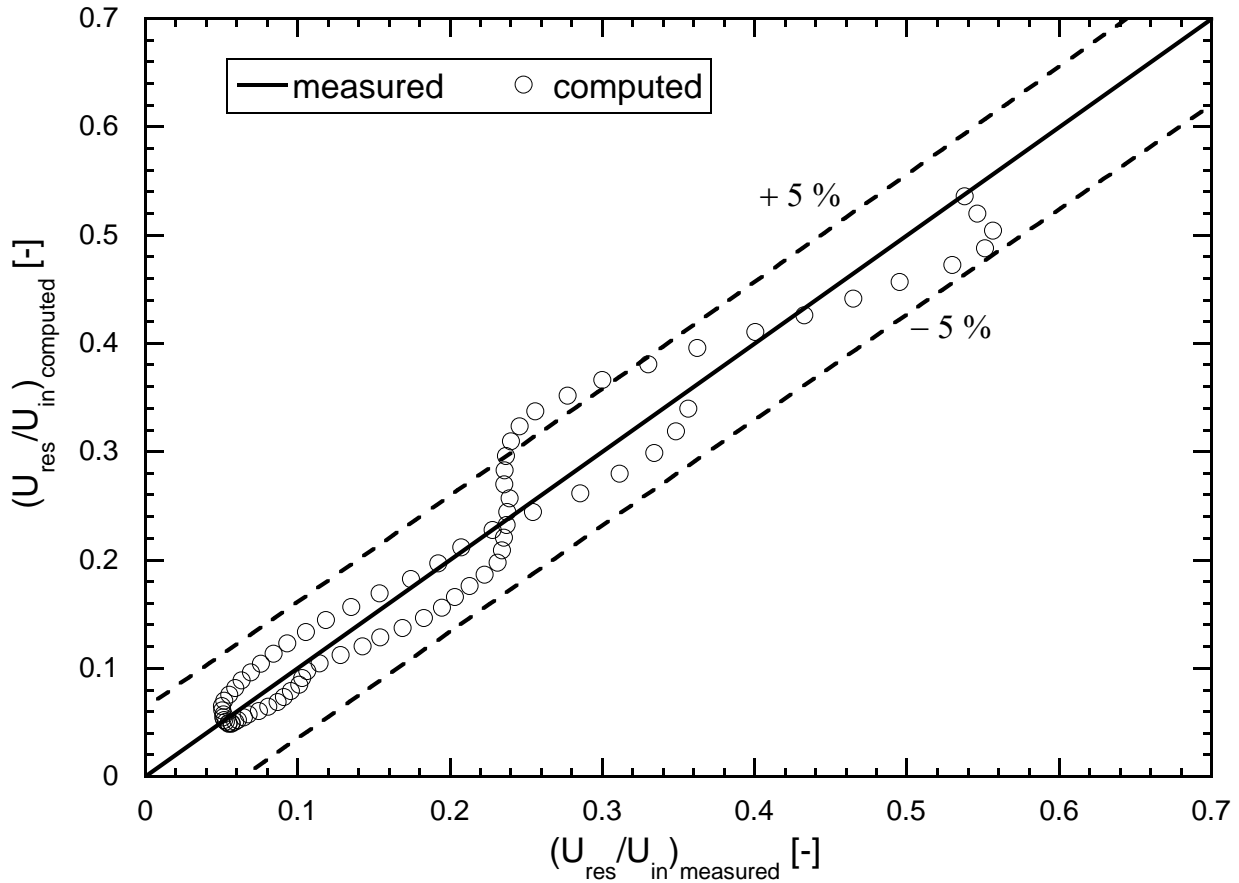


Figure 4.27: Relation for the normalized average velocity of all asymmetric jets along the basin centerline (original formula obtained from polynomial curve fitting, Eq. 4.6) and comparison with measured values. The 95 % confidence interval is ± 0.53 .

and $0.15 \geq Fr_{in} \leq 0.43$. in the range of $2.25 \leq L_c/b \leq 21.75$:

$$\frac{U_{res}}{U_{in}} = 0.39 + 0.44 \cdot \left(\frac{L_c}{b}\right)^{-2} - 0.00017 \cdot \left(\frac{L_c}{b}\right)^2 \quad (4.7)$$

4.9 Influence of geometry shape factor SK of the basin on the normalized average velocity U_{res}/U_{in} for each reservoir

For the development of the empirical approach the moving average of the basin cross sectional time averaged velocity magnitude, U_{res}/U_{in} have been used. Hence, the equations constitute a simplified approach to account for the reduced velocity in the reservoir for

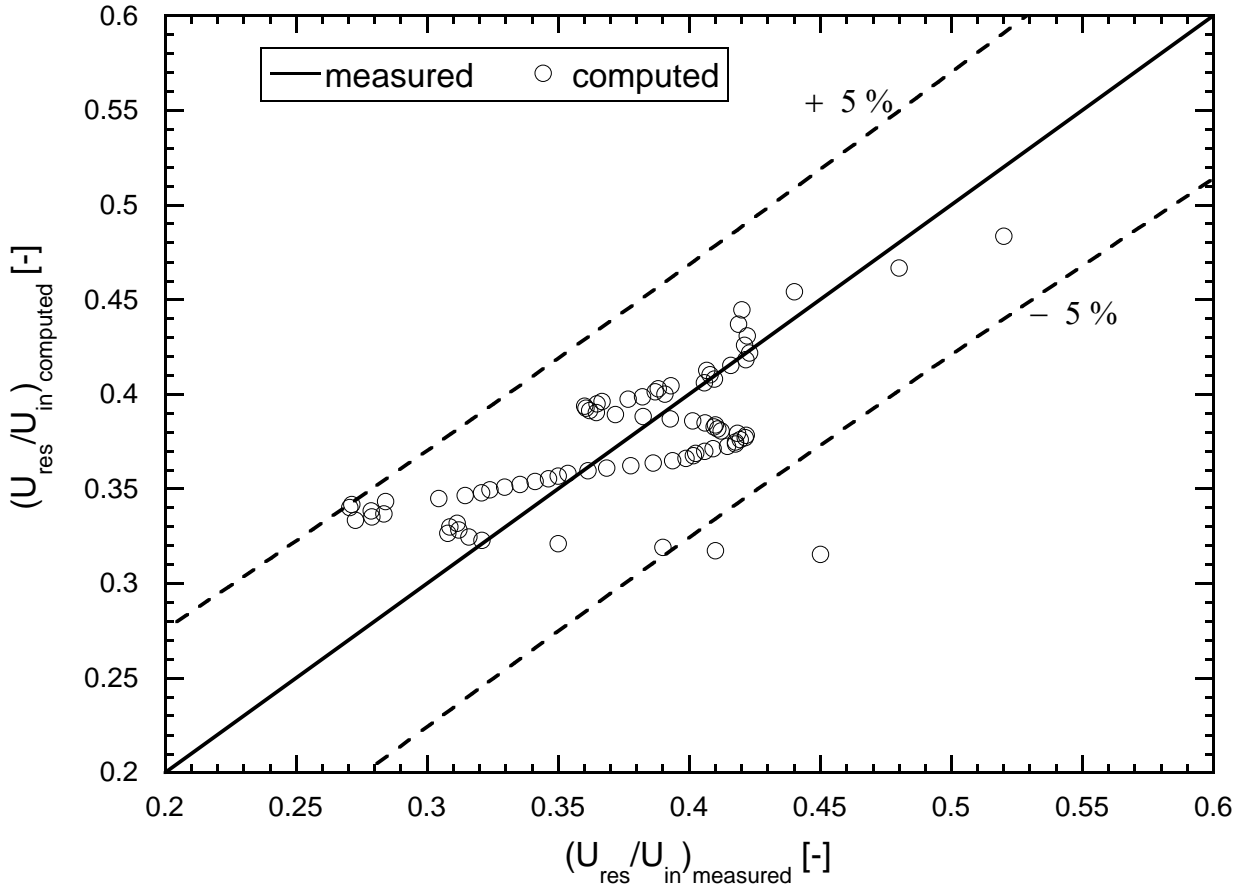


Figure 4.28: Relation for the normalized average velocity of all meandering jets along the basin centerline (original formula obtained from polynomial curve fitting, Eq. 4.7) and comparison with measured values. The 95 % confidence interval is ± 0.8 .

different geometries. The geometry shape factor have been used to develop the equation.

The influence of reservoir geometry on the jet entering velocity into the basin is presented in Figure 4.29. The Figure presents the relationship for all tested geometries represented by SK and average value of U_{res}/U_{in} . Figure 4.29 also shows that, for higher SK , U_{res}/U_{in} increases and can be predicted by Eq. 4.8. The application range of the Eq. 4.8 is $2.92 < SK < 86.60$.

$$\frac{U_{res}}{U_{in}} = 0.88 - 0.33 \cdot \left(\frac{SK}{10}\right)^{-1} \cdot \left(1 + 0.49 \cdot \ln \frac{SK}{10}\right) \quad (4.8)$$

The reservoir design procedure first step is to determine the jet type based on geometry shape factor SK and Fr_{in} . Then predicted the U_{res}/U_{in} ratio from Eq. 4.8.

Prediction of the average velocity of reservoir with specific dimensions is a problem, due to the complexity of the flow pattern. The reduction in the velocity of the entering jet into

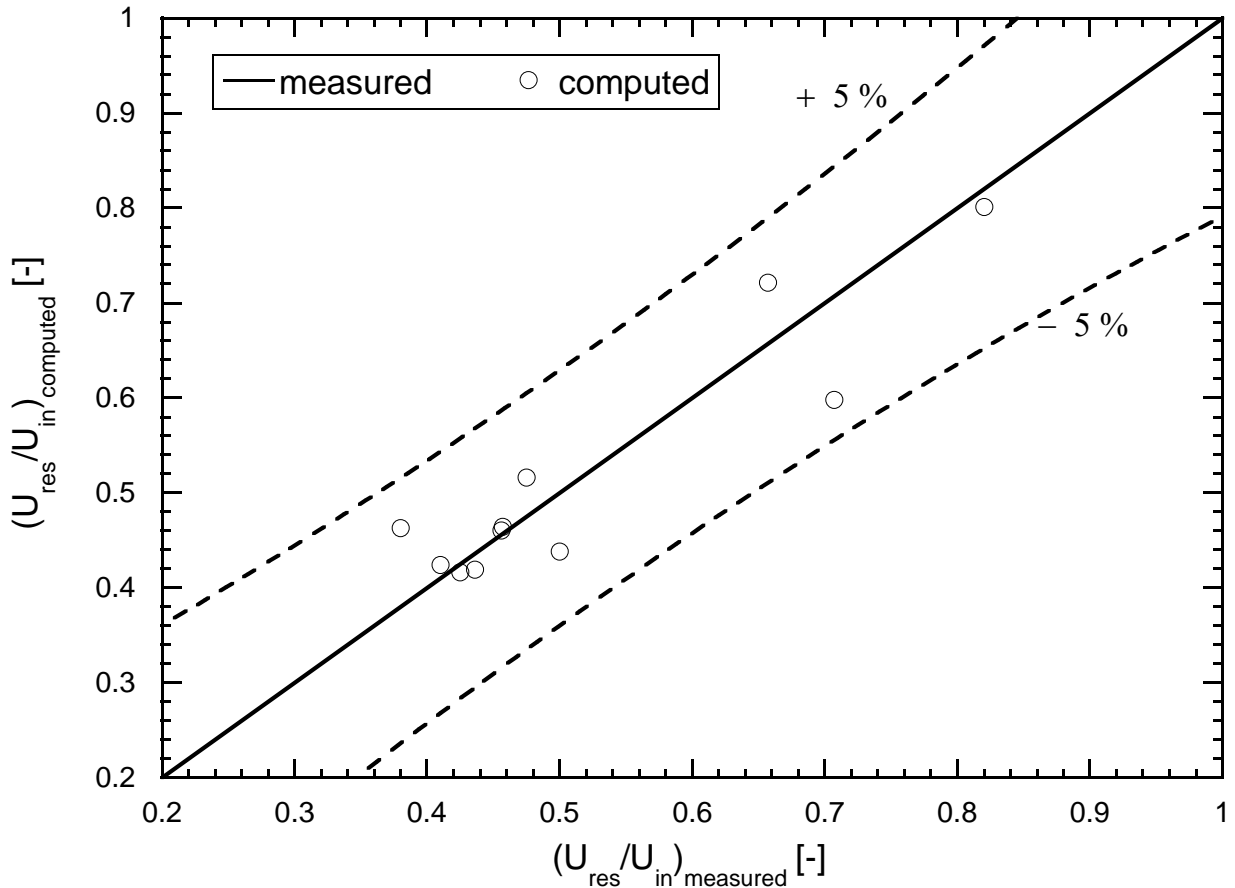


Figure 4.29: Relation for the normalized average velocity over the reservoir (original formula obtained from polynomial curve fitting, Eq. 4.8 and comparison with measured values. The 95 % confidence interval is ± 0.69 .

reservoir can be estimated by using Eq. 4.8.

4.10 Influence of geometry shape factor SK on the reattachment lengths of the upstream recirculation cell in the basin

The geometry shape factor controls the number of circulation cells for specific hydraulic conditions. Moreover the upstream corners circulations are controlling the flow in the center of the reservoir. At a certain geometry shape factor $SK = 5.5$, no flow symmetry is observed. The reattachment length of the upstream circulation cells becomes shorter than the other, and a center circulation appears (Figure 4.5(a)).

Figure 4.30 presents the influence of the geometry on the variation of the lengths of

the right and left circulation cells for flow conditions with $Fr_{in} < 0.1$. The reattachment lengths, normalized with the width of the recirculation cell, is shown as a function of SK . The jet flow type and the corresponding circulation lengths can be predicted from Figure 4.30 based on geometry shape factor value.

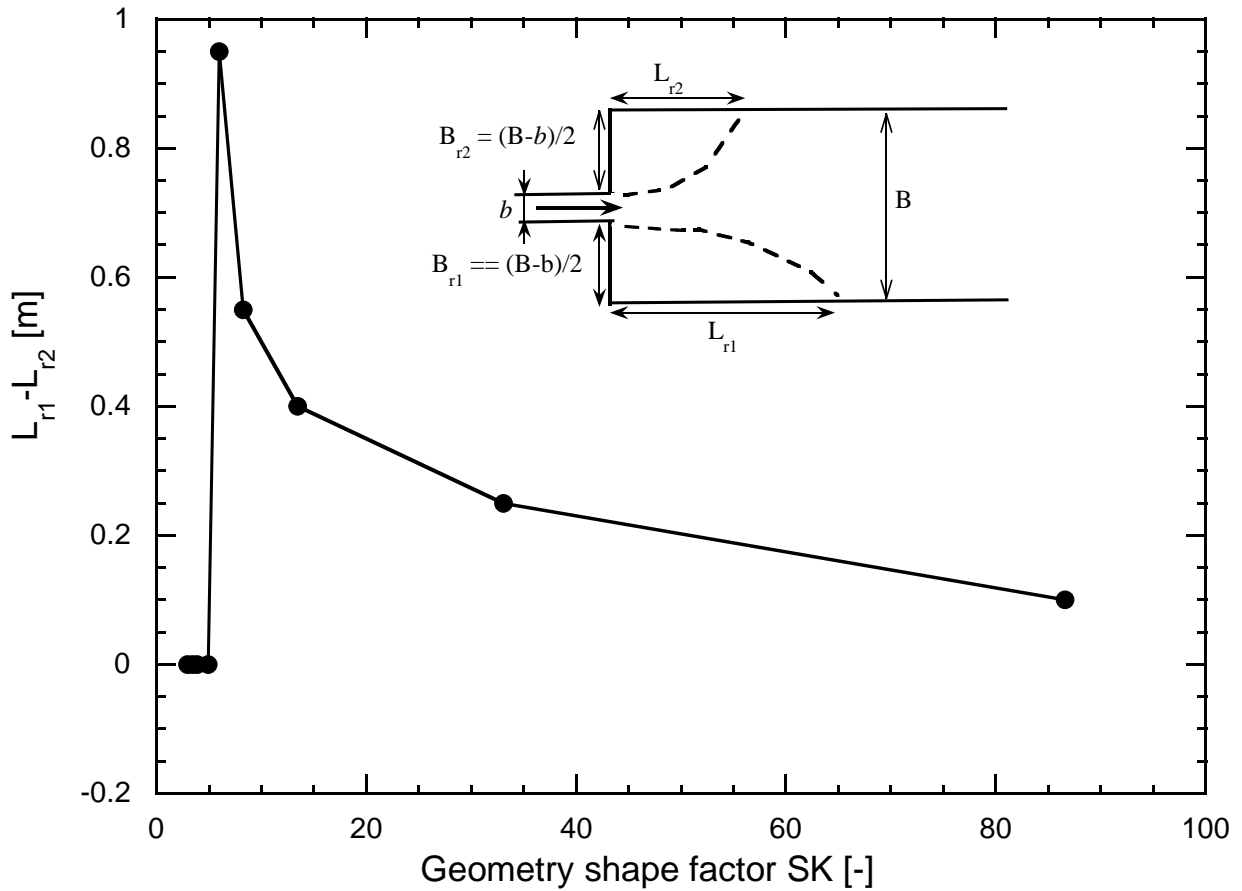


Figure 4.30: Geometry effect on the variation of reattachment lengths $L_{r1} - L_{r2}$ at $Re_{in} = 28000$

For SK up to 5.5 the variations between the reattachment length are zero which means the flow is stable symmetric. While for larger SK the flow still stable but asymmetric with larger and a smaller recirculation length. In Figure 4.30 the bifurcation plot for the normalized reattachment length is compared with normal variation lengths. The figure shows that two bifurcation points exist. However, the differences in the dimensions of the two recirculating zones are evident and its relation with the geometry is well explained by SK .

4.11 Influence of Froude number Fr on the reattachment length $X_r = L_r/B_r$ of the upstream recirculation cell in the basin

Figure 4.31 presents the experimentally measured values of X_{r1} and X_{r2} for all Fr_{in} of a fixed geometry shape factor SK of 5.97. The width of the two upstream recirculation cells is known and equal to the expansion width of the reservoir for axi-symmetric geometry configurations. Based on the measured reattachment length for all inlet Froude number range, the following relationships between the non-dimensional reattachment length X_r and inlet Froude number are developed in Eqs. 4.9 and 4.9:

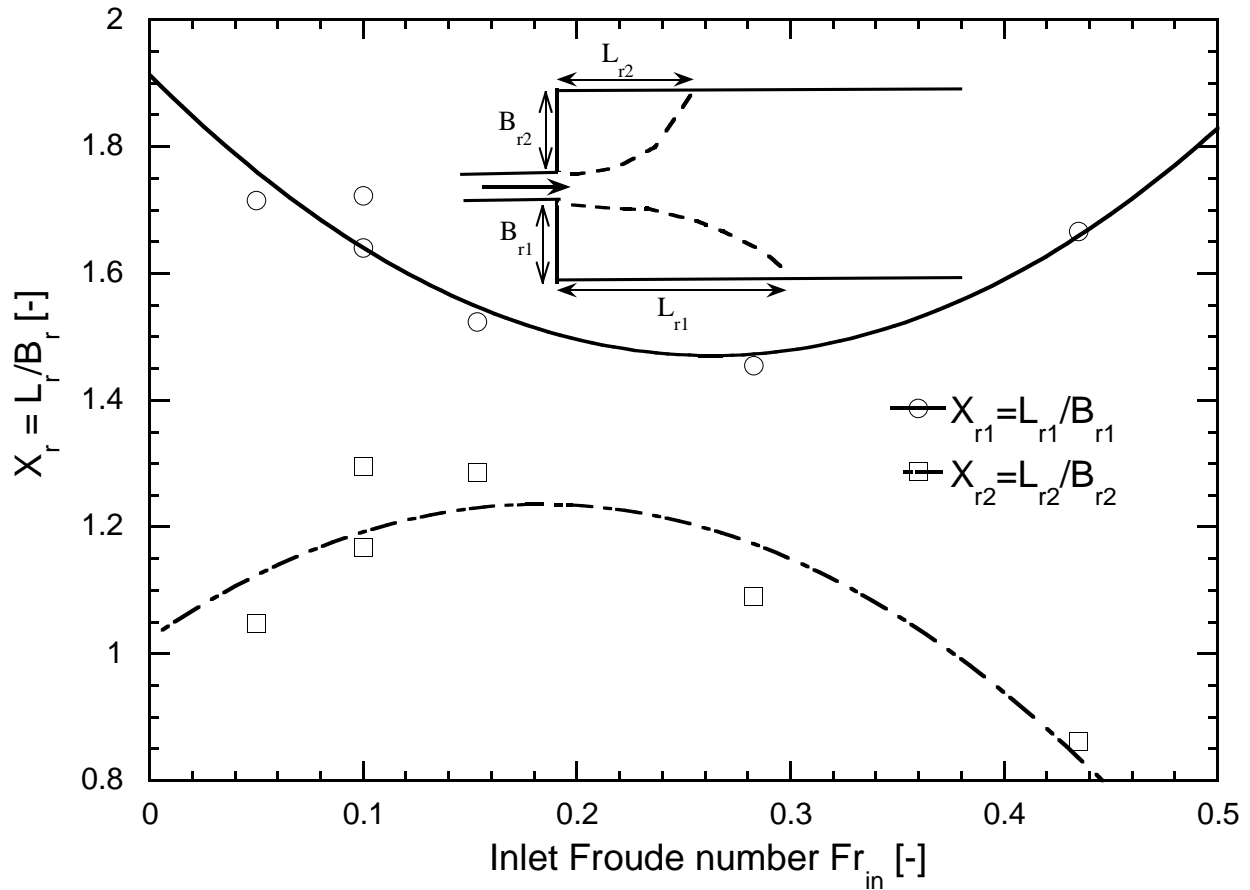


Figure 4.31: Froude number effect on the normalized reattachment length $X_r = L_r/B_r$, where $B_r = \Delta B$, at $Re_{in} = 28000$

$$X_{r1} = 1.9 - 3.36 \cdot Fr_{in} + 6.39 \cdot Fr_{in}^2 \quad (4.9)$$

$$X_{r2} = 1 + 2.31 \cdot Fr_{in} - 6.3 \cdot Fr_{in}^2 \quad (4.10)$$

4.12 Influence of geometry shape factor SK on hydraulic residence time in the basin

Residence time t_r can be used to assess the capability of a reservoir geometry to minimize the sediment before being deposited. Because of the complex geometry of such reservoirs and the likelihood that complete mixing does not occur, the analysis of the hydraulic residence time is not trivial.

The residence time (also called the retention time, or the water age or flushing time), is effectively the average length of time that water molecule (or sediment particle), will remain in a reservoir. The residence time, t_{ri} , is defined as the ratio of the initial reservoir volume V_{res} divided by the average flow rate Q .

In the present study the residence times are between 1.5 and 12.0 min for the tested geometries as shown in Figure 4.32. The relationship between the geometry shape factor SK and the hydraulic initial retention times within the all investigated basins by a series of experimental geometries showed before.

Figure 4.32 shows the residence time as a function of the geometry shape factor SK . The t_r curve (Fig. 4.32) has a bell-shape trend with one spike or hump located at SK of 5.5. The residence time is increasing up to SK of 5.5 and then decreasing for $SK > 5.5$. The residence time for geometries with symmetric and asymmetric flow can therefore be clearly distinguished by the maximum. Moreover, the critical geometry shape factor of 5.5 was found consistent with the previous results of reattachment lengths bifurcation.

4.13 Influence of geometry shape factor SK on relative resident time t_{ri}/t_s of reservoir

Sediment particle with a settling velocity v_{ss} will be trapped if the settling time t_s is lower than the residence time t_r . The settling time t_s is defined as the ratio of water depth to the settling velocity, $t_s = h/v_{ss}$. Then, normalized residence time can be defined by the ratio of initial residence time to settling time t_{ri}/t_s . Finally, an empirical relationship for the clear water phase as shown in Figure 4.33 was established between the relative residence time and the geometry shape factor SK .

Figure 4.33 represents the mean residence time ratio estimates t_{ri}/t_s as a function of SK as represented by Eq. 4.11 and the application range is $2.92 < SK < 86.60$.

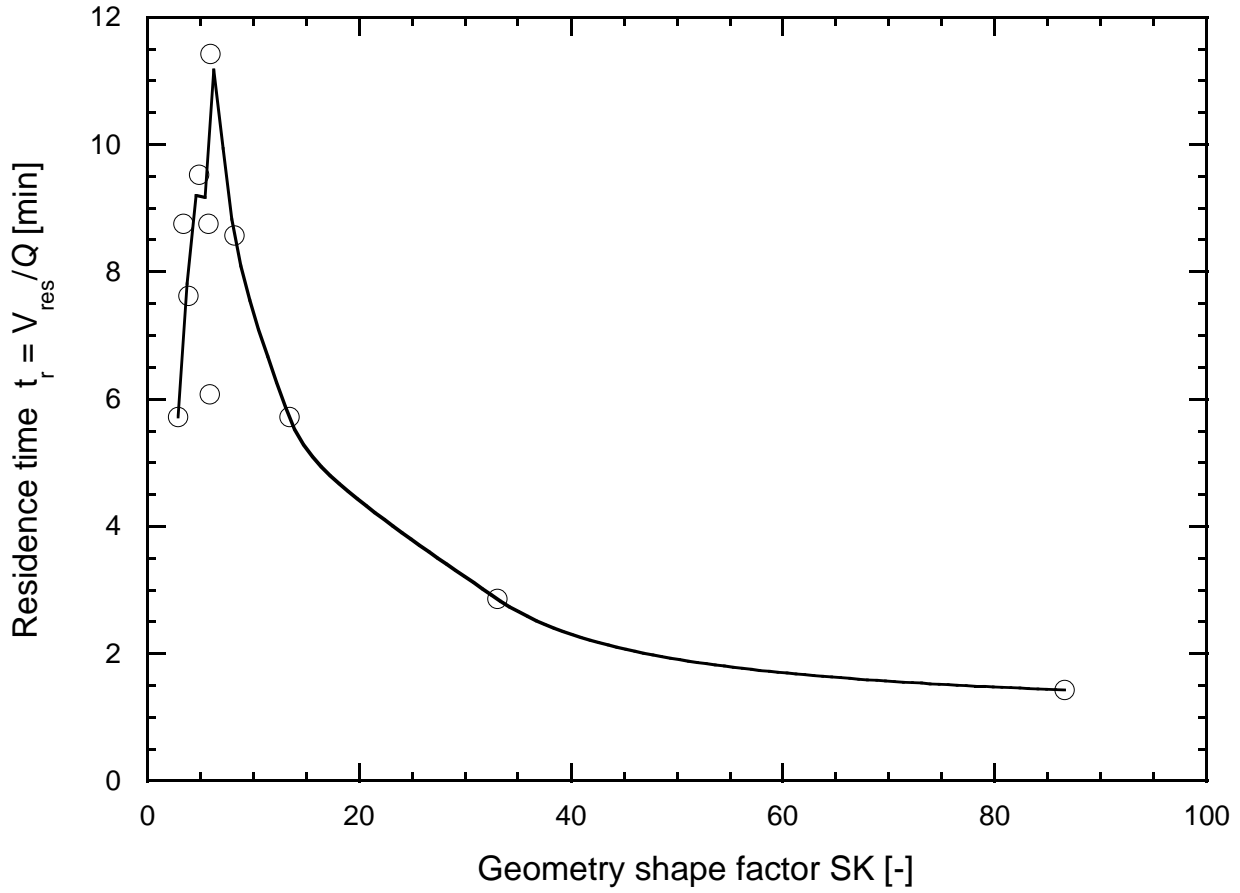


Figure 4.32: Residence time as a function of reservoir geometry shape factor SK .

$$\frac{t_{ri}}{t_s} = -0.85 + \frac{2.3}{SK} + 1.1 \cdot \sqrt{SK/10} \quad (4.11)$$

In Figure 4.33 Equation 4.11 is presented and compared with measured normalized initial residence time t_{ri}/t_s .

4.14 Influence of geometry shape factor SK on reservoir Sedimentation Index SI

The sedimentation index of a reservoir is defined as the ratio of residence (or retention) time to the mean flow velocity through the reservoir and modified later into the following dimensionless form as explained by Verstraeten and Poesen (2000):

$$SI = g \frac{t_r}{U_{res}} \quad (4.12)$$

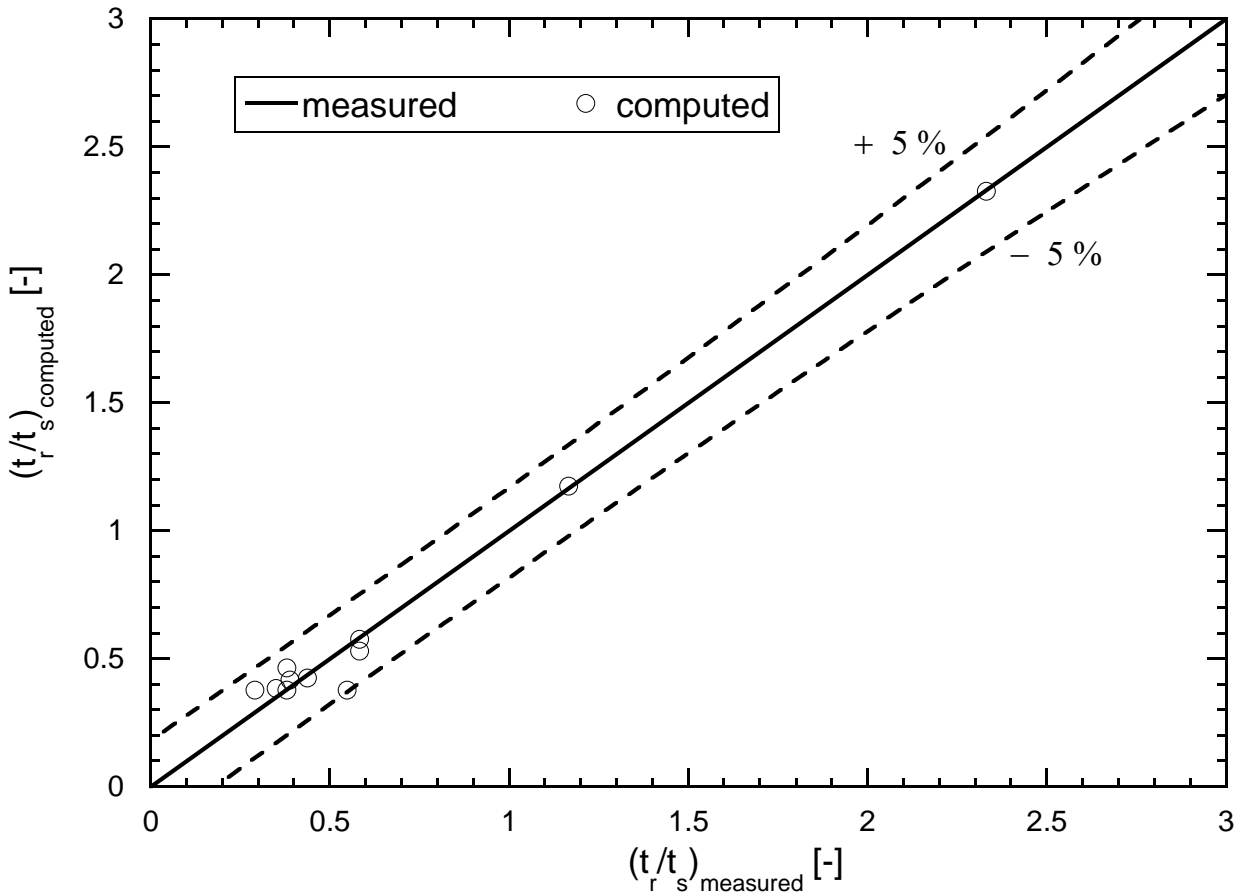


Figure 4.33: Relation for the normalized initial residence time for all geometries (original formula obtained from polynomial curve fitting, Eq. 4.11) and comparison with measured values. The 95 % confidence interval is ± 0.25 .

where t_r is water residence time and for clear water flow $t_r = t_{ri}$ where t_{ri} is the initial residence time; U_{res} is the average flow velocity through the reservoir and g is the gravitational acceleration.

The following relationship between between the sedimentation index SI and the geometry shape factor was produced (Eq. 4.13) was obtained from the clear water phase: :

$$SI = -4922 + 821589 \cdot SK^{-1} \cdot (1 - 2.25 \cdot SK^{-1}) \quad (4.13)$$

The application range of Equation 4.13 is $2.92 < SK < 86.60$.

In Figure 4.34 Equation 4.12 is presented and compared with measured sedimentation index SI .

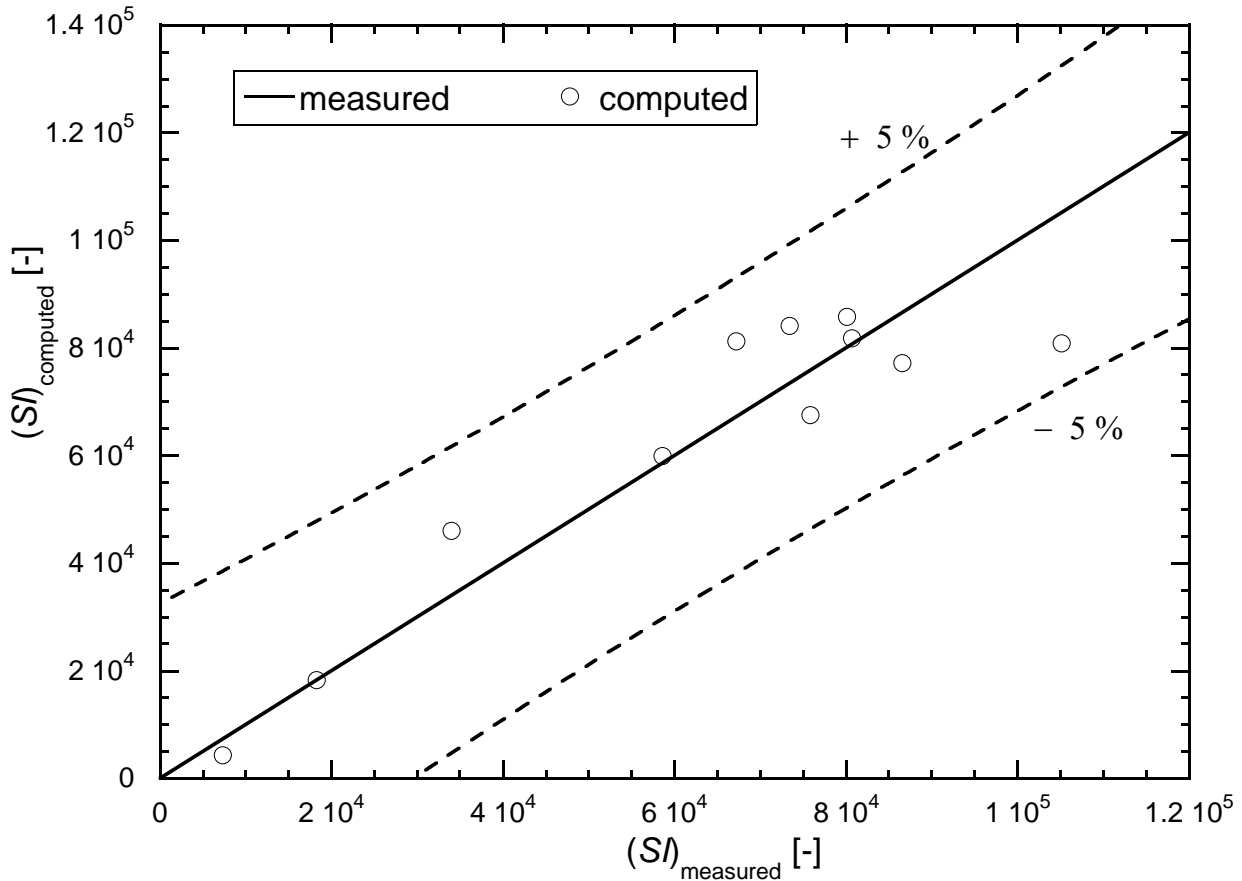


Figure 4.34: Relation for the sedimentation index SI for all geometries (original formula obtained from polynomial curve fitting, Eq. 4.12) and comparison with measured values.

4.15 Conclusions regarding clear water experiments

The experiments revealed a critical geometry shape factor SK , above which an initially symmetric flow will develop towards an asymmetric flow due to the Coanda effect. Through intensive study, it has been found that flow symmetry remains a feature of the flow in reservoirs whose geometry shape factor are less than 5.5.

Thanks to the jet flow regime classifications, the flow structure and separation in a large shallow basin and its relation with geometry could be highlighted through an analysis of streamlines of separation and reattachment, circulation number in each geometry shape factor, and reattachment length relationships. Three types of jet flow regime were classified according to the basin geometry and flow conditions; symmetric with straight jet, meandering with a wavy jet, and asymmetric with question mark jet.

The effects of geometry form were examined for flow in a wide enlargement shallow basin. The influence of the geometric parameters expressed by the geometry shape factor

SK was examined for symmetric inflow and outflow conditions. Although the geometry is symmetric, the flow pattern becomes asymmetric under certain conditions. For $SK > 5.5$, the flow changes from a symmetric structure to an asymmetric structure. For high SK the separating flow bifurcated into asymmetric separation regions and is governed by a critical shape factor at 5.5. The basin length has a strong influence on changing the flow field from an asymmetric flow to a stable symmetric flow. The basin width did not influence the asymmetric separation of the issuing jet.

However, the size of main and secondary eddies were depending on the width. The expansion angle has an influence on the flow pattern and number of circulation cells. The flow instability is increasing by decreasing the expansion jet angle. Flow is asymmetric with one large circulation for semi expansion angle below 40° with symmetric geometric configuration in the up and down stream angles. It can be concluded that the basin geometry influences the behavior of the large turbulence structures, and the flow is quite sensitive to the geometry shape factor.

An asymmetric flow pattern results for Froude number below approximately 0.1 with basin width to water depth ratio $B/h \leq 20$ and geometry shape factor SK below 5.5. A symmetric flow pattern results for Froude numbers above approximately 0.15 with basin width to water depth ratio $B/h \geq 26$ and SK above 5.5. An asymmetric flow pattern results for Reynolds numbers above 14000 with Froude number below approximately 0.1 and basin width to water depth ratio $B/h \leq 20$.

By increasing Fr_{in} to 0.153 (by decreasing water depth) the flow stability and characteristics are completely changed, jet deflection is approximately disappeared and a central meandering jet has been formed with pairing circulation. The meandering behavior is forming by increasing $Fr_{in} = 0.283$ and 0.435 and the flow pattern resembles the von Kármán vortex street pattern. Moreover, the jet has a wavy shape with different curvatures. By decreasing Fr_{in} to 0.05 the jet still deflected to right side and the mean velocity is about 75% of the inlet mean velocity.

Upflow and downflow regions play a key role for the sediment transport from the bed to free surface into the water column. Vertical vortex has been observed which is able to resuspended the sediment particles and keep the suspended one in suspension. Secondary current behavior was observed for the reduced basin width geometry with $SK = 8.25$. The resulting secondary flow arises through a complex interaction between the curved flow, as manifested by the presence of primary eddies formed immediately in the upstream corners, and the boundary layer developed over the bed.

The clear water experiments investigations (i) provides insight into how the onset of asymmetric jet flow structure is forming (ii) gives a quantitative estimation of the reattachment length needed to permit the formation of asymmetric flow structures.

The geometry shape factor SK was used to scale geometry expansion characteristics, such as the reattachment length, for all possible geometries. Moreover, it provides a means

to capture the significant role of the geometry in the bifurcation process between asymmetry and symmetry flow.

In this chapter, equations were developed for several types of flow jet observed in a various large shallow reservoir forms with clear water flow. Several empirical formulas were developed by combinations of all the geometrical dimensionless parameters in which the best fitting relationships were presented. Simple relationship for direct estimation of reattachment lengths X_r for gyres in the asymmetric and symmetric flow structures, as a function of geometry shape factor SK and Froude number have been established.

The normalized residence time t_{ri}/t_s , which is generally referred as the ratio of hydraulic residence time and particle settling time, provides a description of the flow classification and its relationship with geometry shape. These results have implications for the prediction of flow and velocity distribution, for scaling the flow field, and for interpreting CFD results.

The preliminary selection of adequate dimensionless parameters was necessary in order to obtain good results. The normalized residence time is also an important parameter since it classifies the flow according to the geometry. All developed formulas have a general structure which can be physically explained.

Results and analysis of tests with sediments

In this chapter, the results of experiments with sediments are discussed and the effects of geometry on the deposition patterns are investigated. The existence of a morphological equilibrium in the basin by long period test is presented.

Moreover, the effect of the suspended sediment mixture and sediment deposits on the flow field is illustrated. Special attention is given to the mechanism governing the sediment exchange process between the jet and the associated coherent structures.

Finally, the major physical processes responsible for the observed phenomena (asymmetric flow patterns in axi-symmetric geometry) are analyzed.

The last section presents the discussion and conclusions for the investigated phenomena in the axi-symmetric geometries.

In this chapter, the effect of the basin geometry characteristics (Aspect Ratio AR , Expansion Ratio ER , and ratio of expansion area σ) on the sediment deposit characteristics (volume and thickness ratio).

Moreover, several empirical relationships to describe the influence of the reservoir geometry shape factor SK and dimensionless time t/t_r on deposited sediments volume ratio, storage loss, thickness of deposited sediment ratio, sediment intensity and sedimentation index are developed.

5.1 Large coherent structures with and without suspended sediment

The effect of the basin geometry and sediment deposits on the degree of asymmetry of the separated flow was studied in detail. Figures 5.1(a) and (b) present schematic view of the flow pattern, for the reference geometry (T1), with the clear water and the water-sediment mixture, respectively. The clear water phase finding as explained in Section 3.10 is very significant.

It can be noticed in Figure 5.1(a) that the jet issuing from the inlet channel is considerably deviated and three large scale vortices develop, including a main large one rotating anticlockwise in the center part of the basin.

Furthermore, two smaller vortices rotating clockwise are formed in the upstream corners of the basin. The deflected jet works as a vortex shedding region between the main eddy in the center and the triangular one in the upstream right corner.

Moreover, two mixing layers left and right are observed between the main flow and both eddies in Figure 5.1(a). The jet seems to be attracted towards one side of the basin (in the test always to the right side). A second vortex shedding zone in the reverse flow towards the inlet is generated between the main gyre and the small triangular clockwise eddy in the upstream left corner.

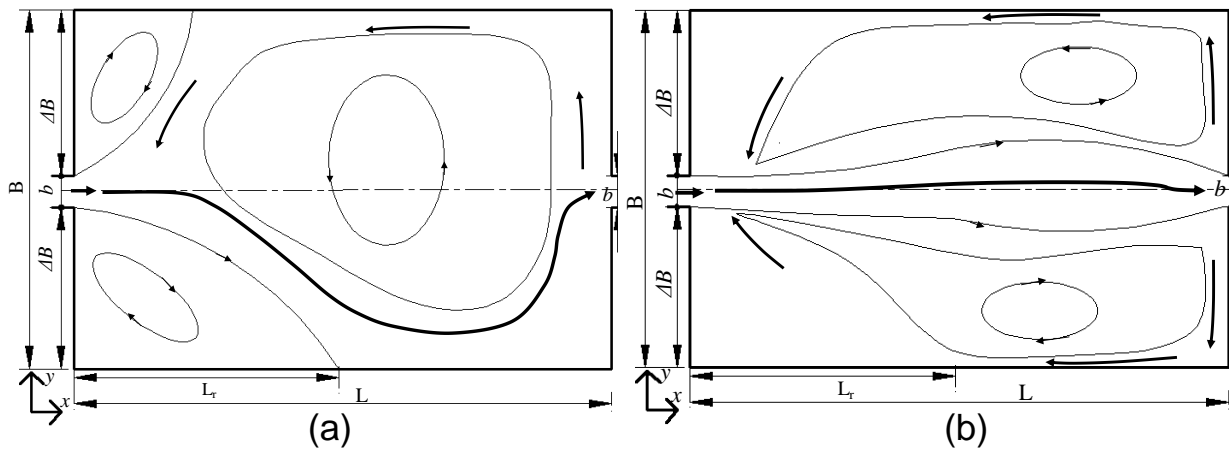


Figure 5.1: Plan view of the reference experimental setup ($L = 6$ m, $B = 4$ m) and definition of the geometrical parameter of the first recirculation cell in the basin (L_r). Discharge $Q = 7.0$ l/s, and water depth $h = 0.2$ m and schematic diagrams of the flow pattern for; (a) clear water, and (b) water-sediment mixture.

Figure 5.1(b) shows the second phase flow feature developed with sediment entrainment. As a result of bed forms and suspended sediment concentrations, the flow field is completely changed. The gyres in the upstream corners disappear and a pattern emerges rather symmetric with respect to the centerline.

The two remaining gyres interact with the jet which shows some tendency to meander. Since the exchange with the upstream corners of the basin is very small, it is expected that not much deposition takes place in those areas. Apparently the changes in the bed forms or effective roughness resulting from the sediment deposition can completely modify the overall flow pattern.

As a conclusion, as sediment is added to the flow, the turbulence is reduced and the mixing lengths decrease which, together with increasing roughness, cause an increase in velocity gradient when compared to clearwater flow.

Several physical mechanisms may be invoked to cause these effects will be explain hereafter.

5.2 Effect of test procedures

In order to investigate the bed evolution with time, two different experimental procedures were tested in order to find a procedure applicable to all tests (Kantoush et al., 2006c). As explained in Section 3.6, the main differences between the tested procedures can be summarized as follows:

Procedure 1: Discontinuous feeding: after each run (90 minutes time steps), the bathymetric measurements are performed after the test interruption.

Procedure 2: Continuous feeding: test interruption occurs after long time step (270 and 540 minutes) of continuous feeding of the water-sediments mixture and accomplishment of measurements.

The flow and deposition pattern comparison with fine sediment for the first three tests (T1, T2, and T3) have been carried out with the same boundary conditions and initial conditions (Table 3.8) but with different test procedure as following:

1. T1: The discontinuous feeding procedure has been used.
2. T2: Test for Series A were repeated with the purpose to check the reproducibility and the model sensitivity.
3. T3: The continuous feeding procedure has been used with the same hydraulic and sediment conditions as previous tests (T1 and T2).

5.3 Flow field comparison

This subsection illustrates a comparison of the time averaged flow patterns evolution with different test procedure, for each run of (T1, T2, and T3). Figures 5.2, 5.3, & 5.4 depict the flow patterns and bed morphology for T1, T2, and T3, respectively. Figures 5.2(a), 5.3(a), & 5.4(a) show that the flow enters in beginning as a plane jet issuing from the narrow leading channel to the wide basin.

After jet issuance, the main flow tends towards the right hand side, generating a large and stable main gyre rotating anticlockwise and two small "triangular" gyres rotating clockwise in the two upstream corners of the basin. The jet appears to be attracted to one of the side-walls.

Its preference for the right side is weak since a stable mirror image of the flow pattern can easily be established by slightly adapting the initial conditions.

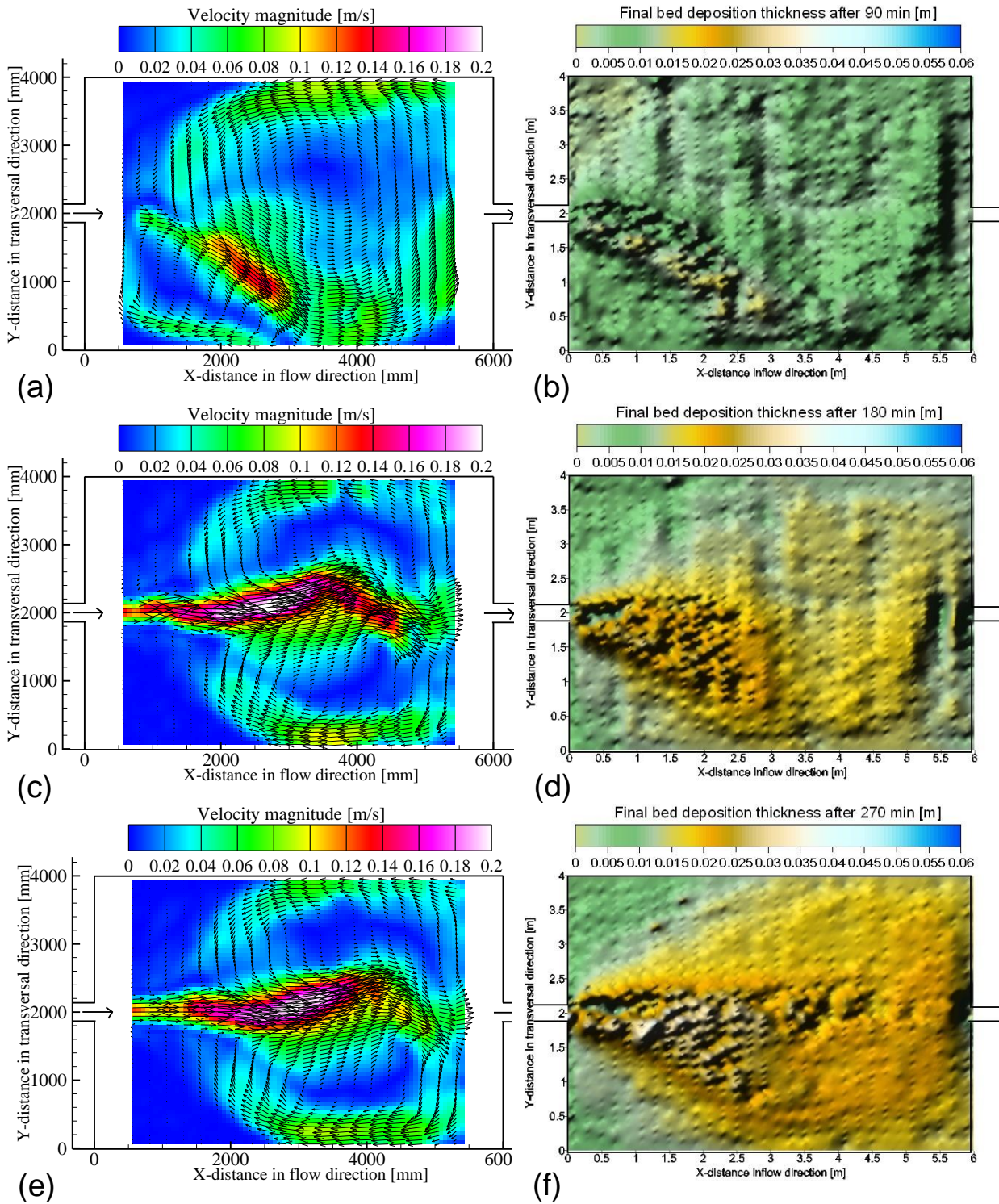


Figure 5.2: Average flow pattern with velocity vectors , (left) and evolution of deposition, (right) for Test1, (T1) for different time steps a, b) 90 min, (c, d) 180 min, (e, f) 270 min

By following the floating particles, it can be noticed that in the first meter from the entrance the particles are straightly entering and, in the next two meters, they deflect to the right until arriving at the reattachment point near the right wall at 2.65 *m* from the entrance.

The particles that do not leave the basin through the outlet channel circulate with the main gyre to arrive near the separation zone at the farthest left side wall. The circulation pattern sustains itself because the inertia of the main gyre pushes the incoming jet aside. An initially smooth bottom favors this inertia dominated pattern.

By comparing the three figures similar gyre patterns are obtained even with different test procedures and different working days.

The inflow mixture behaves like a jet that remains quite separated from the clear water in the basin. After some distance, the shear between both bodies of water moving at a different speed causes mass and momentum exchange and thus eddies that are peeled off from the core of the jet. This peeling off occurs alternatively on both sides of the jet and generates eddies that increase with longitudinal distance.

Furthermore, the jet starts to undulate with a wavelength and amplitude that increase with longitudinal distance. The behavior resembles to a continuously growing instability. This asymmetric and switching flow behavior continues until the downstream end of the reservoir, where the jet is forced to pass through the outlet channel.

During 90 minutes of adding the sediment the observed flow pattern in Figures 5.2(a), 5.3(a), and 5.4(a) did not differ much from the clear water phase, except for the increase in size of the right corner gyre and a downstream shifted reattachment point.

Moreover, the decelerated mean velocity magnitudes in the clear water phase is increased by 50% after 90 *min* of feeding sediment. Apparently this is due to the bed deposition, suspended sediment entrainment and the associated emergence of bed forms.

By comparing the Figures 5.2(a), 5.3(a), and 5.4(a), it can be concluded that similar flow patterns have developed with the two procedures, but with small differences regarding the velocity magnitudes and the reattachment length. Moreover, the deviated jet velocity approximately has the same value as in the inlet channel.

Figures 5.2(c), 5.3(c), and 5.4(c) present the flow patterns after 180 minutes of adding sediment for the three test procedures. As a result of bed deposition with ripple formation and suspended sediment concentrations the flow field is completely changed.

In Figures 5.2(c) and 5.3(c), the main features of the flow pattern are a strong jet towards the outlet with a higher velocity than in the first run (during 90 minutes), and one large eddy on each side of the jet. The gyres in the upstream corners are suppressed if not disappeared and a pattern has emerged that is rather symmetric with respect to the center line.

However, the flow pattern is very complex. The mean flow velocity show the accelerated along the centerline. It is also seen that the remaining two gyres interact with the jet which

shows some tendency to meander. Since the exchange with the upstream corners of the basin is very small, it is expected that not much deposition takes place in those areas.

By comparing the two figures it can be concluded that similar flow patterns have developed with the same test procedure but with small differences regarding the dimensions and strength of the circulation cells. Figure 5.4(c) presents the flow pattern of the continuous test procedure after 180 min of adding sediment. It has a flow structure different from those in Figures 5.2(c), and 5.3(c). Due to the continuous feeding procedure already during the second run the right side gyre starts to enlarge in size and develops into the one shown in Figure 5.4(c). This pattern appears to be rather stable.

With the help of bed evolution measurements and final bed deformation pictures, it can be said that during the transition zone from the initial counterclockwise gyre to the final clockwise gyre the roughness of the bed showed strong local variations.

Apparently the changes in the bed forms or effective roughness resulting from the sediment deposition are capable of completely changing the overall flow pattern and increasing the velocity magnitudes. Through the same mechanism a further development can be expected.

By comparing the three figures the following conclusion can be drawn:

- With *Procedure 1*, the asymmetric flow has been changed to an stable accelerated symmetric flow; due to sediment deposition and suspended sediment effects.
- With *Procedure 2*, the anticlockwise asymmetric jet on the right side flipped to the left side with a clockwise asymmetric jet (Fig. 5.4(c)).

Figures 5.2(e), 5.3(e), and 5.4(e) show the flow patterns that have developed after 270 minutes of adding sediment for the different test procedures. Figures 5.2(e), and 5.3(e) still show symmetric flow patterns with two gyres coupled to the jet flow.

It can be noted that two very weak gyres that might have become laminar or stagnant have hardly any exchange with the main motion. In both figures the same test procedures were used which resulted in virtually identical flow patterns. The flow pattern of the continuous test procedure still show asymmetric as depicted in Figure 5.4(e). It has a low velocity magnitude from those in Figures 5.2(e), and 5.3(e). This measured variation of flow pattern is very interesting and will be explored further in the hereafter sections.

5.4 Comparison of morphological evolution

In this section three tests (T1, T2, and T3) are compared regarding the final bed deposition thickness after each time step. The observation of the bed evolution for Test3 was not possible due to the continuous feeding procedure. Only the final bed thickness deposition

5.4. Comparison of morphological evolution

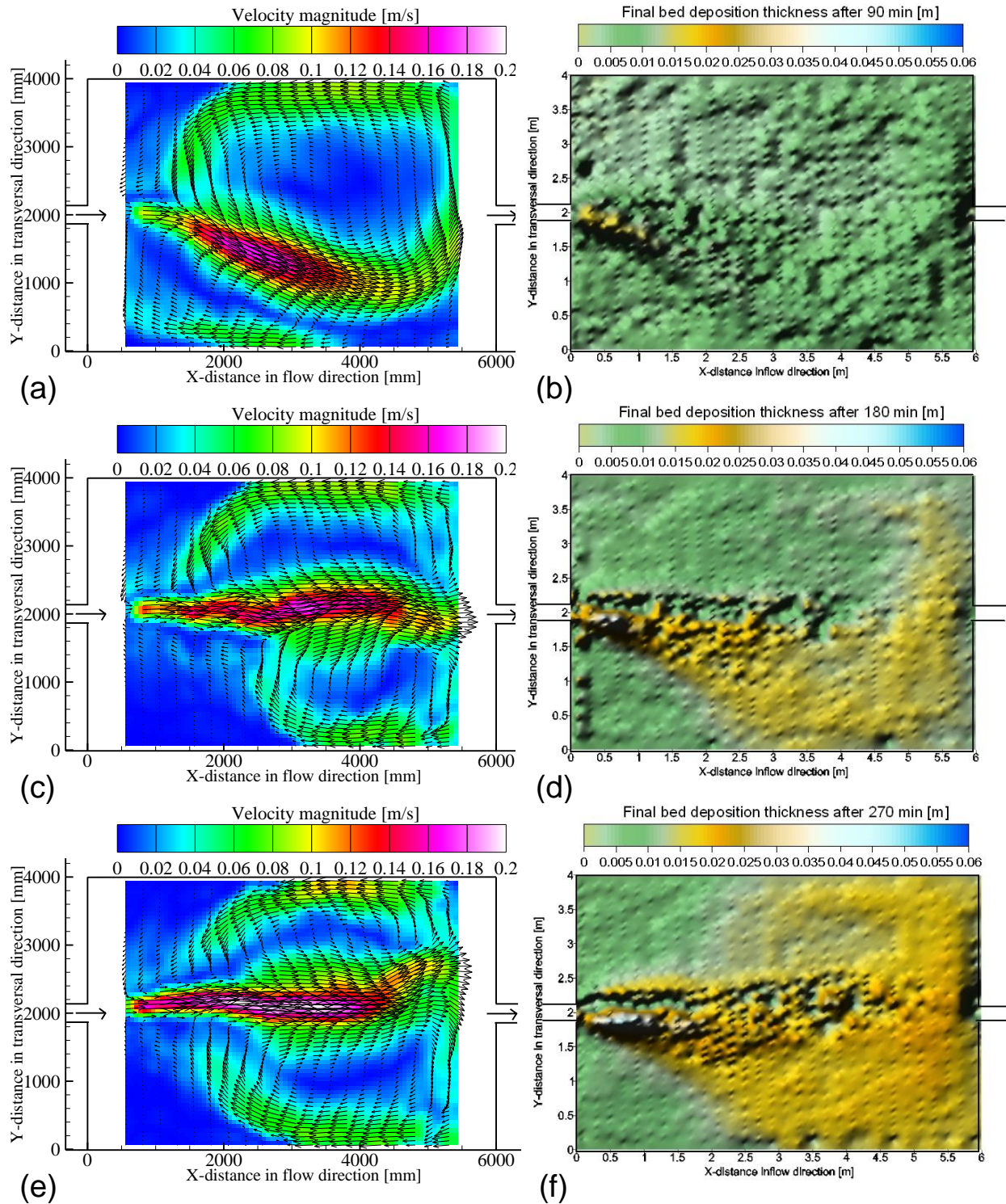


Figure 5.3: Average flow pattern with velocity vectors , (left) and evolution of deposition, (right) for Test2, (T2) for different time steps (a, b) 90 min, (c, d) 180 min, (e, f) 270 min.

was measured after 270 min. For both tested procedures (1&2), two typical features were observed.

The first was development of sediment deposition with ripples formation concentrated on the right hand side and along the centerline later on; the second was concentrated on both right and left sides and very low in the core of the basin.

Figures 5.2(b), and 5.3(b) present a detailed comparison of the sediment thickness layer after 90 min. During 90 minutes, the mixture of water and sediment is advected and diffused throughout the basin following the general flow patterns described above.

The footprint of the flow patterns was clearly visible in the morphology as shown in Figures 5.2(b), 5.3(b), and 5.4(f). The resistance to flow is relatively small for the smooth and plane bed at the start.

However, the flow resistance increases as ripples are being formed. The ripples play an important role in the interaction between the boundary layer flow structures and sediment transport. The asymmetric ripple patterns near the right side wall follow the same direction as the flow pattern shown in Figures 5.2(a), 5.3(a), and 5.4(a). Ripples characteristics were measured manually before cleaning the basin. Moreover, several reference points were taken manually for calibration comparison with the UWS measurements. Nevertheless, some anomalous spikes have been observed.

Figures 5.2(d), and 5.3(d) present the thickness after 180 minutes. It can be easily seen that most of the sediment depositions has take place around the centerline and the downstream part. The sediment concentration and sediment depositions are highest along the centerline of the basin and reduce towards the sides as clearly depicted in Figures 5.2(d), and 5.3(d). Figures 5.3 shows the evolution of the sediment depositions for T2 (repeated test).

The figure shows an almost similar sediment deposition pattern as was found for T1 presented in Figures 5.2. There is a complex relation between flow patterns, sediment exchanges and sediment transport as well. Figures 5.2(f), 5.3(f), & 5.4(f) show the results obtained after 270 min of test run. A submerged channel was formed under the accelerated straight jet trajectory as depicted in Figures 5.2(d), & 5.3(d).

Figures 5.4(f) presents the final bed evolution for the continuous test. It is noticed that the sediment deposition takes place in accordance with the flow patterns of Figures 5.2(a), (c), & (e).

At the beginning ripples start to form near the right side wall leaving the area in the upstream corner void, which is associated with action of the small gyre. It is clearly seen that the deposition at both upstream corners is very small. Most of the sediment deposits right below the main streamlines connected to the inflow channel.

After the flow pattern has changed to the clockwise gyre, a symmetric ripple pattern formed near the left side wall, similar to the one at the right side which formed in the beginning.

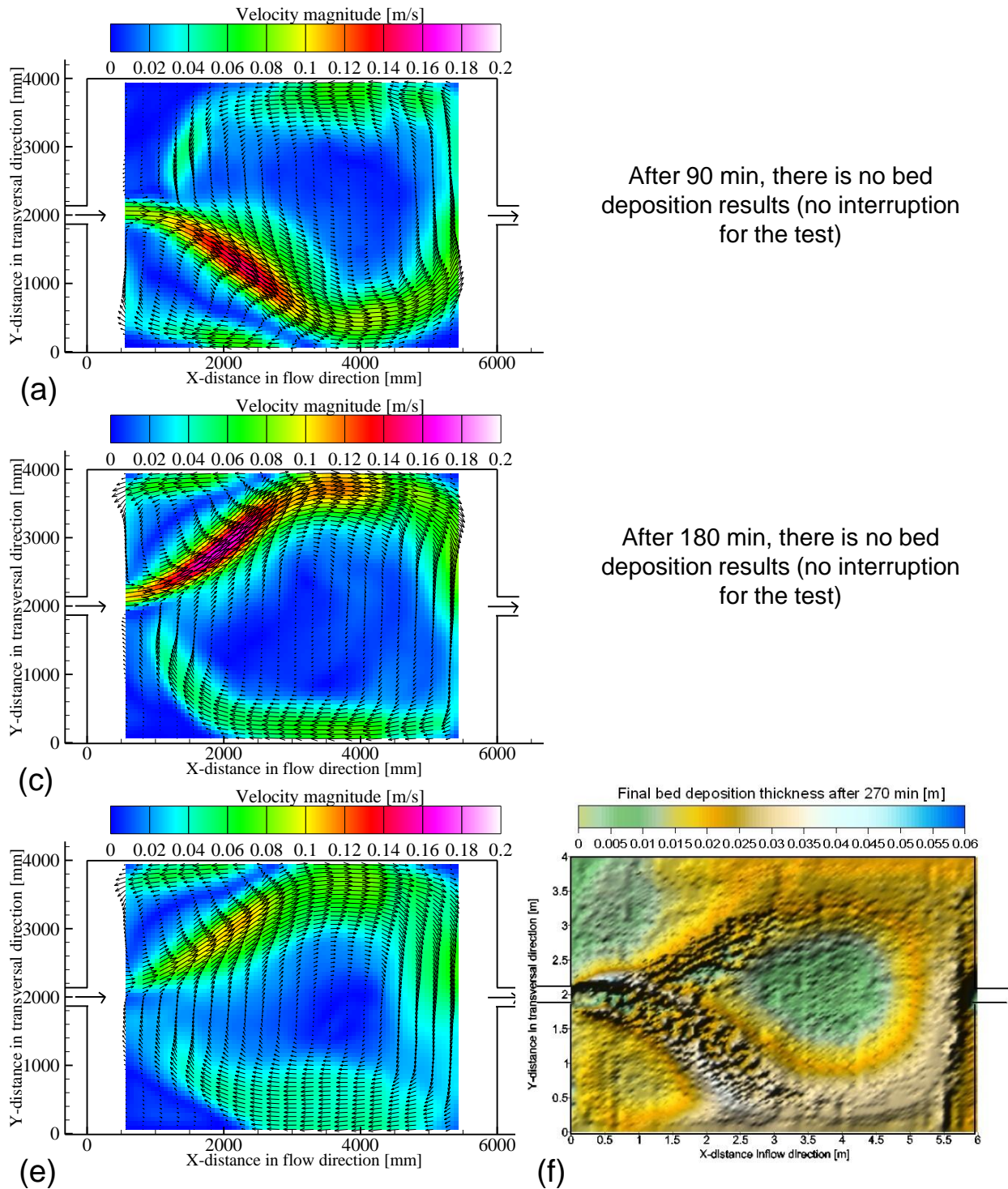


Figure 5.4: Average flow pattern with velocity vectors , (left) and evolution of deposition, (right) for Test3, (T3) for different time steps a, b) 90 min, (c, d) 180 min, (e, f) 270 min.

After a certain period of testing, the deposition on the left side gradually increased

generating a wider bed elevation underneath the jet centerline with a width of approximately three times the inlet channel.

Similarly, in the first few hours of the experiment the elevated bed has reached the right side wall and followed the course of the streamlines down to the outlet channel.

It is remarkable that in the downstream part of the basin the bed is elevated on a rather narrow ridge. There is relatively steep gradients near the inlet channel and the first part of the jet are clearly visible. It is quite likely that on a much larger time scale the relatively quiet zone in the upstream corners and the central part of the main gyre will eventually be filled up with the finest sediment fraction.

According to the above analysis, it may be conclude that the gradual changes during the transitional state are missing due to the effect of the test procedure. To confirm the test procedure effect, Test4 (T4) with continuous feeding and longer time steps were performed as will be explained in Section 5.5.

Based on the next section results, it was found that *90min* enough to develop a stable morphology independently on the test procedure. Due to that most of the experiments were conducted with *270min* total test period with three runs each *90min* and for some selected test different scenario was selected (see Table 3.5)

5.5 Long term morphodynamic equilibrium

Morphological processes occurring in the shallow reservoirs are of obvious practical relevance for the management of reservoirs. In particular, the issue of whether such a simple geometry with that complex behavior may reach an equilibrium state or not, and when it will be happen? Attempts to pursue the same goal on the basis of controlled laboratory observations are not known. This is not surprising as the timescale of morphodynamic evolution is typically much larger than the hydrodynamic timescale.

In spite of these complexities, controlled experimental observations of the morphodynamic evolution of the shallow reservoir are worth pursuing.

In fact, controlled experiments with a simple geometry and boundary conditions provide a check of some of the main mechanisms which drive the evolution process, a goal quite difficult to achieve on the basis of field observations whose interpretation is generally complicated by the large scale of the processes, the more irregular natural geometries and the simultaneous presence of a variety of features whose role cannot be readily isolated.

The aim of the present test (T4) to perform qualitative and quantitative observations of the temporal development of flow patterns and the bed morphology in a rectangular shallow reservoir geometry. To account for progressive morphological evolution and to verify the final achievement of dynamic equilibrium, a long-term test has been performed with durations up to 1080 minutes (18 hrs).

It has to be noticed that these long runs were performed in several time steps 270, 270 and 540 minutes, i.e. the facility has been interrupted to allow bed morphology recording after the three runs. Let us now outline some significant observations on the morphodynamic evolution observed in the reference rectangular reservoir.

The major fact observed is that sediments were deposited in the centerline with the formation of a submerged channels which keeps the flow field more aligned with the center plane. This mechanism is associated with highly suspended sediment and sediment deposition with a highly velocity along the straight jet trajectory.

5.5.1 Morphological evolution and corresponding flow field

The average flow field and the corresponding bed morphology are shown in Figures 5.5 for three different runs (270, 540, and 1080 minutes) allowing a comparison of the long-term bed evolution in the reservoir. The analysis of all the tested long runs lead to establishing some apparently well defined results, which can be summarized as follows:

1. Starting from an initially flat bed reservoir, a slow evolution of bottom topography occurs with two typical features were observed. In the early time running, the first is the development of the sediment deposition with ripples formation concentrated on the right hand side till bed thickness deposition reaches up to 15% of the water depth. These were able to change the flow pattern with a significant reduction of the flow asymmetry.
2. The second is concentrated along the centerline with relatively steep gradients near the inlet channel and the first part of the jet. This is because the velocity gradients in the flow are far steeper in the case of straight jet than the deviated one.
3. The jet is narrower in the the surface than near the bed. Moreover, the deposition gradually increases generating a wider bed elevation underneath the jet centerline.
4. The basin fills up from the center to the walls directions, starting from downstream to upstream direction. With longer period these gradient slopes regions will be eventually filled up with the finest sediment fraction.
5. The increased roughness height associated with mobile sediment may contribute to increase in shear velocity and turbulence intensity.
6. The sediment concentration and sediment deposition are higher right below the main streamlines connected to the inflow channel although of existence of high velocity. Whereas, after 180 min, as a result of ripple formation and suspended sediment concentration the flow field is completely changed.

7. During 540 min (run 2), most of the sediment deposits and suspended concentration are along the center of the basin. A symmetric ripples pattern formed on the middle of the basin is clearly visible.
8. After 540 (run 2), the deposition on the center gradually increased generating a wider bed elevation underneath the jet centerline with a width of approximately three times the inlet channel. There is another longitudinal gradient between the upstream and downstream parts.
9. A tongue shape deposition occurs along the centerline of the basin. The tongue average thickness is of 0.16 m and locates underneath the jet centerline with average width of approximately eight times the inlet channel width.
10. The deposition at both upstream corners is less than in other parts.
11. The exchange of sediment between the jet and the eddies affects the equilibrium configuration significantly. The latter has a strong effect on the entering jet hydrodynamics and on its morphodynamics. It increased due to the generation of the submerged channel which progresses downstream until it reaches a quasi-equilibrium condition. The jet width is reduced on the surface, due to increase of the coupled eddies size and velocity. Most of the bed form features were vanished, as the deposition was fairly fast increased.
12. The equilibrium deposited thickness established at the entrance depends on the reservoir geometry and the sediment exchange on both sides.
13. The volume of the deposited sediments reached 50% of the total reservoir volume after 1080 min (run 3). The reservoir reaches to the equilibrium after 960 min at which the suspended sediment release efficiency reaches 100%.
14. Equilibrium is associated with vanishing the cumulative net of sediment concentration but this does not imply that the instantaneous sediment flux vanishes.

In Figure 5.5(d) after 1080 min (run 3) a uniform deposition occurs. During the first few hours of the run 1, the observed flow pattern did not differ much from the observations described in Section 5.2. After 270 min the of sediment deposition, the flow pattern shows an alternately accelerating with the symmetric jet in Figure 5.5(a), instead of the decelerating with the deflected jet in beginning of the run. Along with the morphological development, the flow pattern showed significant changes for run 1.

After the development of the deposition region along the centerline, the interaction between the upstream corners gyres and the pair of counter rotating vortices is hindered and the upstream circulation slows down, which ultimately leads to their disappearance later on. The final pattern of the bed topography after 270 min is depicted in Figure 5.5(b).

Suspended sediment is transported from the centerline towards the side walls following the large circulation and settles down on its way, forming a higher deposition region on the right side (Fig. 5.5(b)).

The temporal evolution of the contours of sediment bathymetry during the second run is shown in Figure 5.5(d). The evolution of the bed profile in the second run was somewhat similar in many respects to that observed in the first run, even though it displayed a more intense deposition in the center portion of the reservoir and the emerged ripples bed forms had larger wavelength and height. It has to be noted that the velocity gradient is increased when compared to run 1 (Fig. 5.5(a)).

The jet width is narrow with accelerating velocity in the center as shown in the velocity temporal evolution in Figure 5.5(c). Figure 5.5(c) still show symmetric flow patterns with two gyres coupled to the jet flow and same magnitude. Moreover, the velocity magnitude and the strength of the two gyres are increased.

The smooth tongue shape of the inlet after run 3 and the associated diverging character of the flow pattern gives rise to sediment deposition in the form of an elongated central bar and levees bounding the scoured region adjacent to the inlet. This is shown in Figure 5.5(f).

Moreover, the latter described morphodynamic evolution caused a further reduction of the coupled eddies sizes. The observed pattern in Figure 5.5(e) has a significant increasing in the jet effective width. Almost 50% of the basin total volume has been filled by the deposits after 1080 min.

By comparing the three runs in Figure 5.5, it can be concluded that asymmetric flow patterns have developed differently regarding the dimensions and strength of the circulation cells in both sides. Finally, symmetric ripple patterns, could be observed after 270 min of adding sediment.

5.5.2 Comparison of deposition depth for different cross sections

A detailed comparison of cross section bed profiles at four different sections is presented in Figure 5.6 (a, b, c & d). The time evolution of sediment deposits can be seen for the three runs (270, 540 and 1080 min) at cross sections $X1 = 1.5$ m, $X2 = 2.0$ m, $X3 = 3.0$ m and $X4 = 4.5$ m, respectively.

The bed profiles at 90, and 180 min, they are corresponding to Test1 (T1), because the smallest time steps for the long run test (T4) was 270 min. The first 2.0 meters show different bed forms (shape and height) than the last two meters downstream.

Figure 5.6(a) shows depositions in transversal direction of the basin at distance of 1.5 m from the inlet, for the three runs. After 90 min, almost a uniform depositions over the basin with average thickness of 0.015 m is observed. Due to the complete change of the flow pattern after 180 min, sediment deposition rate is slightly increased by 0.005 m.

The bed thickness observed after 270 min(run 1) is almost two times higher than after

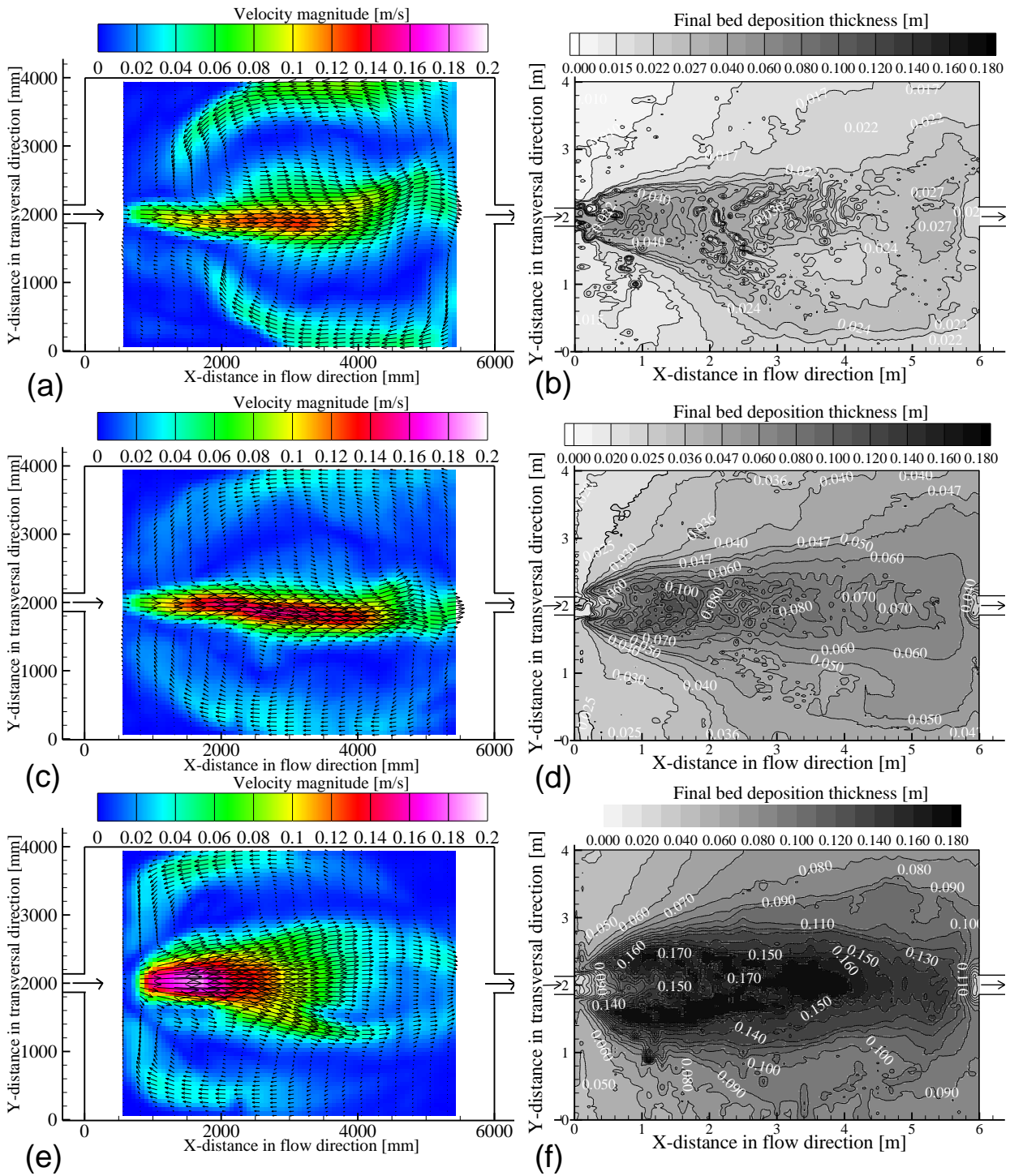


Figure 5.5: Evolution of bed topography and flow vectors with velocity contours at different times (a, b) run 1; 270 min, (c, d) run 2; 540 min, (e, f) run 3; 1080 min. Discharge $Q = 7.0l/s$, water depth $h = 0.2m$ and suspended sediment concentration $C = 3.0g/l$.

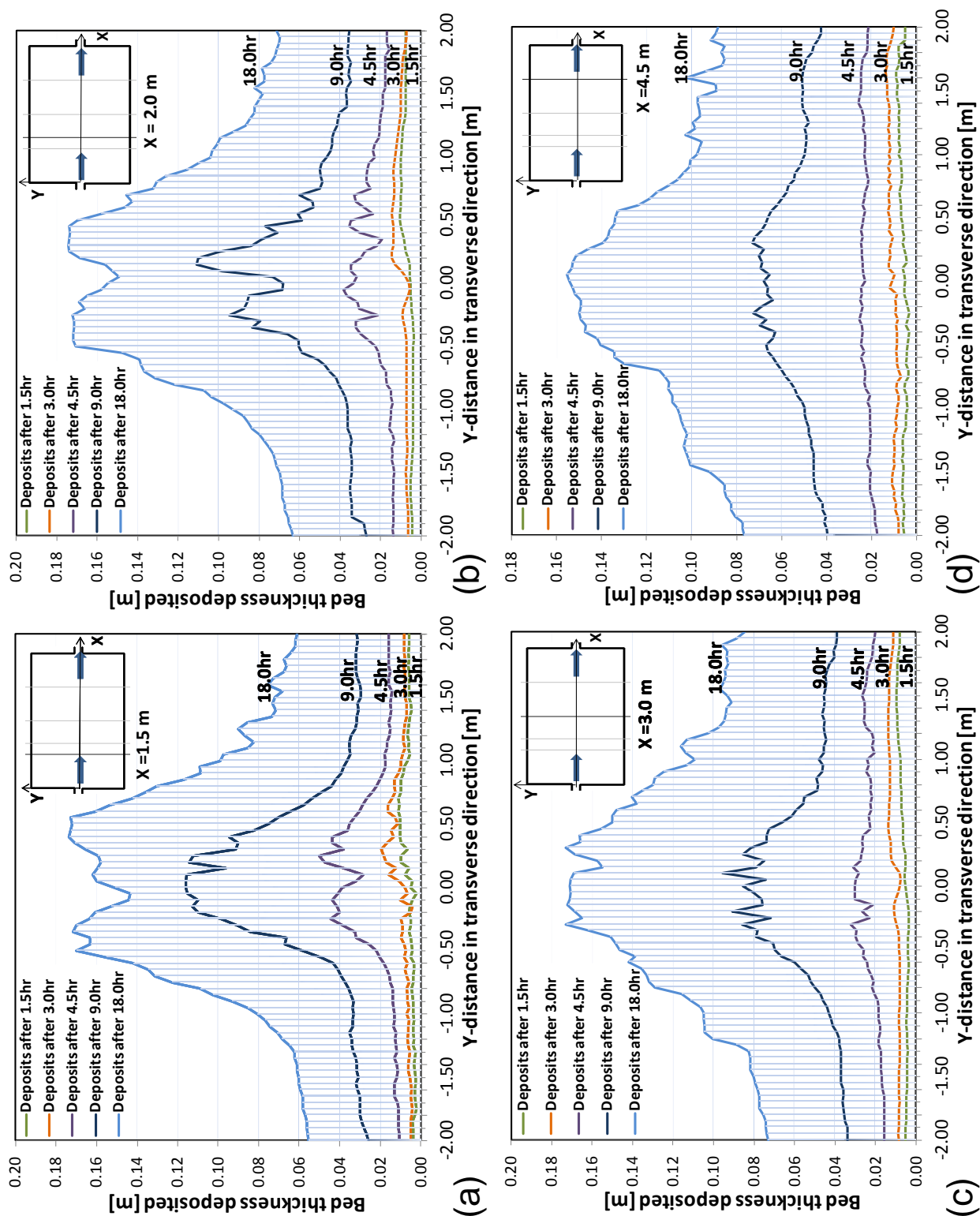


Figure 5.6: Comparison of bed profiles at different cross sections of the basin, (a) $X_1 = 1.5$ m, (b) $X_2 = 2.0$ m, (c) $X_3 = 3.0$ m and (d) $X_4 = 4.5$ for T1, after (1.5, & 3.0) and for T2, after (4.5, 9.0, and 18 hours). Water depth $h = 0.2$ m.

180 min at the center but does not differ much at left and right walls. There are two transverse mild slopes of average 2% to the center.

But after 540 min (run 2) steep slopes appear at both sides. A channel formed on the hill of the deposits along the centerline elevated mount channel forms at the center with a width of 0.75 m after 1080 min (run 3) as shown in Figure 5.6(a).

During 540 min of adding suspended sediment more deposits can be observed at the center and the thickness reaches to 0.17 m after 1080 min (run 3). A horizontal deposited reach with 2.0 m width has been formed along the centerline and still less deposits in the upstream corners. The deposition rate is increased for runs 2 and 3.

It may be concluded that a stable morphology has been reached after 1080 min and almost morphological equilibrium in the basin has been reached for. Bed forms after 270 min deposits show a wavy bed forms (Fig. 5.6(b)).

The bed thickness observed after 540 min is almost three times higher than for 270 min. The bed becomes thicker and even more irregular after 540 min. As the experiment proceeded and equilibrium was as a result, bed forms persisted throughout the three runs. This allowed to follow their development in detail and ascertain that they migrated towards the walls during the second and third runs.

Figure 5.6(c), which shows the final development of bed thickness in the middle of a cross section located at a distance of 3.0 m from the channel inlet, displays the passage of five bed forms characterized by bed deposition speed ranging about 0.5/1 *cm/hr*. For the middle cross section, the influence of the flow deviating towards the centerline of the basin is clearly visible by strongly reduced bed thickness after 180 *min*.

The sediment deposits gradually start to increase again in the middle. The deposition progressively increases after 270 *min* from left wall towards a peak value of 0.03 *m* at the middle section, followed by a small decrease at the right wall. After 1080 *min*, Figure 5.6(c), shows almost similar sediment deposition behavior as presented in Figure 5.6(b).

It can be clearly seen that the deposition layers after 90, 180, and 270 min are parallel with each other and almost a uniform deposition rate is reached at both sides. But after 540 min the sediment deposits formed underwater ridge at the center with mild slopes towards the sides.

After 540 *min* of testing, the deposition on the sides gradually increased generating a wider bed elevation underneath the jet centerline with a width of approximately 1.25 *m*.

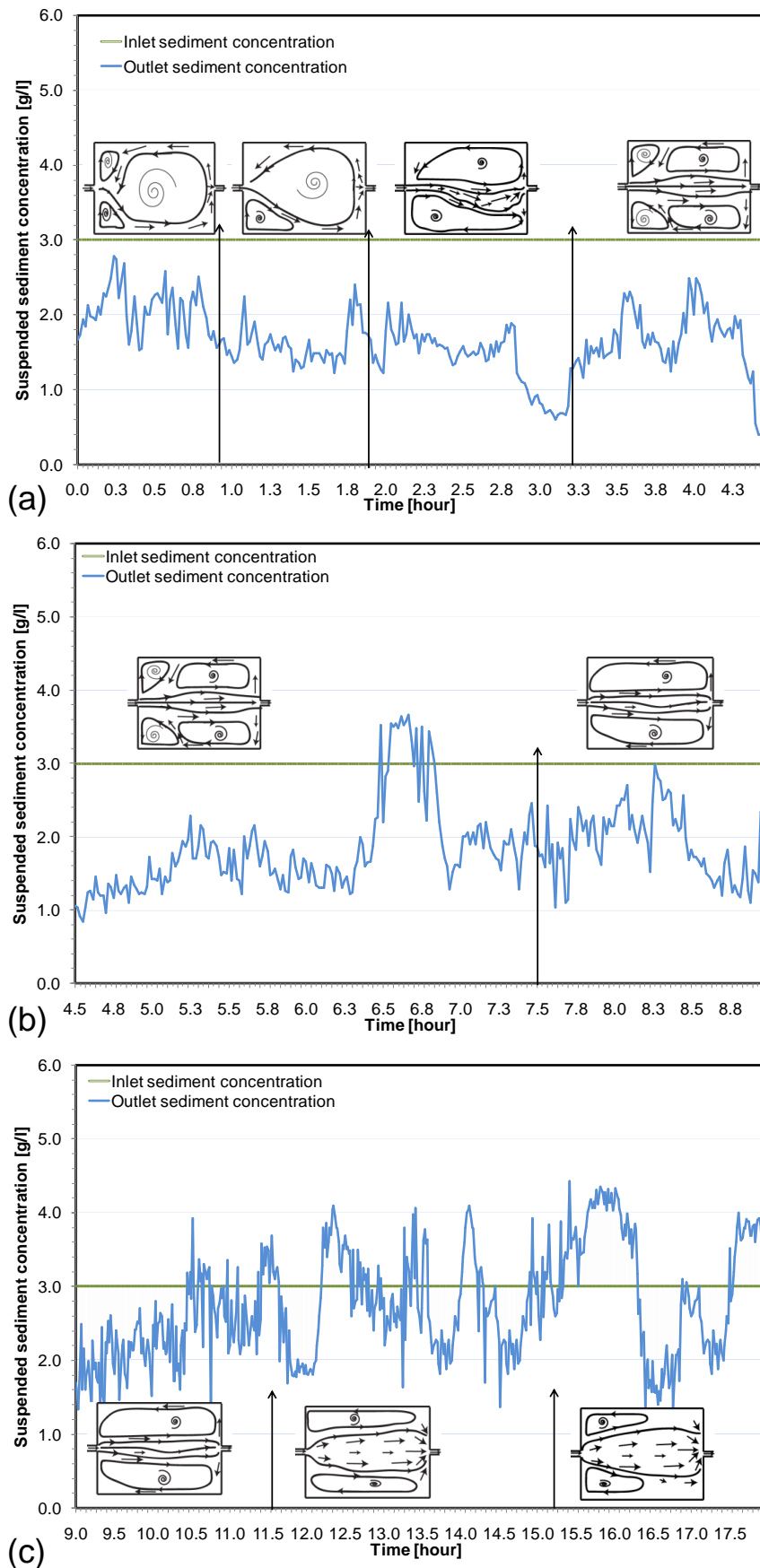


Figure 5.7: Inlet and outlet suspended sediment concentration and sketch of flow patterns, measured every minutes, during (a) run 1; 4.5 hours, (b) run 2; 9.0 hours, (c) run 3; 18.0 hours.

5.5.3 Suspended sediment concentrations and sediment trap efficiency

The suspended sediments concentrations (SSC) at the inlet and outlet channels have been monitored in detail. Since the instruments continuously report SSC, even though these values may be spurious, it was important to scan the data to search for the periods of clogging, i.e. sudden declines in SSC, or periods when SSC remained stable despite significant changes in bed forms, or also sudden changes in flow patterns. Figure 5.7 shows inlet and released SSC from the reservoir every minute and the sketch of the flow pattern during each period.

Figures 5.7(a), (b), and (c) show the time series measured SSC at each time steps, 270, 270, and 540 *min*, respectively. In order to make the graphs easier to view, we chose 270 min periods. The inlet SSC was kept constant of 3 *g/l* with average measurement error of $\pm 5\%$, and only the SSC monitoring at the outlet was available. The sediment release in the beginning of the test for run 1, is low due to the bed formation and mixing exchange between circulations. Then it gradually increases during runs 2 and 3 and relatively stable at the end of run 3. After 960 min of long period, SSC inflow and outflow are approximately equal rates at which the basin reaches to the equilibrium.

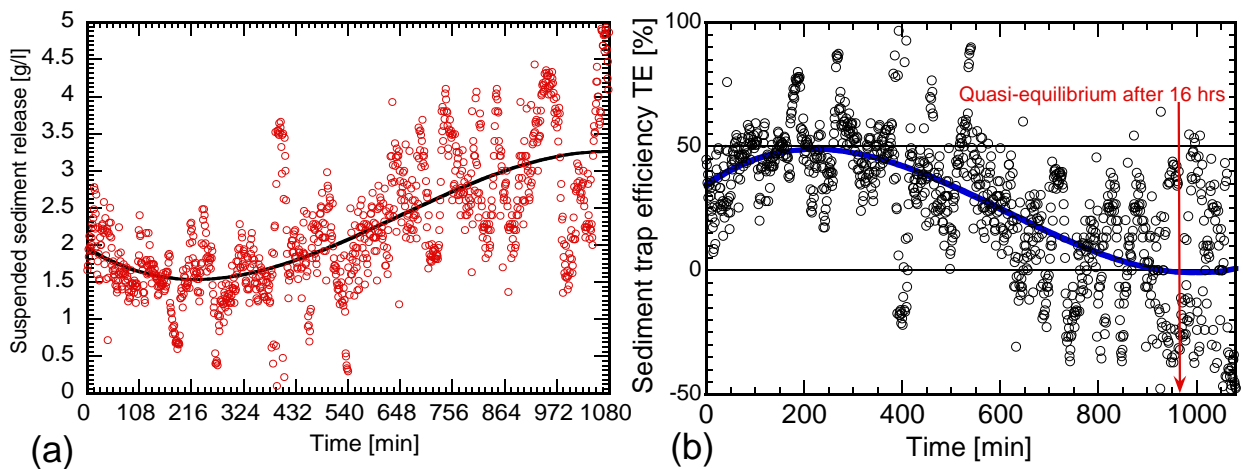


Figure 5.8: Evolution of sediments release E (a), and trap efficiency TE (b), for long run duration (18 *hrs*).

Suspended sediments release for the long duration was used to calculate the sediment release and trap efficiencies, as shown in Figure 5.8(a) and (b), respectively. A general increasing tendency represented by parabolic curve for sediments release can be seen in Figure 5.8(a). The sediments release in the beginning of the test is low due to the bed formation and mixing exchange between internal circulations. Then it gradually increases. Due to the flow deflection to the right side, ripples start to form on the right side and SSC starts to decrease as shown in Figure 5.7(a).

After 3.0 *hrs*, the flow pattern starts to change the direction from right to the center (see Fig. 5.7(a)), and new ripples are formed at the center. The SSC decreases compared to the first run. The presented curve has the same tendency as explained in Figure 5.7.

Continuous shallowing of a reservoir causes diminution in the area of active flow in the reservoir cross section and this process is followed by an increase in flow velocity through the length of the reservoir. Then the trap efficiency for the suspended load reaches zero as shown in Figure 5.8(b).

5.6 Contours of bed deposition and corresponding flow pattern

This section presents a comparison of the final bed depositions and the corresponding flow pattern, for geometries of test (T7, T8, T11, T13, T14 & T16), after 270 minutes. Experimental tests have been conducted systematically by varying width, length and removing corners with different shapes (hexagonal and lozenge).

The bed morphology for a reduced width of $B = 3.0$ m and 2.0 m (T7 & T8) have a uniform deposition rate over entire reservoir surface and symmetric ripple patterns. Flow field remains asymmetric with the reduced width. Moreover, sediment deposits are able to completely change the flow pattern.

By reducing the reservoir length (T11 & T13) the flow is stabilized with a stable symmetrical pattern. By increasing centerline depositions and suspended sediment concentration the left and right circulations along the centerline disappeared with less deposit at both sides.

The behavior is almost similar to a continuously growing instability observed in the reservoir with diamond geometry (T14). Asymmetric and switching flow behavior continues towards the downstream end of the reservoir, where the jet is forced to pass through the outlet channel.

Most of the sediments are deposited directly under the main jet flow trajectory. The sediment was concentrated on both right and left sides and very low in the center of the basin (T14). By cutting the four corners (T16), the flow became more stable, symmetric and has the same behavior as the reduced length reservoirs.

It can be concluded that the reservoir geometry influence the behavior of the large turbulence structures.

Further details of some selected results for clear water and sediment transport about the flow patterns, streamlines, sediment deposition contours, transversal and longitudinal bed deposition thickness sections, and suspended sediment concentrations for all geometries each time steps, are shown in Appendix A.

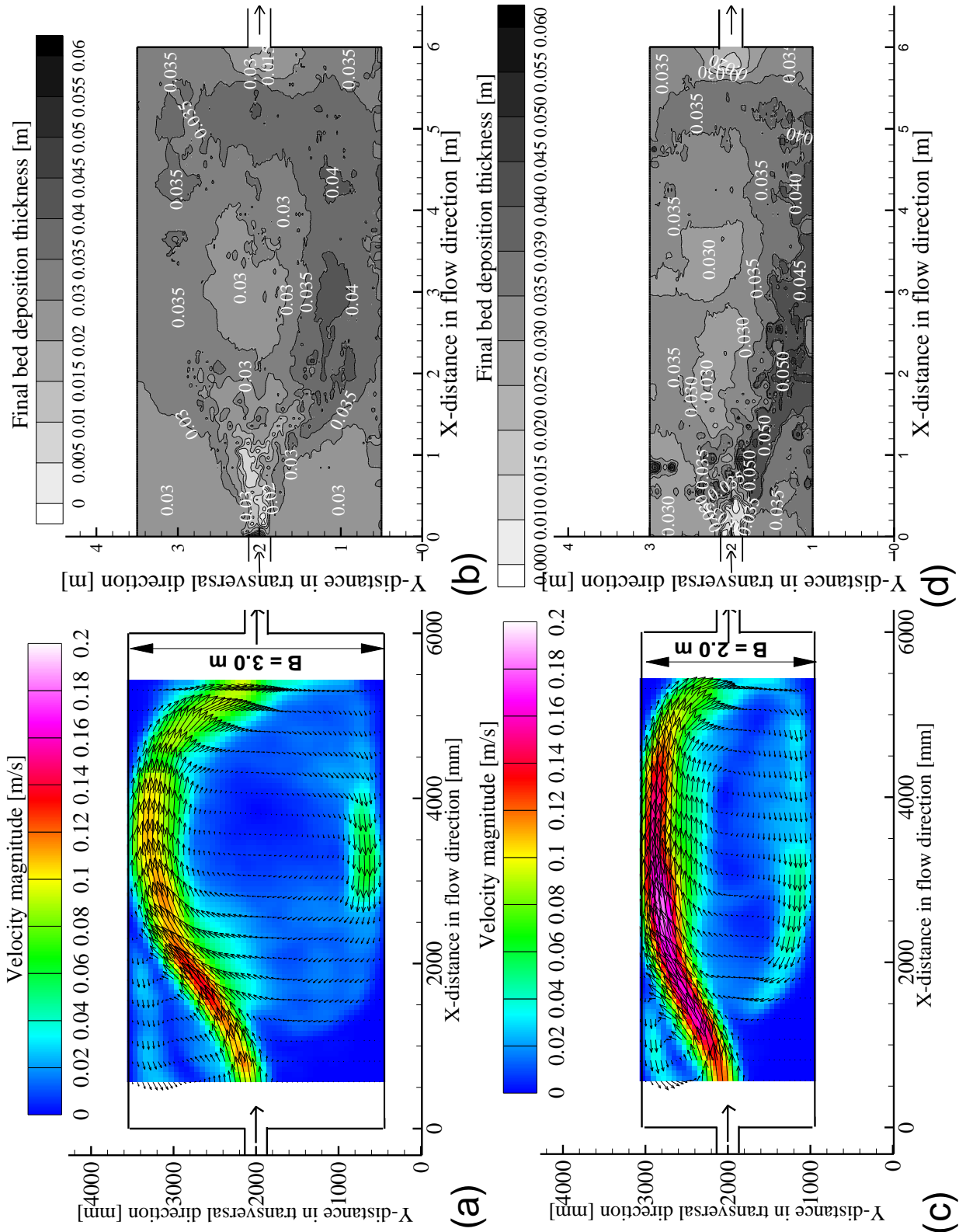


Figure 5.9: Average flow pattern with velocity vectors and bed topography contours at 270 min, for reduced reservoir width B (a) 3.0 m (T7), and (b) 2.0 m (T8).

5.6.1 Effect of reservoir width

To investigate the influence of the rectangular shallow reservoir width on the flow pattern and the associated bed deposition, two different test of $B = 3.0$, and 2.0 m, (T7, and T8), were conducted. The flow field and the bed topography contours are depicted in Figure 5.9. The figure shows a comparison between the two reduced widths at 270 minutes.

During the first hour of the tests, the observed flow pattern was deviated to the right side. But, after two hours the asymmetric jet was flipped from right side to the left one as shown in Figure 5.9(a).

The footprint of these previous stages of the flow patterns are clearly visible in Figure 5.9(b). As a results of the asymmetry flip flop from one side to the other, bed forms persisted throughout the alternately deflected jet. The observed pattern of the bed topography for T7 after 270 minutes is symmetric, as shown in Figure 5.9(b).

A significant differences in reservoir sedimentation occur as a result of reduction in reservoir width. However, the location of the deposited sediment did not vary between the two width (Fig. 5.9(b), and (d)), and furthermore, the location of the sediment deposits are related to the flow field that developed in the basin (Fig. 5.9(a), and (c)).

An asymmetric flow pattern has been observed for all reduced width geometries (T7, and T8). Hence, the reservoir width did not affect the asymmetric separation of the deflected jet.

However, the size of center and the upstream corner eddies were in accordance with the width. By reducing the reservoir width, the decelerating of the deviated jet is reduced. The deviated jet for T8 of width $B = 2.0$ m, is accelerating as shown in Figure 5.9(a). Final deposition patterns were affected by the reservoir width, with more symmetric and uniform distributions on the entire surface, and concentrated deposits on both sides with.

5.6.2 Effect of reservoir length

This section presents a comparison between the two reduced reservoir length for T11 and T13, of length $L = 5$, and 3 m, respectively. The average flow field and the corresponding bed morphology contours after 270 minutes for the reduced reservoir length are shown in Figure 5.10. In the first ten minutes for shorter reservoir lengths with suspended sediment entrainment, the flow is symmetric with one circulation cell on each side of the centerline.

After a short period of 20-40 minutes (according to the basin length), the flow in the reservoir does not show the two circulation pattern. The flow mixture into the reduced reservoir length hinders the two horizontal circulation cell, causing it to disappear after 60 minutes.

The physical details of such flow will be explained in Section 5.9. As seen from the flow patterns plotted for T11 and T13, the flow shown in Figures 5.10(a) and (c) is accelerated along the centerline with no separation or reattachment.

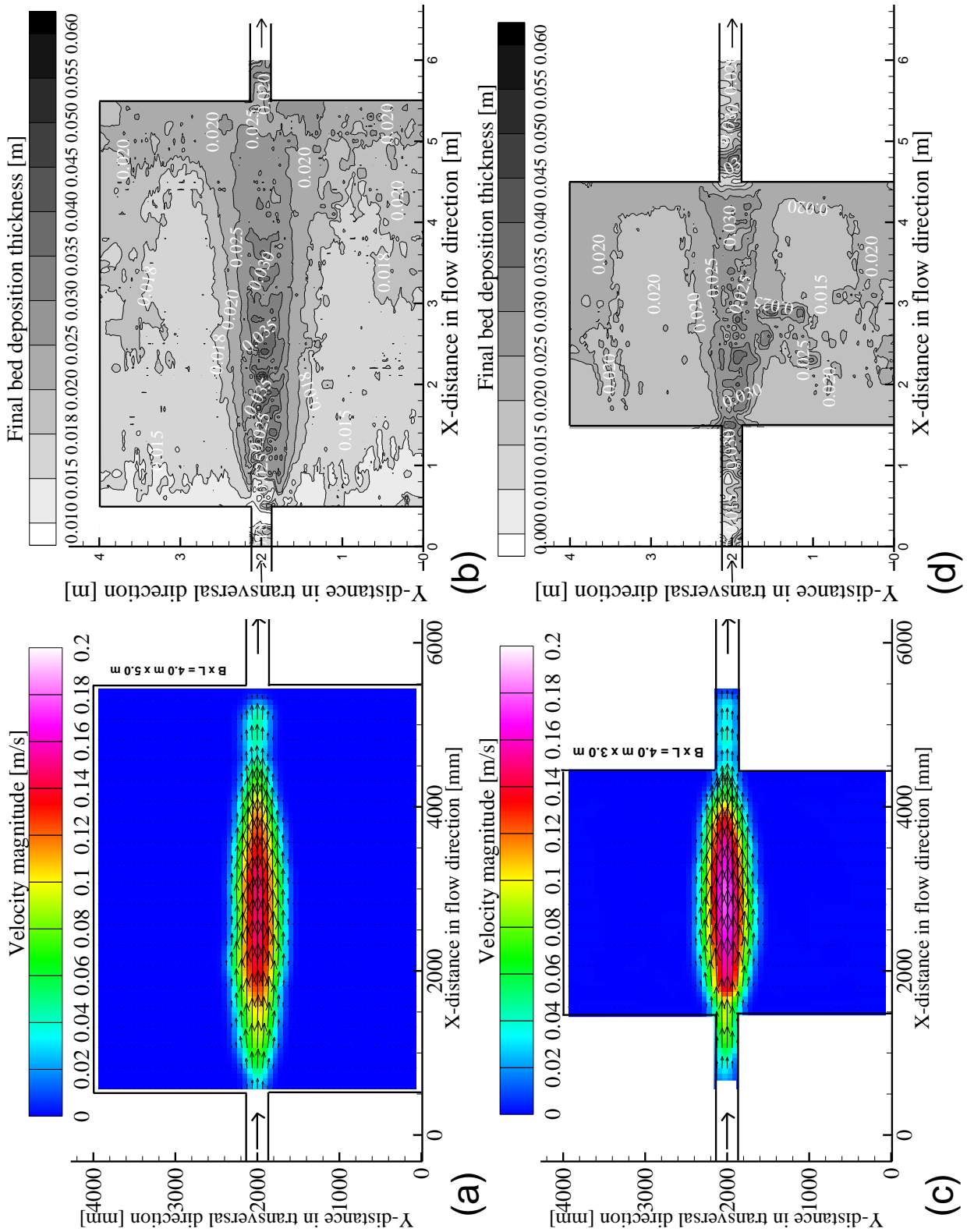


Figure 5.10: Average flow pattern with velocity vectors and bed topography contours at 270 min, for reservoir width length L (a) 5.0 m (T11), and (b) 3.0 m (T13).

The highest flow velocities arose from the inlet jet as it passed straight through the reservoir to the outlet. Figures 5.10(b), and (d) shows a high sediment deposition in the center under the jet trajectory and low deposition near the walls under the reversed jet towards the inlet direction. Revealed clearly by these figures is deposition occurs in the inlet and outlet channels as well. In both the experiments (T11&T13) ripples formed after about 180 minutes.

In the first experiment ripples spread initially along the centerline and near downstream side walls (Fig. 5.10(b)), while in the second they initially concentrated in the middle reach (Fig. 5.10(d)). Note that in the experiment T11 there is a smoothly distributions in the transverse directions from the center to both side wall.

The ripples formations stopped 0.5 m from the outlet in experiment T11, while a remarkable features formed on the whole basin length even in the approach channels of T13. The length of the reservoir plays a critical role in determining the jet flow type and the associated bed deposition pattern. The interested reader is referred to the Appendix A in the CD for further details of the flow patterns, streamlines every thirty minutes.

5.6.3 Effect of semi angle of reservoir entrance

To investigate the general features and differences amongst the various types of expansion semi angle, flow patterns and bed topography after 270 minutes at each of the semi angle $\theta^* = 32^\circ$, and 51.34° are presented in Figures 5.11(a, b), and (c, d), respectively. In the case of the $\theta^* = 32^\circ$ for T14, the flow pattern is asymmetric and the jet asymmetry can flip flop from one side to other as depicted in Figure 5.11(a).

For the later angle, the flow remains asymmetric throughout all the period of its development, during which one main recirculation in the center is exist. After 270 minutes the large circulation was vanishing and only the deviated jet is exist as shown in Figure 5.11(a).

Except for a short period of 30 minutes(during the third run of T14), the flow was meandering along the centerline. All of the flow patterns and stream lines concern T14 are shown in Appendix A on the CD. These observations are in agreement with the pronounced bed form depositions located at right, center, and left evident in Figure 5.11(b).

Considering both Figures 5.11(a) and (b) as a whole, it is evident that the lozenge geometry with $\theta^* = 32^\circ$ is less stable jet comparing to all geometries. This causes the changing from asymmetric left to right to an symmetric flow.

Moreover, the final bed deposition is distributed every where with a final symmetric topography as shown in Figure 5.11(b). The deposition is less in the center region of large circulation cell. while, near the outlet the deposition located at the downstream region was high with a uniform distributions. For the entrance semi angle $\theta^* > 32^\circ$ the flow changes from an asymmetric structures with one main recirculation cell in the center to an symmetric one where the jet is straight with one long recirculation on each side.

Figures 5.11(c) show the flow pattern with velocity magnitudes of the hexagonal geometry with a semi expansion angle of $\theta^* = 51.34^\circ$. The flow was symmetric during the first with two recirculation cells on two sides along the centerline. During the third run the two horizontal circulations were hindered. The flow field was able to mobilize sediments both as bed load and as suspended load throughout the basin length.

A ripple formation was formed along the centerline with less sediment under the circulation cells on both side as shown in Figure 5.11(d). It is interesting to note that, in spite of the horizontal recirculations on both sides were hindered; the sediment depositions still increasing.

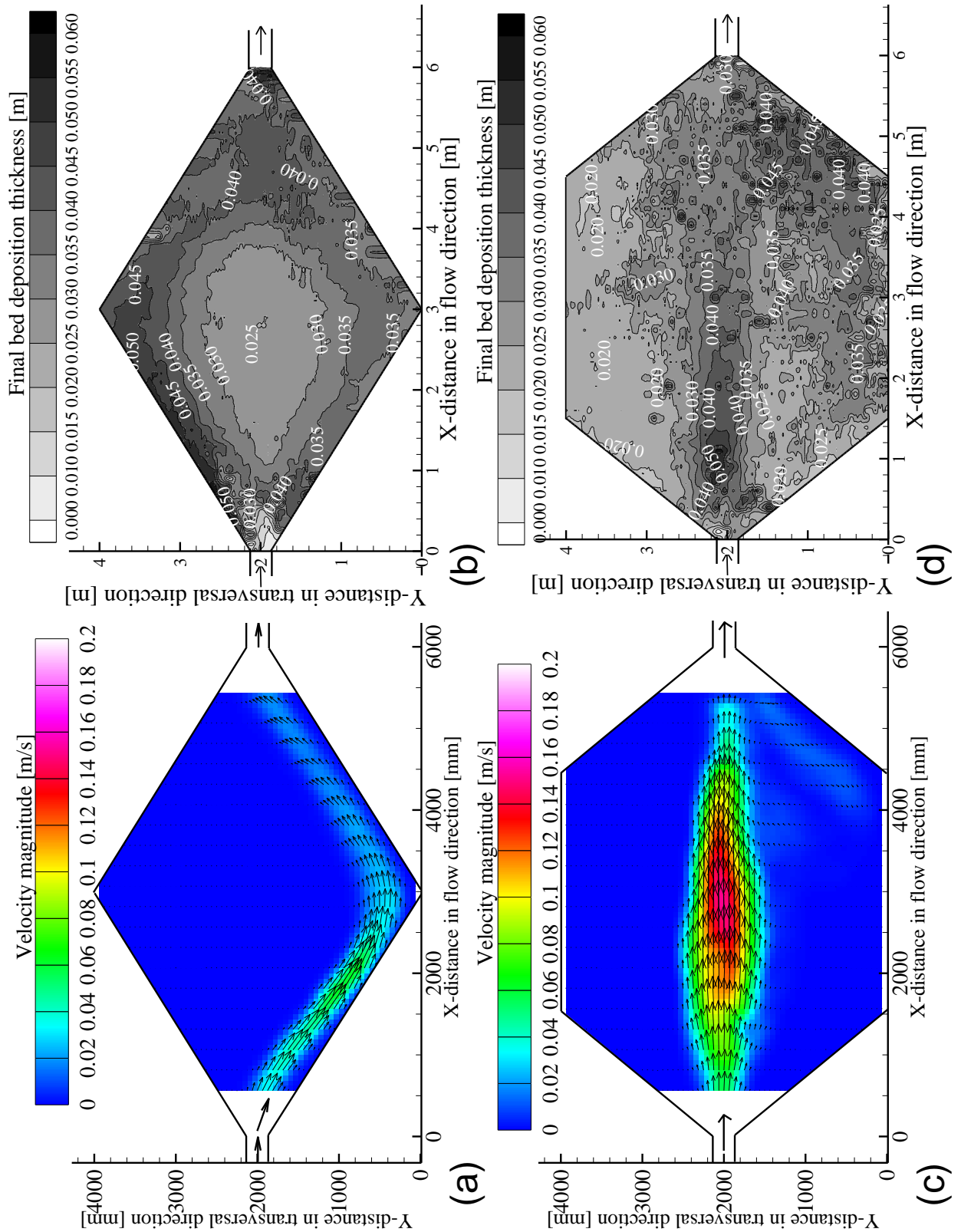


Figure 5.11: Average flow pattern with velocity vectors and bed topography contours at 270 min, for the reduced semi entrance angle θ^* (a) Lozenge geometry with $\theta^* = 32^\circ$ (T14), and (b) Hexagonal geometry with $\theta^* = 51.34^\circ$ (T16).

5.7 Cross and longitudinal sections of deposition thickness

Referring to experiments T7 and T8, the major observation was that sediments were highly deposited in the right side part of the reservoir and scouring just after the inlet. This mechanism is associated with the asymmetric dominant character of the flow field in all the stages of the morphodynamic evolution process. The evolution of the cross-sectionally bed profiles are plotted in Figure 5.12 and the longitudinal axis with the origin located at the inlet of the channel.

Comparison between the bed profiles at 1.5, 3.0, and 4.5 hours for T7, and T8, located at the transversal section of $X_1 = 1.5$, $X_2 = 3.0$, and $X_3 = 4.5$ m, and a longitudinal section at the reservoir center, are shown in Figures 5.12(a), (b), (c), and (d), respectively.

The depositions are progressively increase in the downstream direction. The evolution process increasingly fast with speed of 0.66 cm/hrs, for both experiments T7, and T8. The final bottom profile was slightly concave in the middle where the circulation gyre and slightly convex at the right side and downstream where the jet trajectory.

In fact, the velocity magnitude is increasing by reducing reservoir width. As a result, a fairly deep scour hole develops in the bed profile near the inlet as shown in Figure 5.12(a). Due to the separation region before the outlet channel, deposits are decreasing with a concave shape. To clarify the movement mechanisms of the sediments and the relation with suspended sediments several analysis will be performed. The apparent noise displayed by such profiles is associated with the presence of bed forms.

The evolution of the bed profile in the experiment T8 was somewhat similar in many respects to that observed in the experiment T7, even though it displayed a more uniform deposition in both sides of the basin and the fluctuations of the longitudinal bed profile had longer wavelength as shown in Figure 5.12(d).

The evolution of bed at 1.5, 3.0, and 4.5 hours in the lateral direction at the middle cross section of $X = 3.0$ m, for the reduced lengths experiments T11, and T13 of $L = 5.0$, and 3.0 m, respectively, are shown in Figure 5.13(a). Figure 5.13(b) shows the bed profile in the longitudinal direction at the centerline.

Bed depositions are almost uniform for T8 (width = 2 m), while T7 (width = 3 m) has wavy bed forms along the first 1.5 m and uniform different bed forms further downstream, until 0.5 m before the outlet.

The bed thickness observed for T7 is almost three times higher than for T8. Figure 5.13(a) shows clearly the axi-symmetric distribution of the bed in the transversal direction where the point of maximum exist at the centerline. This observation agrees with the flow pattern results, where the jet is straight with one eddy on each side.

It can be seen that the bed deformation near the wall sides is almost uniform except

for the profiles at 1.5 *hrs*. As a result, the variation rate of bed deformation represented by the longitudinal bed slope is very high at the early stages of flow as can be seen in Figure 5.13(b).

Proceeding with time, this variation becomes slow due to the counteracting effect of the jet flow and the formation of a submerged channel under the centerline which increase in the lateral bed slopes towards the wall.

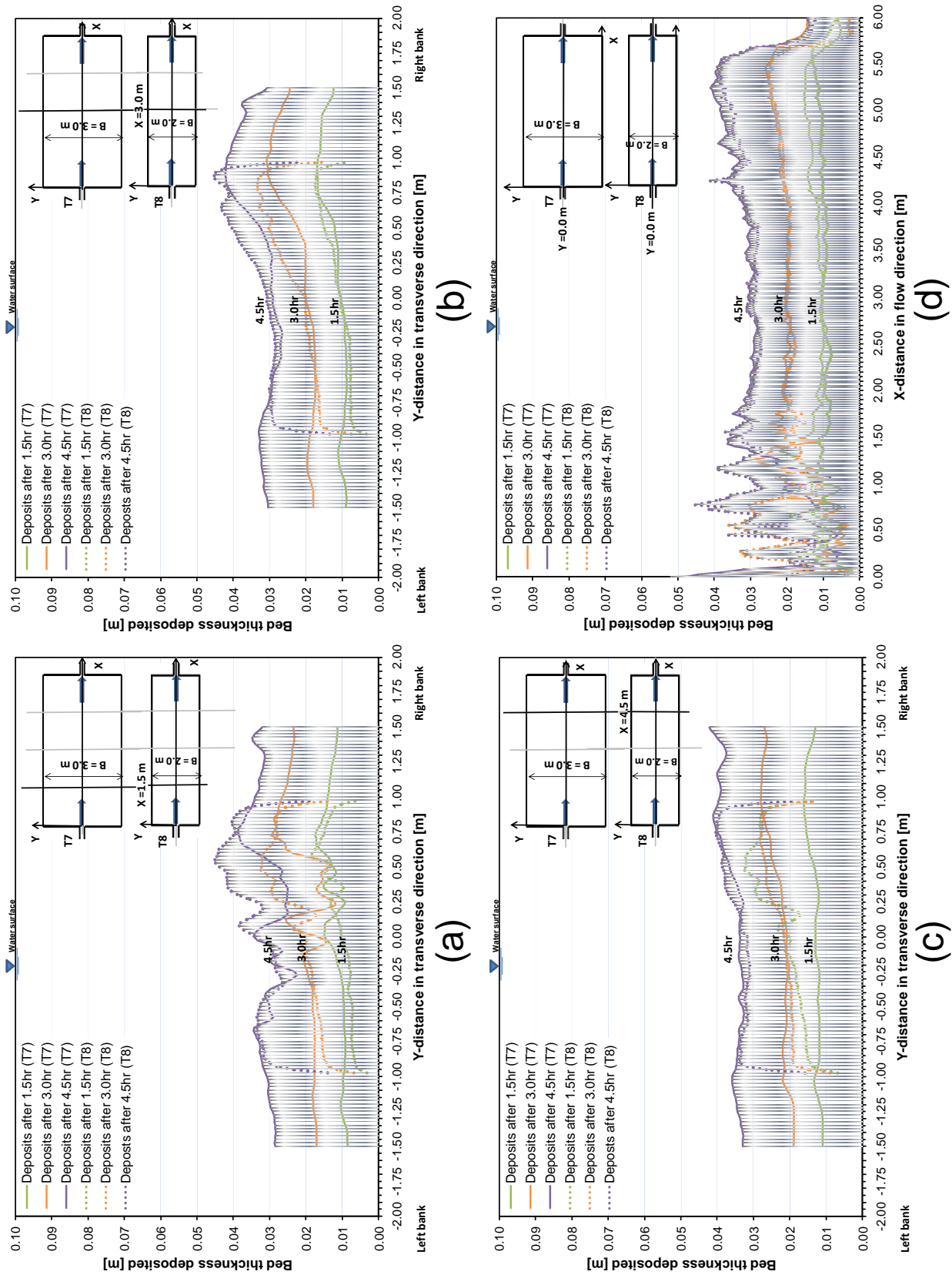


Figure 5.12: Comparison of evolution of the bed profiles between the reduced reservoir widths of $B = 3.0$ m (T7), and 2.0 m (T8) at 1.5, 3.0, and 4.5 hours for (a) cross section at $X_1 = 1.5$ m, (b) cross section at $X_2 = 3.0$ m, (c) cross section at $X_3 = 4.5$ m, and (d) longitudinal section at the centerline of the reservoir.

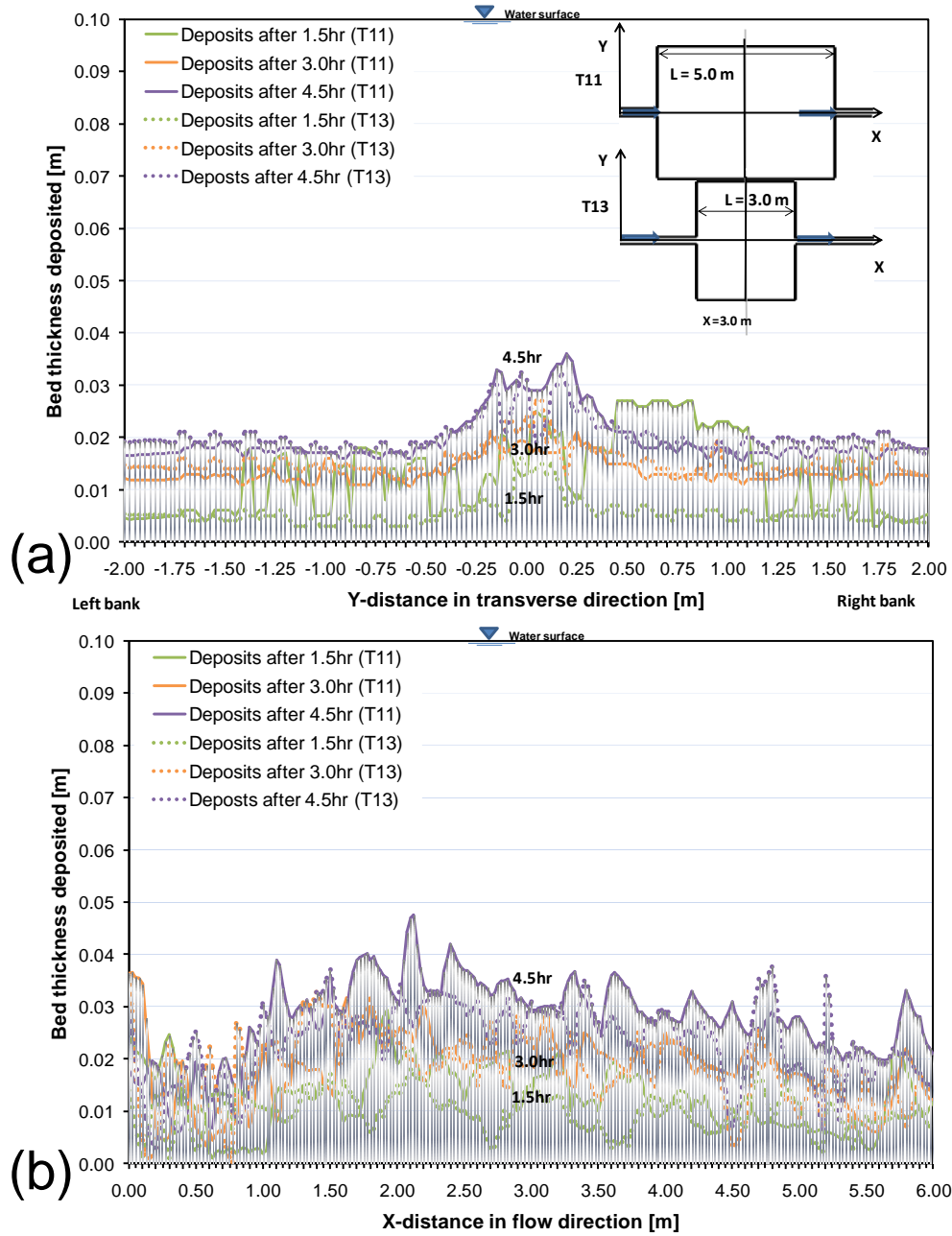


Figure 5.13: Comparison of evolution of the bed profiles between the reduced reservoir lengths of $L = 5.0$ m (T11), and 3.0 m (T13) at 1.5, 3.0, and 4.5 hrs for (a) cross section at $X_2 = 3.0$ m from the main inlet, and (b) longitudinal section at the centerline of the reservoir.

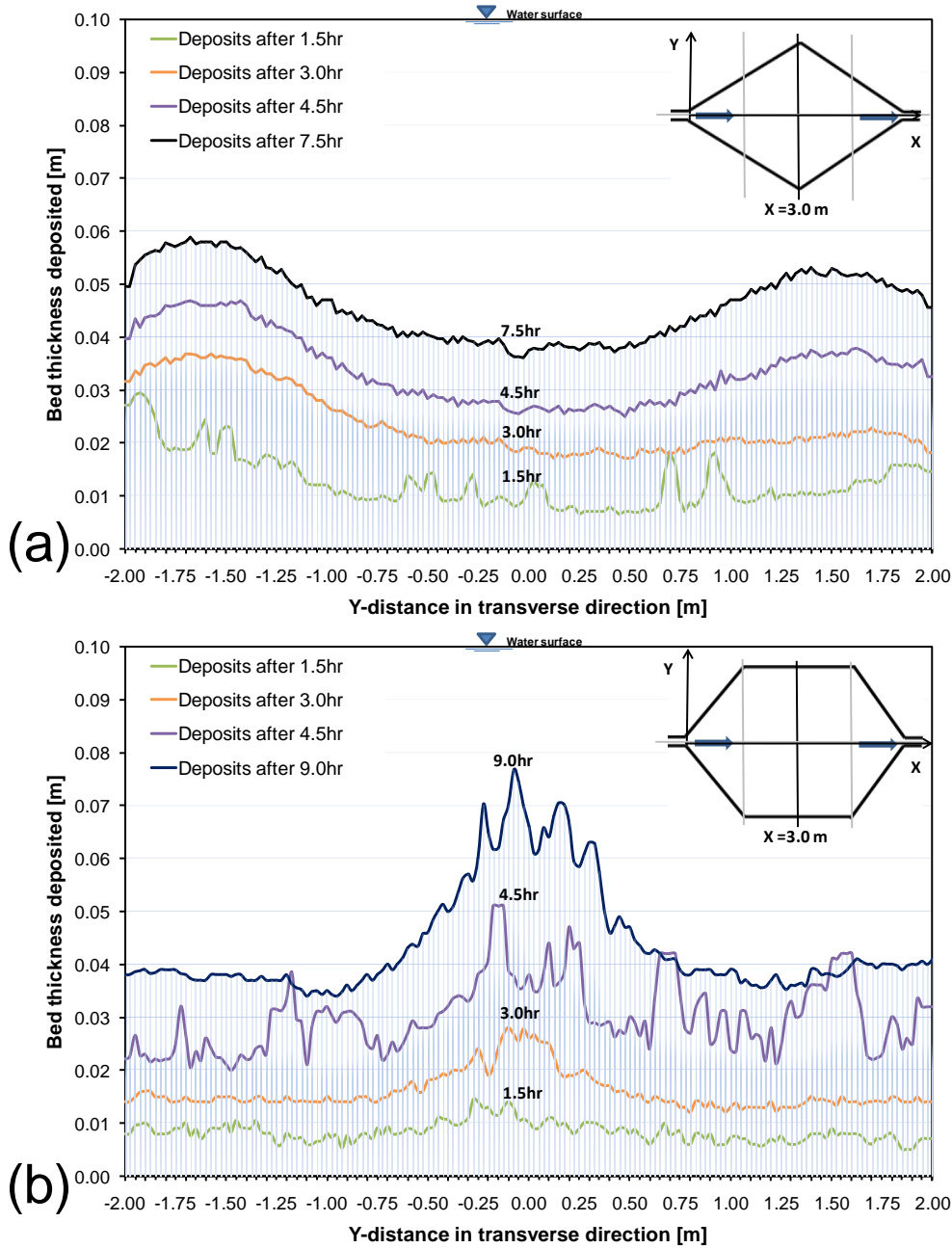


Figure 5.14: Evolution of the transversal bed profiles for the lozenge and the hexagonal geometries at the middle cross section $X_2 = 3.0 \text{ m}$.

Figure 5.14(a) shows the transversal variations of bed topography with time at 1.5, 3.0, 4.5, and 7.5 hours located at the middle cross section $X = 3.0 \text{ m}$, for the lozenge geometry T14. The deposition rate is constant during all stages and is about 0.6 cm/hour .

It can be seen that the magnitudes of deposition increase with time, having higher values near the two side walls and near the downstream end of the reservoir. At an early stage of evolution, the deposition process prevails in the left side. As the bed evolves, the flow pattern switches towards the right side. At the left and right sides the ripples are formed

and later on it formed on the center due to the meandering jet along the center.

Figure 5.14(b) shows the bed profile evolution at 1.5, 3.0, 4.5, 9.0 hours in the transversal direction direction at the middle $X = 3.0$ m, for hexagonal geometry T16. It can be seen that the bed deformation is almost similar to the reduced length experiments profiles (T11 and T13).

In the early stages flow was symmetric with two horizontal circulations on both sides. As a result, the bed profile at 1.5 hour almost uniform over the transversal section. As a result, the bed profile varies with time and reaches a new stable symmetric state with a submerged channel at the center as shown in Figures 5.14(b).

5.8 Suspended sediment concentrations

The shallow reservoir geometry has an effect on the sediment transport from the reservoir inlet to the outlet. A smaller geometry widths or shorter geometry lengths have a high flow velocity and, thus, a high transport sediment in suspension, both in terms of grain size and quantity.

The inlet and outlet instantaneous suspended sediment concentrations (SSC) measured every minutes and schematic sketch for the flow pattern during each periods are shown in Figures 5.15(a), (b), (c), (d), (e and f), and (g and h), for all tested geometry experiments T7, T8, T11, T13, T14, and T16, respectively. The SSC vary widely among geometries based on such factors as geometry shape factor, jet flow type /symmetric, asymmetric, or meandering jet), and bed form depositions. The interruptions points are clearly visible in Figure 5.15, due to the non-continuous of test procedure.

SSC associated with flow patterns. Because of the closed circuits, sediments inflow may rapidly change during the tests, but after controlling the supplied quantity of dry sediments according to online measurements; it stabilized around 3.0 g/l as shown in Figure 5.15.

In Figures 5.15(a), the sediments release in the beginning of the test is low due to the bed formation and mixing exchange between circulations. Then it gradually increases. For the curve showing the first period in Figures 5.15(a and b), SSC release increases during the first 18 minutes, flow needs that time to stabilize after entrainment into stagnant water or initial conditions. Due to the flow deflection to the right side, as shown in down sketch, ripples start to form on the right side; SSC starts to decrease as shown in Figures 5.15(a).

For the second period, SSC are almost constant due to the flow pattern located still at the right side and the formation of the ripples still increasing. But during the third period, the flow patterns start to change the direction from right to the left (see see the upper sketch), and new ripples are formed at the left side.

The SSC decreases compared to the other two periods. By comparing of SSC in the tow Figures 5.15(a and b), SSC for a narrow reservoir width of 2 m is higher than a reservoir

width of 3 m. The flow patterns need almost 18 minutes to stabilize after starting the tests. The suspended sediments affect considerably the flow patterns and dimensions of the turbulence structures.

5.8. Suspended sediment concentrations

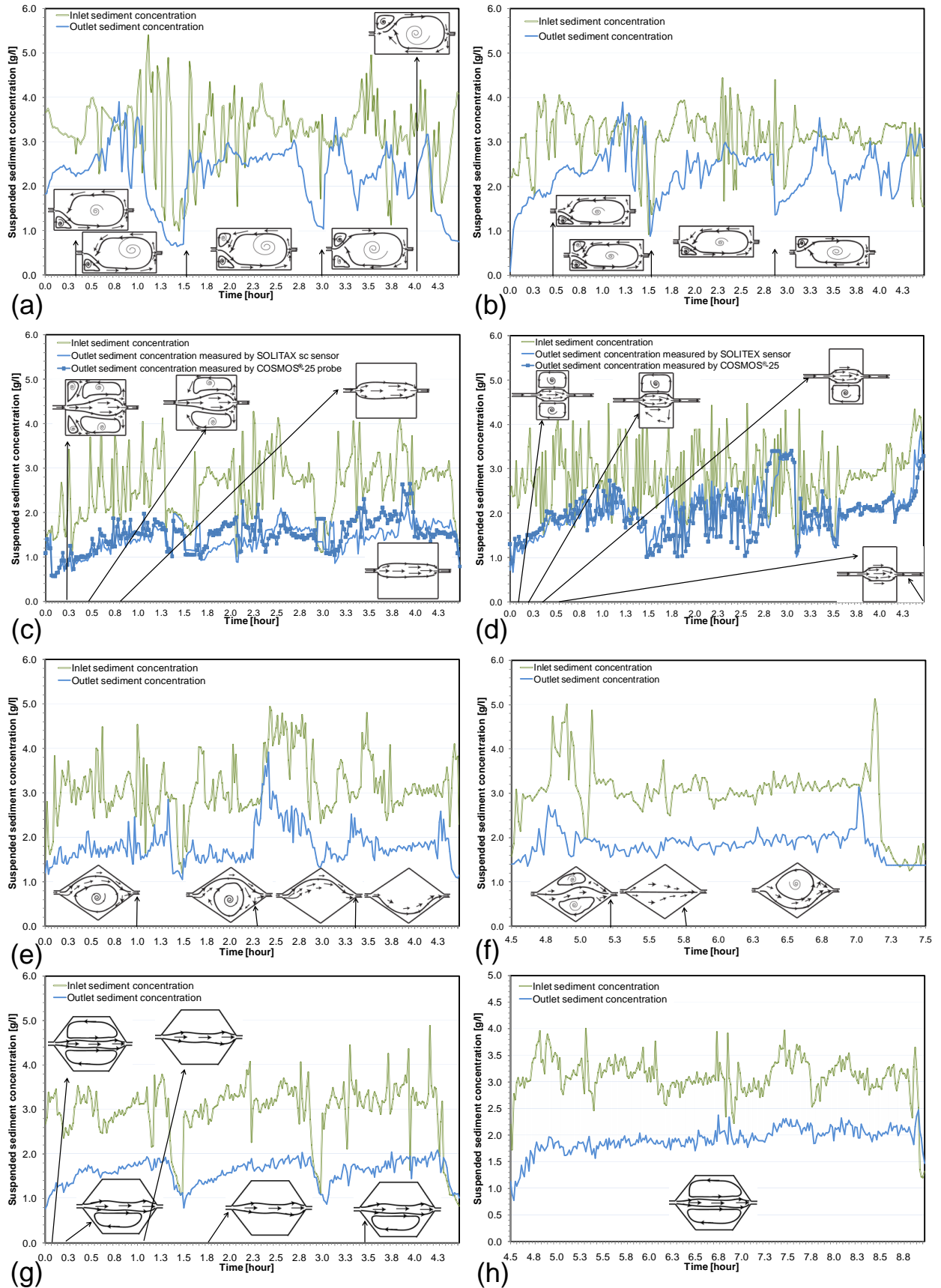


Figure 5.15: Evolution of SSC of various geometries (see also Appendix A)

5.9 Observed phenomena depending on basin geometry

In this section, the observed phenomena of the flow, suspended sediment, and bed topography behavior on a flat bed of various shallow basin geometries are described. The observed phenomena are intriguing. The presence of walnut shells particles moving over a flat bed modulates the flow behavior when compared to clear water flow with the same flow conditions.

In general, the movement of suspended sediment particles can be considered at least as important as the movement of bed load in the reservoir bed development process. The influence of sediment transport on the turbulence characteristics of the carrier fluid has been a subject of great interest for many years as explained in Chapter 2.

First, a description is presented of some observations of the flow during suspended sediment entrainment, followed by some observations and measured characteristics of streamlines, cross sectional velocity, and the corresponding bed deposition. Once uniform flow had been established with the basin, sediment mixture feed was begun as shown in Figure 5.16(a).

Floating white particles were distributed, before sediment feed, on the entire surface of the basin for LSPIV visualization. The evolution of suspended sediment and surface particles in a reduced length shallow reservoir of T13 is shown in Figure 5.16.

The clear water flow in the reduced length reservoir of $L = 3.0$, was symmetric with straight central jet associated with couple eddies on each side as shown in Section 3.10. By entering the sediment particles the white floating particles migrates towards the side walls. As can be observed on the photographs (taken in the reservoir inlet) presented in Figures 5.16(a and b), the flow in the inlet and the basin is turbulent, and vigorous mixing occurs. Almost all floating white particles are swept away from the entering jet and they grouped beside the right and left walls.

Although the details of the flow induced by sediment mixture jet flow is not yet fully understood, fluid is swept away in transversal direction, as shown in Figure 5.16(b).

During and shortly after the injection, an approximately cone-shaped jet forms and evolves into the clear water patch and moves in the downstream direction. During the initial stage (1.00 minutes), the horizontal motions are substantially suppressed and the flow soon becomes laminar. In Figure 5.16(a), a nose jet propagates with a constant average speed and grows rapidly until the buoyancy forces arrest its vertical growth.

At an early stage of evolution, an interesting observation made during the flow of sediment mixture jet puffs into the clear water is the formation of vertical structure moving sediment particles up while the coupled horizontal eddies are being arrested by the sediment stratification.

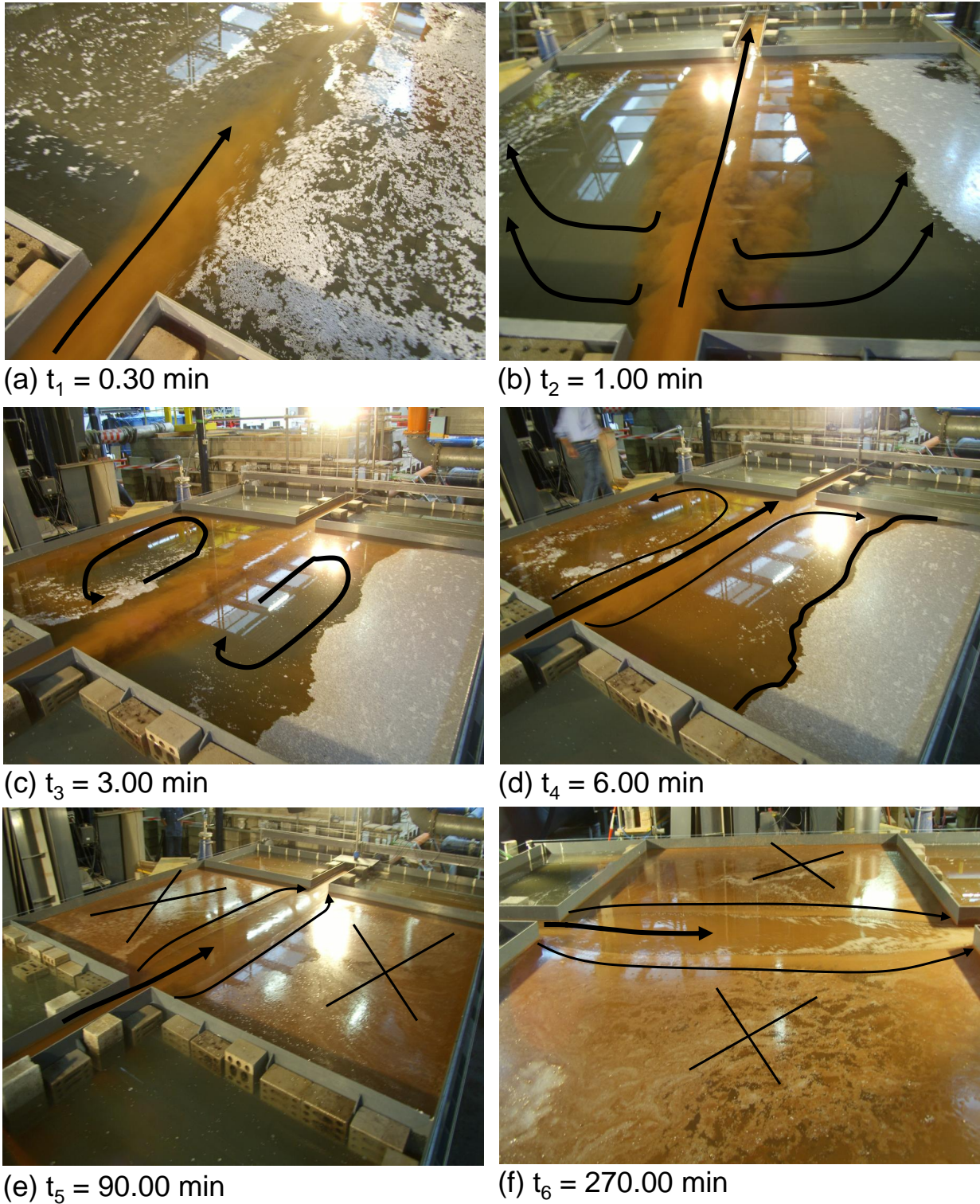


Figure 5.16: Photographs showing the evolution of suspended sediment and floating white particles flow into the reduced length reservoir T13 (length, $L = 3.0$ m, and width, $B = 4.0$), $h = 0.20$ m, $C = 3.0$ g/l, and $Q = 7.0$ l/s.

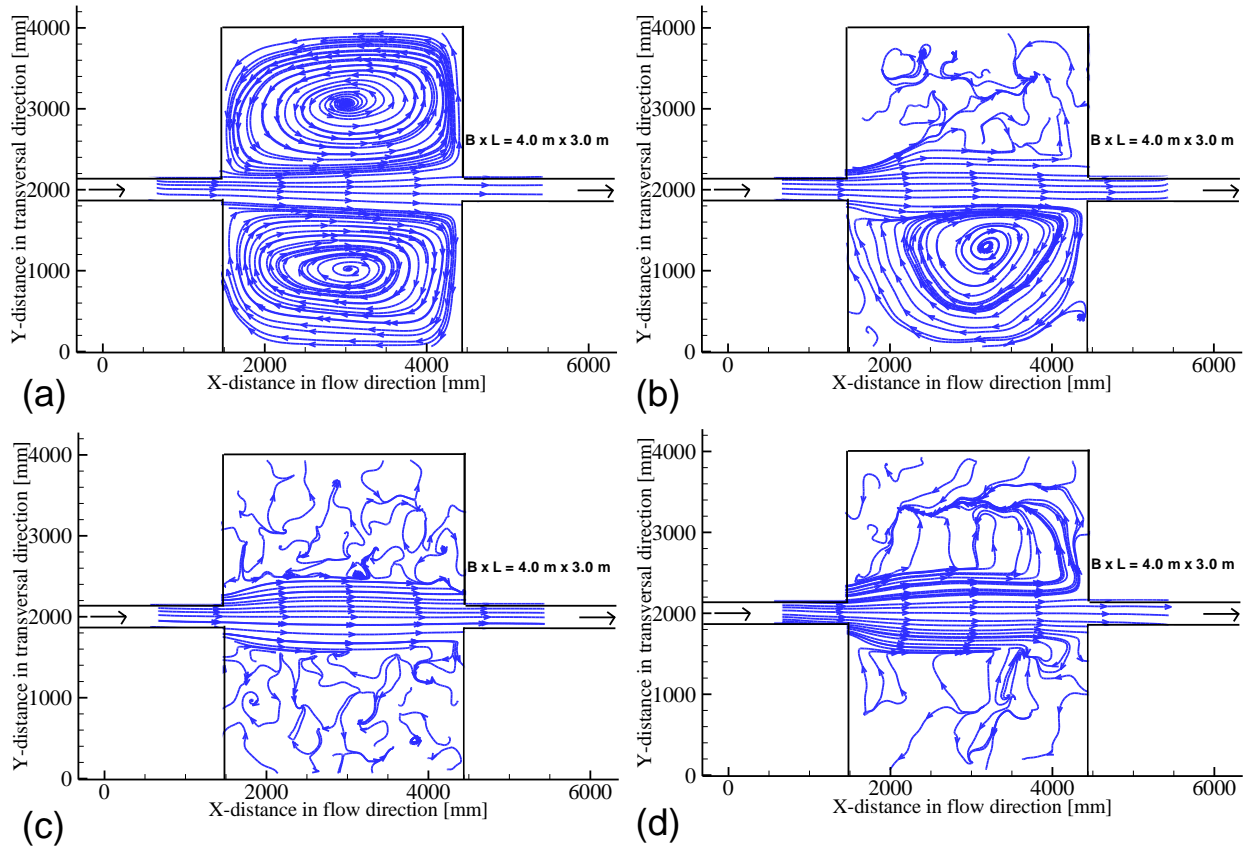


Figure 5.17: The evolution of the streamlines plots for experiment T13 at different time (a) 0.0 (clear water phase), (b) 9.0 min, (c) 90 min, & (d) 270 min.

The sediment particles spreading from up to down and moves near the bottom to up again and subsequent rapid growth with a cone shaped structure protruding into the fluid as shown in Figure 5.16(b). The fluid lost from the sediment spreading is replenished by transversal return currents from bottom to top. The jet width is progressively increasing in downstream direction. The jet seems to be bigger and more outstretched for the bottom layer than the surface in the basin. The sediment mixture jet is a symmetric, linear arrangement of three regions of essentially distributed SSC: an elliptical core with high SSC adjoined by two satellite with low SSC at its longer sides.

When the sediment mixture jet reaches the outlet walls, the jet impinging and the reattachment occurs. Thereafter, the mixture is horizontally propagating at both sides as shown in Figure 5.16(c). During six minutes, SSC propagates over the entire basin surface and on the whole vertical depth as shown in Figure 5.16(d). At later stages, suspended sediments mixed in a homogenous way on the vertical depth. Due to that, the qualitatively vertical observations were difficult. The earlier vortex structures emerges and moves slowly in a straight line along its axis of symmetry.

The evolution of the sediment mixture is continuously developed during 270.0 minutes.

After 90.0 minutes the jet motion is mainly straight and the surface white floating particle were stopped as shown in Figure 5.16(e). A similar behavior was observed at 270 min as shown in Figure 5.16(f).

In order to confirm these observations, surface velocity investigation have been carried out at different time. Figure 5.17(a) shows streamlines in clear water phase. The main features of these streamlines are straight jet from the inlet towards the outlet, and one large eddy on each side of the jet. A sequence of streamlines with suspended sediment entrainment at 9, 90, 270 minutes are shown in Figures 5.17(a, b, c, & d), respectively. Initially in Figure 5.17(b), the jet still straight but the left side horizontal circulation was stopped. It can be observed that the horizontal surface circulations were stopped completely at the last two stages as shown in Figure 5.17(c, & d).

Figure 5.18(a) show the spanwise longitudinal velocity distribution located at the middle of the basin with clear water and sediment phases. The evolution of the bed topography profiles after 1.5, 3.0, 4.5 hours of sediment entrainment is clearly visible in Figure 5.18(b).

The mean axial velocity profiles of Figure 5.18(a) are all symmetric with equal circulation regions on left and right for clear water phase. During the initial growth, the turbulent motions are dominated by the inertia forces. During the sediment evolution, the horizontal left recirculation was arrested and the right circulation velocity is reduced.

Generally speaking, the flow in the sediment state shows alternately accelerating and decelerating patterns with time at the centerline. At later stages, the surface horizontal circulations were suppressed, but sediment deposits on both side still increasing with time as shown in Figure 5.18(b).

Moreover, high sediment deposition and concentration were formed at the center while the axial mean velocities are high. Sediment deposition is increasing near the side walls although the horizontal surface eddies were suppressed. In order to justify these observations, an interpretation taking into consideration the following two important driving mechanisms is required: the cross-stream and streamwise components of sediment transport.

The cross-stream sediment transport is produced due to the overturning motions or the secondary currents. This circulation moves the sediments from the center of the basin to the wall sides in the lateral direction. This process occurs rapidly at the early stage of bed evolution and then slows down the deposition rate, as can be seen in Figure 5.18(b).

Figures 5.19 and 5.20 present the interaction of flow structures with bed topography for the reference geometry experiment T1 ($B = 4.0$ m & $L = 6.0$ m). The figures help to understand the evolution of jet flow behaviors and types when they reach the topography normally, from deep to shallow water depth (due to deposition variations)).

The reference experiment provide a physical evidence of typical interactions of flow strictures with bed topography. Figures 5.19(a, b, c, & d) show the evolution of streamlines over bed topography at time 0.15, 1.50, 3.00, and 4.50 hours, respectively. Figure 5.20(a) presents a comparison of the mean streamwise velocity u for clear water phase and with

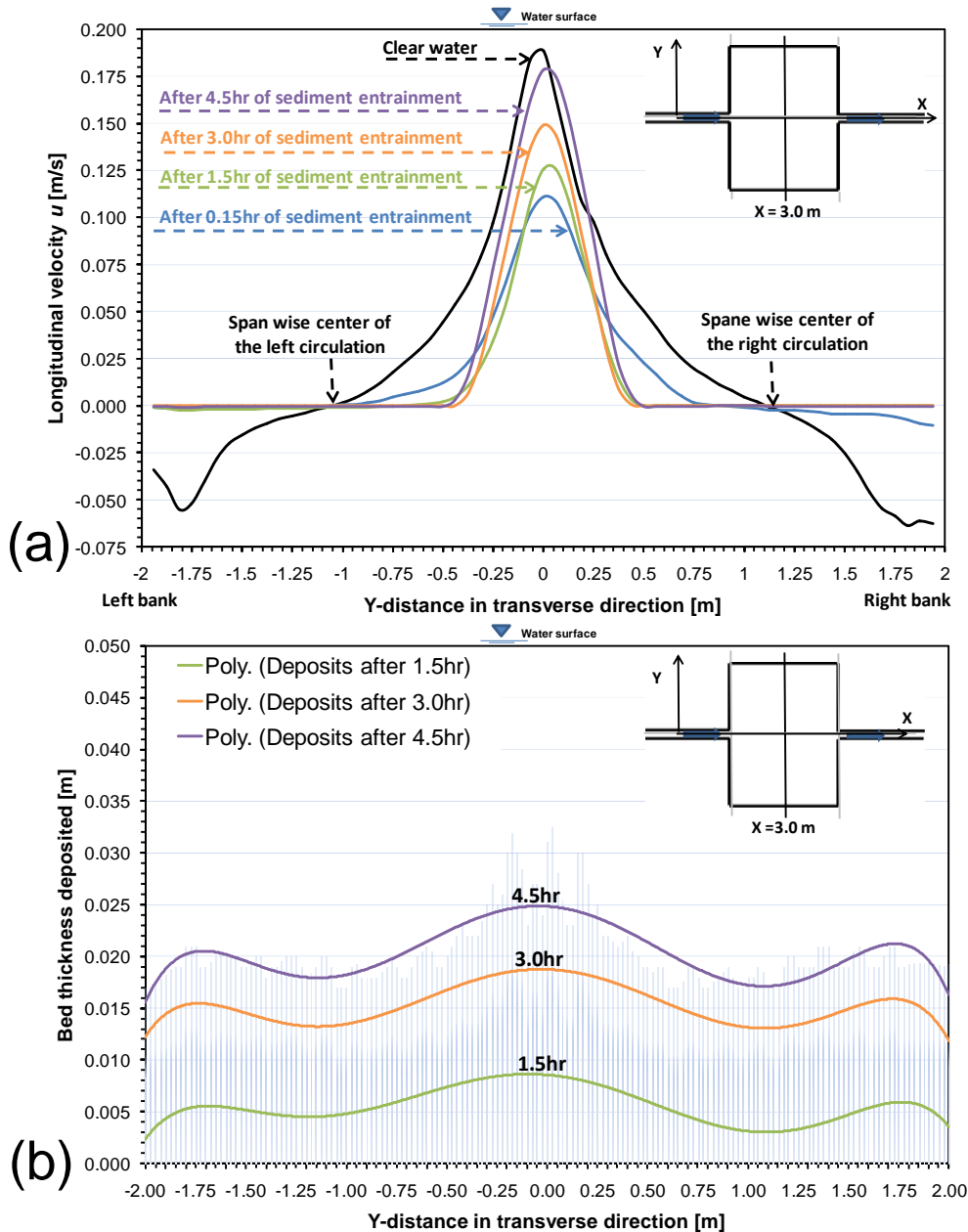


Figure 5.18: Comparison of, (a) streamwise velocity profiles and, (b) Bed topography, for T13 at the middle basin cross section

sediment at different time 0.15, 1.50, 3.00, and 4.5 hours.

Figure 5.20(a) shows the mean axial velocity distributions of the cross sectional streamwise velocity located at $X = 1.5$ m from the reservoir inlet. The evolution of the bed topography at the same cross section at time 1.5, 3.0, and 4.5 hrs, are shown in Figure 5.20(b).

For the case with less deposited thickness (thicknesses of about 0.05 times the flow depth), at $(t = 0.15 - 1.5$ hrs) see Figure 5.20(b), the jet crosses the topography with a deflected streamlines as shown in Figures 5.19(a, & b). This deflection has been clearly explained before in Section 5.1.

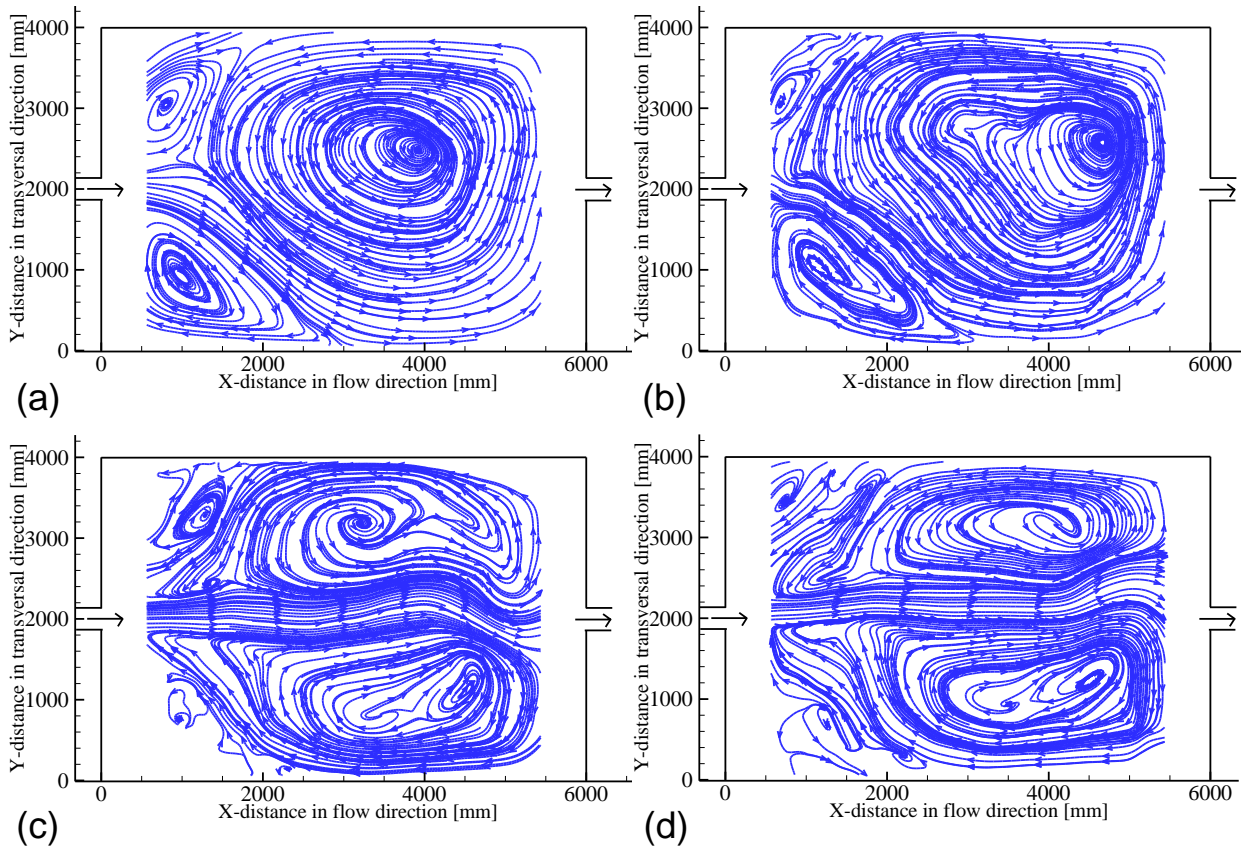


Figure 5.19: The evolution of the streamlines plots for experiment T1 at different time (a) 0.15 hrs, (b) 1.50 hrs, (c) 3.00 hrs, & (d) 4.5 hrs.

The streamwise velocity u profile is clearly asymmetric and the peak velocity is located away from the centerplane at $Y = 0.0$ as shown in Figure 5.20(a). On the right and left side at $Y = 1.75$ and -1.5 m of the basin there are recirculation regions with negative velocities. During period of 1.5 hrs the velocity profiles have the same right deflected profiles.

This indicates that the less deposited thickness was not able to affect on the flow structures. For the case with high deposited thickness (thicknesses of about 0.15 times the flow depth), in contrast, the jet is not able to cross the topography as shown in Figures 5.19(c & d).

The jet reaches the right side from the deep to shallow region. This new bed topography prevents the jet to move towards the shallow region (high deposited thickness). In this case, the jet is deviated to the centerline and forming two circulations on each side. The switching of the jet from right to the centerline direction are clearly visible in Figure 5.20(a).

Moreover, a velocity acceleration can be clearly observed. The results show that the interaction strongly depends on the deposition height and on the geometry. They are able to completely change the flow structures.

It must be noticed that this behavior was observed in several experiments. Of course,

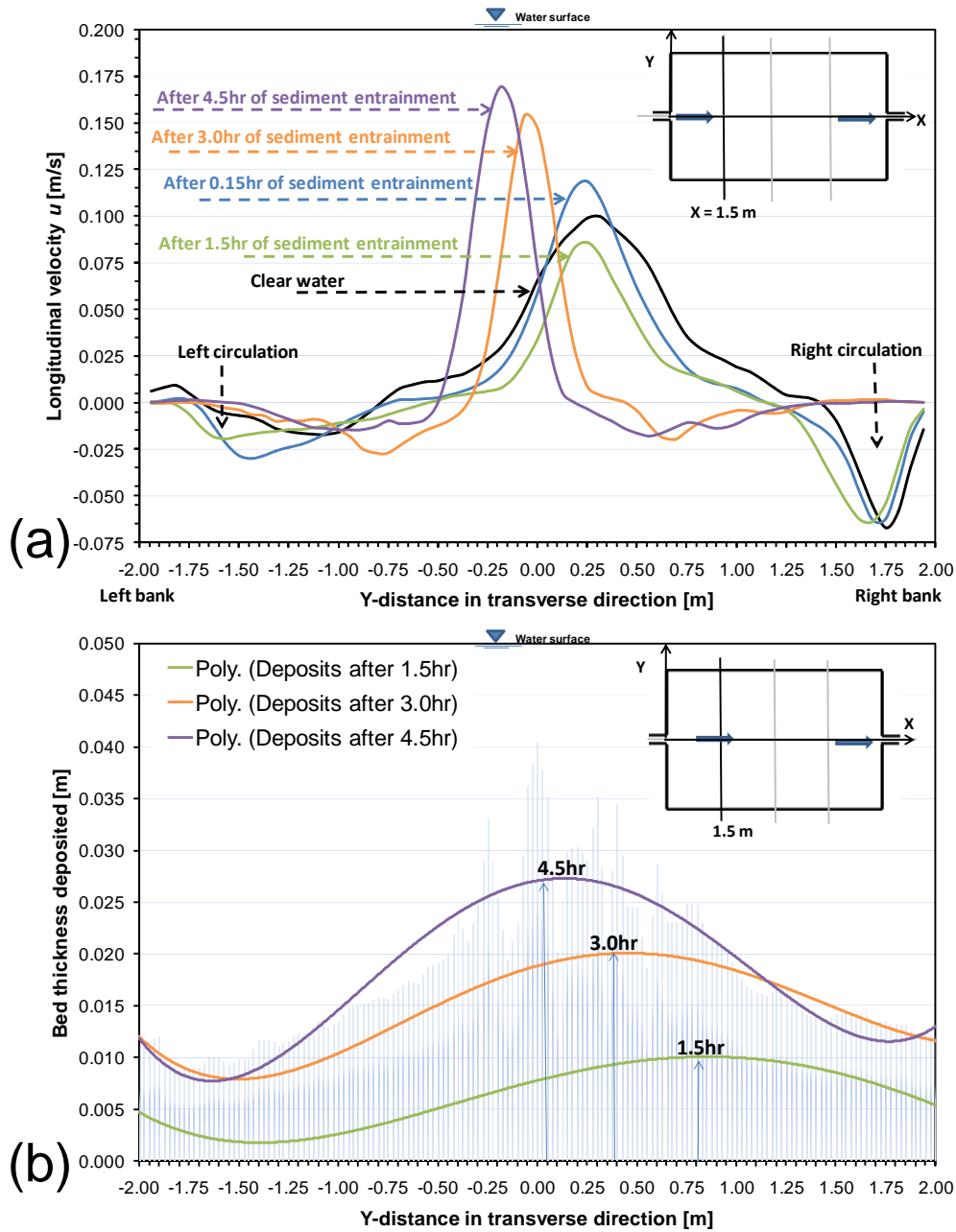


Figure 5.20: Comparison of, (a) streamwise velocity profiles and, (b) Bed topography, for T1 at cross section located at $X = 1.5$ m from the basin inlet.

the measured streamlines were not identical because the geometrical configurations imply inevitable variations on its effect and initial velocity. As example, similar results have been explained in Section 5.6.1 of the reduced width geometries.

Most of these processes are involved in the studied experiments with different geometry shapes. The results show that the flow behavior depends crucially on the deposits height. Another important result is the formation of a jet alongside the center, and the creation of new structure associated with the sediment deposits interaction.

5.9. Observed phenomena depending on basin geometry

When suspended sediment is added to the turbulent flow over a plane bed in shallow basin with various forms and transported as bed and suspended load the experiments revealed:

1. The large horizontal coherent structures are substantially suppressed compared to clear water flow with similar flow conditions. This is indicating that sediment loading is affecting the flow pattern and the horizontal momentum exchange.
2. Incorporating fine sediment transport increases the growth rate of the velocity.
3. Suspended sediment and deposition height stabilize the flow and change the flow pattern from asymmetric with clear water to symmetric with sediments.
4. Ripples and bed form deposits with a thickness reaching 15% of the water height are directly responsible for changes in flow structure.
5. High sediments concentrations and deposits form along the main jet while the high velocity occurs, due to the formation of a large mixing layer between the primary and secondary gyres.
6. Sediment deposits are increased while there is no horizontal surface motions.

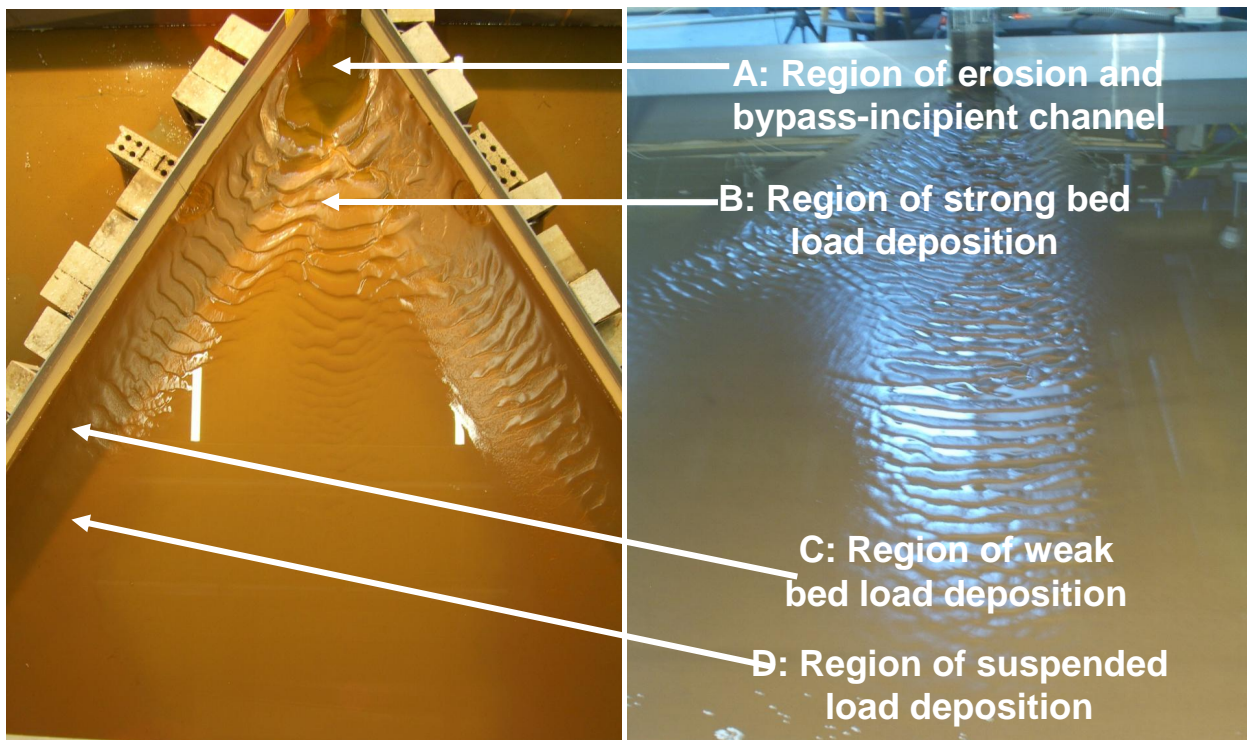


Figure 5.21: Photographes of final bed forms and classifications of bed forms.

5.10 Classification of bed forms and final bed deposit

A number of previous studies attempt to explain and classify the type of bed forms generated under given flow conditions. In the following paragraphs, bed form classifications and the final sediment deposit observed in the experimental shallow reservoir geometries are described. The bed forms observed in the experiments are identified according to the classification methods in literature.

The final bed forms of the experimental results can be classified conveniently as in Figure 5.21. Although geometrical configurations vary between jets types, (deflected, straight, and meandering) the bed forms characteristics are the same due to the universality of the jet deceleration and acceleration mechanism. Different bed form characteristic were observed by alter the ratio of across-stream and downstream velocity magnitude as will be explained in Section 5.11.

All of the features of the deposit of the turbulent jet flow in the shallow basin shown in Figure 5.21, can be explained by convolving the sediment flux process at the bed (erosion, bypass, suspension deposition) with the spatially decaying velocity field.

For the purpose of classification of bed forms the morphological regions (A, B, C, and D) for flow pattern over a walnut shells bed can be distinguished as follows (see also Figure 5.21):

- A) Region of erosion and bypass-incipient channel surrounded by levees due to flow separation and strong turbulence in the jet region has great potential for eroding the substrate creating a flute-like erosional scour.
- B) Region of strong bed load deposition after jet separation and before reattachment again.
- C) Region of weak bed load deposition after reattachment
- D) Region of pure suspension deposition region near the walls, circulation cells and near the outlet.

In this paragraph only bed forms of the region B (Fig. 5.21) are considered. The observed bed forms are identified and compared with different regime predictors and classification methods from literature. The length of developed bed forms (ripples) is denoted by Λ , the height is referred to as Δ and the ratio $\Delta/\Lambda = \delta$ is called bed form steepness. The analysis shows that for all experiments the dominant bed features are ripples.

Immediately after the start of all experiments with suspended sediments, ripples were observed to form throughout the whole length of all jet types (deflected or straight). Ripples length Λ observed in the experiments fell in the range (11-17 cm) while their height Δ attain values ranging about 1 cm.

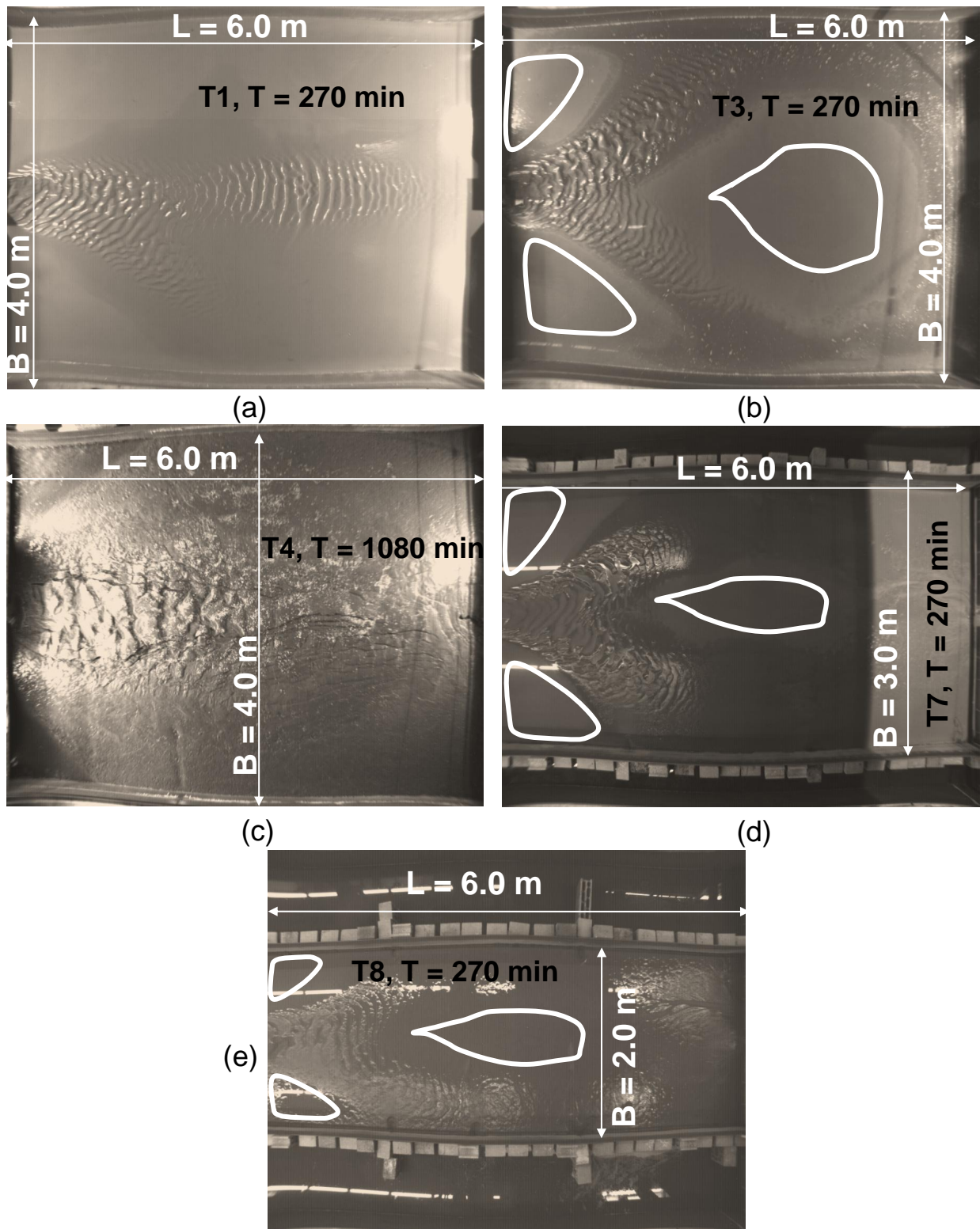


Figure 5.22: Morphological features for various geometry with asymmetric flow structures. Plane view pictures taken after the end of experiment.

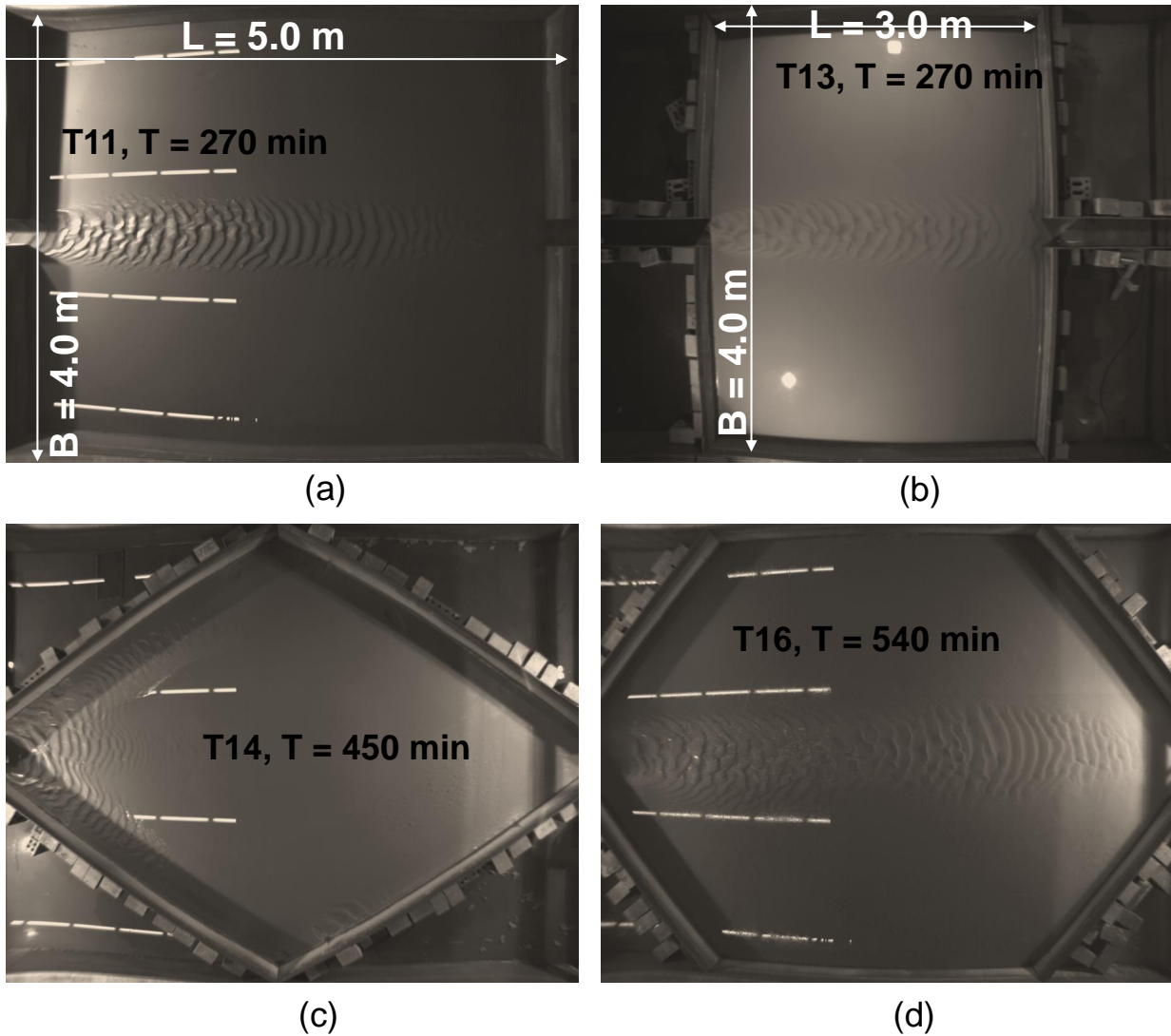


Figure 5.23: Morphological features for various geometry with symmetric flow structures. Plane view pictures taken after the end of experiment.

Migrating bed forms and their deposits are features containing helpful information regarding flow and deposition processes. A series of pictures for several laboratory geometries were taken in order to elucidate final bed forms and sediment transport processes over flat bed. In Figures 5.22 and 5.23 final bed morphology photographs for all experiments with asymmetric and symmetric flow structures are presented, respectively.

An interesting feature displayed by the shape of these bed forms was the presence of a distinct correlation between the orientation of their symmetry and asymmetry and the type the flow patterns.

It has to be noted that the bed evolution has a somewhat oscillating and unstable character: this feature arises from the complex interaction between the large-scale coherent structures generated by the shear layer issued from the sharp edges of the inlet and the

mobile bed. This is clarified by the sequence of topography fields measured at different times.

5.11 Efficiency of flushing

The initial storage of the experimental shallow reservoirs with different geometries have been reduced due to the sediment deposit causing a negative effects on the operation of the reservoir. Considering the importance of this issue, two modes of flushing operation for control of sedimentation were performed in several experiments. In order to investigate the effect of flushing and the effectiveness during of free flow and Drawdown flow, ten experiments have been conducted.

The final bed morphology formed previously for each geometry was used as the initial bed topography for the two modes of flushing. The entire experiments lasted for two days.

In the next subsection investigations of the flow pattern and the associated bed topography for free flow with normal water depth and drawdown flushing in various shallow reservoir geometries will be presented.

5.11.1 Free flow flushing flow and bed morphology

A detailed description of two representative experiments (T1 and T16) provide a general view of the asymmetric and symmetric jet flow experiments of free flow flushing. The final bed morphology obtained from both experiments were used as the initial topography for clear water test. Here, clear water without sediment was introduced into the basin to investigate the further bed evolution under those circumstances.

Figure 5.24 shows the flow velocity with vectors and the bed topography contours after two days of free flow flushing. In the free flow flushing the amount of the flushed sediments depend on many parameters such as water depth, discharge released, the size of the outlets, the geometry of the reservoir, the size and the kind of the deposited of the sediments in the reservoir.

The hydraulic conditions were kept constant during pressure flushing ($Q = 7.0l/s$ and $h = 0.20m$). Laboratory experiments were carried out to investigate the flushing processes during free flow flushing. Figures 5.24(a and c) present the flow patterns for two different geometry After stopping the flow, clear water (without sediment) has been injected into the basin to investigate the further evolution of the bed for free flow flushing.

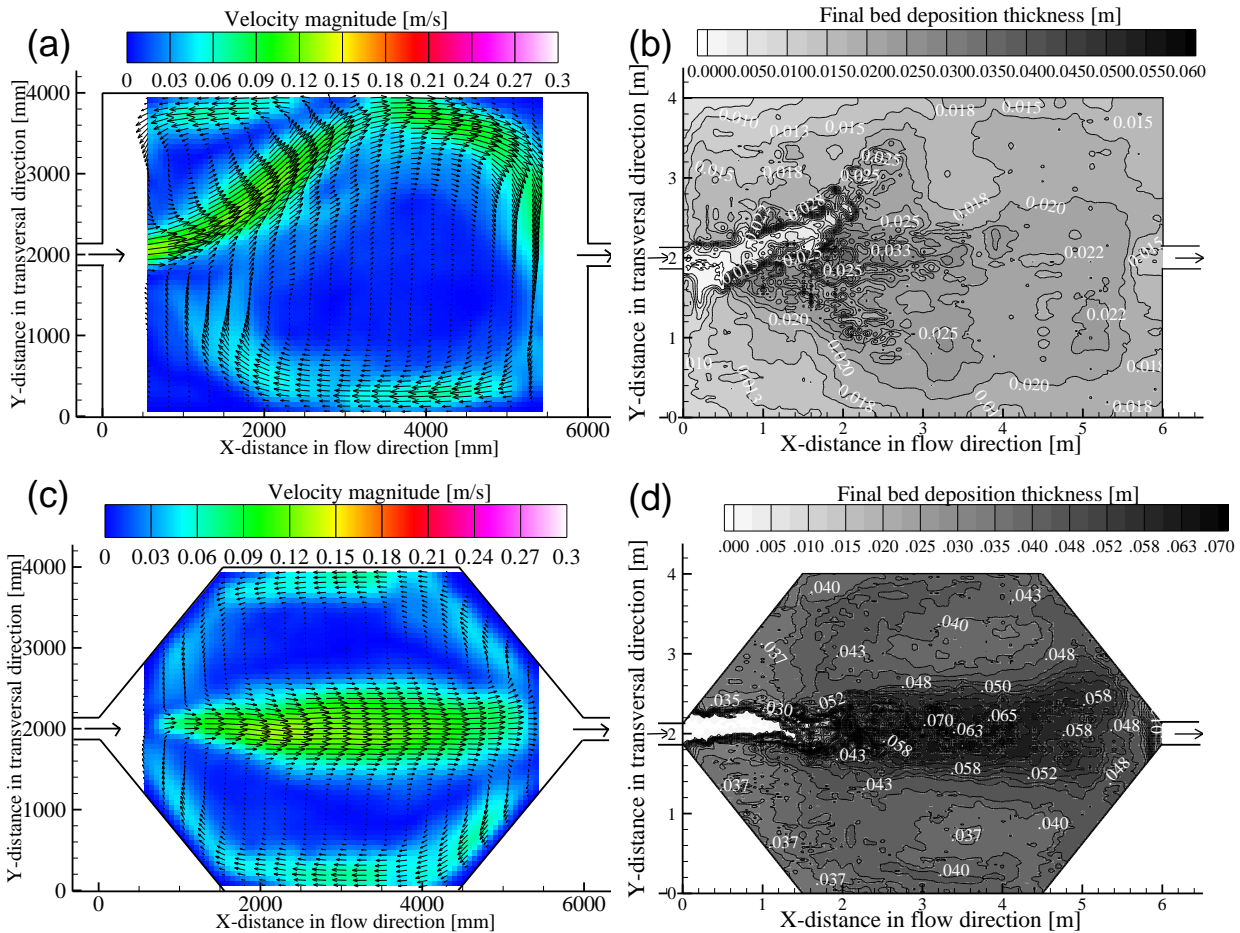


Figure 5.24: Flow velocity with vectors and bed topography contours after two days of free flow flushing ($Q = 7.0 \text{ l/s}$ and $h = 0.2 \text{ m}$) of experiments (a, b) T1, and (c, d) T16.

The flow pattern in Figure 5.24(a) was asymmetric with deviated jet and three circulation cells. After restarting the flow it chooses the easiest path from the inflow to the outflow gate along the left side wall.

The sedimentation from the previous period has apparently become too much of an obstacle to result in a symmetric flow pattern. If flushing takes place under a sustained water level, only a very limited area in the reservoir is cleared as showed by the bed topography contours in Figure 5.24(b). The sediment deposit scoured in the vicinity of the inlet and the deflected jet within a very short period of time (8.0 hours).

The experiments lasted after that 40 hours without any changes neither in flow structures nor in bed topography. During the test the released suspended sediment concentration was measured at the outlet. In about 10 minutes after the flow was started, the SSC was high and afterward the outlet discharge was almost clear. A tongue shaped crater called flushing channel was formed by the flushing flow.

Once the flushing channel was formed and there is no sediment moving into the channel, the water flowing through the outlet is clear, that is the formation of channel is fairly stable and no sediment will be removed from the flushing channel afterward. Symmetric flow pattern was observed in the hexagonal geometry experiment (T16) as shown in Figure 5.24(c).

The flow patterns that are brought about by the entrance jet, bed topography and the reservoir geometry, are control the location and the size of the scoured channel. The circulation cells in the initial clear-water with flat bed are rotating faster than in the pressure flushing case. Figures 5.25(a&b) present the final bed deformation after two days of clear

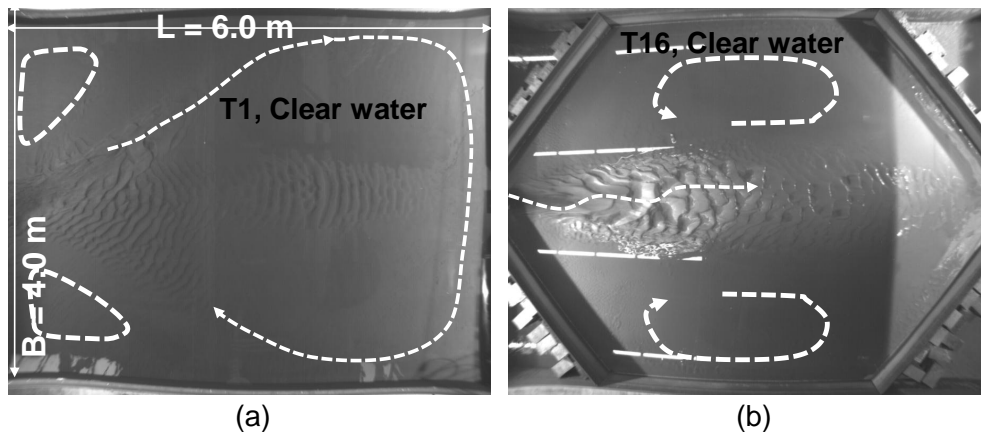


Figure 5.25: Photographs of eroded channel at the end of reservoir experiments after two days of free flow flushing (a) T1, (b) T16.

water test for T1 and T2, respectively. Also, the jet trajectories and the horizontal circulation cells are shown by schematically sketch. The most important change was found in the erosion of the bed near the entrance.

No significant change has been observed anymore between the respective bed profiles after that period. Hence, for these flow and sediment conditions, the bed might be considered as stable. After the channel was formed its location is rather stable, and difficult to shift as its depth enforces the flow pattern to follow the channel path.

In generally, the scour channel geometry which can be typically developed in the reservoirs after a pressure flushing, influenced by factors including submerged angle of repose of the sediment, inflow and outflow of water and sediment, outlet geometry, characteristic of the sediments, etc.

It seems that the the same channel geometry was obtained with two different geometry shape. Free flow sediment flushing method has local effects in sediment disposal and is recommended when local disposal of the sediment deposits is intended. The results of the present study revealed that the location and the size of the formed channel is depending on the jet flow type and characteristics.

5.11.2 Drawdown flushing flow and bed morphology

The experiments in drawdown flushing were started by opening the outlet gate and the water depth reached to 10 cm in the basin. After that the pump was turned on with normal discharge of $Q = 7.0 \text{ l/s}$. In the drawdown flushing case the discharge was kept constant as before and the water depth dropped by half than before.

Figure 5.26 shows the flow structure and final bed thickness contours after two days of drawdown flushing in various reservoir geometries. If the water surface can be drawdown significantly to generate high flow velocity near the outlet, the flow starts to erode a wide channel.

At that stage, a significant amount of sediment deposits was flushed through the reservoir, and the initial channel deepened and widened as a result of the strong jet flow and erosion. An extremely high SSC around $C = 10 - 20 \text{ g/l}$, was measured. Eroded sediments are transported progressively downstream forming a flushing channel located either at the side wall or straight at the centerline. It depends on the flow structure and basin geometry shape factor as will be shown in the following chapters.

Figure 5.26(a) shows the flow pattern of the reduced reservoir width (T8) with asymmetric flow structure. Initially all deposited sediment resuspended with the high velocity jet trajectory which deviated to the left side wall. The flushing channel location was clearly visible by the resuspended sediment which was rapidly released during 30 minutes. This followed by a short period of very rapid widening of the flushing channel forming a wide advancing front. Then, after a sudden change in the rate of widening, the flushing channel continues to widen at a more gradual rate.

The final channel form and bed morphology contours is shown in Figure 5.26(b). The jet trajectory path was eroded and high deposition under the circulation cell. Fine suspended sediments were carried and deposited on the right side and on the left upstream corner of the reservoir, by the reverse eddies that are generated by the jet flow separation.

The flow structure was stable and did not change during 48 hours and the fixed bottom of the reservoir was exposed after erosion. The channel did not develop along the shortest path from inflow to outflow, but developed toward the left side. Figure 5.28(b) show the final configuration of the channel after experiment T8.

The channel location and size were varied by reducing the reservoir length than by reducing the reservoir width as can be seen in Figures 5.26(b&d). A straight flushing channel was formed in the processes of drawdown flushing for the reduced reservoir length (T13). For shorter reservoir length experiments the flushing channel width is variant with the reservoir length. The channel width is increasing in downstream direction with a T-shape channel as shown in Figure 5.26(d).

The channel width developed as time elapsed, increased smoothly with time and reached a dynamically stable state in the whole length(Fig. 5.26(d)). The banks of the channel have

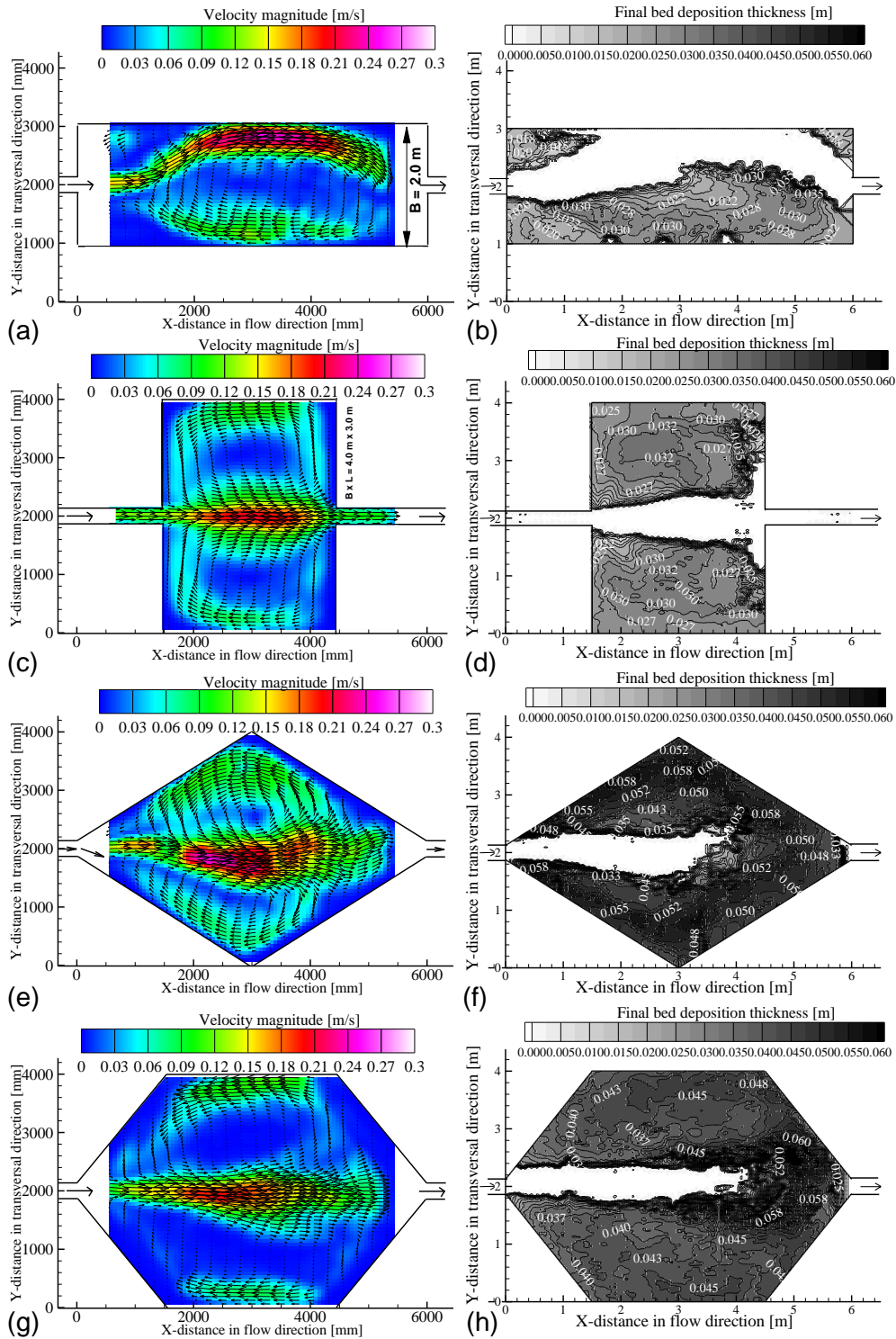


Figure 5.26: Flow velocity with vectors and bed topography contours after two days of drawdown flushing ($Q = 7.0\text{ l/s}$ and $h = 0.1\text{ m}$) of experiments (a, b) T8, (c, d) T13, (e, f) T14, and (g, h) T16

a mild slope in the jet shedding regions (streamwise and reverse jets). The flow pattern shown in Figure 5.26(c) is symmetric with two circulation cells on both sides. The circulation

velocity was able to erode two transversal channels on both outlet wall side. the transversal eroded deposit was elevated up with the reverse flow.

Figures 5.26(e and f) present the flow field and bed morphology for the reduced entrance angle $\theta^* = 32^\circ$ (lozenge geometry). The flow pattern in Figure 5.26(e) shows a meandering jet along the centerline with two coupled eddies on both sides. The flow was asymmetric with one large circulation for the same geometry but on a flat bed and 20 cm water depth.

The final bed deposition was able to change the flow pattern. Eroded sediments are transported progressively downstream forming a narrow advancing front over which the flow fans out. Due to the fanning out of the flow it losses its transporting capacity and causes the front to built up to form an underwater-ridge before the outlet (see Fig. 5.26(f and h)). If the water level is drawn down during flushing, the sediment removal can be divided into several phases. Flushing is most effective during the first hours after the stored water in the reservoir has been released.

A stable flushing narrow channel was created by the flushing flow in a short period. The footprint of the central meandering jet was clearly visible in the channel front, which was deviated to the left side following the jet.

The jet is straight and strong until 3 m length from the inlet and after that it was shifted left. The jet was meandering after the middle section in one meter length before reattachment. From the above results, it can be concluded that outflow sediment discharge and the channel characteristics are in accordance with the reservoir geometry as well as the discharge and water depth.

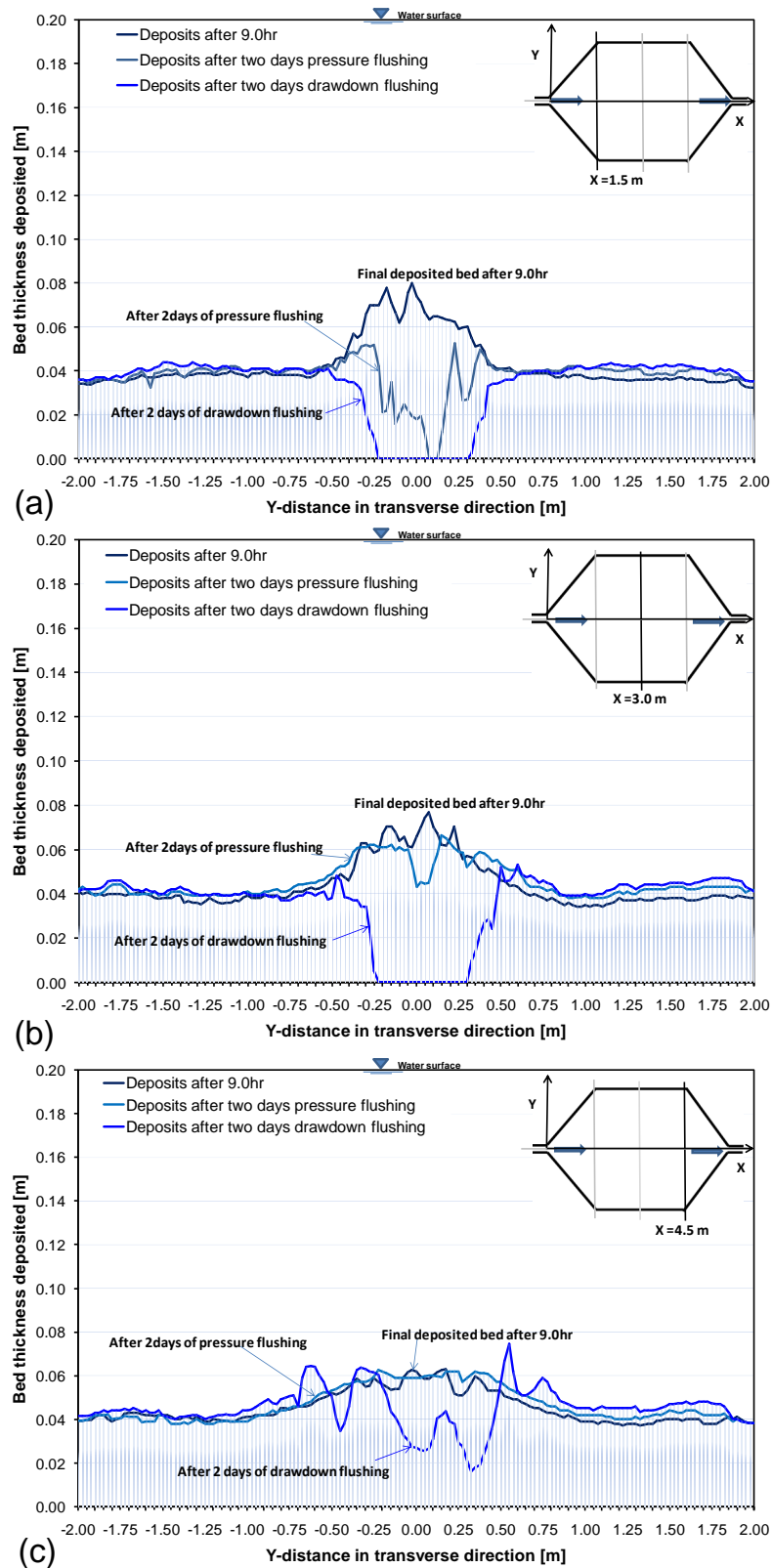


Figure 5.27: Comparison of bed thickness profiles of final deposition after 9.0 hours, free flow and drawdown flushing after two days for T16 at three different cross sections (a) $X_1 = 1.5$ m, (b) $X_2 = 3.0$ m, and (c) $X_3 = 4.5$ m from the basin inlet.

By increasing the jet expansion angle to $\theta^* = 51.34^\circ$ the jet meandering behavior disappear. The flow pattern shown in Figure 5.26(g) for the hexagonal geometry is symmetric with straight jet along the centerline and one eddy on each side. The jet reattachments and the eddy size are similar on both side. The channel flushing is straight with width double size of the inlet channel width $b = 0.25m$. the channel length is in accordance with the reattachment points locations as shown in Figure 5.26(h).

A detailed comparison evolution for the final bed profiles before flushing, after pressure and after drawdown flushing, for the hexagonal geometry experiments T16 are presented in Figures 5.27(a, b, &c) at three different cross sections $X1 = 1.5$ m, $X2 = 3.0$ m, and $X3 = 4.5$ m, from the inlet, respectively.

After 9.0 hours of sediment entrainment an underwater-ridge on the whole central basin basin was built. With pressure flushing the jet was able to wash out the peak part of the ridge and forming a triangular shape cross section as shown in Figure 5.27(a) at the first cross section $X1 = 1.5m$. But with drawdown flushing the whole ridge washed out and a flushing channel was formed with a trapezoidal cross section with bottom width of 0.5 m (two times the inlet channel).

There is no bed thickness variation on both sides with the two modes of flushing. For the second cross section shown in Figure 5.27(b), the ridge did not change under pressure flushing, but it was flushed out with drawdown mode. The channel cross section size and geometry is same as $X1$.

The right side bed thickness was elevated by 1 *cm* with the drawdown flushing. Figure 5.27(c) shows the bed thickness at $X3 = 4.5$ m, where the channel flushing cross section is reduced and forming a complex bed forms in the center. The final bed morphology for all discussed results geometries are presented in Figures 5.28(a, b, c, d, e, & f).

In general, the function of the flushing channel is to reduce the sediment concentration around the entrance of basin and to prevent hydraulic structures from abrasion by sediments. The increasing of erosion and thus the increasing of sedimentation has caused the sediment level at the downstream to increase significantly.

The width of the channel is in accordance with the inlet channel, flow pattern, water depth, discharge, and the outlet conditions. If flushing is allowed to continue for such a long time the channel erosion diminishes, the longitudinal eroded depths are closely related to the depositional pattern in the reservoir.

The flow structures and sediment deposition patterns of drawdown flushing system have been investigated. A larger volume in the reservoir generally generates a higher flushing flow depth and velocity in the flushing channel. The larger reservoir volume will induce higher bed shear stress, and hence produces more effective flushing/removal of sediments on the bed.

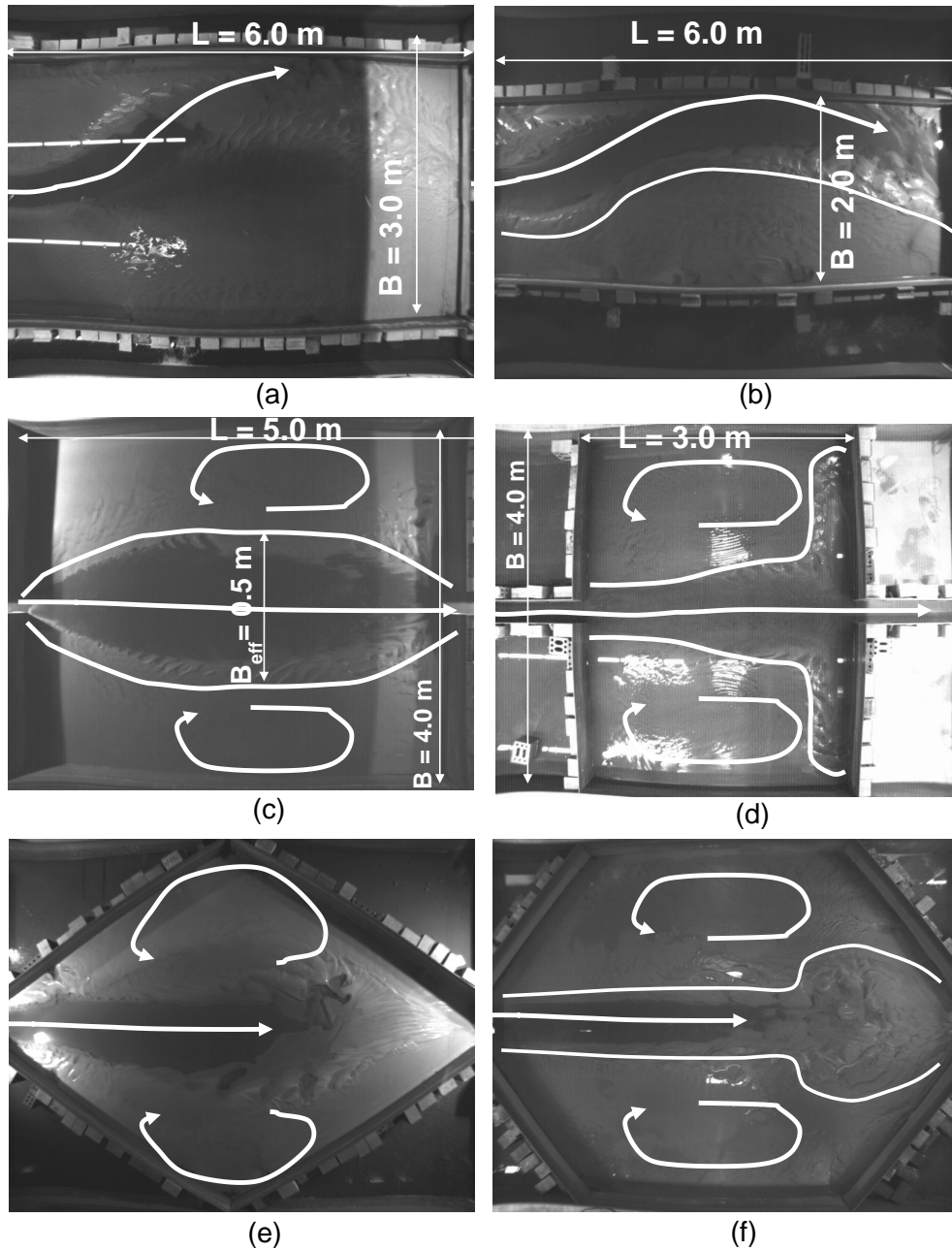


Figure 5.28: Photographs of eroded channel at the end of reservoir experiments after two days of drawdown flushing (a) T7, (b) T11, (c) T14, and (d) T16.

5.12 Influence of reservoir geometry on sedimentation characteristics

5.12.1 Influence of aspect ratio of reservoir on storage loss SR

Various geometrical configurations with different aspect ratio $AR = L/B$, where L and B is length and width of the basin, respectively, hydraulic and sediment conditions have been analyzed.

The temporal evolution of the silting ratio which can be defined by the deposited volume of sediments V_{dep} divided by the volume of water initially stored in the reservoir V_{res} is shown in Figure 5.29. The figure depicts the relationship between the silting ratio and the aspect ratio of different reservoir.

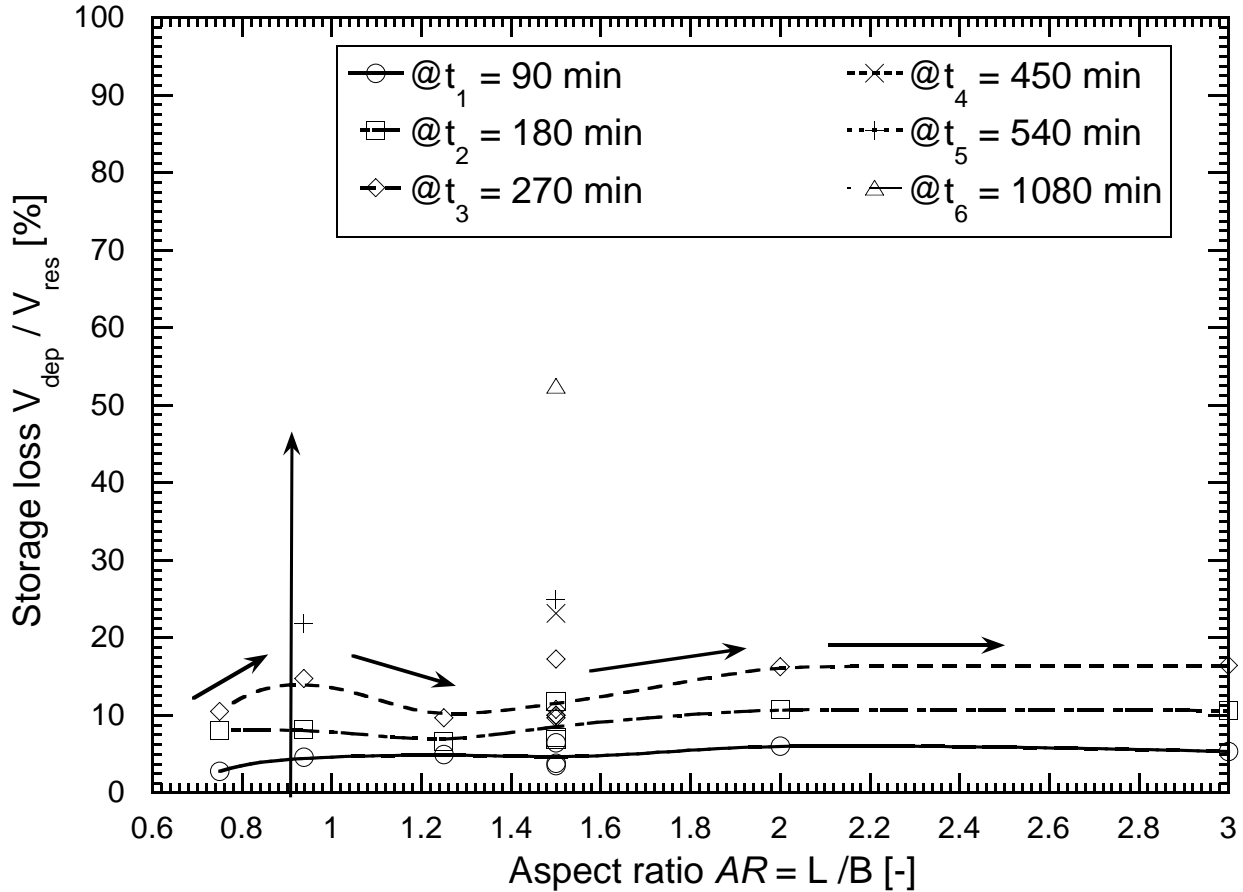


Figure 5.29: Influence of Aspect Ratio $AR = L/B$ on storage loss V_{dep}/V_{res} .

The evolution of the silting ratio at 90, 180, 270, 450, 540 and 1080 minutes for aspect ratio $AR = L/B$ of about 0.75 to 3.00 are shown in Figure 5.29. Silting ratio increases with the aspect ratio of the reservoir, except for AR between 1 and 1.5. In beginning of experiment for $t_1 = 90$ minutes, silting ratio was almost uniform of 4% for all geometries.

The evolution of the silting ratio in the second and third periods were somewhat similar in many respects to that observed in the first run, even though it displayed a more silting ratio at large AR .

Note that the silting ratio gradient is increased when compared to run 1 (Fig. 5.29). Silting ratio is increasing with time and almost 53% of the original storage volume was deposited after 1080 min.

The obtained silting ratio curves in Figure 5.29 have a fast and high peak at low aspect ratio of 0.9. It decreases for a higher AR until 1.25. It increases again for aspect ratio larger

than 1.25. The Aspect Ratio AR of the reservoir plays a critical role in determining the sediment deposition volume and silting ratio.

It can be concluded that the reservoirs with large aspect ratio have high silting ratio, as shown in Figure 5.29.

5.12.2 Influence of expansion ratio of reservoir on storage loss

This section presents the evolution of silting ratio and its relationship with Expansion Ratio ER . To investigate the influence of the ER on the silting ratio, six different runs were plotted in Figure 5.30.

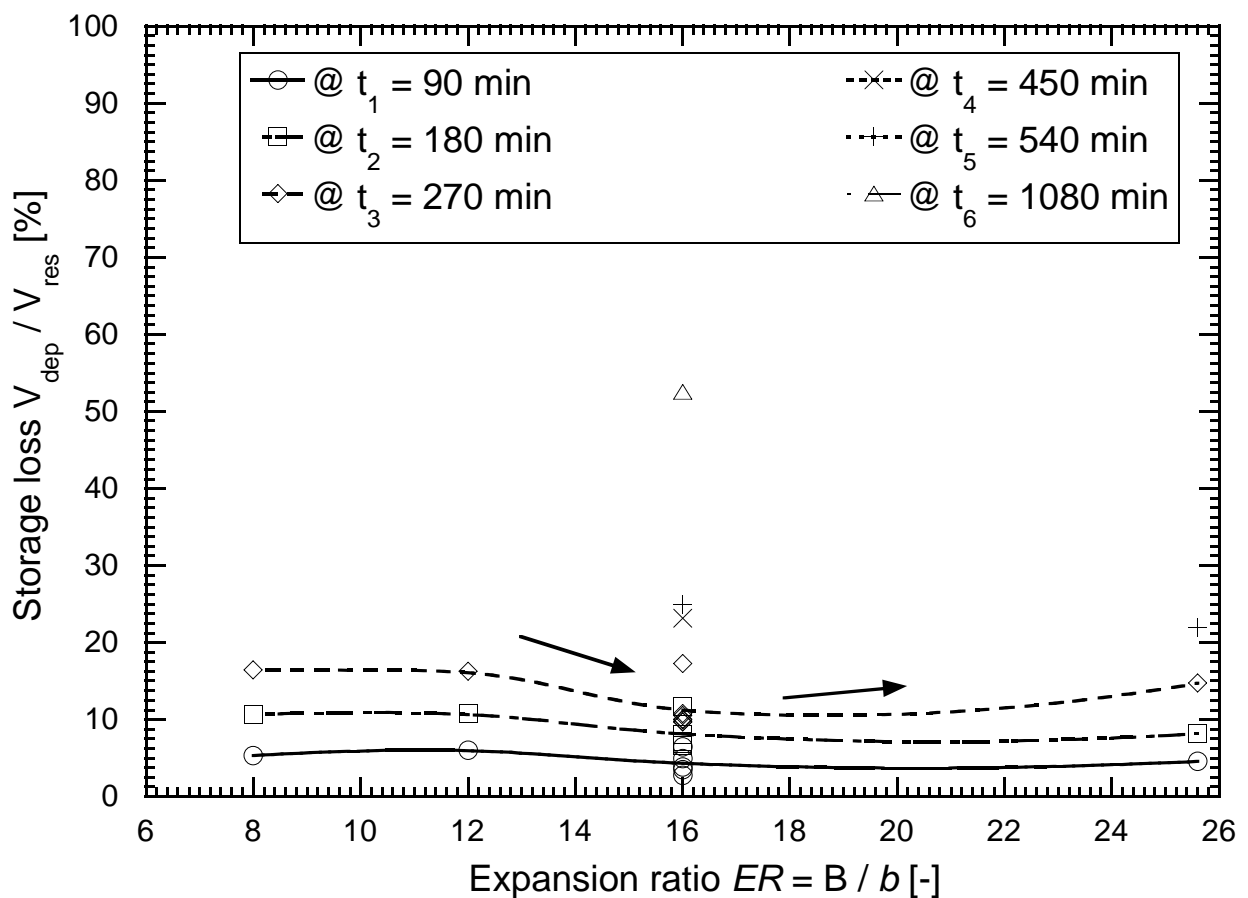


Figure 5.30: Influence of Expansion Ratio $ER = B/b$ on storage loss V_{dep}/V_{res} .

The silting ratio is almost constant and uniform by increasing the expansion ratio as depicted in Figure 5.30 for the first and second period. At 270 min silting ratio start to gradually increase by increasing ER .

The evolution of the silting ratio is almost constant between expansion ratio of about 8 to 12. Finally it can be concluded that Expansion Ratios ER has no significant effect on the silting ratio during t_1 and t_2 .

The general tendency of silting process is inversely proportional to expansion ratio ER , e.g. a higher silting ratio is to be expected in a narrow reservoir with lower expansion ratio, as shown in Figure 5.30.

5.12.3 Influence of normalized expansion area $\sigma = A_{exp}/A_t$ on storage loss

The relation between normalized expansion area and the storage loss, (which can be defined as the ratio deposited sediment volume to the initial reservoir capacity, after 90, 180, 270, 450, 540 and 1080 minutes), are presented in Figure 5.31.

The normalized expansion area is the ratio of expansion area A_{exp} , to the total surface area of the basin A_t . Storage loss is gradually increases with σ until reach to the first peak. Then a gradually decreasing is occurred till it reaches to the second peak.

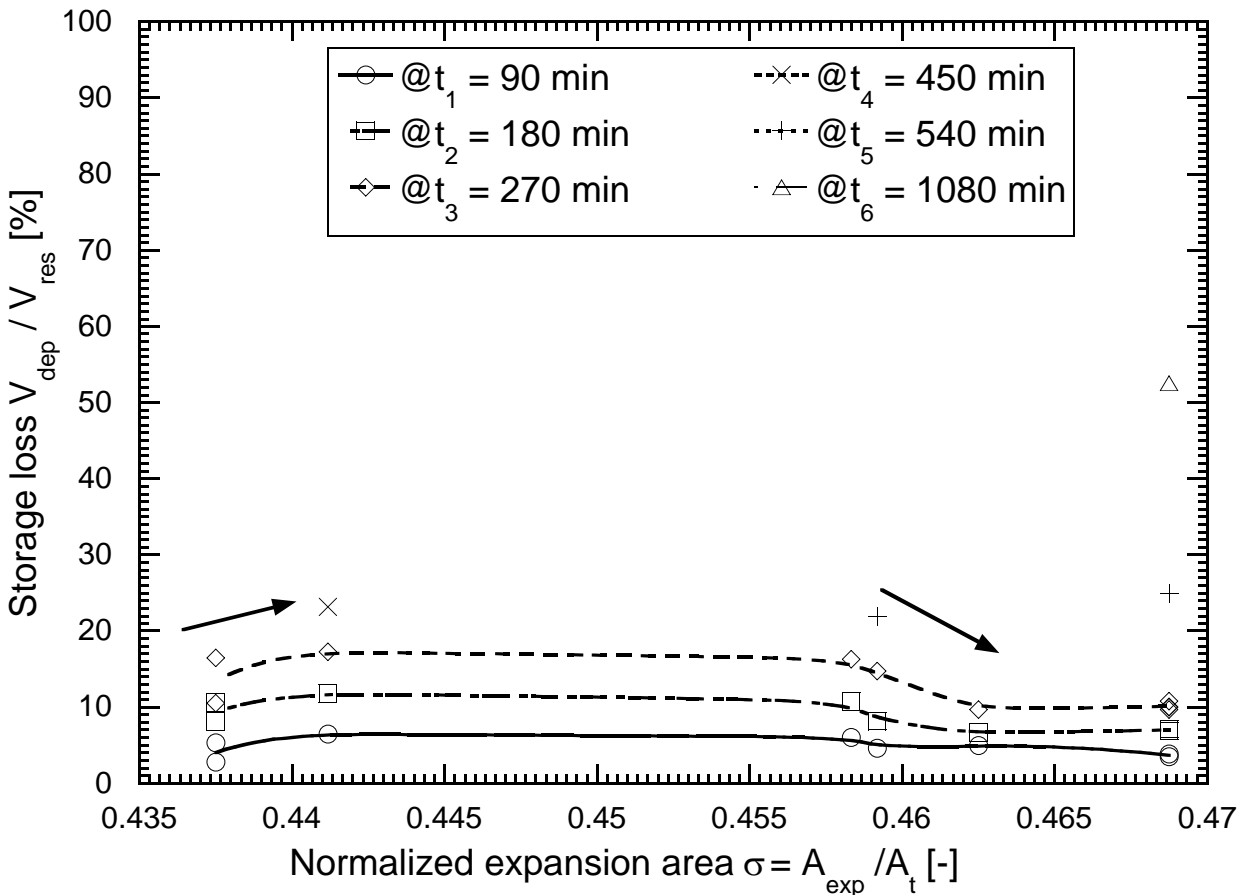


Figure 5.31: Influence of normalized expansion area $\sigma = A_{exp}/A_t$ on the storage loss V_{dep}/V_{res} .

The normalized expansion area σ has a moderate effect on the storage loss. The highest storage loss was observed between σ of 0.44 and 0.46. The normalized expansion area of

0.47 showed lowest silting intensity. The silting evolution process for these ratios is given in Figure 5.31.

In the period of time from t_1 to t_2 , reservoirs have lost 12% of their capacity. It was stated that the capacities of reservoirs investigated was reduced by 20% after the third period and the reduction rate was significantly high during the last run t_6 before it reach to equilibrium state.

Long run period for the reference reservoir geometry was 53% silted. It can be concluded that the higher silting ratios for the smaller reservoirs in size.

5.13 Influence of geometry shape factor SK on storage loss SR

5.13.1 Time normalized by actual residence time of reservoir

Actual residence time t_r is defined as the ratio of actual water volume in reservoir (difference between initial and dead deposits volumes) to the average flow rate. Time t is the duration of the inflow of suspended sediment to reservoir.

An empirical relationship correlating the storage loss SR with geometry shape factor SK and t^* dimensionless time $t^* = t/t_r$, was developed.

To predict the storage loss evolution two independent variables which represent the geometry effect SK and dimensionless time t^* were used. The geometry shape factor has a strong correlation with storage loss and R-squared of 0.96.

In Figure 5.32 Equation 5.1 is presented and compared with measured storage loss SR .

For the determination of the silting ratio at specific time and geometry configurations of the reservoir (Fig. 5.32) the expression developed is referred to (Eq. 5.1). The application range of Eq. 5.1 is $2.92 < SK < 13.42$ and $8 \geq t^* \leq 200$.

$$SR = \frac{V_{dep}}{V_{res}} = 0.25 \cdot t^* + 200 \cdot SK^{-2} \cdot (1.2 + \ln \frac{SK}{10}) \quad (5.1)$$

where t^* ratio of duration of suspended sediment inflow to actual water residence of reservoir $t^* = t/t_r$, storage loss SR is the ratio of cumulative deposited volume after specific running time V_{dep} and the initial reservoir volume before deposition V_{res} ($SR = V_{dep}/V_{res}$), SK is the geometry shape factor $SK = (P/\sqrt{A_t}) \cdot AR \cdot D_{exp}$, where P is the wetted perimeter of the length of the side walls, A_t is the total surface area of the reservoir, AR is aspect ratio of the reservoir, and $D_{exp} = R/\Delta B$ is expansion density of the reservoir.

For the same data another empirical formula, Eq. 5.2, was developed by using the product of the geometry shape factor SK and the dimensionless time t^* . The application range of Eq. 5.2 is $2.92 < SK < 13.42$ and $8 \leq t^* \leq 200$.

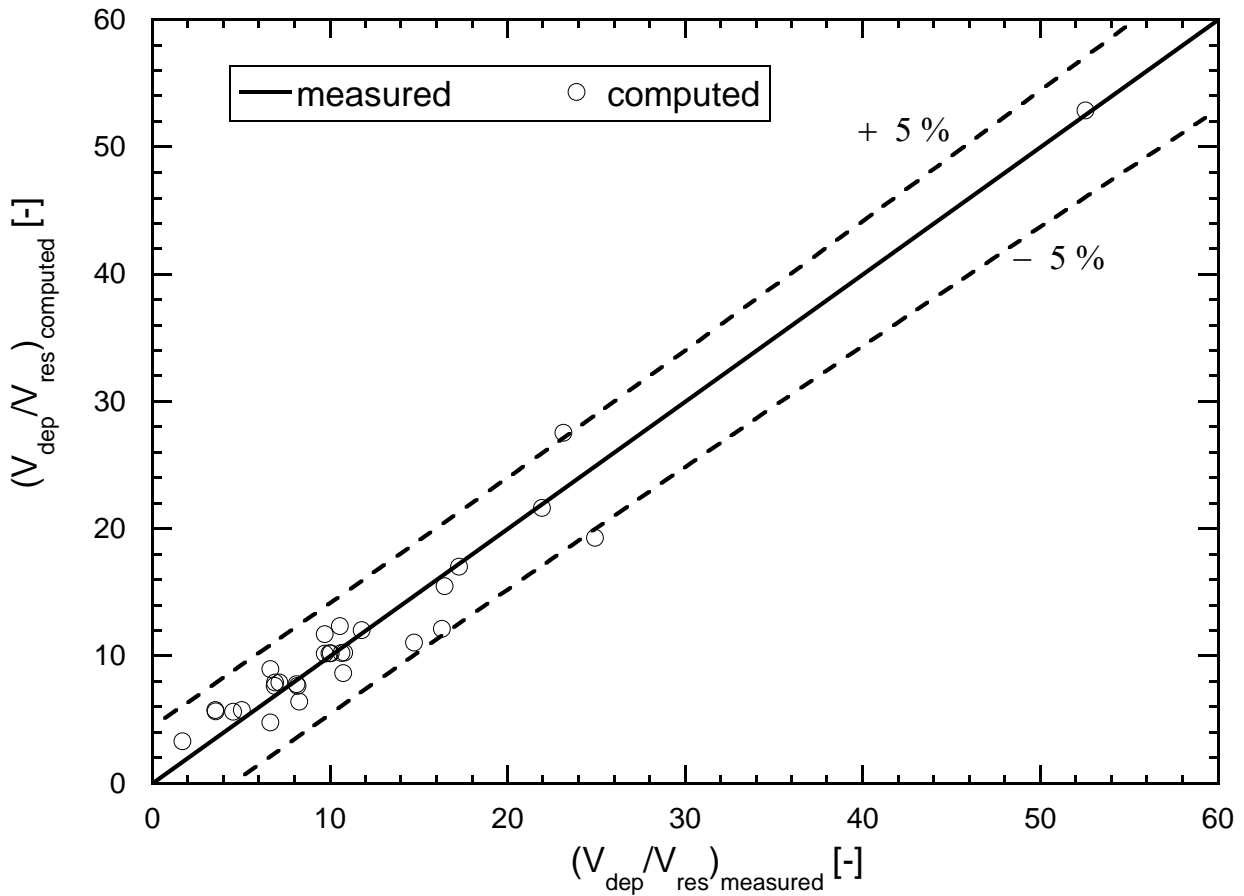


Figure 5.32: Relation for the storage loss SR (original formula obtained from polynomial curve fitting of three parameters (SR , SK , and t^*), Eq. 5.1) and comparison with measured values. The 95 % confidence interval is ± 0.49 .

$$SR = \frac{V_{dep}}{V_{res}} = 19 + 4.6 \cdot \ln \frac{SK \cdot t^*}{1000} + 18.3 \cdot \left(\frac{SK \cdot t^*}{1000} \right)^3 \quad (5.2)$$

The storage loss relationship follows same function in Figure 5.32 and the correlation between SR and $SK \cdot t^*$ may be given in the form of Eq. 5.2.

A comparison between the measured and computed storage loss of Eq. 5.2 is shown in Figure 5.33.

It can be concluded that Eq. 5.1 has a high R^2 value of 0.96, whereas with Eq. 5.2 R^2 is 0.82, which is still acceptable. Several formula were tested and the highest correlation value is presented.

Moreover, with a simple multiplication of two dimensionless numbers SK and t^* , an accepted equation could be obtained.

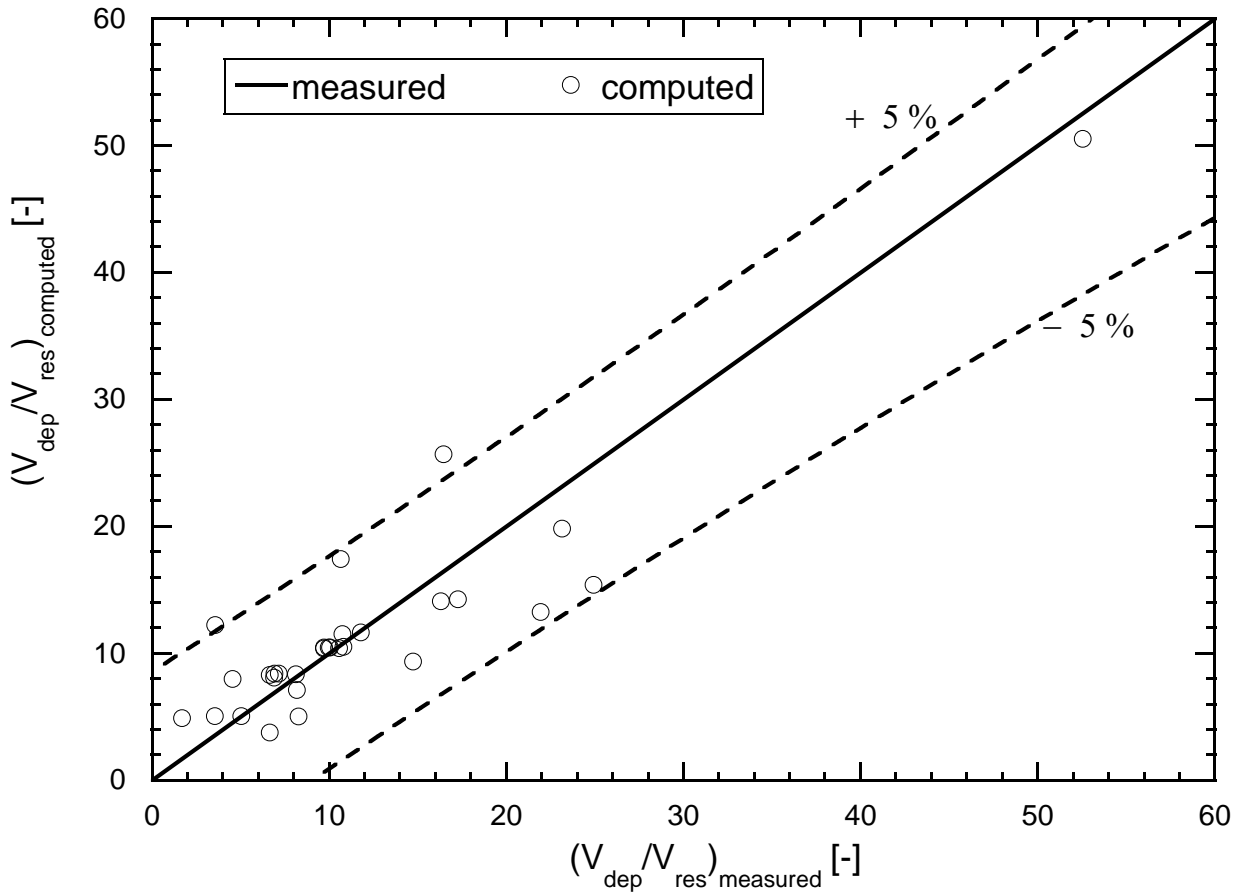


Figure 5.33: Relation for the storage loss SR (original formula obtained from polynomial curve fitting of three parameters (SR , and $SK \cdot t^*$), Eq. 5.2) and comparison with measured values. The 95 % confidence interval is ± 0.79 .

5.13.2 Time normalized by initial residence time of reservoir

Initial residence time t_{ri} is the ratio of initial reservoir volume to average flow rate in reservoir. In this section the previous two equations (Eqs. 5.1 and 5.2) will be established by using initial residence time instead of actual one.

An empirical relationship correlating the storage loss SR with geometry shape factor SK and t^{**} relative time $t^{**} = t/t_{ri}$, was developed in Eq. 5.3, and the application range is $2.92 < SK < 13.42$ and $8 \leq t^{**} \leq 95$

$$SR = \frac{V_{dep}}{V_{res}} = 0.44 \cdot t^{**} - 5.4 + 375 \cdot SK^{-2} \cdot \left(1 + 0.8 \cdot \ln \frac{SK}{10}\right) \quad (5.3)$$

An empirical relationship correlating the storage loss SR with the product of geometry shape factor SK and the relative time t^{**} was developed in Eq. 5.4, and the application range is $2.92 < SK < 13.42$ and $8 \geq t^{**} \leq 95$

$$SR = \frac{V_{dep}}{V_{res}} = 6.9 + \left(\frac{SK \cdot t^{**}}{100}\right)^3 (1 - 0.5 \cdot \ln \frac{SK \cdot t^{**}}{100}) \quad (5.4)$$

where t^{**} relative time of suspended sediment inflow to initial water residence of reservoir $t^{**} = t/t_{ri}$, storage loss SR is the ratio of cumulative deposited volume after specific running time V_{dep} and the initial reservoir volume before deposition V_{res} ($SR = V_{dep}/V_{res}$), SK is the geometry shape factor $SK = (P/\sqrt{A_t}) \cdot AR \cdot D_{exp}$, where P is the wetted perimeter of the length of the side walls, A_t is the total surface area of the reservoir, AR is aspect ratio of the reservoir, and $D_{exp} = R/\Delta B$ is expansion density of the reservoir.

5.14 Effect of geometry shape factor SK on mean relative deposited thickness

In this section geometry influence on the relative deposited thickness. The water depth has an significant effect on the flow and sediment deposition behaviors. Due to that the thickness of deposited sediment d was normalized by the water depth h .

The main task of this investigation was an attempt to derive a formula to predict the deposition thickness in the reservoir for specific water depth, geometry characteristics and time. Two different approaches were used for that.

In the beginning a combination of one dependant variable d/h and two independent variables, SK and t^* , was tested. With d/h and $SK \cdot t^*$, a high correlation was obtained owing a R^2 value of 0.85. Figure 5.34 shows the measured and computed relative deposited thickness from the relationship between $SK \cdot t^*$, and d/h being the relative deposited thickness normalized by water depth in the reservoir.

A simple nonlinear formula was developed in Eq. 5.5 by using Stata software.

$$\frac{d}{h} = 0.2 \cdot \left(1 + \left(\frac{SK \cdot t^*}{1000}\right)^3\right) - \frac{0.035}{\sqrt{(SK \cdot t^*)/1000}} \quad (5.5)$$

Where d/h is ratio of average thickness of deposited sediment over the reservoir at specific period to the water depth at the same period, t/t_r is ratio of t the duration of the suspended sediment inflow to t_r the actual water residence time in reservoir at the same period, and SK is the reservoir geometry factor.

In Figure 5.34 Equation 5.5 is presented and compared with measured relative deposited thickness d/h .

In order to find a suitable expression for d/h the genetic program GPKernel (Genetic Programming Kernel) developed by M. Keijzer and V. Babovic at the Danish Hydraulic Institute (DHI) has been used.

Based on experimental flume study empirical model for prediction of the mobile bed evolution near the side weir was developed using GPKernel (Rosier, 2007). The program

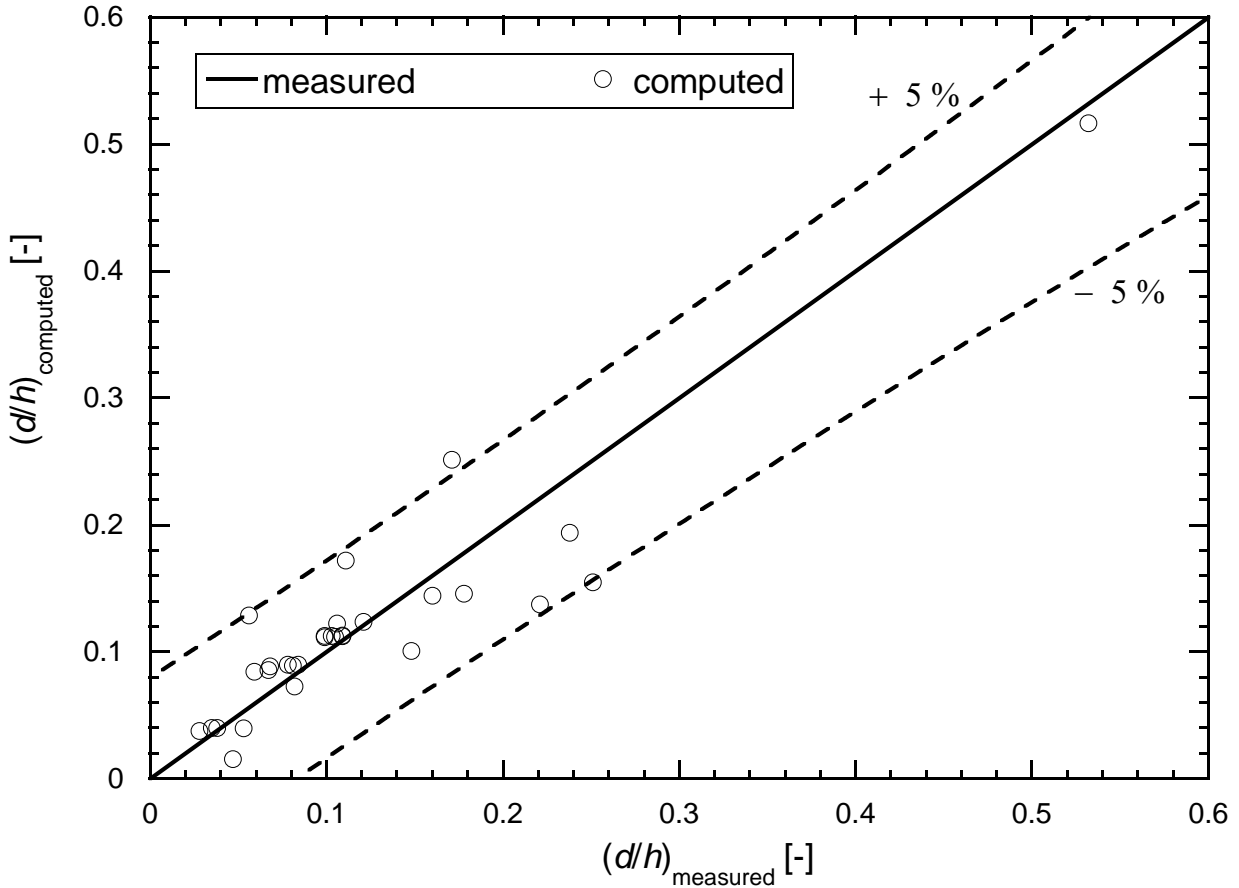


Figure 5.34: Relation for the relative deposited thickness d/h (original formula obtained from polynomial curve fitting of three parameters (SR , and $SK \cdot t^*$), Eq. 5.5) and comparison with measured values.

looks for mathematical relations based on a set of input parameters, constants, operations, genetic parameters and user-defined targets.

Introducing the parameters d/h , SK , and t^* to the genetic program several relations in the form d/h were obtained in a very complex expression. Therefore, a regroupement of terms and omission of terms of minor influence the rather complex expression can be reduced to Equation (Eq. 5.6).

A comparison between both expression (original and simplified) is shown in Figure 5.35. Based on the physical meaning and the degree of correlation expressed in terms of R^2 -values the following equation has been selected ($R^2 = 0.96$):

$$\frac{d}{h} = \frac{-0.38 \cdot t^{**} \cdot (SK^{-1} - 0.39)}{3 \cdot SK + SK / (0.46 \cdot t^{**} + 3 \cdot SK + t^{**} / SK)} \quad (5.6)$$

Where d/h is ratio of average thickness of deposited sediment over the reservoir at specific period to the water depth at the same period, t^{**} is the relative time and it can be define

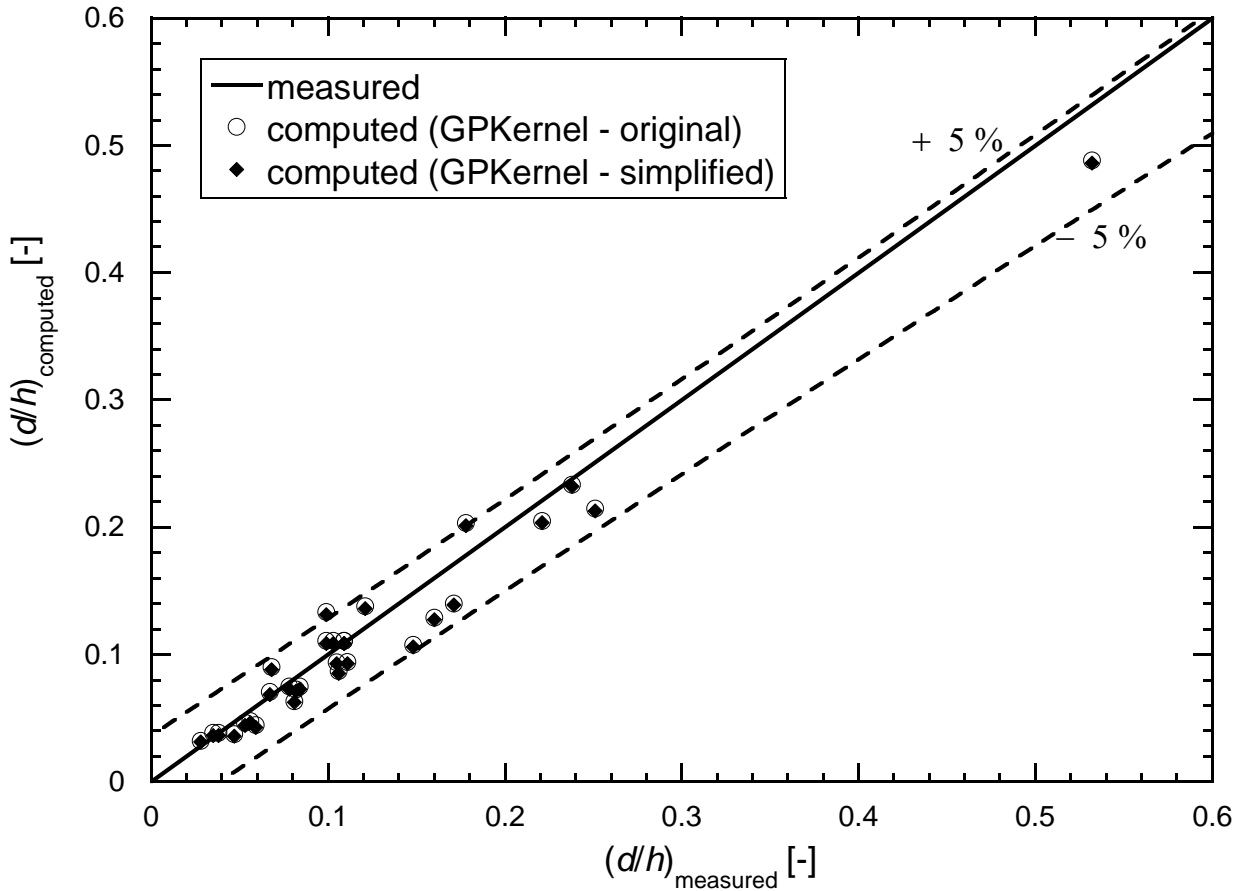


Figure 5.35: Relation for the relative deposited thickness with relative time (simplified formula obtained from GPKernel, Eq. 5.6) and comparison with the original GPKernel-formula and measured values. The 95 % confidence interval is ± 0.9 .

as $t^{**} = t/t_{ri}$ is ratio of t the duration of the suspended sediment inflow to t_{ri} the reservoir initial residence time before deposition, and SK is the reservoir geometry factor.

5.15 Discussions and conclusions

5.15.1 Influence of sediment feeding test procedure

Similar flow patterns was developed with the two procedures, but with small differences regarding the velocity magnitudes and the reattachment length. Moreover, the deviated jet velocity approximately has the same value as in the inlet channel.

It was found that 90 *min* was enough to develop a stable morphology independently on the test procedure. Due to that most of the experiments were conducted with 270*min* total test period with three runs each 90*min* and for some selected test different scenario was selected.

5.15.2 Influence of test duration

Results of the long run experiment provide some understanding of the general picture whereby an equilibrium configuration may be established in a large rectangular simple geometry communicating through an inlet with shallow basin: the basic observation emerging from the experiment is the fact that the bed elevation established close to the inlet at equilibrium results from the readjustment of the whole profile.

A strong interaction between flow field and bottom topography also occurs in the basin inlet region with a quasi equilibrium state.

The reservoir reaches to the quasi-equilibrium after 16 hours at which the suspended sediment release efficiency reaches 100%. The results help to understand the flow mechanism and the sediment exchange process. The prediction of sediment behavior lies in the prediction of flow behavior and the results are very sensitive to the geometry and the morphodynamic conditions.

The deposition pattern is obviously strongly influenced by the inlet jet deviation and, in turn, material deposits are able to change later the pattern of the flow structure. The volume of the deposited sediments reached 50% of the total reservoir volume after 18 hours.

Finally, bed forms were observed to develop and evolve in the basin throughout the experiments. Bed forms exhibit features shared by ripples and Barchan-shaped ripples were formed. The mechanisms controlling the morphological equilibrium at the basin, an important role is also played by the jet flow type and accompanied eddies. By increasing the sediment deposition and water become very shallow the presence of significant vertical vorticity shedding from the inlet carrying sediments resuspended in the surf zone is vanishing.

5.15.3 Influence of basin geometry and bed forms

The reservoir width did not affect the asymmetric separation of the deflected jet. Final deposition patterns were affected by the reservoir width, with more symmetric and uniform distributions on the entire surface, and concentrated deposits on both sides with. It is interesting to note that, in spite of the horizontal recirculations on both sides were hindered with reduced reservoir length; the sediment depositions still increasing.

The highest sediment deposition and concentration was found along the main jet flow, where the velocity is highest. The flow pattern was stable, with high roughness over the entire bed. However, after some time, ripples developed underneath the main jet, with thicknesses of about 0.15 times the flow depth. These were able to change the flow pattern.

For shape factor of the reservoir $SK < 5.5$, the more uniform were the depositions over the entire surface. Furthermore, the time evolution of deposition patterns with different reservoir geometries could be assessed.

The experiments revealed the interaction between flow pattern and bed forms. Although the geometry is perfectly symmetric, deposition and flow patterns are asymmetric for geom-

etry shape factor $SK > 5.5$. The depositions and flow structure remains asymmetric with reduced width of the reservoir and disappear when reducing the length of the reservoir.

5.15.4 Conclusions regarding phenomena

It was shown that the reduction of horizontal vortex take place by entering the sediment mixture.

As sediment is added to the flow, the turbulence is reduced and the mixing lengths decrease which, together with increasing roughness, cause an increase in velocity gradient when compared to clearwater flow. The turbulence was generated locally by the horizontal entrainment of a mixture into the basin with stagnant water. The jet pulse created a region of three-dimensional turbulent flow, characterized by mixing and entrainment. Then the size of the turbulence increased rapidly. During the subsequent stage of sediment settled down, the horizontal motions are suppressed and eventually the mixed region becomes flat and the motion becomes quasi vertical.

5.15.5 Conclusions regarding flushing

Experiments showed that under free flow a flushing nose can be formed in a very short time and only relatively small amount of sediment was flushed out. This has confirmed the observations by Di Silvio (1990), Shaun (1989), Wan (1986), Dawans et al. (1986), and Jihn-Sung (1995).

During drawdown flushing, different flushing channel shapes (curved, straight, and cone) was formed with different geometry. The width of the channel is in accordance with the inlet channel, flow pattern, water depth, discharge, and the outlet conditions. If flushing is allowed to continue for such a long time the channel erosion diminishes, the longitudinal eroded depths are, clearly, closely related to the depositional pattern in the reservoir. The flow structures and sediment deposition patterns of drawdown flushing system have been investigated. A larger volume in the reservoir generally generates a higher flushing flow depth and velocity in the flushing channel. The larger reservoir volume will induce higher bed shear stress, and hence produces more effective flushing/removal of sediments on the bed. A significant amount of sediment deposits was flushed through the reservoir.

To effectively apply the flushing processes for removing deposits, the location, depth, and width of the flushing channel can be changed by modifications of the geometry. The channel attracts the jet and stabilizes the flow structures over the entire surface. For the experiments with drawdown flushing sediments it is considered relevant to know the channel width and depth in order to estimate the gain of the reservoir capacity. Due to the sensitivity of the flow pattern to the boundary conditions, initial conditions, and the geometry (and changes in time), it is difficult to predicate the exact location of the flushing channel.

Trapping and flushing efficiencies

The results and analysis of ten laboratory experiments on trap and flushing efficiencies are presented. The evolution of the sediment trap efficiency in the reservoir was calculated for each experiment. The influence of the characteristics the reservoir geometry as Aspect Ratio AR , Expansion Ratio ER , Expansion area ratio σ , and Expansion density ratio and geometry shape factor SK , on trap and flushing efficiencies were investigated.

Moreover, several empirical formulas to describe the relationship between the reservoir geometry and sediment trap efficiency as well as flushing efficiency for two modes of flushing were developed. Another empirical formula for drawdown flushing describe the function between the geometry shape factor and the channel characteristics which forms during flushing.

6.1 Definition of trap efficiency

The trap efficiency of a reservoir is a measure of the ability of the reservoir to cause deposition of inflowing sediment. It is usually expressed as the percentage of incoming sediment which is trapped by the reservoir. Important factors influencing the trap efficiency are the sediment characteristics, the retention or residence time, and the flow dynamics of the reservoir.

The standard predictor of trap efficiency has been the Brune curve (Brune, 1953), an empirical relationship graphing trap efficiency as a function of average residence time. The average residence or retention time is defined to the capacity-inflow ratio, the reservoir capacity (volume) divided by the average annual inflow (volume per year) of water and sediment, as shown in Figure 2.9 in Chapter 2. The Brune curve gives only a rough estimate of trap efficiency because:

- the capacity-inflow ratio is not very descriptive of flow dynamics.
- no distinction is made as the source or type of the sediment.

Lesser known but more descriptive predictors of trap efficiency are the Churchill curves

(Brune, 1953), empirical relations graphing the percentage of incoming sediment passing through the reservoir (100 percent minus the trap efficiency) as a function of the sedimentation index of the reservoir. This index is defined to be ratio of the average retention time to the average velocity of water within the reservoir; it describes the depositional environment better than the capacity-inflow ratio alone because it includes some reservoir flow dynamics. Moreover, there are two Churchill curves, the distinction being the source of the sediment. One curve describes (100 percent minus) the trap efficiency for sediment produced from the watershed immediately tributary to the reservoir. The other curve describes (100 percent minus) the trap efficiency for sediment produced upstream and which has already passed through one or more reservoirs. If everything else were equal, upstream sediment would be finer than local sediment, and less likely to be trapped.

The trap efficiency of a reservoir is the percentage of incoming sediment which is trapped by the reservoir. In the present study trap efficiency has been calculated from two different measurements variables:

- Volumes of sediment inflow and deposited
- Suspended sediment concentrations at inlet and outlet channel

6.2 Prediction of trap efficiency

The deposited sediment volume as in Eq. 6.1, and suspended sediment concentration SSC as in Eq. 6.2 were used to calculate the trap efficiency TE by two different approaches. The first approach is based on the measured deposited volume at the end of a certain period after the entrance of the sediments. TE was calculated for each experiment at three to five periods. The sediment trap efficiency for the first approach is defined as the ratio between the deposited volume and the basin to the entering sediment volume which was calculated from the known weight of dry sediment in the mixing tank.

$$TE = \frac{V_{dep}}{V_{in}} \quad (6.1)$$

where TE is the sediment trap efficiency, V_{dep} is the deposited sediment volume after a certain period in the basin and V_{in} is the volume of the entering sediments from the inlet channel.

The second approach for calculating TE is based on SSC measurements and is defined as the ratio between SSC released from the basin minus SSC entering and the SSC entering the reservoir in a given period.

$$TE = \frac{C_{in} - C_{out}}{C_{in}} \quad (6.2)$$

where C_{in} is the entering suspended sediment concentration and C_{out} is the released suspended sediment concentration.

6.2.1 Influence of Aspect Ratio AR of reservoir on trap efficiency TE

The trap efficiency varied as a function of the reservoir aspect ratio, AR , as shown in Figure 6.1 with the evolution of TE at six measurement periods.

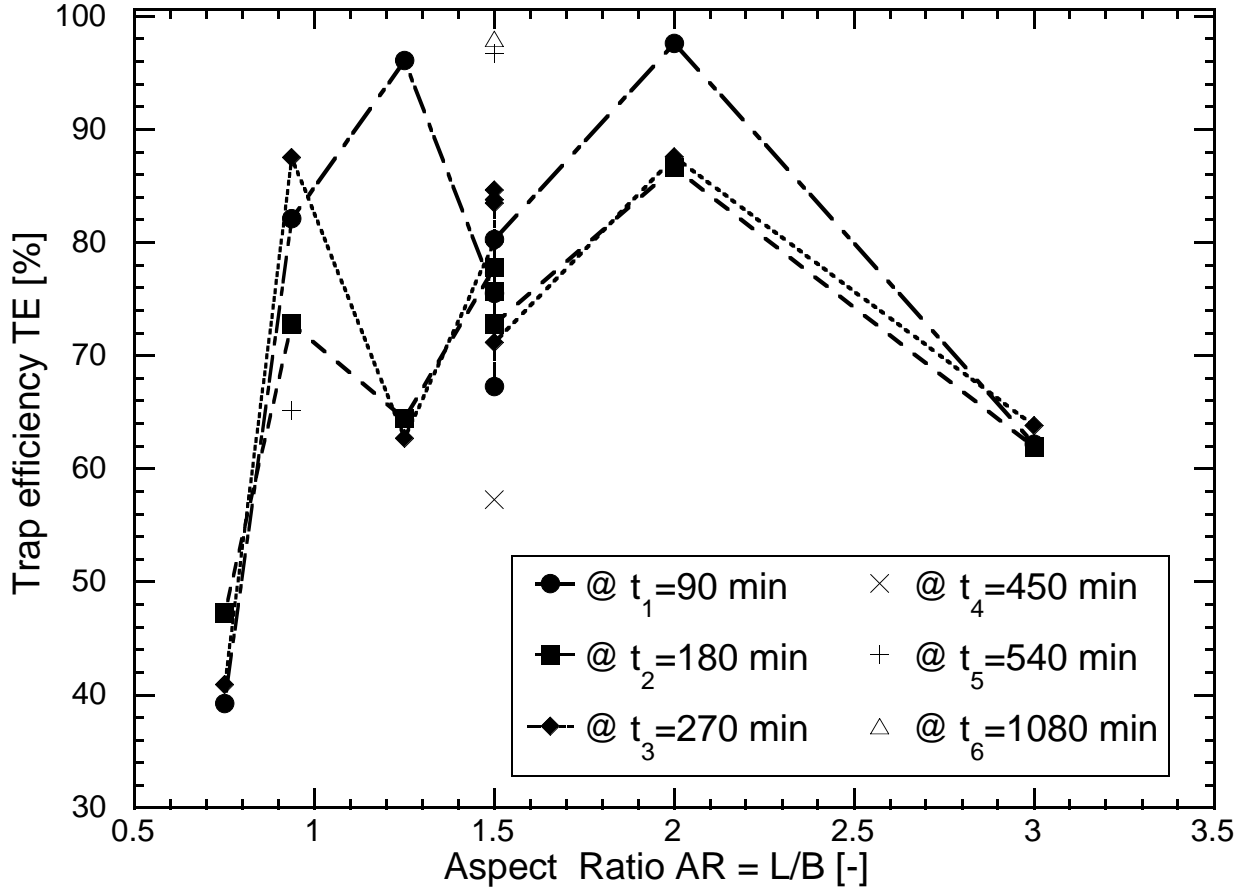


Figure 6.1: Influence of Aspect Ratio $AR = L/B$ on trap efficiency V_{dep}/V_{in} of the reservoir

The trap efficiency is ranging from 110% at t_6 of 1080 minutes ($AR = 1.5$) to 38% at t_1 of 90 minutes ($AR = 0.75$). At the early period $t_1 = 90$ min, two peaks were formed at AR of 1.25 and 2. Trap efficiency is growing with increasing AR and reaches a critical AR . Then it decreases while AR is increasing.

The TE curves at $t_2 = 180$ min and $t_3 = 270$ min have approximately the same trend as for t_1 . Apparently the reservoirs did not reach the equilibrium state and flow pattern was changing during these three periods. The reservoir reached to a quasi equilibrium state during the longest test duration $t_6 = 1080$ min, since the observed TE passed 100%. Equilibrium is associated with vanishing the cumulative net of sediment concentration but this does not imply that the instantaneous sediment flux vanishes.

It can be concluded that TE increases with increasing reservoir aspect ratio until it reached the peak at TE . Then it decreases with increasing aspect ratio as shown in Figure 6.1.

6.2.2 Influence of Expansion Ratio ER of reservoir on trap efficiency TE

The influence of the Expansion Ratio ER on the trap efficiency TE is illustrated in Figure 6.2. The evolution of the trap efficiency is compared for six different runs at 90, 180, 270, 450, 540, and 1080 minutes. Several data points are located at $ER = 16$ which indicated that expansion ratio is not representative for geometries with a fixed width and variable length.

Trap efficiency increases with increasing ER till it reaches $ER = 12$ where TE is almost 100%. The minimum TE was obtained for a basin with $ER = 16$. For higher ER , the trap efficiency decreases again.

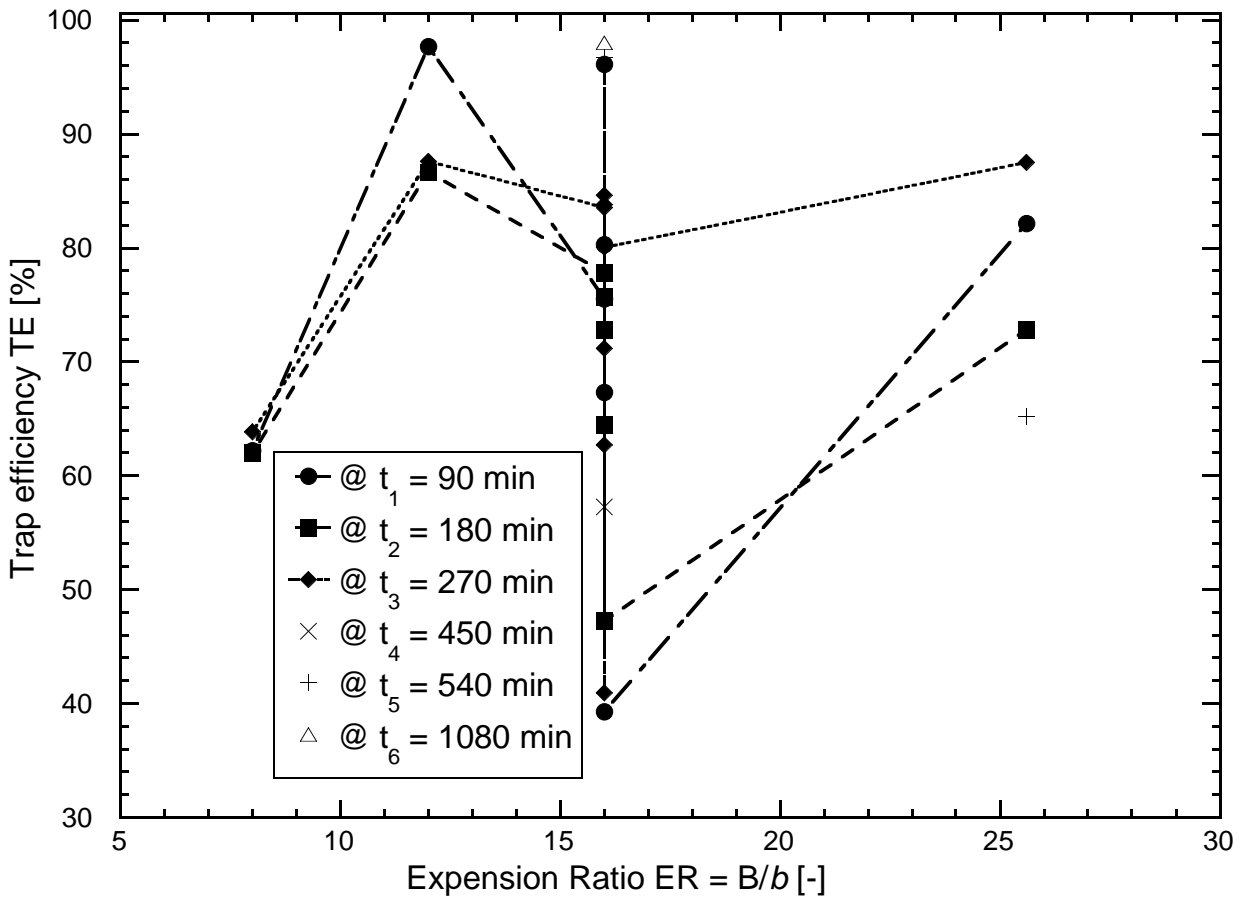


Figure 6.2: Influence of Expansion Ratio $ER = B/b$ on trap efficiency of reservoir V_{dep}/V_{in}

There is no significant changes of TE evolution for narrow reservoirs with low of $ER = 8$. In contrast, trapped rates were reduced by 15% by increasing ER .

6.2.3 Influence of normalized expansion area $\sigma = A_{exp}/A_t$ on trap efficiency TE

The effect of expansion area ratio is defined as ratio of expansion to total areas. Its influence on TE is shown on Fig. 6.3.

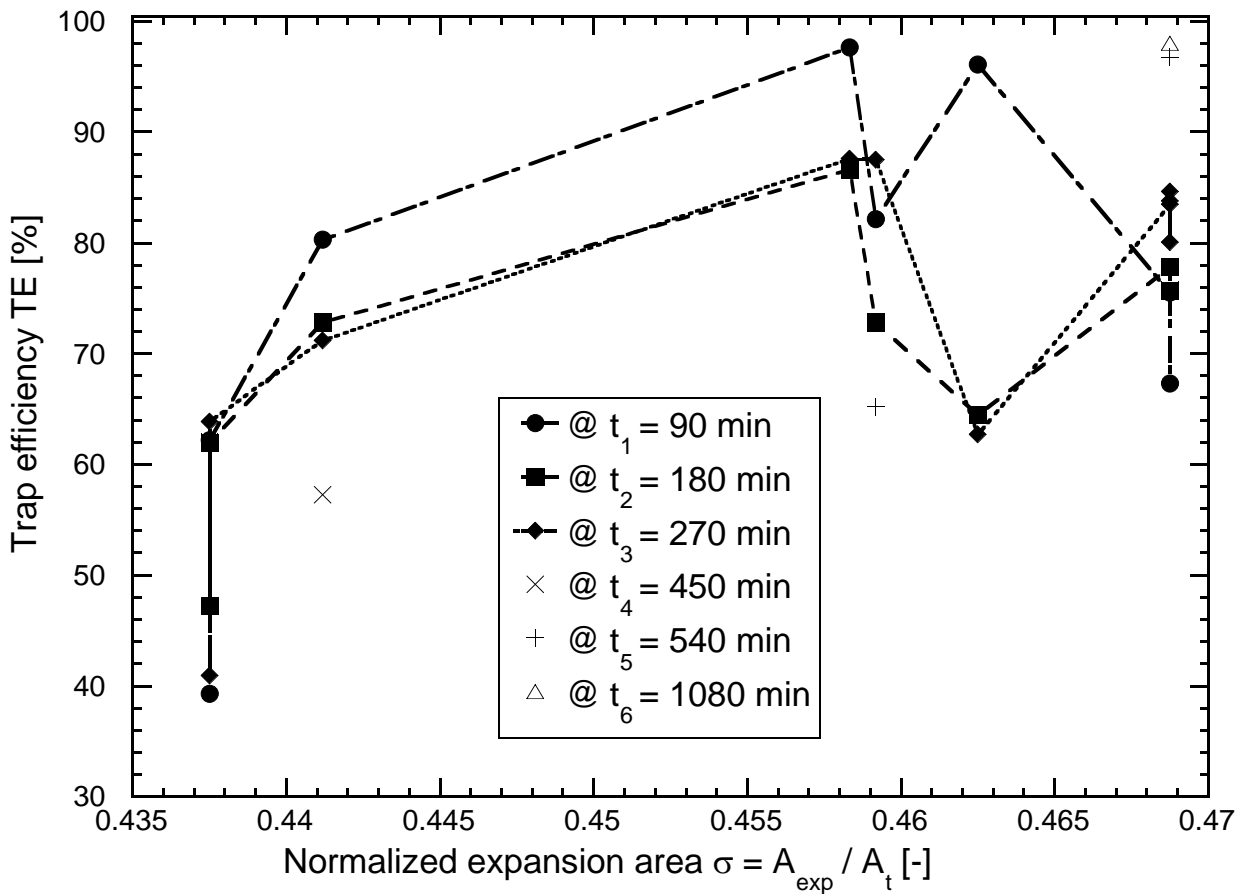


Figure 6.3: Influence of expansion area ratio $\sigma = A_{exp}/A_t$ on trap efficiency of reservoir V_{dep}/V_{in}

At the first period $t_1 = 90min$, trap efficiency increases with increasing expansion area ratio σ until a maximum value of almost 100% is obtained. Then it decreases again for higher expansion area ratio. Almost the same trend was found at t_2 and t_3 as well.

Nevertheless, it is believed that trap efficiency has a proportional trend with expansion area ratio.

6.2.4 Influence of expansion aspect ratio $AR_{exp} = L/\Delta B$ on trap efficiency TE

The evolution of trap efficiency as a function of expansion aspect ratio $AR_{exp} = L/\Delta B$ was investigated as shown in Figure 6.4. Trap efficiency increased with increasing expansion aspect ratio, which can be defined as the ratio of expansion length to the expansion width. It reaches a maximum TE at $AR_{exp} = 3.2$ before it decreases again with for higher AR_{exp} .

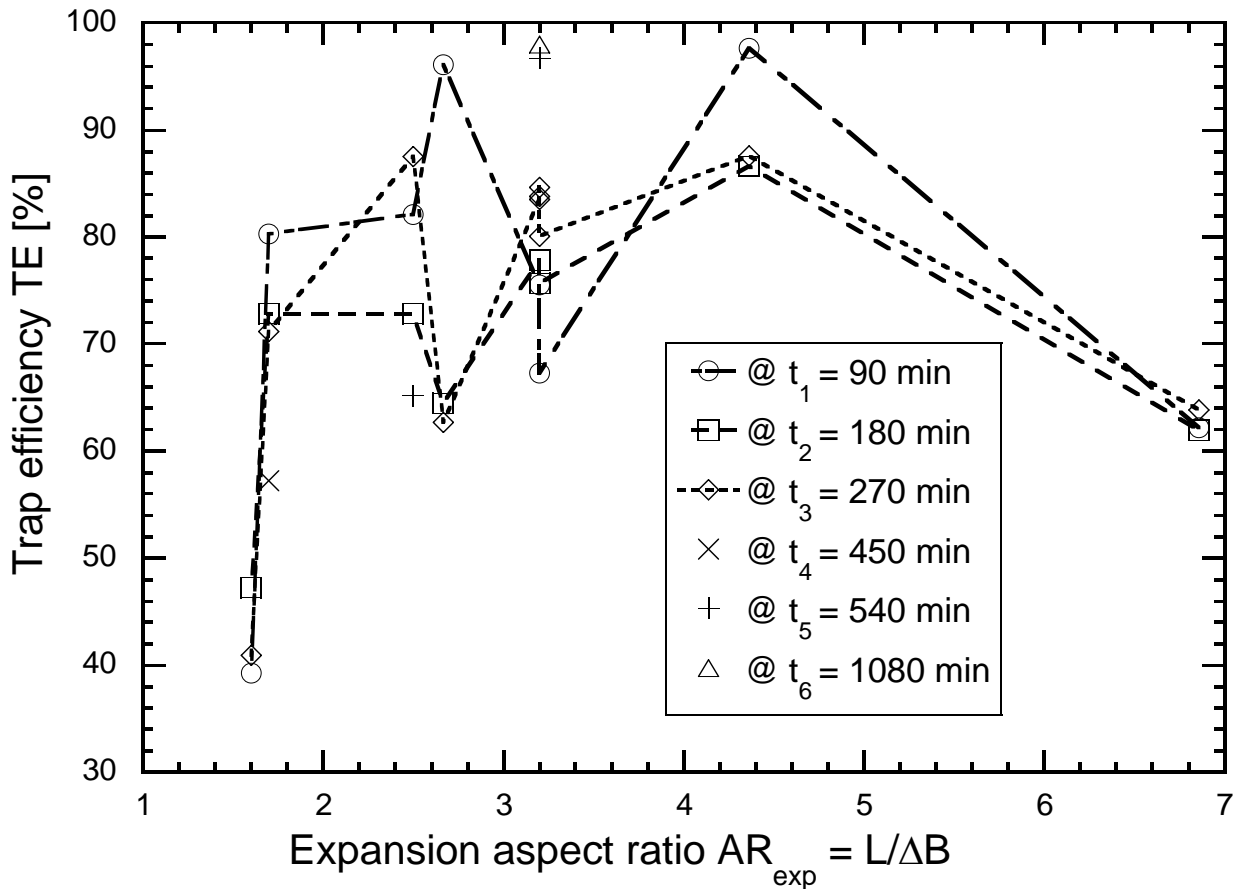


Figure 6.4: Influence of expansion aspect ratio $AR_{exp} = L/\Delta B$ on trap efficiency of reservoir V_{dep}/V_{in}

The trap efficiency after $t_1 = 90$ min raised to a peak, afterwards it reduced by almost 15%. then apparently increased again to asymptotically reaching 100% before decreasing again with further increase of expansion aspect ratio. In the second and third runs the second rise in trap efficiency originated from $AR_{exp} = 2.65$ as shown in Figure 6.4.

6.2.5 Influence of geometry shape factor SK on trap efficiency TE

The before analyzed non-dimensional geometrical parameters (AR , ER , σ , and A_{exp}) did not show a clear influence on trap efficiency when considering each parameters alone. Therefore a set of several combination of these parameters were used and checked versus trap efficiency. It was found that geometry shape factor SK has a great influence on most of the dimensionless results parameters e.g., trap efficiency, storage losses percentage, sedimentation index, and silting intensity as well.

The geometry shape factor SK is defined as the $SK = \frac{P}{\sqrt{A_t}} \cdot AR \cdot D_{exp}$; where P is the wetted perimeter of the length of the side walls, and $AR = L/B$ is the aspect ratio. L and B are length and width, A_t is the total surface area of the basin, D_{exp} is the expansion density $D_{exp} = R/\Delta B$ where R is the distance from the edge of channel to the edge of the basin.

Figures 6.5(a) and (b) show a comparison of geometry effect on trap efficiency calculated from (two approaches) sediment volume and suspended sediment concentration measurements, respectively. In these figures the evolution of trap efficiency for both approaches and its relationship with geometry shape factor was depicted.

It is clearly visible in Figure 6.5(a), that TE decreases with increasing geometry shape factor. The evolution of trap efficiency is increased with time and it reached quasi equilibrium during the last period of last run. There is some differences from sediment volume and suspended sediment measurements approaches arises due to the closed hydraulic circuit which was used for reduced reservoir width experiments. These differences mainly due to the inflow suspended sediment concentration was higher due to very fine particle which could not deposited at the settling basin.

An empirical relationship between trap efficiency and geometry shape factor SK was developed from all experiments and measurements results in Eq. 6.3:

$$TE = \frac{V_{dep}}{V_{in}} = 95 - 360 \cdot SK^{-2} - 12 \cdot \left(\frac{SK}{10}\right)^3 \quad (6.3)$$

The application range of Eq. 6.3 is $2.92 < SK < 13.42$.

The normalized time t/t_s effect on tap efficiency TE for all experiments geometry shape factor SK , were investigated and depicted each geometry separately in Figure 6.6. Where t/t_s is the normalized time of the suspended sediment inflow by t_s the time of settling sediment velocity. It is clearly visible that the smaller geometry shape factor trapped less sediments and the evolution of trap efficiency can be approximated by a fitting decreasing curve as shown in Figure 6.6 for $SK = 2.92$. It can be conclude that the distance between inlet and outlet of the reservoir has a great influence of trap efficiency. Therefore, it is favorable when you design a reservoir to select a short distance between inlet and outlet.

By increasing SK to 3.41 trap efficiency increased by almost 35% and the evolution curve has S shape with decreasing tendency at the end of the experiment. With further increasing for geometry shape factor still trap efficiency increases as shown in Figure 6.6

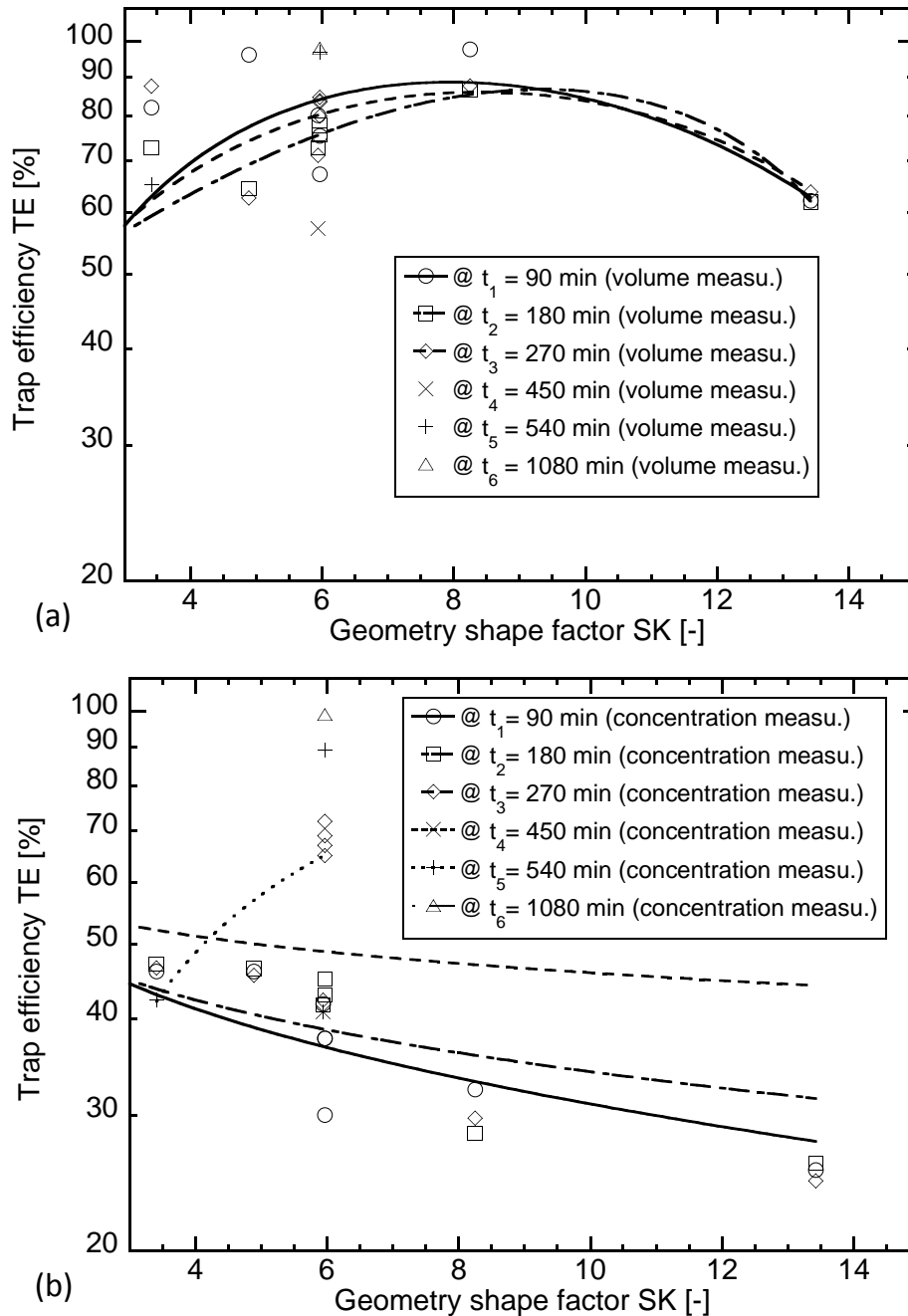


Figure 6.5: Influence of geometry shape factor SK on the trap efficiency TE calculated from (a) volume measurements approach (b) (a) suspended sediment concentration measurements approach

at t_1 and SK of 4.89. Moreover, the evolution of trap efficiency still decreasing same as the geometries has low SK . In contrast the tendency increased with further increasing of geometry shape factor SK of 5.97, 8.25, and 13.42 as shown in Figure 6.6.

It is clearly visible that the evolution tendency of TE depends on geometry shape factor and it could be classified and linked with the type of jet flow as shown in Figure 6.7.

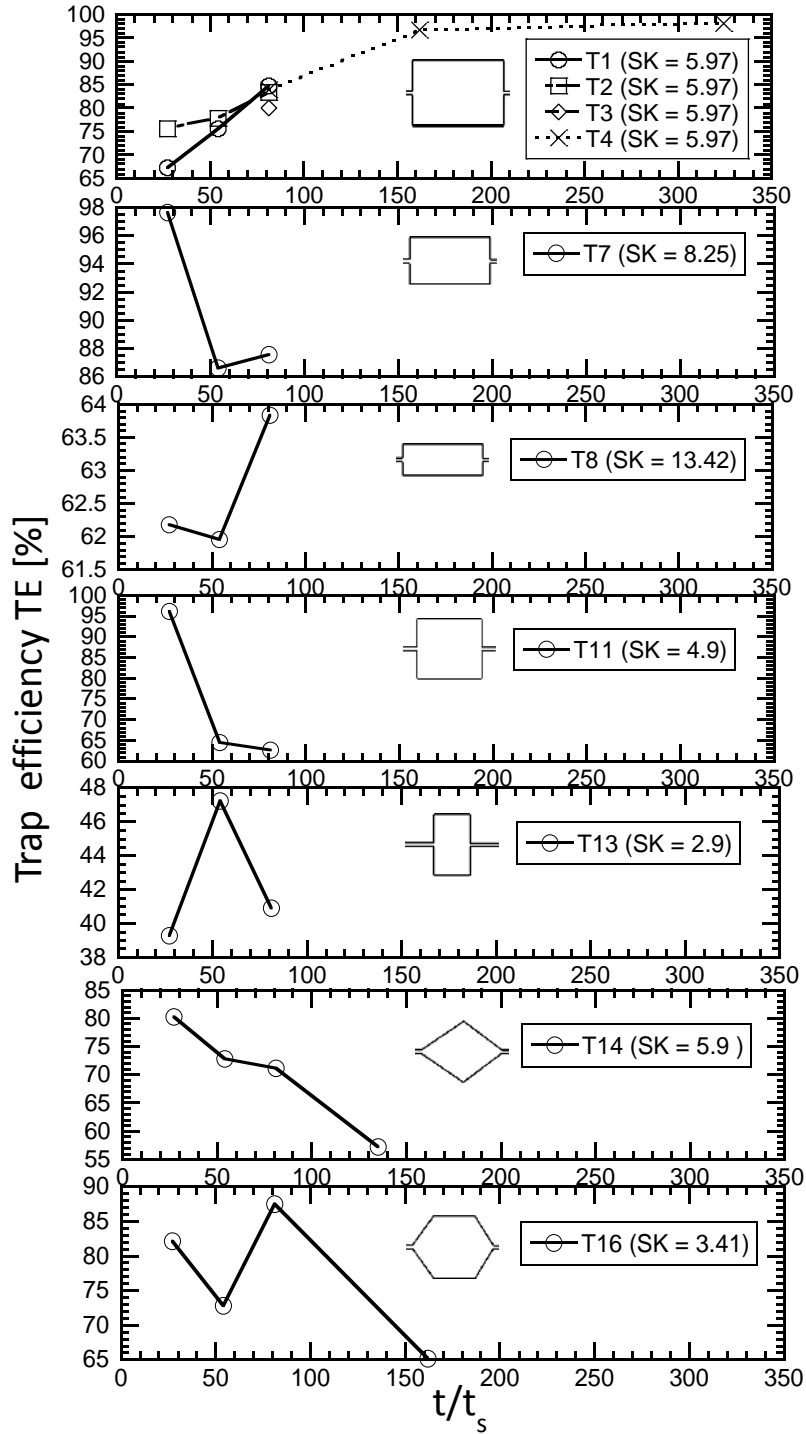


Figure 6.6: Influence of normalized time t / t_s on trap efficiency of various geometry shape factor SK

According to the discussed results of all experiments of different time period the evolution of trap efficiency can be classified to different curves as shown in Figure 6.7. The evolution of trap efficiency has increased and decreased tendencies according to the geometry shape

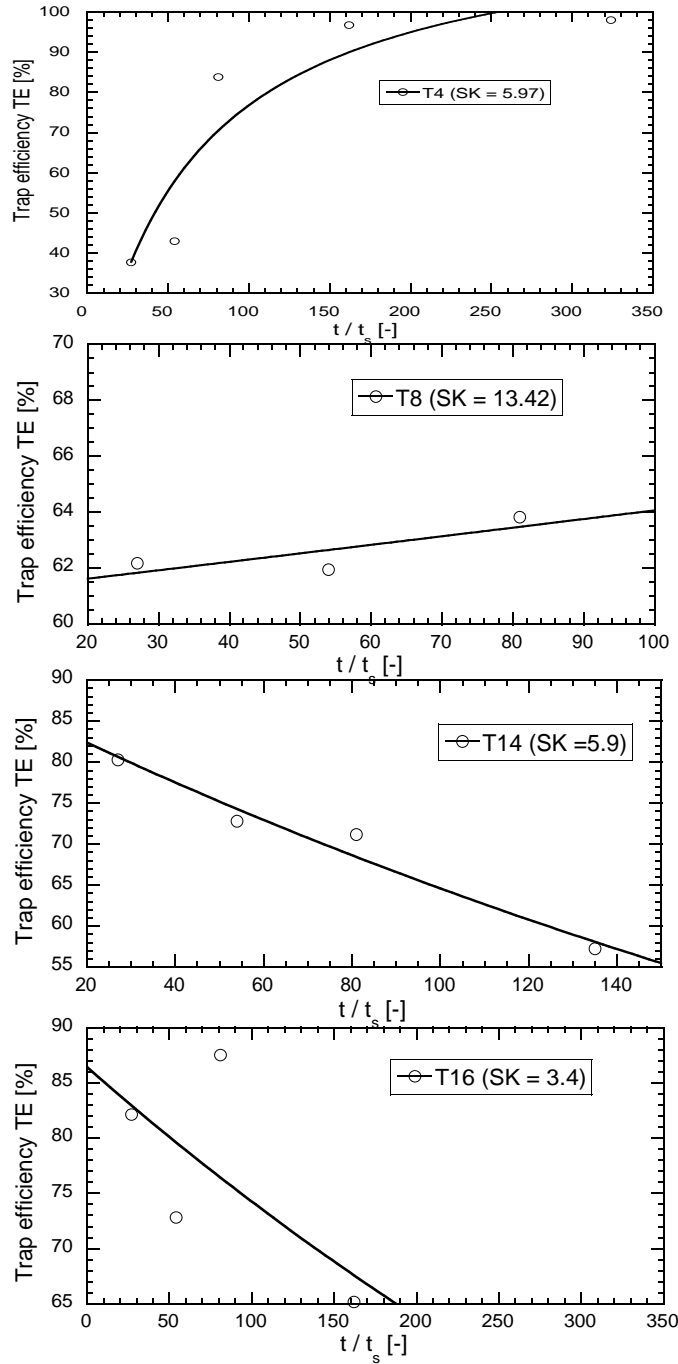


Figure 6.7: Classification of the evolution tendency of trap efficiency curve according to geometry shape factor SK

factor and jet flow type as well. The increasing tendency of the evolution curve was found for geometries with $SK > 5.5$, and decreasing one for $SK < 5.5$ as shown in Figure 6.7. It has to be said that most of these curves were representing a short periods of 270 minutes, except for three experiments with long run tests (experiments with SK of 5.97, 3.41 and 2.92).

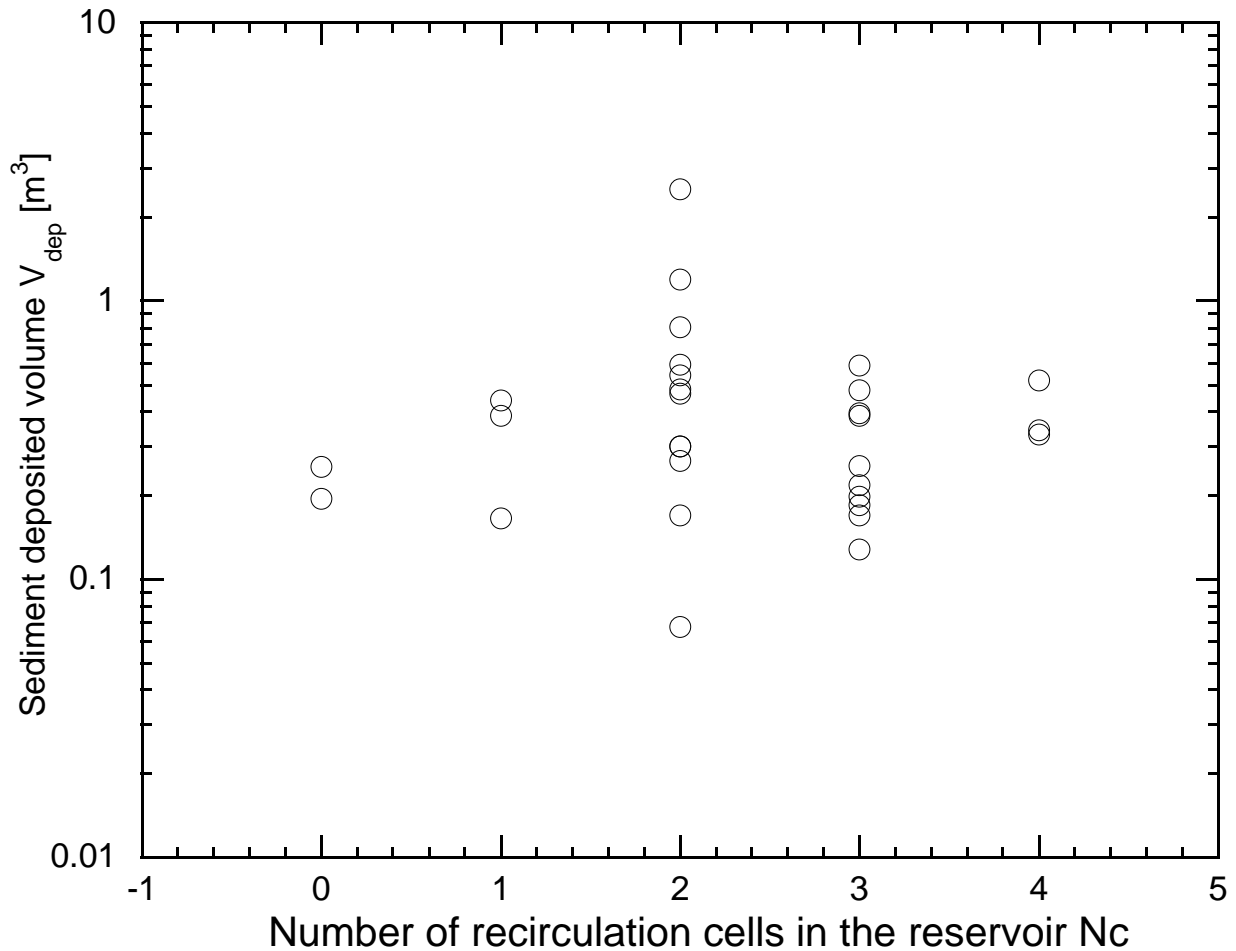


Figure 6.8: Relationship between number of flow recirculation cells and deposited volume

It is believed that the number of recirculation cells which exist with the flow pattern are in accordance with the flow and sediment deposition behavior as shown in Figure 6.8. By increasing the number of recirculation cells (number of eddies) accompanied the flow pattern, the deposited volume increased. So with no recirculations and if flow was straight from inlet to outlet, the minimum deposited volume was obtained as shown in Figure 6.8. Either with one or three recirculation cells the deposited volume was less and it increased with number of recirculation cells of 2 or 4. It can be concluded that a low or an odd number of circulation cells are preferable to reduce the deposit of sediments.

A long run test for reference geometry shape factor of 5.97 was carried out until the quasi equilibrium state was reached this. The total duration of the test was 1080 minutes. The evolution of the trap efficiency for reference test is shown in Figure 6.9.

Evolution of trap efficiency with time can be approached by the following empirical Eq. 6.4 was defined from the results in Figure 6.9. The application range of Equation 6.4 is $27 \leq t/t_s \leq 324$

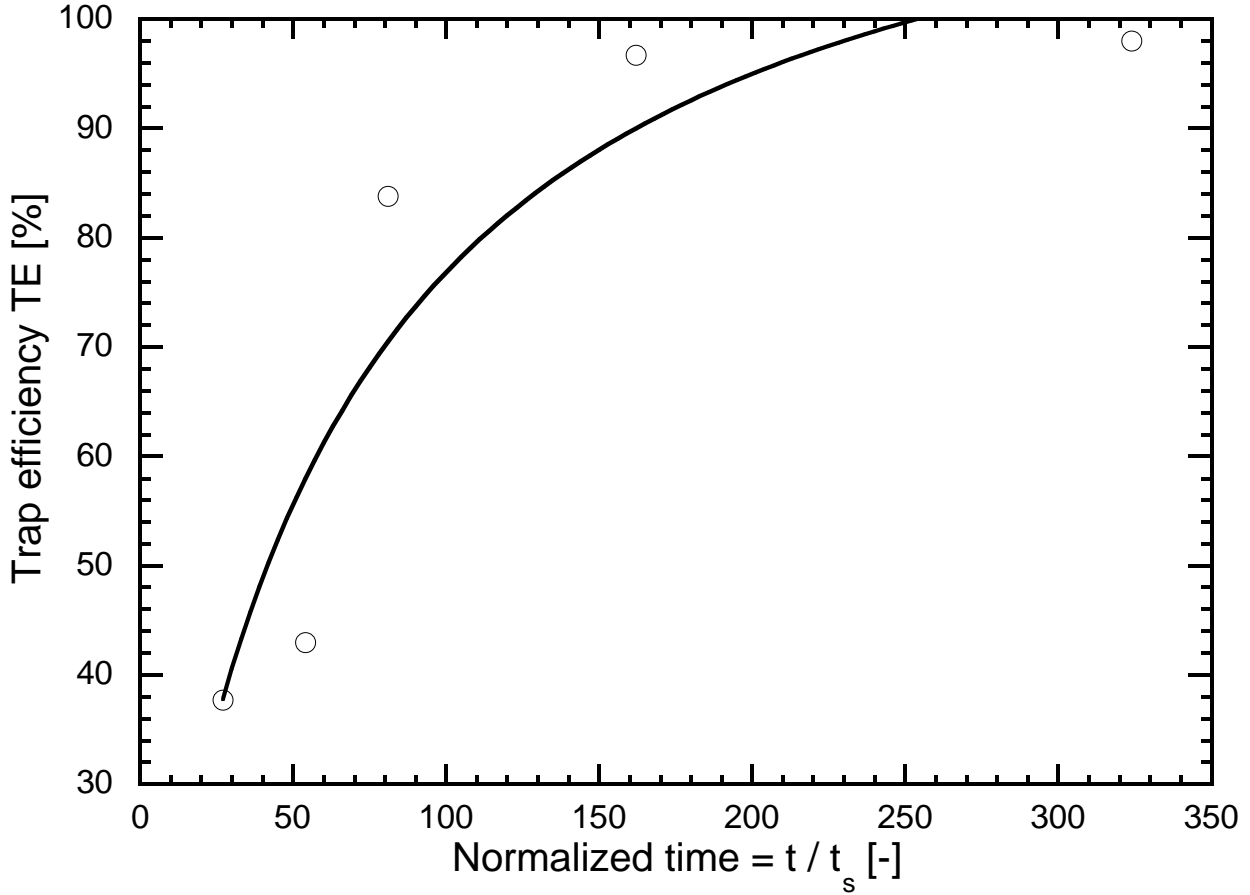


Figure 6.9: The evolution of trap efficiency for the long run test of 1080 minutes for the reference geometry with $SK = 5.97$ with normalized time t/t_s

$$TE = \frac{120 \cdot (t/t_s)}{58 + (t/t_s)} \quad (6.4)$$

where TE is the trap efficiency in percentage and normalized time is ratio of duration of suspended sediment inflow to the actual residence time t/t_r .

As expected time is an important parameter which affects the trap efficiency as illustrated in Figure 6.9. Hence, time effect should be considered when determining the trap efficiency of a reservoir geometry influenced by suspended sediments. Therefore, the following empirical formula Eq. 6.5 was developed to predict the trap efficiency by combination of the geometry shape factor and ratio of running to actual residence times t/t_r .

$$TE = \frac{C_{in} - C_{out}}{C_{in}} = 13.5 - 0.055 \cdot (t^*) + 1700 \cdot SK^{-2} \cdot \left(1 + 0.72 \cdot \ln \frac{SK}{10}\right) \quad (6.5)$$

where TE is the trap efficiency at specific time $t^* = t/t_r$ and geometry which is represented by shape factor SK . The application range of Eq. 6.5 is $2.92 < SK < 13.42$ and $8 \geq t^* \leq 200$.

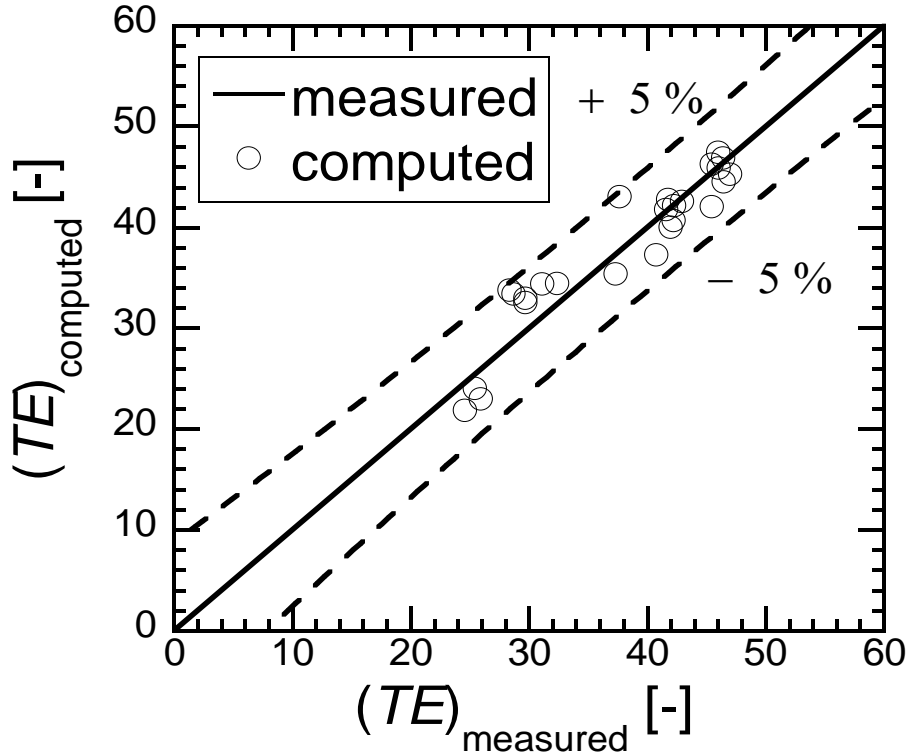


Figure 6.10: Relation for the trap efficiency TE with SK , t^* and , Eq. 6.5) and comparison with measured values. The 95 % confidence interval is ± 0.49 .

In Figure 6.10 Equation 6.5 is presented and compared with measured trap efficiency TE .

6.2.6 Influence of relative residence time t_r/t_s on trap efficiency TE

A strong link seems to exist between actual residence time, trap efficiency and geometry shape factor. Therefore, the settling time was used to normalize the residence time. A statistical evaluation of the dimensionless relative residence time t_r/t_s , and geometry shape factor SK as two independent parameters and the trap efficiency as dependent parameter was performed to find a relationship between these three parameters. The obtained relationship is:

$$TE = \frac{V_{dep}}{V_{in}} = 30 + 11.2 \cdot \frac{t_r}{t_s} + 32.5(SK/10)^3 \cdot (1 - 2.85 \ln(SK/10)) \quad (6.6)$$

where TE is the trap efficiency in percentage, t_r , is the residence and t_s the settling time, and SK is the geometry shape factor.

6.3 Influence of geometry shape factor SK on reservoir Sedimentation Index SI

As already mentioned, the trap efficiency of a reservoir is the percentage of incoming sediment which is trapped by the reservoir. The standard predictor of trap efficiency is the Brune curve, expressing trap efficiency as a function of the capacity-inflow ratio of the reservoir. If the average flow velocity of water in the reservoir is known, then the sedimentation index of the reservoir can be calculated. Then the less well known but more descriptive Churchill curves can be used to predict the trap efficiency. Churchill's curves have not been revised since their introduction in 1948, even though more data are available than what were used originally. Moreover, Churchill curves do not consider the geometry effect. Therefore the influence of the reservoir geometry and the dimensionless time on the the sedimentation index was analyzed as shown in Figure 6.11.

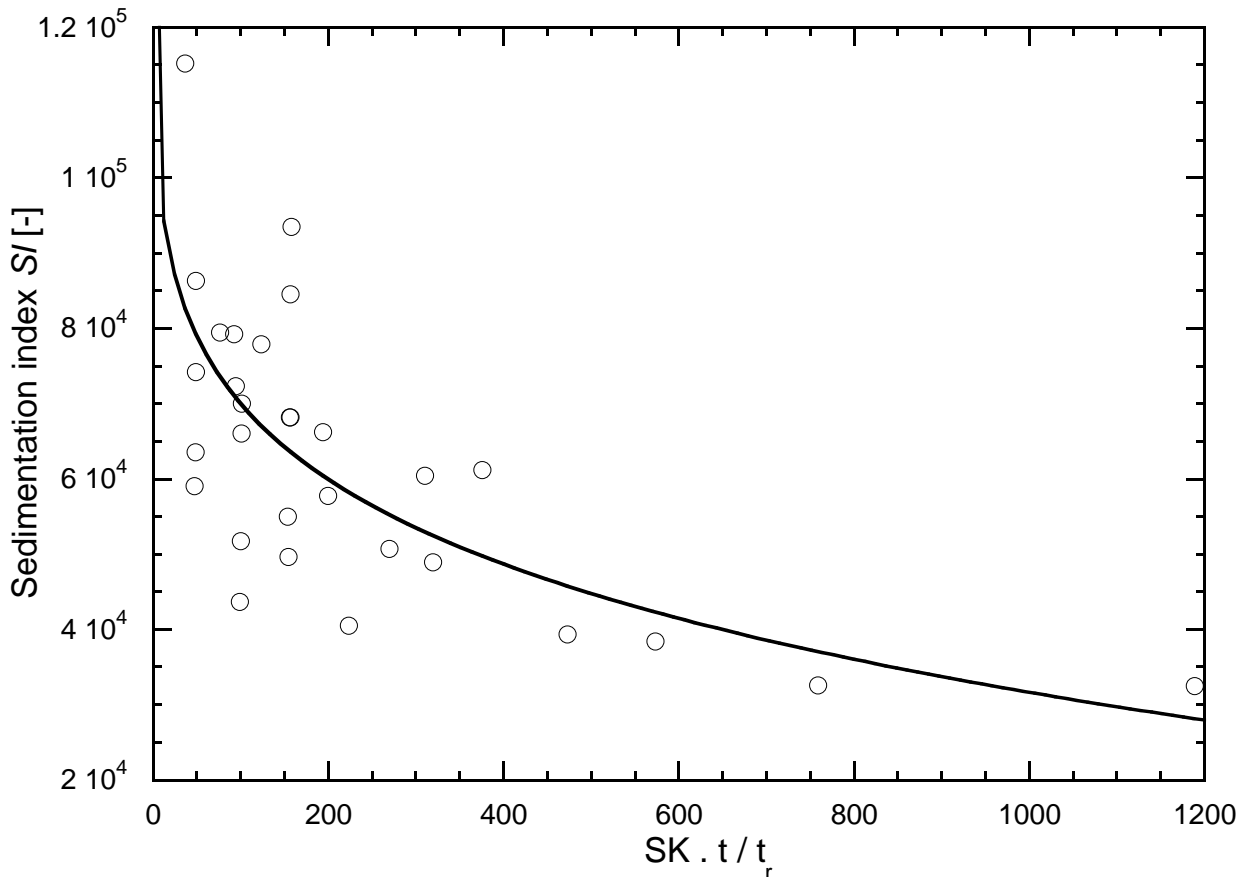


Figure 6.11: The influence of geometry shape factor and sedimentation index.

$$SI = g \frac{t_r}{U_{res}} = 80076 - 47766 \cdot \sqrt{\frac{SK \cdot (t/t_r)}{1000}} + 28 \cdot \left(\frac{SK \cdot (t/t_r)}{1000}\right)^{-2} \quad (6.7)$$

where SI is the sedimentation index which is defined as $g \frac{t_r}{U_{res}}$ where t_r is the residence time, U_{res} is the average velocity in the reservoir, t/t_r is ratio of t the reservoir running period to t_r the reservoir residence time at the same period, and SK is the reservoir geometry factor. The application range of Eq. 6.7 is $8 < t/t_r < 200$ and $2.92 < SK < 13.42$.

6.4 Influence of sedimentation index SI on sediment release efficiency RE

The relationship between the percent of sediments passing through a reservoir and its sedimentation index SI has been produced in (Eq. 6.8) and the curve is shown in Figure 6.12.

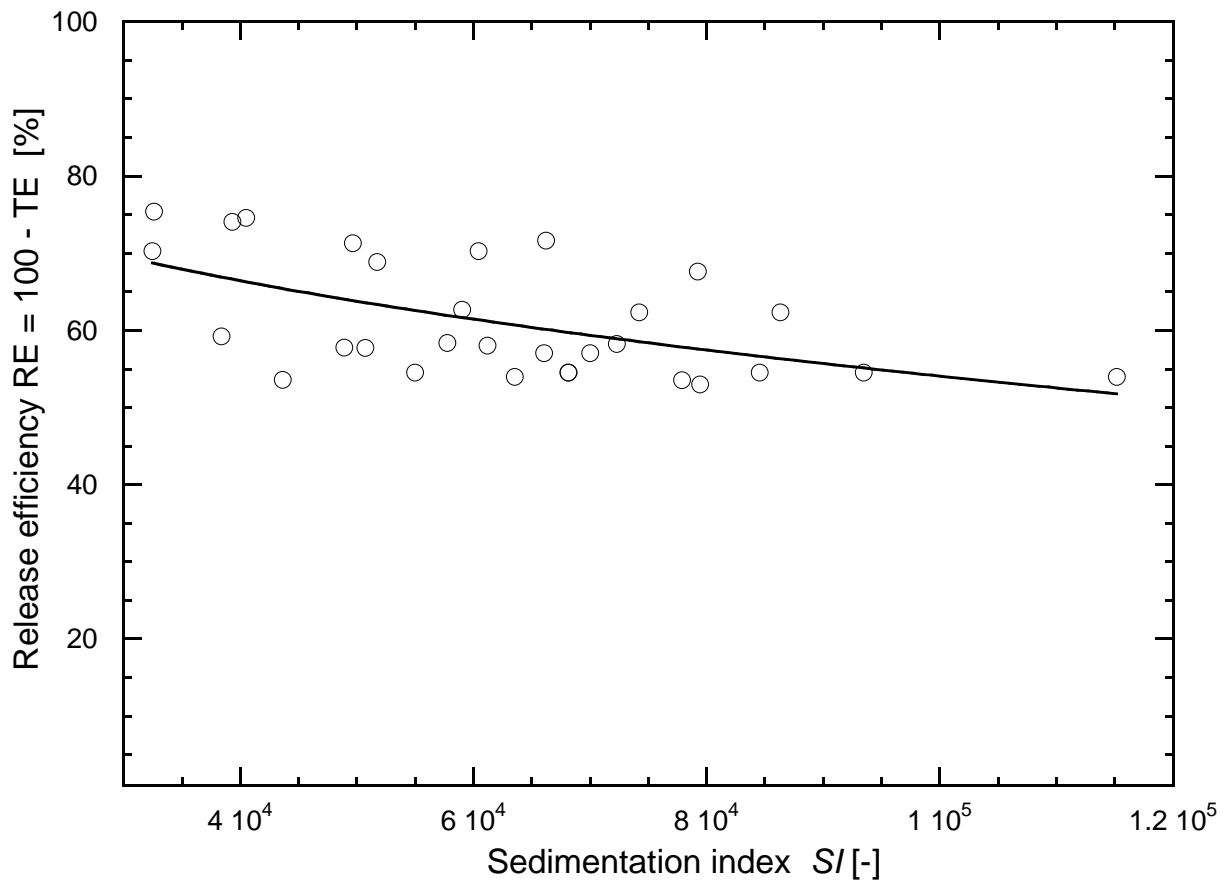


Figure 6.12: The influence of the sedimentation index on the release efficiency RE of the reservoir.

$$RE = 74 - 0.0002 \cdot SI \quad (6.8)$$

where SI is the sedimentation index which is defined as $g \frac{t_r}{U_{res}}$ where t_r is the residence time, U_{res} is the average velocity in the reservoir, RE is percent of sediment released from the reservoir $RE = 100 - TE$. The application range of Eq. 6.8 is $50718 < SI < 86340$ and $2.92 < SK < 13.42$.

6.5 Prediction of flushing efficiency

Efficiency of flushing of suspended sediment through the reservoir is important to determine the feasibility of flushing operations according to the designed reservoir. In the present study, measured data for each run were recorded after one time of a flushing with clear water was performed during two days. With the total cumulative deposited sediment at the end of each experiment and the volume of flushed sediments during this procedure, flushing efficiency, FE, is defined as:

$$FE = \frac{V_{flushed}}{V_{df}} \quad (6.9)$$

where $V_{flushed}$ volume of flushed sediment with clear water after two days, V_{df} total cumulative deposited volume after a specific period.

6.5.1 Free flow flushing

Figure 6.13 shows the correlation between efficiency of free flow flushing with normal flow depth and the geometry shape factor. With increasing the geometry shape factor SK the free flow efficiency increases as it can be seen in Fig 6.13.

The flushing efficiency is fairly low with a maximum value of 10% for the most narrow reservoir with SK of 13.42. Qualitatively, it was found that almost all of the removed sediment from the final deposited one was flushed out in the one third of the flushing duration.

The developed correlation from Figure 6.13 between free flow flushing efficiency and geometry shape factor SK can be approached by Eq. 6.10 and the application range is $2.92 < SK < 13.42$.

$$FE = 0.81 + 0.47 \cdot SK \quad (6.10)$$

6.5.2 Drawdown flushing

Flushing efficiency is an index to describe the effectiveness of hydraulic flushing. With lowering the water depth in the reservoir to half of the normal water depth, the efficient drawdown flushing as a function of geometry shape factor were plotted in Figure 6.14.

It was observed that the drawdown flushing efficiency increases with higher geometry shape factor. The drawdown flushing was higher compared to the free flow flushing. The minimum flushing efficiency was 20% for the largest geometry shape factor. Additionally,

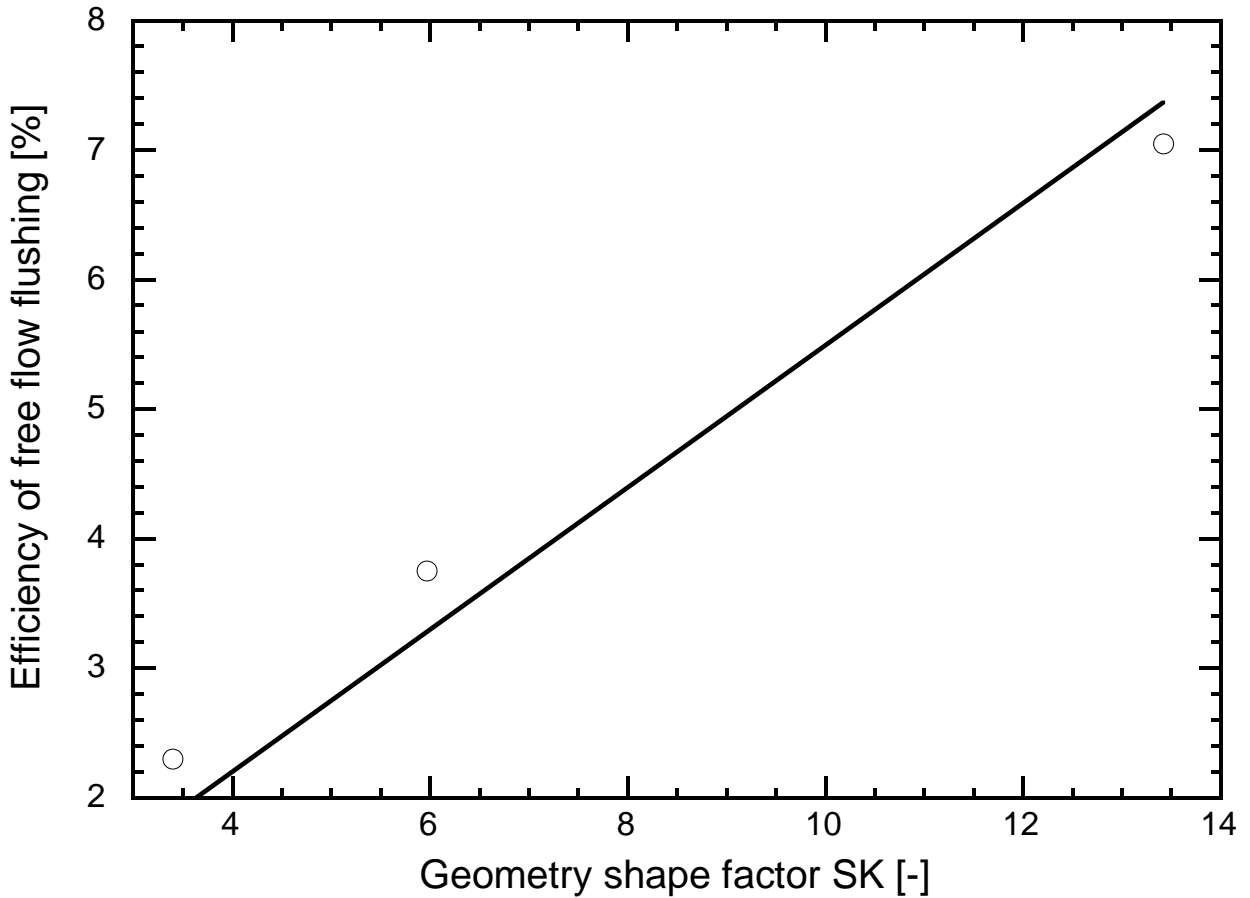


Figure 6.13: Influence of geometry shape factor on the efficiency of free flow flushing

the maximum drawdown flushing efficiency reached almost 65% for the highest geometry shape factor as shown in Figure 6.14. It was found qualitatively that almost fifty percent of the total volume removed sediments were flushed out in the one fourth of the flushing duration.

Drawdown flushing efficiency was correlated with the geometry shape factor the empirical relationship formula in Eq. 6.11. The application range of Eq. 6.11 is $2.92 < SK < 13.42$.

$$FE = \frac{V_{flushed}}{V_{dep}} = 103 + 12.4 \cdot (SK/10)^{-2} - 65.75 \cdot (SK/10)^{-1} \quad (6.11)$$

6.5.2.1 Characteristics of the channel forming during drawdown flushing

Several geomorphic studies indicated that the width of the channel and flow discharge are significantly correlated. In the present study the discharge was constant and only the geometry shape was changing. Therefore, an empirical relationships between the characteristics of the flushing channel (width, and length) and geometry shape factor SK were developed.

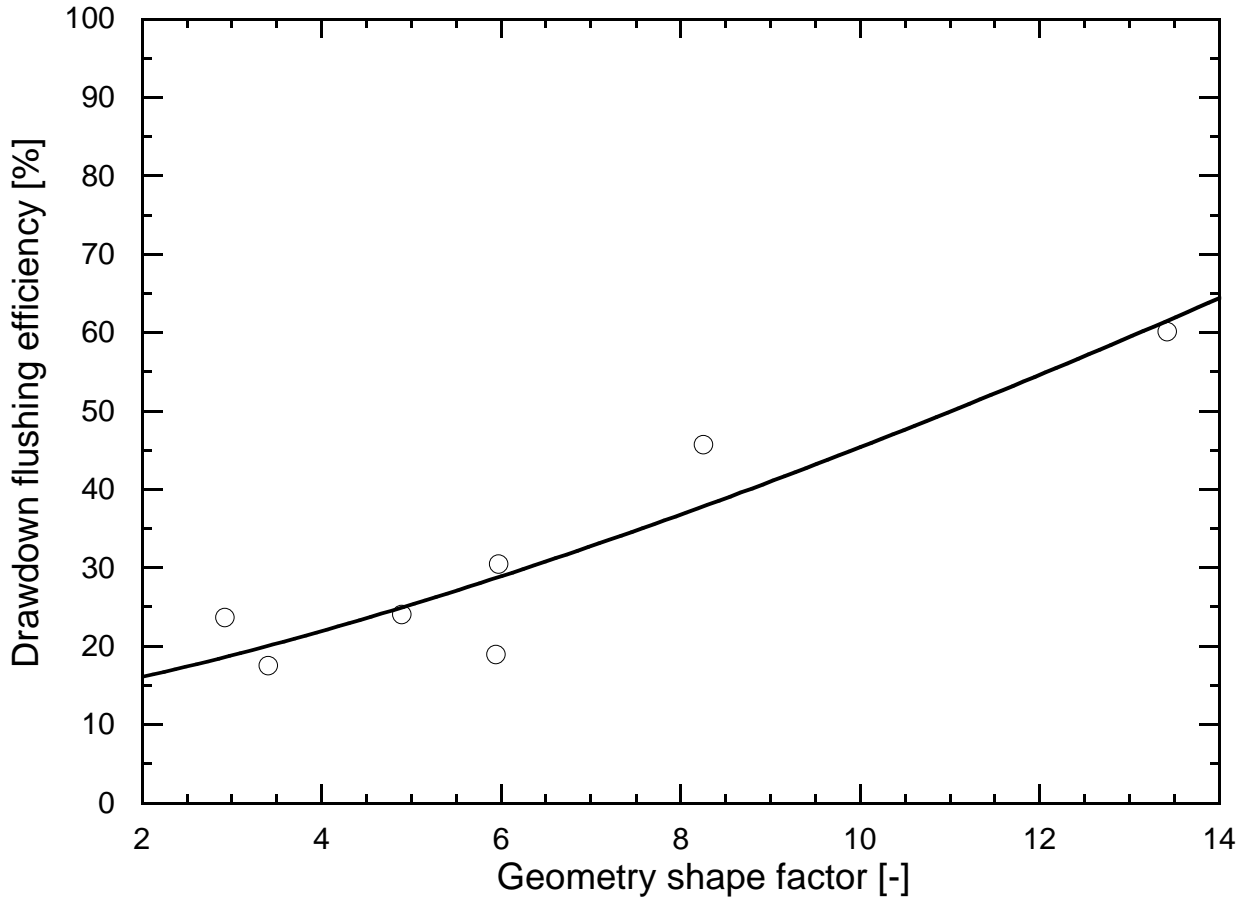


Figure 6.14: Influence of the geometry shape factor on efficiency of the drawdown flushing

A simple empirical equation (Eq. 6.12) was developed to predict the flushing channel width for a specific geometry. The width of the drawdown flushing channel b_{eff} was normalized by the width of the inlet channel b .

$$\frac{b_{eff}}{b} = 2.81 + 800 \cdot SK^3 \cdot (4.375 \cdot \ln(SK/10) - 1) \quad (6.12)$$

where b_{eff} is the width of the flushing channel, b is the inlet channel width, and SK is the geometry shape factor.

To predict the flushing length l_{eff} which was normalized by the inlet channel width b as was a function of geometry shape factor of the basin the following empirical relationship could be obtained from the experiments

$$\frac{l_{eff}}{b} = 26.85 + 6430 \cdot SK^2 \cdot (1 - 0.074 \cdot SK) \quad (6.13)$$

where l_{eff} is the length of the flushing channel, b is the inlet channel width, and SK is the geometry shape factor.

Furthermore the measured channel characteristics l_{eff} and b_{eff} could be fitted by a empirical relationship depending on the geometry shape factor as well. Before that the area of flushing channel was normalized by the total surface area of each tested experiments as $\Delta A = \frac{A_{fc}}{A_t}$, where $A_{fc} = b_{eff} \cdot l_{eff}$ and A_t is the total area of the reservoir. The obtained equation is:

$$\Delta A = \frac{A_{fc}}{A_t} = -52 + 44.3/(\sqrt{SK/10}) + 24.1 \cdot (SK/10)^3 \quad (6.14)$$

Numerical simulation

7.1 Methodology of numerical study

Preliminary studies were done in which two different codes, namely academic (CCHE2D & WOLF2D) and commercial (FLOW-3D), were applied to simulate the flow and sediment in a shallow reservoir with a rectangular geometry.

After choosing a possible code, simulations were carried out to model the conducted experiments in the laboratory reservoir with different geometries. The results of numerical simulations, with and without sediment, were compared to experiments and the numerical model was calibrated.

7.2 Preliminary simulations

Preliminary simulations were conducted in three steps. As the first step, a preliminary evaluation and comparison of different computer programs (both commercial and academic codes) has been performed before experimental set-up. A *2D* numerical simulation of the hydrodynamics and suspended sediment transport allowed to pre-define the different reservoir geometries to be tested on the physical model. The results showed the complexity of the flow and sediment interaction with the geometry (Kantoush et al., 2005).

After the experimental set-up has been installed and having preliminary experimental results, the second step was carried out. The second step was to model the two-phase flow, using CCHE2D. This code was used to model experiments with Walnut shells. The model was calibrated by results of experimental modeling. The second step results were published in Kantoush et al. (2006a, 2007c).

The third step was to model the flow, using WOLF2D (Dewals, 2006; Erpicum, 2006), developed at the University of Liege and based on an original finite volume scheme. A series of experimental and numerical simulations were done with the objective of testing

the sensitivity to different parameters in the numerical modeling. The influence of the basin geometry on the flow field has been investigated experimentally and numerically. Different options and formulations are analyzed, especially when they concern and influence the length of the basin. For each case the obtained flow pattern comparison from the laboratory measurements and the simulation were compared. The simulations focused on the ability of the numerical model to predict the transition between stable and unstable configurations. The WOLF2D numerical model leads to accurate results for the flow in a number of basin geometries and for various hydraulic conditions (Dewals et al., 2008).

7.2.1 First step: numerical results obtained from simulations with Flow-3D and CCHE2D

7.2.1.1 Model description

Simple reservoir geometry has been simulated in order to study whether the relevant processes can be reproduced mathematically, and what features are controlling the phenomena. The model has been represented by a simple rectangular grid spacing of about 0.10 m in the flow direction and 0.05 m in the transverse direction. A median grain size of $d_{50} = 0.20\text{mm}$ was used to represent the suspended sediment. A suspended sediment concentration of $C = 5.0\text{ kg/m}^3$ has been injected upstream. A total discharges of $Q = 5.0\text{ l/s}$ A flow depth of $h = 0.20\text{ m}$ and a bed roughness $n = 0.01$ have been used as boundary and initial conditions. The FLOW-3D software package is being used to solve for flow, sediment transport, and evolution of sediment concentration in reservoirs, under conditions specified at the boundaries of the numerical domain. FLOW-3D solves the nonlinear Navier-Stokes equations in three-dimensions, and uses the Volume-of-Fluid (VOF) method to track fluid-fluid or fluid-sediment interfaces (Hirt and Nichols, 1981). FLOW-3D incorporates several turbulence closure schemes but these cannot be used with the shallow water module which has been used for the computations.

7.2.1.2 Boundary conditions

The following boundary conditions have been applied to both models:

- Inlet section: Flow and suspended load discharges are prescribed.
- Outlet section: Water surface elevation is assumed to be constant.
- Wall boundary: Total slip condition for flow, and zero normal gradient condition for suspended load is assumed.
- Bottom roughness: Manning's n value of 0.01 has been used for both models.

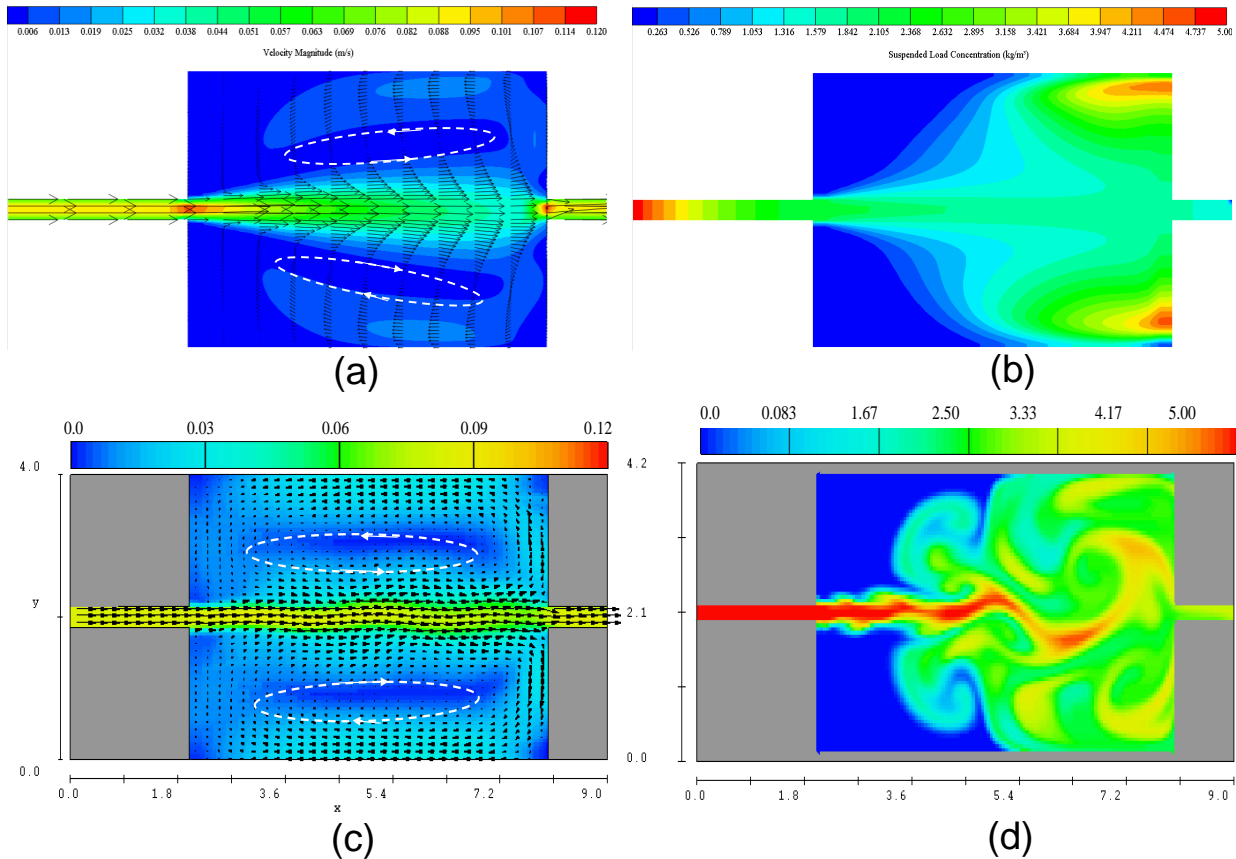


Figure 7.1: Stationary flow field and velocity magnitude computed by (a) CCHE2D, (c) FLOW-3D and suspended sediment concentration computed by (b) CCHE2D, (d) FLOW-3D, for the initial reservoir conditions (plane bed, constant discharge, $\kappa - \varepsilon$).

Figure 7.1(a) presents the stationary flow field obtained by CCHE2D, starting from an initial condition of stagnant water and a plane bed and using a $\kappa - \varepsilon$ closure scheme. The flow pattern was found to agree reasonably with the laminar flow computed by FLOW-3D as shown in Figure 7.1(c). It was found that two large recirculation eddies develop along both sides of the basin. Several scenarios have been simulated with the same geometry and changing the boundary and initial conditions in both programs. Figure 7.1(b and d) show the suspended sediment concentration calculated by CCHE2D and FLOW-3D, respectively. Although both patterns coincide in a general manner, substantial differences can be noticed locally, due to the different flow assumptions made.

Figure 7.2(a and b) present a detailed comparison of suspended sediment concentrations and flow velocity magnitudes computed by both models along the centerline of the flow. Suspended sediment concentrations and flow velocity magnitudes are in good agreement for both models.

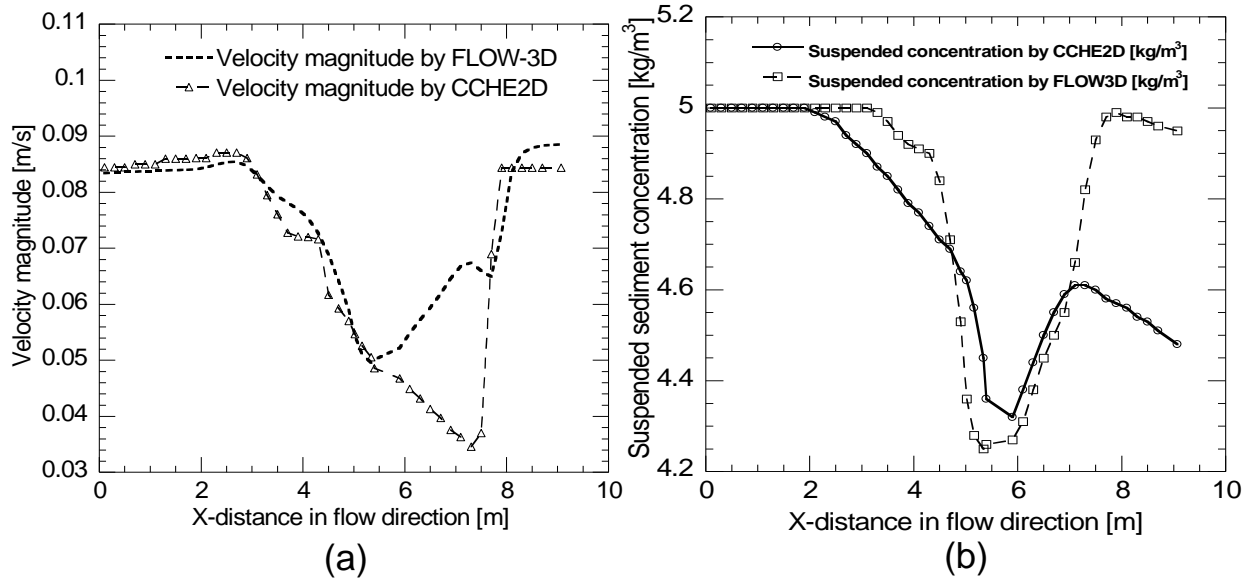


Figure 7.2: Longitudinal section at the basin centerline for (a) velocity magnitude, (b) suspended sediment distributions, computed by CCHE2D and FLOW-3D.

7.2.2 Second step: numerical results obtained by simulations with CCHE2D compared with experiments

For the comparison with the physical experiments the code CCHE2D was used.

A series of numerical simulations is presented and compared with scaled laboratory experiments, with the objective of testing the sensitivity to different flow and sediment parameters and different turbulence closure schemes. Different scenarios are analyzed and a detailed comparison of preliminary laboratory tests and some selected simulations are presented.

The computational model CCHE2D was developed by NCCHE (National Center for Computational Hydroscience and Engineering) and is a depth-integrated 2D hydrodynamic and sediment transport model based on a variant of the finite element method (Jia and Wang, 2001; Wu, 2001). The model is used to predict river flow patterns and related bed and/or bank erosion for both uniform and non-uniform sediment transport. Both depth-averaged $\kappa - \varepsilon$ and eddy viscosity turbulence closures are available. The effects of secondary flow in curved channels on the bed-load direction are modeled, but not the effects on fluid momentum and sediment transport rate. The rate and direction of the bed-load transport is adjusted according to the bed slope.

CCHE2D was used for its capabilities to simulate suspended sediment transport. Suspended transport occurs mostly at a non-equilibrium state and is usually simulated by non-equilibrium transport models. CCHE2D implements a full non-equilibrium transport

model for bed-material load (bed load plus suspended load). Non-equilibrium approaches are proposed for cases where sediment transport occurs mainly as bed load, as suspended load, or as full total load, respectively. Also, the model simulates the transport of non-uniform sediment mixtures with multiple size classes. Several formulas for fractional non-cohesive sediment transport capacity and movable bed roughness are provided.

7.2.2.1 Governing equations

7.2.2.1.1 Hydrodynamic model The depth-averaged model is applicable to shallow water flows and is governed by the depth-integrated continuity and Navier-Stokes equations:

Continuity equation:

$$\frac{\partial Z}{\partial t} + \frac{\partial hu}{\partial x} + \frac{\partial hv}{\partial y} = 0 \quad (7.1)$$

Momentum equations:

$$\frac{\partial u}{\partial t} + u \frac{\partial u}{\partial x} + v \frac{\partial u}{\partial y} = -g \frac{\partial Z}{\partial x} + \frac{1}{h} \left[\frac{\partial(h\tau_{xx})}{x} + \frac{\partial(h\tau_{xy})}{y} \right] - \frac{\tau_{bx}}{\rho h} + f_{cor}v \quad (7.2)$$

$$\frac{\partial v}{\partial t} + u \frac{\partial v}{\partial x} + v \frac{\partial v}{\partial y} = -g \frac{\partial Z}{\partial y} + \frac{1}{h} \left[\frac{\partial(h\tau_{yx})}{x} + \frac{\partial(h\tau_{yy})}{y} \right] - \frac{\tau_{by}}{\rho h} + f_{cor}u \quad (7.3)$$

where u and v are the depth-integrated velocity components in x and y directions, respectively; t is the time; g is the gravitational acceleration; Z is the water surface elevation; ρ is the density of water; h is the local water depth; f_{cor} is the Coriolis parameter; τ_{xx} , τ_{xy} , τ_{yx} and τ_{yy} are depth integrated Reynolds stresses; and τ_{bx} and τ_{by} are shear stresses on the bed surface.

7.2.2.1.2 Sediment transport model A brief introduction of CCHE2D sediment transport is presented here. More details can be found in Wu (2001).

As shown in Figure 7.3, the water depth is divided into two zones: the suspended-load zone and bed-load zone. The thickness of the bed-load zone δ is strictly speaking related to the saltation height of the sediment particles and, hence, a variable. However, to simplify the problem, δ may be taken as twice the sediment diameter (Einstein, 1950). Following this conventional treatment, Figure 7.3 defines the bed-load zone to range from z_b to $z_b + \delta$, and the suspended-load zone to range from $z_b + \delta$ to z_s . Here $\delta = 2d$, and d is the sediment diameter.

In case of non-uniform sediment transport, the sediment mixture can be divided into several size classes. For each size class, the three-dimensional convection-diffusion equation of sediment transport is:

$$(1 - \dot{p}) \frac{\partial z_{bk}}{\partial t} + \frac{\partial(\delta \overline{c_{bk}})}{\partial t} + \frac{\partial q_{bkx}}{\partial x} + \frac{\partial q_{bky}}{\partial y} = -E_{bk} + D_{bk} \quad (7.7)$$

where \dot{p} is the porosity of bed material; c_{bk} is the average concentration of bed load at the bed-load zone; q_{bkx} and q_{bky} , are the components of bed load transport rate in x - and y directions, usually being written as $q_{bkx} = \alpha_{bx} q_{bk}$ and $q_{bky} = \alpha_{by} q_{bk}$; α_{bx} and α_{by} are direction cosines of bed load movement, which is assumed to be along the direction of bed shear stress; q_{bk} is the bed load transport rate of k^{th} size class. The first term on the left hand side of Eq. 7.7 stands for bed change, which results from the sediment exchange between the moving sediment and the bed material.

7.2.2.2 Morphological processes

When the equilibrium transport model is adopted for bed load, the bed change can be calculated from the bed load continuity Eq. 7.7:

$$(1 - \dot{p}) \frac{\partial z_{bk}}{\partial t} + \frac{\partial(\delta h C_{tk})}{\partial t} + \frac{\partial(q_{bkx} + q_{skx})}{\partial x} + \frac{\partial(q_{bky} + q_{sly})}{\partial y} = 0 \quad (7.8)$$

where q_{skx} and q_{sly} are the suspended load transport rates in x - and y -directions, defined by $q_{skx} = U h C_k + \epsilon_s h \partial C_k / \partial x$ and $q_{sly} = V h C_k + \epsilon_s h \partial C_k / \partial y$. Usually the diffusion terms in q_{skx} and q_{sly} are neglected.

When the non-equilibrium transport model is adopted for bed load, the calculation of bed change can be determined by either the bed load continuity equation or the overall sediment continuity Eq. 7.8. The flow field is computed under steady-state conditions, i.e. the velocity difference between two consecutive time steps is less than 1%. Sediment transport is then computed and used to compute erosion and deposition rates, followed by a bed topography update. After this bed topography update the flow field has to be recomputed. Yet, as long as the bed variations are small, the flow field will be very similar. Hence, no direct coupling between flow and morphology is thus accounted for.

7.2.2.3 Initial Conditions

The required initial conditions include the initial channel geometry and initial bed material gradation. For a complete simulation of sediment transport, information on sediment properties, sediment transport capacity, non-equilibrium adaptation length and movable bed roughness should be given. The sediment properties include the sediment grain size, specific gravity (default value: 2.65), grain shape factor (default value: 0.7) and bed material porosity. The sediment transport capacity, non-equilibrium adaptation length and the movable roughness are determined by empirical formulas.

7.2.2.4 Empirical Formulas

Lots of formulas are available for fractional non-cohesive sediment transport. CCHE2D code proposes four sediment transport capacity formulas accounting for the hiding and exposure effects of non-uniform sediment are always considered. The sediment transport capacity is determined by Van Rijn (1984a,b,b) formula, Wu et al. (2000) formula, SEDTRA module (Garbrecht et al., 1995), the modified Ackers and White's formula (Proffit and Sutherland., 1983), or the modified Engelund and Hansen's formula (Wu and Vieira, 2000). The SEDTRA module uses three different formulas to calculate sediment transport capacities for different size ranges: Laursen (1958) formula for size classes from 0.01 to 0.25 *mm*, (Yang, 1973) formula for size classes from 0.25 to 2.0 *mm*, and (Meyer-Peter and Mueller's, 1948) formula for size classes from 2.0 to 50.0 *mm*.

7.2.2.5 Turbulence closure

Two turbulence closures are available in CCHE2D: the eddy viscosity model (parabolic, mixing length models) and the two-dimensional $\kappa - \epsilon$ model (Jia and Wang, 2001, 1999). In equations (2) and (3), the Reynolds stresses are approximated based on the Boussinesq's assumption:

$$\tau_{xx} = 2v_t \frac{\partial u}{\partial x} \quad (7.9)$$

$$\tau_{xy} = v_t \left(\frac{\partial u}{\partial y} + \frac{\partial v}{\partial x} \right) \quad (7.10)$$

$$\tau_{yy} = 2v_t \frac{\partial v}{\partial y} \quad (7.11)$$

7.2.2.5.1 Eddy viscosity model Two zero-equation eddy viscosity models are available in the model. The first one is the Depth-Integrated Parabolic Model (DIPM), in which the eddy viscosity v_t is calculated by the following formula:

$$v_t = \frac{A_{xy}}{6} \kappa U^* h \quad (7.12)$$

where A_{xy} is an adjustable coefficient of eddy viscosity, κ is the von Karman constant, and U^* is the shear velocity. The second eddy viscosity model is the Depth-Integrated Mixing Length Model (DIMLM). The eddy viscosity v_t is calculated by the following equation:

$$v_t = \bar{l}^2 \sqrt{2\left(\frac{\partial u}{\partial x}\right)^2 + 2\left(\frac{\partial v}{\partial x}\right)^2 + 2\left(\frac{\partial u}{\partial x} + \frac{\partial v}{\partial x}\right)^2 + 2\left(\frac{\partial \bar{U}}{\partial z}\right)^2} \quad (7.13a)$$

$$\bar{l} = \frac{1}{h} \int \kappa z \sqrt{\left(1 - \frac{z}{h}\right)} dz = \kappa h \int_0^1 \lambda \sqrt{1 - \lambda} d\lambda \approx 0.267 \kappa h \quad (7.13b)$$

$$\frac{\partial \bar{U}}{\partial z} = C_m \frac{U^*}{\kappa h} \quad (7.13c)$$

where C_m is a coefficient with a value of 2.34375 so that Eq. 7.13 will cover Eq. 7.12 in the case of a uniform flow in which all horizontal velocity gradients vanish.

7.2.2.5.2 Two dimensional $\kappa - \epsilon$ model In this model, differential equations are introduced for the turbulent kinetic energy k and the rate of dissipation of turbulent energy ϵ , where

$$k = \frac{1}{2} \bar{u}_i \bar{u}_i \quad (7.14)$$

and

$$\epsilon = \mu_t \frac{\partial \bar{u}_i}{\partial x_j} \frac{\partial \bar{u}_i}{\partial x_j} \quad (7.15)$$

The depth-integrated governing equations for k and ϵ are:

$$\frac{\partial k}{\partial t} + u \frac{\partial k}{\partial x} + v \frac{\partial k}{\partial y} - \frac{\partial}{\partial x} \left[\frac{v_t}{\sigma_k} \frac{\partial k}{\partial x} \right] - \frac{\partial}{\partial y} \left[\frac{v_t}{\sigma_k} \frac{\partial k}{\partial y} \right] = P - \epsilon + P_{kV} \quad (7.16)$$

$$\frac{\partial \epsilon}{\partial t} + u \frac{\partial \epsilon}{\partial x} + v \frac{\partial \epsilon}{\partial y} - \frac{\partial}{\partial x} \left[\frac{v_t}{\sigma_\epsilon} \frac{\partial \epsilon}{\partial x} \right] - \frac{\partial}{\partial y} \left[\frac{v_t}{\sigma_\epsilon} \frac{\partial \epsilon}{\partial y} \right] = c_{1\epsilon} \frac{\epsilon}{k} - c_{2\epsilon} \frac{\epsilon^2}{k} + P_{\epsilon V} \quad (7.17)$$

where

$$P = \bar{u}_i \bar{u}_j u_{i,j} = v_t \left[2\left(\frac{\partial u}{\partial x}\right)^2 + 2\left(\frac{\partial v}{\partial y}\right)^2 + 2\left(\frac{\partial u}{\partial x} + \frac{\partial v}{\partial y}\right) \right]$$

and

$$P_{kV} = C_k \frac{U^3}{h}, \quad P_{\epsilon V} = C_\epsilon \frac{U^4}{h^2}, \quad U^* = \sqrt{c_f(u^2 + v^2)}, \quad C_k = \frac{1}{\sqrt{c_f}}, \quad C_\epsilon = 3.6 \frac{c_{2\epsilon}}{c_f^{3/4}} \sqrt{c_\mu}$$

and c_f is the friction coefficient. From the local values of k and ϵ , a local eddy viscosity can be evaluated as

$$v_t = \frac{c_\mu k^2}{\epsilon} \quad (7.18)$$

In the above equations, the following values are used for the empirical constants:

$$c_\mu = 0.09, \quad c_{1\epsilon} = 1.45, \quad c_{2\epsilon} = 1.90, \quad \sigma_k = 1.0, \quad \sigma_\epsilon = 1.3$$

7.2.2.6 Results of numerical computations

Numerical simulations have been performed to test the sensitivity of the different model parameters and to compare them with the laboratory experiment. The results are described hereafter. Confirm the laboratory model; a simple rectangular basin has been simulated. This basin has a rectangular grid spacing of 0.05 *m* in both flow and transverse directions.

Table 7.1 shows descriptions of runs and values of parameters used.

7.2.2.6.1 Boundary conditions and parametric analysis In the depth-averaged 2D simulation of sediment transport, the inflow sediment discharge must be given at each inlet boundary. The simulations are summarized in Table 7.1. They are compared with the numerical reference simulation A-2, for which boundary conditions and further details are summarized in Table 4. For the sediment transport calculation, the inflow sediment discharges.

To reduce the complexity of the system, specific processes such as sediment sorting are not included for the moment.

The analysis has been done according to Table 7.2. The sensitivity of the parameters is discussed hereafter. Beside the simulations referenced in Table 7.2, some further runs are also discussed.

7.2.2.6.2 Influence of turbulence closure Three types of turbulence closures were used in run series A, B, and C. Depth-integrated parabolic and mixing length based on eddy viscosity models were used in run series A and B. Both eddy viscosity models were tested for a wide range of values of the adjustable coefficient A_{xy} (values between 1 and 1000). The output values were defined for a 1.5 *hrs* run time. The presentation of the results uses the following procedure:

1. For each model and for different parametric values, four figures are shown: velocity magnitude, kinematic eddy viscosity, suspended sediment concentration and bed elevation.
2. A longitudinal section has been taken along the basin centerline.

7.2.2.7 Run series A (see Table 7.1)

A depth-integrated parabolic eddy viscosity model was used, with A_{xy} ranging from 1, 2, ... to 1000. Results are presented for $A_{xy} = 1, 50, \text{ and } 150$. Figure 7.4 shows the results of Run A – 1 where ($A_{xy} = 1$). Figure 7.4a presents the velocity magnitudes and vectors. The water-sediment mixture flows from the narrow inlet channel into the much wider basin.

At first, the inflow mixture behaves like a jet that remains quite separated from the clear water in the basin. After some distance, the shear between both bodies of water moving

Table 7.1: Summary of numerical runs.

Series	Run	Turbulence	Characteristic	Parameters			
				No	closure	features	A_{xy}
A	A-1	DIPM	different turbulence closure	1			
	A-2	DIPM	models were used:	50			
	A-3	DIPM	DIPM, DIMLM, $k - \epsilon$.	150			
B	B-1	DIMLM	A_{xy}	2			
	B-2	DIMLM	varies for	20			
C	C	$k - \epsilon$	series A and B.				
D	D-1	DIPM	two different		0.00009		
	D-2	DIPM	grain sizes		0.00015		
M	M-1	DIPM	mixing layer			0.025	
	M-2	DIPM	thickness δ_m			0.05	
	M-3	DIPM	varies			0.1	
L	L-1	DIPM	long				1.5
	L-2	DIPM	time				3
	L-3	DIPM	runs				4.5
	L-4	DIPM					9
MO	MO-1	DIPM	clear water flow on developed				1.5
	MO-2	DIPM	from a movable bed which				65
	MO-3	DIPM	Run A-2, erosion of the developed bed				133

at different speeds causes mass and momentum exchange and thus eddies are peeled off from the core of the jet. This peeling off occurs alternatively on both sides of the jet and generates eddies that increase in size with longitudinal distance. Furthermore, the jet starts to undulate with a wavelength and amplitude that increase with longitudinal distance. This behavior resembles a continuously growing instability.

Figure 7.4b shows the kinematic eddy viscosity. As the eddy viscosity is directly related to the shear velocity (see Eqs. 7.2 and 7.3), its behavior is similar to velocity (Figure 7.4a). From the lowest to the highest flow velocities in the basin, the eddy viscosity changes by up to one order of magnitude.

Figure 7.4c presents the suspended sediment distribution. The initial concentration in the inlet channel equals 3.0 kg/m^3 . This concentration diffuses throughout the basin following the general velocity and eddy viscosity pattern described above. Nevertheless, the sediment concentration pattern does not undulate as much as velocity and remains more or less symmetric. Finally, Figure 7.4d shows the final bed elevations after 4.5 hours of testing.

Table 7.2: Boundary conditions for reference run.

Boundary conditions	Symbol	Value	Dimension
water discharge	Q_w	0.007	$[m^3/s]$
downstream water level	h	0.2	$[m]$
sediment concentration	Q_s	4	$[kg/m^3]$
sediment density	ρ_s	1500	$[kg/m^3]$
sediment diameter	d_{50}	0.00009	$[m]$
sediment porosity	p	0.4	$[-]$
wall boundary condition	-		
bottom slope	J	0	$[\%]$
Model			
basin width	B	4	$[m]$
basin length	L	6	$[m]$
grid spacing	Δx	0.05	$[m]$
width/length of inlet channel	b/l_{in}	0.25/1.0	$[-]$
width/length of outlet channel	b/l_{out}	0.25/1.0	$[-]$
Manning roughness coefficient	n	0.015	$[-]$
Modelling parameters			
mixing layer thickness	δ_m	0.05	$[m]$
adaptation length for bed load	l_s	0.35	$[m]$
adaptation factor for suspended load	α	0.2	$[-]$
transport mode	total load as suspended load		
transport capacity formula	Schoklitsch (1937)		

Similar to the sediment concentration distribution, the bed change remains symmetric and shows maximum values of up to 0.09 m, i.e. about 45 % of the initial water depth.

Figure 7.5 shows the results for run A-2. The eddy viscosity parameter has a value of $A_{xy} = 50$, resulting in viscosities 50 times higher than the first run.

Figure 7.5a presents the simulated stationary flow field with velocity magnitudes and vectors. In contrast with the flow pattern of Run A-1, the flow pattern computed here is found to agree fairly well with the experimental observations, showing the incoming jet deflecting towards the left-hand side of the basin, combined with a large eddy on the right-hand side and a small eddy in the left corner of the upstream part of the reservoir. The jet apparently diffuses much faster than for run A-1.

It was found that this flow pattern can switch to a reverse pattern with the jet positioned on the right-hand side and the eddy along the left-hand side. This could be numerically achieved by changing the initial state or the local geometry of the reservoir. The kinematic eddy viscosity presented in Figure 7.5b follows the same pattern and diffuses much faster.

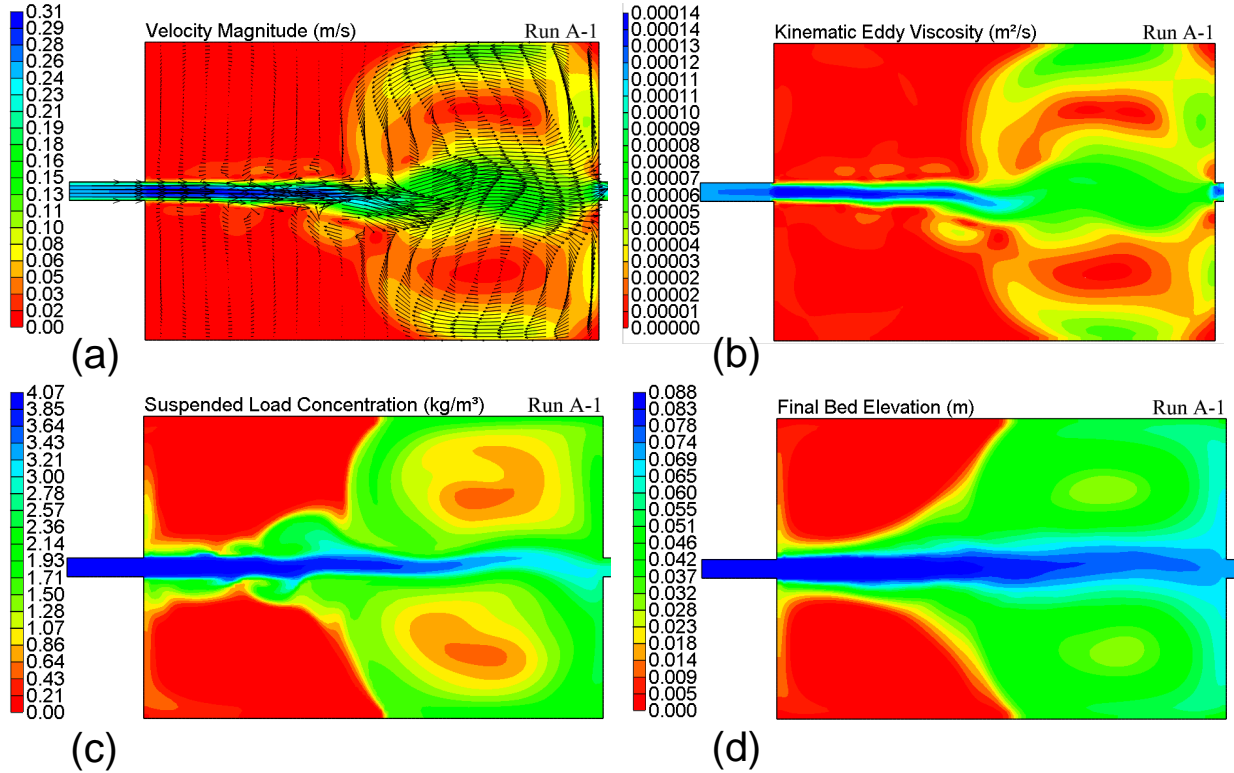


Figure 7.4: Results for numerical simulation run A – 1: a) stationary flow field with velocity vectors and magnitudes, b) kinematic eddy viscosity, c) suspended load concentration, and d) final bed elevation results.

By further increasing A_{xy} , towards 150, small eddies start to form at each corner of the basin, similar to the eddy that is observed in run A-2 along the left hand side of the reservoir for $A_{xy} = 50$.

For A_{xy} more than 150, the flow starts to become more and more symmetric, with two small eddies at the entrance reservoir corners as shown in Figure 7.6a for run A-3. Finally, for A_{xy} between 500 and 1000 four small eddies are generated at each corner of the basin. The morphology in Figure 7.5d (Run A-2) shows that the flow pattern concentrates the depositions on the left hand side.

Figure 7.6 shows the results for Run A–3 with $A_{xy} = 150$. The flow pattern in Figure 7.6a shows symmetric behavior with two small eddies in both corners near the entrance of the reservoir and a centralized jet flow that diffuses very fast.

Similarly, the kinematic eddy viscosity, the suspended sediment concentration and sediment depositions are highest along the centreline of the basin and reduce towards the sides as shown in Figures 7.6b- 7.6d. It can be concluded that with higher values of the kinematic eddy viscosity, the flow and sediment deposition behave in a quasi-symmetric manner.

The mirrors of flow pattern and bed deformation shown in Figure 7.5 are most similar

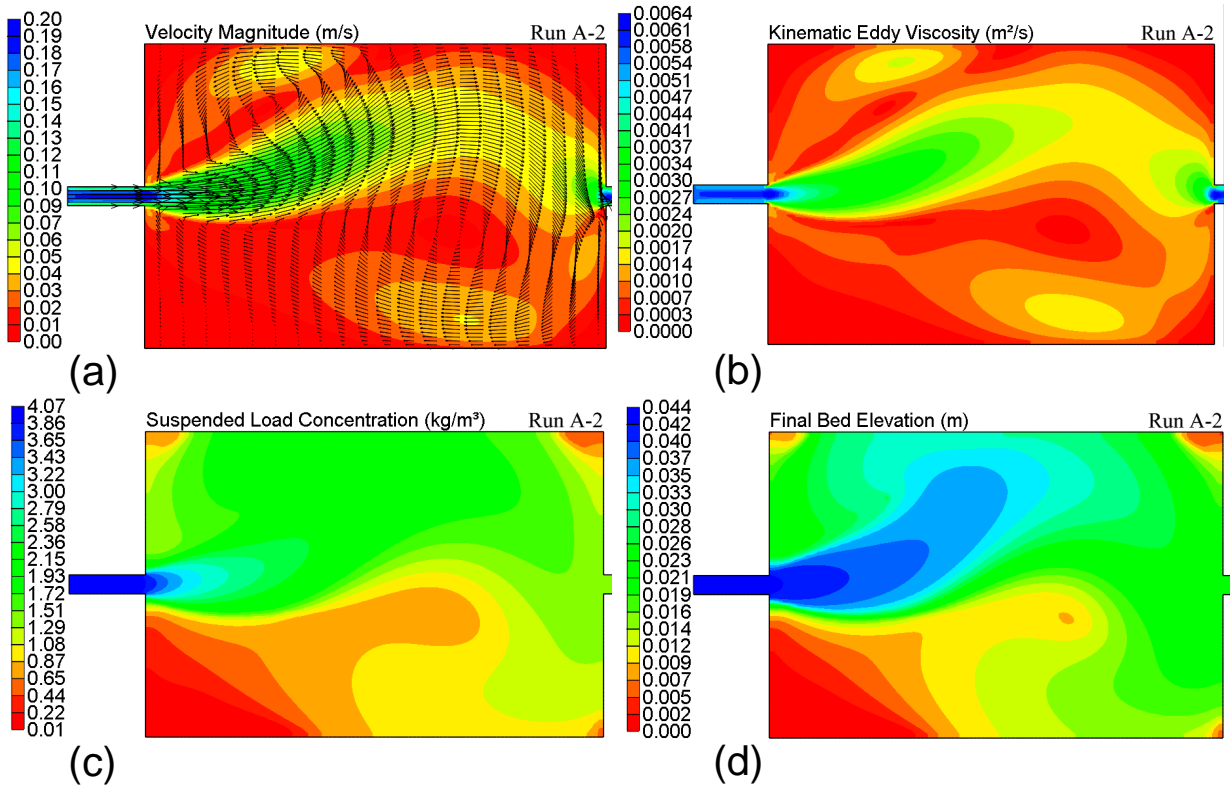


Figure 7.5: Results for numerical simulation run A – 2: a) stationary flow field with velocity vectors and magnitudes, b) kinematic eddy viscosity, c) suspended load concentration, and d) final bed elevation results.

to those observed in the laboratory experiments. The corresponding range of A_{xy} values is situated between 20 and 120. Hence, when using the laboratory experiments as a reference, using a depth-integrated parabolic eddy viscosity model, with eddy viscosities between $0.001 \text{ m}^2/\text{s}$ and $0.006 \text{ m}^2/\text{s}$, seems to provide the qualitatively most plausible results.

7.2.2.8 Run series B (see Table 7.1)

Series B uses a depth-integrated mixing layer model (hereafter; DIMLM). Figures 7.7 and 7.8 present the results of Runs B-1 and B-2 respectively. Analysis of these runs is quite similar to the one performed for run series A.

Several simulations have been carried out with A_{xy} values varying between 1 and 100. Figures 7.7 and 7.8 show the results for $A_{xy} = 2$ and 20 respectively. The lowest value thereby generates flow and sedimentation patterns very similar to the ones observed for run A – 1. The highest value is very similar to the results obtained for run A – 3.

As a first-hand conclusion, the DIMLM turbulence closure model seems less suitable to reproduce the flow and sediment patterns observed during the laboratory experiment.

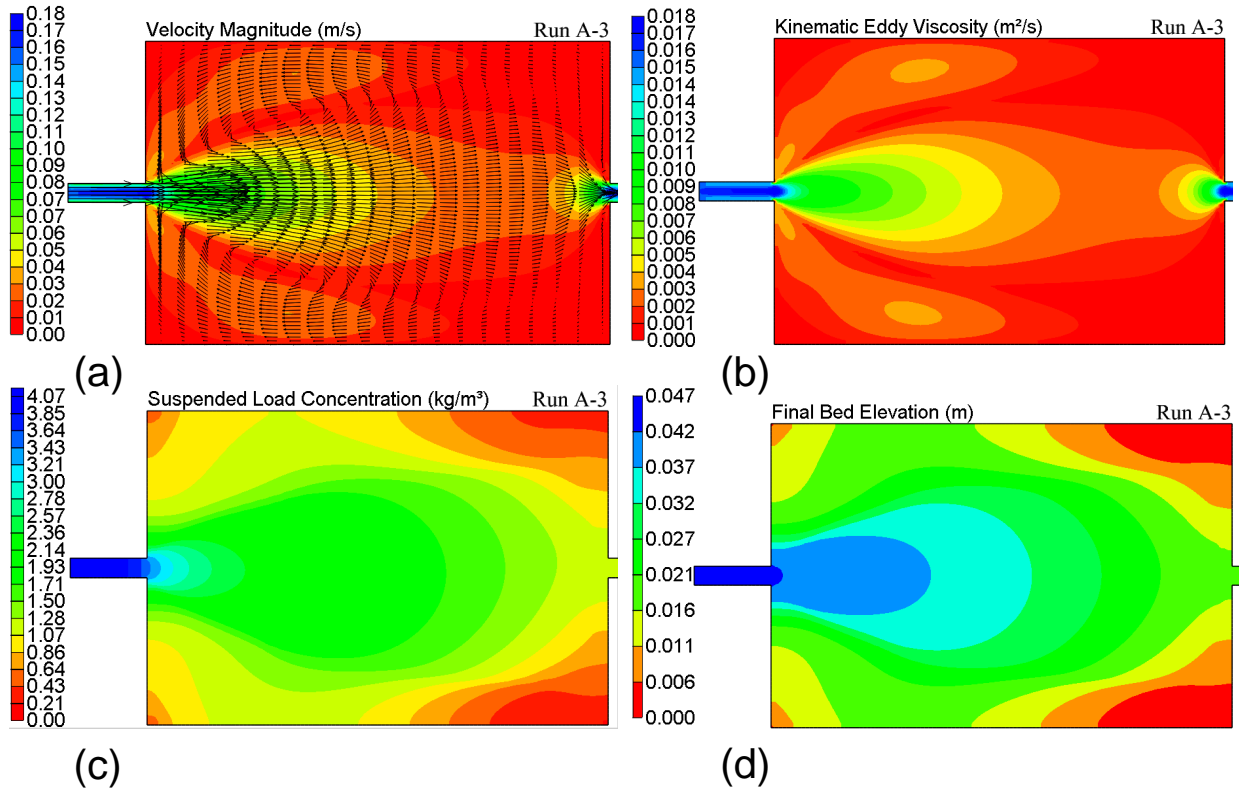


Figure 7.6: Results for numerical simulation run A – 3: a) stationary flow field with velocity vectors and magnitudes, b) kinematic eddy viscosity, c) suspended load concentration, and d) final bed elevation results.

7.2.2.9 Run series C (see Table 7.1)

Run series C uses the two-equation $k - \epsilon$ turbulence model. Figure 7.9a shows the velocity magnitude and vectors and Figure 7.9b the corresponding kinematic eddy viscosity. It was found that two large recirculation eddies develop along both sides of the basin. The flow pattern is perfectly symmetric and differs from the experimental one.

7.2.2.10 Comparison of the different run series along the basin centreline

Figure 7.10 to Figure 7.14 present a detailed comparison of velocity magnitude, kinematic eddy viscosity, suspended sediment concentration, and final bed elevation along the basin centreline of all previous run series. Velocity distributions for run series A, B, and C are similar in the inlet channel. At the interface between inlet channel and basin, a sudden velocity increase occurs, followed by a gradual decrease throughout the whole basin length.

For low eddy viscosities (runs A-1 and B-1), the velocity trace agrees with the flow pattern meandering along the centreline. At the outlet of the basin, all runs exhibit similar flow behavior: at 0.50 m upstream of the outlet section, the velocity progressively increases

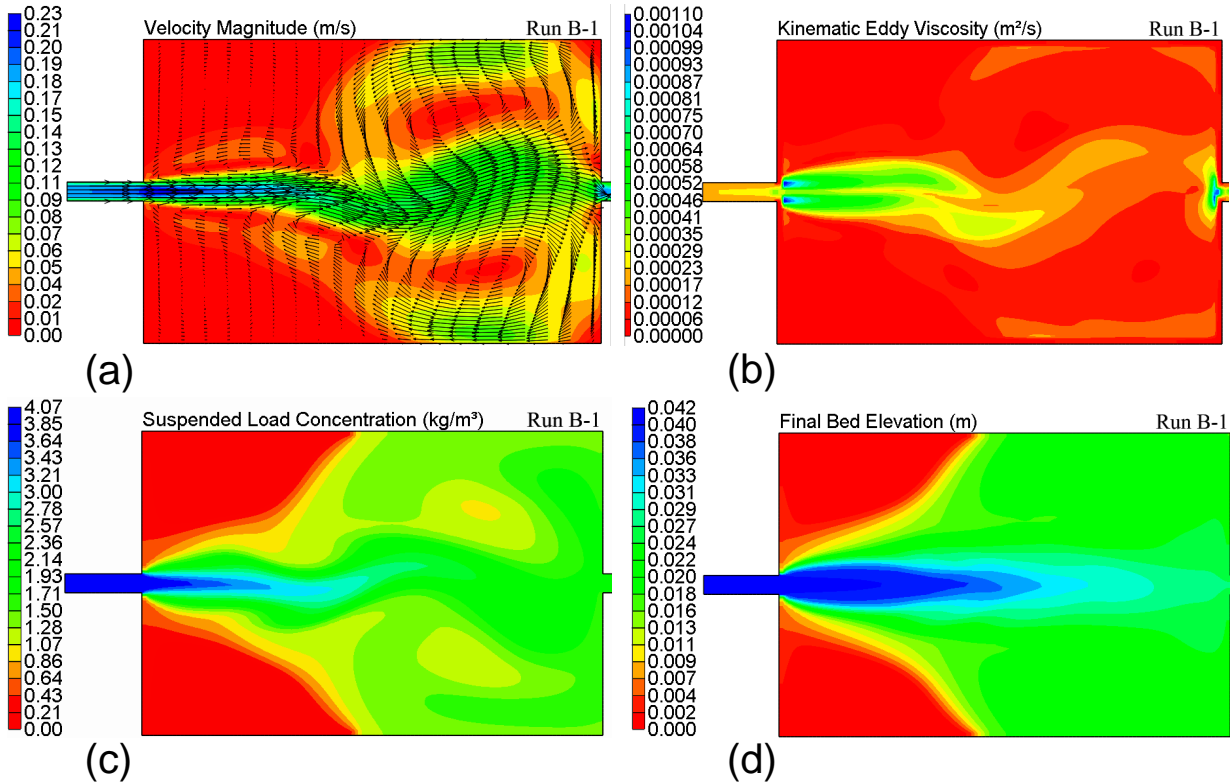


Figure 7.7: Results for numerical simulation run B – 1: a) stationary flow field with velocity vectors and magnitudes, b) kinematic eddy viscosity, c) suspended load concentration, and d) final bed elevation results.

towards a peak value at the outlet section itself, followed by a small decrease and finally stabilization of the velocity profile inside the outlet channel.

The appearance of the peak value is generated by the sudden geometric change, which generates a weak plunging water surface at the constriction and thus increasing velocity values. The centreline velocity inside the basin decreases with increasing eddy viscosity (run series A-2 and A-3).

Figure 7.11 compares the longitudinal changes in eddy viscosity for runs A, B, and C, while Figure 7.12 shows a comparison between the predicted bed profiles for runs A-2, A-3, B-1, and B-2 along the center line of the basin. For run A-2, the influence of the flow deviating towards the left-hand side of the basin is clearly visible by strongly reduced bed thickness. Also, due to the recirculation eddy, the sediment deposits gradually start to increase again in front of the outlet.

Figure 7.13 shows similar trends for the suspended sediment concentration along the centreline of the basin, with, run A-2 exhibiting a low suspended sediment concentration in the middle of the basin. Moreover, for run B-1, the sediment concentration oscillates in the middle of the basin.

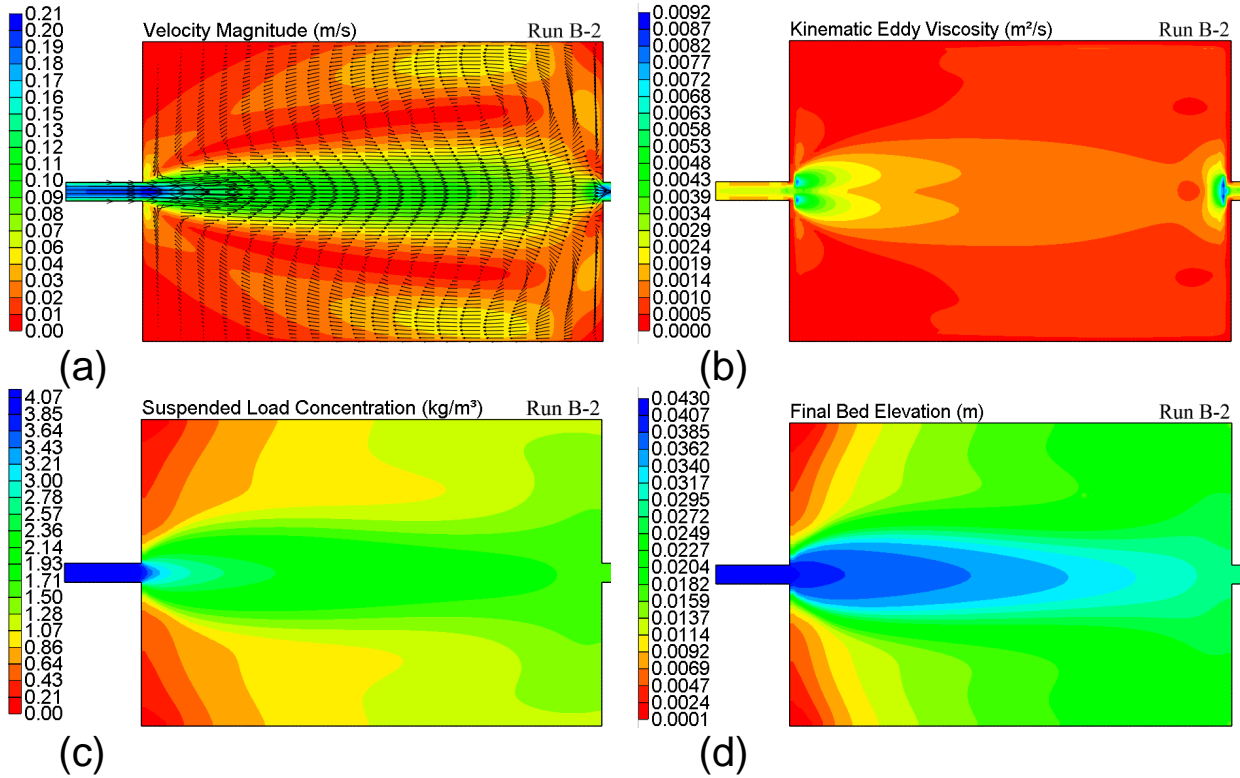


Figure 7.8: Results for numerical simulation run B – 2: a) stationary flow field with velocity vectors and magnitudes, b) kinematic eddy viscosity, c) suspended load concentration, and d) final bed elevation results.

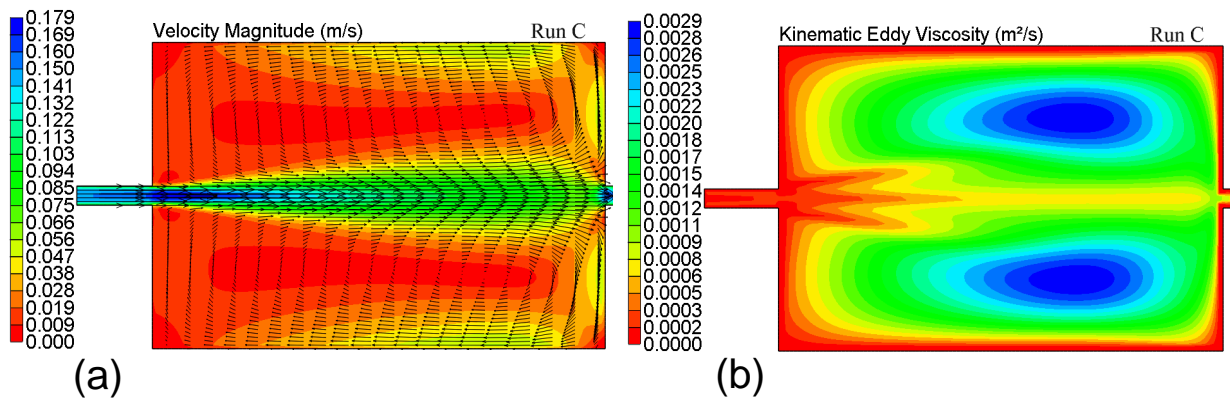


Figure 7.9: Results for numerical simulation run C: a) stationary flow field with velocity vectors and magnitudes, b) kinematic eddy viscosity.

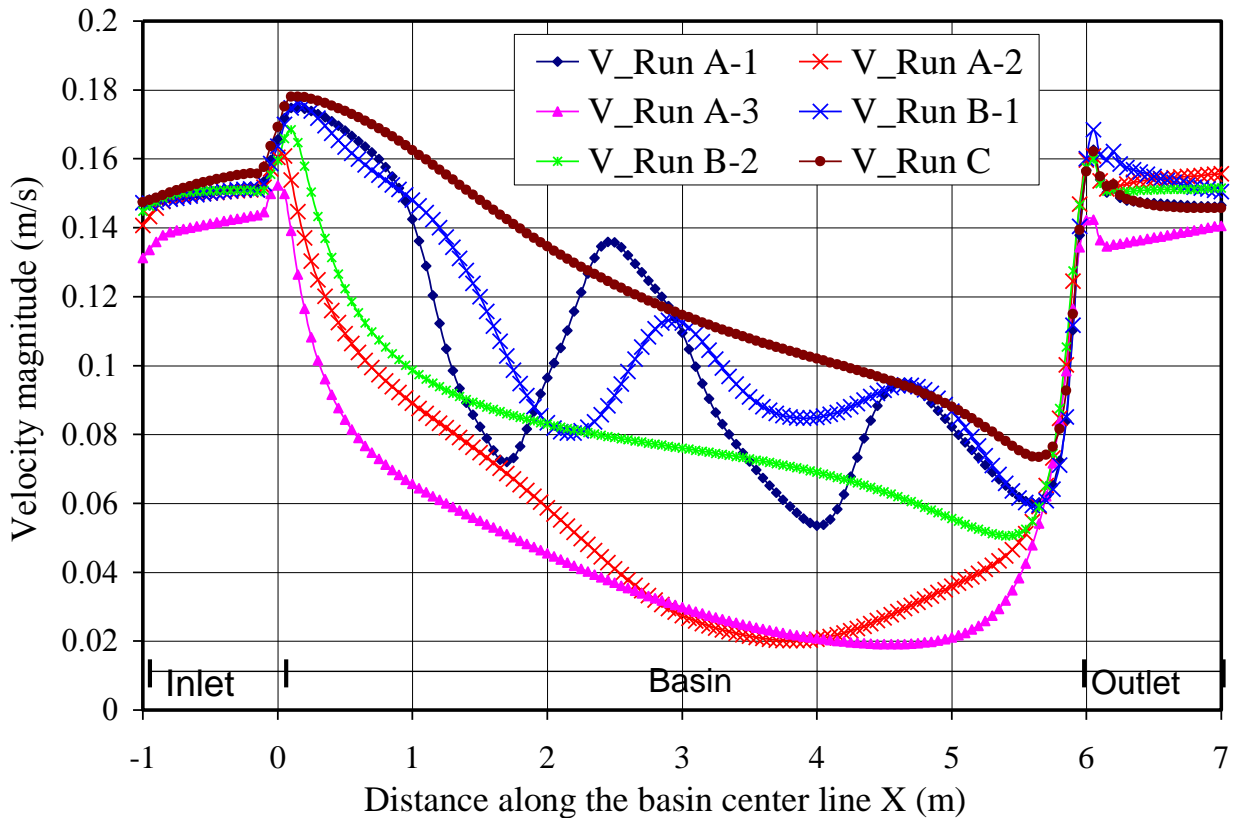


Figure 7.10: Comparison of depth-averaged velocity magnitude along basin centreline for run series A, B, and C.

7.2.2.11 Influence of grain size distribution

Two different simulations have been conducted with a modification of the grain size curve towards extreme grain sizes, with the sediment inflow rate being the similar to the one used during the reference laboratory experiment. The turbulence model used is the Depth-Integrated Parabolic Model (DIPM). Hence, run D-1 uses $d_{50} = 0.09 \text{ mm}$ and run D-2 $d_{50} = 0.15 \text{ mm}$.

Figure 7.14a compares the resulting bed profiles along the centreline of the basin. Despite the fact that the final bed morphology was expected to be different, both results were found to be similar. The reason for this is not clear yet, but might be due to the relatively short duration of the runs (only 1.5 hrs). Longer duration experiments will be performed in the near future.

7.2.2.11.1 Influence of bottom layer thickness The mixing layer represents that part of the sediment at the bed that can be exchanged with the sediment transported by the flow. The bed material gradation usually varies with the vertical direction, so the bed material above the non-erodible layer is divided into several layers, as shown in Figure 7.15.

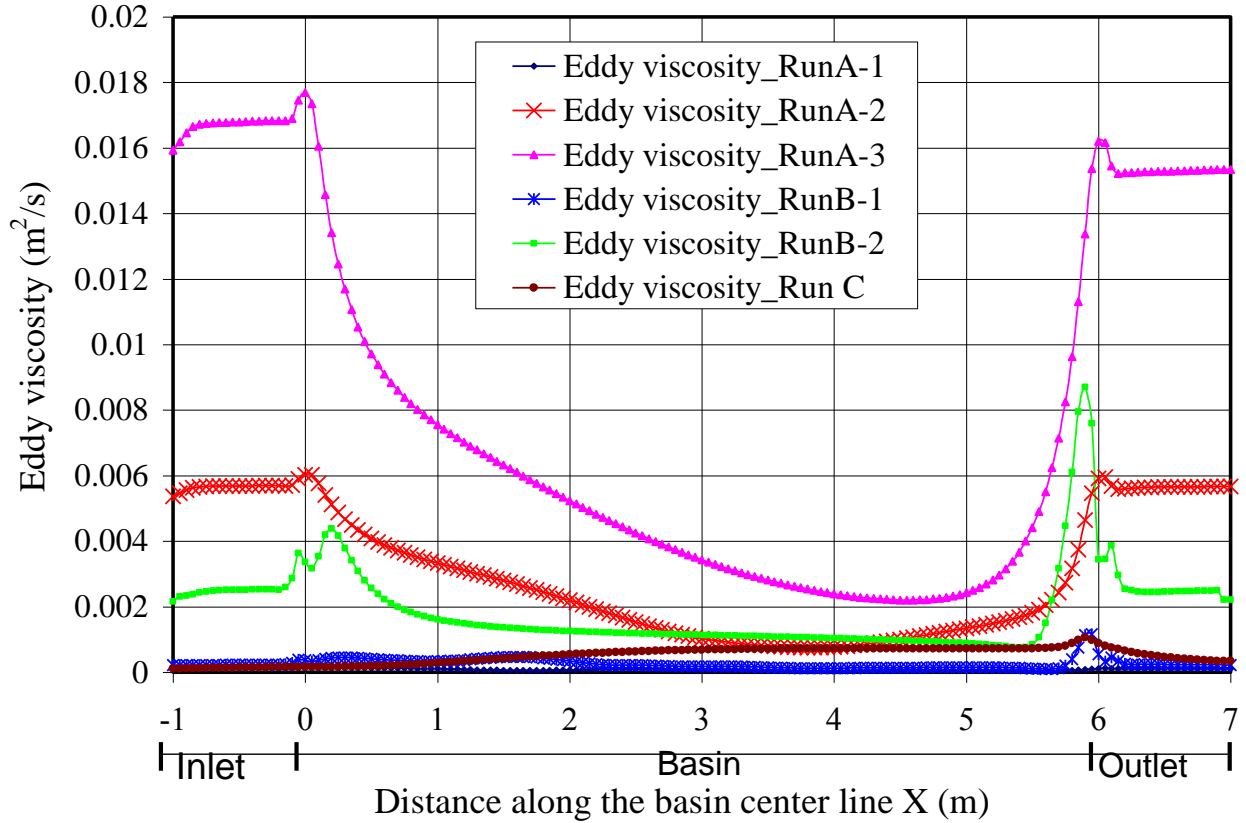


Figure 7.11: Comparison of kinematic eddy viscosity along basin centreline for run series A, B, and C

The top layer is the mixing layer, whereas the second one is the subsurface layer. The variation of bed material gradation in the mixing layer is determined by (Wu, 1991)

$$\frac{\partial(\delta_m p_{bk})}{\partial t} = \frac{\partial z_{bk}}{\partial t} + P_{bk}^* \left(\frac{\partial \delta_m}{\partial t} - \frac{\partial z_b}{\partial t} \right) \quad (7.19)$$

where p_{bk} is the bed material gradation in the mixing layer; δ_m is the thickness of the mixing layer, which is related to the flow and sediment conditions as well as the bed deformation; $\partial z_b / \partial t$ is the total bed deformation rate, $\partial z_b / \partial t = \sum_{k=1}^N \partial z_{bk} / \partial t$; N is the total number of size classes; P_{bk}^* is p_{bk} when, $\partial m / \partial t - \partial z_b / \partial t \leq 0$ and P_{bk}^* is the bed material gradation in the subsurface layer when $\partial m / \partial t - \partial z_b / \partial t > 0$. The bed material gradations in the layers under the mixing layer are determined by using the mass conservation law.

The objective of run series M is to test the sensitivity of the model to this exchangeable control volume. M-1, M-2, and M-3 were performed with mixing layer thicknesses of 0.025, 0.05 and 0.1 m respectively. For numerical reasons (i.e., deposition during a one time step should not exceed mixing layer thickness), the time step has been reduced proportionally for these runs.

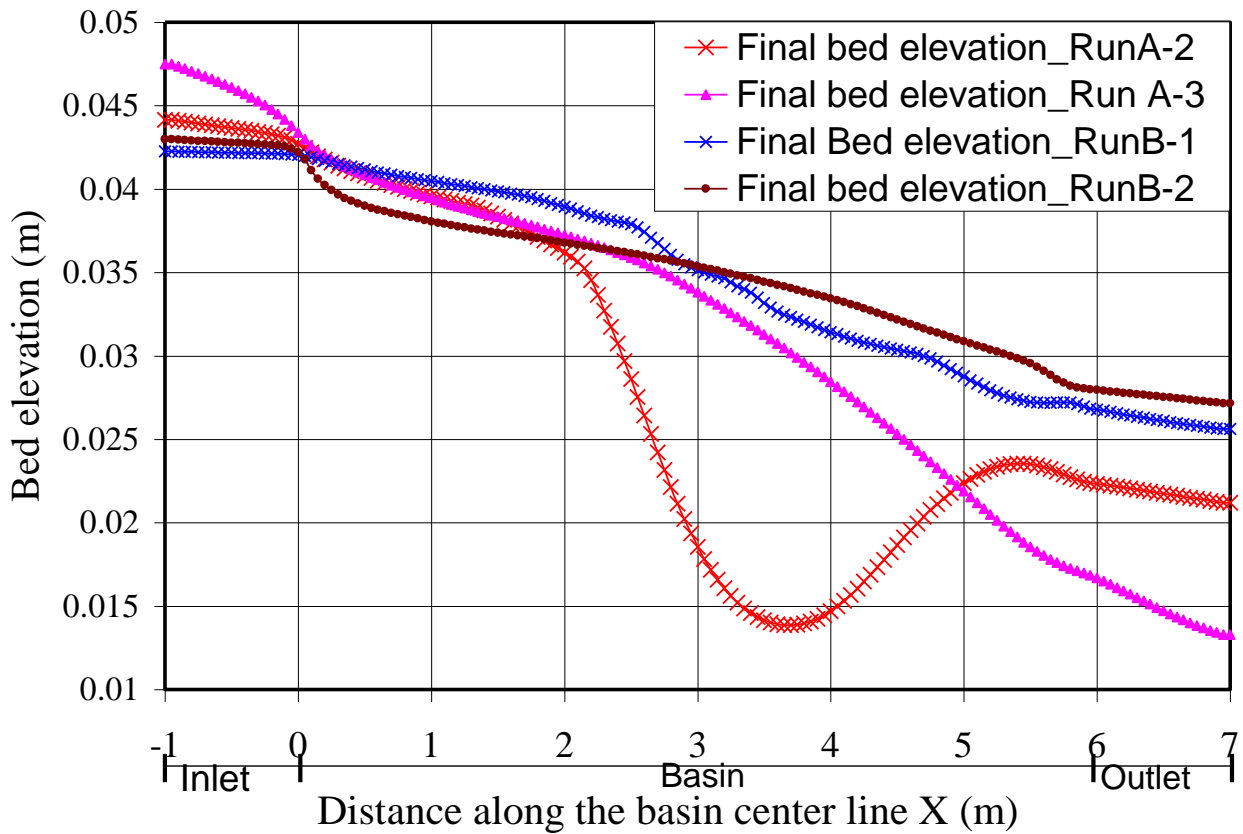


Figure 7.12: Comparison of bed profiles along basin centreline for run series A and B

Figure 7.14b shows the bed elevation along the centreline of the basin for the three runs. By increasing the mixing layer thickness till $1/4$ of the water depth, bed elevation increases see Figure 23 for curve M1 and M2. But for higher values of the mixing layer (half of the water depth bed elevation decreases as shown in Figure 7.14b for curve M3 which overlaps with curve M1.

7.2.2.11.2 Influence of duration of run time Figure 7.14c shows the evolution of the sediment depositions at different run time periods (1.5 hrs, 3.0 hrs, 4.5 hrs, and 9.0 hrs) along the centreline of the basin. The figure shows almost constant bed thickness within the first time period. Bed thickness increases and is less homogenous along the centreline after 3.0 and 4.5 hours. Beds become thicker and even more irregular after 9.0 hours. It may be concluded that a stable morphology has not yet been reached after 9.0 hours and that longer runs would be needed to attain morphological equilibrium in the basin.

7.2.2.11.3 Influence of movable bed The bed morphology obtained for run B-2 was used as initial bathymetry for run series MO as shown in Figure 7.14d. Clear water without

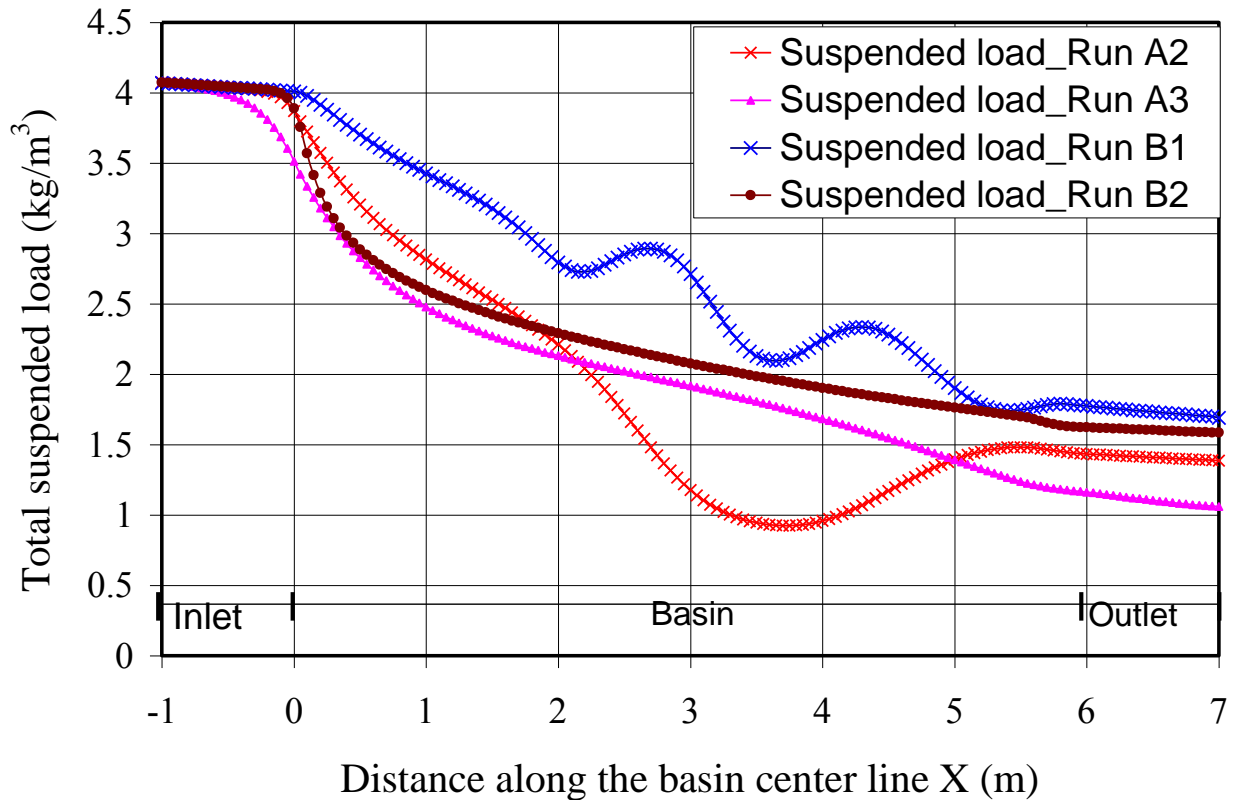


Figure 7.13: Comparison of suspended load concentration along basin centreline for run series A and B.

sediment was injected into the basin to investigate the bed evolution for MO1, MO2, and MO3 at different time periods (1.5 hrs, 65 hrs and 133 hrs). Between 65 and 133 hrs, no significant change is observed anymore between the respective bed profiles. Hence, for these flow and sediment conditions, the basin might be close to its morphological equilibrium.

As a conclusion, A_{xy} has a significant effect on flow patterns, velocity distributions, sediment concentrations and bed forms.

7.2.2.11.4 Comparison of experimental and numerical results A detailed comparison of flow field and morphological development between the experimental model and numerical simulation Run A2 is presented.

7.2.2.11.5 Flow map Figure 7.16 shows that the numerically computed velocity vectors are acceptable and generally in a good agreement with the experimentally observed vectors.

Figure 7.17 compares the computed and measured axial velocity magnitude at the basin centreline. In the inlet channel, experimentally observed velocity distributions are approx-

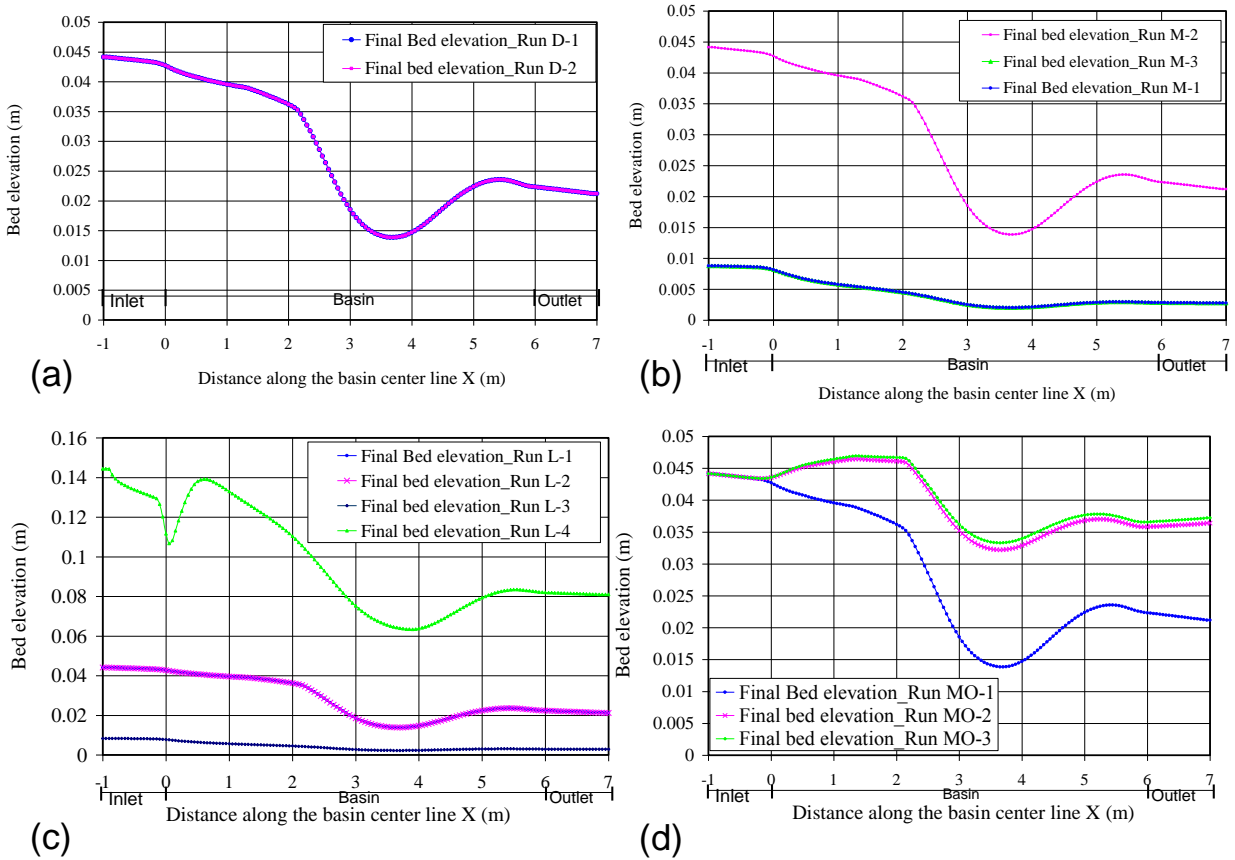


Figure 7.14: Comparison of bed profiles along basin centreline for: a) run series D, b) run series M, c) run series L and d) run series MO.

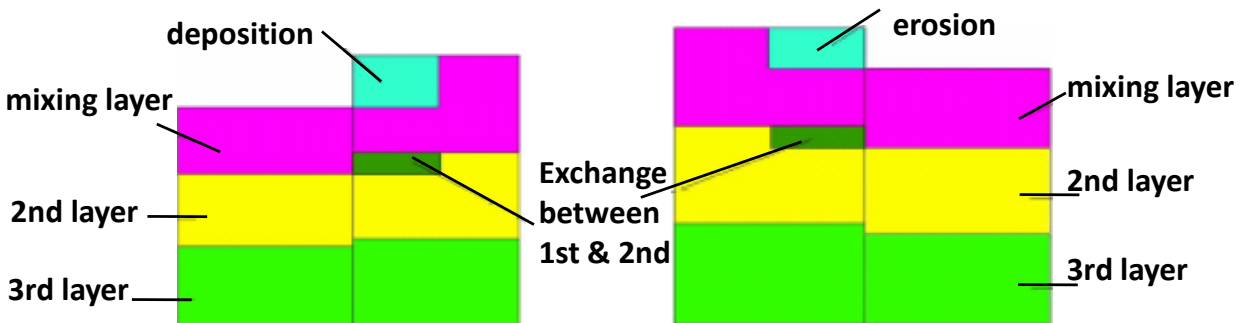


Figure 7.15: Multiple-layer sorting model of bed material gradation.

imately the same. At the interface between inlet channel and basin, a sudden velocity increase is observed in the computations, followed by a gradual decrease throughout the whole basin length.

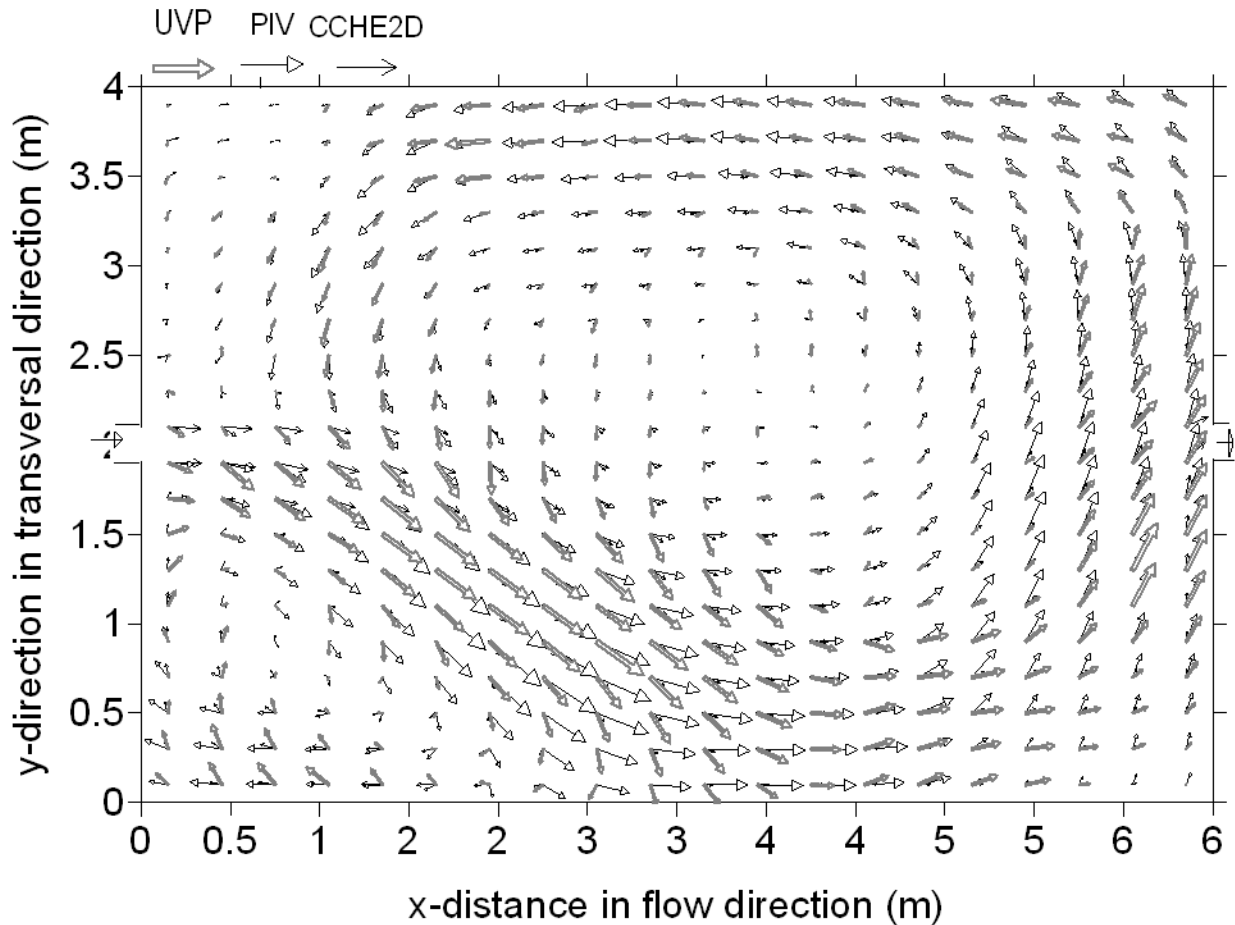


Figure 7.16: Comparison of velocity magnitude vectors recorded by UVP and LSPIV with numerically simulated velocity magnitude vectors (run *A* – 2).

7.2.2.12 Conclusions regarding the simulations with CCHE2D

Comparison has been made between a laboratory experiment with a rectangular reference geometry and depth-averaged numerical simulations with CCHE2D. The laboratory experiments show that suspended sediment transport and deposition are determined by the initial flow pattern and by the upstream and downstream boundary conditions.

Three major horizontal eddies developed influencing the sediment deposition pattern. Although asymmetric flow patterns are privileged, a symmetric pattern can appear from time to time. This particular behavior could also be reproduced by the two-dimensional depth-averaged flow and sediment transport model CCHE2D.

In spite of the symmetric setup, these generally produced an asymmetric flow pattern that can easily switch sides depending on the assumptions made for the initial and boundary conditions. When using the laboratory experiment as a reference, the most reliable numerical results have been obtained with a parabolic depth-averaged eddy viscosity model.

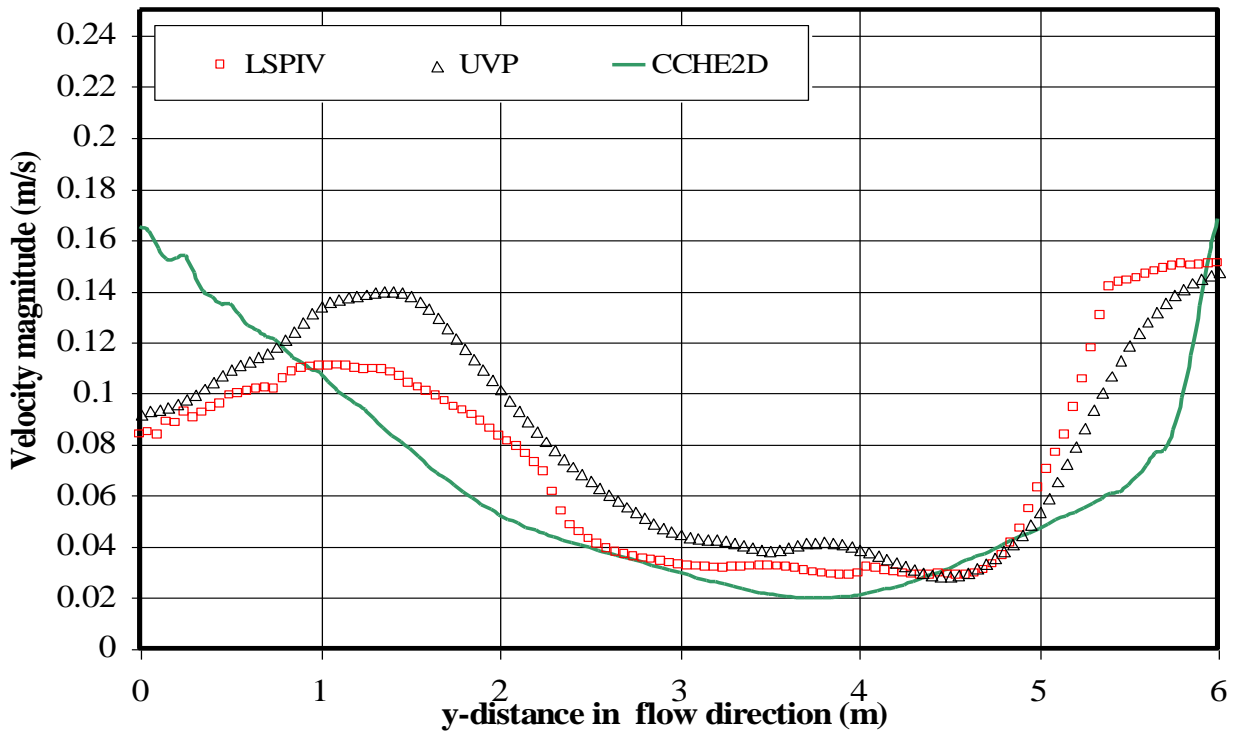


Figure 7.17: Comparison of depth-averaged velocity magnitude recorded by UVP and LSPIV with numerically simulated velocity magnitude (run *A - 2*). Longitudinal profile is taken along the basin centreline.

It was found that the flow patterns are quite sensitive to boundary and initial conditions. Also, strongly asymmetric flow and morphological patterns frequently developed during the experiments. These patterns could be simulated numerically by use of a parabolic eddy viscosity model.

7.2.3 Third step: numerical simulation with WOLF2D

The WOLF2D model is based on the two-dimensional depth-averaged equations of volume and momentum conservation, namely the shallow-water equations. In the shallow-water approach the only assumption states that velocities normal to a main flow direction are smaller than those in the main flow direction. Details about the model and the simulated results are given in Dewals et al. (2008).

WOLF2D boundary conditions:

1. The value of the specific discharge is prescribed as an inflow boundary condition. Besides, the transverse specific discharge is set to zero at the inflow.
2. The outflow boundary condition is a constant water surface elevation: 0.2 m.

3. At solid walls, the component of the specific discharge normal to the wall is set to zero.
4. For the purpose of evaluating the diffusive terms, the gradients of the unknowns must also be specified at the boundaries. These gradients in the direction parallel to the boundary are set to zero for simplicity, while the gradients of the variables in the direction normal to the boundary are properly evaluated by finite difference between the value at the boundary and the value at the center of the adjacent cell.

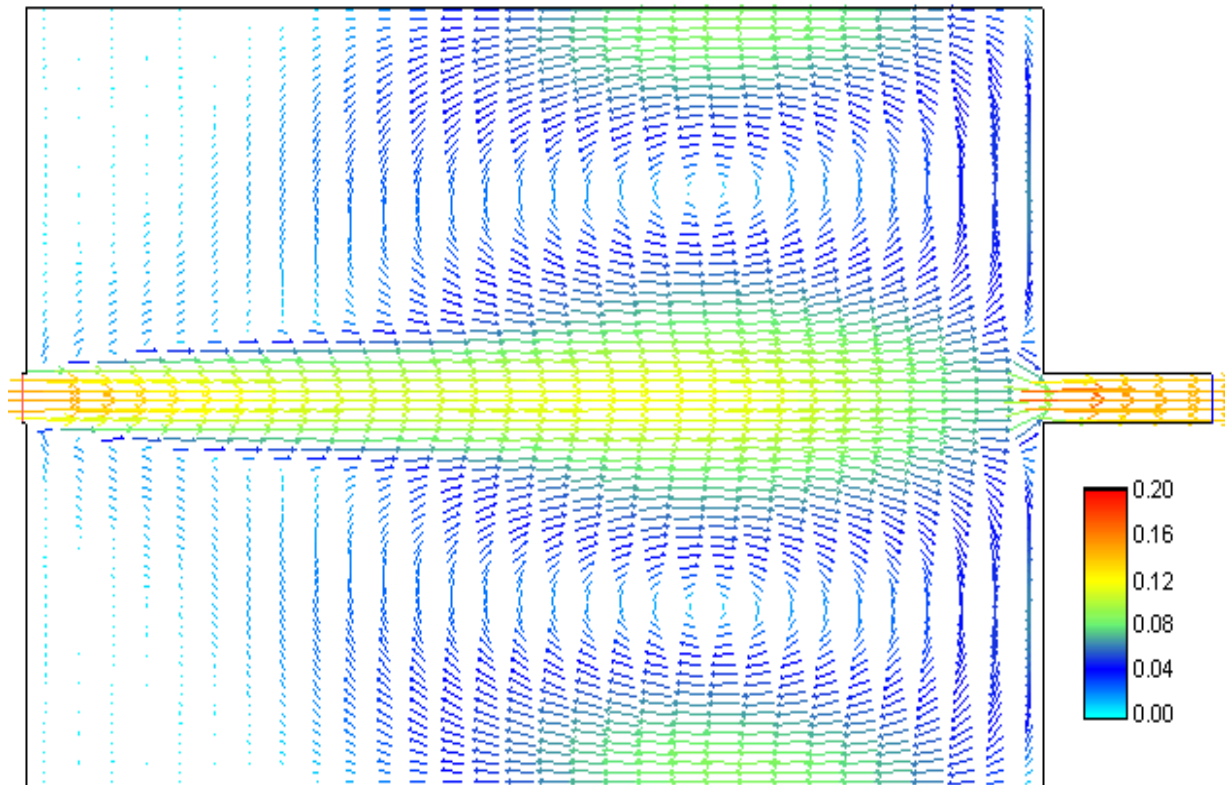


Figure 7.18: Flow field simulated with a uniform specific discharge profile at inflow (algebraic turbulence closure). Velocity magnitude in m/s.

Simulated results First simulation was performed based on the geometry and inflow/outflow conditions of the physical model. The simulation is run until a steady-state flow field is reached. This obtained simulated flow field is perfectly symmetric (see Fig. 7.18).

Although not in agreement with experimental observations, this result was expected since neither the mathematical model nor the algorithm implementation are supposed to break the perfect symmetry of input data.

Consequently, this first simulation result demonstrates that the model does not include any spurious numerical artifact tending to introduce dissymmetry in a problem with per-

fectly symmetric input data. According to the first simulations all the the solution for the full domain always converges to a symmetric solution.

A non-symmetric solution can be obtained only with a non-symmetric initial and boundary flow field. However, according to the laboratory experiments, this symmetric flow field is unstable. Therefore, a second series of simulations has been undertaken with slightly disturbed distributions of the specific discharge at the inflow, in order to test the stability of the numerical solution.

Instead of being uniform, the cross-sectional profile of the specific discharge is specified with a linear variation along the width of the inlet channel:

$$q_{in}(y) = q_0 + q_1 \frac{2y}{b} \quad (7.20)$$

where q_{in} (m^2/s) denotes the actual value specified as inflow boundary condition, q_0 (m^2/s) is the reference value (total discharge divided by channel width) and q_1 (m^2/s) measures the magnitude of the linear variation b (m) designates the width of the inlet channel.

As shown on Figure 7.19b), considering this minor change in the inflow boundary condition with $q_1/q_0 = 2\%$ leads to a totally different flow field.

In order to verify that the simulated flow field does not significantly depend on the arbitrary value selected for the disturbance, five simulations have been run with q_1/q_0 varying between 1 % and 5 %. In every case, the flow field remains very close to that one observed at the laboratory (Figure 7.19). For disturbance intensities between 1% and 5%, it is almost no effect on the simulated result.

The output of the numerical model becomes now essentially consistent with experimental observations.

Indeed, the deviation of the main jet is reproduced. The three main vortices highlighted experimentally are also properly predicted by the numerical model. The simulated reattachment length L_{r1} evaluated at 2.53 m which is only 2.5% shorter than the experimental of 2.6 m.

The slight perturbation introduced here has an amazingly strong effect on the results because of the unstable nature of the symmetric flow field. As a consequence, it can be concluded that the numerical model is able to reproduce the high sensitivity of the real flow to external disturbances and hence the unstable nature of the symmetric solution. It must be noted that same simulation result can also be obtained, with a uniform specific discharge profile as inflow boundary conditions, by starting the computation with a flow field initially deviated. In this case, the non-symmetric initial condition acts as a disturbance

Numerical model is able to predict the transition between stable and unstable configurations. The stability of a symmetric flow field is analyzed by considering "quasi-symmetric" input data. Quasi-symmetric; input data means symmetric geometry, outflow conditions

and initial conditions, but slightly disturbed inflow boundary condition, according to relation. A geometric configuration will be referred to as stable if a symmetric flow field remains stable for quasi-symmetric input data.

On the contrary, the configuration will be said to be unstable if, for quasi-symmetric input data, a symmetric flow field becomes unstable and the actual steady solution deviates considerably from the symmetric one. The last three configurations (Figure 7.19c, f, and h) are found to permit a stable symmetric flow field, while the geometry shown in Figure 7.19b) does not.

This classification between stable and unstable configurations obtained from the 2D numerical simulations is in perfect agreement with experimental results. Hence, it may be emphasized that the numerical model succeeds in reproducing the transition between basin lengths enabling a stable symmetric flow field and those leading to flow instability.

All configurations turn out to lead to instability of a symmetric flow field. This conclusion can be drawn equally either from the experimental results or from the numerical ones, which means again that the numerical model performs very well in identifying both the stable and the unstable configurations.

A series of numerical simulations with the objective of testing the sensitivity to different parameters in the numerical modeling have been carried out, but only results of different bottom roughness $n_b = 0.01, 0.02, 0.03$ and $0.04 \text{ s/m}^{1/3}$ are presented hereafter (Figure 7.20).

For the comparison between symmetric and non-symmetric results a suitable quantitative indicator of the "intensity" of the non-symmetry of the flow field is introduced. It consists in evaluating the first moment m of the u -velocity field with respect to the centerline of the basin. The indicator is defined in non-dimensional form as follows:

$$m(x) = \frac{1}{B} \int_{-B/2}^{B/2} \frac{u(x,y) - U}{U} \frac{2y}{B} dy = \frac{1}{B} \int_{-B/2}^{B/2} \left(\frac{u}{U} - 1\right) \frac{2y}{B} dy = \frac{2}{UB^2} \int_{-B/2}^{B/2} u y dy \quad (7.21)$$

where U (m/s) is a reference velocity. The following value has been considered: $U = Q/(Bh_0)$, where h_0 (m) corresponds to the water depth at the down-stream boundary condition, Q (m^3/s) is the total discharge and B (m) the basin width. For any flow field which is symmetric with respect to the centerline, the moment remains equal to zero. For non-symmetric flow fields, the moment quantifies the deviation of the actual velocity profile compared to a symmetric profile. For instance, $m = 1$ if the velocity profile varies linearly between both side-walls of the basin with a difference between maximum velocity and mean velocity equal to three times the mean velocity.

In the upstream part of the basin, negative values of m corresponds to an anti-clockwise rotating vortex, while in the rest of the basin, positive values of m indicate a clockwise rotating vortex. Bottom roughness effect on the flow symmetry and stability as well is clearly visible in Figure 7.20. The resistance to flow is relatively small for the smooth and bed ($n_b = 0.01$), but with the increasing of n_b values the first moment m is decreasing.

7.2.3.1 Conclusion regarding simulations with WOLF2D

Laboratory experiments and numerical simulations for a large rectangular shallow basin show that the basin geometry has a strong influence on the flow pattern. It is therefore highly depending on the boundary, the initial flow conditions and the geometry. The present research gives a detailed numerical and experimental comparison of shallow flows in a series of rectangular basins for which experimental data is available.

The experimental results include flow visualization for four different basin geometries (varying length of the basin). For symmetric input data, the numerical model provides a perfectly symmetric result. However, if the inflow boundary condition is slightly disturbed, the numerical model performs well in reproducing both the symmetric and non symmetric flow patterns observed at the laboratory. On one hand, for the geometries corresponding to an observed non-symmetric flow field, the numerical model converges towards a completely deviated flow field, in very satisfactory agreement with laboratory measurements. The result is essentially insensitive to the arbitrary amplitude of the small disturbances superimposed to the inflow boundary condition.

Comparisons between experimental data and numerical results are presented. They demonstrate a reasonable agreement. On the other hand, for the geometries corresponding to an observed symmetric flow field, the slight disturbances introduced up-stream are quickly damped and the computed steady flow field is found almost symmetric. Moreover, the numerical model accounts for wall roughness, which appears decisive for properly reproducing the third vortex, located in the upper part of the basin, in the case of non-symmetric flow fields.

7.3 Discussions and conclusions

Although the simulations show that a 2D depth-averaged model can be used to reproduce the observed flow patterns in the laboratory, it is believed that future improvement of the modeling technique can lead to more reliable predictions. For a better approximation of the eddies and jets it is recommended to use a more detailed model for horizontal turbulence. For instance techniques such as 3D LES (three dimensional large eddy simulation) can be considered.

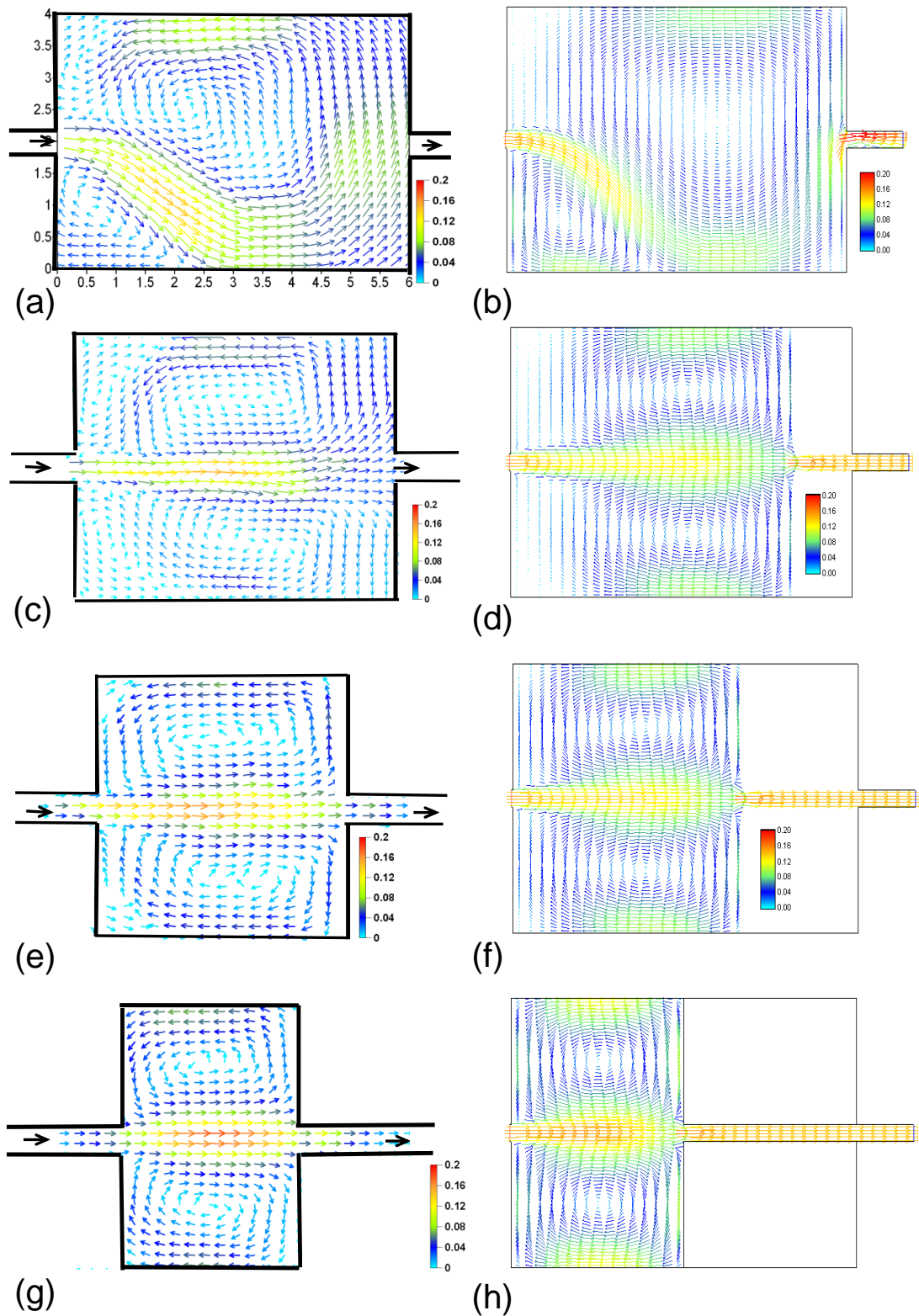


Figure 7.19: Measured and simulated average flow pattern with velocity vectors in a rectangular basin with a constant width of 4 m and four different lengths a, b) 6 m, c, d) 5 m, e, f) 4 m, and g, h) 3 m, respectively.

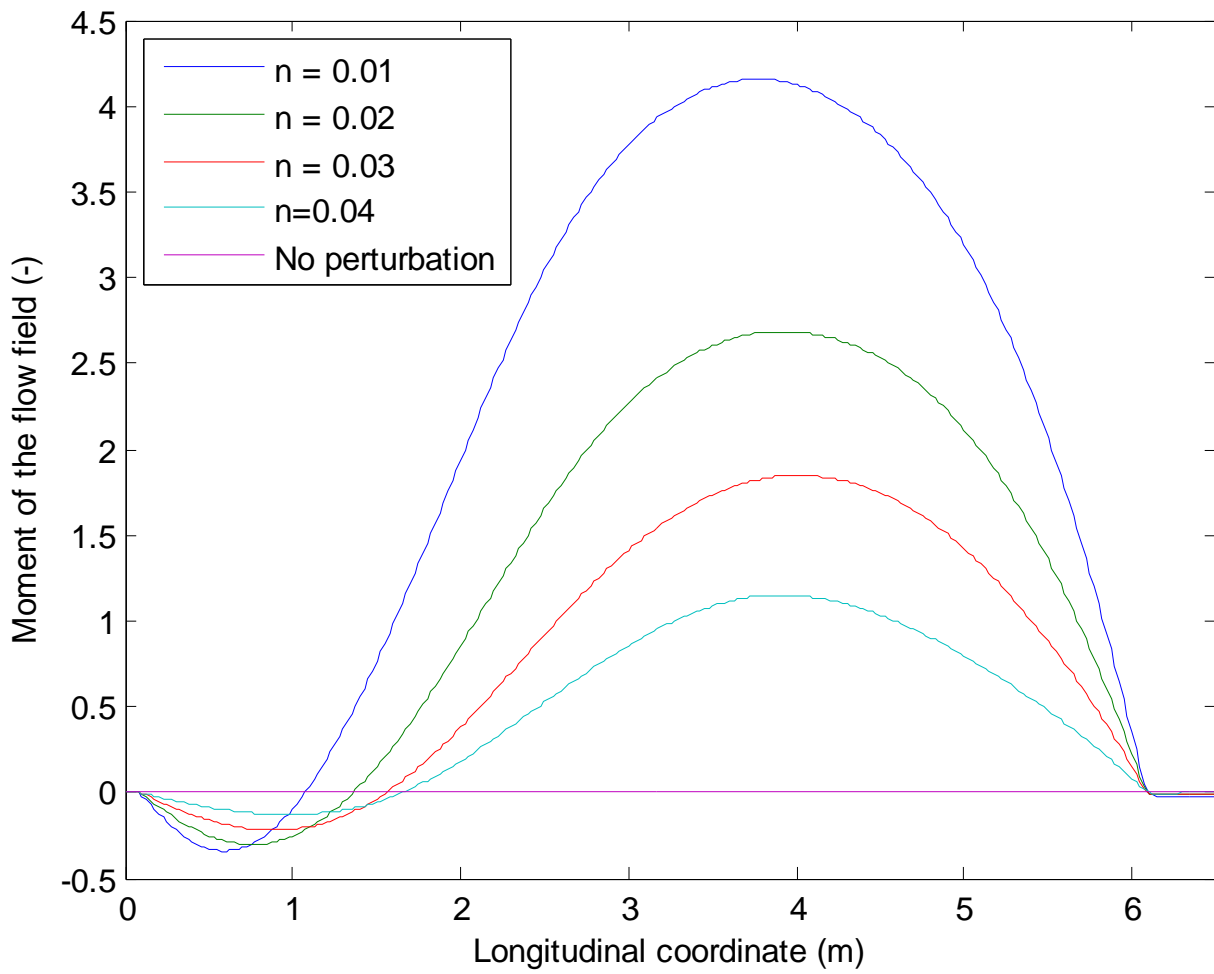


Figure 7.20: Simulated non-dimensional moment m of the flow field in the rectangular basin of 6 m by 4 m.

Summary, Conclusions, Recommendations and Outlook

8.1 Summary and Conclusions

8.1.1 Problematic of control silting processes in shallow reservoirs by design of a suitable geometry form

Controlling of sediment deposition in reservoirs is a major goal of planning, design and operation. The challenge is preserve and extend, if possible, the useful life of a reservoir.

Reservoir sedimentation endangers useful reservoir volume for flood control, hydropower generation, irrigation, water supply, recreation and environmental purposes. Sediment deposition in reservoirs reduces the storage capacity and generates a risk of blockage of intake structures as well as sediment entrainment in hydropower schemes. Over the years as the sediments accumulate, the reservoir loses its storage capacity.

Designers of multipurpose reservoirs are often faced with the challenge of finding and predicting the reservoir siltation. The deposition behavior of fine sediments is an important process, which still is not fully known. The intensity of silting in reservoirs depends on several factors. One main factor is certainly the reservoir geometry. The prediction of the flow pattern and the evolution of the deposition are of great interest for designers of new basins.

The main motivation of the research work was to study the effect of reservoir geometry on flow, sedimentation, and trap efficiency in shallow basins. This should allow to define the optimal shape of the geometry and the management rules of the reservoir. For the first time systematic experimental investigations of the evolution of large water body structures and the associated morphological processes of deposition by suspended sediment in shallow basins with 16 different geometries have been carried out. Furthermore a comparison was

made with the results of numerical modeling.

8.1.2 Experimental set-up, measurement equipment

Sixteen experiments with clear water and water-sediment mixture were performed in a recirculating hydraulic large installations. The experimental tests have been conducted in a rectangular shallow basin with inner maximum dimensions of 6 *m* in length and 4 *m* in width. The inlet and outlet rectangular channels are both 0.25 *m* wide and 1 *m* long.

The influence of different shallow reservoir geometries, with variable widths and lengths as well as expansion angles have been achieved experimentally. To investigate the effect of basin width on the flow and sedimentation processes, first the 6 *m* long basin was performed (Figure 3.5). The width was then reduced successively from 4 to 3 to 2, to 1, and to 0.50 *m* (Figure 3.5). In a second step the effect of basin length was examined by reducing the length of the rectangular shallow basin from 6 *m* to 5, to 4, and to 3 *m* successively (Figure 3.5). Also geometries with three expansion angles were tested (Figure 3.5). To model suspended sediment flow in the laboratory model, crushed walnut shells with a median grain size $d_{50} = 50 \mu m$, and a density of 1500 kg/m^3 was used in all tests.

Several parameters were measured during every test, namely: 2*D* surface velocities, 3*D* velocity profiles, thickness of the deposited sediments, concentration of sediment inflow and outflow, water level in the basin and discharge.

The main measurement techniques employed include ultrasonic probes for measuring water levels, an Ultrasonic Velocity Profiler device (UVP) for measuring 3*D* velocity components and Large Scale Particle Image Velocimetry technique (LSPIV) for measuring surface velocity fields. Furthermore two turbidity meter sensors were installed at the inlet and outlet channels for online suspended sediment measurements. To measure bed morphology evolution a Miniature echo sounder (UWS) was used.

8.1.3 Geometrical parameters, hydraulic and sediment conditions

The geometry shape factor defined as $SK = (P/\sqrt{A_t}) \cdot AR \cdot D_{exp}$ was used to scale expansion characteristics, such as the reattachment length, for all tested geometries, where: P is the wetted perimeter of the length of the side walls; A_t is the total surface area of the basin; $AR = L/B$ is the aspect ratio; $D_{exp} = R/\Delta B$ is the jet expansion density, ΔB is the depth of lateral expansion, and R is the distance from the side edge of channel to the edge of the basin. Such a geometry shape factor allows also to highlight the significant role of the geometry in the bifurcation process between asymmetry and symmetry flow. The different test configurations revealed the effect of geometry on the degree of asymmetry of the separated flow in the basin.

A discharge of $Q = 7 \text{ l/s}$ and a water depth $h = 0.20 \text{ m}$ was used for all experiments, except for two experiments (T5 and T6). These hydraulic conditions were chosen to fulfil the sediment transport requirements. Thus, for all tests, Froude number ($0.05 \leq Fr \leq 0.43$) was small enough and Reynolds number is $14000 \leq Re \leq 28000$) to ensure subcritical and fully developed turbulent flow conditions. During all tests the suspended sediment concentration at the inlet was kept constant with $C = 3.0 \text{ g/l}$.

8.1.4 general phenomena observed with clear water and suspended sediment

The jet entering into the basin developed initially in a symmetric flow for all tested geometries. But the asymmetry phenomenon of the jet in axi-symmetric geometry is due to an deceleration of the axial velocity along the centerline which leads to an increase in the velocity on one side (Figures 4.1(a) and 4.2(a)). This results in a local reduced pressure on that region which in turn tends to amplify the deflection of the jet (Coanda effect).

The Coanda jet is defined as the wall jet along the curved wall. The flow of fluid with a curved jet is accompanied with the decrease of the pressure behind the curvature jet near the wall corner. The pressure on the wall drops below the surrounding pressure resulting in the attachment of the fluid flow to the wall. The increase of one corner gyre increases its size compared to one on the other side. Both of them control the center gyre.

Once these resulting gyres were established across the basin, flow asymmetry is maintained. Simultaneously, an axial acceleration of the velocity increases the centrifugal forces, which tends to re-establish the symmetry of the flow pattern. A balance between those two effects is reached in the steady state.

Upflow and downflow regions play a key role for the sediment transport from the bed to the free surface into the water column. Vertical vortices have been observed which are able to re-suspended the sediment particles and to keep them in suspension. Secondary current behavior was observed for a reduced basin width with geometry shape factor of SK of 8.25 (rectangular basin 6 m long and 3 m wide). Secondary flow arises through a complex interaction between the curved flow, as manifested by the presence of primary eddies formed immediately in the upstream corners, and the boundary layer developing over the bed.

When suspended sediment is added to the turbulent flow over a plane bed in shallow basin with various forms and transported as bed and suspended load, the following was observed:

1. The large horizontal coherent structures substantially were suppressed compared to clear water flow with similar flow conditions. This indicates that sediment transport is affecting the flow pattern and the horizontal momentum exchange.

2. Suspended sediment and deposition height stabilize the flow and change the flow pattern from asymmetric with clear water to symmetric with sediments.
3. Ripples and bed form deposits with a thickness reaching about 15% of the water depth are directly responsible for the change of the flow structure.
4. High sediment concentrations and deposits form along the main jet where the high velocity occurs, due to the formation of a large mixing layer between the primary and secondary gyres.
5. Sediment deposits are increased while there is no horizontal surface motions.

8.1.5 Results of experiments with clear water flow

Jet flow regimes could be classified conveniently by the geometry shape factor SK and the inlet Froude number Fr_{in} . Three distinct and characteristic flow regimes were observed, namely (i) symmetric (straight jet), (ii) asymmetric (deflected jet with a question mark shape) and (iii) a central meandering jet. The occurrence of each is well-determined by SK and Fr_{in} as follows:

- Asymmetric flow pattern:

$$Fr \leq 0.1, B/h \leq 20, SK > 5.5$$

- symmetric flow pattern:

$$Fr \geq 0.1, B/h \geq 26, SK < 5.5$$

where B/h is the basin width to depth ratio.

The influence of the geometrical parameters expressed by the shape factor SK was examined for symmetric inflow and outflow conditions. Although the reference rectangular geometry is symmetric, the flow pattern became asymmetric under certain conditions. By reducing the basin length and for the hexagonal forms, the flow is stabilized with a stable symmetrical pattern. The basin width did not influence the asymmetric separation of the issuing jet. By removing the upstream corners, the two corner gyres disappeared and only the core gyre is formed. No changes occurred by removing the downstream corners in the diamond geometry shape.

It can be concluded that the basin geometry influences the behavior of the large turbulence structures, and the flow is quite sensitive to the geometry shape factor.

By decreasing the shape factor SK below 5.5, the flow becomes more stable and symmetric. The second flow behavior developed with a shorter basin length and for a hexagonal geometry. In the latter case, the flow became even more stable and symmetric with four

large vortices. By reducing SK to 2.92, the number of symmetric gyres is reduced to two (coupled) circulation cells along the centerline. The upstream corner vortices disappear completely. In conclusion, in tested axi-symmetric rectangular configurations, the flow become symmetric if $SK < 5.5$ and asymmetric if $SK > 5.5$.

The water depth has also a significant effect on the flow pattern and the vortex structure. For $Fr_{in} \leq 0.10$ flow is asymmetric and the entering jet is deflected to one side. By increasing the Froude number a central meandering jet is created. The Reynolds number has less effect on the flow structure for the studied range ($14000 < Re < 28000$).

The clear water experiments investigations (i) provided a better insight into how the onset of asymmetric jet flow structure is forming (ii) gives a quantitative estimation of the reattachment length required for the formation of asymmetric flow structures.

8.1.6 Empirical approaches for prediction of mean velocity ratio in reservoir, reattachment lengths, relative residence time and sedimentation index

As explained before, the jet flow structure in the reservoir can be predicted by the geometry shape factor SK and the Froude number Fr . For the prototype application, usually the reservoir dimensions are known and therefore the geometry shape factor can be calculated.

Once the flow type structure according to the geometry shape factor SK are classified, as explained in before, the following empirical relationships for estimating the ratio of the mean velocity in reservoir and the mean inlet velocity U_{res}/U_{in} along the centerline of the basin have been obtained from the systematic experiments:

- Geometry shape factor $2.92 < SK < 5.5$, $0.05 \leq Fr_{in} \leq 0.1$, and $2.25 \leq L_c/b \leq 21.75$ (Eq. 4.5):

$$\frac{U_{res}}{U_{in}} = 0.097 \cdot \frac{L_c}{b} \cdot \left(1 - \ln \frac{L_c}{10 \cdot b}\right)$$

- Geometry shape factor $5.5 < SK < 86.6$, $0.05 \leq Fr_{in} \leq 0.1$, and $2.25 \leq L_c/b \leq 21.75$ (Eq. 4.6):

$$\frac{U_{res}}{U_{in}} = 0.68 - 0.066 \cdot \frac{L_c}{b} + 0.00011 \cdot \left(\frac{L_c}{b}\right)^3$$

- Geometry shape factor $2.92 < SK < 86.6$, $0.15 \leq Fr_{in} \leq 0.43$, and $2.25 \leq L_c/b \leq 21.75$ (Eq. 4.7):

$$\frac{U_{res}}{U_{in}} = 0.39 + 0.44 \cdot \left(\frac{L_c}{b}\right)^{-2} - 0.00017 \cdot \left(\frac{L_c}{b}\right)^2$$

where L_c/b ratio of axial distance of the basin and inlet channel width, U_{res}/U_{in} ratio of the mean velocity magnitude in the reservoir and in the inlet channel along the centerline.

For estimation of the mean velocity in the reservoir the prediction of the silting index is important.

Another empirical formula to predict the average velocity ratio U_{res}/U_{in} over the whole reservoir as a relation with SK was developed for the application range of is $2.92 < SK < 86.60$ (Eq. 4.8).

$$\frac{U_{res}}{U_{in}} = 0.88 - 0.33 \cdot \left(\frac{SK}{10}\right)^{-1} \cdot \left(1 + 0.49 \cdot \ln \frac{SK}{10}\right)$$

The geometry shape factor is also controlling the number of circulation cells exist for specific hydraulic conditions. The number of recirculation cells in the basin can be estimated from Figure 4.16(c) in Section 4.4.

The reattachment length L_r of the entering jet was normalized with the recirculation width $B_r = \Delta B$ which is the equal to lateral expansion width ΔB in axi-symmetric reservoirs. Empirical relationship for direct estimation of the reattachment lengths X_r of gyres as a function of geometry shape factor SK (Eqs. 4.1, 4.2, 4.3, and 4.4) and Froude number (Eqs. 4.9 and 4.9) have been established.

Furthermore an empirical function between geometry shape factor SK and normalized initial residence time t_{ri}/t_s , which is generally referred to as the ratio of water residence time and particle settling time could be found for the application range of $2.92 < SK < 13.42$ (Eq. 4.11).

$$\frac{t_{ri}}{t_s} = -0.85 + \frac{2.3}{SK} + 1.1 \cdot \sqrt{SK/10} \quad (Eq. 4.11)$$

With the prediction of the mean velocity in the reservoir also a relationship between the sedimentation index SI and the geometry shape factor SK (Eq. 4.13) could be found for $2.92 < SK < 86.60$:

$$SI = -4922 + 821589 \cdot SK^{-1} \cdot (1 - 2.25 \cdot SK^{-1})$$

All these empirical formulas clearly show the importance of the geometry shape factor SK when defining the new reservoir design.

The geometry of the reservoir can be selected if possible according to the flow and hydraulic conditions. Moreover, for a certain geometry the flow structure type, number of recirculation and its reattachment lengths can be predicted with the help of the developed clear water formulas.

8.1.7 Results of experiments with suspended sediment

Compared to the experiments with clear water, the flow behavior in the basin changed in the presence of suspended sediments.

Bed forms and final sediment deposits were systematically observed in the experiments with different shallow reservoir geometries. Although jets types vary for the different geometrical configurations (deflected asymmetric, straight symmetric and meandering), the bed form characteristics remain the same. Immediately after the beginning of all experiments with suspended sediments, ripples formed throughout the whole length for all jet types (deflected or straight). The observed ripples length Λ in the experiments were in the range of 11 to 17 *cm* while their height Δ reached values of about 1 *cm*. An interesting feature revealed by the shape of these bed forms was the presence of a distinct correlation between the orientation of their symmetry and asymmetry and the type of the flow pattern.

A strong interaction between flow field and bottom topography also occurs in the basin inlet region with a quasi equilibrium state. There, most of the bed form features disappeared, as the deposition was fairly fast increased.

The deposition pattern was strongly influenced by the inlet jet deviation. In turn, sediment deposits were able to change later the pattern of the flow structure.

For the reference geometry (basin 4*6 *m*) two typical deposition pattern were observed. In the first case the sediment depositions with ripples formation concentrated on the right hand side and later on along the centerline. In the second case the deposits were concentrated on both right and left sides and remained very low in the center of the basin.

It may be concluded that the number of recirculation cells which exist in the basin have a strong influence on the flow and sediment deposition behavior. By increasing the numbers of recirculation cells (number of eddies) the deposited volume of sediments in the basin increased.

8.1.8 Empirical relationships for prediction of storage losses and relative deposition thickness in a shallow basin

Based on the performed experiments the storage losses can be estimated with the following empirical relationships:

- Application range is $2.92 < SK < 13.42$ and $8 \leq t^* \leq 200$ (Eq. 5.1):

$$SR = \frac{V_{dep}}{V_{res}} = 0.25 \cdot t^* + 200 \cdot SK^{-2} \cdot (1.2 + \ln \frac{SK}{10})$$

- Application range is $2.92 < SK < 13.42$ and $8 \leq t^{**} \leq 95$ (Eq. 5.3):

$$SR = \frac{V_{dep}}{V_{res}} = 0.44 \cdot t^{**} - 5.4 + 375 \cdot SK^{-2} \cdot (1 + 0.8 \cdot \ln \frac{SK}{10})$$

Furthermore the relative deposition thickness can be estimated by:

- Application range is $2.92 < SK < 13.42$ and $8 \leq t^* \leq 200$ (Eq. 5.5):

$$\frac{d}{h} = 0.2 \cdot (1 + (\frac{SK \cdot t^*}{1000})^3) - \frac{0.035}{\sqrt{SK \cdot (t^*)/1000}}$$

- Application range is $2.92 < SK < 13.42$ and $8 \leq t^{**} \leq 95$ (Eq. 5.6):

$$\frac{d}{h} = \frac{-0.38 \cdot t^{**} \cdot (SK^{-1} - 0.39)}{3 \cdot SK + SK/(0.46 \cdot t^{**} + 3 \cdot SK + t^{**}/SK)}$$

where

SR : is the silting defined as ratio of cumulative deposited volume after specific running time V_{dep} and the initial reservoir volume before deposition V_{res} ($SR = V_{dep} / V_{res}$),

SK : is the geometry shape factor $SK = (P/\sqrt{A_t}) \cdot AR \cdot D_{exp}$

P : is the wetted perimeter of the length of the side walls

A_t : is the total surface area of the reservoir

AR : is aspect ratio of the reservoir

$D_{exp} = R/\Delta B$ is expansion density of the reservoir.

d/h : is relative thickness of deposited sediment over reservoir at specific period normalized by the water depth at the same period

t^* : is the dimensionless time which can be define as ratio of duration of suspended sediment inflow to actual water residence of reservoir $t^* = t/t_r$

t^{**} : is the normalized time and it can be define as $t^{**} = t/t_{r_i}$ is ratio of t the duration of the suspended sediment inflow to t_{r_i} the reservoir initial residence time before deposition.

8.1.9 Trapping and flushing efficiencies

8.1.9.1 Trap efficiency

The trap efficiency of a reservoir is the percentage of incoming sediment which is trapped by the reservoir. The standard predictors of trap and release efficiencies are the Brune and Churchill curves. Churchill's curves have not been revised since their introduction in 1948, even though more data are available than what were used originally. Moreover, Churchill curves do not consider the geometry effect. Therefore the influence of the reservoir geometry and the dimensionless time on the the trap efficiency were considered to developed an empirical relationship in Eq. 6.5:

- Application range is $8 \leq t^* \leq 200$ (Eq. 6.4):

$$TE = \frac{120 \cdot (t^*)}{58 + (t^*)}$$

Hence, time effect should be considered when determining the trap efficiency of a reservoir geometry influenced by suspended sediments. Therefore, the following empirical formula Eq. 6.5 was developed to predict the trap efficiency by combination of the geometry shape factor and ratio of running to residence times t / t_r .

- Application range is $2.92 < SK < 13.42$ and $8 \leq t^* \leq 200$ (Eq. 6.5):

$$TE = \frac{C_{in} - C_{out}}{C_{in}} = 13.5 - 0.055 \cdot (t^*) + 1700 \cdot SK^{-2} \cdot (1 + 0.72 \cdot \ln \frac{SK}{10})$$

A strong link seems to exist between actual residence time, trap efficiency and geometry shape factor. Therefore, the settling time was used to normalize the residence time. The obtained relationship is in Eq. 6.6.

- Application range is $2.92 < SK < 13.42$ and $1.4 \leq \frac{t_r}{t_s} \leq 3.3$ (Eq. 6.6):

$$TE = \frac{V_{dep}}{V_{in}} = 30 + 11.2 \cdot \frac{t_r}{t_s} + 32.5(SK/10)^3 \cdot (1 - 2.85 \ln(SK/10))$$

If the average flow velocity of water in the reservoir is known as developed in Section 8.1.6, then the sedimentation index of the reservoir can be calculated. An empirical relationship between the sedimentation index, geometry shape factor, and dimensionless time was developed in Eq. 6.7.

- Application range is $2.92 < SK < 13.42$ and $8 \leq t^* \leq 200$ (Eq. 6.7):

$$SI = g \frac{t_r}{U_{res}} = 80076 - 47766 \cdot \sqrt{\frac{SK \cdot t^*}{1000}} + 28 \cdot \left(\frac{SK \cdot t^*}{1000}\right)^{-2}$$

For estimating the release efficiency in shallow reservoirs based on the correlation between the sedimentation index SI and sediment release efficiency an empirical linear relationship was developed in Eq. 6.8.

- Application range is $2.92 < SK < 13.42$ and $8 \leq t^{**} \leq 95$ (Eq. 6.8):

$$RE = 74 - 0.0002 \cdot SI$$

TE : trap efficiency in percentage

t^* : dimensionless time t/t_r

t : duration of suspended sediment inflow

t_r : actual residence time for the case with clear water

$t_r = t_{ri}$

t_s : settling time of sediment particle

SI : sedimentation index $g \frac{t_r}{U_{res}}$

U_{res} : average velocity in the reservoir

8.1.9.2 Flushing efficiency and flushing channel formation

Efficiency of flushing of suspended sediment through the reservoir is important to determine the feasibility of flushing operations for different reservoir conditions. In the present study, final bed morphology formed previously during the test for each geometry was used as the initial condition for two modes of flushing. The entire experiments lasted for two days. With the total cumulative deposited sediment at the end of each experiment and the volume of flushed sediments during this procedure, flushing efficiency, FE, is defined as:

$$FE = \frac{V_{flushed}}{V_{df}}$$

where $V_{flushed}$ volume of flushed sediment with clear water after two days, V_{df} total cumulative deposited volume in the reservoir after a specific period.

8.1.9.2.1 Free flow flushing without lowering reservoir level Free flow flushing has only a very local effect. Therefore it can be applied only to remove sediment deposited around the entrance of the inlet channel under the action of the main jet. The most important bed change occurred by the erosion near the entrance. After the channel was formed its location remained rather stable. Experiments showed that under pressurized flow a flushing nose can be formed in a very short time but only relatively small amount of sediment was flushed out.

The free flow flushing efficiency was fairly low with a maximum value of 10% for the most narrow reservoir with $SK = 13.42$. Qualitatively, it was found that almost all of the removed sediment from the final deposited one was flushed out in the one third of the flushing duration.

The developed correlation between free flow flushing efficiency and geometry shape factor SK can be approached by Eq. 6.10 for the application range of is $2.92 < SK < 13.42$.

$$FE = 0.81 + 0.47 \cdot SK$$

8.1.9.2.2 Drawdown flushing During drawdown flushing, three channel shapes (curved, straight, and cone) were formed with the different basin geometries. The width of the channel depends on the inlet channel width, the flow pattern, and the geometry shape factor. The flow structures and sediment deposition patterns of drawdown flushing system have been investigated. A larger volume in the reservoir generally generates a higher flow depth and velocity in the flushing channel.

To apply the flushing efficiently for removing deposits, the width, length, and location of the flushing channel can be changed by modifications of the geometry shape factor. The flushing channel attracts the jet and stabilizes the flow structures over the entire basin. For the experiments with drawdown flushing it is important to know the channel width and length in order to estimate the gain of the reservoir capacity. Due to the sensitivity of the flow pattern on the boundary conditions, initial conditions and the geometry (and changes in time), it is difficult to predicate the exact location of the flushing channel.

Drawdown flushing efficiency could be correlated with the geometry shape factor by empirical relationship formula in Eq. 6.11 within the application range of $2.92 < SK < 13.42$:

$$FE = \frac{V_{flushed}}{V_{dep}} = 103 + 12.4 \cdot (SK/10)^{-2} - 65.75 \cdot (SK/10)^{-1}$$

8.1.9.2.3 Characteristics of flushing channel forming during drawdown flushing

Several geomorphic studies indicated that the width of the channel and flow discharge are significantly correlated. In the present study the discharge was constant and only the geometry shape was changing.

A simple empirical equation (Eq. 6.12) could be found to predict the flushing channel width for a specific geometry in the range of $2.92 < SK < 13.42$.

$$\frac{b_{eff}}{b} = 2.81 + 800 \cdot SK^3 \cdot (4.375 \cdot \ln(SK/10) - 1)$$

where b_{eff} is the width of the flushing channel, b is the inlet channel width, and SK is the geometry shape factor.

The flushing length l_{eff} could also be expressed as a function of geometry shape factor of the basin for $2.92 < SK < 13.42$ by the following empirical relationship could be obtained from the experiments

$$\frac{l_{eff}}{b} = 26.85 + 6430 \cdot SK^2 \cdot (1 - 0.074 \cdot SK)$$

where l_{eff} is the length of the flushing channel, b is the inlet channel width, and SK is the geometry shape factor.

Furthermore the measured channel characteristics l_{eff} and b_{eff} could be fitted by an empirical relationship depending on the geometry shape factor as well. The area of flushing

channel was normalized by the total surface area of each tested experiments as $\Delta A = \frac{A_{fc}}{A_t}$, where $A_{fc} = b_{eff} \cdot l_{eff}$ and A_t is the total area of the reservoir. The obtained equation is:

$$\Delta A = \frac{A_{fc}}{A_t} = -52 + 44.3/(\sqrt{SK/10}) + 24.1 \cdot (SK/10)^3$$

It has to be noted that all empirical relationships developed are restricted to boundary and hydraulic conditions of experiments defined by: $0.375 \leq h/b \leq 0.8$ where h/b is the inlet channel width to depth ratio, $0.05 \leq Fr \leq 0.43$, and $14000 \leq Re \leq 28000$.

8.1.10 Numerical simulation

Numerical simulations were performed by using three different codes, with FLOW-3D, CCHE2D, and WOLF 2D software solving the shallow-water equations. Three turbulence closure schemes $\kappa - \varepsilon$, parabolic eddy viscosity model, and mixing length eddy viscosity model were exploited and compared.

Although the experimental set-up is axi-symmetric, the flow and deposition were asymmetric. Two scenarios were simulated, with and without inlet perturbations. For without perturbation input data, the numerical model provides a perfectly symmetric result. However, if the inflow boundary condition is disturbed by a slightly non uniform velocity distribution, the numerical model was able to produce the asymmetric flow pattern as observed in the laboratory experiments.

On one hand, for the geometries corresponding to an observed non-symmetric flow field, the numerical model converges towards a completely deviated flow field, the global pattern of which is consistent with laboratory observations. For the geometries corresponding to an observed symmetric flow field, the slight disturbances introduced upstream are quickly damped and the computed steady flow field is found almost symmetric.

The 2D simulations were found to succeed in predicting the influence of the length and width of the basin on the global flow pattern. Numerical and experimental results were compared by means of the first moment of the longitudinal velocity field about the centreline of the basin and they were in good agreement.

Although the simulations show that a 2D depth-averaged model can be used to reproduce the observed flow patterns in the laboratory, it is believed that future improvement of the modeling technique can lead to more reliable predictions. For a better approximation of the eddies and jets it is recommended to use a more detailed model for horizontal turbulence. For instance techniques such as fully 3D approaches (three dimensional large eddy simulation) can be considered.

8.2 Answers to practical questions

The study focuses on the influence of geometry of shallow reservoirs on flow pattern and sedimentation processes by suspended sediments and gives answers to the questions given in Section 1.3:

Flow patterns and sedimentation process

How functions the processes of flow and sedimentation patterns in shallow reservoirs under suspended load?

Although the flow is shallow, three-dimensionality of the flow controls the function processes between flow and sedimentation patterns. Furthermore, upflow and downflow regions play a key role for the sediment transport from the bed to the free surface into the water column. Vertical vortices are able to resuspended particles and to keep them in suspension. Secondary flow arises through a complex interaction between the curved flow, as manifested by the presence of primary eddies formed immediately in the upstream corners, and the boundary layer developing over the bed. The changes in the bed forms or relative roughness resulting from the sediment deposition are capable of completely changing the overall flow pattern. The flow pattern was stable, with high roughness over the entire bed. The increased roughness height associated with mobile sediment may contribute to increase in shear velocity and turbulence intensity. However, after some time, ripples developed underneath the main jet, with thicknesses of about 0.15 times the flow depth. There is a correlation between the orientation of bed form symmetry and asymmetry and the type the flow patterns. Finally, high deposition form along the main jet due to the formation of a large mixing layer between the primary and secondary recirculation cells. Through the same mechanism a further development can be expected.

What is the mechanism governing the sediment exchange process between the jet entering the reservoir and the associated turbulence structures?

By entering the mixture of suspended sediment a reduction of horizontal vortex take place. As sediment is added to the flow, the turbulence is reduced and the mixing lengths decrease which, together with increasing roughness, cause an increase in velocity gradient when compared to clearwater flow. The turbulence was generated locally by the horizontal entrainment of a mixture into the basin with stagnant water. The jet pulse created a region of three-dimensional turbulent flow, characterized by mixing and entrainment. Then the size of the turbulence increased rapidly. During the subsequent stage of sediment settling, the horizontal motions are suppressed and eventually the mixed region becomes flat and the motion becomes quasi vertical. The cross-stream sediment transport is produced due to the overturning motions or the secondary currents. This circulation moves the sediments from

the center of the basin to the wall sides in the lateral direction. This process occurs rapidly at the early stage of bed evolution and then slows down the deposition rate.

What is the morphodynamic evolution of the jet flow in the reservoir?

A slow evolution of bottom topography occurs with two typical features on right and centerline of the basin. The jet is narrower in the the surface than near the bed and the deposition gradually increases generating a wider bed elevation underneath the jet centerline. Then the basin fills up from the center to the walls directions, starting from downstream to upstream direction. With longer period these gradient slopes regions will be eventually filled up with the finest sediment fraction. A tongue shape deposition occurs along the centerline of the basin. The tongue average thickness is of 0.16 m and locates underneath the jet centerline with average width of approximately eight times the inlet channel width. The deposition at both upstream corners is less than in other parts. The exchange of sediment between the jet and the eddies affects the equilibrium configuration significantly. The latter has a strong effect on the entering jet hydrodynamics and on its morphodynamics. It increased due to the generation of the submerged channel which progresses downstream until it reaches a quasi-equilibrium condition. The jet width is reduced on the surface, due to increase of the coupled eddies size and velocity. Most of the bed form features were vanished, as the deposition was fairly fast increased.

Is it possible for a simple reservoir geometry to obtain a long term morphodynamic equilibrium and when it will be reached?

The possible existence of a long term equilibrium (where inflow of suspended sediment concentration is equal to released suspended sediment concentration) was observed in the basin (4*6 m) after 16 hours where the suspended sediment release efficiency reached 100%.

Influence of reservoir geometry

What is the influence of the shallow reservoir geometry on the flow and bed deposition behaviors and the main mechanism controlling the morphodynamic evolution?

Reducing the width of the basin did not affect the asymmetric separation of the deflected jet. Final deposition patterns were influenced by the reservoir width, with more symmetric and uniform distributions on the entire surface. Increasing the length of the reservoir plays a critical role on the jet flow type and the associated bed deposition pattern. The jet flow and sediment deposit were stable and symmetric. The same behavior was observed for the hexagonal geometry. For a geometry shape factor $SK < 5.5$, the depositions became more uniform and symmetric over the entire surface. The geometry shape factor SK is able to predicted flow velocity in reservoir, jet flow type, sediment deposition thickness and trap efficiency. Flow becomes symmetric if $SK < 5.5$ and asymmetric if $SK > 5.5$.

Which geometry of the shallow reservoir has to be chosen in order to minimize the sedimentation processes?

Geometry of lozenge form with large instabilities of flow pattern and one recirculation cell is favorable for minimizing the sedimentation.

Which flow behavior and hydraulic condition is optimal in view of minimizing sedimentation?

Asymmetric flow pattern with a large stagnant zones and one circulation cell or less number of gyres are favorable to minimize retention of sediments.

What is the relationship between the reservoir geometry and sediment trap efficiency?

A strong link seems to exist between actual residence time, trap efficiency and geometry shape factor. Therefore, the settling time was used to normalize the residence time. The obtained relationship is in Eq. 6.6.

$$TE = \frac{C_{in} - C_{out}}{C_{in}} = 13.5 - 0.055 \cdot (t^*) + 1700 \cdot SK^{-2} \cdot (1 + 0.72 \cdot \ln \frac{SK}{10})$$

How the geometry of the reservoir influences the relative deposited thickness?

$$\frac{d}{h} = \frac{-0.38 \cdot t^{**} \cdot (SK^{-1} - 0.39)}{3 \cdot SK + SK / (0.46 \cdot t^{**} + 3 \cdot SK + t^{**} / SK)}$$

Operation and flushing

How the reservoir has to be operated in order to reduce sedimentation and which mode gives the best flushing efficiency?

Reservoirs can be operated after sediment deposition by drawdown flushing. Different flushing channel shapes (curved, straight, and cone) will be formed in accordance with the geometry shape factor SK . The width of the channel is in accordance with the inlet channel, flow pattern, water depth, discharge, and the outlet conditions. If flushing is allowed to continue for such a long time the channel erosion diminishes, the longitudinal eroded depths are closely related to the depositional pattern in the reservoir. A larger volume in the reservoir generally generates a higher flushing flow depth and velocity in the flushing channel. The larger reservoir volume will induce higher bed shear stress, and hence produces more effective flushing/removal of sediments on the bed. A significant amount of sediment deposits was flushed through the reservoir. To effectively apply the flushing processes for removing deposits, the location, depth, and width of the flushing channel can be changed by modifications of the geometry or installation of islands or a movable wall near

the inlet jet. The channel attracts the jet and stabilizes the flow structures over the entire surface. For the experiments with drawdown flushing sediments it is considered relevant to know the channel width and depth in order to estimate the gain of the reservoir capacity. Due to the sensitivity of the flow pattern to the boundary conditions, initial conditions, and the geometry (and changes in time), it is difficult to predicate the exact location of the flushing channel.

What is the location, width and depth of the channel which forms during flushing? How influences the geometry shape factor on the flushing efficiency?

To predict the flushing channel width for a specific geometry

$$\frac{b_{eff}}{b} = 2.81 + 800 \cdot SK^3 \cdot (4.375 \cdot \ln(SK/10) - 1)$$

and the flushing length l_{eff} could also be expressed as a function of geometry shape factor by the following formula:

$$\frac{l_{eff}}{b} = 26.85 + 6430 \cdot SK^2 \cdot (1 - 0.074 \cdot SK)$$

Numerical simulation

What is the most appropriate numerical model available to simulate the observed flow and sedimentation structures?

The most appropriate numerical model which is able to simulate the experimental tests with complex geometries. Moreover, it can predicted and simulate the prototype in less time and error. Furthermore, simulations for the evolution of sediment depositions can be extended. To be able to investigate the geometry effect on the flow, sediment deposition, and trap efficiency, the developed equations have to be added to the numerical codes, in order to take into account the interactions between geometry, flow, settling of sediment, bed deposition, and suspended sediment effect. It is more useful to develop, verify and validate that model with the observed experimental flow and deposition patterns.

8.3 Recommendations for design of shallow reservoirs

This section outlines the design procedures for the geometry of reservoir.

To minimize the retention of sediments, the following recommendations, can be given as rules of thumb:

1. Flow pattern and number of recirculation cells

An asymmetric flow pattern with a low number of circulation cells is favorable to reduce the exchange processes between flow, bed deposition and suspended sediment. By increasing the number of recirculation cells (number of eddies) the deposited volume will increase. Flow pattern with large stagnant zones in the basin allows a portion of flow to pass the basin in a time period less than the settling time. Therefore, the empirical Equation 4.11 should be used for defining the reservoir hydraulic conditions.

2. Residence time:

It can be used to normalize the duration of suspended sediment inflow into the reservoir. Moreover, the normalized residence time which is generally referred to as the ratio of hydraulic residence time and particle settling time, provides a description of the flow classification. The normalized residence time is strongly influenced by the geometry shape factor of the basin which influence for the prediction of flow and velocity distribution, for scaling the flow field, and for interpreting CFD results throughout the flow behavior of the different basin geometries. The preliminary selection of adequate dimensionless parameters was necessary in order to obtain good results.

3. Geometry of basin (length, width, corners, shape factor and expansion angles)

The trap efficiency is reducing with time with the lozenge form, but trapping is high in the beginning. With the lozenge form the jet could expanded on all the basin geometry. However, drawdown flushing should be with that geometry in order to make storage space available for the subsequent deposits. According to the proposed empirical formula, removal efficiency can be estimated. The length of the reservoir plays a critical role in determining the jet flow type and the associated pattern of the bed deposition. The use of an elongated basin increases the retention of sediments. The maximum Aspect Ratio (Length to width ratio) of reservoir should be 1.5. For higher ratios the sediment deposition will increase too fast. The minimum Aspect Ratio should be above 0.75, to minimize sedimentation. Although an asymmetric flow pattern is favored, a symmetric pattern can persist for quite a long time with shorter distance between inlet and outlet. A symmetric flow pattern is recommended with drawdown flushing which will be able to flush the formed deposited channel under the jet. Larger Expansion Ratio (width of reservoir to the width of the inlet channel) between 1.5 to 0.75 are preferred to minimize sedimentation. By removing the upstream corners, the stability of flow is much decreasing, because the corners are controlling the other circulation cells inside the basin. On the other hand, the half angle of the expansion jet should be less or equal 32° . The geometry shape factor is an important factor to predicted the flow and sediment deposition in the reservoir. It is difficult to give only one single value which can minimize the sedimentation. However, a favorable range for geometry shape factor between 3.0 to 6.0 can be recommended.

4. Flow and sediment instabilities

Large instabilities of flow with sediment occurred for the geometry form of lozenge with one circle eddy in the center of the basin. Therefore, the deposited volume was reduced with time which is favorable for minimizing the sedimentation.

This research on the effect of the geometry of shallow reservoirs is a first step in developing new procedure to control or prevent reservoir sedimentation due to suspended sediment. The empirical equations developed from the experimental study can give a first estimation.

The presented procedure may be interesting in combination with other traditional methods, such as flushing. Moreover, the flushing efficiency and channel formation characteristics can be predicted from the developed equations in this study.

The applications from the present study are not only restricted to reservoir sedimentation, but can be extended to other shallow flow related problems, as for example jet flow.

8.4 Outlook and further Research

For the first time, the evolution of the flow and deposition processes for sixteen shallow reservoir geometries have been carried out in the present study. The originality of the work can be summarized in the following five points:

1. For the first time systematical investigations of the influence of shallow reservoir geometry on the flow and sediment deposition processes were performed. Detailed description of the full processes of flow and sediment deposition patterns constitutes a first step in understanding the geometry effects and the flow sediment interactions.
2. The observed phenomena of the flow, suspended sediment, and bed topography behavior on a flat bed of various shallow basin geometries were explained. The observed phenomena are intriguing.
3. Combinations between four measurement devices of LSPIV for two dimensional velocity every thirty minutes, Mini-Echo Sounder to measure the bed evolutions every ninety minutes, UVP to measure three dimensional velocity profiles, and SOLITAX turbiditymeter probes for online measurements of inlet and outlet suspended sediment concentration.
4. Developing several empirical formulas to predict the flow and sediment deposition behaviors.
5. Preliminary design procedures and recommendations for engineering practices.

The experiments were started with the basic rectangular geometry, followed by different systematically configurations with the aim to find the more optimal geometries. Tracer experiments and velocity measurements were performed in the model to determine the hydraulic behavior of the reservoir.

The following points are suggested to be addressed in a possible follow up of the present research:

1. Database of carried experimental tests is suitable for numerical validation. After validations and verifications of numerical code, a case study application should be performed.
2. For a better approximation of the flow structures and the jet behaviors it is recommended to use a more detailed model for three dimensional turbulence. For instant techniques such as three-dimensional large eddy simulation as fully *3D* approaches can be considered. Three-dimensional numerical simulations can assess the pressure distribution variations effect over the entire reservoir, on the symmetric and asymmetric flow behavior.
3. There is a need to study the secondary current effect and vertical vorticity in the shallow reservoir geometry. Furthermore, the sediment-transport model should be extended with multiple grain size fractions, suspended sediment concentrations, and convection-diffusion processes for suspended sediment.
4. Further physical experiments for:
 - a) Asymmetric geometrical configurations: Series of configurations could be tested by varying the locations of inflow and outflow. To study the influence of the outlet channel width to stabilize the deflected jet at the center. What is the optimal outlet width at which the deflected jet with the reference rectangular geometry becomes symmetric at the center. Symmetric and asymmetric inflow and outflow conditions for polygonal and curved geometries could be also of interest. There is a considerable scope for further research in this area.
 - b) Influence of Froude number on sediment deposition pattern: experiments with other hydraulic conditions to investigate the effect of discharge and water depth with sediment transport. Particularly experimental investigations concerning the effect of Reynolds number on the symmetry and asymmetry of the flow should be done with a simple geometry.
 - c) Influence of suspended sediment concentration on flow and sediment: experiments with other sediment characteristics and suspended concentration in order to investigate the effect of the grain size distribution and sediment concentration.

- d) Although the simulations showed that a 2D depth averaged model can be used to reproduce the observed hydrodynamic features in the clear water experiments, future improvements of the modeling technique is required to have more reliable predictions, especially with sediment transport models.
- e) Geometry shape factor SK between 13.4 and 86: the present study gives a large range for geometry shape factor SK between 2.9 and 86.6 with clear water test. On the other hand, the range of geometry shape factor with sediment phase is small between 3.4 and 13.4. Therefore, it is recommended to do test for the same range as with clear water experiments.

Acknowledgements

My first and last gratitude to the Almighty " Allâh ", the God of all mankind, for giving me the health, strength, patient, and faith to undertake this work. In my human endeavors, I humbly implore him to grant that my labor my serve all the living.

Then

I wish to express my sincere gratitude to my supervisor Prof. Dr. Anton Schleiss, Professor and director of Laboratory of Hydraulic Constructions (LCH), Swiss Federal Institute of Technology (EPFL), Switzerland, who introduced me to the fascinating world of Reservoir Sedimentation, and continuously gave me invaluable guidance, suggestions, and encouragement during the period of carrying out this study. I offer my heartfelt thanks to him for his support to enable me to attend many international conferences in and outside Switzerland. I am indebted to him, for giving me the chance to study in his laboratory.

During my Master studies in Japan I was searching for a PhD position, I sent for Prof. Scartezzini my CV and he encouraged me to apply for doctoral school program. Moreover, he introduced me to Prof. Schleiss. I must express boundless thanks to Prof. Dr. Jean-Louis Scartezzini, Professor and director of Solar Energy and Building Physics Laboratory and Doctoral School Program of Environment at EPFL, Switzerland, from whom I derived stimulus and encouragement through applying for doctoral school program, without which I will not have that excellent chance to continue my PhD study.

I would like to acknowledge my deep and sincere gratitude to Dr. Dr Jean-Louis Boillat, senior research associate at LCH, who opened his heart and his library to give me his knowledge, his time and his effort to teach me, to encourage me and guide me through my research work. Moreover, we had a lot of discussions on politics, religion, social topics, and etc.

My sincere thanks are also extended to Dr Erik Bollaert, for his discussion, encouragement, advice, and English correction.

The author acknowledges the financial support by the Swiss Federal Office for Water and Geology FOWG (now Federal Office for the Environment FOEN) in the framework of

Acknowledgements

the project "Rhone-Thur - sustainable use of rivers".

I appreciated a lot to meet and discuss with Prof. Wim Uijttewaal, Associate Professor of Department of Civil Engineering of Delft, The Netherland, during his visits in Lausanne as invited professor.

I'm indebted to Dr G. De Cesare, who was always ready to help and discuss about reservoir sedimentation and laboratory instruments. I would like to thank Dr K. Blankaert, for his scientific exchange and result discussions. I do not forget the sympathy of Dr Mohamed Farhat from Hydraulic Machines Laboratory for his substantial support in developing LSPIV system. I am grateful to Haroon Anwar for his help with Matlab, and Gonzalo Medina Arellano from Departamento de Matematicas y Estadistica, Universidad Nacional de Colombia, for his great continuous support with Latex.

I am deeply thankful to Prof. Michel Piroton, Prof. and director of HACH (Hydrodynamique Appliquée et Constructions Hydrauliques), Liège, Belgium, for discussions on numerical simulation. He has also participated to the present work during the Post-Doctoral stay of Dr Benjamin Dewals, by conducting numerical simulations. I would also like to thank Benjamin who collaborated in simulating the experimental results, during his PostDoc at LCH-EPFL.

My thanks for providing support on numerical simulations with CCHE2D are due to Dr Yaxoin Zhange, Dr. Dalmo Ferreira, Prof. Yafi Jia, and Prof. Moustafa Altinakar from National Center for Computational Hydroscience and Engineering (NCCHE).

I am highly appreciating the help of Dr. Azin Amini for her help with latex , writing equations, corrections, and list of symbols. Special thanks for Dr. Burkhard Rosier for his precious help with GPKernel programming, Dr. Mohamed Fawzy for STATA programming and statistics, and Fadi Hachem for translating my Résumé, Haroon Anwer for his help to develop Matlab codes for treatment of UVP measurements.

Gratitude is dedicated to the members of the jury, Prof. Hans-Erwin Minor, Prof. Michel Piroton, and Prof. Wim Uijttewaal, who have honored me by accepting to review and evaluate this thesis, and Prof. André Mermoud for accepting to be the president of my PhD thesis jury.

A word of appreciation is due to the Head and staff of Civil Engineering Department, Alexandria University for their invaluable teaching of the fundamentals of hydraulics, irrigation, water resources and civil engineering subjects. Sincere thanks and indebtedness are due to my respected teachers in Irrigation and Hydraulics Department, Alexandria University.

I would like to thank Mr. Edgar Bastian, and Chevalier, from Le service audiovisuel SAVE *Réalisateur* groupe Audiovisuel at EPFL and Madame Liliane Dufresne from University of Lausanne (UNIL), Institut de minéralogie et géochimie for her great help with laser granulometry of walnut shells.

Experimental study could be difficult without a strong technical support from Michel Teuscher. My thanks are, therefore, addressed to him and also to Jean-Marck Terraz, Frigile,

Louis Schneiter, Eric Pantillon, for preparing experimental basin, even if it was the most smelling desalting basin at EPFL.

During my study I have to deal with more than ten companies for laboratory instrument, sediment material, plastic seeding particle for PIV and Software. I am grateful for all of the following companies for free samples and sending for me all instrument:

- Met-Flow SA, Lausanne, Switzerland for support and providing probes. My special thanks to Olivier Marriete for providing technical support for conducting UVP measurements;
- ehd imaging in Germany for the camera and the software;
- DANTEC in France and Germany, for FlowManager PIV post-processing program;
- General Acoustics in Germany for instrument of UltraLab UWS for measuring sediment thickness;
- NIPPON WALNUT Co. in Japan, AGRINDUSTRIA s.n.c. in Italy, & Carlo SA, Switzerland for sediment materials;
- Züllig and Dr. Lange in Switzerland for Turbidity meters for suspended sediment concentrations measurements.

LCH has a wonderful work team consisting of internationally, multi-languages, and cultural people. I wish to place on record my sincere thanks to my friends and colleagues at LCH for being my family in Switzerland. I'm proud and happy of making wonderful friendships with: Azin, Burkhard, Tobias, Alexandre, Pedro, Selim, Fréd, Philippe, Rémi, Matteo, Marcelo, Jolanda, Javier, Fadi, Jean-Marc, Martin, Ali, and Michael.

A word of appreciation is due to the Moslems community (GMU) at EPFL, for all brothers and sisters. I wish it was possible for me to name them all.

I would like to express my acknowledgments to many friends in Switzerland, Walid, Ismail, Bernerad, Galal, Hassan, Mourad, Ahmad, Haitham, Nor-Eldine, Ezz-Eldine, Nacereldine, Nabil, Othman, Wagdy, Maged, Selim, Mohamed, Kariem, Omar, Malika, Lila, Lila, Nihal, Emanuela, and Jamila.

I wish to express my grateful to my family and Rasha's family for their encouragement and praying for me throughout the course of this study.

Last but not least, my sincere gratitude to my darling, Rasha, for her persistent love, continuous support, and enormous patience.

References

- Adrian, R. J. (1991). Particle-imaging techniques for experimental fluid mechanics, ann. rev. *Fluid Mech.*, 23:261–268. 96
- Ahrens, J. P. (2000). The fall velocity equation. *J. Waterw., Port, Coastal, Ocean Eng.*, 126(2):99–102. 87
- Alavian, V. and Chu, V. H. (1985). Turbulent exchange flow in a shallow compound channel. In *Proc. 21th Congress International Association Hydraulic Research*, volume 3, pages 446–451. 45
- Altinakar, M., Graf, W. H., and Hopfinger, E. (1996). Flow structure in turbidity currents. *J. Hydr. Res.*, 34(5):713–718. 89, 100
- Altinakar, M. S. (1988). *Weakly depositing turbidity current on a small slope*. PhD thesis, No. 738, Swiss Federal Institute of Technology, EPFL, Lausanne, Switzerland. 88
- Anderson, A. G. (1953). The characteristics of sediment waves formed by flow in open channels. In *Proceedings of the Third Midwestern Conference on Fluid Mechanics*, pages 379–395. University of Minnesota, Institute of Technology. 69
- Annandale, G. W. (1987). *Reservoir sedimentation developments in water science*. Elsevier Publishers BV, Amsterdam, the Netherlands. 56
- Ashworth, P., Best, J., Leddy, J., and Geehan, G. (1994). The physical modelling of braided rivers and deposition of fine-grained sediment. In *Process Models and Theoretical Geomorphology*, John Wiley & Sons Ltd, pages 115–139, Chichester, UK. 84
- Babarutsi, S., Ganoulis, J., and Chu, V. H. (1989). Experimental investigation of shallow recirculating flows. *J. Hydr. Eng.*, 115:906–925. 47
- Bagnold, R. A. (1954). Experiments on gravity free dispersion of large solid spheres in a newtonian fluid under shear. In *Proc. R. Soc. Lond. A*, pages 49–63. 66

References

- Bagnold, R. A. (1956). The flow of cohesionless grains in fluids. In *Proc. R. Soc. Lond. A*, volume A, pages 234–297. 68
- Bagnold, R. A. (1966). An approach to the sediment transport problem from general physics. *US. Geological Survey Professional Paper, Washington, D.C*, page 422. 67
- Bagnold, R. A. (1973). The nature of saltation and of bed load transport in water. In *Proc. R. SOC. A*, volume 332, pages 473–504. 67
- Balachandar, R., Ramachandran, S., and Tachie, M. F. (2000). Characteristics of shallow turbulent near wakes at low reynolds numbers. *Journal of Fluids Engineering*, 122:302–308. 43
- Balachandar, R. and Tachie, M. F. (2001). A study of boundary layer-wake interaction in shallow water layer. *Journal of Fluid Dynamics Research*, 16:511–521. 43
- Batchelor, G. K. (1977). The effect of brownian motion on the bulk stress in a suspension of spherical particles. *Journal of Fluid Mechanics*, 83:97–117. 69
- Battaglia, F., Tavener, S. J., Kulkarni, A. K., and Merkle, C. L. (1997). Bifurcation of low reynolds number flows in symmetric channels. *AIAA Journal*, 35:97–117. 50
- Batuca, D. G. and Jordaan, J. M. (2000). *Silting and desilting of reservoirs*. A. A. Balkema, Rotterdam. 50, 53, 62
- Bennett, S. J. and Bridge, J. S. (1995). An experimental study of flow, bedload transport and bed topography under conditions of erosion and deposition and comparison with theoretical models. *Sedimentology*, 42:117–146. 72
- Best, J. L. (1992). On the entrainment of sediment and initiation of bed defects: insights from recent developments within turbulent boundary layer research. *Journal of Sedimentology*, 39:797–811. 69
- Best, J. L. (1993). On the interaction between turbulent flow structure, sediment transport and bedform development: some considerations from recent experimental research. In Clifford, N. J., French, J. R., and Hardisty, J., editors, *Turbulence, Perspectives on Flow and Sediment Transport*, pages 61–92, New York. Wiley. 69
- Best, J. L. and Ashworth, P. (1994). A high-resolution ultrasonic bed profiler for use in laboratory flumes. *Journal of Sedimentary Research*, 24:279–288. 100
- Boillat, J.-L. and Pougatsch, H. (2000). State of the art of sediment management in Switzerland. In *International Workshop and Symposium on Reservoir Sedimentation Management*, Tokyo, Japan. 53

- Bollaert, E., Irniger, P., and Schleiss, A. (2000). River rehabilitation through a multi-purpose reservoir. In *HYDRO 2000, Making Hydro more Competitive: Sediment Management*, pages 183–192, Venice, Italy. 85
- Booij, R. (1986). Metingen van uitwisselingen tussen haven en rivier, in dutch. Technical report, Section Hydr. Engrg. Dep. Civil Engrg., Delft Univ. of Technology. 43
- Booij, R. (2003). Measurements and large eddy simulations of the flows in some curved flumes. *Journal of Turbulence*, 4:8–15. 43
- Brown, C. B. (1943). Discussion of sedimentation in reservoirs, by j. witzig. In *The American Society of Civil Engineers*, volume 69, pages 1493–1500. 55, 56, 58, 64, 65
- Brown, C. B. (1958). *Sediment transportation*. Wiley, New York. 58, 73
- Brown, G. L. and Roshko, A. (1974). On density effects and large structure on mixing layers. *Journal of Fluid Mechanics*, 64:775–816. 47
- Brune, G. M. (1953). Trap efficiency of reservoirs. *Transactions of the American Geophysical Union*, 34:407–418. 55, 58, 59, 73, 239, 240
- Bureau of Reclamation, U. (1987). Design of small dams. Technical report, Water Resources Technical Publication, U.S. Government Printing Office. 55, 61
- Buttling, S. and Shaw, T. L. (1973). Predicting the rate and pattern of storage loss in reservoirs. In *Tansactions of the Eleventh International Congress of Large Dams*, volume 1, pages 565–580, Madrid, Spain. International Commission on Large Dams. 58
- Carmer, C. F., Rummel, A., and Jirka, G. H. (2002). Combined planar measurements of flow velocity and mass concentration in shallow turbulent flow, part II: Application of coupled pivpca technique to turbulent shallow wake flows. In *Int. Conf. Hydr. Meas. & Exp. Meth.*, Estes Park. CO. ASCE and IAHR. 43
- Chang, F. and Richards, D. (1971). Deposition of sediment in transient flow. *Journal of the Hydraulics Division-ASCE*, 97(6). 75
- Chang, H. (1967). Hydraulics of rivers and deltas. Technical report, Ph.D Dissertation, Colorado State University. 74
- Chang, H. H. (1982). Mathematical model for erodible channels. *Journal of the Hydraulics Division-ASCE*, 108(5). 74
- Chanson, H. (2000). Boundary shear stress measurements in undular flows: Application to standing wave bed forms. *Water Resourources Research*, 36:3036–3076. 69

References

- Chen, D. and Jirka, G. H. (1995). Experimental study of boundary layer-wake interaction in shallow water layer. *Journal of Fluid Dynamics Research*, 16:11–41. 43
- Chen, D. and Jirka, G. H. (1997). Absolute and convective instabilities of plane turbulent wakes in a shallow water layer. *Journal of Fluid Mechanics*, 338:157–172. 43
- Chen, D. and Jirka, G. H. (1998). Linear stability analysis of turbulent mixing layers and jets in shallow water layers. *Journal of Hydraulic Research*, 36(5):815–829. 45
- Chen, Y. H., Lopez, J. L., and Richardson, E. V. (1978). Mathematical modeling of sediment deposition in reservoir. *Journal of the Hydraulics Division-ASCE*, 104(12):1605–1616. 54
- Cheng, N. S. (1982). Simplified settling velocity formula for sediment particle. *Journal of Hydraulic Engineering*, 123(2):149–152. 87
- Cherdron, W., Durst, F., and Whitelaw, J. H. (1978). Asymmetric flows and instabilities in symmetric ducts with sudden expansion. *Journal of Fluid Mechanics*, 84(2):13–31. 48, 49
- Choi, H. G. and Joseph, D. D. (2001). Fluidization by lift of 300 circular particles in plane poiseuille flow by direct numerical simulation. *Journal of Fluid Mechanics*, 438:101–128. 70
- Chu, V. and Babarutsi, S. (1988). Confinement and bed-friction effects in shallow turbulent mixing layer. *Journal of Hydraulic Engineering*, 114:1257–1274. 43, 45, 46
- Chu, V. H., Wu, J.-H., and Khayat, R. E. (1991). Stability of transverse shear flows in shallow open channels. *Journal of Hydraulic Engineering*, 117(10):1370–1388. 45
- Churchill, M. A. (1948). Discussion of analysis and use of reservoir sedimentation data. 55, 60, 73
- Coleman, N. (1981). Velocity profiles with suspended sediment. *Journal of Hydraulic Research*, 19:211–229. 72
- Coleman, S. E. and Fenton, J. D. (2000). Potential flow instability theory and alluvial stream bed forms. *Journal of Fluid Mechanics*, 418:101–117. 69
- Coleman, S. E. and Melville, B. W. (1994). Bedform development. *Journal of Hydraulic Engineering*, 120:544–560. 69
- Coleman, S. E. and Melville, B. W. (1996). Initiation of bed forms on a flat sand bed. *Journal of Hydraulic Engineering*, 122:301–310. 69

- Colombini, M., Seminara, G., and Tubino, M. (1987). Finite amplitude alternate bars. *Journal of Fluid Mechanics*, 181:213–232. 69
- Crowe, C. T. (1993). Modelling turbulence in multiphase flows. *Engineering Turbulence Modelling & Experiments*, pages 899–913. 71, 72
- Dantec Dynamics (2007). www.dantecdynamics.com. 97, 99, 334
- De Cesare, G. and Boillat, J.-L. (2006). Flow velocity measurements using ultrasound doppler method -10 years experience in hydraulic modeling. In *Proc. 5th International Symposium on Ultrasonic Doppler Methods for Fluid Mechanics and Fluid Engineering ISUD*, pages 113–116, ETH Zurich, Switzerland. 93
- De Cesare, G. and Lafitte, R. (2007). Outline of the historical development regarding reservoir sedimentation. In *32nd Congress of IAHR, Harmonizing the Demands of Art and Nature in Hydraulics*, Venice, Italy. 52, 54
- De Cesare, G., Schleiss, A., and Hermann, F. (2001). Impact of turbidity currents on reservoir sedimentation. *Journal of Hydraulic Engineering*, 127(1):6–16. 56, 93
- Dewals, B. (2006). Une approche unifiée pour la modélisation d’écoulements à surface libre, de leur effet érosif sur une structure et de leur interaction avec divers constituants. PhD thesis (in french). Technical report, University of Liège. 259
- Dewals, B. J., Kantoush, S. A., Erpicum, S., Piroton, M., and Schleiss, A. J. (2008). Analysis of flow instabilities in shallow rectangular basins. *Journal of Environmental Fluid Mechanics*, 8(1):31–54. 260, 282
- Dietrich, W. E. (1982). Settling velocity of natural particles. *Water Resources Research*, 18(6):1615–1626. 87
- Dinehart, R. L. (1999). Correlative velocity fluctuations over a gravel river bed. *Water Resources Research*, 35:569–582. 69
- Dingler, J., Boylls, J., and Lowe, R. L. (1977). A high frequency sonar for profiling small scale subaqueous bed forms. *Marine Geology*, 24:279–288. 100
- Dracos, T., Giger, M., and Jirka, G. H. (1992). Plane turbulent jets in a bounded fluid layer. *Journal of Fluid Mechanics*, 241:587–614. 44
- Drohan, W. (1911). The silting up of reservoirs and canals and some methods for preventing same. *Engin. and Contract*, 35:56–58. 64
- Durst, F., Melling, A., and Whitelaw, J. H. (1974). Low Reynolds number flow over a plane symmetric sudden expansion. *Journal of Fluid Mechanics*, 64:111–128. 47, 48, 49

References

- Durst, F., Pereira, J. F. C., and Tropea, C. (1993). The plane symmetric sudden-expansion flow at low Reynolds numbers. *Journal of Fluid Mechanics*, 248:567–581. 50
- Dyer, K. R. and Soulsby, R. L. (1988). Sand transport on the continental shelf. *Annual Revision Fluid Mechanics*, 20:295–324. 75
- Eakin, H. M. (1939). Instructions for reservoir sedimentation surveys, in silting of reservoirs. Technical report, U.S. Department of Agriculture, Technical Bulletin. 52
- Einstein, E. A. and Chien, N. (1955). Effects of heavy sediment concentration near the bed on velocity and sediment distribution. Technical report, Univ. of California, Berkeley, and U.S. Army Corps of Engrs., Missouri River Div. 67, 71
- Elata, C. and Ippen, A. T. (1961). The dynamics of open channel flow with suspensions of neutrally buoyant particles. Technical report, Technical Report No.45, Hydrodynamics Lab, MIT. 67
- Elghobashi, S. (1994). On predicting particle-laden turbulent flows. *Applied Scientific Research*, 52:309–329. 72
- Elghobashi, S. and Truesdell, G. C. (1993). On the way interaction. *Journal of Multiphase Flow*, 21:151–173. 72
- Emttea, R., Fujita, I., Muste, M., and Krufer, A. (1997). Particle Image Velocimetry for whole field measurement of ice velocities. *Cold Regions Science and Technology*, 26:97–112. 96
- Engelund, F. (1966). Hydraulic resistance in alluvial streams. In *Proc. Am. Soc. Civ. Eng.*, volume 92, pages 315–326. 68, 69
- Engelund, F. and Fredsøe, F. (1982). Sediment ripples and dunes. *Annual Revision Fluid Mechanics*, 14:13–37. 68
- Engelund, F. and Hansen, E. (1966). Investigations of flow in alluvial streams. Technical report, Acta Polytechnica Scandinavica, Civil Engineering and Building Construction Series No.35. Finnish Academy of Technology. 69
- Engelund, F. and Hansen, E. (1967). *A monograph on sediment transport in alluvial streams*. In: Teknisk Vorlag, Copenhagen, Denmark, 62 p. 66, 87
- Erpicum, S. (2006). Contribution à la modélisation de la turbulence en écoulements quasi-tridimensionnels à surface libre. maillage adaptatif multibloc et calage objectif des paramètres. PhD thesis (in french). Technical report, University of Liège. 259

- Fan, J. and Morris, G. L. (1992). Reservoir sedimentation II: Reservoir desiltation and long-term, storage capacity. *Journal of Hydraulic Engineering*, 118(3):370–384. 53, 56, 63, 65
- Fearn, R., Mullin, T., and Cliffe, K. A. (1990). Nonlinear flow phenomena in a symmetric sudden expansion. *Journal of Fluid Mechanics*, 211:595–608. 48, 49, 50
- Feng, Z.-G. and Michaelides, E. E. (2002). Particle motion and interparticle forces close to a solid boundary using the Lattice-Boltzmann method. *Physics of Fluids*, 14:49–60. 70
- Foster, I. D. L., Millington, R., and Grew, R. G. (1992). The impact of particle size controls on stream turbidity measurements, some implications for suspended sediment yield estimation, in Erosion and Sediment Transport Monitoring Programmes in River Basins. *IAHS Publications*, 210:51–62. 104
- Foumeny, E., Aingham, D. B., and Walker, A. J. (1996). Bifurcations of incompressible flow through plane symmetric channel expansions. *Journal of Computers and Fluids*, 25:335–351. 50
- Fujita, I., Muste, M., and Kruger, A. (1998). Large scale particle image velocimetry for flow analysis in hydraulic engineering applications. *Journal of Hydraulic Research*, 36(3):397–414. 96
- Garbrecht, J., Kuhnle, R., and Alonso, C. (1995). A sediment transport capacity formulation for application to large channel networks. *Journal of Soil and Water Conservation*, 50(5):527–529. 266
- Garcia, M. H. (1994). Depositional turbidity currents laden with poorly stored sediment. *Journal of Hydraulic Engineering*, 120(11):1240–1263. 100
- Gerkema, T. (2000). A linear instability analysis of tidally generated sand waves. *Journal of Fluid Mechanics*, 417:303–322. 69
- Gibbs, R. J., Mathews, M. D., and Link, D. A. (1971). The relationship between sphere size and settling velocity. *Journal of Sedimentary Petrology*, 44(1):7–18. 87
- Giger, M., Dracos, T., and Jirka, G. H. (1991). Entrainment and mixing in plane turbulent jets in shallow water. *Journal of Hydraulic Research*, 29:615–641. 44
- Gippel, C. J. (1995). Potential of turbidity monitoring for measuring the transport of suspended solids in streams. *Hydrological Processes*, 9:83–97. 104
- Gore, R. A. and Crowe, C. T. (1989). Effects of particle size on modulating turbulent intensity. *International Journal of Multiphase Flow*, 15:279–285. 70, 72

References

- Gottschalk, L. C. (1952). Measurement of sedimentation in small reservoirs. *Transactions of the American Soc. civ. Engrs*, 117:59–71. 58
- Graf, W. H. (1971). *Hydraulics of sediment transport*. McGraw-Hill, New York. 69, 87
- Graf, W. H. (1983). The hydraulics of reservoir sedimentation. *International Water Power and Dam Construction*, 35(4):45–52. 73, 75
- Graf, W. H. (1984). *Storage losses in reservoirs*. *Water Power and Dam Construction*, April. 60
- Grass, A. J. (1970). Initial instability of fine sand bed. *Journal of Hydraulic Engineering*, 96:619–632. 69
- Gust, G. and Southard, J. B. (1983). Effects of weak bedload on the universal law of the wall. *Journal of Geophysic Research*, 88:5939–5952. 72
- Gvelesiani, L. G. and Shmaltzel, N. P. (1968). *Reservoir silting at hydroelectric station, energy*. Moscow (in Russian). 64, 65
- Gvelesiani, L. G. and Shmaltzel, N. P. (1971). Studies of storage work silting of hydroelectric power plants on mountain rivers and silt deposition fighting. In *Proceedings of the XIV Congress of the IAHR*, volume 5, pages 17–20. Hydraulic research and its impact on the environment. 65
- Haan, C. T., Barfield, B. J., and Hayes, J. C. (1994). *Design hydrology and sedimentology for small catchments*. San Diego, Academic Press. 62
- Hallermeier, R. J. (1981). Terminal settling velocity of commonly occurring sand grains. *Sedimentology*, 28(6):859–865. 87
- Hancock, G. and Willgoose, G. (2001). The production of digital elevation models for experimental model landscapes. *Earth Surf Processes Landforms*, 26:475–490. 87, 100
- Heineman, H. G. (1961). Sediment distribution in small flood retarding reservoirs in the missouri basin loess hills. *Agricultural Research Service*, pages 41–44. 73
- Heinemann, H. G. (1981). A new sediment trap efficiency curve for small reservoirs. *Water Resources Bulletin*, 17:825–830. 60
- Heinemann, H. G. (1984). *Reservoir trap efficiency*. Erosion and sediment yield: some methods of measurement and modelling, Norwich: GeoBooks, Norwich. 57
- Heller, P., Bollaert, E., and Schleiss, A. (2005). Potential synergies of multipurpose run-of-river hydroelectric powerplants. In *Proceedings of the XXXI IAHR Congress, Theme C*, pages 2121–2130, Seoul, Korea. 85

- Heller, P., Pellaud, M., Bollaert, E., Schleiss, A., and Schlaepfer, R. (2007). River rehabilitation through a multi-purpose reservoir. In *32nd Congress of IAHR, Harmonizing the Demands of Art and Nature in Hydraulics*, Venice, Italy. 85
- Hersberger, D. S. (2002). Measurement of 3d flow field in a 90° bend with ultrasonic doppler velocity profiler. In *Third International Symposium on Ultrasonic Doppler Methods for Fluid Mechanics and Fluid Engineering*, pages 59–66. 93
- Hetsroni, G. (1989). Particles turbulence interaction. *International Journal of Multiphase Flow*, 5:735–746. 70, 72
- Hinze, J. O. (1975). *Turbulence*. McGraw-Hill, New York, USA. 66, 89
- Ho, C. M. and Huerre, P. (1984). Perturbed free shear layers. *Annual Review of Fluid Mechanics*, 16:365–424. 43
- Hotchkiss, R. H. and Parker, G. (1991). Shock fitting of aggradational profiles due to backwater. *Journal of Hydraulic Engineering*, 117(9):1129–1144. 56
- Huang, L. and Chiang, Y. L. (2001). The formation of dunes, antidunes, and rapidly damping waves in alluvial channels. *Int. J. Numer. Anal. Methods Geomech.*, 25:675–690. 69
- Huang, L. H. and Chiang, Y. L. (1999). Bed form formation in alluvial channels. In Jayawardena, A., Lee, J., and Wang, Z., editors, *River Sedimentation*, pages 93–99, Rotterdam. Balkema. 69
- Huang, L. H. and Song, C. H. (1993). Dynamic response of poroelastic bed to water waves. *Journal of Engineering Mechanics*, 119:1003–1020. 69
- Huerre, P. and Monkewitz, P. A. (1990). Local and global instabilities in spatially developing flows. *Annual Review of Fluid Mechanics*, 22:473–539. 43
- International Committee on Large Dams, I. (1996). Dealing with reservoir sedimentation Guidelines and case studies. 115. 53
- Irish, J. L. and White, T. E. (1998). Coastal engineering applications of high resolution lidar bathymetry. *Coastal Engineering*, 35:47–71. 100
- Ismail, H. M. (1951). Turbulent transfer mechanism and suspended sediments in closed channels. In *ASCE*, volume 77, pages 1–26. 67
- Itakura, T. and Kishi, T. (1980). Open channel flow with suspended sediments. *Journal of the Hydraulics Division-ASCE*, 106:1325–1343. 72

References

- Jia, Y. and Wang, S. S. (2001). Cche2d: Two-dimensional hydrodynamic and sediment transport model for unsteady open channel flows over loose bed, technical report no. ncche-tr-2001-1. Technical report, National Center for Computational Hydroscience and Engineering, Univ. of Mississippi, Ole Miss, Oxford, Miss. 262, 264, 266
- Jia, Y. and Wang, S. S. Y. (1999). Numerical model for channel flow and morphological change studies. *J. Hydraulic. Eng., ASCE*, 125(9):924–933. 266
- Jirka, G. H. and Uijttewall, W. (2003). Shallow flows: a definition. In *International symposium on shallow flows*, pages 3–11, Delft, The Netherlands. Balkema. 41
- Jowett, I. (1984). Sedimentation in new zealand hydroelectric schemes. *Water International*, 9:172–173. 64
- Julien, P. Y. (1995). *Erosion and sedimentation*. Cambridge University Press, Cambridge, England. 69
- Kantoush, S. A. (2007). Symmetric or asymmetric flow patterns in shallow rectangular basins with sediment transport. In *32nd Congress of IAHR, John F. Kennedy Student Competition*, Venice, Italy. 45
- Kantoush, S. A., Boillat, J.-L., and Schleiss, A. J. (2007a). Economical large scale piv measurements at the surface of different shallow reservoir geometries. In *Hydraulic Measurements & Experimental Methods Conference, HMEM 2007, EWRI of ASCE & IAHR*, Lake Placid, NY, USA. 98
- Kantoush, S. A., Boillat, J.-L., and Schleiss, A. J. (2007b). Evolution of sediment deposition and flow patterns in a rectangular shallow reservoir under suspended sediment load. In *5th IAHR symposium on river, coastal and estuarine morphodynamics*, University of Twente, The Netherlands. 79
- Kantoush, S. A., Bollaert, E., Boillat, J.-L., and Schleiss, A. (2005). Suspended load transport in shallow reservoirs. In *Final Proc. XXXI IAHR Congress. Korea Water Resources Association*, pages 1787–1799, Seoul, South Korea. 75, 77, 85, 259
- Kantoush, S. A., Bollaert, E., Boillat, J.-L., and Schleiss, A. J. (2006a). Sedimentation processes in shallow reservoirs comparison of numerical and experimental simulations. In *Proc. of 7th International Conference on HydroScience and Engineering*, Philadelphia, USA. 259
- Kantoush, S. A., Bollaert, E., Boillat, J.-L., and Schleiss, A. J. (2007c). Experimental and numerical modeling of sedimentation in rectangular shallow reservoirs: a first comparison. *International Journal of Sediment Research*. 259

- Kantoush, S. A., Bollaert, E., De Cesare, G., Boillat, J.-L., and Schleiss, A. (2006b). Flow investigation in a rectangular shallow reservoir using UVP, LSPIV and numerical model. In *Proceeding of the 5th International Symposium on Ultrasonic Doppler Methods for Fluid Mechanics and Fluid Engineering*, pages 129–133, ETH Zurich, Switzerland. 93
- Kantoush, S. A., Bollaert, E., and Schleiss, A. J. (2007d). Influence of the width of a rectangular shallow reservoir on sedimentation behavior and trap efficiency. In *32nd Congress of IAHR, Special Session of Reservoir Sedimentations*, Venice, Italy. 47, 49
- Kantoush, S. A., De Cesare, G., Boillat, J.-L., and Schleiss, A. J. (2008). Flow field investigation in a rectangular shallow reservoir using uvp, lspiv and numerical modeling. *Journal of Flow Measurement and Instrumentation*, 19(3-4):139–144. 92
- Kantoush, S. A. and Schleiss, A. J. (2007). Large scale piv- measurements at the surface of different shallow reservoir geometries. *Journal of Visualization*. 46, 92, 98
- Kantoush, S. A., Schleiss, A. J., and Balzerek, H. (2007e). Evaluation of miniecho sounder measurements to estimate sediment thickness in shallow reservoirs. In *Hydraulic Measurements & Experimental Methods Conference, HMEM 2007*, Lake Placid, NY, USA. EWRI of ASCE & IAHR. 92
- Kantoush, S. A., Uijttewaal, W., Bollaert, E., Boillat, J.-L., and Schleiss, A. J. (2006c). Experimental study of suspended sediment transport and deposition in a rectangular shallow reservoir. In *IAHR Proc. of the International Conference on Fluvial Hydraulics*, pages 1623–1631, Lisbon, Portugal. Taylor & Francis Group. 177
- Kantoush, S. K., Boillat, J.-L., Bollaert, E., and Schleiss, A. J. (2007f). Influence of shallow reservoir geometry on the flow pattern and sedimentation process by suspended sediments. In *Mesures d'aménagements des cours d'eau pour la protection contre les crues, l'environnement, la société et l'économie*, pages 35–52, Lausanne, Switzerland. 97
- Karim, F. (1999). Bed-form geometry in sand-bed flows. *Journal of Hydraulic Engineering*, 125(12):1253–1261. 68
- Kennedy, J. F. (1963). The mechanics of dunes and antidunes in erodible-bed channels. *Journal of Fluid Mechanics*, 16:521–544. 68, 69
- Kobus, H. (1980). *Hydraulic Modeling*. Pitman, Boston, Mass. 84
- Kostic, S., Parker, G., and Marr, J. (2002). Role of turbidity currents in setting the foreset slope of clinoforms prograding into standing fresh water. *Journal of Sedimentary Research*, 72(3):353–362. 56

References

- Krumdieck, A. and Chamot, P. (1979). Sediment flushing at the Santo Domingo reservoir. *International Water Power and Dam Construction*, pages 25–30. 64, 65
- Kulick, J. D., Fessler, J. R., and Eaton, J. K. (1994). Particle response and turbulence modification in fully developed channel flow. *Journal of Fluid Mechanics*, 277:109–134. 72
- Ladd, A. J. C. (1994). Numerical simulations of particulate suspensions via a discretized Boltzmann equation. Part 1: Theoretical foundation. *Journal of Fluid Mechanics*, 271:285–309. 70
- Ladd, A. J. C. (1996). Sedimentation of homogeneous suspensions of non-brownian spheres. *Physics of Fluids*, 9:491–499. 70
- Lague, D., Crave, A., and Davy, P. (2003). Laboratory experiments simulating the geomorphic response to tectonic uplift. *Journal of Geophysical Research*, 108(B1). 100
- Lai, J. S. and Shen, H. W. (1996). Flushing sediment through reservoirs. *Journal of Hydraulic Research*, 34(2):237–255. 75
- Langendoen, E. J. (2001). of the effectiveness of selected computer models of depth average free surface flow and sediment transport to predict the effects of hydraulic structures on river morphology. Technical report, Rep., prepared for WES Vicksburg, National Sedimentation Laboratory, Agricultural Research Service. 75
- Lara, J. M. and Sanders, J. I. (1970). The 1963&1964 Lake Mead survey. Technical report, US Bureau of Reclamation. 73
- Laursen, E. (1958). The total sediment load of streams. *J. Hydraul. Div., Am. Soc. Civ. Eng.*, 54(1):1–36. 266
- Lewis, J. and Eads, R. (1996). Turbidity controlled suspended sediment sampling. *Watershed Management Council Newsletter*, 6(4):4–5. 104
- Lin, B. and Falconer, R. A. (1996). Numerical modeling of three dimensional suspended sediment for estuarine and coastal waters. *Journal of Hydraulic Research*, 34(4):435–456. 75
- Lyn, D. A. (1988). A similarity approach to turbulent sediment laden in open channels. *Journal of Fluid Mechanics*, 193:1–26. 72
- Lyn, D. A. (1991). Resistance in flat bed sediment laden flows. *J. Hydr. Engrg., ASCE*, 117:94–114. 72

- Lyn, D. A. (1992). Turbulence characteristics of sediment laden flows open channels. *Journal of Hydraulic Engineering*, 118:971–988. 72
- Mahmood, K. (1987). Reservoir sedimentation: Impact, extent, and mitigation. Technical report, World Bank. 52, 64
- Mertens, W. (1985). Model tests for sedimentation process in reservoirs. In *In Proceedings of EUROMECH 192*, Munich, Neubiberg. 73
- Met-Flow (2005). *UVP Monitor, User's guide*. 92
- Mizukami, M., Parthasarathy, R. N., and Faeth, G. M. (1992). Particle generated turbulence in homogeneous dilute dispersed flows. *International Journal of Multiphase Flow*, 18:397–412. 70
- Mizushima, J., Okamoto, H., and Yamagushi, H. (1996). Stability of flow in a channel with a suddenly expanded part. *Physics of Fluids*, 8:2933–2942. 50
- Moreton, D., Ashworth, P., and Best, J. (2002). The physical scale modelling of braided alluvial architecture and estimation of subsurface permeability. *Basin Research*, 14:265–286. 84
- Morris, G. (1995). Reservoir sedimentation and sustainable development in india: problem scope and remedial strategies. In *Sixth International Symposium on River Sedimentation, Management of Sediment: Philosophy, Aims, and Techniques*, pages 53–61, New Delhi. Balkema. 63
- Morris, G. L. and Fan, J. (1998). *Reservoir sedimentation handbook Design and management of dams, reservoirs, and watersheds for sustainable use*. McGraw Hill. 53, 54, 64
- Mueller, A. (1973). Turbulence measurements over a movable bed with sediment transport by laser anemometry. In *Proc., 15th Cong., Int. Assn. Hydr. Res.*, volume 1, pages 1–7. 72
- Munro, R., Dalziel, S., and Jehan, H. (2004). An pattern matching technique for measuring sediment redeposition levels. *Exp. in Fluids*, 37:399–408. 100
- Murthy, B. N. (1977). Life of reservoir. *Central Board of Irrigation and Power*. 52, 61
- Muste, M. and Patel, V. C. (1997). Velocity profiles for particles and liquid in open channel flow with suspended sediment. *Journal of Hydraulic Engineering, ASCE*, 123(9):742–751. 71
- Nelson, J.M., S. R. M. S. and Drake, T. (1995). Role of near-bed turbulence structure in bed load transport and bed form mechanics. *Water Resources Res.*, 31:2071–2086. 69

References

- Nizéry, A., Braudeau, G., and Bonnin, J. (1953). La station du Sautet pour l'étude de l'alluvionnement des réservoirs. In *2e journ. Œuvres de l'hydraulique*, pages 180–215. 63
- Nouh, M. (1989). The Von Karman coefficient in sediment laden flow. *J. Hydr. Res.*, 27:477–499. 71
- Oehy, C. (2003). *Effects of obstacles and jets on reservoir sedimentation due to turbidity currents*. PhD thesis, communications LCH, No. 15, Swiss Federal Institute of Technology. 93, 100
- Olsen, N. R. B. (1991). *A three dimensional numerical model for simulation of sediment movements in water intakes*. PhD thesis, University of Trondheim. 75
- Ortel, H. J. (1990). Wakes behind blunt bodies. *Annual Review of Fluid Mechanics*, 22:529–564. 43
- Ouwa, Y., Watanabe, M., and Asawo, H. (1981). Flow visualization of a two dimensional water jet in a rectangular channel. *Japanese Journal of Applied Physics*, 20(1):243–247. 48, 49
- Ouwa, Y., Watanabe, M., and Matsuoka, Y. (1986). Behavior of a confined plane jet in a rectangular channel at low reynolds number I: General flow characteristics. *Japanese Journal of Applied Physics*, 25:754–761. 49
- Papadopoulos, G., Battaglia, F., and Arik, E. (1999). An experimental and numerical study of 3d flow past double sided expansions. In *In 30th AIAA Fluid Dynamics Conference*. 50
- Parker, G. and Coleman, N. (1986). Simple model of sediment laden flows. *Journal of Hydraulic Engineering, ASCE*, 112:356–375. 72
- Patankar, N. A., Ko, T., Choi, H. G., and Joseph, D. D. (2001). A correlation for the lift off of many particles in plane Poiseuille flows of Newtonian fluids. *J. Fluid Mech.*, 445:55–76. 70
- Pazwash, H. (1982). Sedimentation in reservoirs case of sefidrud dam. In *3rd Congress of the ADP, IAHR*, volume Cc7, pages 215–223, Bandung, Indonesia. 53
- Pemberton, E. L. (1978). Reservoir sedimentation. In *Proceedings of the US-Japan binational seminar on sedimentation and erosion*, Honolulu, Hawaii. 60
- Proffit, G. and Sutherland, A. (1983). Transport of non-uniform sediment. *Journal of Hydraulic Research*, 21:33–43. 266

- Qi, D. (2000). Simulation of fluidization of cylindrical multiparticles in a three dimensional space. *Int. J. Multiphase Flow*, 27:107–118. 70
- Qian, N. (1982). Reservoir sedimentation and slope stability, technical and environmental effects. In *14th International Congress on Large Dams*, volume III, pages 639–690, Transactions, Rio de Janeiro, Brazil. 63
- Qihua, R., Guangquian, W., and Lubo, L. (1999). Computer simulation of evolution of wind blown ripples. In Jayawardena, A., Lee, J., and Wang, Z., editors, *River Sedimentation*, pages 721–726, Rotterdam. Balkema. 69
- Ramírez, C. and Rodríguez, A. (1992). History of the cachì reservoir. sedimentological studies in the cachì reservoir, Costa Rica: Sediment inflow, reservoir sedimentation, and effects of flushing. Technical Report UNGI Rapport Nr 81, Uppsala University, Department of Physical Geography. 65
- Rashidi, M., Hetsroni, G., and Banerjee, S. (1990). Particle turbulence interaction in a boundary layer. *Int. J. Multiphase Flow*, 16:935–949. 70
- Raudkivi, A. J. (1997). Ripples on a stream bed. *Journal of Hydraulic Engineering, ASCE*, 123:58–64. 66, 68, 69
- Raudkivi, A. J. and Witte, H. H. (1990). Development of bed features. *Journal of Hydraulic Engineering*, 116:1063–1079. 69
- Rayan, M. A. (1980). Influence of solid particles in suspension on some turbulent characteristics. *Multiphase transport: Fundamentals, reactor safety, applications*, 4:969–991. 72
- Rechsteiner, G. (1996). Ablagerungen im Stausee Gebidem und einige ihrer Folgen (Sedimentation in the Gebidem hydroelectric reservoir and some of its consequences). Technical report, Internationales Symposium Verlandung von Stauseen und Stauhaltungen, Sedimentprobleme in Leitungen und Kanälen. 65
- Reynolds, A. J. (1965). Waves on the erodible bed of an open channel. *J. Fluid Mech.*, 22:113–133. 68
- Richards, K. and Robert, A. (1986). Laboratory experiments with the hr multipurpose profile follower on a rippled sad bed. Technical report, University of Cambridge, Department of Geography Working Paper. 100
- Richards, K. J. (1980). The formation of ripples and dunes on an erodible bed. *J. Fluid Mech.*, 99:597–618. 68

References

- Rienössl, K. and P., S. (1982). Sedimentation of small reservoirs in the high alps. In *Fourteenth International Congress on Large Dams*, volume III, pages 65–82, Transactions, Rio de Janeiro, Brazil. 64
- Rogers, C. B. and Eaton, J. K. (1991). The effect of small particles on fluid turbulence in a flat-plate turbulent boundary layer in air. *Phys. Fluids*, A(3):928–937. 72
- Rooij, F., Dalziel, S. B., and Linden, P. F. (1999). Electrical measurement of sediment layer thickness under suspension flows. *Exp. in Fluids*, 26:470–474. 100
- Roshko, A. (1976). Structure of turbulent shear flows: A new look. *AIAA Journal*, 14:1349–1357. 47
- Roshko, A. (1981). The plane mixing layer - flow visualization results and three dimensional effects. *Lecture Notes in Physics*, 136:208–217. 47
- Rosier, B., Boillat, J.-L., and Schleiss, A. J. (2004a). Mapping of bed morphology for lateral overflow using digital photogrammetry. In *2nd International Conference on Scour and Erosion-ICSE-2*, Singapore. 100
- Rosier, B., Jordan, F., De Cesare, G., Boillat, J.-L., and Schleiss, A. (2004b). Determination of velocity profiles and bed morphology using uvp transducers to investigate the influence of lateral overflow on mobile bed. In *4th International Symposium on Ultrasonic Doppler Methods for Fluid Mechanics and Fluid Engineering, ISUD 4*, pages 47–50, Sapporo, Japan. 93
- Ruddy, B. C. (1987). Sediment discharge in muddy creek and the effect of sedimentation rate on the proposed Wolford mountain reservoir near Kremmling. Technical Report 87-4011, Colorado. Water Resour. Investigation Rep. 54
- Rummel, A., Carmer, C. F., and Jirka, G. H. (2002). Combined planar measurements of flow velocity and mass concentration in shallow turbulent flow part1: Development of a planar concentration analysis (pca) system. In *Int. Conf. Hydr. Meas. and Exp. Meth.*, Estes Park. CO. ASCE and IAHR. 43
- Schleiss, A. and Oehy, C. (2002). Verlandung von Stauseen und Nachhaltigkeit. *Wasser, energie, luft*, 94(7/8):227–234. 35, 36, 52
- Schlichting, H. (1979). *Boundary Layer Theory*. McGraw Hill. 89
- Schoklitsch, A. (1935). und kolkabwehr (The silting of reservoirs and scour prevention). page 178pp, Vienna. 64

- Schoklitsch, A. (1937). *Handbuch des Wasserbaues (English translation by S. Shulits, 1930)*. Springer, Vienna, Austria. 73, 270
- Shapira, M., Degani, D., and Weihs, D. (1990). Stability and existence of multiple solutions for viscous flow in suddenly enlarged channels. *Computers and Fluids*, 18:239–258. 49
- Shen, H. W. and Julien, P. Y. (1993). *Erosion and sediment transport. Handbook of Hydrology*. McGraw-Hill, New York. 54
- Shieh, C.-L., Tseng, C.-M., and Hsu, S. (2001). and geometric similarity of alluvial deltas. *Journal of Hydraulic Engineering, ASCE*, 127(1):17–29. 74, 86
- Sloff, C. J. (1991). Reservoir sedimentation: a literature survey. Technical report, Communications on Hydraulic and Geotechnical Engineering Faculty of Civil Engineering, Delft University of Technology. 52, 61, 64
- Sloff, C. J. (1997). *Sedimentation in reservoirs*. Comm. on hydr. and geotechn. engrg., Delft University of Technology. 53
- Sloff, C. J., Jagers, H., and Kitamura, Y. (2004). Study on the channel development in a wide reservoir. In *Proc. River Flow*, pages 811–819, Napoli, Italy. 74
- Smith, J. D. (1970). Stability of a sand bed subjected to a shear flow of low froude number. *J. Geophys. Res.*, 75:928–940. 68, 69
- Soares, E. F., Unny, T. E., and Lennox, W. C. (1982). Conjunctive of deterministic and stochastic models for predicting sediment storage in large reservoirs. *J. Hydrol.*, 59:83–105. 54
- Sobey, I. and Drazin, P. (1986). Bifurcations of twodimensional channel flows. *Journal of Fluid Mechanics*, 171(Oct):263–287. 49
- Sobey, I. J. (1985). Observation of waves during oscillatory channel flow. *J. of Fluid Mech.*, 151:395–406. 49, 50
- Stevens, J. C. (1936). The silt problem. *Transactions of the American Society of Civil Engineers*, 101:207–288. 65
- Stoker, J. J. (1957). *Water waves*. Interscience Publishers, New York. 41, 43
- Stovin, V. R. (1996). *The prediction of sediment deposition in storage chambers based on laboratory observations and numerical simulation*. PhD thesis, Univ. of Sheffield. 74
- Stovin, V. R. and Saul, A. J. (2000). Computational fluid dynamics and the design of sewage storage chambers. *J. CIWEM*, 14(2):103–110. 73, 74, 75

References

- Strand, R. I. and Pemberton, E. L. (1982). *Reservoir sedimentation. Technical Guideline for Bureau of Reclamation*. 54
- SUMI, T. (2005). Sediment flushing efficiency and selection of environmentally compatible reservoir sediment management measures. In *Proceedings of the International Symposium on Sediment Management and Dams, Topic1 Sediment Management and Dams*, pages 9–22, Yokohama, Japan. 63
- Takeda, Y. (1995). Velocity profile measurement by ultrasonic doppler method. *Experimental Thermal and Fluid Science*, 10(4):444–453. 92, 93
- Talstra, H., Uijttewall, W., and Stelling, G. S. (2006). Emergence of large-scale coherent structures in shallow separating flow. In *IAHR Proc. of the International Conference on Fluvial Hydraulics*, pages 261–269, Lisboa, Portugal. 47
- Tarela, P. and Menendez, A. (1999). A model to predict reservoir sedimentation. *Lakes & Reservoirs: Research & Management*, 4:121–133. 56
- Tolouie, E., West, J. R., and Billam, J. (1993). Sedimentation and desiltation in the sefid rud reservoir, iran. *Geomorphology and sedimentology of lakes and reservoirs*, pages 125–138. 52
- Townsend, A. A. (1976). *The structure of turbulent shear flow, second edition*. Cambridge University Press, Cambridge. 44
- Troutt, T. R., Scheelke, B., and Norman, T. R. (1984). Organized structures in a reattaching separated flow field. *Journal of Fluid Mechanics*, 143:413–427. 47
- Tsuji, Y. and Morikawa, Y. (1982). Ldv measurements of an air solid two phase flow in a horizontal pipe. *J. Fluid Mech.*, 120:385–406. 70
- Tsuji, Y., Morikawa, Y., and Shiomi, H. (1984). Ldv measurements of an air solid two phase flow in a vertical pipe. *J. Fluid Mech.*, 139:417–434. 70
- Uijttewaal, W. and Booij, R. (2000). Effects of shallowness on the development of free-surface mixing layer. *Journal of Physics of Fluids*, 12:392–402. 43
- Uijttewaal, W., Lehmann, D., and Mazijk, A. v. (2001). Exchange processes between a river and its groyne fields: Model experiments. *J. Hydr. Engrg.*, 127:928–936. 96
- Uijttewaal, W. and Tukker, J. (1998). Development of quasi two dimensional structures in a shallow free surface mixing layers. *Journal Exp. Fluids*, 24:192–200. 45
- Umeyama, M. and Gerritsen, F. (1992). Velocity distribution in uniform sediment laden flow. *J. Hydr. Engrg., ASCE*, 118:229–245. 72

- Van Rijn, L. C. (1984a). Sediment transport: Part I: Bed load transport. *Journal of Hydraulic Engineering*, 110(10):1431–1456. Reviewed - Key Document. 66, 266
- Van Rijn, L. C. (1984b). Sediment transport: Part II – Suspended load transport. *Journal of Hydraulic Engineering*, 110(11):1613–1641. Reviewed - Key Document. 66, 87, 266
- Van Rijn, L. C. (1984c). Sediment transport: Part III – Bed forms and alluvial roughness. *Journal of Hydraulic Engineering*, 110(12):1733–1754. Key Document. 68
- Van Rijn, L. C. (1987). *Mathematical Modeling of Morphological Processes in the Case of Suspended Sediment Transport*. PhD thesis, University of Technology Delft. Absent. 75
- Van Rijn, L. C., Van Rossum, H., and Termes, P. (1990). Field verification of 2-d and 3-d suspended-sediment models. *Journal of Hydraulic Engineering*, 116(10):1270–1288. 75
- Vanoni, V. A. (1946). Transportation of suspended sediment by running water. *Trans., ASCE*, 111:67–133. 67, 71
- Vanoni, V. A. (1975). Sedimentation engineering. *the ASCE Task Committee for the Preparation of the Manual on Sedimentation Committee of the Hydraulics Division, ASCE*. 55
- Vanoni, V. A. and Nomicos, G. N. (1960). Resistance properties in sediment laden streams. *Trans., ASCE, Paper No.3055*, 125:1140–1175. 67, 71
- Verstraeten, G. and Poesen, J. (2000). Estimating trap efficiency of small reservoirs and ponds, an overview of existing methods and the implications for the assessment of sediment yield. *Progress in Physical Geography*, 24(2):219–251. 62, 170
- Vischer, D. and Hager, W. (1998). *Dam Hydraulics*. John Wiley & Sons, New York. 56, 63
- Wagner, E., Karlsböck, N., and Niedermühlbichler, H. (1996). Spülung des speichers margaritze flushing of the margaritze reservoir. In *Internationales Symposium Verlandung von Staueeen und Stauhaltungen, Sedimentprobleme in Leitungen und Kanälen*, pages 123–136, ETH Zürich, Versuchsanstalt für Wasserbau, Hydrologie und Glaziologie der Eidgenössischen Technischen Hochschule Zürich (in German). 65
- Weitbrecht, V., Kühn, G., and Jirka, G. H. (2002). Large scale PIV measurements at the surface of shallow water flows. *Flow Meas. and Instr.*, 13:237–245. 96
- Williams, K. L. and Jackson, D. R. (1998). Bistatic bottom scattering: model, experiments, and model and data comparison. *J. Acoustical Soc. Am.*, 103:169–181. 100
- Williamson, C. H. K. (1996). Vortex dynamics on the cylinder wake. *Annual Review of Fluid Mechanics*, 22:477–539. 43

References

- Wu, C. M. (1989). Hydraulic properties of reservoir desilting. In *Proceedings of XXIII Congress of the IAHR, Hydraulics and the Environment, Technical Session B: Fluvial Hydraulics*, pages B587–B593, Ottawa. 64, 65
- Wu, W. (1991). The study and application of 1-d, horizontal 2-d and their nesting mathematical models for sediment transport. phd., dissertation. Technical report, Wuhan University of Hydraulic and Electric Engineering, China. 277
- Wu, W. (2001). CCHE2D sediment transport model (version 2.1), tech. rep. no. ncche-tr-2001-3. Technical report, National Center for Computational Hydroscience and Engineering, Univ. of Mississippi, Ole Miss, Oxford, Miss. 262, 263
- Wu, W., Rodi, W., and Wenka, T. (2000). 3d numerical modeling of flow and sediment transport in open channels. *J. of Hydraulic Engineering, ASCE*, 126:4–15. 266
- Wu, W. and Vieira, D. (2000). One-dimensional channel network model CCHE1D 2.0 technical manual, Technical Report No. NCCHE-TR-2000-1. Technical report, National Centre for Computational Hydroscience and Engineering, The University of Mississippi. 266
- Xingkui, W. and Ning, Q. (1989). Turbulence characteristics of sediment laden flow. *J. Hydr. Engrg., ASCE*, 115:781–800. 72
- Yalin, M. S. (1971). *Theory of Hydraulic Models*. Macmillan, London. 84
- Yalin, M. S. and da Silva, A. M. F. (2001). *Fluvial processes*. IAHR and Balkema, Delft. 68, 69
- Yang, C. T. (1973). Incipient motion and sediment transport. *J. Hydraul. Div., Am. Soc. Civ. Eng.*, 99(10):1679–1704. 266
- Yarin, L. P. and Hetsroni, G. (1994). Turbulence intensity in dilute two phase flows I: Effect of particle-size distribution on the turbulence of the carrier fluid. *Int. J. Multiphase Flow*, 20:1–16. 72
- Yucel, O. (1977). investigation on reservoir delta formation in a laboratory flume. In *Proc. 7th IAHR Congress*, Baden Baden. 74
- Yucel, O. and Graf, W. H. (1973). Bed load deposition in reservoirs. In *Proc. 15th IAHR Congress*, Istanbul, Turkey. 74

List of Figures

1.1	Methodology and different phases of the research work	37
2.1	Photos of The Lido and Malamocco inlets of the Venice Lagoon and two shallow reservoir geometries in Germany	42
2.2	2D coherent structures generation of the mixing layer experiment at LCH	44
2.3	Experiment at LCH with shallow jet with 2DCS generation in a lozenge geometry	46
2.4	The vortex street-like instability of a shallow turbulent wake flow in a rectangular reservoir	48
2.5	Classification of reservoirs	51
2.6	Factors influencing the trap efficiency of reservoirs	56
2.7	Trap efficiency related to capacity-catchment area ratio (after Gottschalk, 1952)	58
2.8	Trap efficiency as a function of capacity-catchment area ratio (after Brown, 1958)	59
2.9	Trap efficiency as a function of capacity/annual inflow ratio (after Brune, 1953)	59
2.10	Churchill's (1948) curve for local and upstream sediment, relating trap efficiency to a sedimentation index	60
2.11	Release efficiency RE versus sedimentation index RE	61
2.12	The Brune and Churchill trap efficiency curves	62
3.1	Conceptual chart comprising all the possible factors which influence the experimental set-up	78
3.2	Schematic view of the experimental installation for the open circuit tests	79

3.3	Plan view of the experimental installation for the closed circuit tests	80
3.4	Photos of different part of the experimental facilities	81
3.5	Geometry with dimensions of all basins used in the test series .	82
3.6	Photos of configurations of basins of the test series	83
3.7	Grain size distribution of selected sediment	90
3.8	Microscopic photograph of the sediment particles used in the experiments	91
3.9	Above: Scheme of UVP installations and data acquisition, Below: Plane view and dimensions of UVP	93
3.10	Frame positions and file format of velocity raw data acquisition and UVP technical specifications	94
3.11	3D velocity decomposition	96
3.12	Scheme of 3D treatment and the geometry support dimensions	96
3.13	Above: Scheme of UVP installations and data acquisition, Below: Plane view and dimensions of UVP	97
3.14	Scheme of LSPIV installations and data acquisition	97
3.15	Specification steps of LSPIV methodology (Dantec Dynamics, 2007)	99
3.16	Typical PIV image pairs and the basic principle scheme of PIV	99
3.17	Principle of distance measurement by UWS	102
3.18	Miniature echo sounder mounted on the frame measuring before and after depositions	103
3.19	Suspended sediment concentration sensors of ZÜLLIG and HACH LANGE companies	105
3.20	Optical measuring principle and infra red duo scatterd light principle	106
3.21	Laboratory calibration for the walnut material suspension concentration	107
3.22	Installed turbidity meter in the upstream and downstream leading channel	108
3.23	Experimental test procedures for the reference rectangular geometry with suspended sediment	111
3.24	Walnut shells mixture at the inlet and outlet of the basin in different geometry form	112
3.25	Definition of the geometrical parameters of the test configurations	115
3.26	Graphical analysis of the relation between different dimensionless parameters of geometry SK (x-axis), normalized velocity in reservoir, and relative deposited thickness (y-axis)	121

4.1	Symmetric streamline and geometrical parameters of the recirculation cells	129
4.2	Asymmetric streamline and geometrical parameters of the recirculation cells	130
4.3	Time development of flow vectors and velocity magnitude for geometry with shape SK of 5.97	132
4.4	Time development of streamlines for geometry with shape SK of 5.97	133
4.5	Average flow pattern with velocity vectors for seven different geometries with asymmetric behavior	136
4.6	Streamlines for clear water flow for seven different geometries with asymmetric behavior	137
4.7	Mean vorticity for seven different geometries with asymmetric behavior	138
4.8	Average flow pattern with velocity vectors for four different geometries with symmetric behavior	139
4.9	Streamlines for clear water flow for four different geometries with symmetric behavior	140
4.10	Mean vorticity for four different geometries with asymmetric behavior	141
4.11	Average flow pattern with velocity vectors for the reference geometry with shape factor $SK = 5.97$ and three different water depth with meandering behavior	142
4.12	Mean streamlines for the reference geometry with shape factor $SK = 5.97$ and three different water depth with meandering behavior	143
4.13	Mean vorticity for the reference geometry with shape factor $SK = 5.97$ and three different water depth with meandering behavior	144
4.14	Average velocity vectors with ratio of velocity U_{res}/U_{in} for the reference geometry with $SK = 5.97$ with five different hydraulic conditions	145
4.15	Streamlines for the reference geometry with $SK = 5.97$ with five different hydraulic conditions	146
4.16	Geometry effect on the reattachment lengths X_r and circulations number at $Re = 28000$	149
4.17	Comparison of velocity magnitude vectors from UVP, LSPIV .	150
4.18	Three-dimensional plot of vertical velocity contour and streamlines at different planes of the reference geometry	152

4.19	Three-dimensional plot of vertical velocity contour and streamlines at different planes of the reservoir geometry with $SK = 8.25154$	
4.20	V-W velocity vector and U-contour plots for flow $Re = 28000$, at different cross streamwise planes of the reservoir geometry .	155
4.21	The normalized mean velocity U_{res}/U_{in} for symmetric and asymmetric jet in the axial and transverse sections for $Re = 28000$.	156
4.22	The normalized mean velocity U_{res}/U_{in} in Test1 with various Froude and Reynolds numbers in the axial and transverse sections	158
4.23	Scheme for regime classification of jet flow types	159
4.24	Time averaged mean velocity magnitude for symmetric, meandering, and asymmetric jets along the basin centerline	161
4.25	Time averaged mean longitudinal velocity for symmetric, asymmetric, and meandering jet flow regime at the basin centerline	162
4.26	Relation for the normalized average velocity of all symmetric jets along the basin centerline and comparison with measured values	163
4.27	Relation for the normalized average velocity of all asymmetric jets along the basin centerline and comparison with measured values	164
4.28	Relation for the normalized average velocity of all meandering jets along the basin centerline and comparison with measured values	165
4.29	Measured versus predicted normalized average velocity ratio in reservoir	166
4.30	Geometry effect on the variation of reattachment lengths $L_{r1} - L_{r2}$ at $Re_{in} = 28000$	167
4.31	Froude number effect on the reattachment lengths X_{r1} at $Re_{in} = 28000$	168
4.32	Residence time as a function of reservoir geometry shape factor SK	170
4.33	Relation for the normalized initial residence time for all geometries and comparison with measured values	171
4.34	Relation for the sedimentation index SI for all geometries and comparison with measured values	172
5.1	Plan view of the reference geometry, definition of the geometrical parameters and schematic diagram of the flow pattern . .	176
5.2	Average flow pattern with velocity vectors and evolution of deposition for Test1, (T1) for different time steps	178

5.3	Average flow pattern with velocity vectors and evolution of deposition for Test2, (T2) for different time steps	181
5.4	Average flow pattern with velocity vectors and evolution of deposition for Test3, (T3) for different time steps	183
5.5	Evolution of bed topography and flow vectors with velocity contours at different time	188
5.6	Evolution of bed thickness measured at four different cross sections	189
5.7	Inlet and outlet suspended sediment concentration and sketch of flow patterns during 18 hours	191
5.8	Evolution of sediments release E and trap efficiency TE for long run duration (18 <i>hrs</i>)	192
5.9	Average flow pattern with velocity vectors and bed topography at 270 min, for reduced reservoir widths	194
5.10	Average flow pattern with velocity vectors and bed topography at 270 min, for reduced reservoir length	196
5.11	Average flow pattern with velocity vectors and bed topography at 270 min, for the reduced semi entrance angle	199
5.12	Comparison of evolution of the bed profiles between the reduced reservoir widths at different time	202
5.13	Comparison of evolution of the bed profiles between the reduced reservoir length at different time	203
5.14	Evolution of the transversal bed profiles for the lozenge and the hexagonal geometries	204
5.15	Time series of SSC of various geometries	207
5.16	Photographes showing the evolution of suspended sediment and the surface floating particles entering in a short length shallow reservoir geometry	209
5.17	The evolution of the streamlines plots for experiment T13 . . .	210
5.18	Middle cross section for, (a) streamwise velocity profiles and, (b) Bed topography, for T13 at different time	212
5.19	The evolution of the streamlines plots for experiment T1 . . .	213
5.20	Comparison of, (a) streamwise velocity profiles and, (b) Bed topography, for T1 at cross section $X = 1.5$ m	214
5.21	Photographes of final bed forms for two different expansion angles	215
5.22	Morphological features for various geometry with asymmetric flow structures	217
5.23	Morphological features for various geometry with symmetric flow structures	218

5.24	Flow velocity with vectors and bed topography contours after two days of free flow flushing of two different experiments . . .	220
5.25	Photographs of eroded channel at the end of reservoir experiments after two days of free flow flushing	221
5.26	Flow pattern and bed topography contours after two days of drawdown flushing for four different experiments	223
5.27	Comparison of bed thickness profiles of final deposition after 9.0 hours, free flow and drawdown flushing after two days for T16 at three different cross sections	225
5.28	Photographs of eroded channel at the end of reservoir experiments after two days of drawdown flushing	227
5.29	Influence of Aspect Ratio on the silting ratio of reservoir . . .	228
5.30	Influence of Expansion Ratio on the silting ratio of reservoir .	229
5.31	Influence of normalized expansion area on the storage loss . . .	230
5.32	Relation for the storage loss SR and comparison with measured values	232
5.33	Relation for the storage loss SR with $SK \cdot t^*$ and comparison with measured values	233
5.34	Relation for the relative deposited thickness d/h with $SK \cdot t^*$ and comparison with measured values	235
5.35	Relation for the relative deposited thickness with relative time and comparison with measured values (simplified formula from GPKernel)	236
6.1	Influence of Aspect Ratio on the trap efficiency of reservoir . .	241
6.2	Influence of Expansion Ratio on the trap efficiency of reservoir	242
6.3	Influence of ratio of surface area of expansion and the total area of the reservoir on the trap efficiency of reservoir	243
6.4	Influence of expansion aspect ratio on the trap efficiency of reservoir	244
6.5	Influence of geometry shape factor SK on the trap efficiency TE	246
6.6	Influence of dimensionless time on trap efficiency of various geometry shape factor SK	247
6.7	Classification of the evolution tendency of trap efficiency curve according to geometry shape factor SK	248
6.8	Relationship between number of flow recirculation cells and deposited volume	249
6.9	The evolution of trap efficiency for the long run test of 1080 minutes for the reference geometry with normalized time . . .	250

6.10	Relation for the trap efficiency TE with SK , t^* and comparison with measured values	251
6.11	The influence of geometry shape factor and sedimentation index	252
6.12	The influence of the sedimentation index on the release efficiency RE of the reservoir	253
6.13	Influence of geometry shape factor on the efficiency of free flow flushing	255
6.14	Influence of the geometry shape factor on efficiency of the draw-down flushing	256
7.1	Stationary flow field with velocity magnitude and suspended sediment concentration computed by CCHE2D and FLOW-3D for the initial reservoir conditions (plane bed, constant discharge, $\kappa - \varepsilon$)	261
7.2	Longitudinal section for velocity magnitude and suspended sediment concentrations computed by CCHE2D and FLOW-3D .	262
7.3	General configuration of sediment transport in CCHE2D . . .	264
7.4	Results for numerical simulation run A – 1	271
7.5	Results for numerical simulation run A – 2	272
7.6	Results for numerical simulation run A – 3	273
7.7	Results for numerical simulation run B – 1	274
7.8	Results for numerical simulation run B – 2	275
7.9	Results for numerical simulation run C	275
7.10	Comparison of depth-averaged velocity magnitude along basin centreline for run series A, B, and C	276
7.11	Comparison of kinematic eddy viscosity along basin centreline for run series A, B, and C	277
7.12	Comparison of bed profiles along basin centreline for run series A and B	278
7.13	Comparison of suspended load concentration along basin centreline for run series A and B	279
7.14	Comparison of suspended load concentration along basin centreline for run series A and B	280
7.15	Multiple-layer sorting model of bed material gradation	280
7.16	Comparison of velocity magnitude vectors recorded by UVP and LSPIV with numerically simulated velocity magnitude vectors	281
7.17	Comparison of depth-averaged velocity magnitude recorded by UVP and LSPIV with numerically simulated velocity magnitude	282

7.18	Flow field simulated with a uniform specific discharge profile at inflow (algebraic turbulence closure). Velocity magnitude in m/s	283
7.19	Measured and simulated average flow pattern with velocity vectors in a rectangular basin with a constant width of 4 m and four different lengths	287
7.20	Simulated non-dimensional moment m of the flow field in the rectangular basin of 6 m by 4 m	288
A1.1	Time average flow pattern with velocity vectors and streamlines with clear water (Test1)	353
A1.2	Time average flow pattern and streamlines after 10 minutes of the first period with sediments (Test1)	354
A1.3	Time average flow pattern and streamlines after 30 minutes of the first period with sediments (Test1)	354
A1.4	Time average flow pattern and streamlines after 60 minutes of the first period with sediments (Test1)	355
A1.5	Time average flow pattern and streamlines after 90 minutes of the first period with sediments (Test1)	355
A1.6	Time average flow pattern and streamlines after 10 minutes of the second period with sediments (Test1)	356
A1.7	Time average flow pattern and streamlines after 30 minutes of the second period with sediments (Test1)	356
A1.8	Time average flow pattern and streamlines after 60 minutes of the second period with sediments (Test1)	357
A1.9	Time average flow pattern and streamlines after 90 minutes of the second period with sediments (Test1)	357
A1.10	Time average flow pattern and streamlines after 10 minutes of the third period with sediments (Test1)	358
A1.11	Time average flow pattern and streamlines after 30 minutes of the third period with sediments (Test1)	358
A1.12	Time average flow pattern and streamlines after 60 minutes of the third period with sediments (Test1)	359
A1.13	Time average flow pattern and streamlines after 90 minutes of the third period with sediments (Test1)	359
A1.14	Time average flow pattern and streamlines of the free flow flushing with water depth $h = 20cm$ (Test1)	361
A1.15	Time average flow pattern and streamlines of the drawdown flushing with water depth $h = 10cm$ (Test1)	361

A1.16	Contours of deposition pattern after the first period run after 1.5 hour (Test1)	364
A1.17	Contours of deposition pattern after the first period run after 3.0 hour (Test1)	365
A1.18	Contours of deposition pattern after the first period run after 4.5 hour (Test1)	366
A1.19	Contours of deposition pattern after the free flow flushing period run after 48 hour (Test1)	367
A1.20	Evolution of sediment deposits for four periods runs at cross section $X_1 = 1.5m$ (Test1)	369
A1.21	Evolution of sediment deposits for four periods runs at cross section $X_2 = 3.0m$ (Test1)	370
A1.22	Evolution of sediment deposits for four periods runs at cross section $X_3 = 4.5m$ (Test1)	371
A1.23	Evolution of sediment deposits for four periods runs at center-line longitudinal section $Y = 2.0m$ (Test1)	372
A1.24	Time average flow pattern with velocity vectors and streamlines with clear water measured by UVP (Test1)	375
A1.25	Comparison of velocity magnitude vectors obtained from UVP and LSPIV measurement (Test1)	376
A2.1	Time average flow pattern with velocity vectors and streamlines with clear water (Test2)	379
A2.2	Time average flow pattern and streamlines after 60 minutes of the third period with sediments (Test2)	380
A2.3	Time average flow pattern and streamlines after 90 minutes of the third period with sediments (Test2)	380
A3.1	Time average flow pattern with velocity vectors and streamlines with clear water (Test3)	383
A3.2	Time average flow pattern and streamlines after 240 minutes of the first period with sediments (Test3)	384
A3.3	Time average flow pattern and streamlines after 270 minutes of the first period with sediments (Test3)	384
A3.4	Contours of deposition pattern after the first period run after 4.5 hour (Test3)	387
A3.5	Evolution of sediment deposits for 4.5 hours run at cross section $X_3 = 4.5m$ (Test3)	389
A3.6	Evolution of sediment deposits for four periods runs at center-line longitudinal section $Y = 2.0m$ (Test3)	390

A4.1	Time average flow pattern with velocity vectors and streamlines with clear water (Test4)	393
A4.2	Time average flow pattern and streamlines after 480 minutes of the third period with sediments (Test4)	394
A4.3	Time average flow pattern and streamlines after 510 minutes of the third period with sediments (Test4)	394
A4.4	Time average flow pattern and streamlines after 540 minutes of the third period with sediments (Test4)	395
A4.5	Inflow and released suspended concentration of sediments from the reservoir during the first period of 4.5hours (Test4)	397
A4.6	Inflow and released suspended concentration of sediments from the reservoir during the second period of 4.5hours (Test4)	398
A4.7	Inflow and released suspended concentration of sediments from the reservoir during the third period of 9.0hours (Test4)	399
A4.8	Contours of deposition pattern after the third period run after 18.0 hour (Test4)	402
A4.9	Evolution of sediment deposits for three periods runs at cross section $X_1 = 1.5m$ (Test4)	404
A4.10	Evolution of sediment deposits for three periods runs at cross section $X_2 = 3.0m$ (Test4)	405
A4.11	Evolution of sediment deposits for three periods runs at cross section $X_3 = 4.5m$ (Test4)	406
A4.12	Evolution of sediment deposits for four periods runs at center-line longitudinal section $Y = 2.0m$ (Test4)	407
A5.1	Time average flow pattern with velocity vectors and streamlines with clear water depth of $h_1 = 0.20m$ (Test5)	410
A5.2	Time average flow pattern with velocity vectors and streamlines with clear water depth of $h_2 = 0.15m$ (Test5)	412
A5.3	Time average flow pattern with velocity vectors and streamlines with clear water depth of $h_3 = 0.10m$ (Test5)	414
A5.4	Time average flow pattern with velocity vectors and streamlines with clear water depth of $h_4 = 0.075m$ (Test5)	416
A6.1	Time average flow pattern with velocity vectors and streamlines with clear water for (Test6) of low discharge	419
A6.2	Time average flow pattern and streamlines after 10 minutes of the first period with sediments (Test6)	420
A6.3	Time average flow pattern and streamlines after 30 minutes of the first period with sediments with (test6) of low discharge (Test6)	420

A6.4	Time average flow pattern and streamlines after 60 minutes of the first period with sediments with (test6) of low discharge (Test6)	421
A6.5	Time average flow pattern and streamlines after 90 minutes of the first period with sediments with (test6) of low discharge (Test6)	421
A7.1	Time average flow pattern with velocity vectors and streamlines with clear water (Test7)	424
A7.2	Time average flow pattern and streamlines after 60 minutes of the third period with sediments (Test7)	425
A7.3	Time average flow pattern and streamlines after 90 minutes of the third period with sediments (Test7)	425
A8.1	Time average flow pattern with velocity vectors and streamlines with clear water (Test8)	428
A8.2	Time average flow pattern and streamlines after 60 minutes of the third period with sediments (Test8)	429
A8.3	Time average flow pattern and streamlines after 90 minutes of the third period with sediments (Test8)	429
A8.4	Time average flow pattern and streamlines of the drawdown flushing with water depth $h = 10cm$ (Test8)	431
A8.5	Inflow and released suspended concentration of sediments from the reservoir during the first, second and third period of 4.5hours (Test8)	433
A8.6	Contours of deposition pattern after the third period run after 4.5 hour (Test8)	436
A8.7	Contours of deposition pattern for the drawdown flushing period run after 48 hour (Test8)	437
A8.8	Sediment deposits comparison for third and flushing periods run at cross section $X_2 = 3.0m$ from the entrance (Test8) . . .	439
A8.9	Sediment deposits comparison for third and flushing periods run at cross section $X_3 = 4.5m$ from the entrance (Test8) . . .	440
A8.10	Evolution of sediment deposits for three periods runs at centerline longitudinal section $Y = 2.0m$ (Test8)	441
A9.1	Time average flow pattern with velocity vectors and streamlines with clear water (Test9)	444
A10.1	Time average flow pattern with velocity vectors and streamlines with clear water (Test10)	447
A11.1	Time average flow pattern with velocity vectors and streamlines with clear water (Test11)	450

A11.2	Time average flow pattern and streamlines after 60 minutes of the third period with sediments (Test11)	451
A11.3	Time average flow pattern and streamlines after 90 minutes of the third period with sediments (Test11)	451
A11.4	Time average flow pattern and streamlines of the drawdown flushing with water depth $h = 10cm$ (Test11)	453
A11.5	Inflow and released suspended concentration of sediments from the reservoir during the first, second and third period of 4.5hours (Test11)	455
A11.6	Contours of deposition pattern after the first period run after 1.5 hour (Test11)	458
A12.1	Time average flow pattern with velocity vectors and streamlines with clear water for the square geometry (Test12)	461
A13.1	Time average flow pattern with velocity vectors and streamlines with clear water (Test13)	464
A13.2	Time average flow pattern and streamlines after 60 minutes of the third period with sediments (Test13)	465
A13.3	Time average flow pattern and streamlines after 90 minutes of the third period with sediments (Test13)	465
A13.4	Inflow and released suspended concentration of sediments from the reservoir during the first, second and third period of 4.5hours (Test13)	467
A13.5	Contours of deposition pattern after the first period run after 1.5 hour (Test13)	470
A13.6	Contours of deposition pattern after the second period run after 3.0 hour (Test13)	471
A14.1	Time average flow pattern with velocity vectors and streamlines with clear water (Test14)	474
A14.2	Time average flow pattern and streamlines after 120 minutes of the fourth period with sediments (Test14)	475
A14.3	Time average flow pattern and streamlines after 150 minutes of the fourth period with sediments (Test14)	475
A14.4	Time average flow pattern and streamlines after 180 minutes of the fourth period with sediments (Test14)	476
A14.5	Time average flow pattern and streamlines of the drawdown flushing with water depth $h = 10cm$ (Test14)	478
A14.6	Inflow and released suspended concentration of sediments from the reservoir during the first, second and third period of 4.5hours (Test14)	480

A14.7	Inflow and released suspended concentration of sediments from the reservoir during the fourth period of 3.0hours (Test14) . .	481
A14.8	Inflow and released suspended concentration of sediments from the reservoir during the flushing period of 48hours (Test14) . .	482
A14.9	Contours of deposition pattern after the first period run after 1.5 hour (Test14)	485
A14.10	Contours of deposition pattern after the second period run after 3.0 hour (Test14)	486
A14.11	Contours of deposition pattern after the third period run after 4.5 hour (Test14)	487
A14.12	Contours of deposition pattern after the fourth period run after 7.5 hour (Test14)	488
A14.13	Contours of deposition pattern for the drawdown flushing period run after 48 hour (Test14)	489
A14.14	Evolution of sediment deposits for four periods runs at cross section $X_1 = 1.5m$ (Test14)	491
A14.15	Evolution of sediment deposits for four periods runs at cross section $X_2 = 3.0m$ (Test14)	492
A14.16	Evolution of sediment deposits for four periods runs at cross section $X_3 = 4.5m$ (Test14)	493
A14.17	Sediment deposits comparison for fourth and flushing periods run at cross section $X_1 = 1.5m$ from the entrance (Test14) . .	494
A14.18	Sediment deposits comparison for fourth and flushing periods run at cross section $X_2 = 3.0m$ from the entrance (Test14) . .	495
A14.19	Sediment deposits comparison for fourth and flushing periods run at cross section $X_3 = 4.5m$ from the entrance (Test14) . .	496
A14.20	Evolution of sediment deposits for four periods runs at center-line longitudinal section $Y = 2.0m$ (Test14)	497
A15.1	Time average flow pattern with velocity vectors and streamlines with clear water for the square geometry (Test15)	500
A16.1	Time average flow pattern with velocity vectors and streamlines with clear water (Test16)	503
A16.2	Time average flow pattern and streamlines after 210 minutes of the fourth period with sediments (Test16)	504
A16.3	Time average flow pattern and streamlines after 240 minutes of the fourth period with sediments (Test16)	504
A16.4	Time average flow pattern and streamlines of the free flow flushing with water depth $h = 20cm$ (Test16)	506

List of Figures

A16.5	Time average flow pattern and streamlines of the drawdown flushing with water depth $h = 10cm$ (Test16)	507
A16.6	Inflow and released suspended concentration of sediments from the reservoir during the first, second and third period of 4.5hours (Test16)	509
A16.7	Inflow and released suspended concentration of sediments from the reservoir during the fourth period of 4.5hours (Test16) . .	510
A16.8	Test phases, measurement and procedures pictures during four runs (Test16)	511
A16.9	Plan view of the final bed depositions features after the fourth period 9.0 hour (Test16)	512
A16.10	Downstream looking of final deposition with ripple formations details after 9.0 hour (Test16)	513
A16.11	Plan view of the final bed depositions features after the 48 hour of free flow flushing (Test16)	514
A16.12	Downstream looking of final deposition with ripple formations details after 48 hour of free flow flushing (Test16)	515
A16.13	Plan view of the final bed depositions features after 48 hour of drawdown flushing (Test16)	516
A16.14	Downstream looking of final deposition with ripple formations details after 48 hour of drawdown flushing (Test16)	517
A17.1	Time average flow pattern with velocity vectors and streamlines with clear water for the square geometry (Test17)	520

List of Tables

2.1	Classification of most commercially and academic available computational models	76
3.1	Hydraulic conditions of experiments	86
3.2	Comparison of different characteristic particle sizes and the corresponding settling velocities of fine crushed walnut shells.	88
3.3	List of parameters describing the physical properties and grain size distribution curve for the sediment material.	91
3.4	Model parameters and instrumentation used	92
3.5	Model parameters and instrumentation	110
3.6	Geometrical properties and configurations of different tests	118
3.7	Hydraulic conditions for all tested configurations with clear water	124
3.8	Sediment conditions for all tested configurations with suspended sediment . .	126
7.1	Summary of numerical runs	269
7.2	Boundary conditions for reference run (simulation A-2)	270

Experimental Test Results for Different Geometries

Appendix gives selected experimental results and measured data for different reservoir geometries. The complete data of all test configurations is available at the Laboratory of Hydraulic Constructions (LCH) upon request.

- A1. Results of reference rectangular reservoir geometry of length 6.0m, and width 4.0m, with three test duration (1.5hour for each) [Test1]
- A2. Repeated test results of rectangular reservoir geometry of length 6.0m, and width 4.0m [Test2]
- A3. Continues test results of rectangular reservoir geometry of length 6.0m, and width 4.0m [Test3]
- A4. Long-term test results of rectangular reservoir geometry of length 6.0m, and width 4.0m [Test4]
- A5. Results of rectangular reservoir geometry of length 6.0m, and width 4.0m, different Froude numbers [Test5]
- A6. Results of rectangular reservoir geometry of length 6.0m, and width 4.0m, different R_n [Test6]
- A7. Results of rectangular reservoir geometry of length 6.0m, and width 3.0m [Test7]
- A8. Results of rectangular reservoir geometry of length 6.0m, and width 2.0m [Test8]
- A9. Results of rectangular reservoir geometry of length 6.0m, and width 1.0m [Test9]

A10. Results of rectangular reservoir geometry of length 6.0m, and width 0.5m [Test10]

A11. Results of rectangular reservoir geometry of length 5.0m, and width 4.0m [Test11]

A12. Results of rectangular reservoir geometry of length 4.0m, and width 4.0m [Test12]

A13. Results of rectangular reservoir geometry of length 3.0m, and width 4.0m [Test13]

A14. Results of lozenge reservoir geometry [Test14]

A15. Results of cutted upstream corners of rectangular reservoir geometry of length 6.0m, and width 4.0m [Test15]

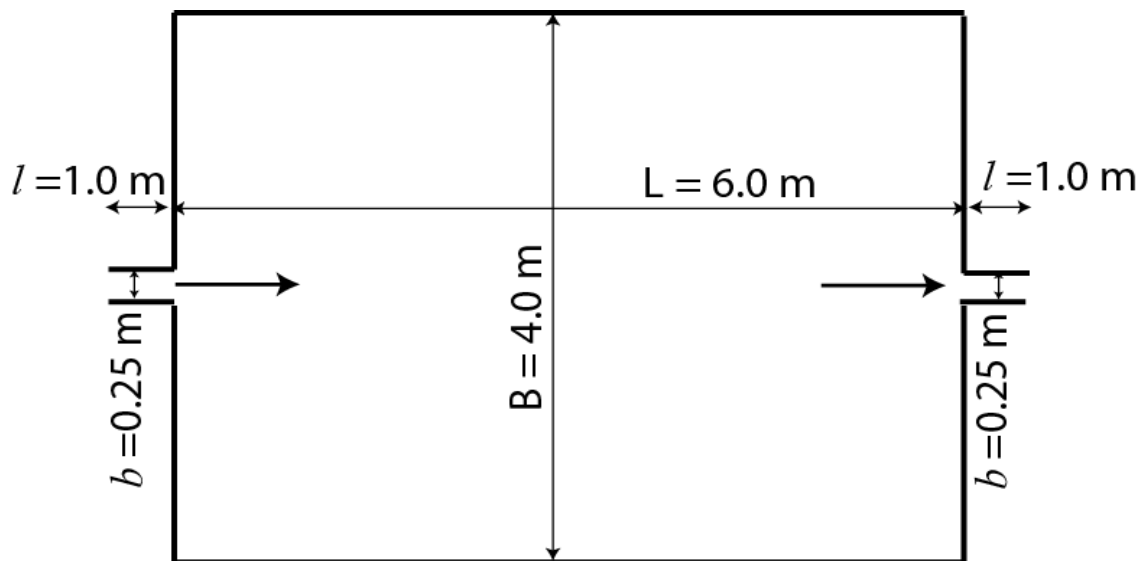
A16. Results of hexagonal reservoir geometry [Test16]

A17. Results of rectangular channel geometry of length 6.0m, and width 0.25m [Test17]

Every reservoir geometry results are given for the measured quantities:

1. Surface velocity LSPIV-measurements
 - Flow pattern with clear water
 - Flow field with Sediment water mixture
2. Suspended sediment concentration
3. Bed deposition morphology
 - Bathymetric contour lines
 - Cross sections
 - Centerline longitudinal section
 - Final deposition pictures
4. 3-D velocities UVP-measurements

A1 Results of rectangular geometry Test1



A1.1 Surface velocity obtained by (LSPIV) measurements

Results of flow field with the velocity magnitude and streamlines obtained for the following flow and sediment characteristic:

- Discharge $Q = 7.0$ [l/s]
- Water depth $h = 0.2$ [m]
- Froude Number $F_r = 0.1$
- Reynolds number $Re = 28000$
- Sediment diameter $d_{50} = 50$ [μ]
- Sediment density $\rho = 1500$ [kg/m³]
- Suspended sediment concentration $C = 3.0$ [g/l]

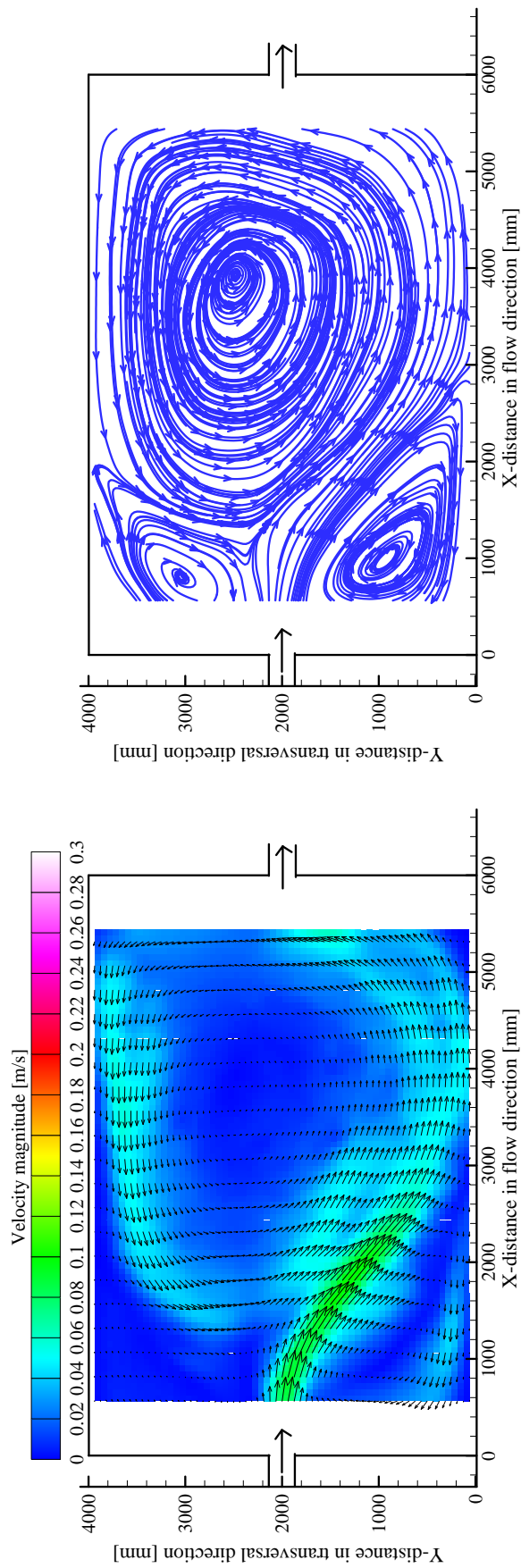


Figure A1.1: Time average flow pattern with velocity vectors (left); streamlines (right) with clear water after stable state

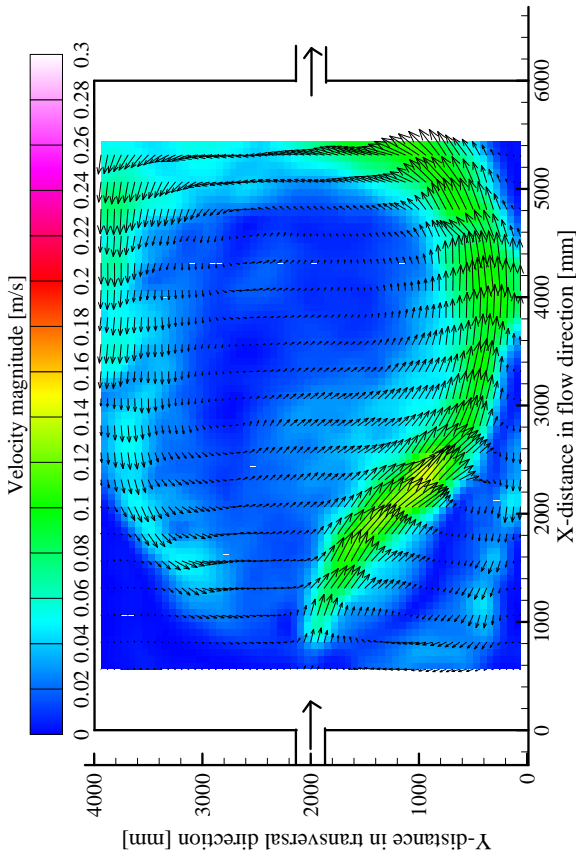


Figure A1.2: Time average flow pattern (left); streamlines (right) after 10 minutes of the first period with sediments

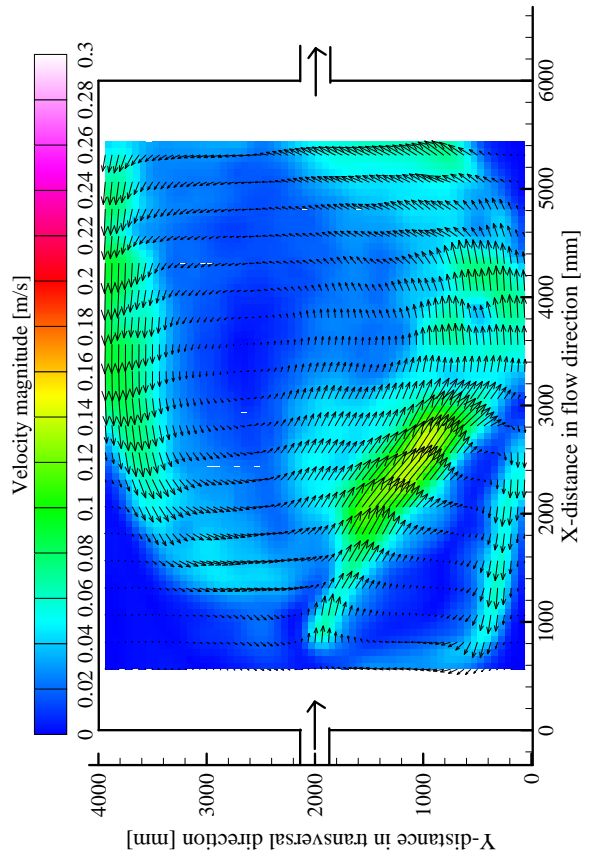
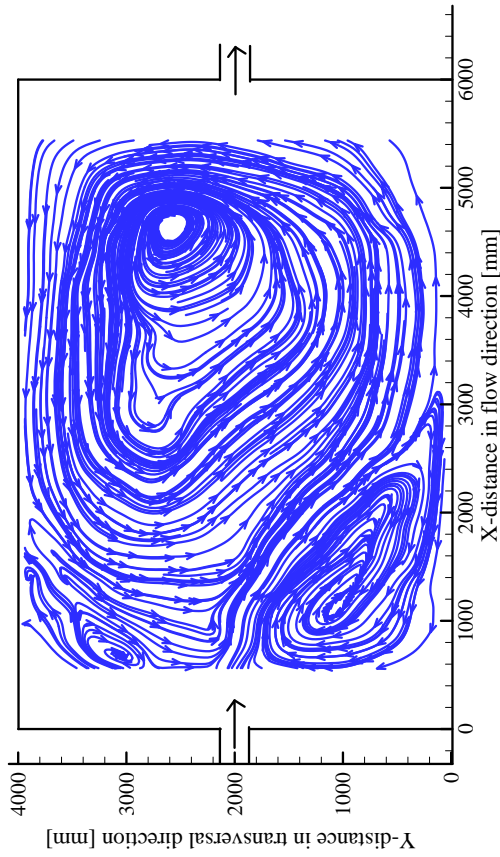
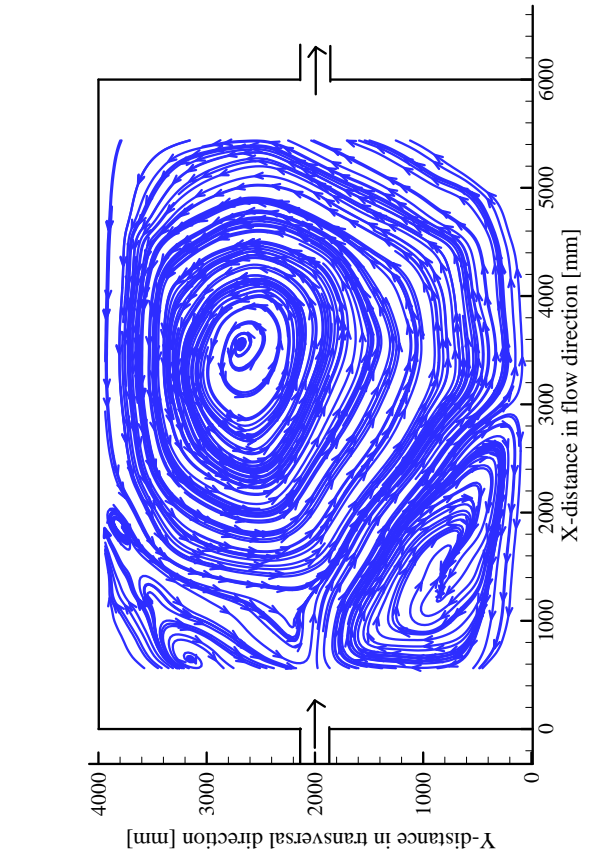


Figure A1.3: Time average flow pattern (left); streamlines (right) after 30 minutes of the first period with sediments



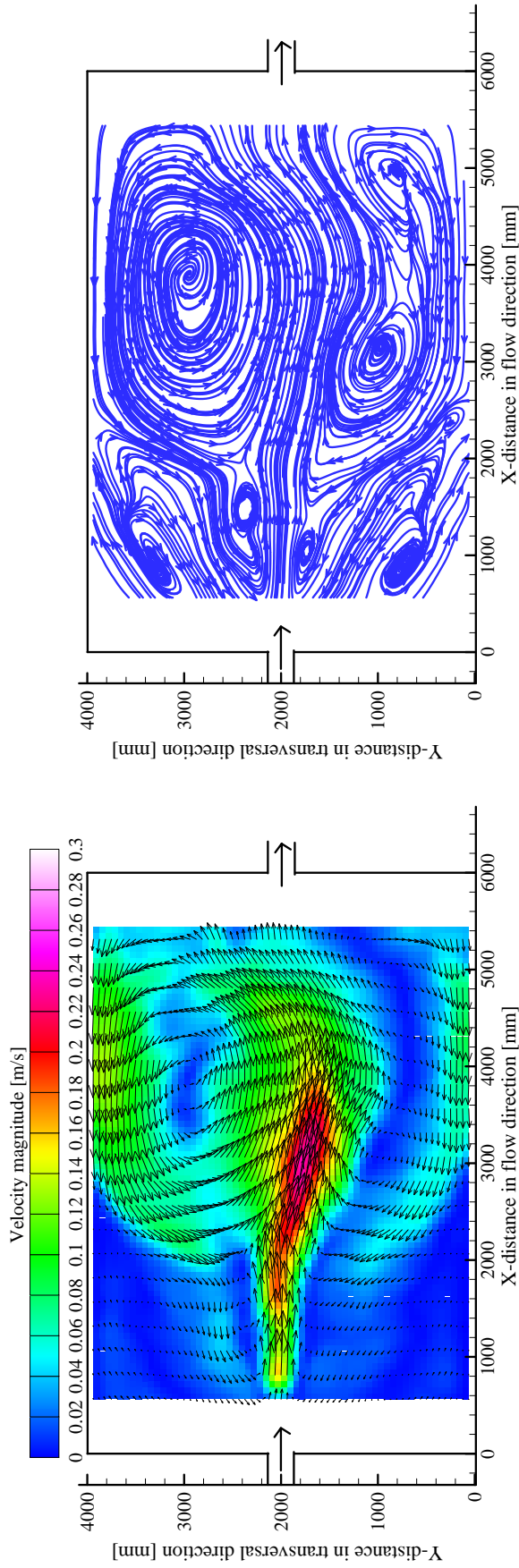


Figure A1.4: Time average flow pattern (left); streamlines (right) after 60 minutes of the first period with sediments

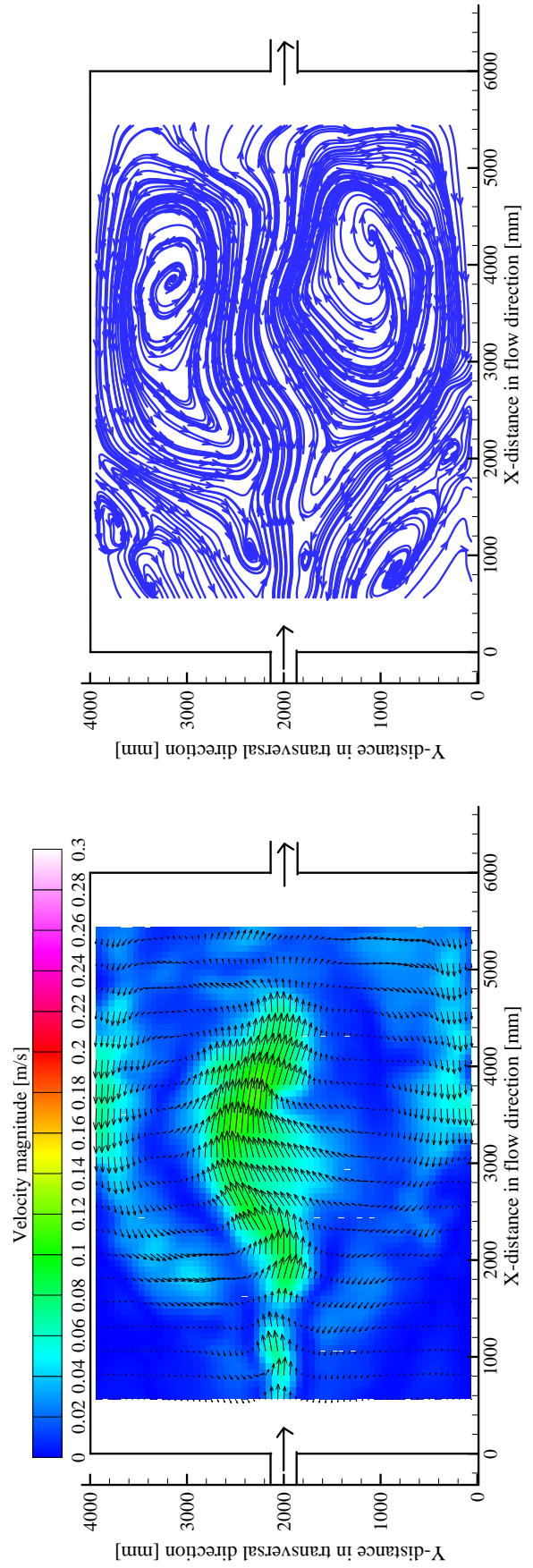


Figure A1.5: Time average flow pattern (left); streamlines (right) after 90 minutes of the first period with sediments

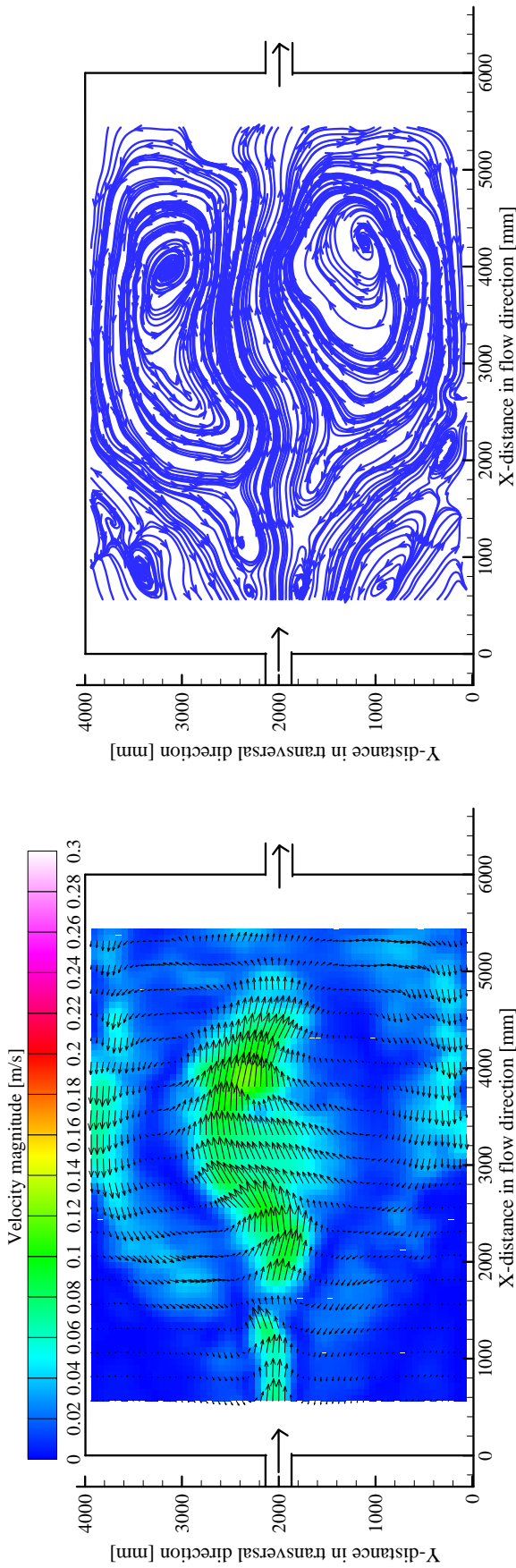


Figure A1.6: Time average flow pattern (left); streamlines (right) after 10 minutes of the second period with sediments

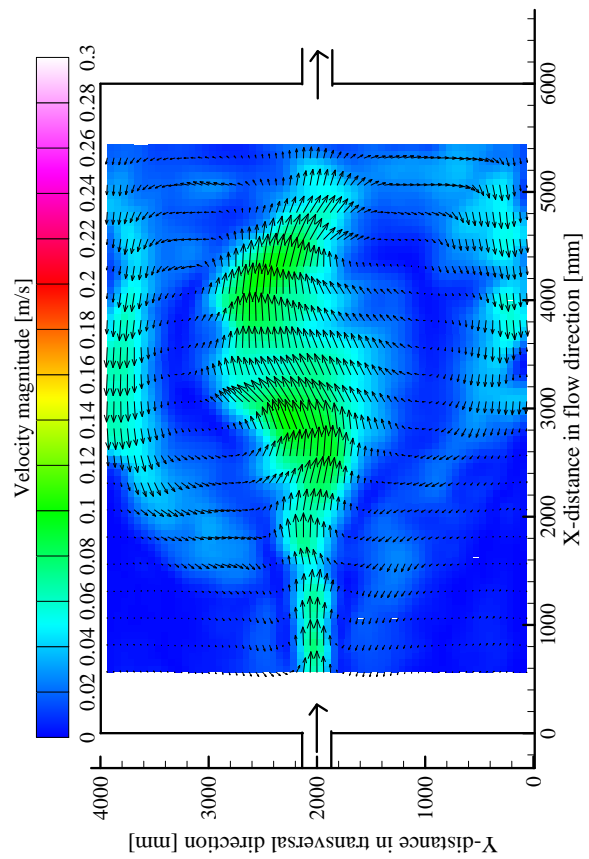


Figure A1.7: Time average flow pattern (left); streamlines (right) after 30 minutes of the second period with sediments

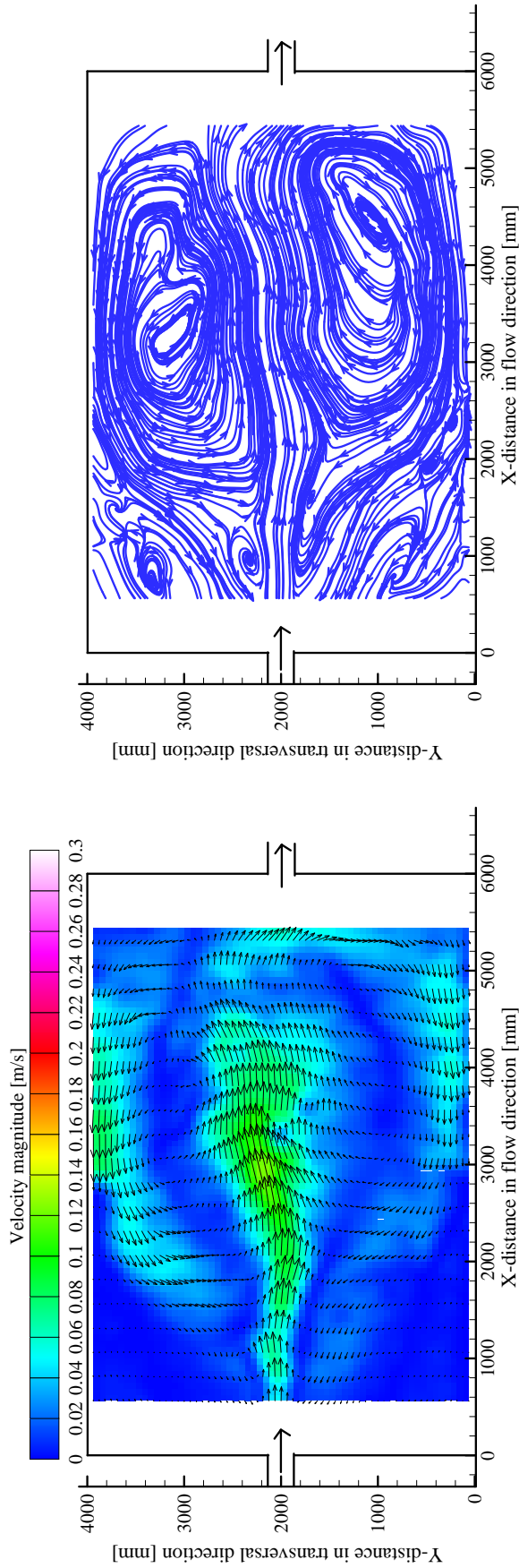


Figure A1.8: Time average flow pattern (left); streamlines (right) after 60 minutes of the second period with sediments

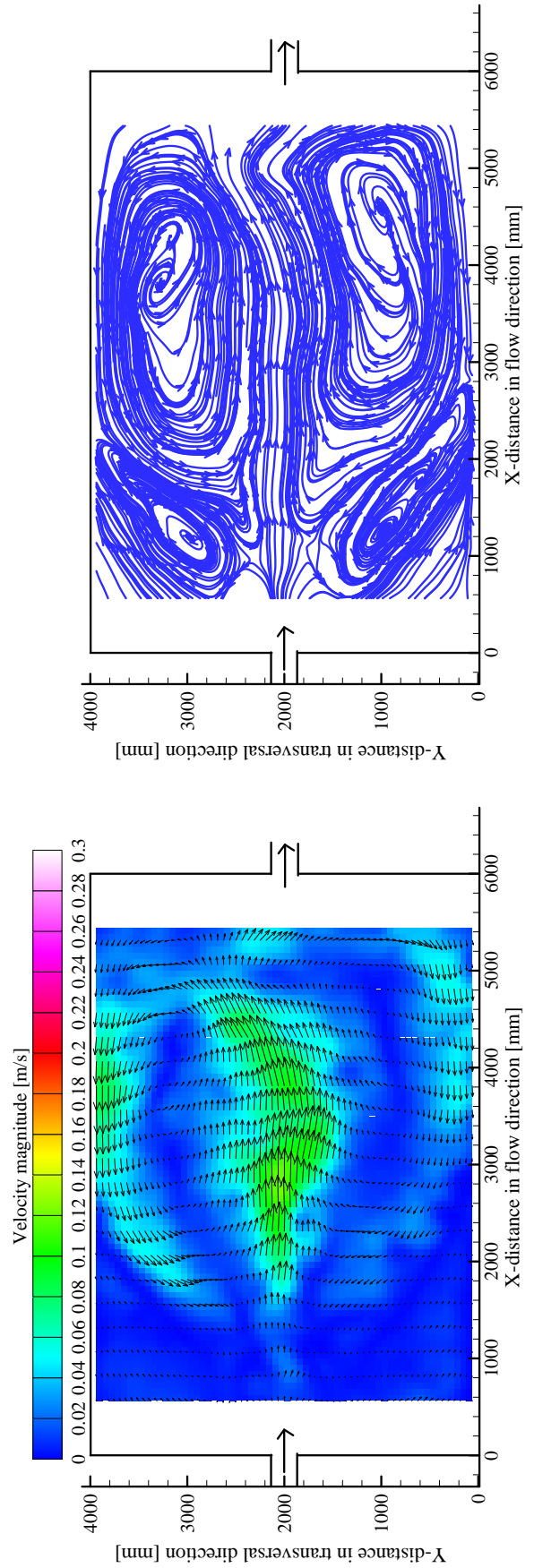


Figure A1.9: Time average flow pattern (left); streamlines (right) after 90 minutes of the second period with sediments

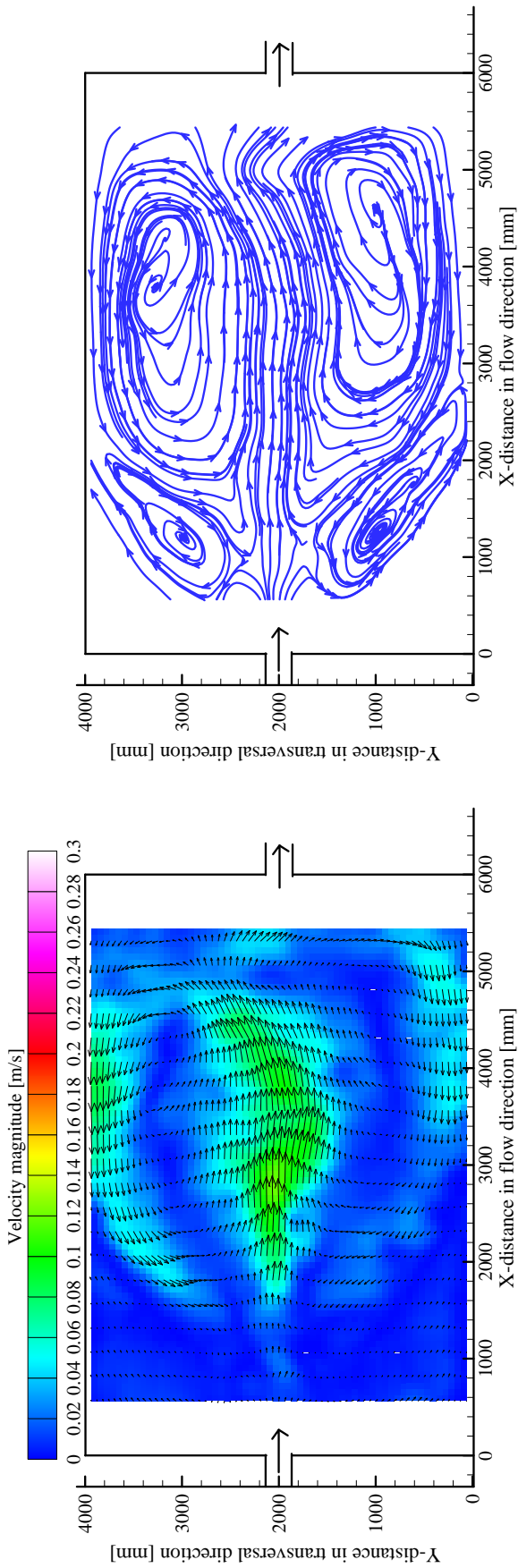


Figure A1.10: Time average flow pattern (left); streamlines (right) after 10 minutes of the third period with sediments

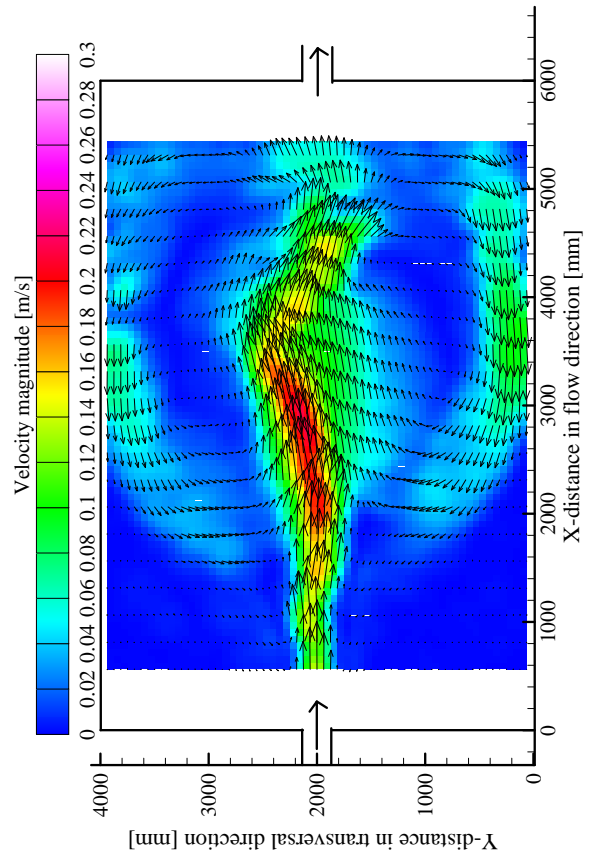


Figure A1.11: Time average flow pattern (left); streamlines (right) after 30 minutes of the third period with sediments

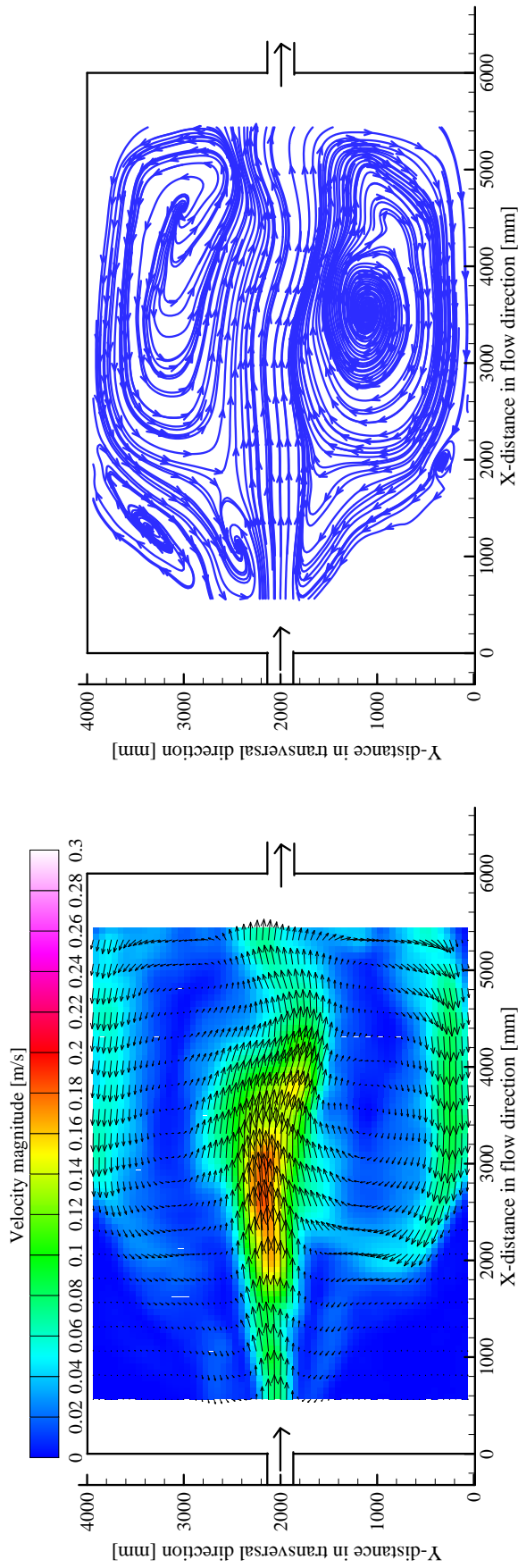


Figure A1.12: Time average flow pattern (left); streamlines (right) after 60 minutes of the third period with sediments

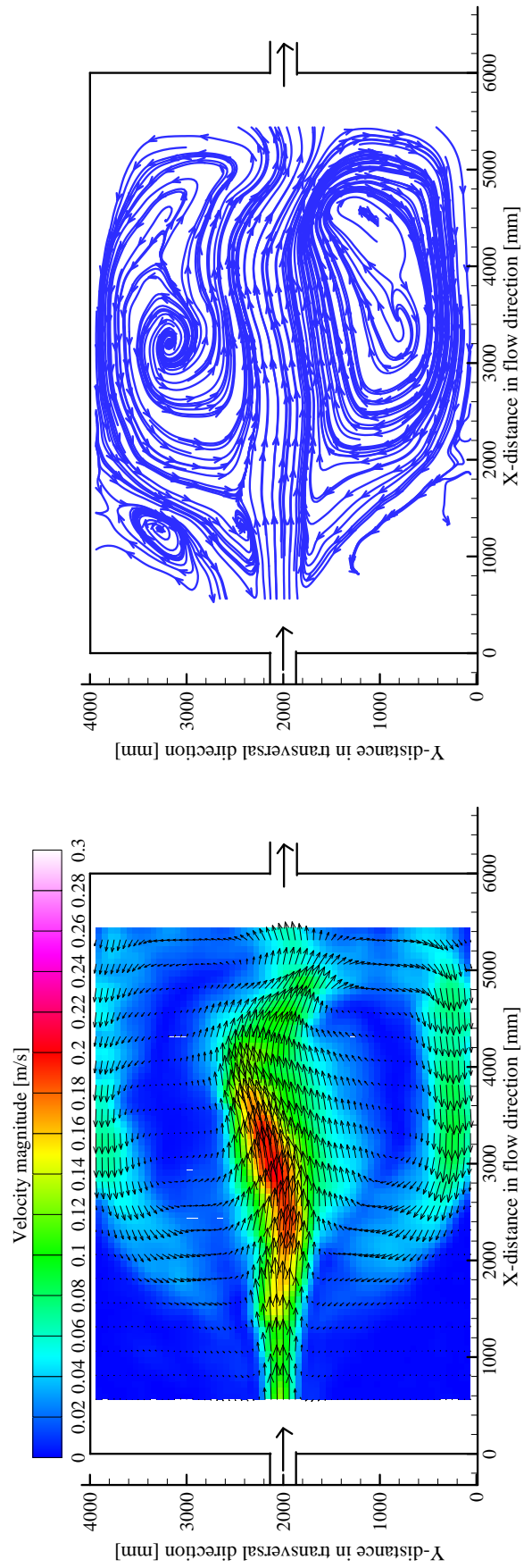


Figure A1.13: Time average flow pattern (left); streamlines (right) after 90 minutes of the third period with sediments

A1.2 Two days flushing with clear water over the final bed deposition of the third period (4.5 hours)

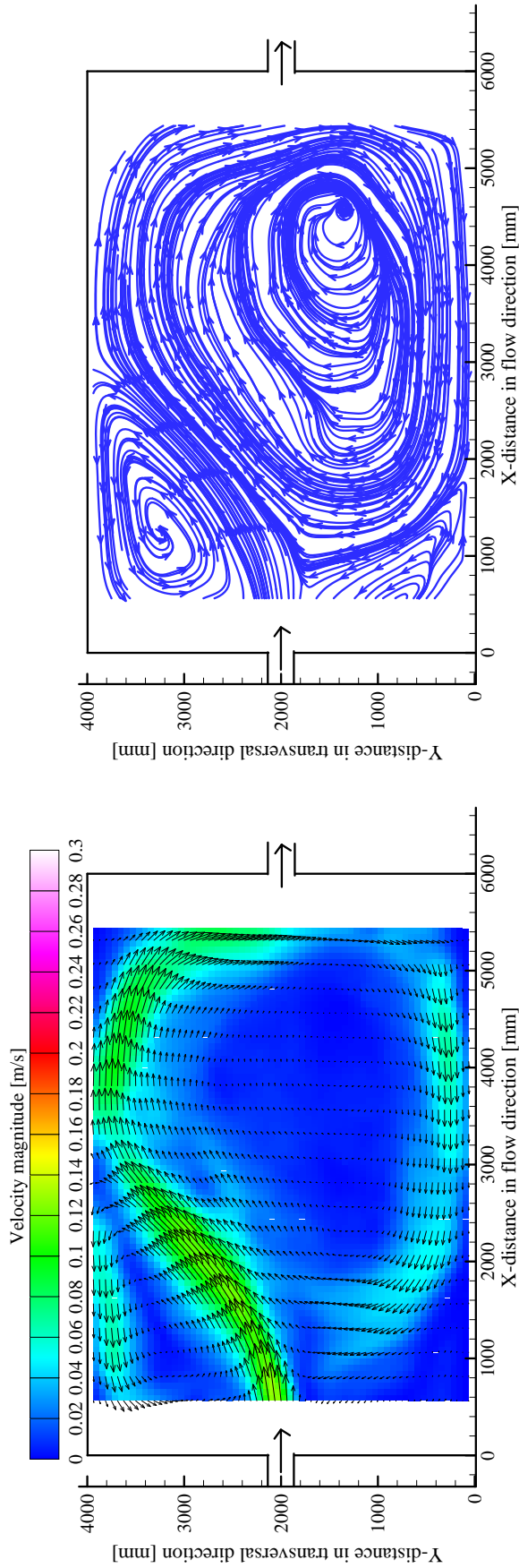


Figure A1.14: Time average flow pattern (left); streamlines (right) of the free flow flushing with water depth $h = 20\text{cm}$

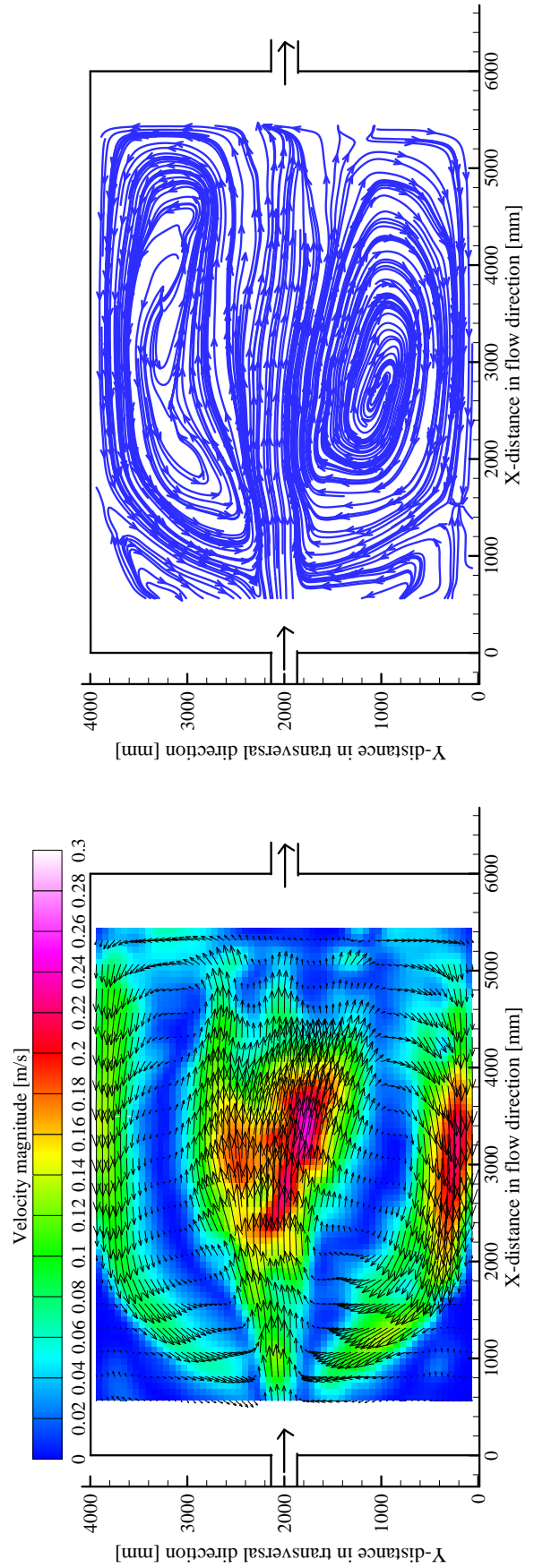


Figure A1.15: Time average flow pattern (left); streamlines (right) of the drawdown flushing with water depth $h = 10\text{cm}$

A1.3 Measurements of bed thickness deposition obtained by Mini Echo Sounder for Test1

Results of morphological evolution obtained for the following flow and sediment characteristic:

- Discharge $Q = 7.0$ [l/s]
- Water depth $h = 0.2$ [m]
- Froude Number $F_r = 0.1$
- Reynolds number $Re = 28000$
- Sediment diameter $d_{50} = 50$ [μ]
- Sediment density $\rho = 1500$ [kg/m³]
- Suspended sediment concentration $C = 3.0$ [g/l]

A1.3.1 Depositions contours

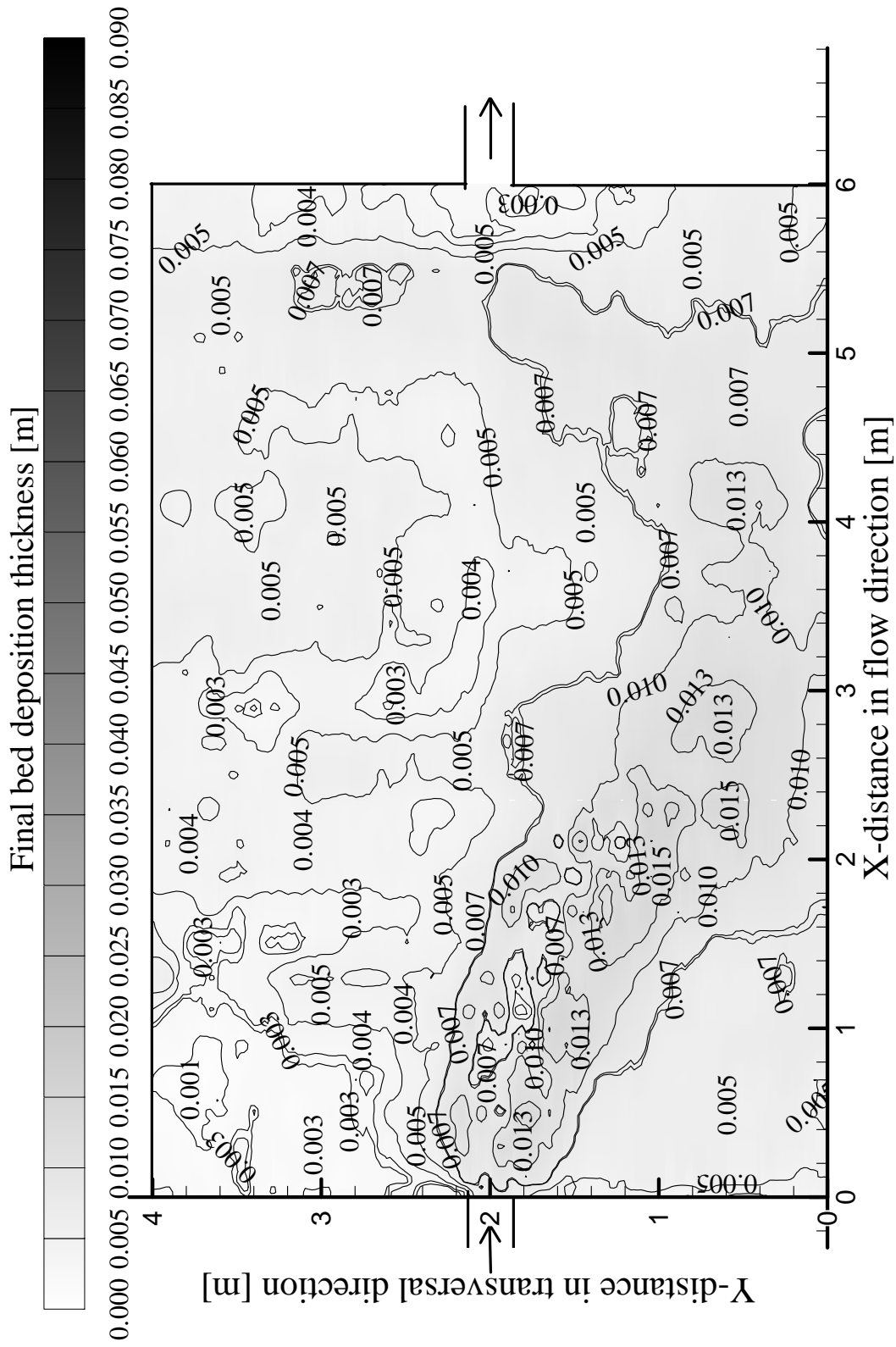


Figure A1.16: Contours of deposition pattern after the first period run after 1.5 hour

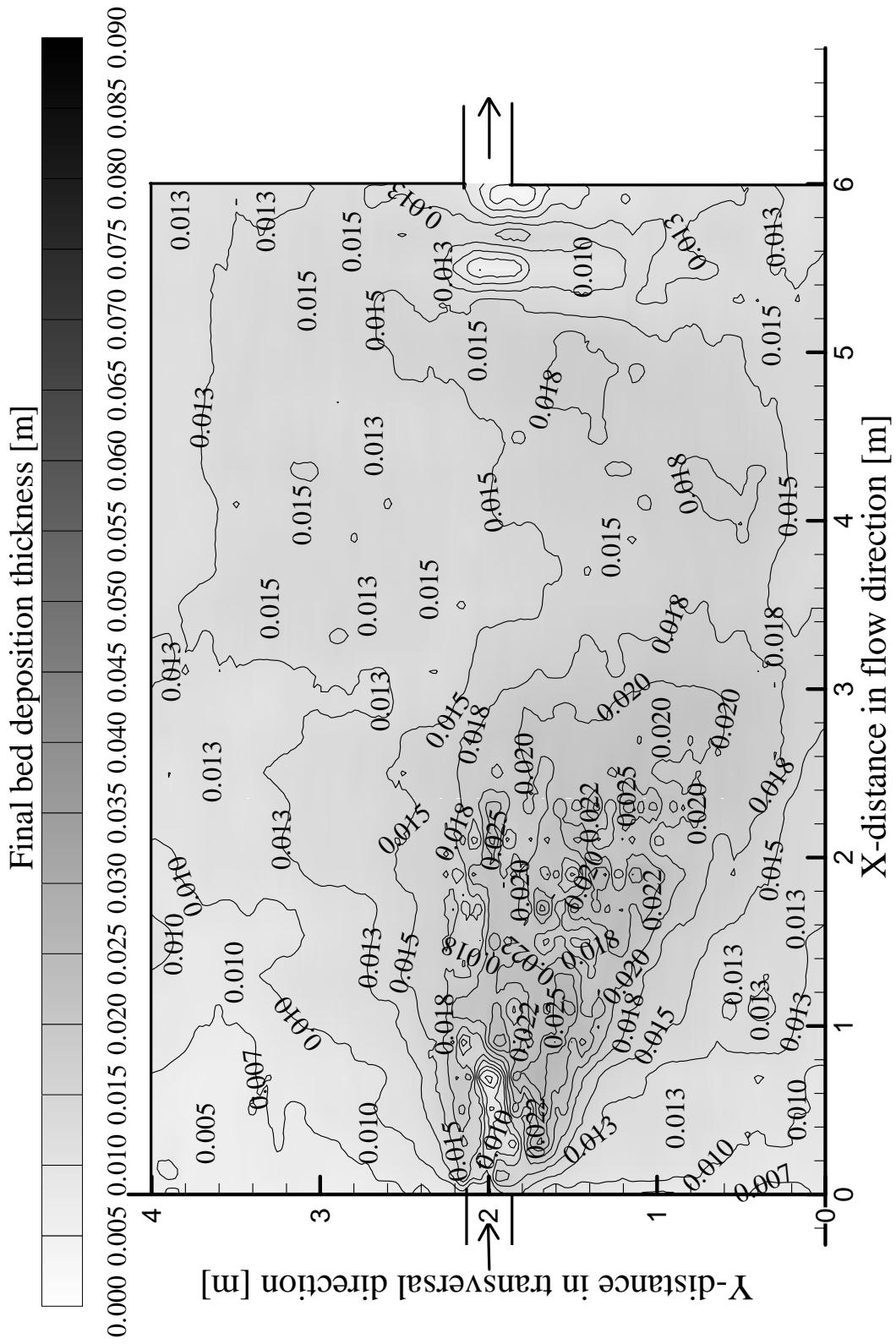


Figure A1.17: Contours of deposition pattern after the first period run after 3.0 hour

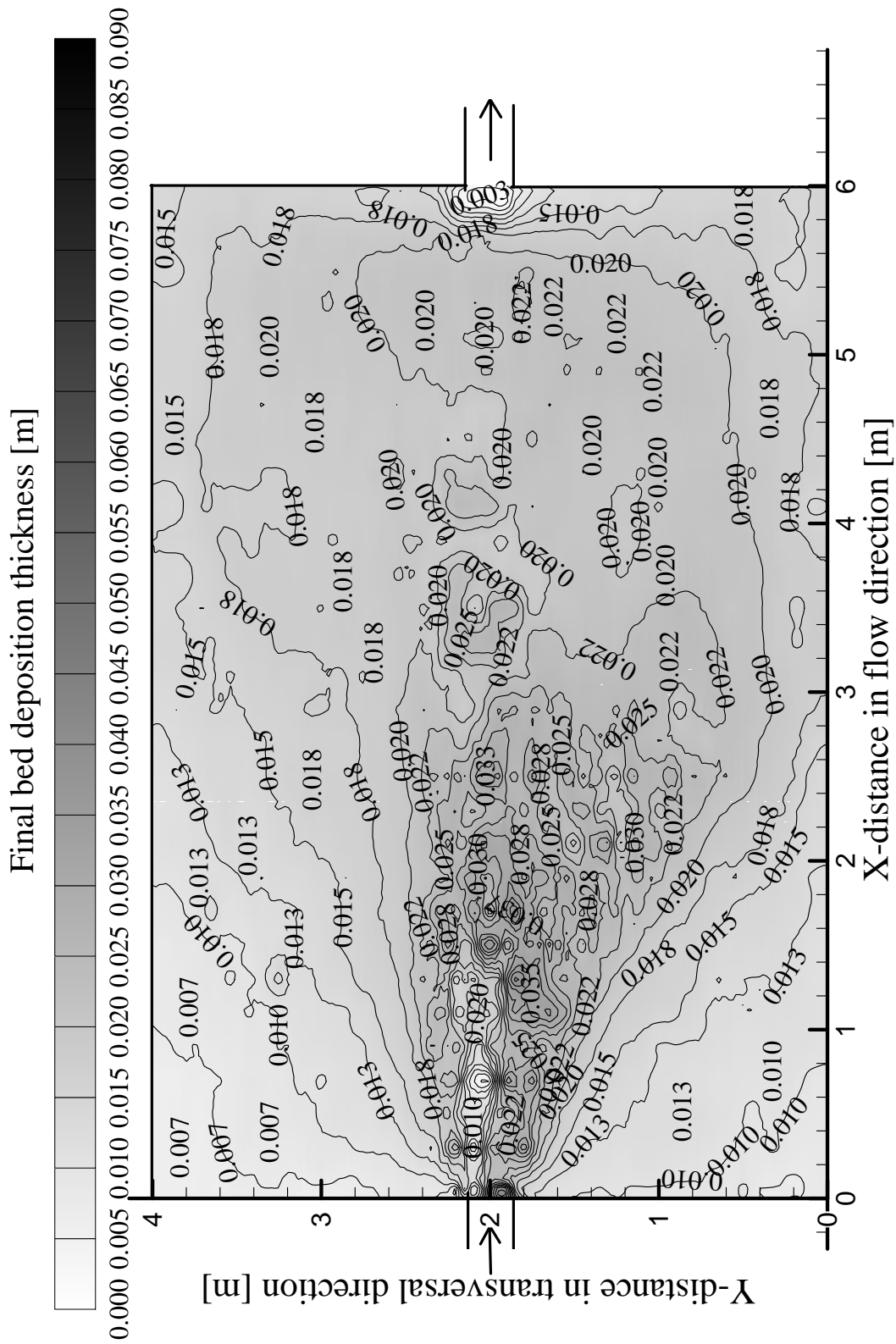


Figure A1.18: Contours of deposition pattern after the first period run after 4.5 hour

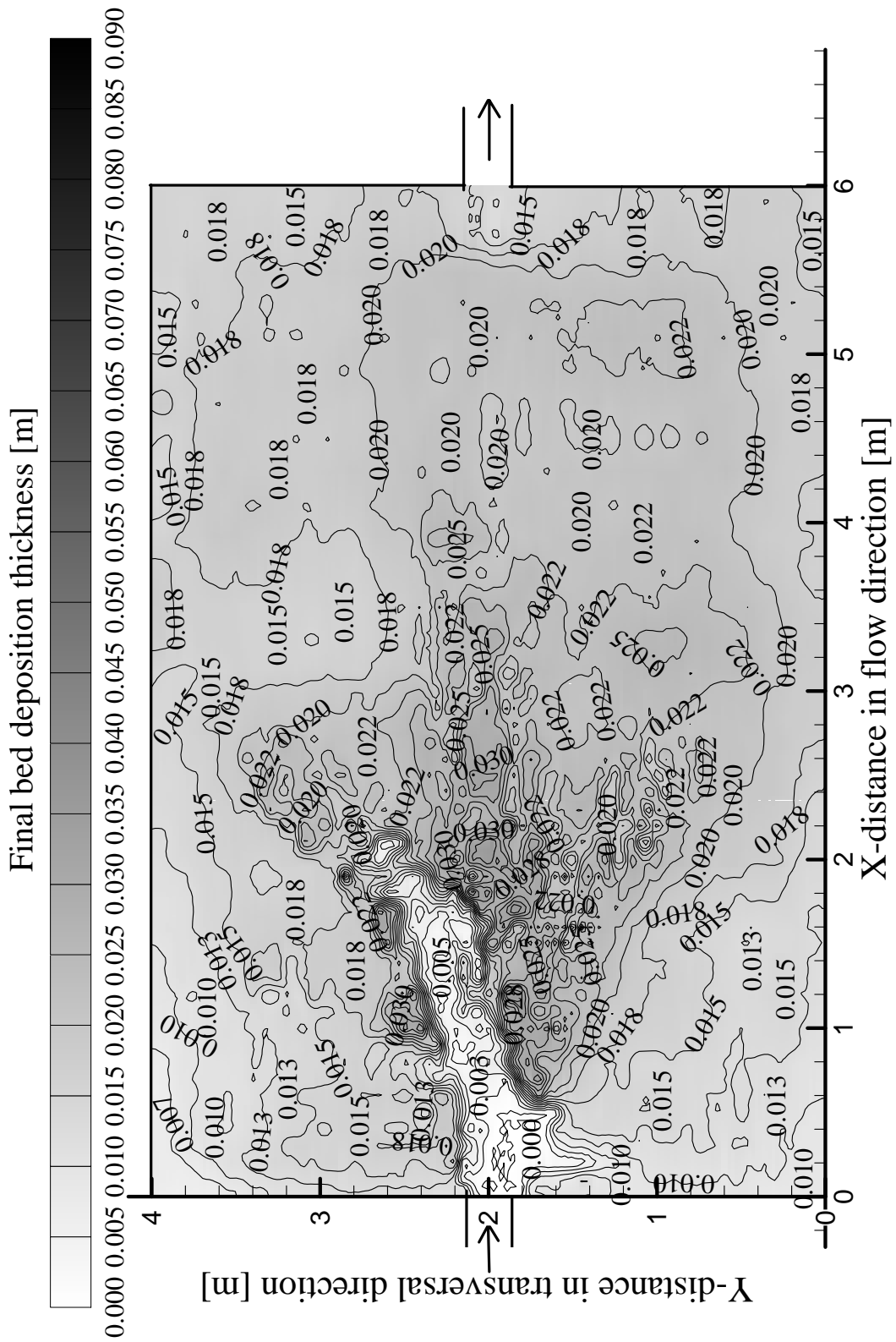


Figure A1.19: Contours of deposition pattern after the free flow flushing period run after 48 hour

A1.3.2 Bed thickness cross and longitudinal sections

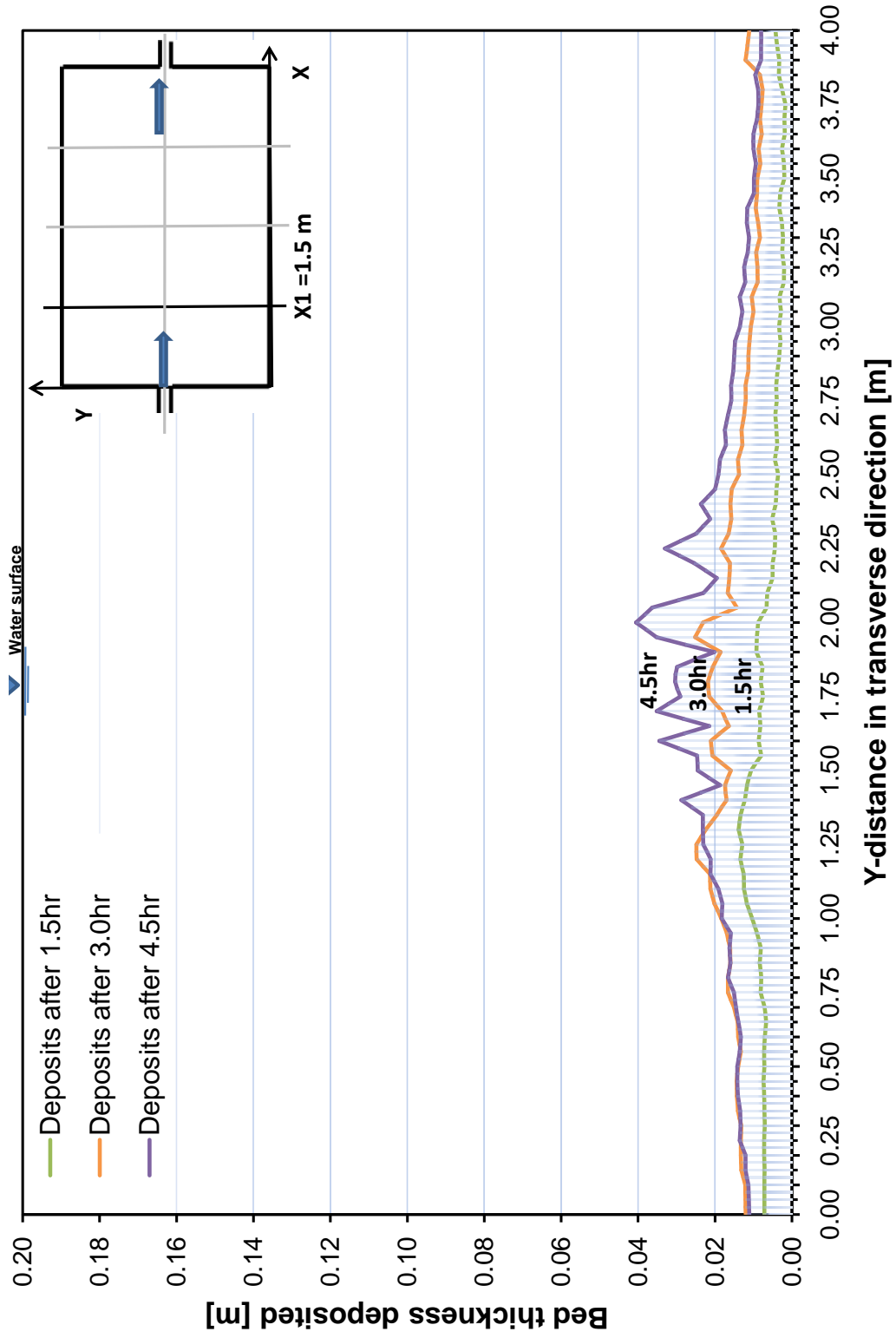


Figure A1.20: Evolution of sediment deposits for four periods runs at cross section $X_1 = 1.5m$ from the entrance

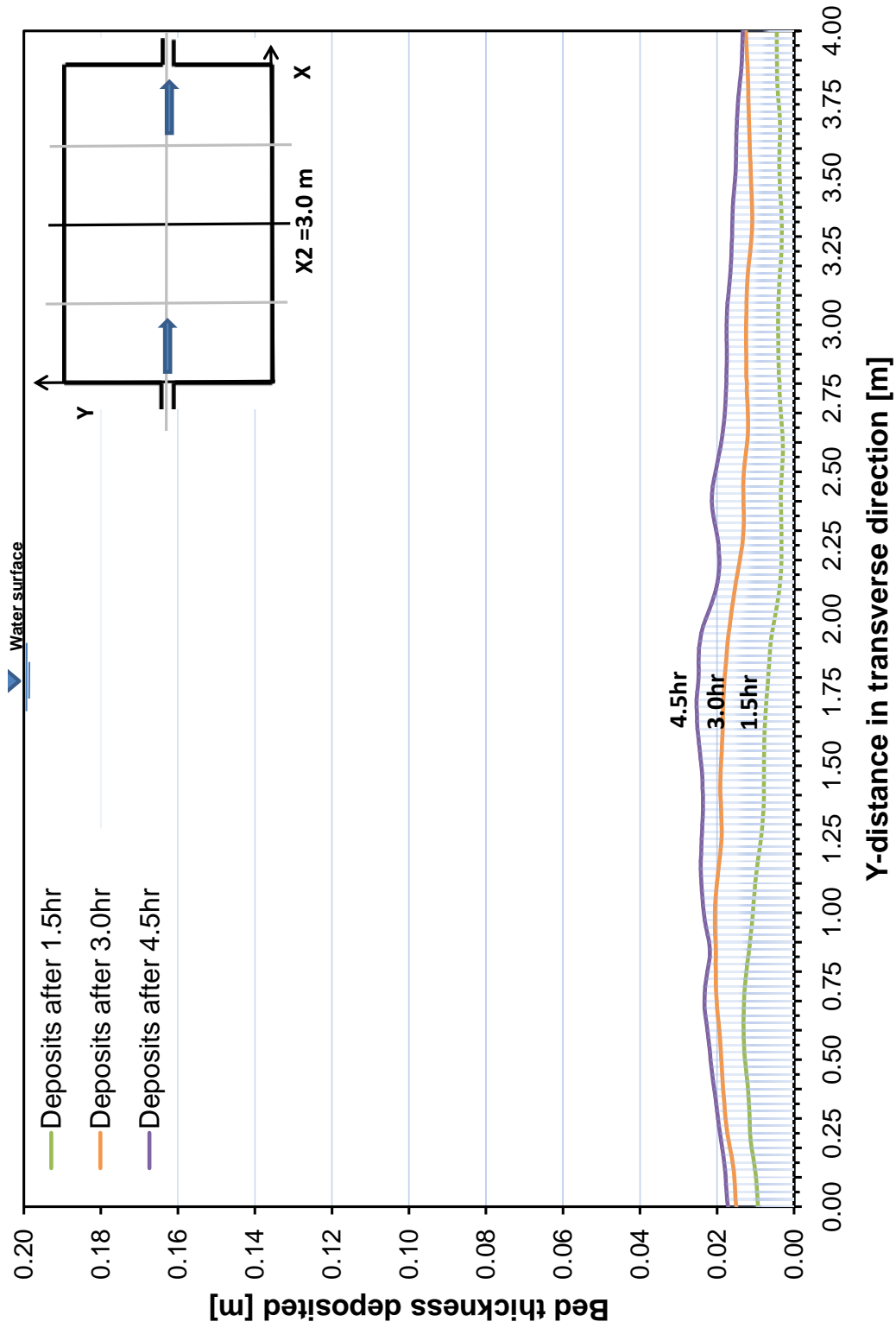


Figure A1.21: Evolution of sediment deposits for four periods runs at cross section $X_2 = 3.0m$ from the entrance

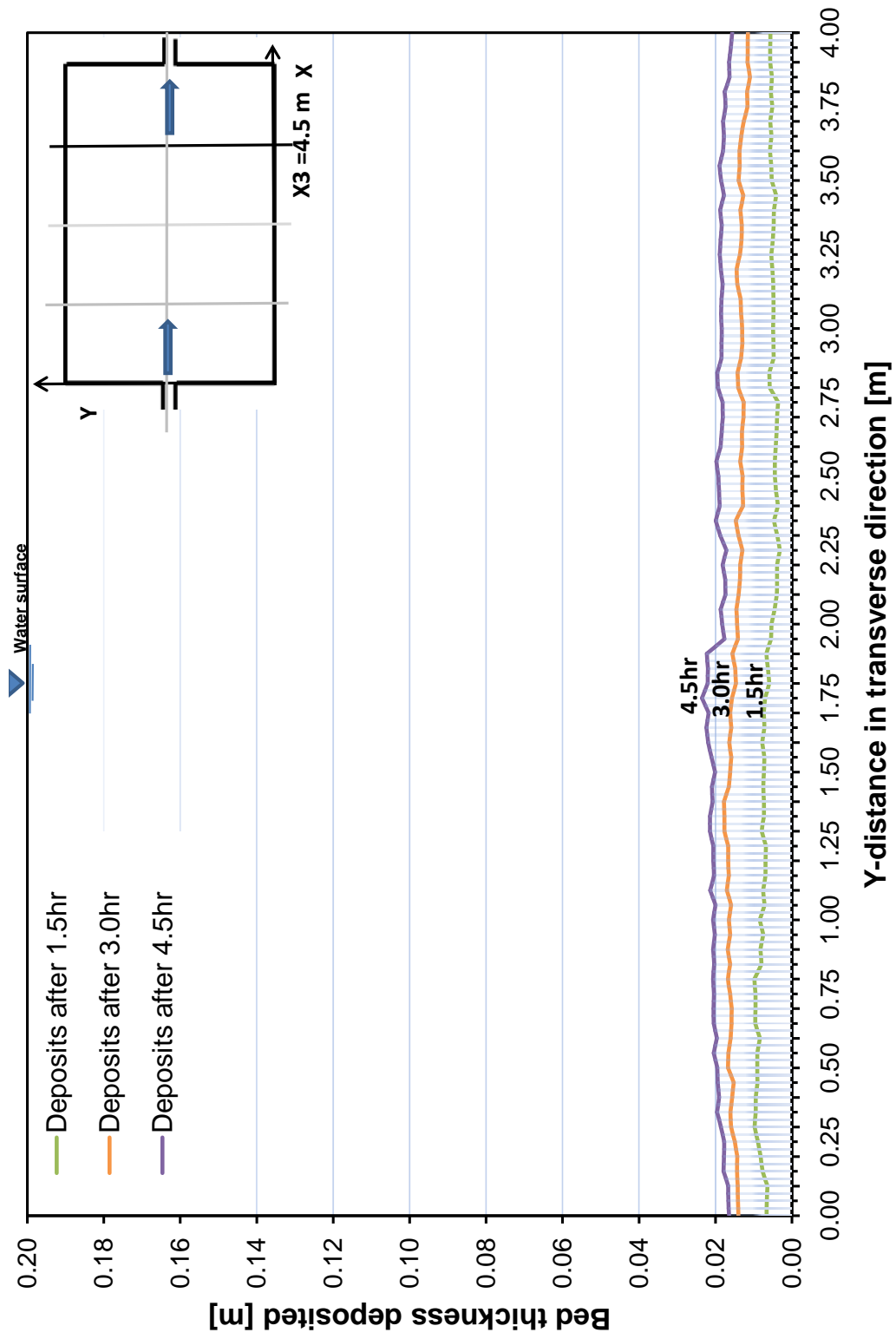


Figure A1.22: Evolution of sediment deposits for four periods runs at cross section $X_3 = 4.5m$ from the entrance

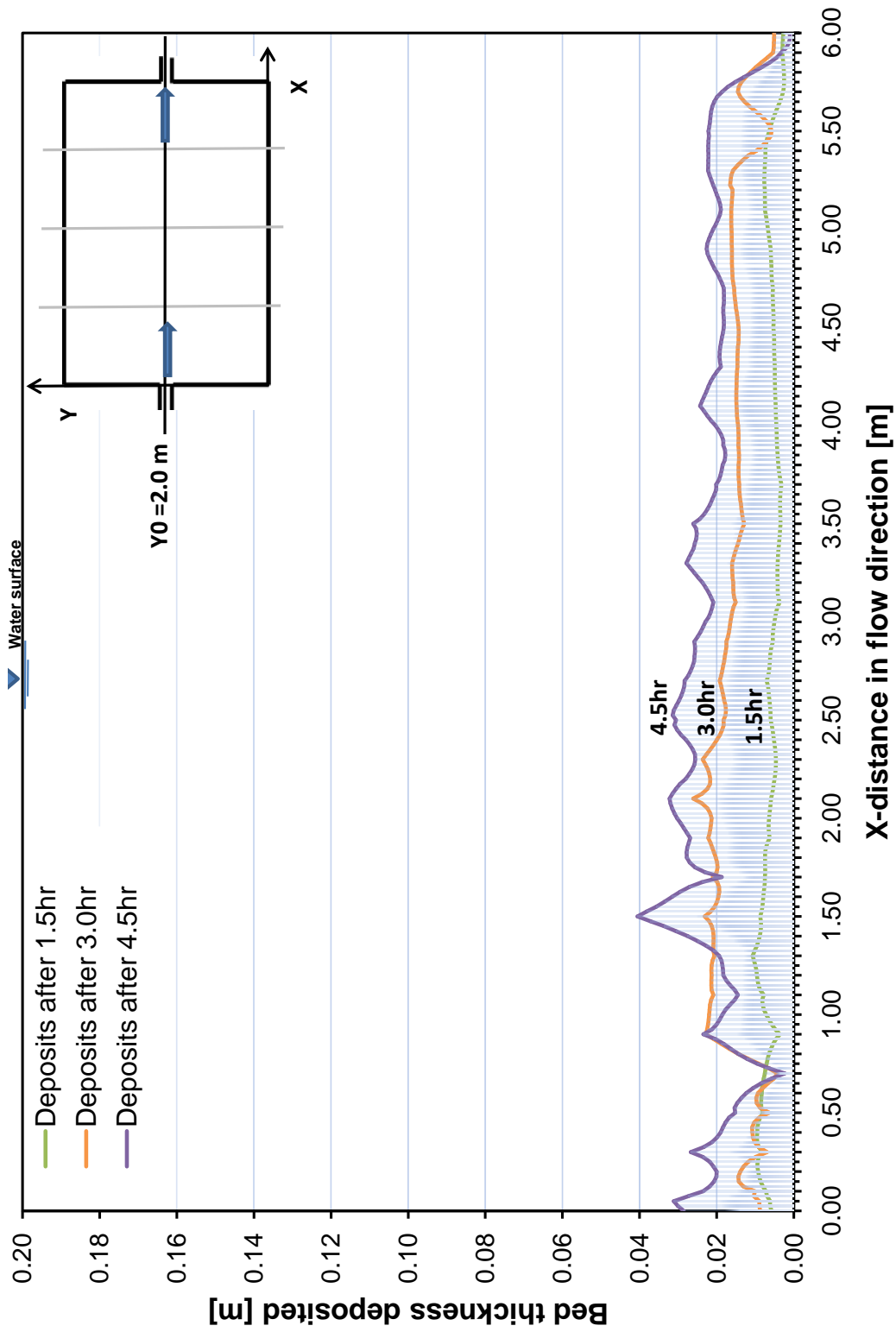


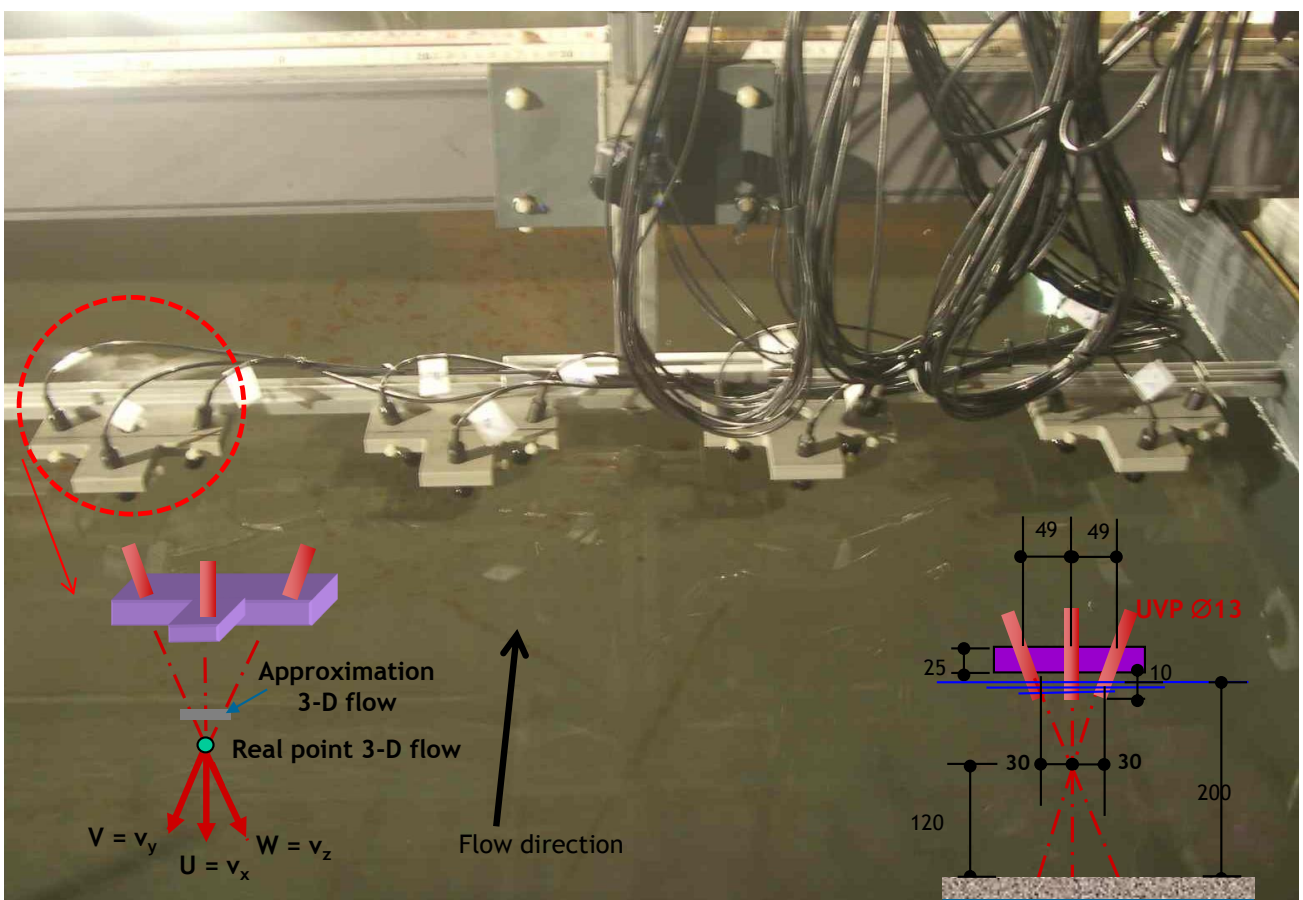
Figure A1.23: Evolution of sediment deposits for four periods runs at centerline longitudinal section $Y = 2.0m$

A1.4 3D velocity measurements obtained by Ultrasound Velocity Profiler (UVP)

Results of 3D velocities (U, V, and W) for the following flow and sediment characteristic:

- Discharge $Q = 7.0$ [l/s]
- Water depth $h = 0.2$ [m]
- Froude Number $F_r = 0.1$
- Reynolds number $Re = 28000$
- Sediment diameter $d_{50} = 50$ [μ]
- Sediment density $\rho = 1500$ [kg/m³]
- Suspended sediment concentration $C = 3.0$ [g/l]

A1.4.1 Results of 3D UVP measurements for the initial state with clear water



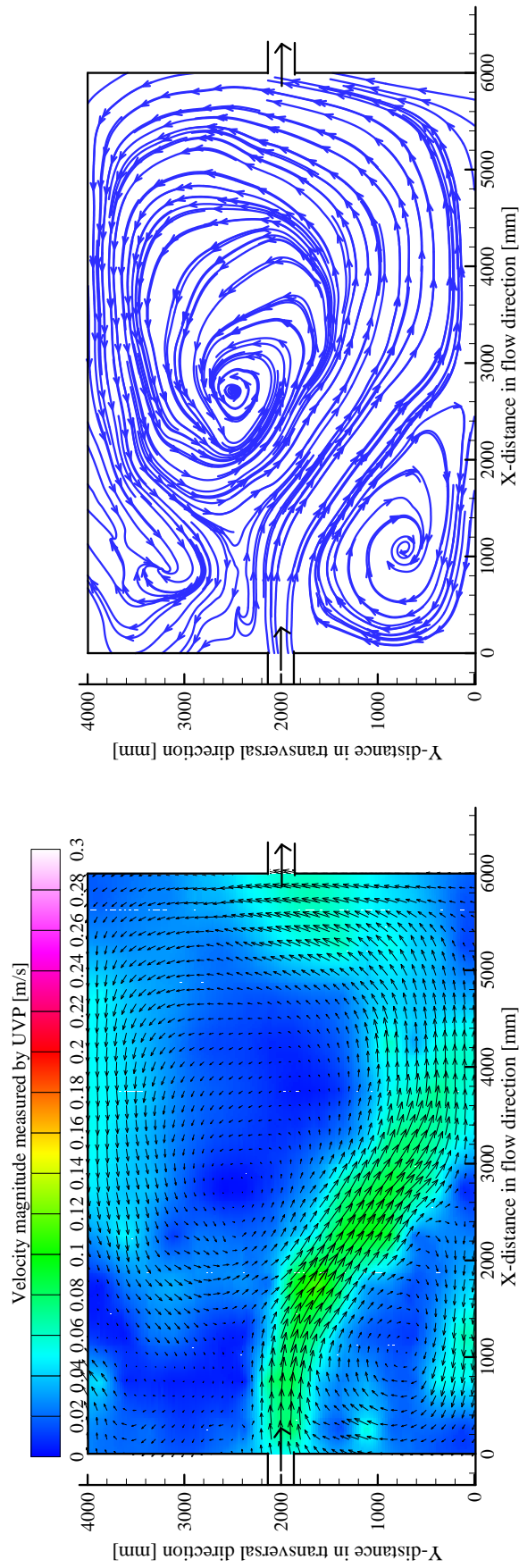


Figure A1.24: Time average flow pattern with velocity vectors (left); streamlines (right) with clear water after stable state at the 3D intersection of the 3 probes

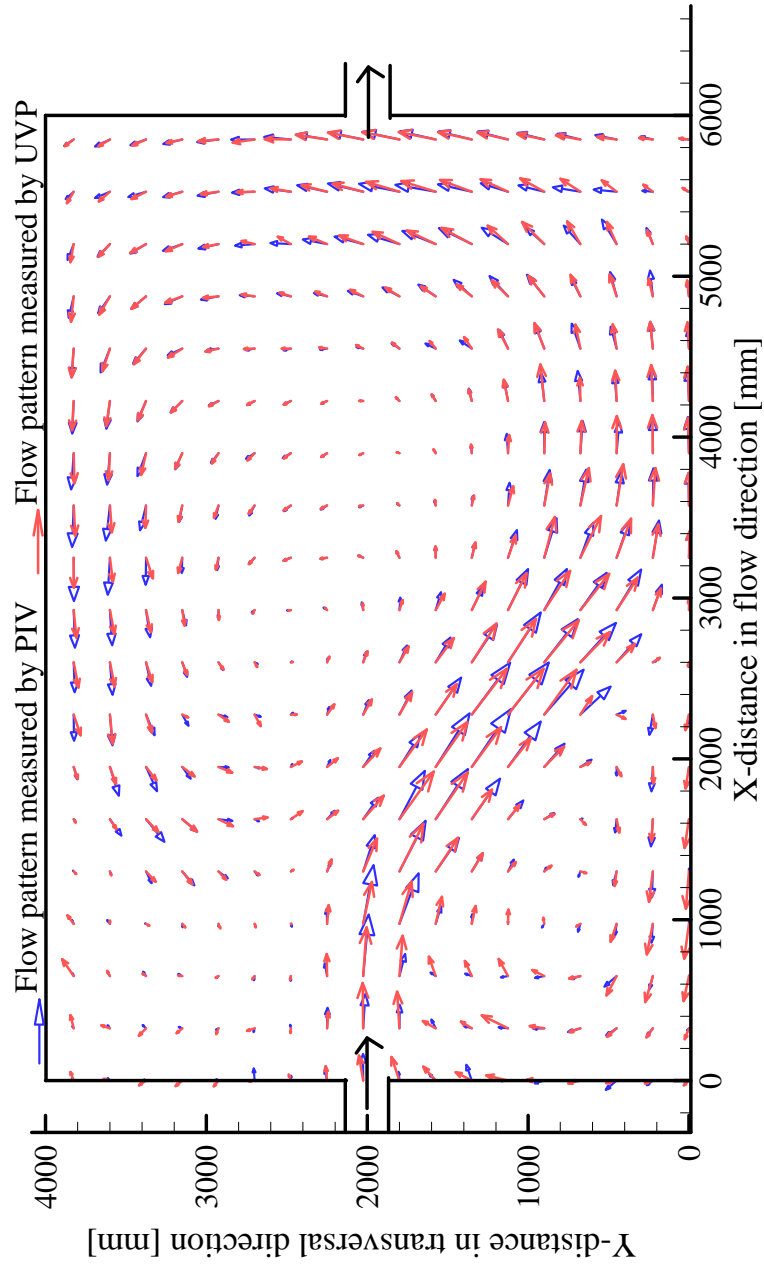
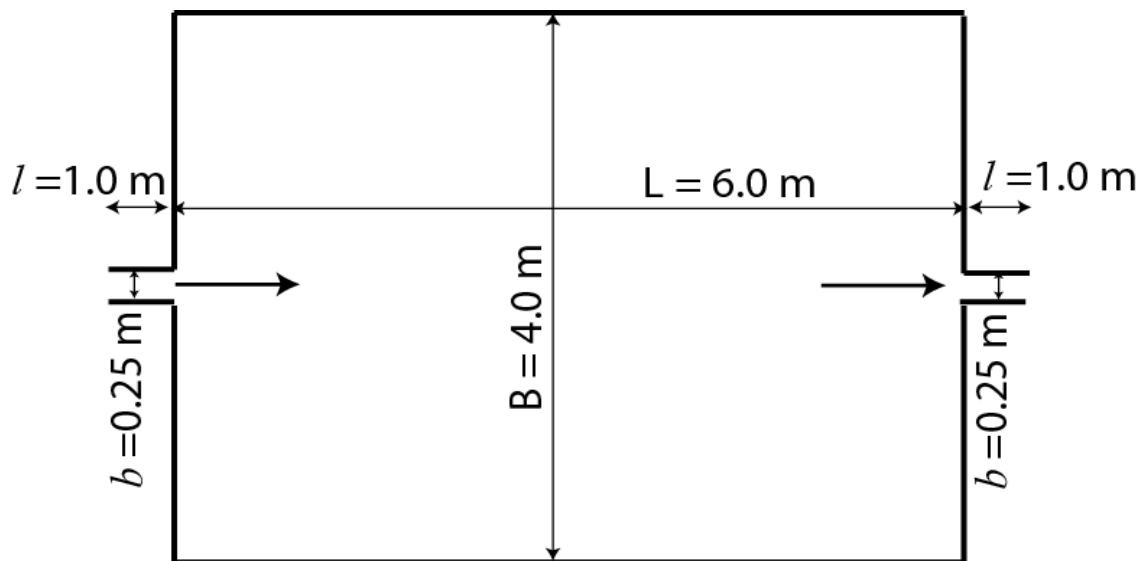


Figure A1.25: Comparison of velocity magnitude vectors obtained from UVP and LSPIV measurement

A2 Results of rectangular geometry Test2



A2.1 Surface velocity obtained by (LSPIV) measurements

Results of flow field with the velocity magnitude and streamlines obtained for the following flow and sediment characteristic:

- Discharge $Q = 7.0$ [l/s]
- Water depth $h = 0.2$ [m]
- Froude Number $F_r = 0.1$
- Reynolds number $Re = 28000$
- Sediment diameter $d_{50} = 50$ [μ]
- Sediment density $\rho = 1500$ [kg/m³]
- Suspended sediment concentration $C = 3.0$ [g/l]

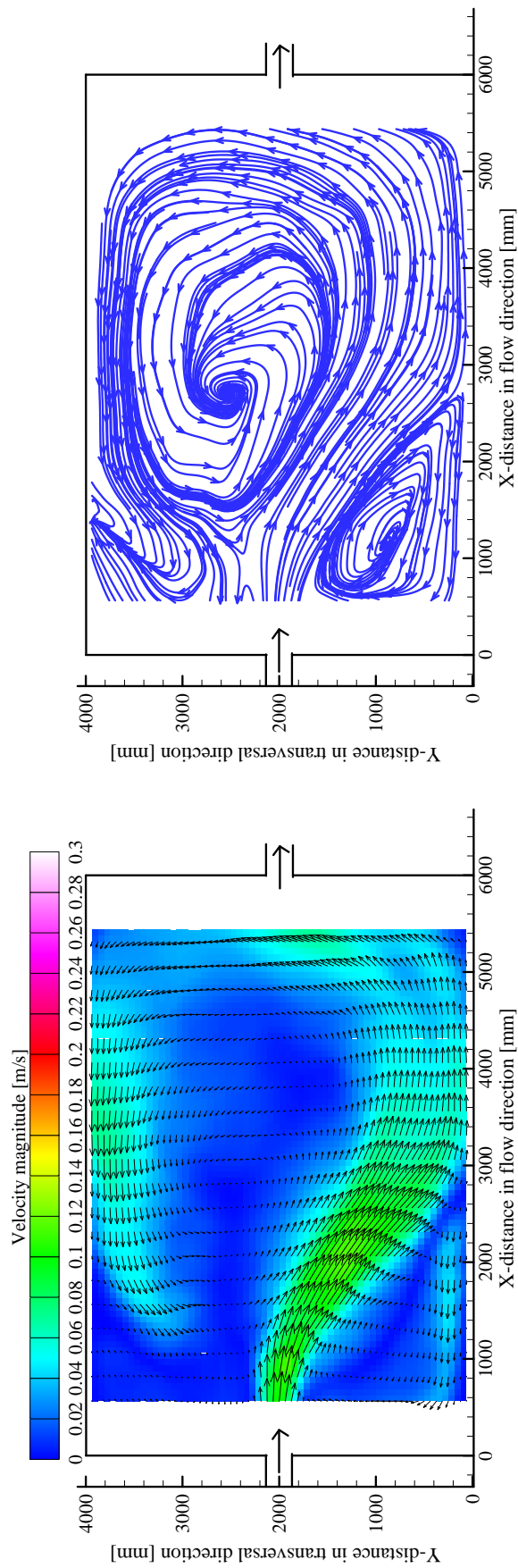


Figure A2.1: Time average flow pattern with velocity vectors (left); streamlines (right) with clear water after stable state

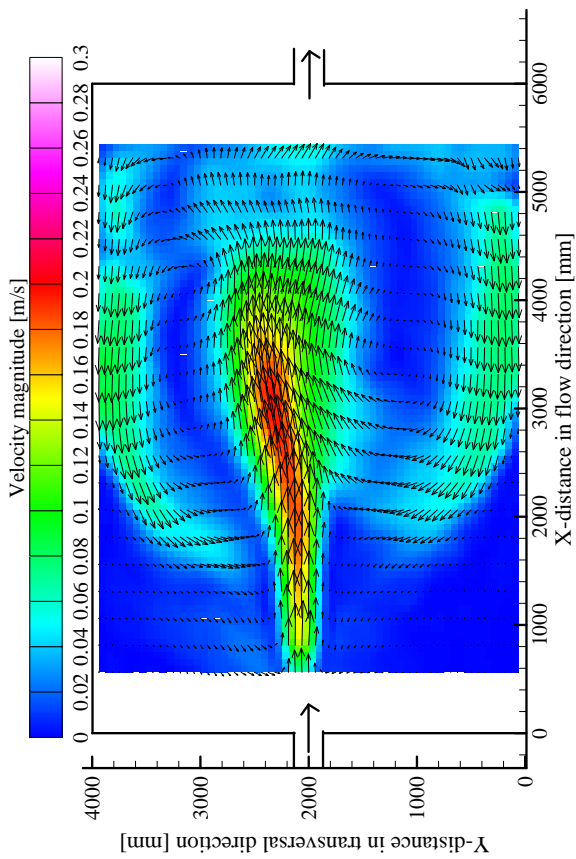


Figure A2.2: Time average flow pattern (left); streamlines (right) after 60 minutes of the third period with sediments

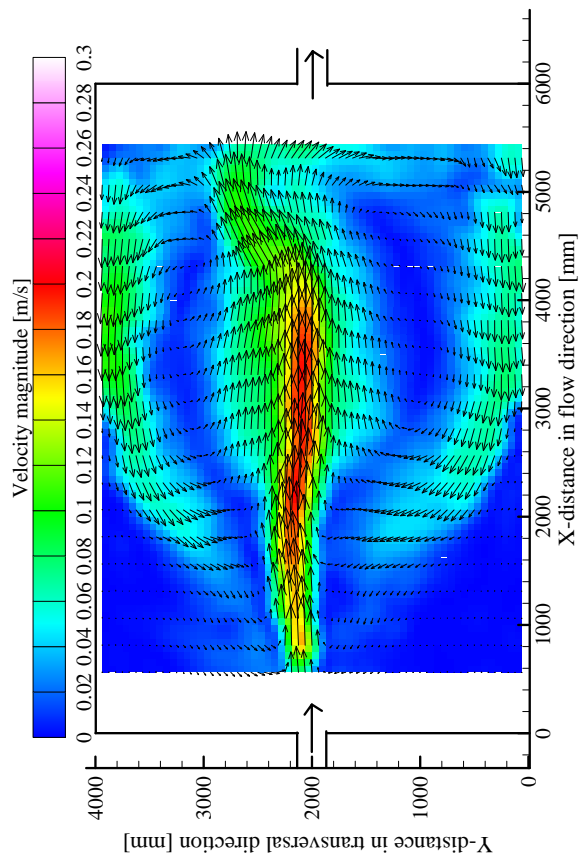
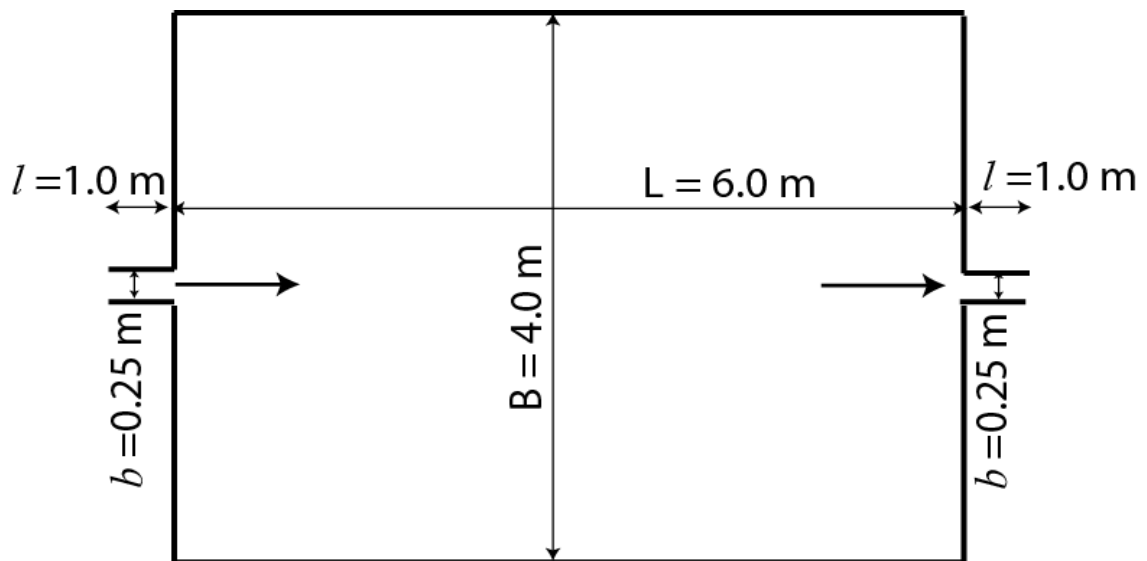


Figure A2.3: Time average flow pattern (left); streamlines (right) after 90 minutes of the third period with sediments

A3 Results of rectangular geometry Test3



A3.1 Surface velocity obtained by (LSPIV) measurements

Results of flow field with the velocity magnitude and streamlines obtained for the following flow and sediment characteristic:

- Discharge $Q = 7.0$ [l/s]
- Water depth $h = 0.2$ [m]
- Froude Number $F_r = 0.1$
- Reynolds number $Re = 28000$
- Sediment diameter $d_{50} = 50$ [μ]
- Sediment density $\rho = 1500$ [kg/m³]
- Suspended sediment concentration $C = 3.0$ [g/l]

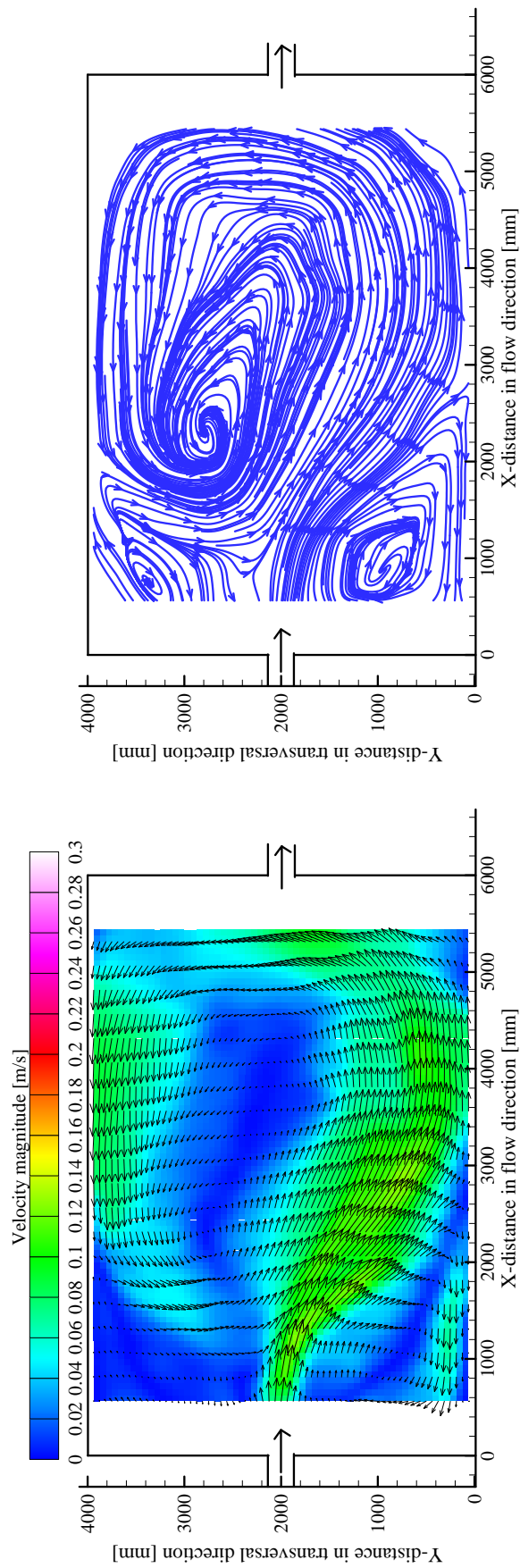


Figure A3.1: Time average flow pattern with velocity vectors (left); streamlines (right) with clear water after stable state

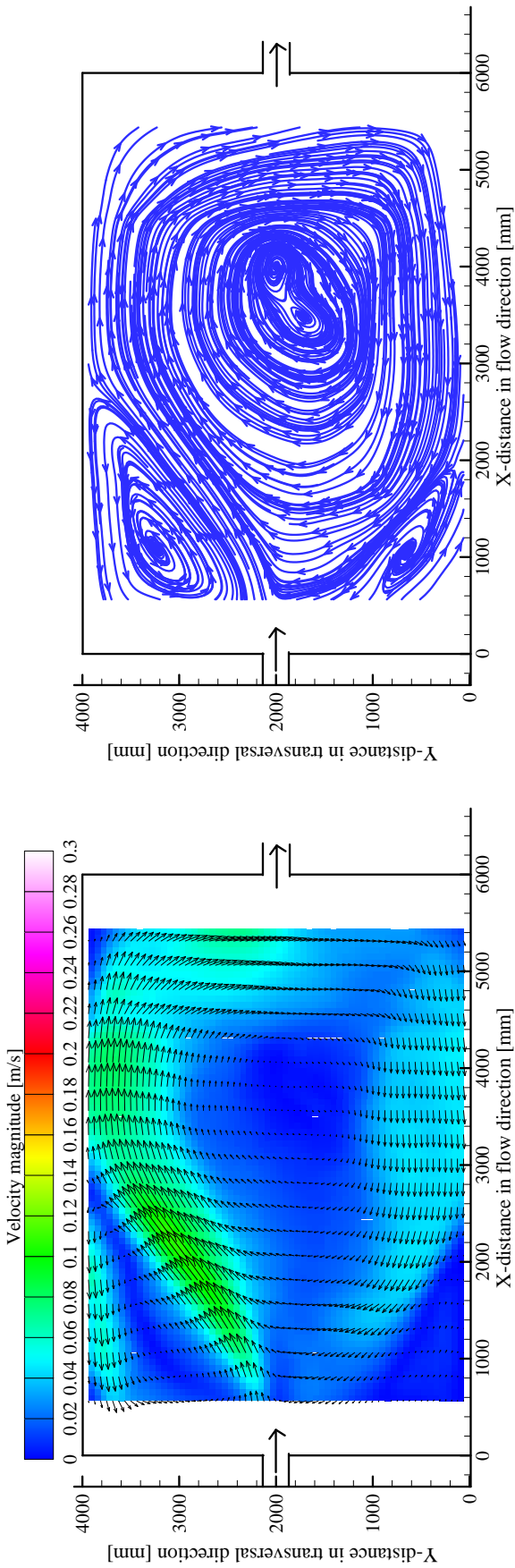


Figure A3.2: Time average flow pattern (left); streamlines (right) after 240 minutes of the first period with sediments

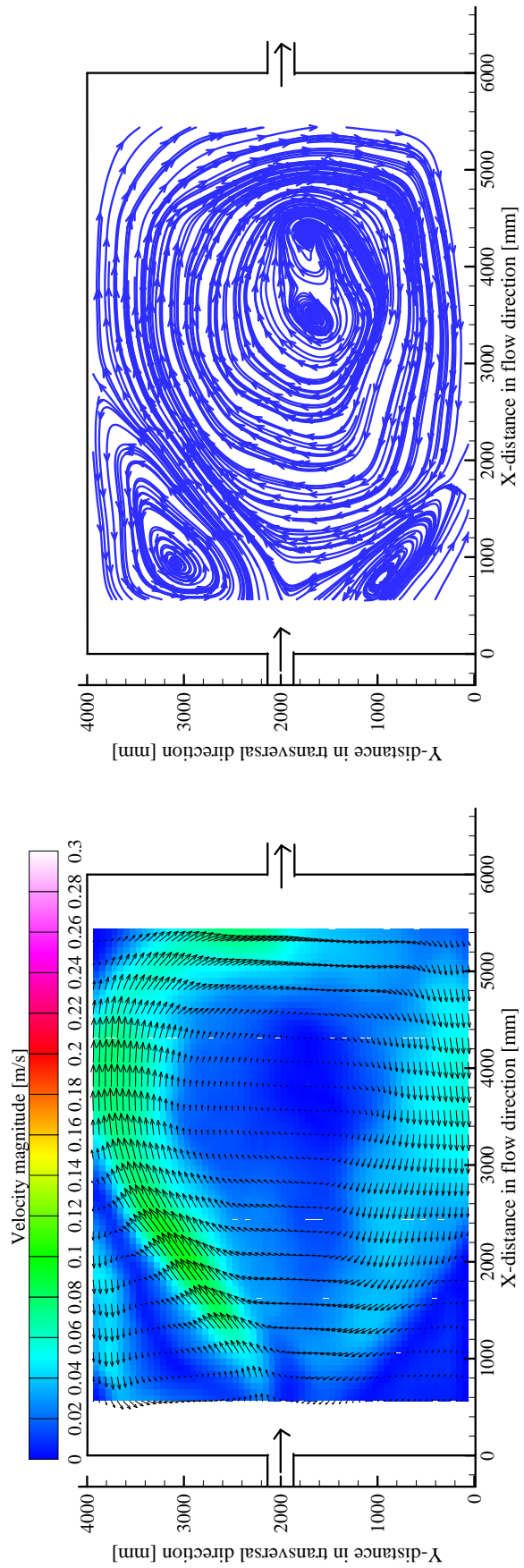


Figure A3.3: Time average flow pattern (left); streamlines (right) after 270 minutes of the first period with sediments

A3.2 Measurements of bed thickness deposition obtained by Mini Echo Sounder

Results of morphological evolution obtained for the following flow and sediment characteristic:

- Discharge $Q = 7.0$ [l/s]
- Water depth $h = 0.2$ [m]
- Froude Number $F_r = 0.1$
- Reynolds number $Re = 28000$
- Sediment diameter $d_{50} = 50$ [μ]
- Sediment density $\rho = 1500$ [kg/m^3]
- Suspended sediment concentration $C = 3.0$ [g/l]

A3.2.1 Depositions contours

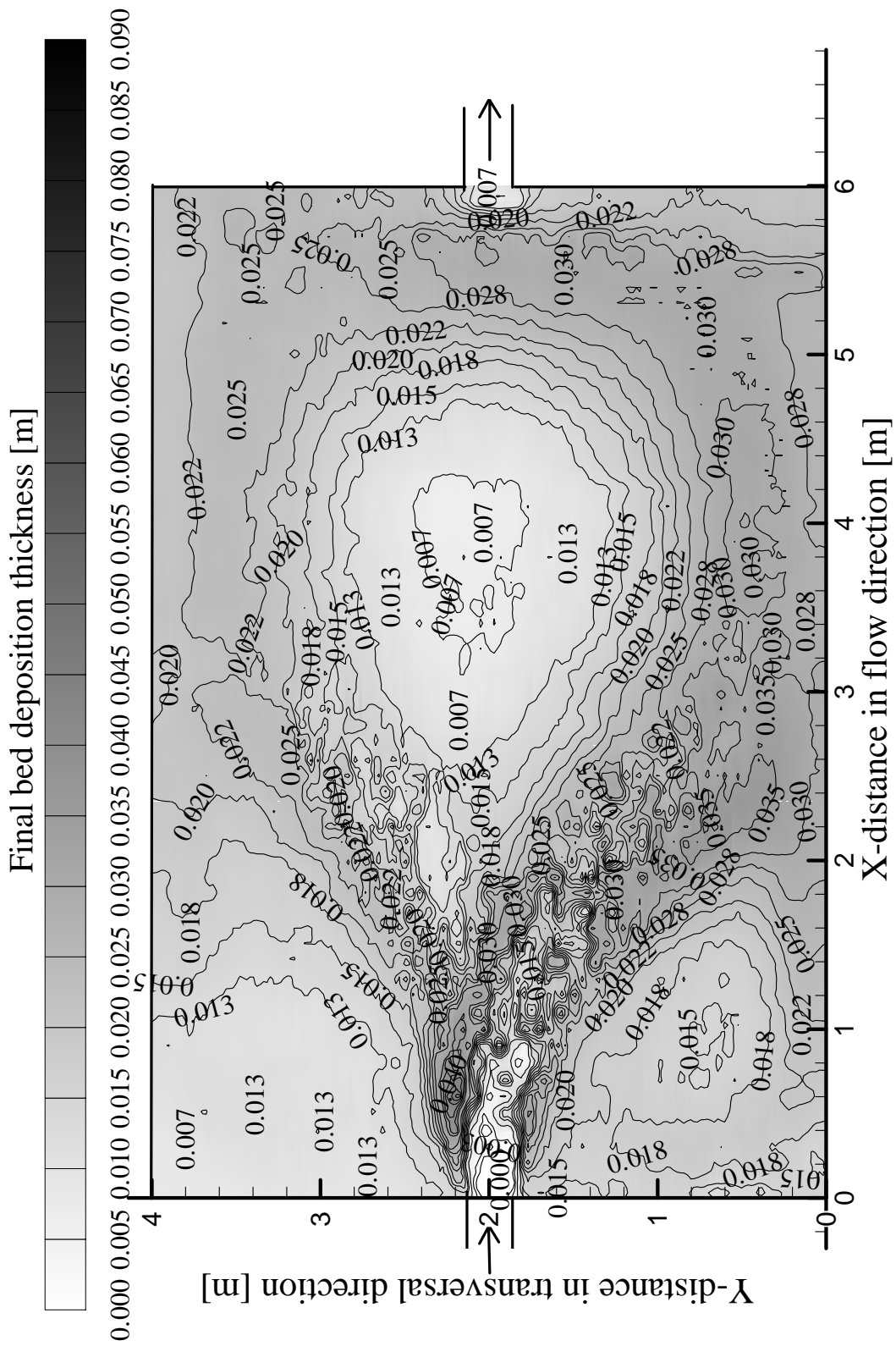


Figure A3.4: Contours of deposition pattern after the first period run after 4.5 hour

A3.2.2 Bed thickness cross and longitudinal sections

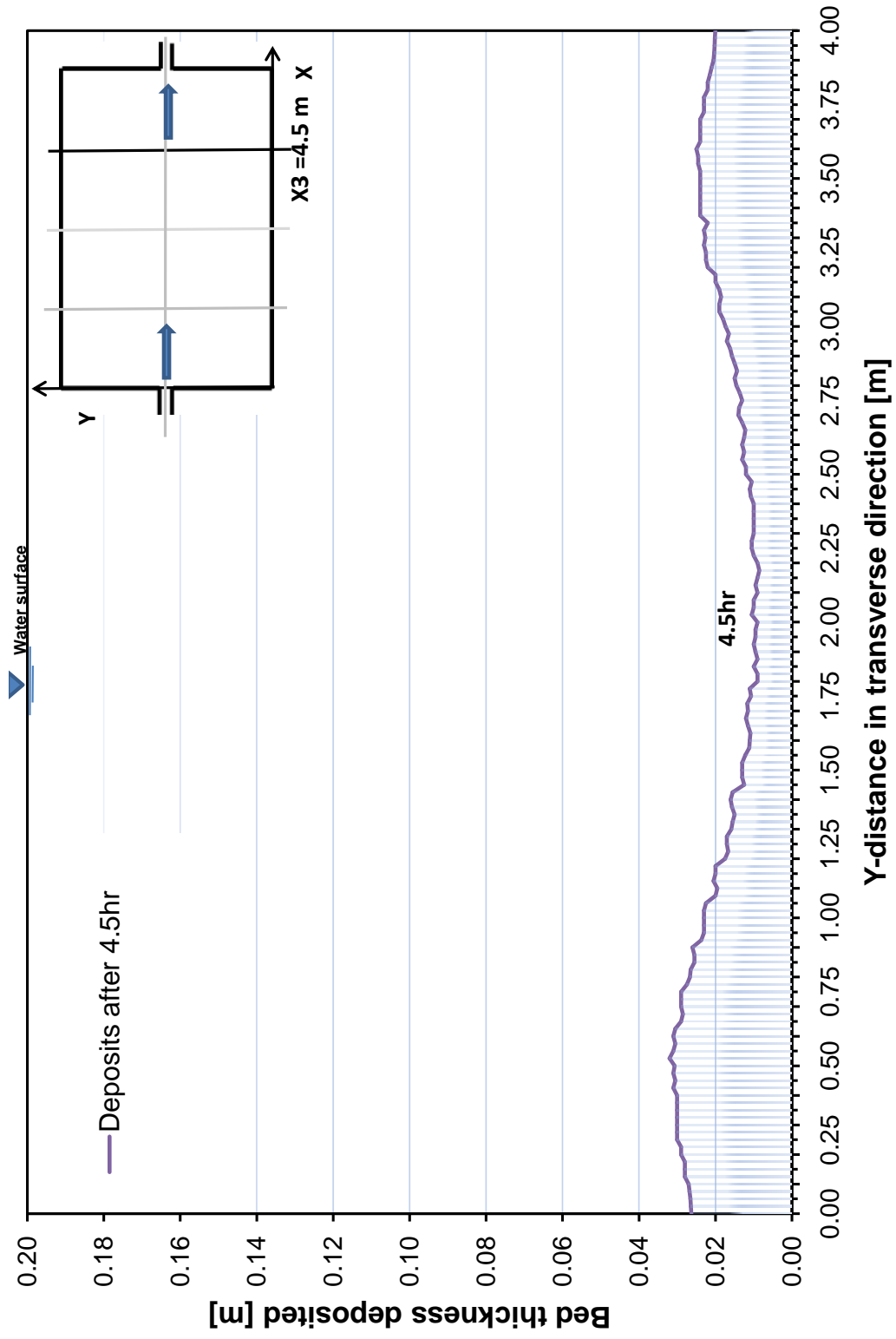


Figure A3.5: Evolution of sediment deposits for four periods runs at cross section $X_3 = 4.5m$ from the entrance

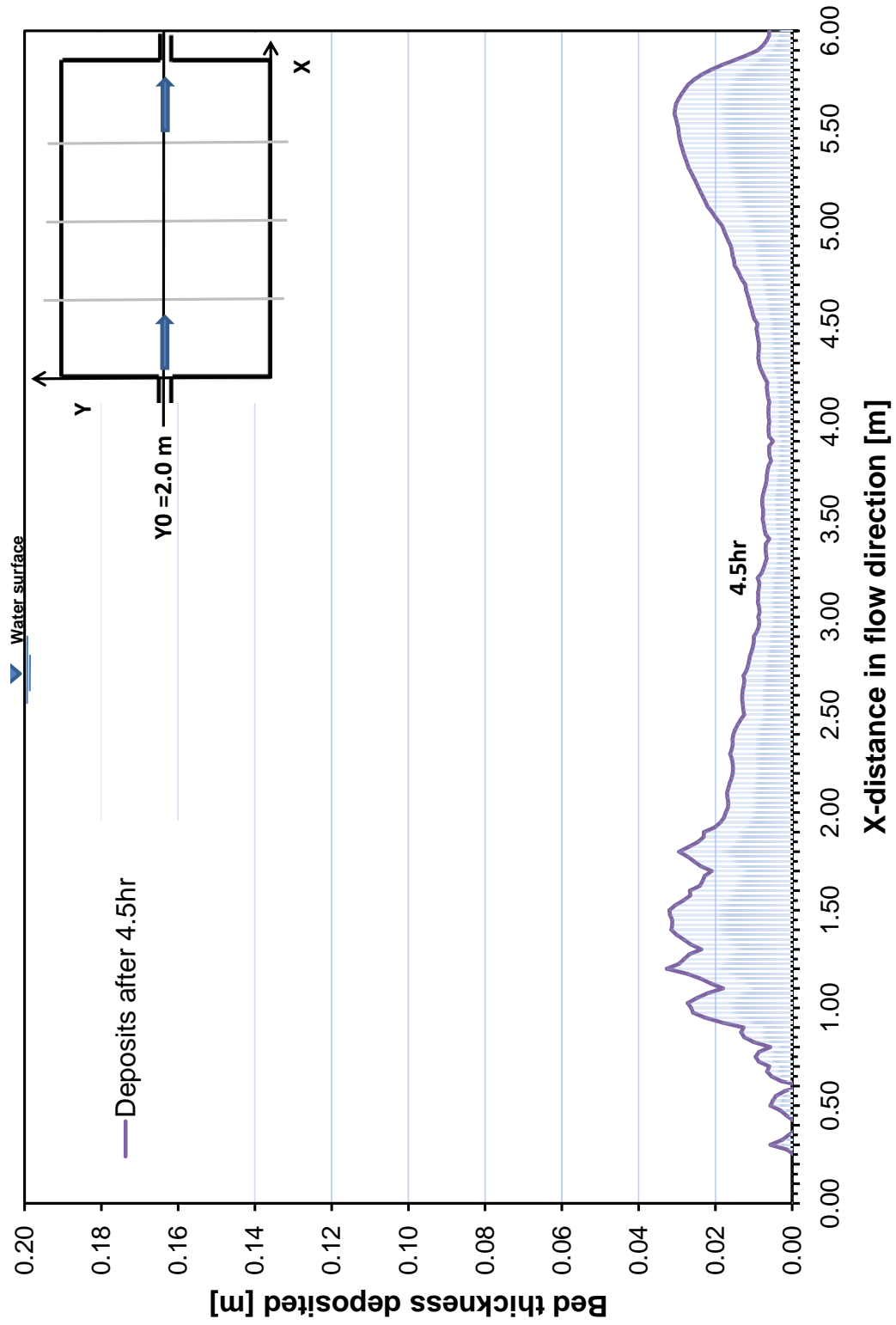
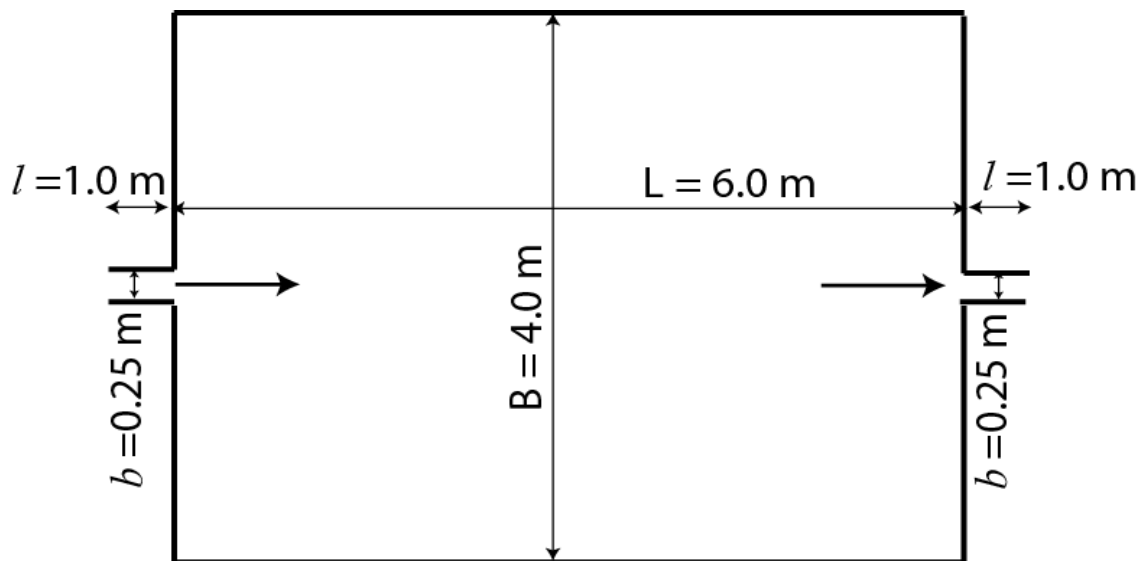


Figure A3.6: Evolution of sediment deposits for four periods runs at centerline longitudinal section $Y = 2.0\text{m}$

A4 Results of rectangular geometry Test4



A4.1 Surface velocity obtained by (LSPIV) measurements

Results of flow field with the velocity magnitude and streamlines obtained for the following flow and sediment characteristic:

- Discharge $Q = 7.0 [l/s]$
- Water depth $h = 0.2 [m]$
- Froude Number $F_r = 0.1$
- Reynolds number $Re = 28000$
- Sediment diameter $d_{50} = 50 [\mu]$
- Sediment density $\rho = 1500 [kg/m^3]$
- Suspended sediment concentration $C = 3.0 [g/l]$

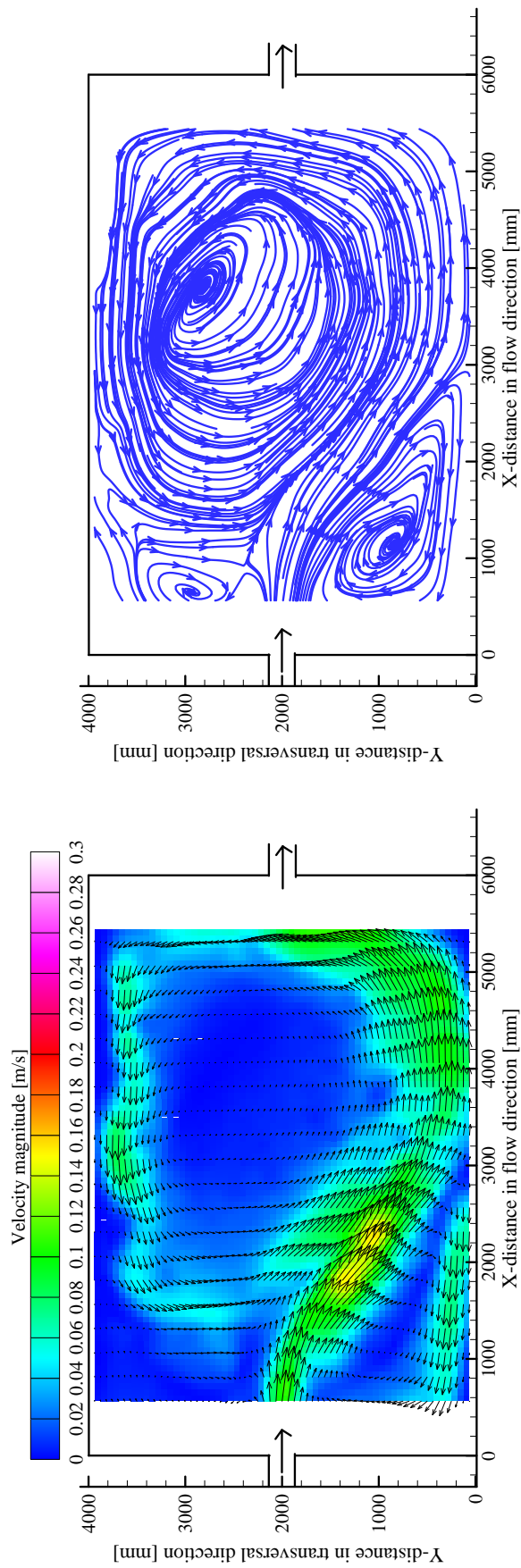


Figure A4.1: Time average flow pattern with velocity vectors (left); streamlines (right) with clear water after stable state

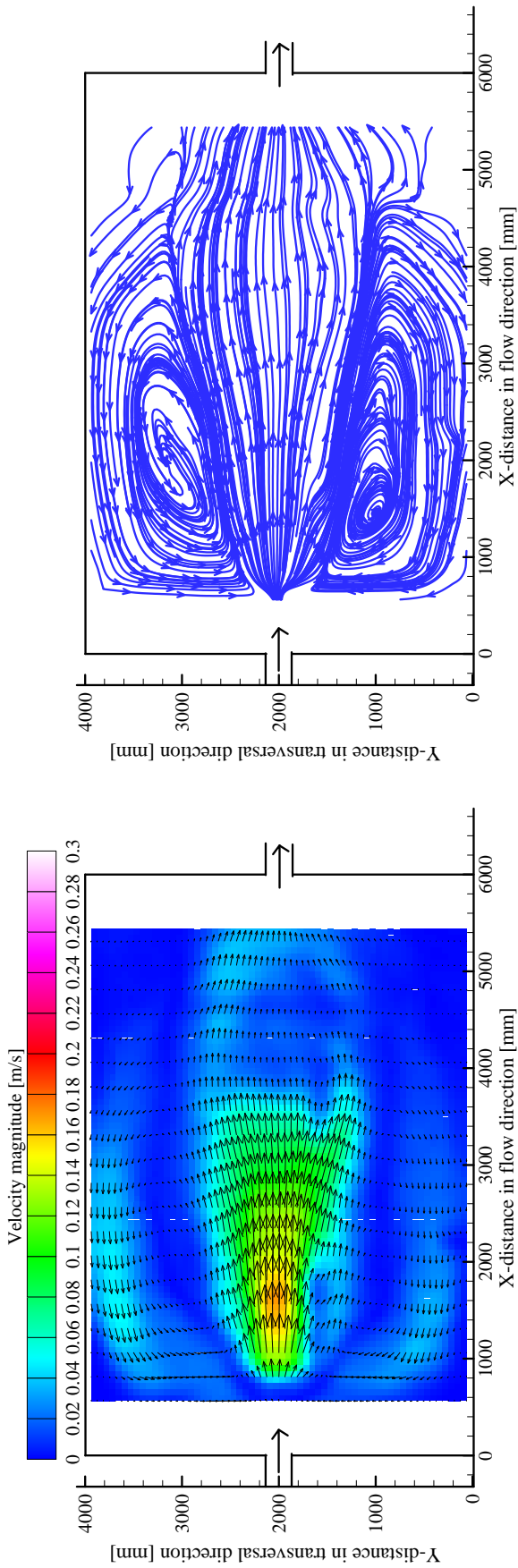


Figure A4.2: Time average flow pattern (left); streamlines (right) after 480 minutes of the third period with sediments

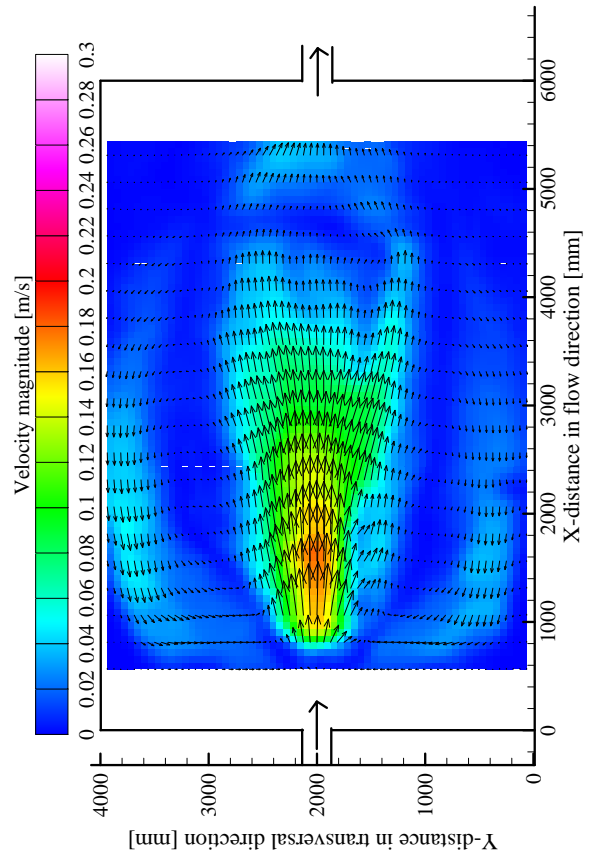


Figure A4.3: Time average flow pattern (left); streamlines (right) after 510 minutes of the third period with sediments

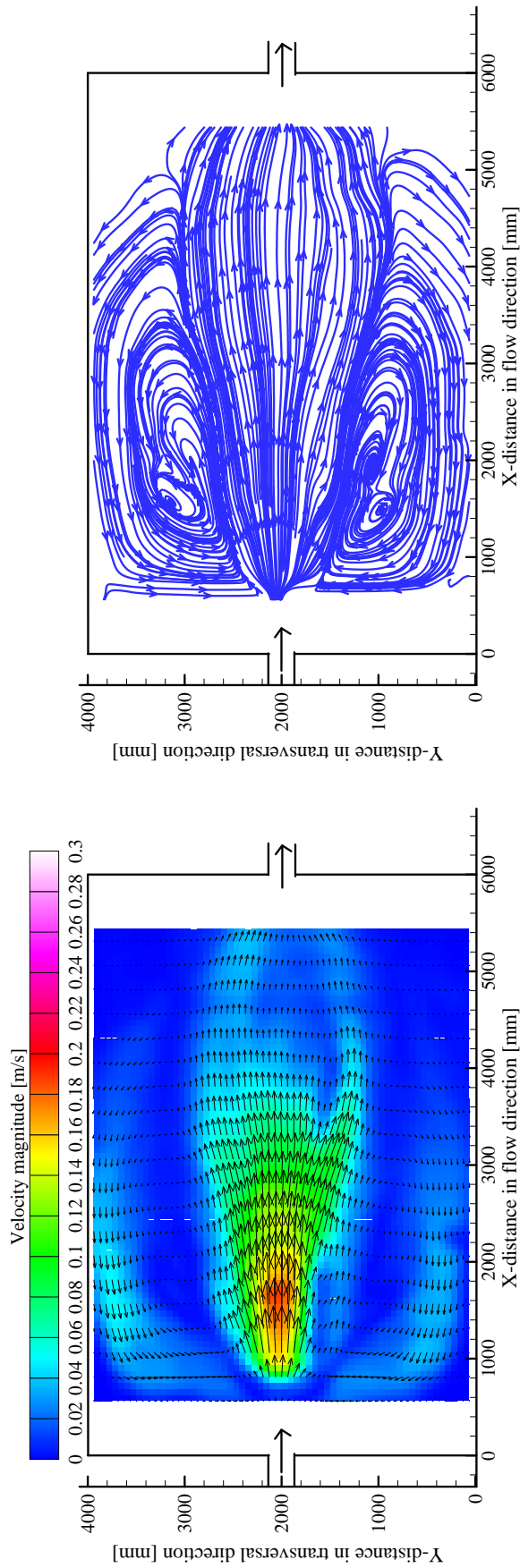


Figure A4.4: Time average flow pattern (left); streamlines (right) after 540 minutes of the third period with sediments

A4.2 Measurements of suspended sediment concentration obtained by turbiditymeter

Results of sediment concentration obtained for the following flow and sediment characteristic:

- Discharge $Q = 7.0$ [l/s]
- Water depth $h = 0.2$ [m]
- Froude Number $F_r = 0.1$
- Reynolds number $Re = 28000$
- Sediment diameter $d_{50} = 50$ [μ]
- Sediment density $\rho = 1500$ [kg/m³]
- Suspended sediment concentration $C = 3.0$ [g/l]

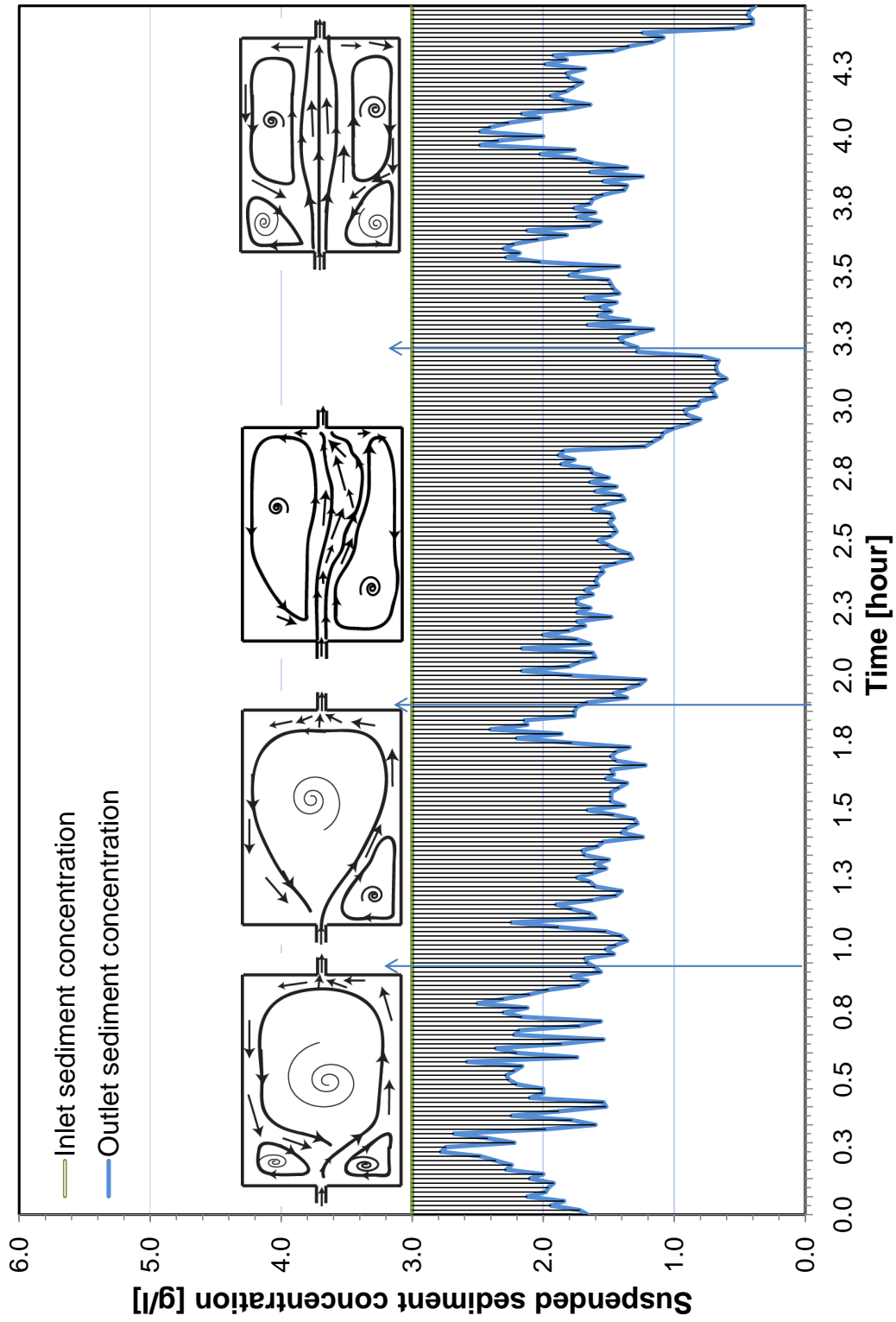


Figure A4.5: Inflow and released suspended concentration of sediments from the reservoir during the first period of 4.5hours, measured every minute

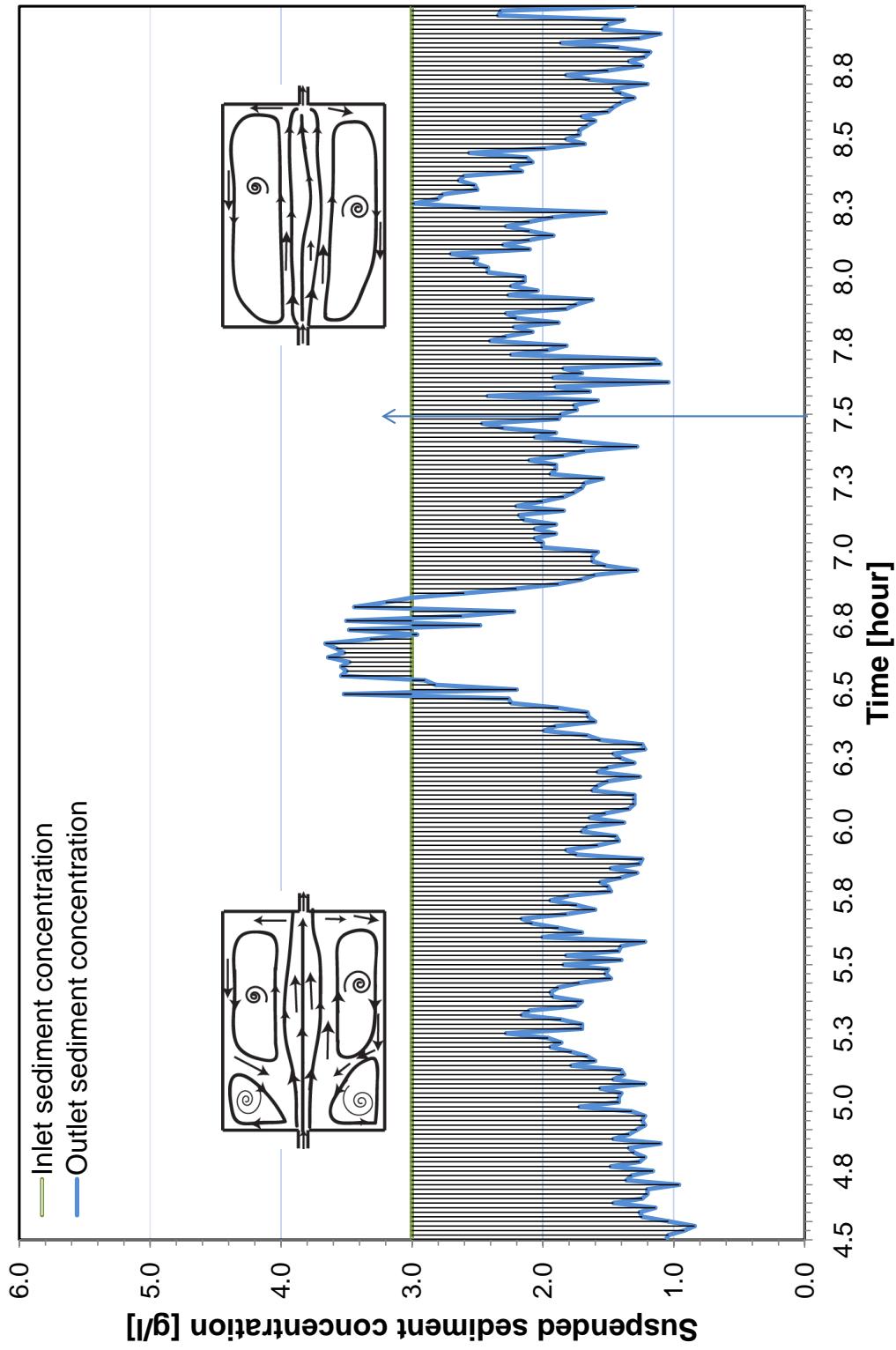


Figure A4.6: Inflow and released suspended concentration of sediments from the reservoir during the second period of 4.5hours, measured every minute

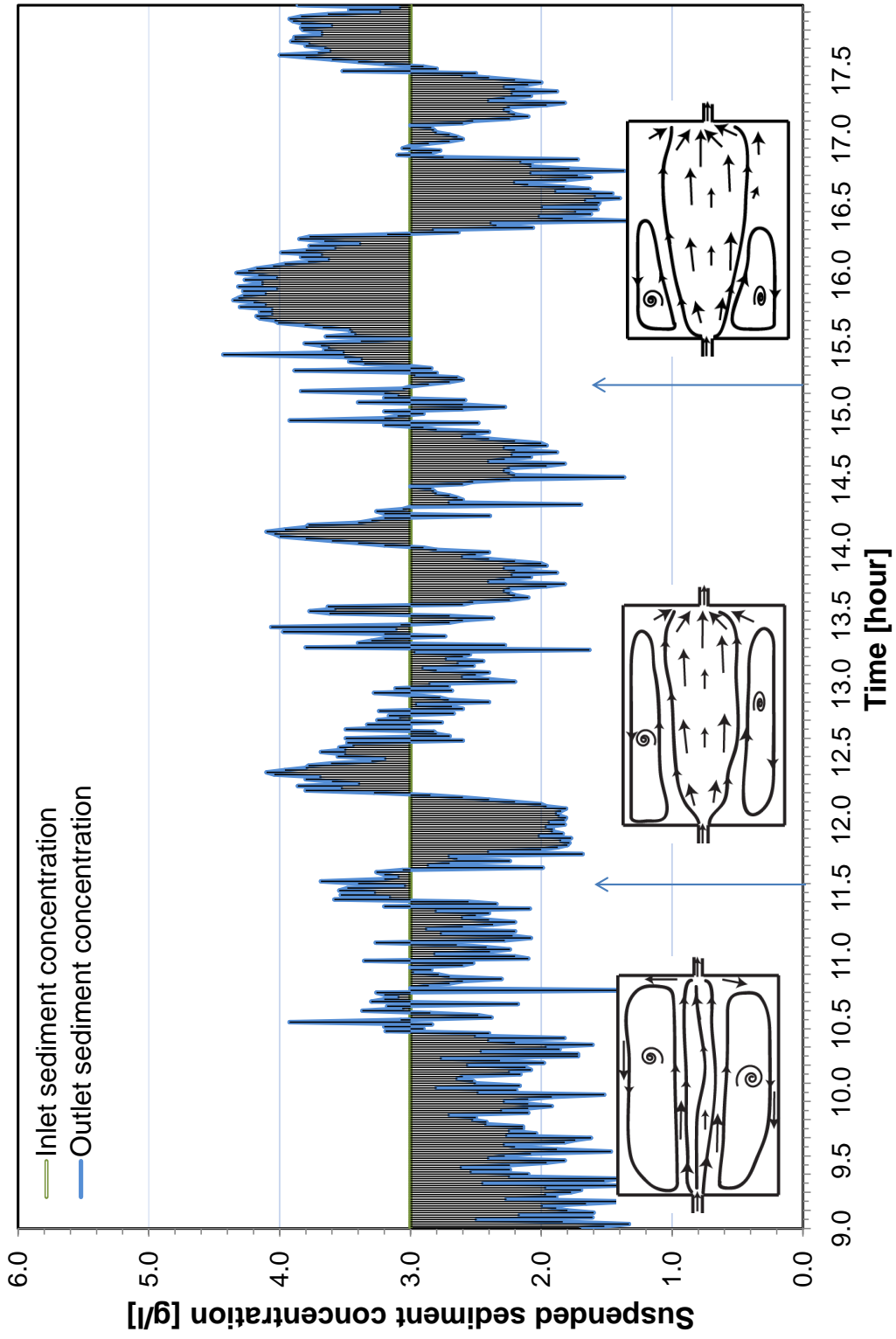


Figure A4.7: Inflow and released suspended concentration of sediments from the reservoir during the third period of 9.0hours, measured every minute

A4.3 Measurements of bed thickness deposition obtained by Mini Echo Sounder

Results of morphological evolution obtained for the following flow and sediment characteristic:

- Discharge $Q = 7.0$ [l/s]
- Water depth $h = 0.2$ [m]
- Froude Number $F_r = 0.1$
- Reynolds number $Re = 28000$
- Sediment diameter $d_{50} = 50$ [μ]
- Sediment density $\rho = 1500$ [kg/m³]
- Suspended sediment concentration $C = 3.0$ [g/l]

A4.3.1 Depositions contours

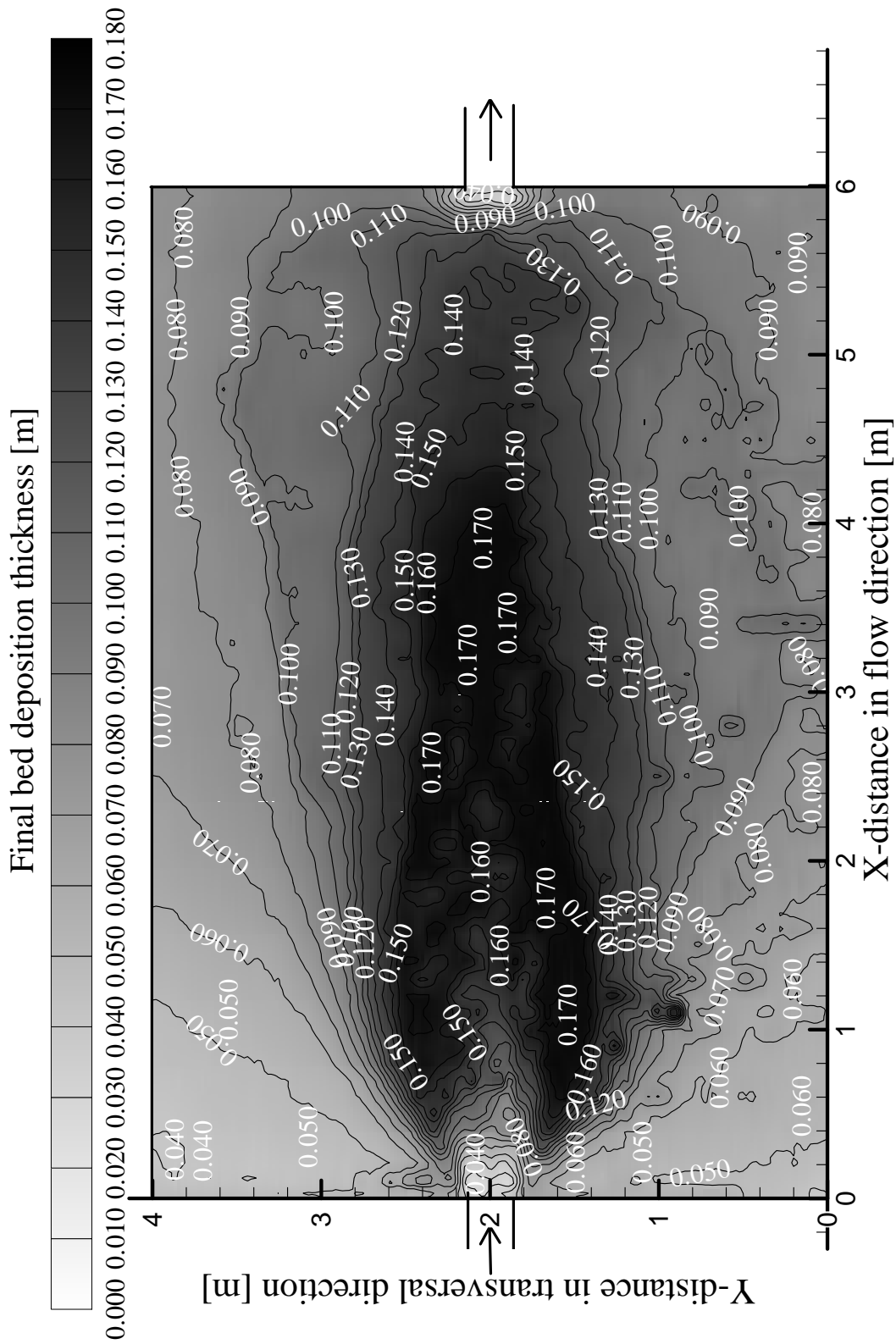


Figure A4.8: Contours of deposition pattern after the third period run after 18.0 hour

A4.3.2 Bed thickness cross and longitudinal sections

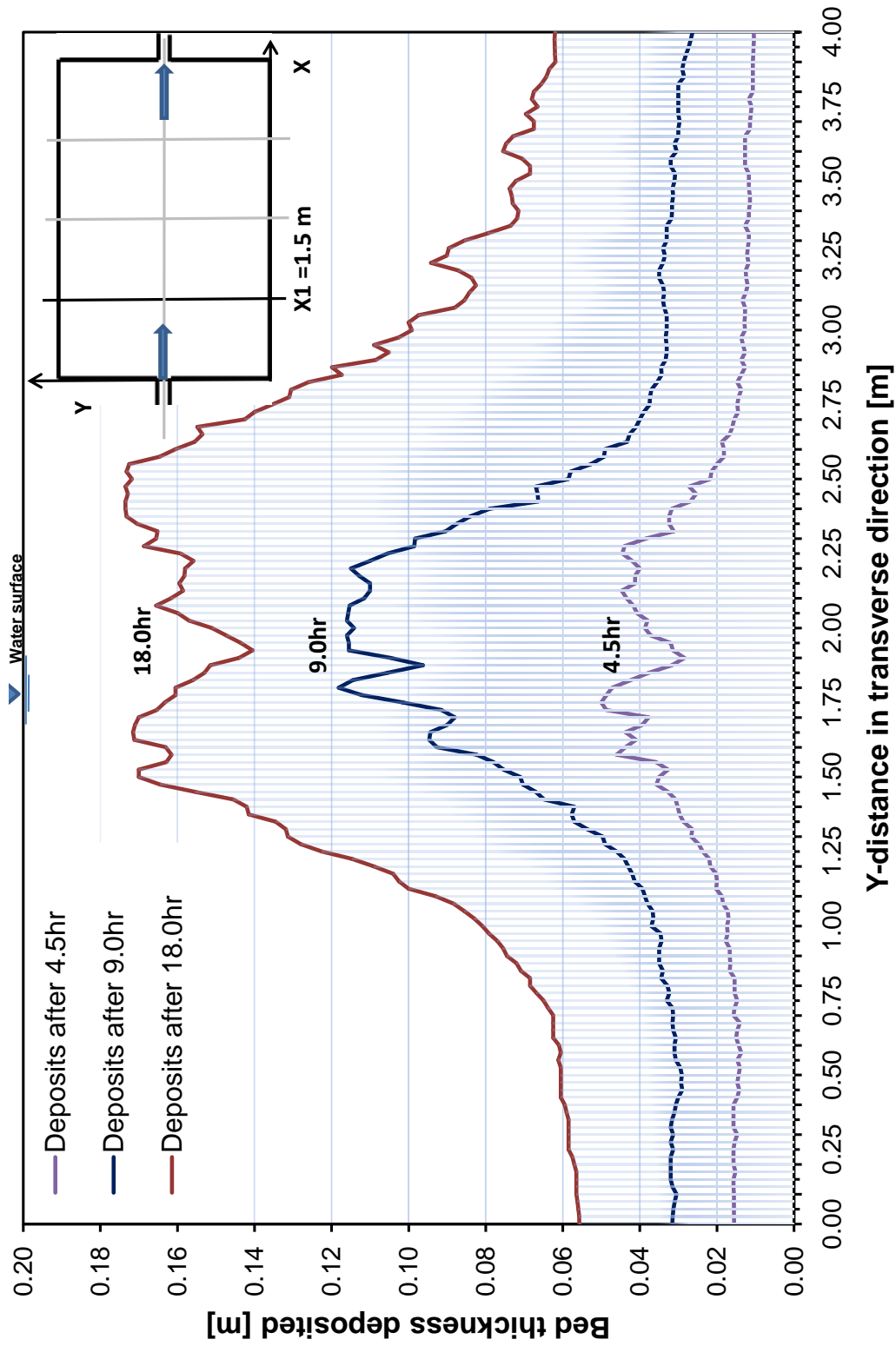


Figure A4.9: Evolution of sediment deposits for three periods runs at cross section $X_1 = 1.5\text{m}$ from the entrance

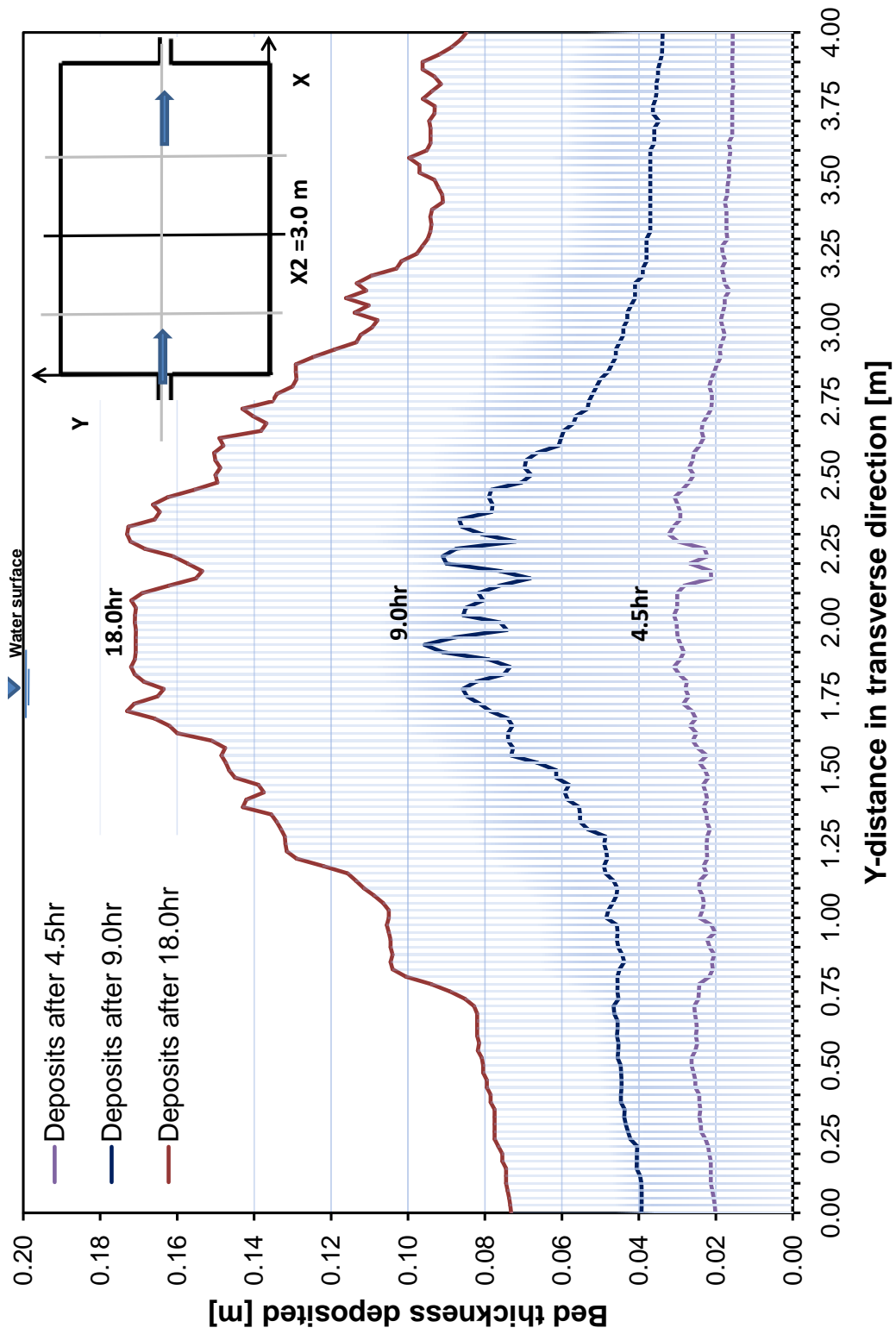


Figure A4.10: Evolution of sediment deposits for three periods runs at cross section $X_2 = 3.0\text{ m}$ from the entrance

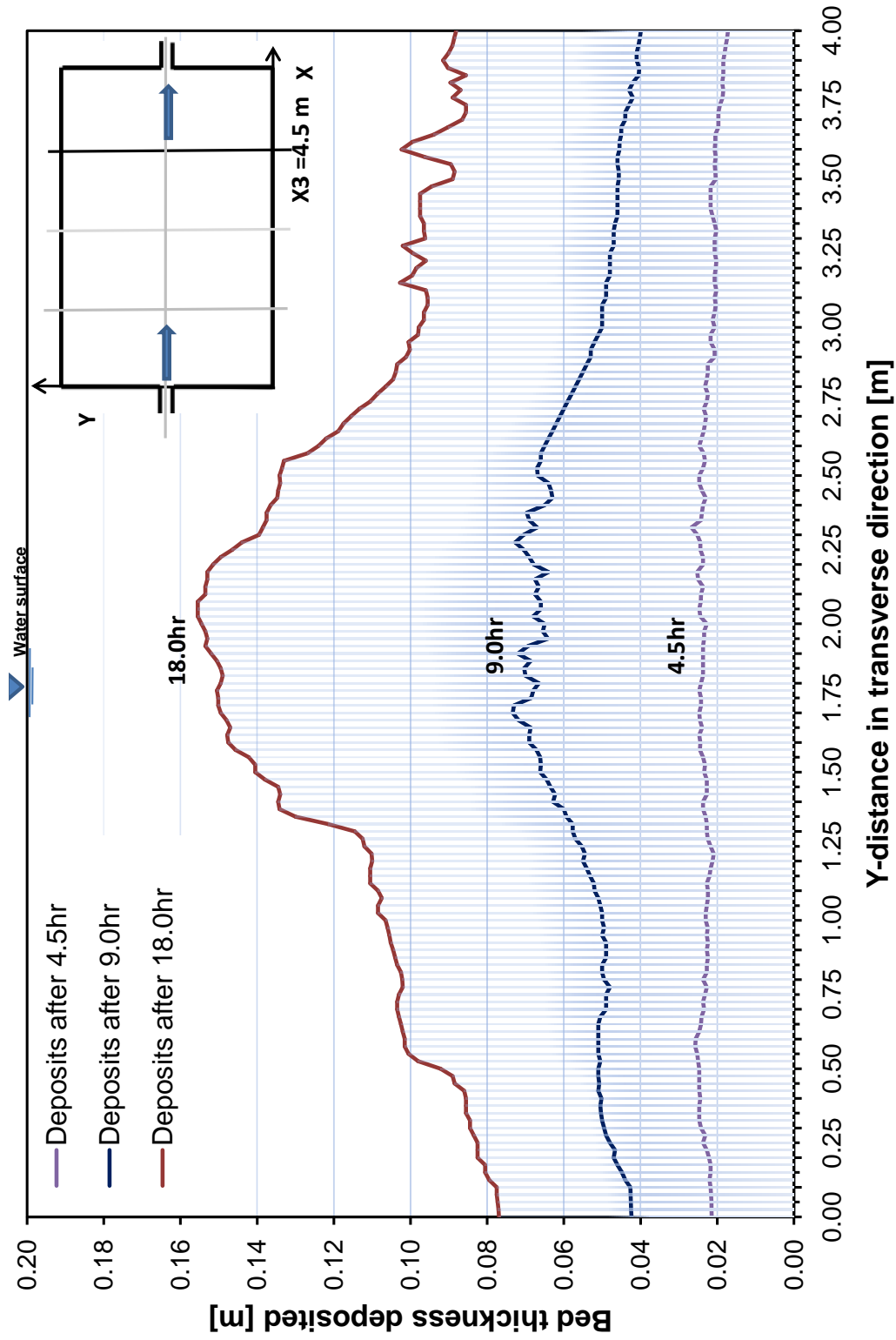


Figure A4.11: Evolution of sediment deposits for three periods runs at cross section $X_3 = 4.5m$ from the entrance

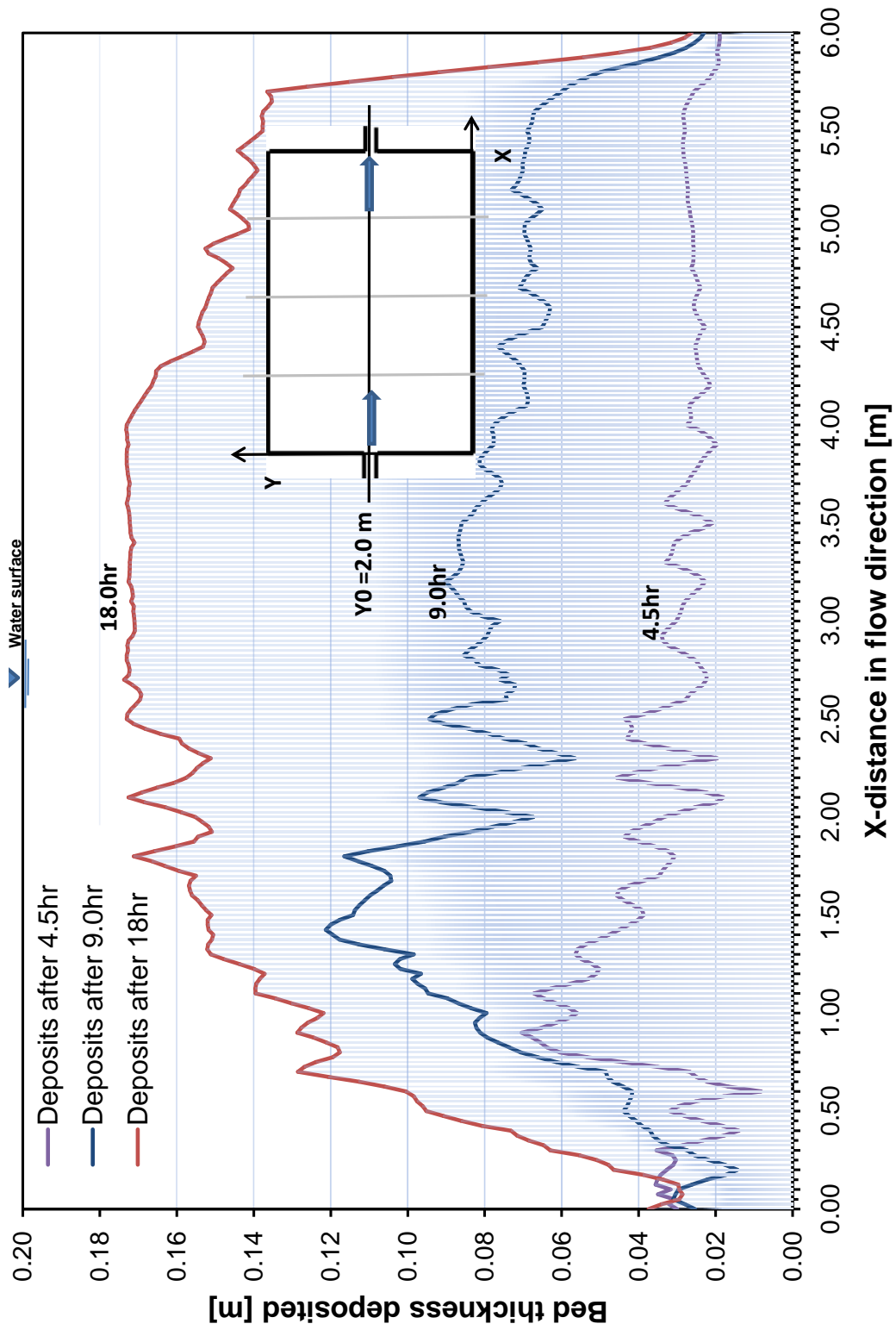
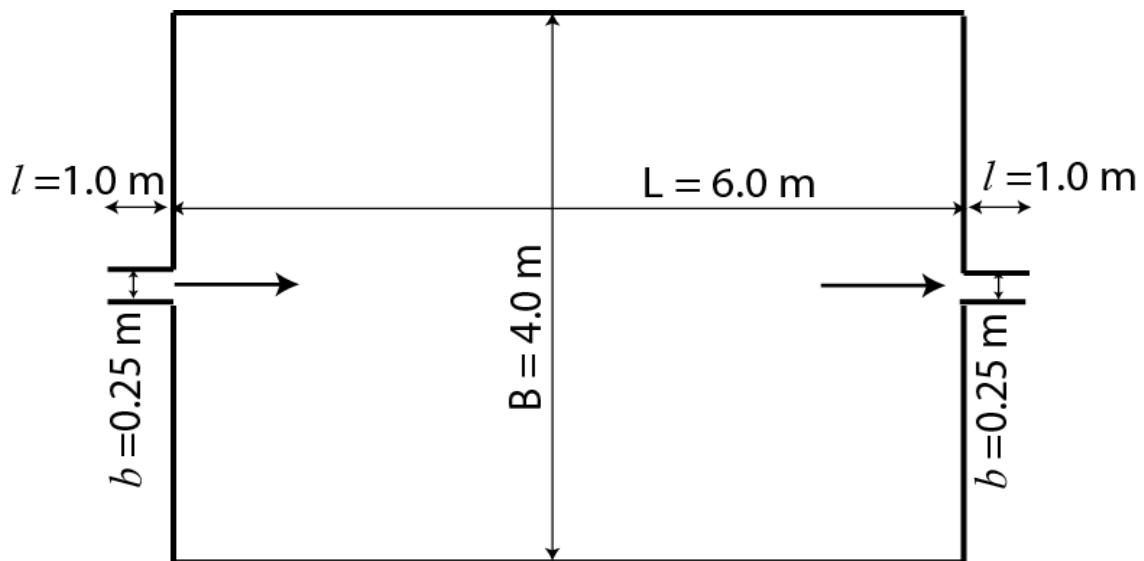


Figure A4.12: Evolution of sediment deposits for four periods runs at centerline longitudinal section $Y = 2.0m$

A5 Results of rectangular geometry Test5



A5.1 Surface velocity obtained by (LSPIV) measurements with clear water depth of $h_1 = 0.2m$ for Test5

Results of flow field with the velocity magnitude and streamlines obtained for the following flow characteristic:

- Discharge $Q = 7.0 [l/s]$
- Water depth $h = 0.2 [m]$
- Froude Number $F_r = 0.1$
- Reynolds number $Re = 28000$

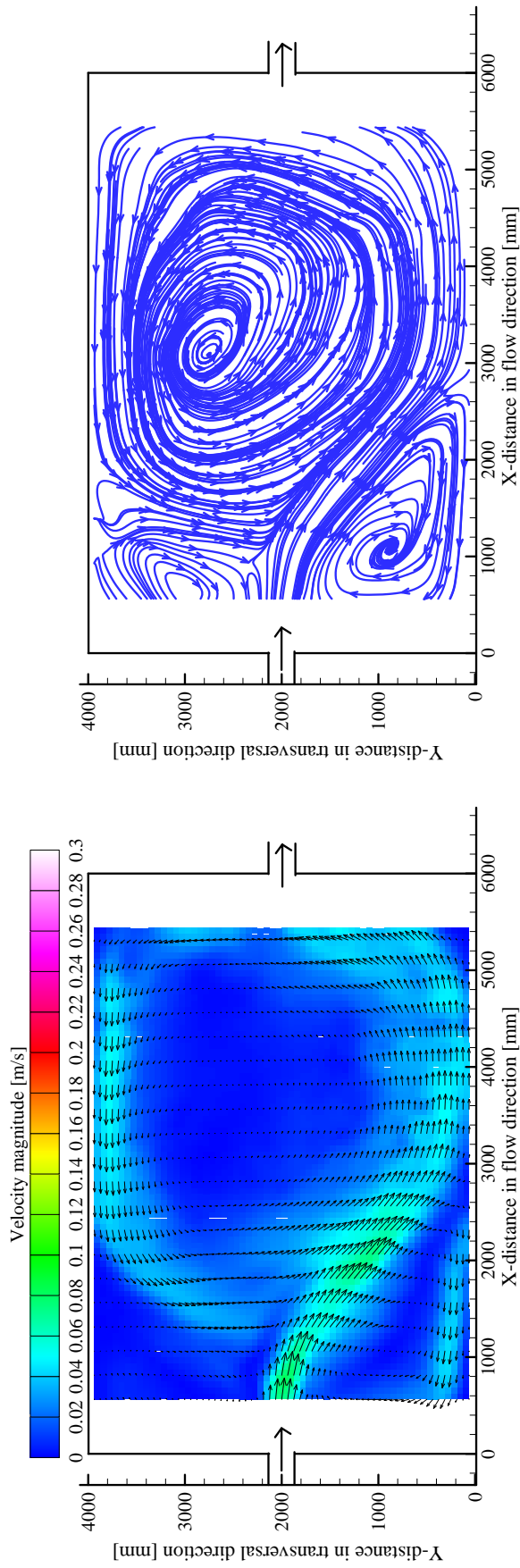


Figure A5.1: Time average flow pattern with velocity vectors (left); streamlines (right) with clear water depth of $h_1 = 0.2m$ after stable state

A5.2 Surface velocity obtained by (LSPIV) measurements with clear water depth of $h_2 = 0.15m$ for Test5

Results of flow field with the velocity magnitude and streamlines obtained for the following flow characteristic:

- Discharge $Q = 7.0 [l/s]$
- Water depth $h = 0.15 [m]$
- Froude Number $F_r = 0.15$
- Reynolds number $Re = 28000$

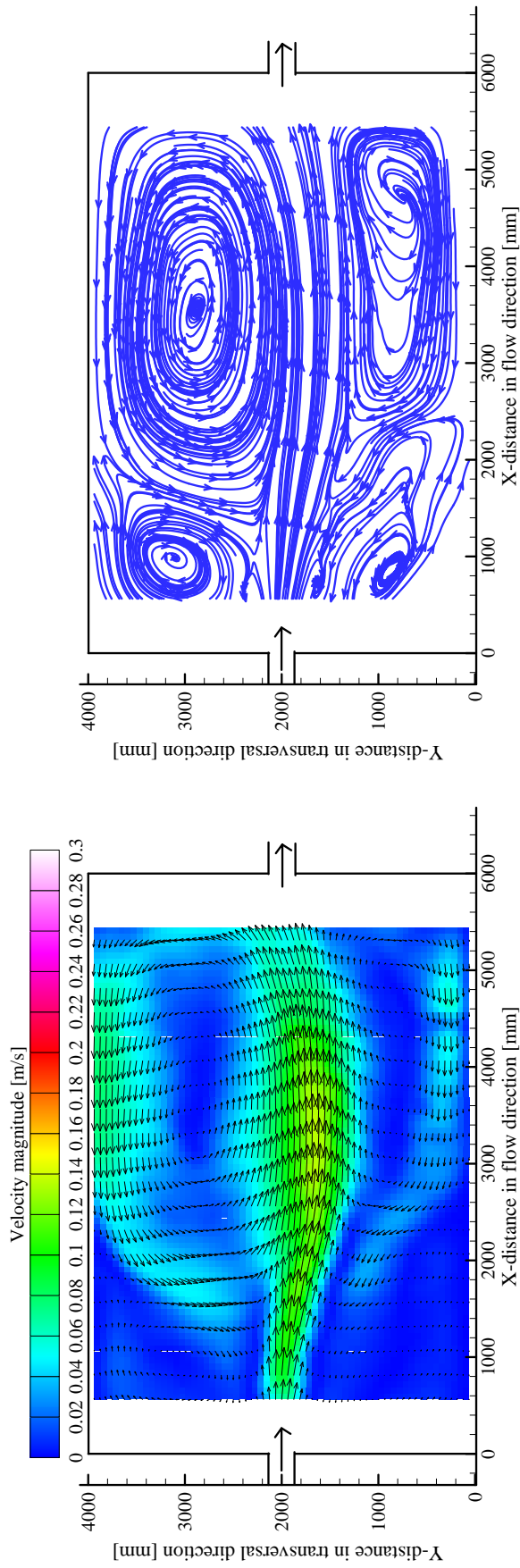


Figure A5.2: Time average flow pattern with velocity vectors (left); streamlines (right) with clear water depth of $h_2 = 0.15m$ after stable state

A5.3 Surface velocity obtained by (LSPIV) measurements with clear water depth of $h_3 = 0.10m$ for Test5

Results of flow field with the velocity magnitude and streamlines obtained for the following flow characteristic:

- Discharge $Q = 7.0 [l/s]$
- Water depth $h = 0.10 [m]$
- Froude Number $F_r = 0.28$
- Reynolds number $Re = 28000$

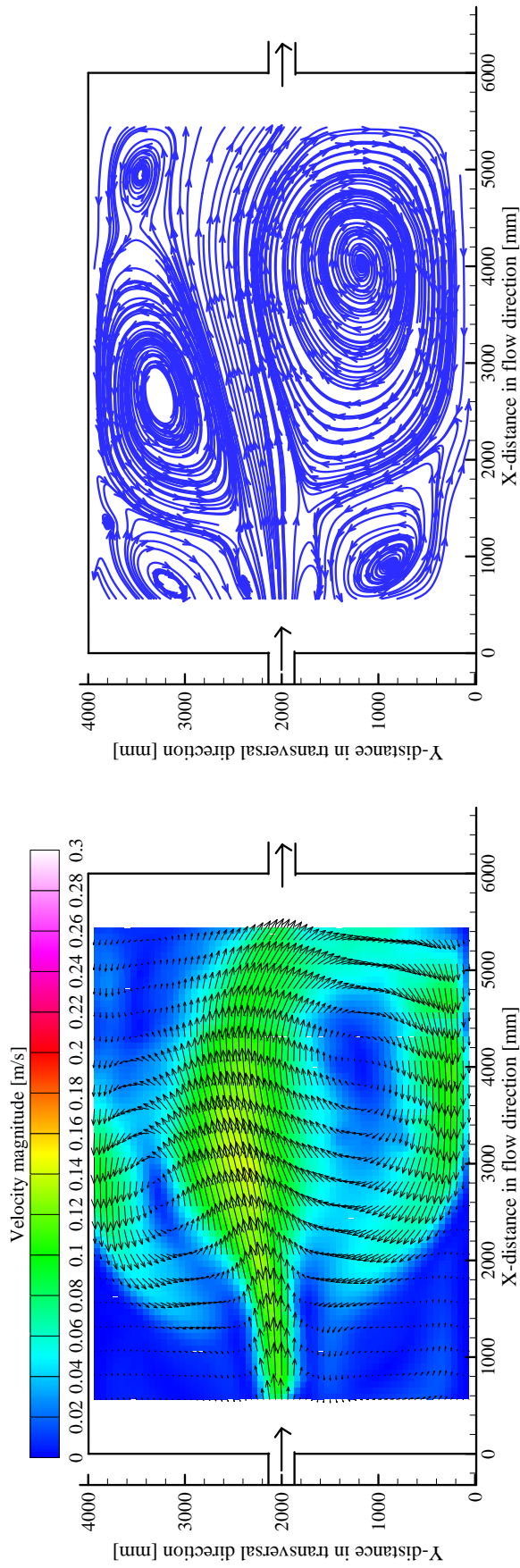


Figure A5.3: Time average flow pattern with velocity vectors (left); streamlines (right) with clear water depth of $h_3 = 0.10m$ after stable state

A5.4 Surface velocity obtained by (LSPIV) measurements with clear water depth of $h_4 = 0.075m$ for Test5

Results of flow field with the velocity magnitude and streamlines obtained for the following flow characteristic:

- Discharge $Q = 7.0 [l/s]$
- Water depth $h = 0.075 [m]$
- Froude Number $F_r = 0.43$
- Reynolds number $Re = 28000$

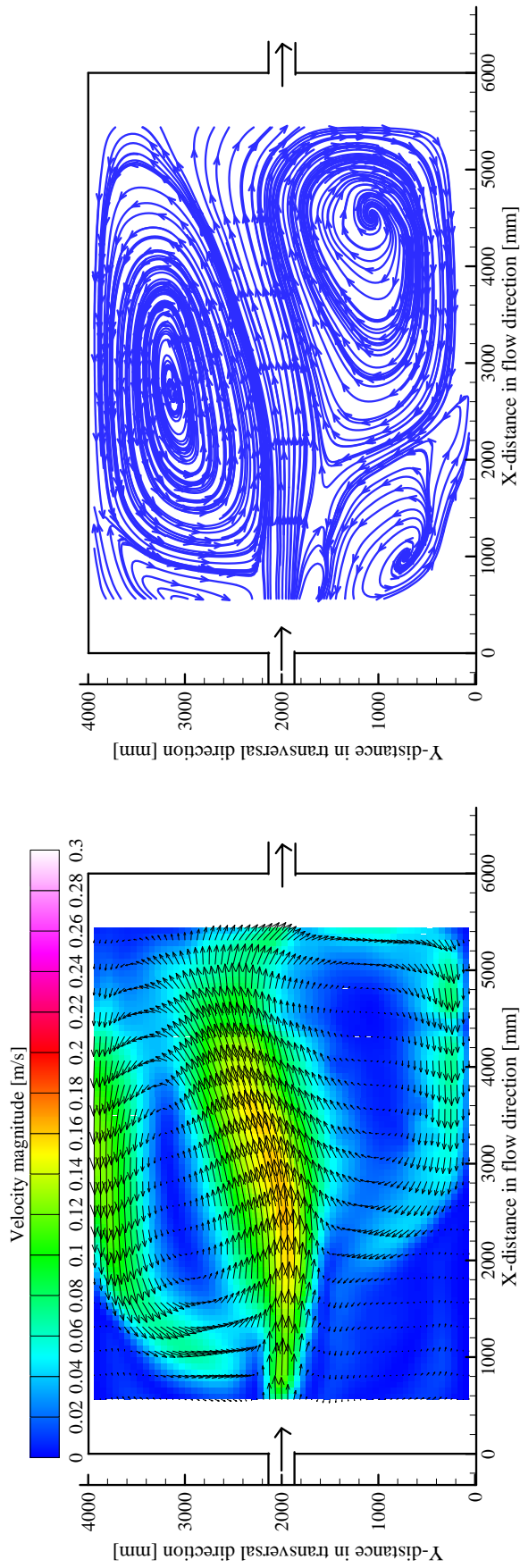
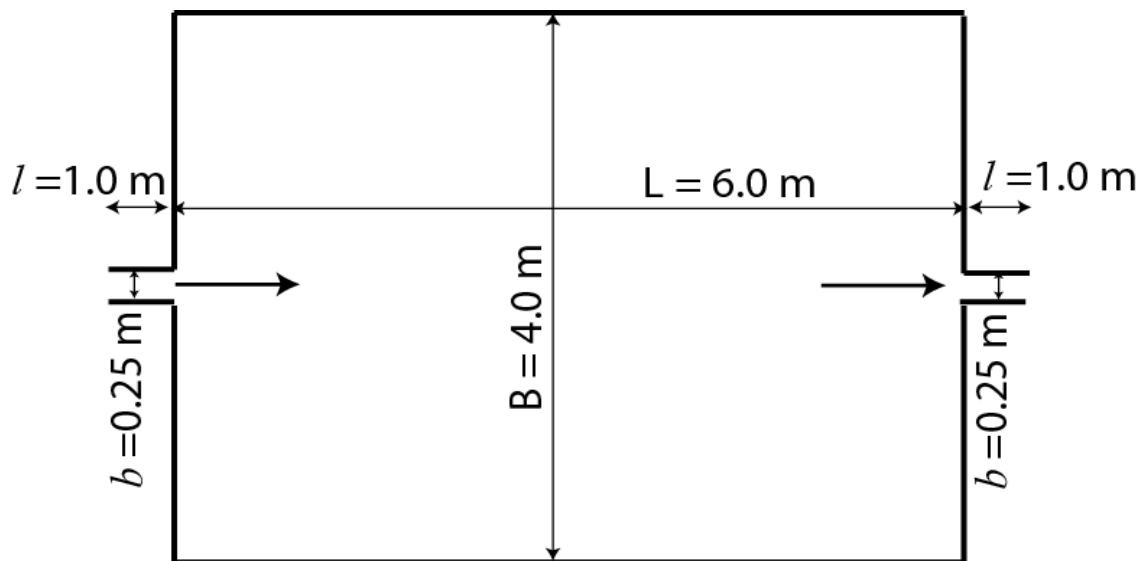


Figure A5.4: Time average flow pattern with velocity vectors (left); streamlines (right) with clear water depth of $h_4 = 0.075m$ after stable state

A6 Results of rectangular geometry Test6



A6.1 Surface velocity obtained by (LSPIV) measurements for (Test6) of low discharge

Results of flow field with the velocity magnitude and streamlines obtained for the following flow and sediment characteristic:

- Discharge $Q = 3.5 [l/s]$
- Water depth $h = 0.2 [m]$
- Froude Number $F_r = 0.05$
- Reynolds number $Re = 14000$
- Sediment diameter $d_{50} = 50 [\mu]$
- Sediment density $\rho = 1500 [kg/m^3]$
- Suspended sediment concentration $C = 3.0 [g/l]$

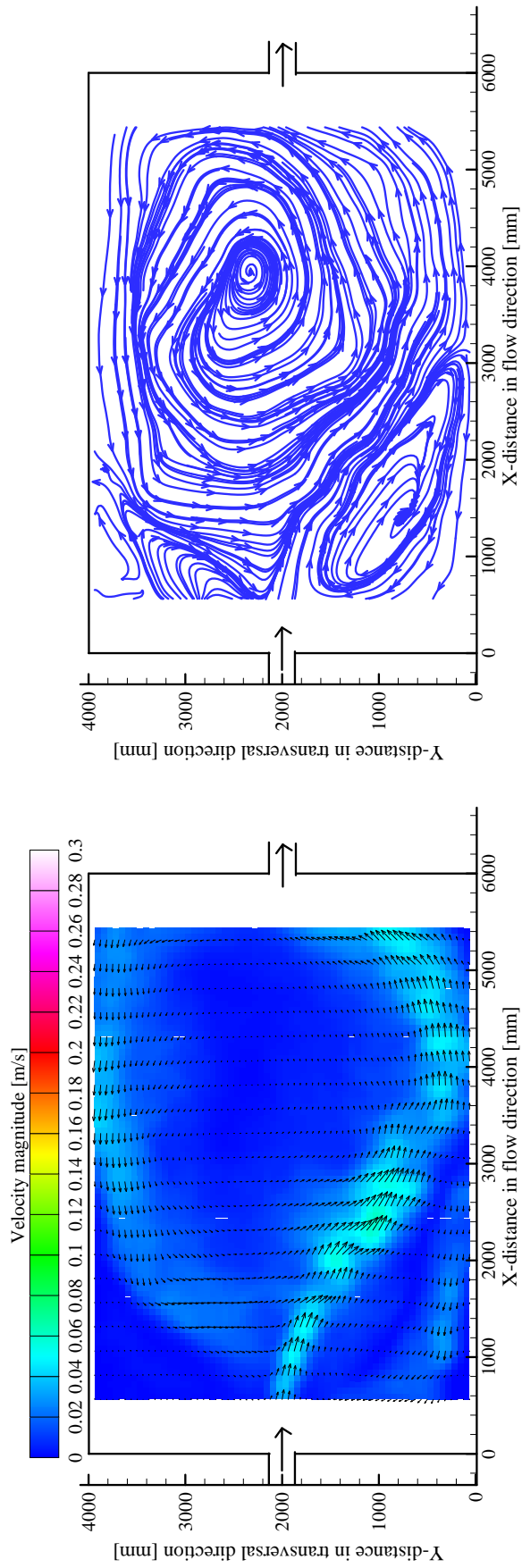


Figure A6.1: Time average flow pattern with velocity vectors (left); streamlines (right) with clear water after stable state for (Test6) of low discharge

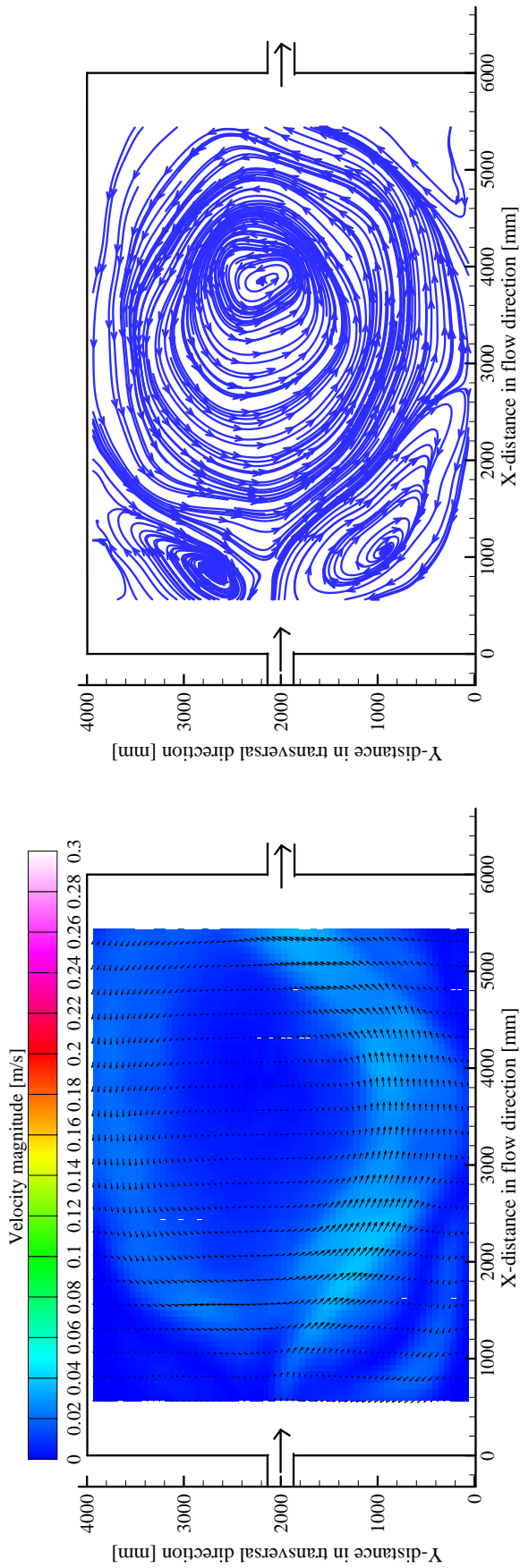


Figure A6.2: Time average flow pattern (left); streamlines (right) after 10 minutes of the first period with sediments

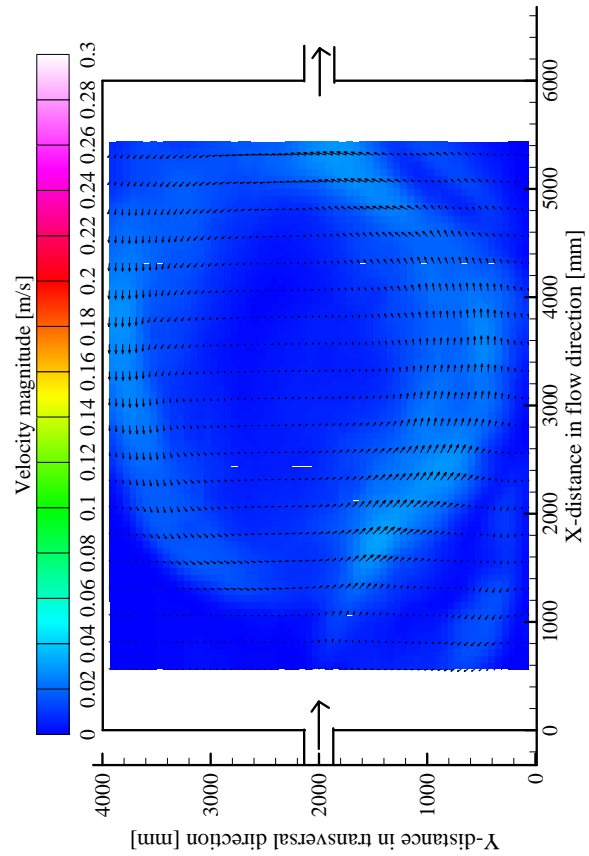


Figure A6.3: Time average flow pattern (left); streamlines (right) after 30 minutes of the first period with sediments

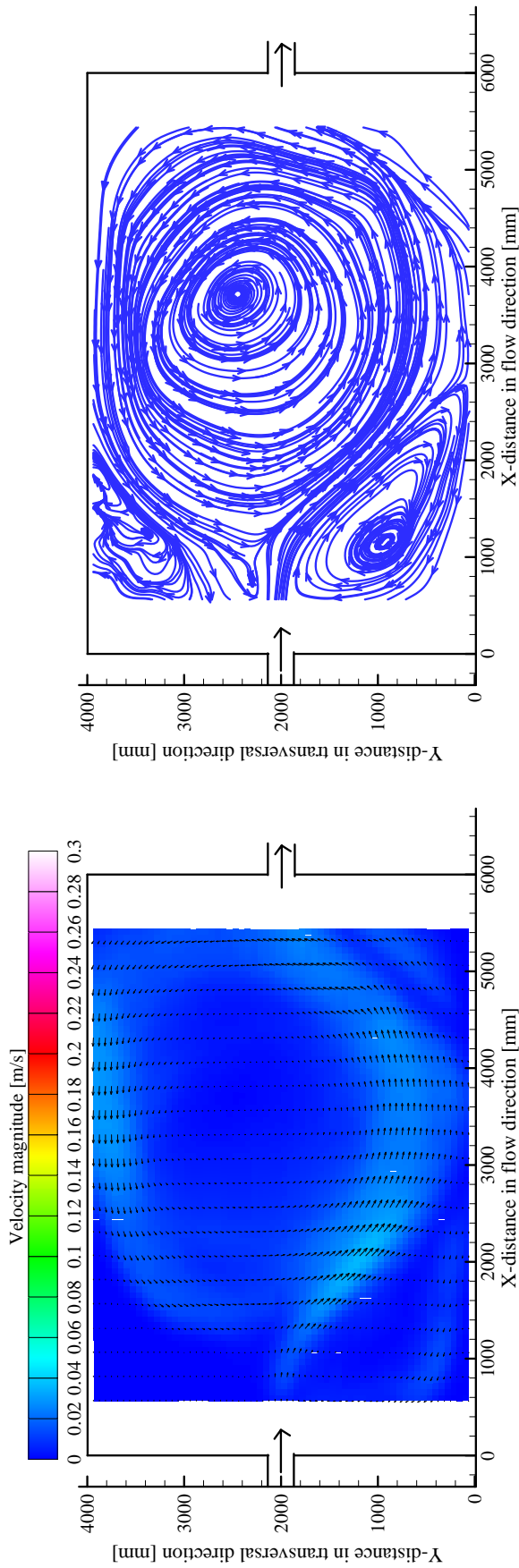


Figure A6.4: Time average flow pattern (left); streamlines (right) after 60 minutes of the first period with sediments

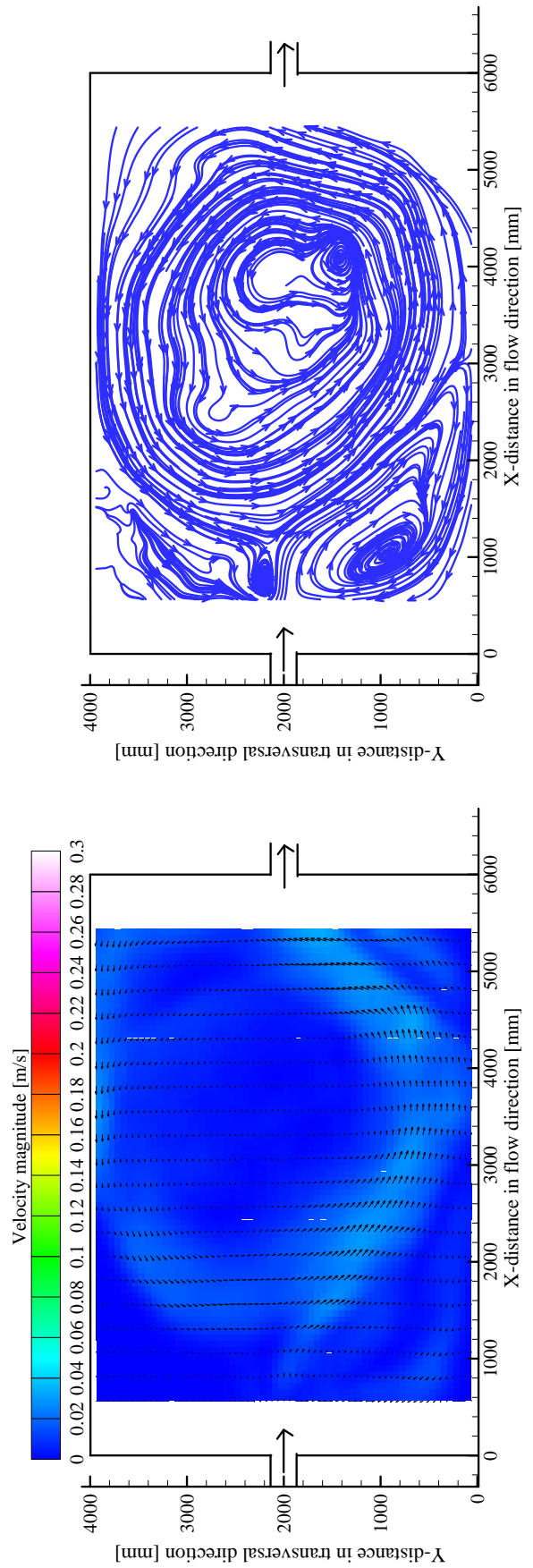
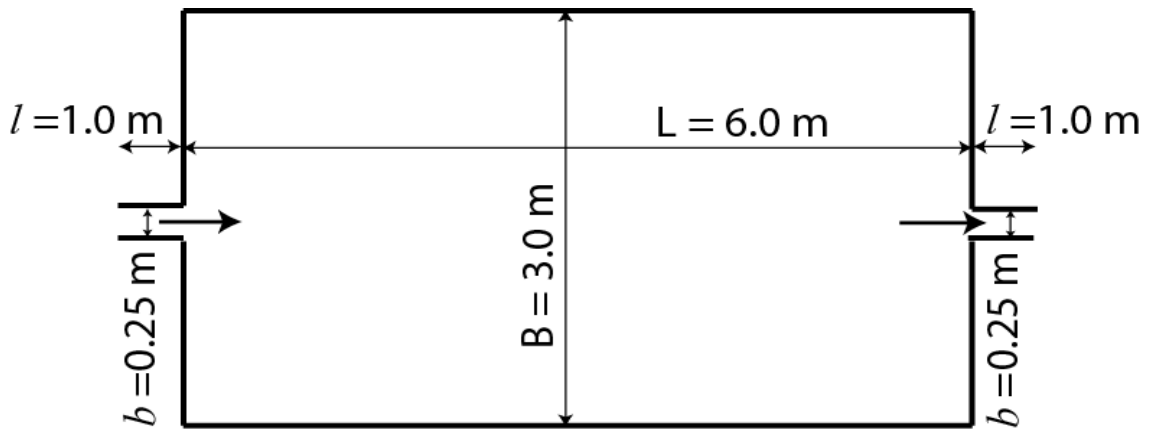


Figure A6.5: Time average flow pattern (left); streamlines (right) after 90 minutes of the first period with sediments

A7 Results of rectangular geometry Test7



A7.1 Surface velocity obtained by (LSPIV) measurements

Results of flow field with the velocity magnitude and streamlines obtained for the following flow and sediment characteristic:

- Discharge $Q = 7.0$ [l/s]
- Water depth $h = 0.2$ [m]
- Froude Number $F_r = 0.1$
- Reynolds number $Re = 28000$
- Sediment diameter $d_{50} = 50$ [μ]
- Sediment density $\rho = 1500$ [kg/m³]
- Suspended sediment concentration $C = 3.0$ [g/l]

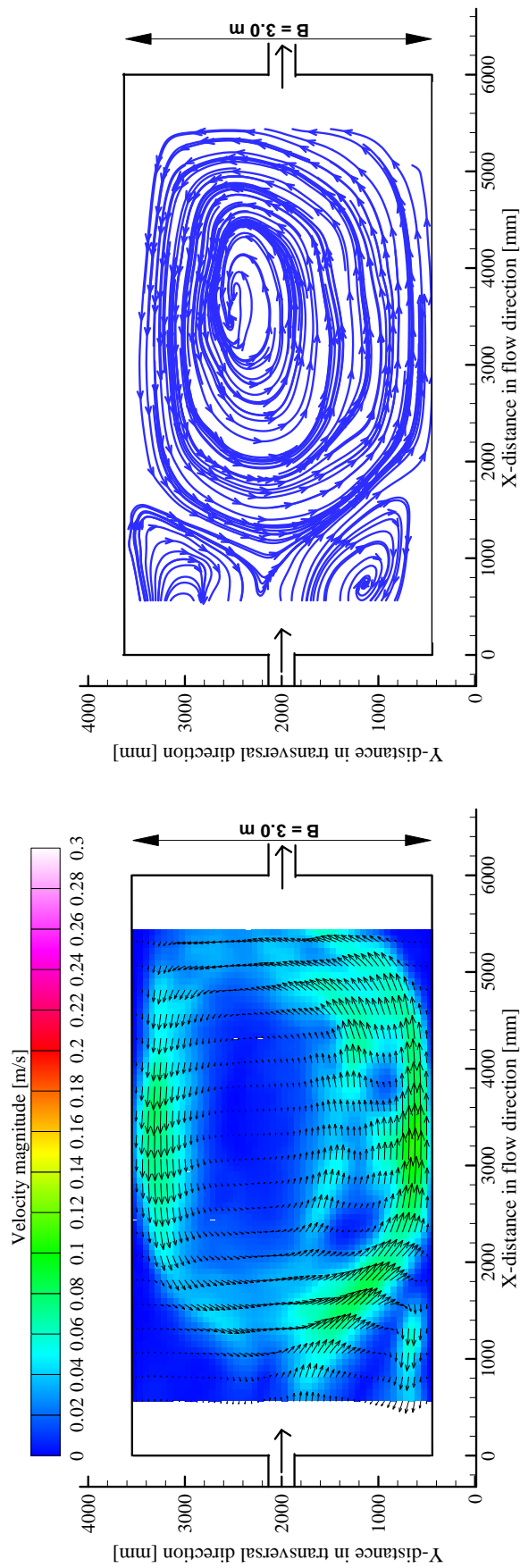


Figure A7.1: Time average flow pattern with velocity vectors (left); streamlines (right) with clear water after stable state

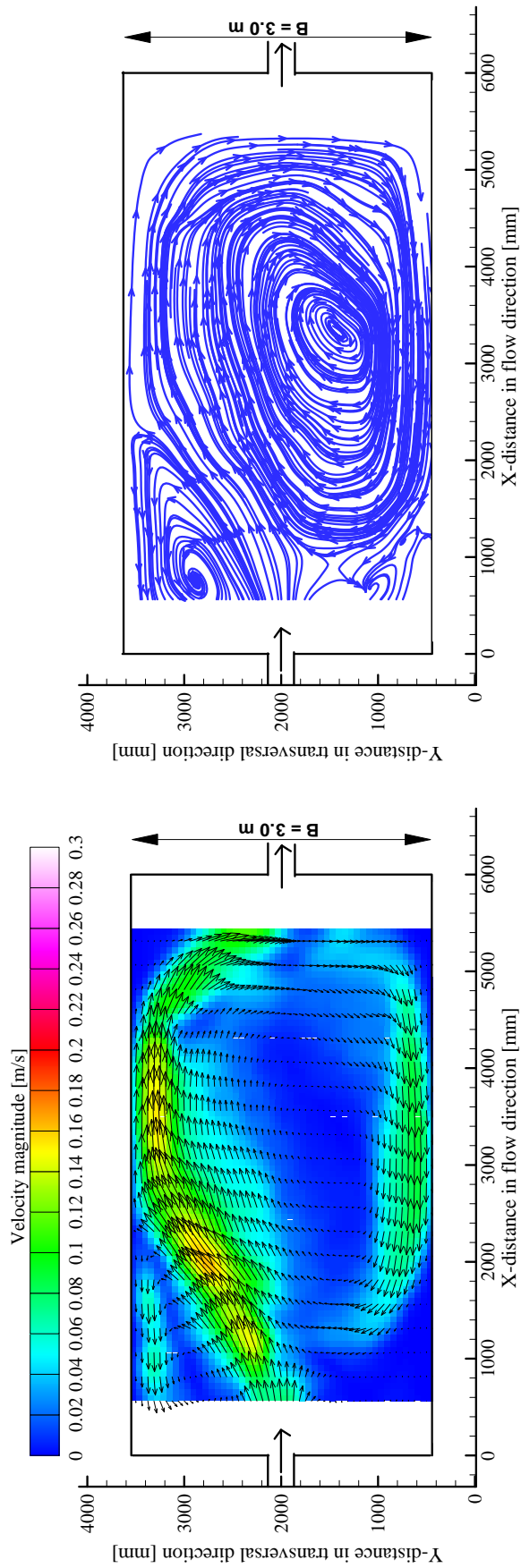


Figure A7.2: Time average flow pattern (left); streamlines (right) after 60 minutes of the third period with sediments

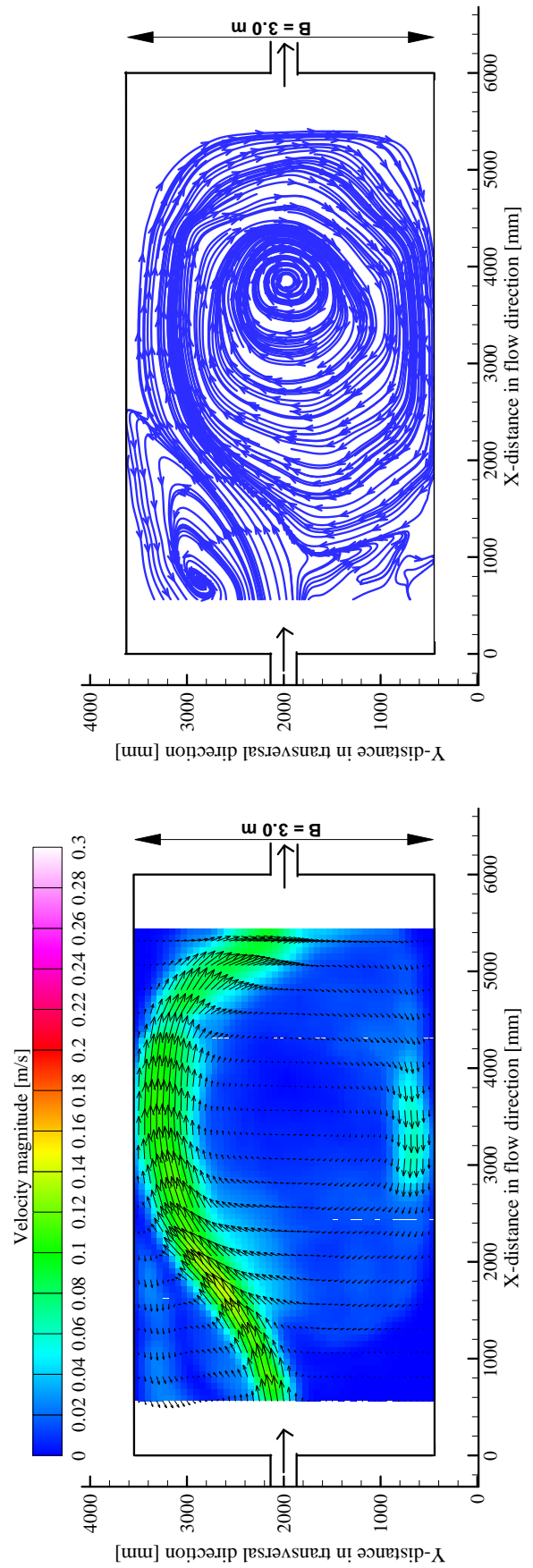
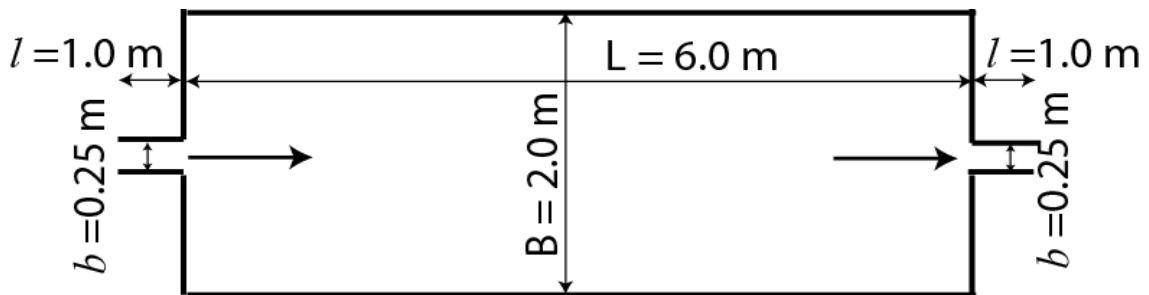


Figure A7.3: Time average flow pattern (left); streamlines (right) after 90 minutes of the third period with sediments

A8 Results of rectangular geometry Test8



A8.1 Surface velocity obtained by (LSPIV) measurements

Results of flow field with the velocity magnitude and streamlines obtained for the following flow and sediment characteristic:

- Discharge $Q = 7.0$ [l/s]
- Water depth $h = 0.2$ [m]
- Froude Number $F_r = 0.1$
- Reynolds number $Re = 28000$
- Sediment diameter $d_{50} = 50$ [μ]
- Sediment density $\rho = 1500$ [kg/m³]
- Suspended sediment concentration $C = 3.0$ [g/l]

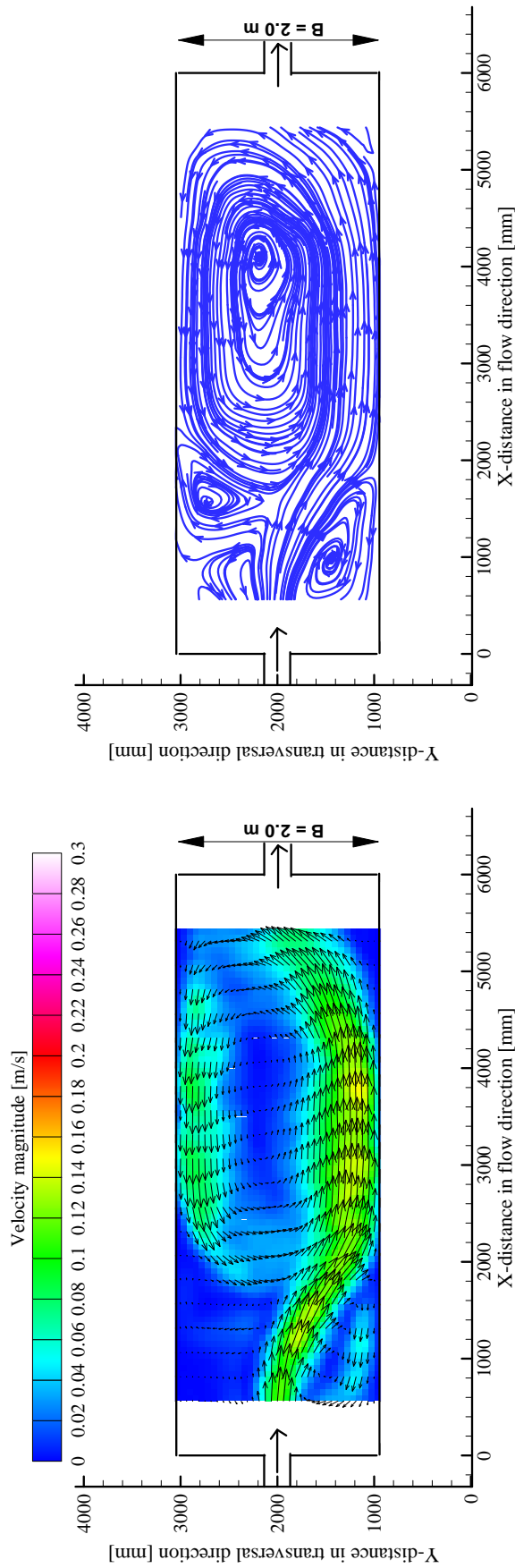


Figure A8.1: Time average flow pattern with velocity vectors (left); streamlines (right) with clear water after stable state

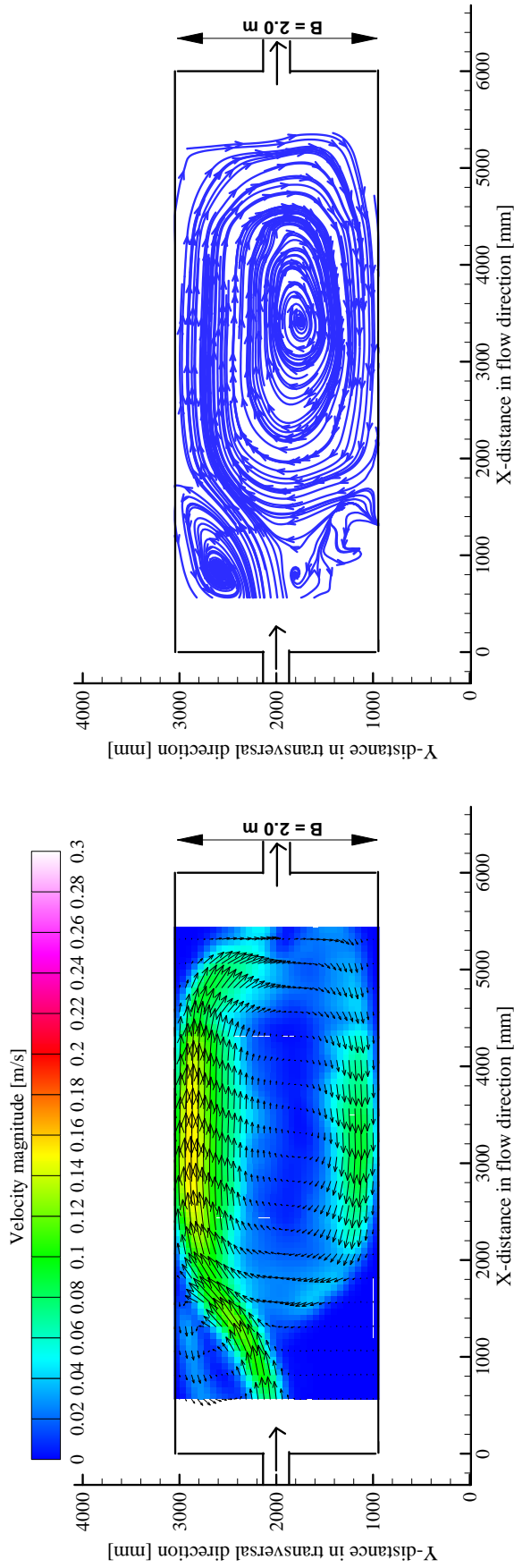


Figure A8.2: Time average flow pattern (left); streamlines (right) after 60 minutes of the third period with sediments

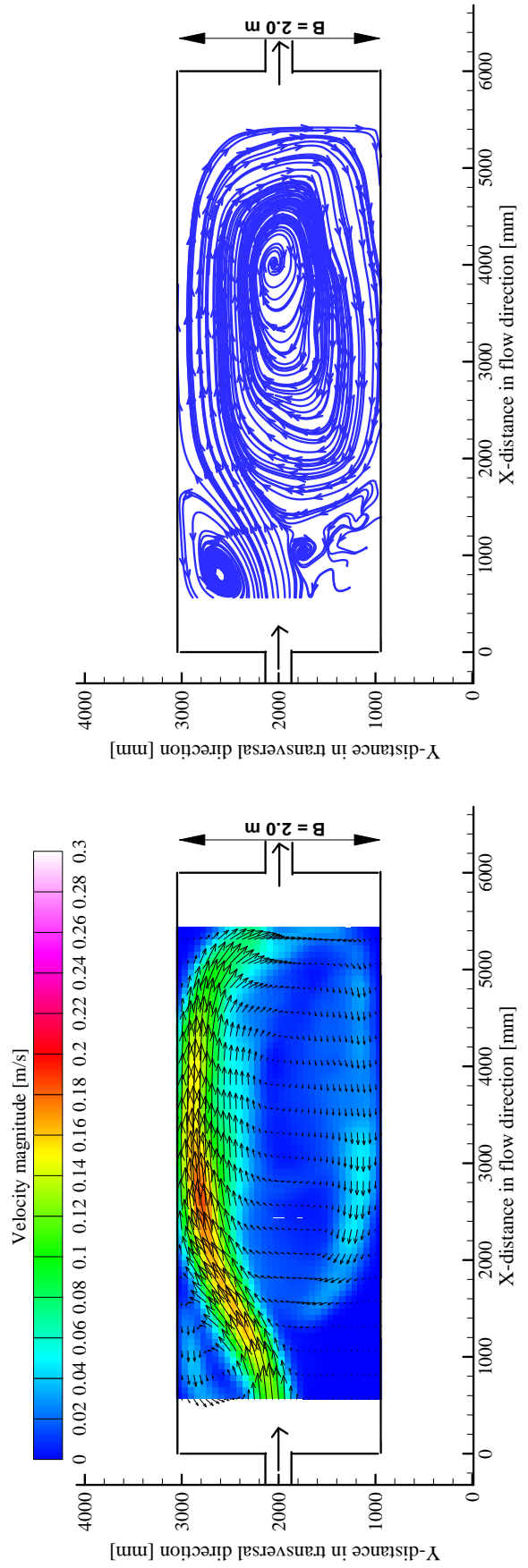


Figure A8.3: Time average flow pattern (left); streamlines (right) after 90 minutes of the third period with sediments

A8.2 Two days flushing with clear water over the final bed deposition of the third period (4.5 hours)

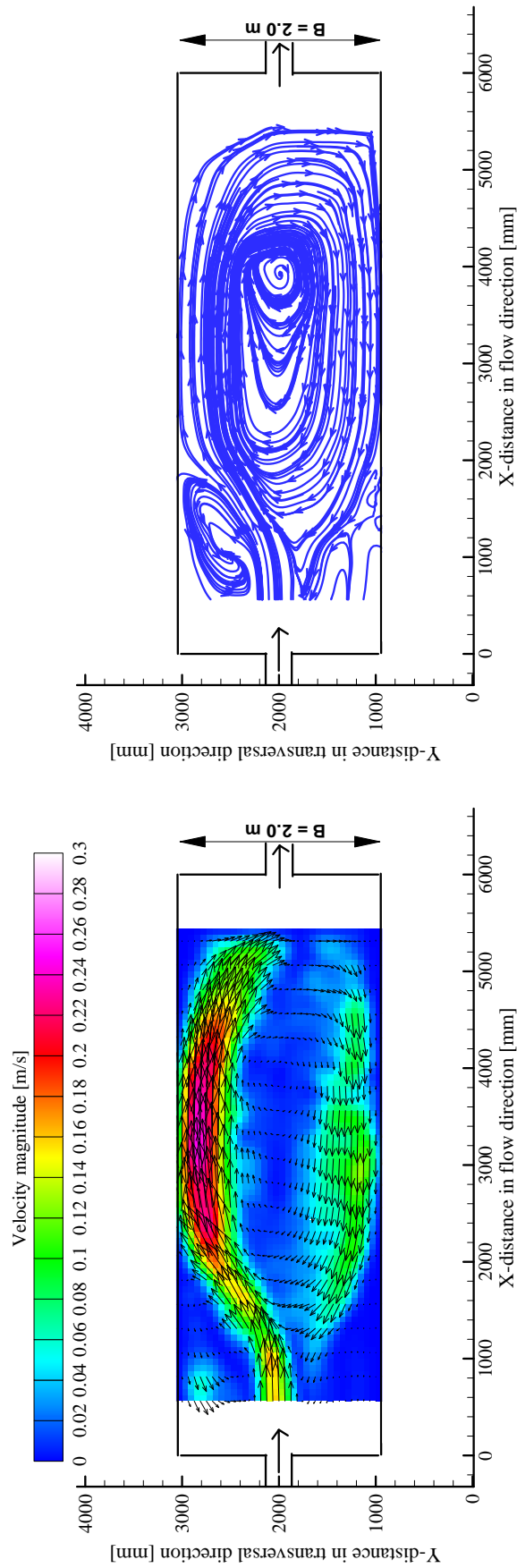


Figure A8.4: Time average flow pattern (left); streamlines (right) of the drawdown flushing with water depth $h = 10 \text{ cm}$

A8.3 Measurements of suspended sediment concentration obtained by turbiditymeter

Results of sediment concentration obtained for the following flow and sediment characteristic:

- Discharge $Q = 7.0$ [l/s]
- Water depth $h = 0.2$ [m]
- Froude Number $F_r = 0.1$
- Reynolds number $Re = 28000$
- Sediment diameter $d_{50} = 50$ [μ]
- Sediment density $\rho = 1500$ [kg/m³]
- Suspended sediment concentration $C = 3.0$ [g/l]

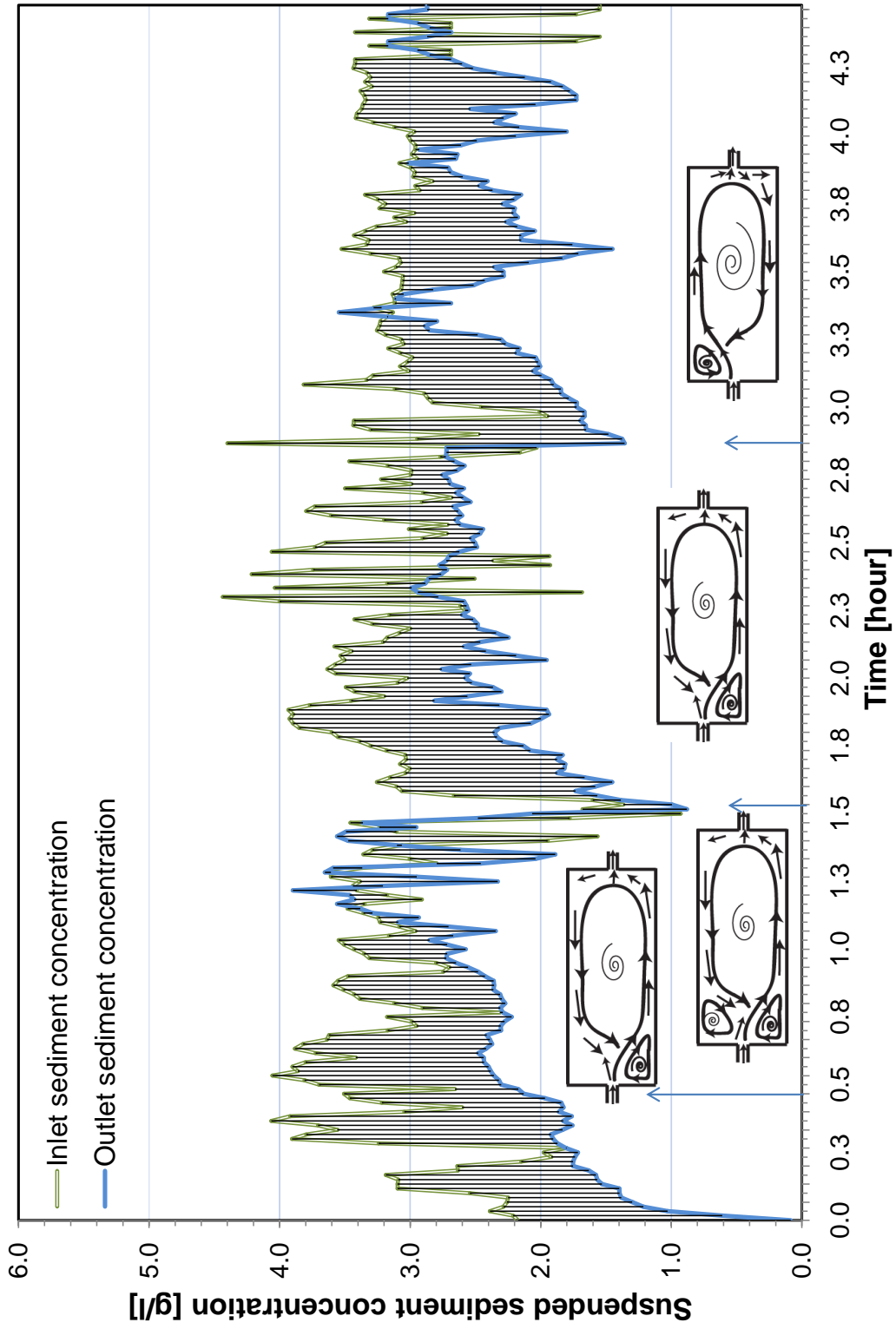


Figure A8.5: Inflow and released suspended concentration of sediments from the reservoir during the first, second and third period of 4.5 hours, measured every minute

A8.4 Measurements of bed thickness deposition obtained by Mini Echo Sounder

Results of morphological evolution obtained for the following flow and sediment characteristic:

- Discharge $Q = 7.0$ [l/s]
- Water depth $h = 0.2$ [m]
- Froude Number $F_r = 0.1$
- Reynolds number $Re = 28000$
- Sediment diameter $d_{50} = 50$ [μ]
- Sediment density $\rho = 1500$ [kg/m³]
- Suspended sediment concentration $C = 3.0$ [g/l]

A8.4.1 Depositions contours

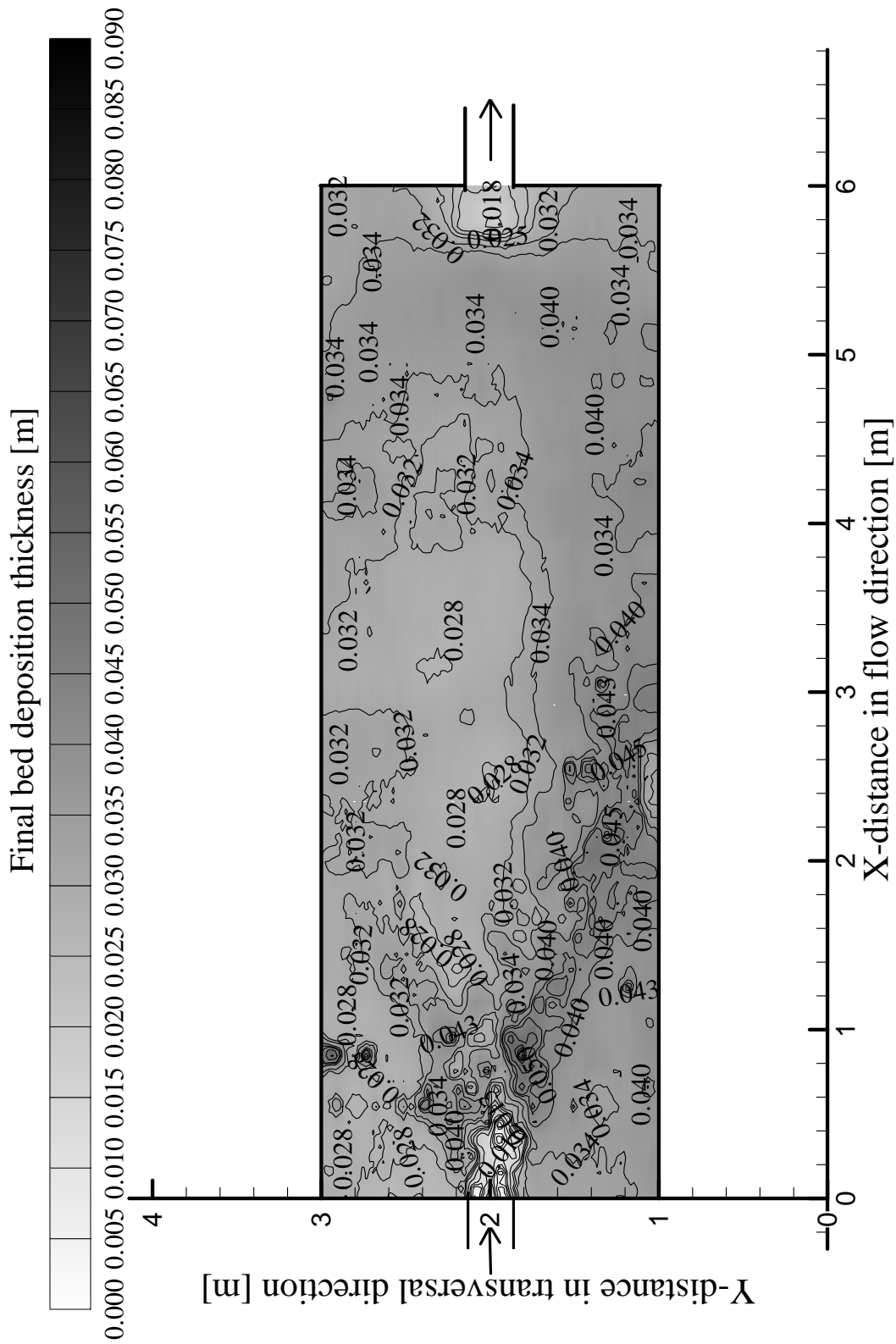


Figure A8.6: Contours of deposition pattern after the third period run after 4.5 hour

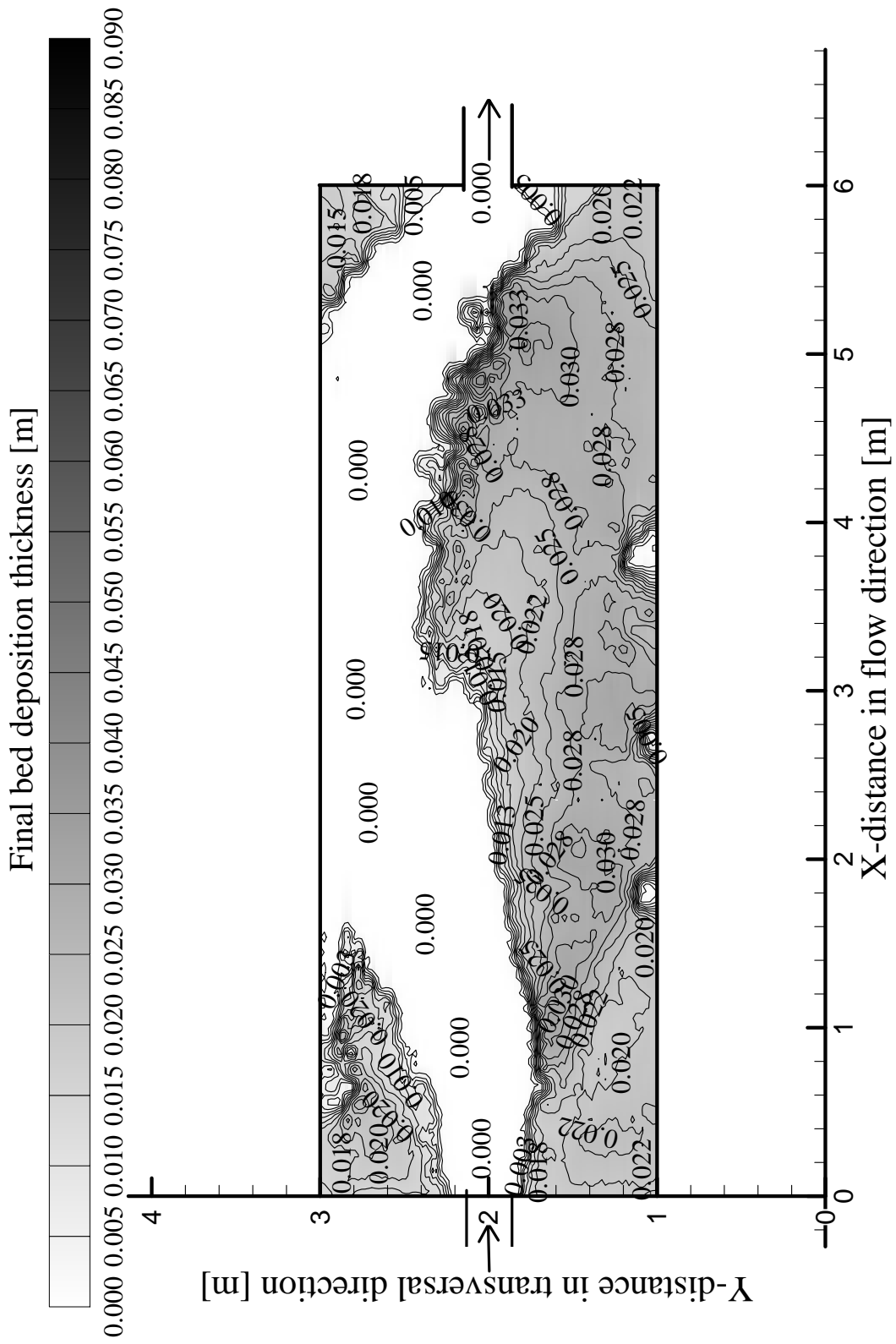


Figure A8.7: Contours of deposition pattern for the drawdown flushing period run after 48 hour

A8.4.2 Bed thickness cross and longitudinal sections

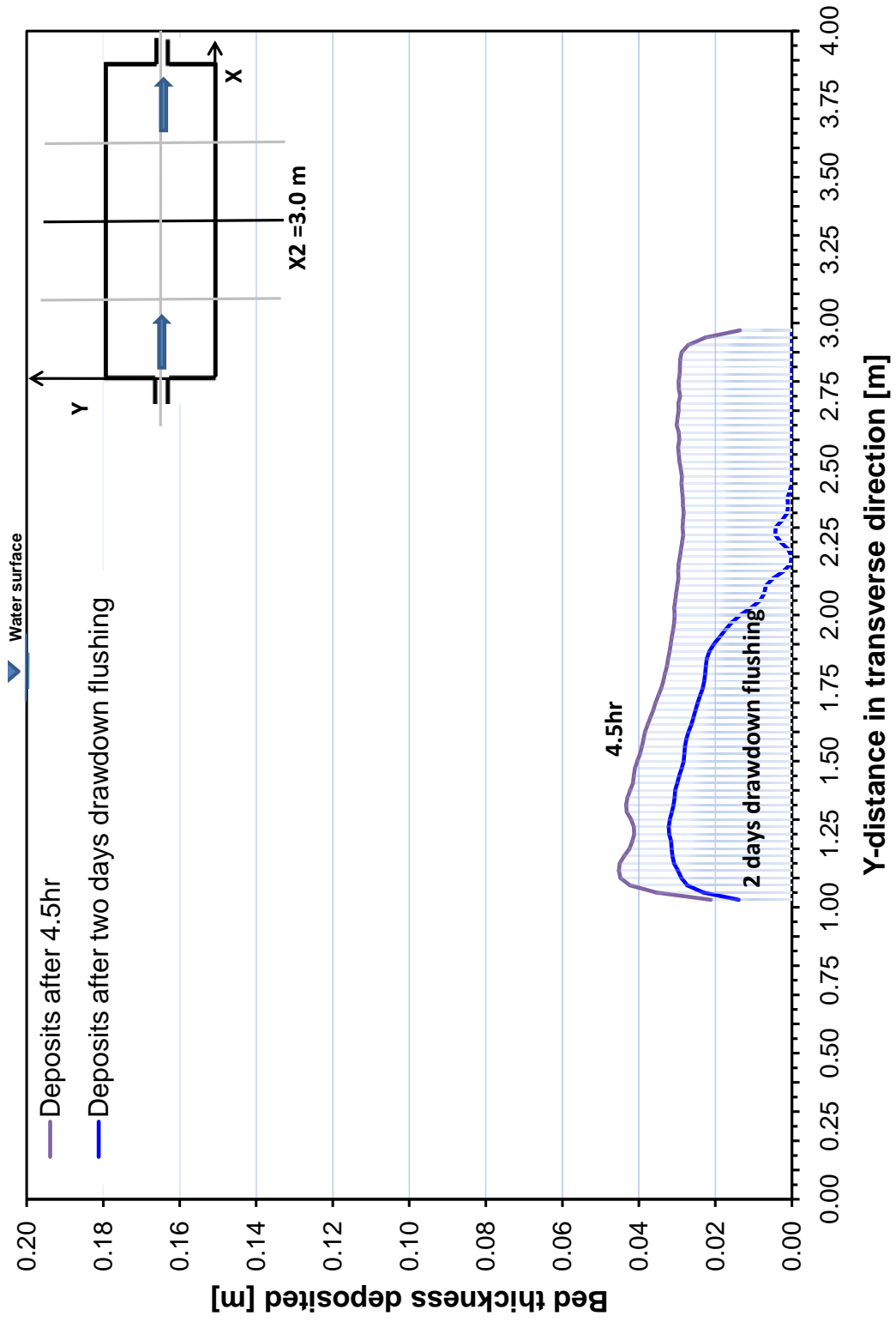


Figure A8.8: Sediment deposits comparison for third and flushing periods run at cross section $X_2 = 3.0m$ from the entrance

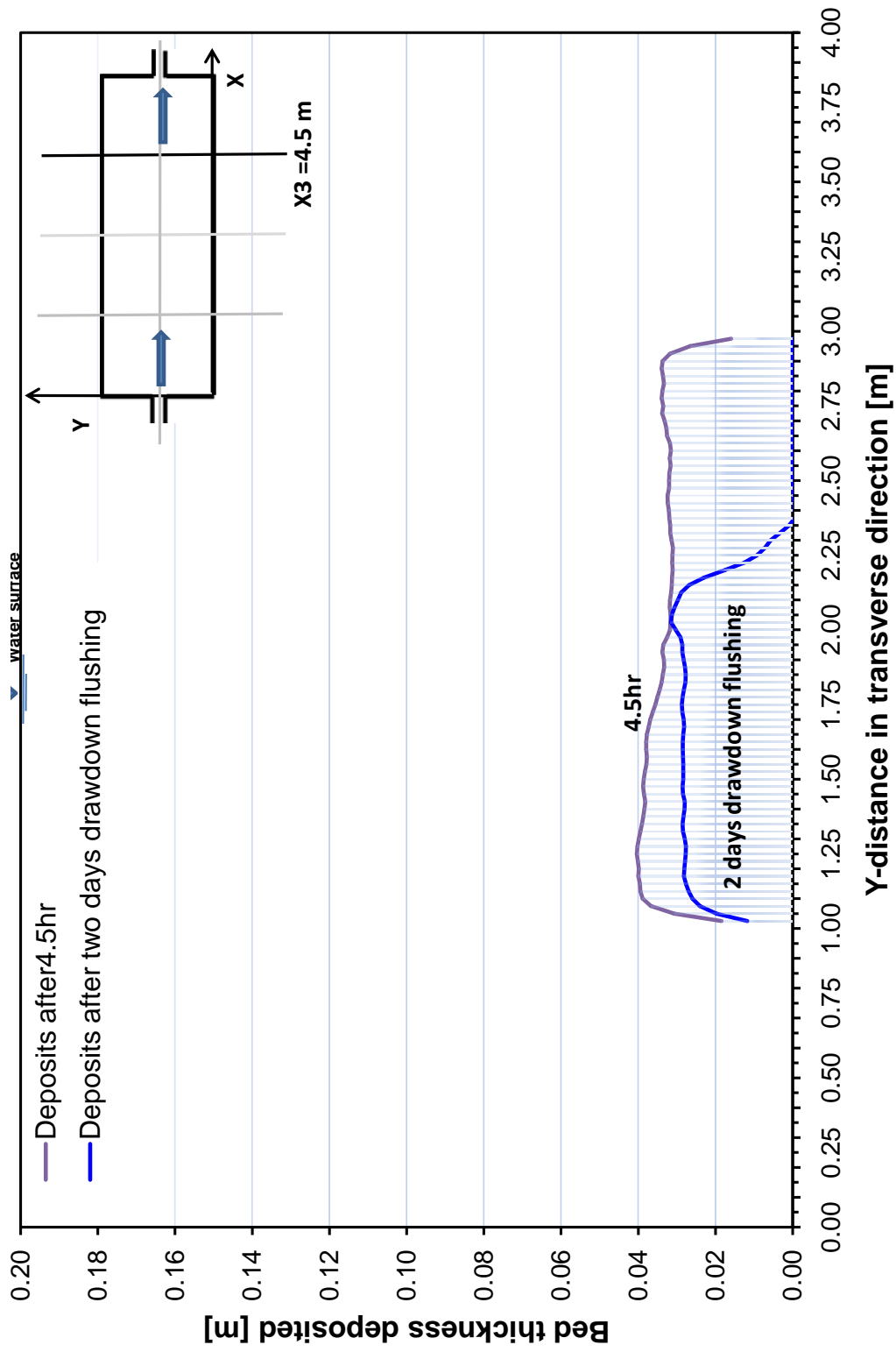


Figure A8.9: Sediment deposits comparison for third and flushing periods run at cross section $X_3 = 4.5\text{m}$ from the entrance

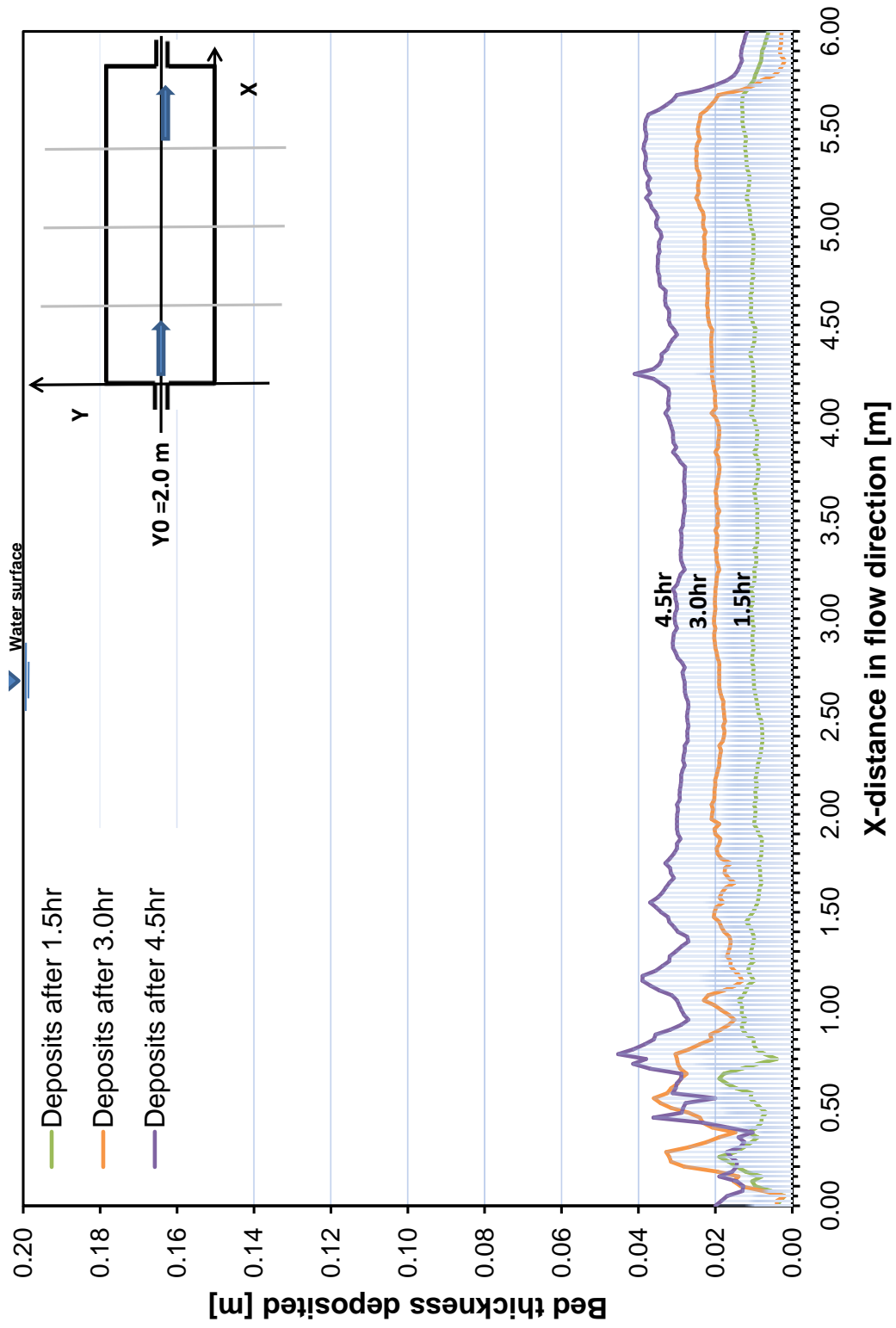
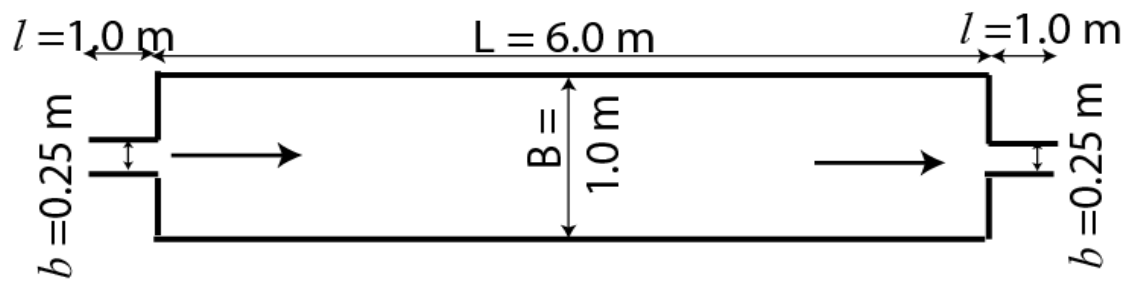


Figure A8.10: Evolution of sediment deposits for three periods runs at centerline longitudinal section $Y = 2.0m$.

A9 Results of rectangular geometry Test9



A9.1 Surface velocity obtained by (LSPIV) measurements with clear water for Test9

Results of flow field with the velocity magnitude and streamlines obtained for the following flow characteristic:

- Discharge $Q = 7.0$ [l/s]
- Water depth $h = 0.2$ [m]
- Froude Number $F_r = 0.1$
- Reynolds number $Re = 28000$

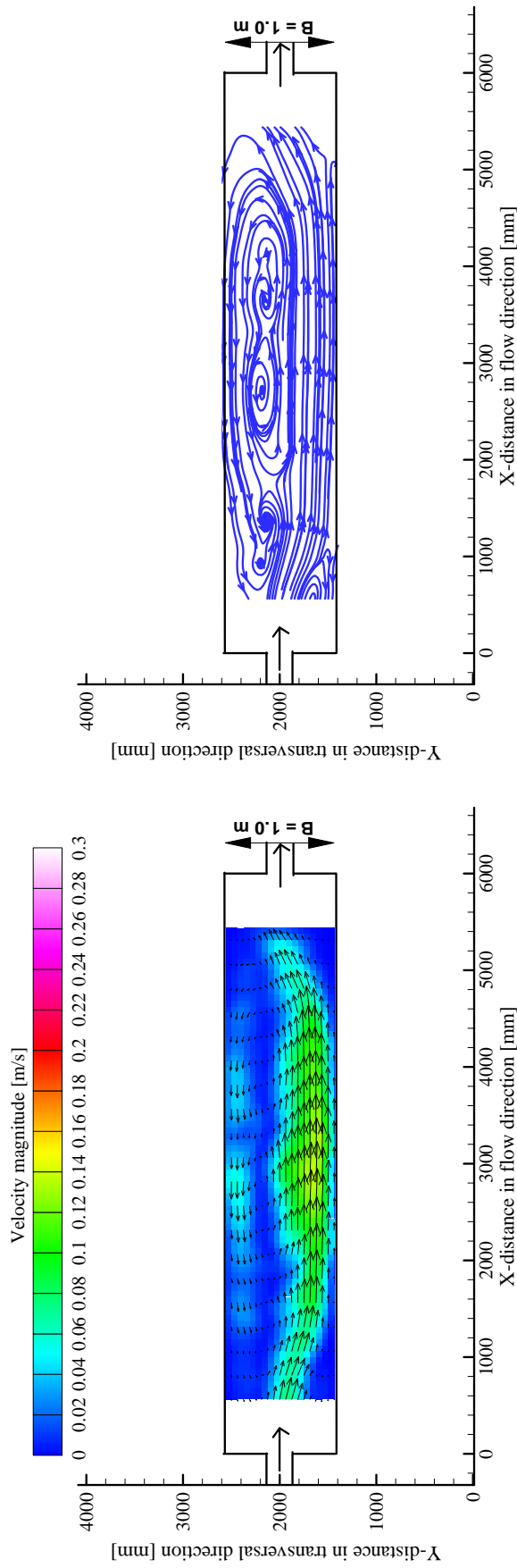
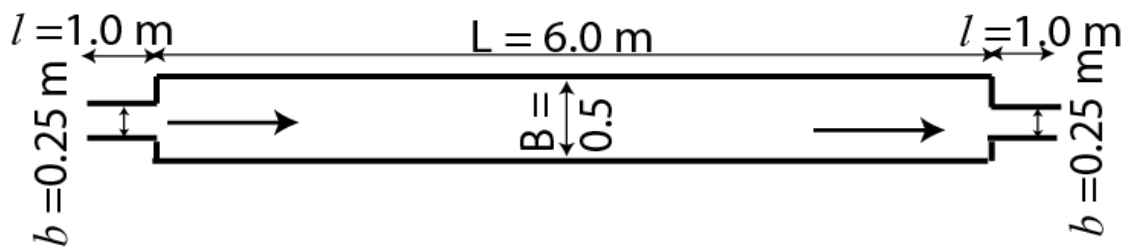


Figure A9.1: Time average flow pattern with velocity vectors (left); streamlines (right) with clear water after stable state

A10 Results of rectangular geometry Test10



A10.1 Surface velocity obtained by (LSPIV) measurements with clear water for Test10

Results of flow field with the velocity magnitude and streamlines obtained for the following flow characteristic:

- Discharge $Q = 7.0 [l/s]$
- Water depth $h = 0.2 [m]$
- Froude Number $F_r = 0.1$
- Reynolds number $Re = 28000$

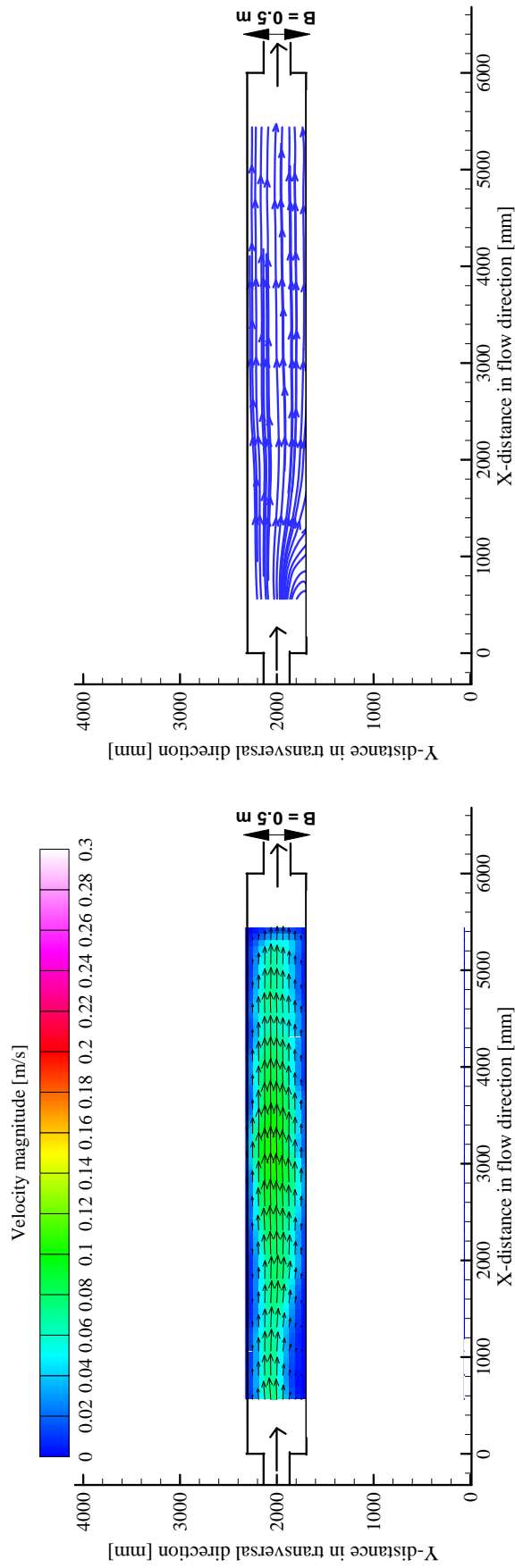
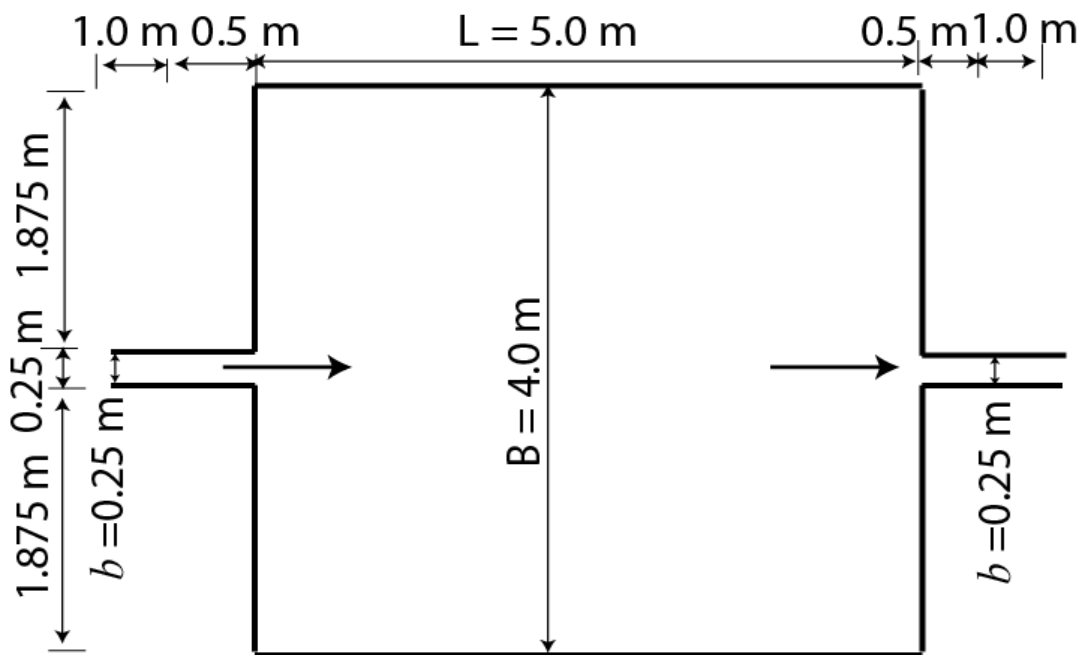


Figure A10.1: Time average flow pattern with velocity vectors (left); streamlines (right) with clear water after stable state

A11 Results of rectangular geometry Test11



A11.1 Surface velocity obtained by (LSPIV) measurements

Results of flow field with the velocity magnitude and streamlines obtained for the following flow and sediment characteristic:

- Discharge $Q = 7.0$ [l/s]
- Water depth $h = 0.2$ [m]
- Froude Number $F_r = 0.1$
- Reynolds number $Re = 28000$
- Sediment diameter $d_{50} = 50$ [μ]
- Sediment density $\rho = 1500$ [kg/m³]
- Suspended sediment concentration $C = 3.0$ [g/l]

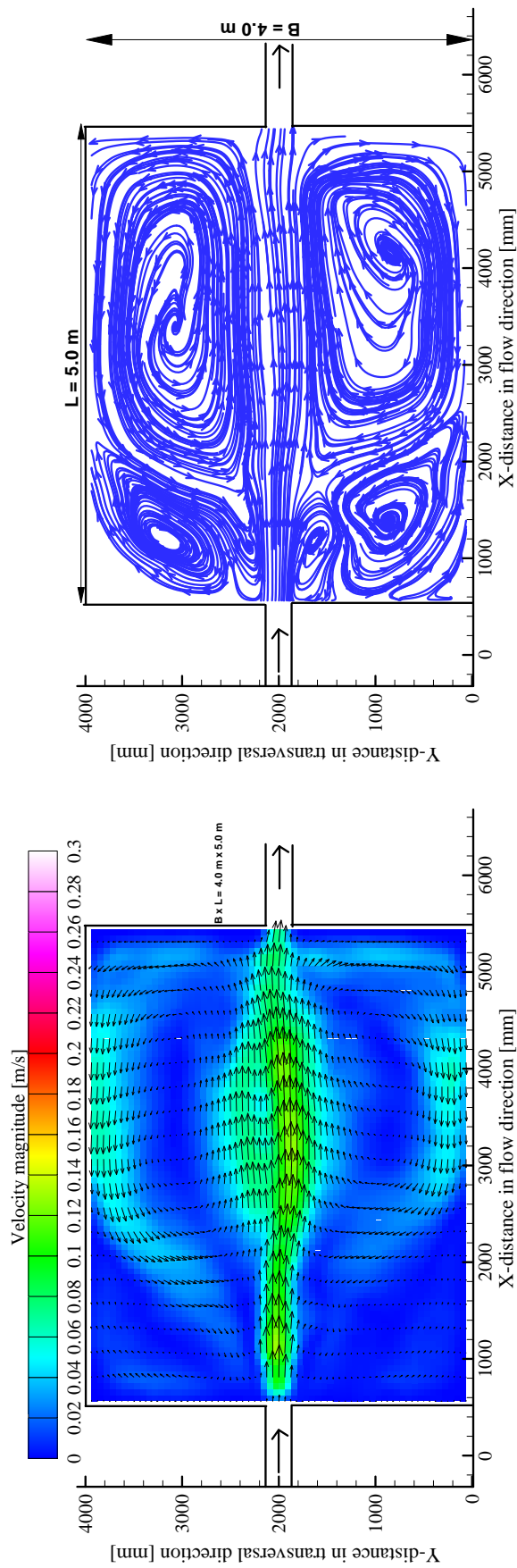


Figure A11.1: Time average flow pattern with velocity vectors (left); streamlines (right) with clear water after stable state

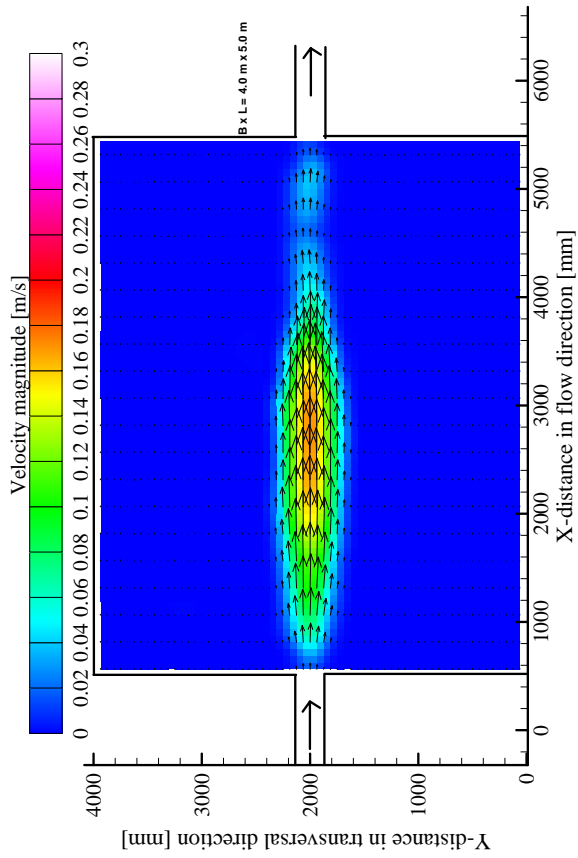


Figure A11.2: Time average flow pattern (left); streamlines (right) after 60 minutes of the third period with sediments

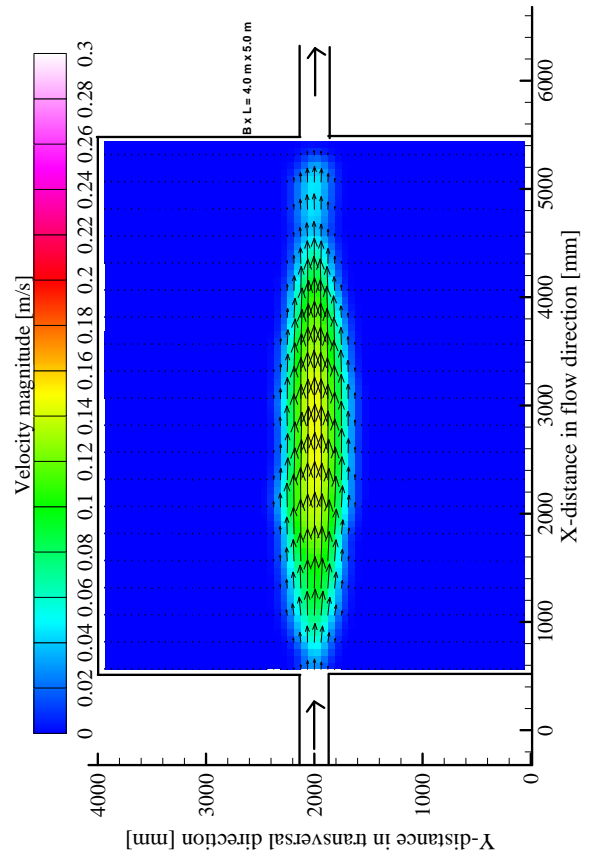


Figure A11.3: Time average flow pattern (left); streamlines (right) after 90 minutes of the third period with sediments

A11.2 Two days flushing with clear water over the final bed deposition of the third period (4.5 hours)

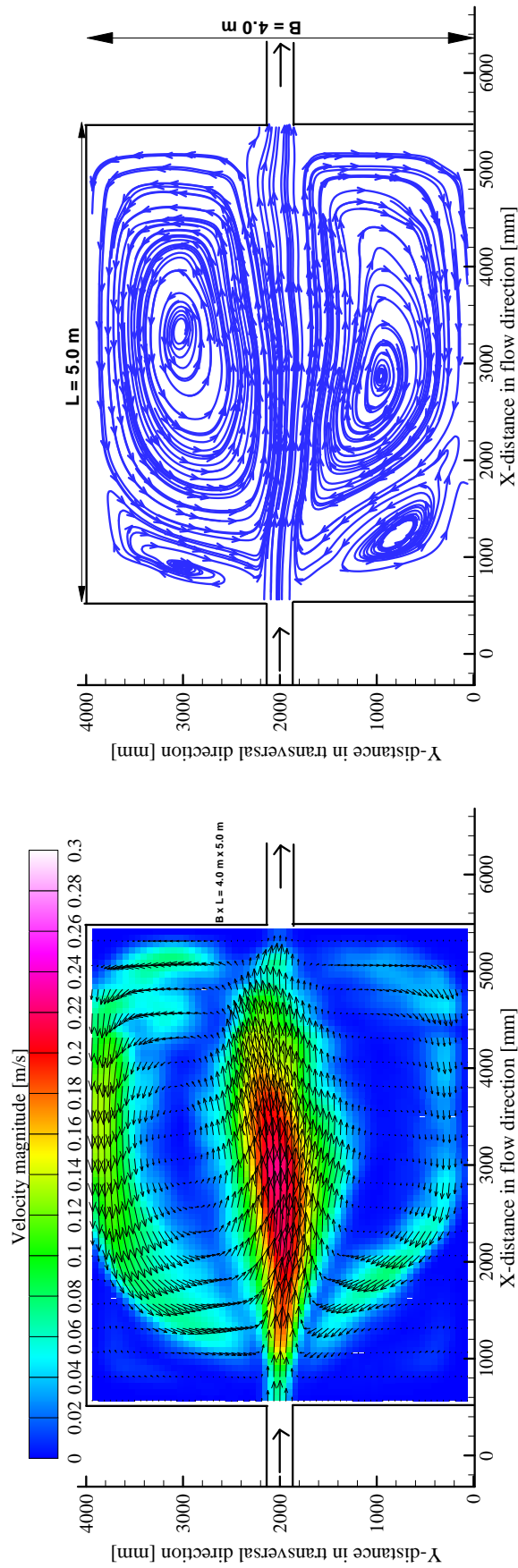


Figure A11.4: Time average flow pattern (left); streamlines (right) of the drawdown flushing with water depth $h = 10 \text{ cm}$

A11.3 Measurements of suspended sediment concentration obtained by turbiditymeter

Results of sediment concentration obtained for the following flow and sediment characteristic:

- Discharge $Q = 7.0$ [l/s]
- Water depth $h = 0.2$ [m]
- Froude Number $F_r = 0.1$
- Reynolds number $Re = 28000$
- Sediment diameter $d_{50} = 50$ [μ]
- Sediment density $\rho = 1500$ [kg/m³]
- Suspended sediment concentration $C = 3.0$ [g/l]

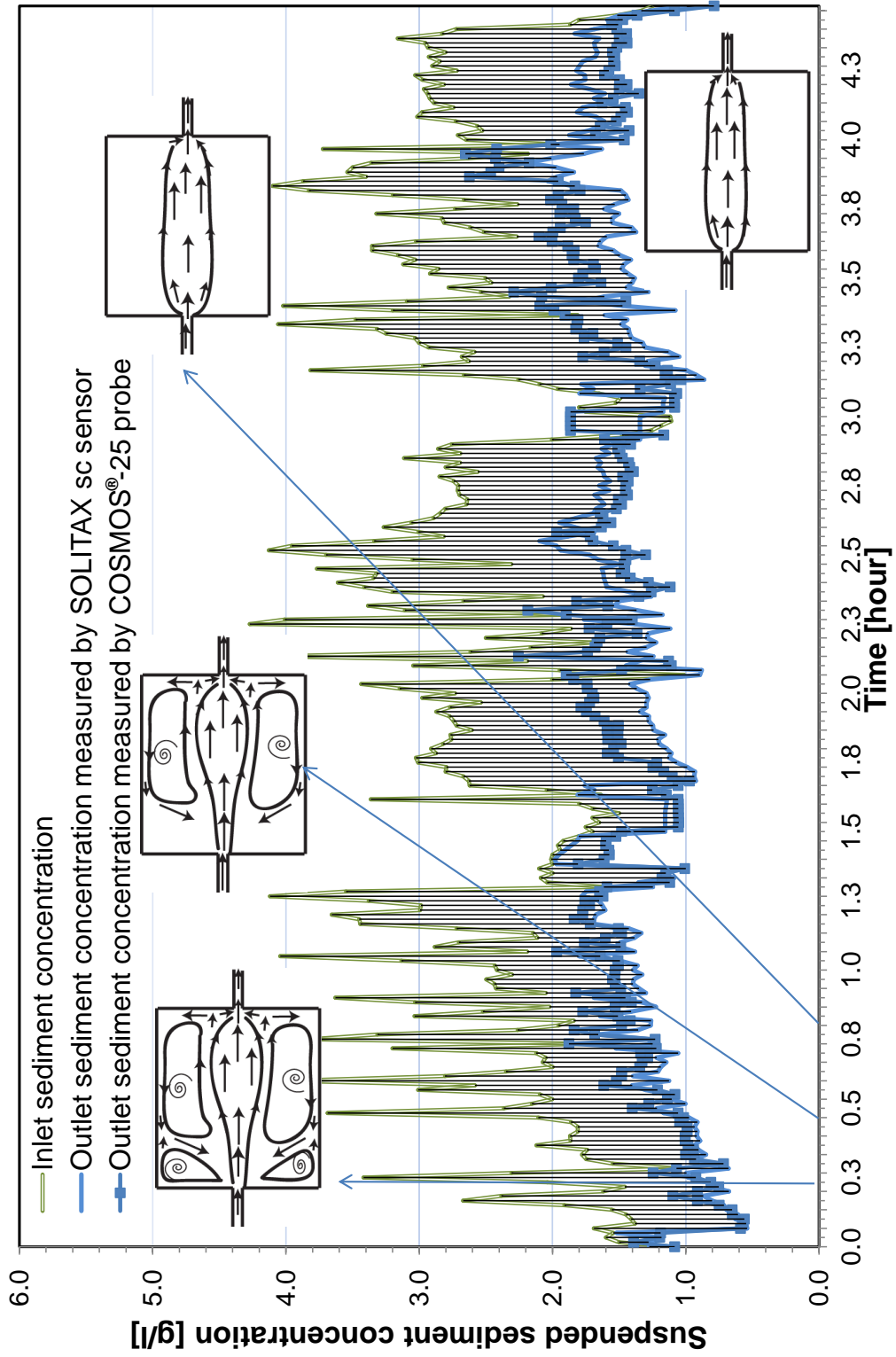


Figure A11.5: Inflow and released suspended concentration of sediments from the reservoir during the first, second and third period of 4.5 hours, measured every minute

A11.4 Measurements of bed thickness deposition obtained by Mini Echo Sounder

Results of morphological evolution obtained for the following flow and sediment characteristic:

- Discharge $Q = 7.0$ [l/s]
- Water depth $h = 0.2$ [m]
- Froude Number $F_r = 0.1$
- Reynolds number $Re = 28000$
- Sediment diameter $d_{50} = 50$ [μ]
- Sediment density $\rho = 1500$ [kg/m^3]
- Suspended sediment concentration $C = 3.0$ [g/l]

A11.4.1 Depositions contours

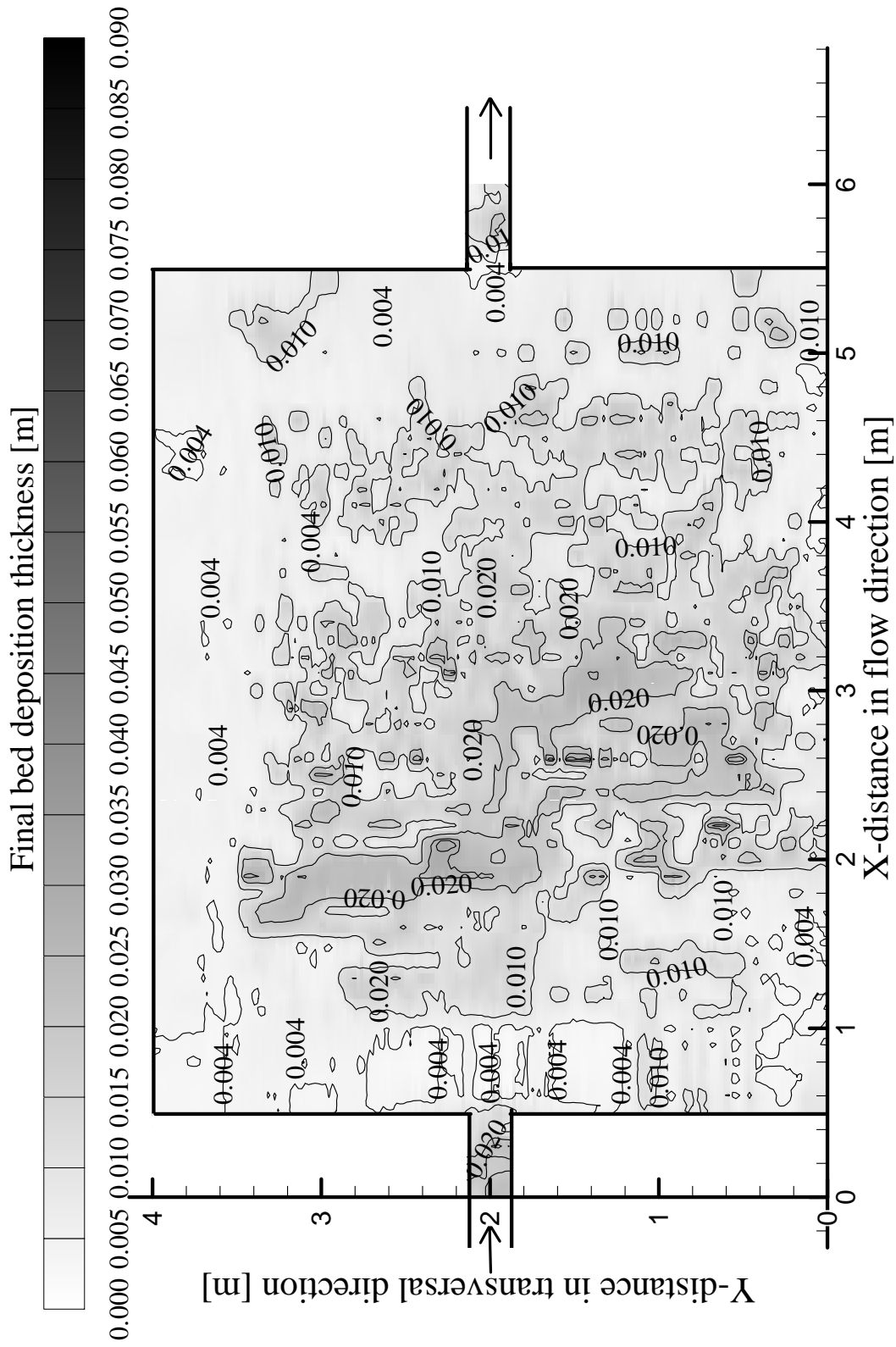
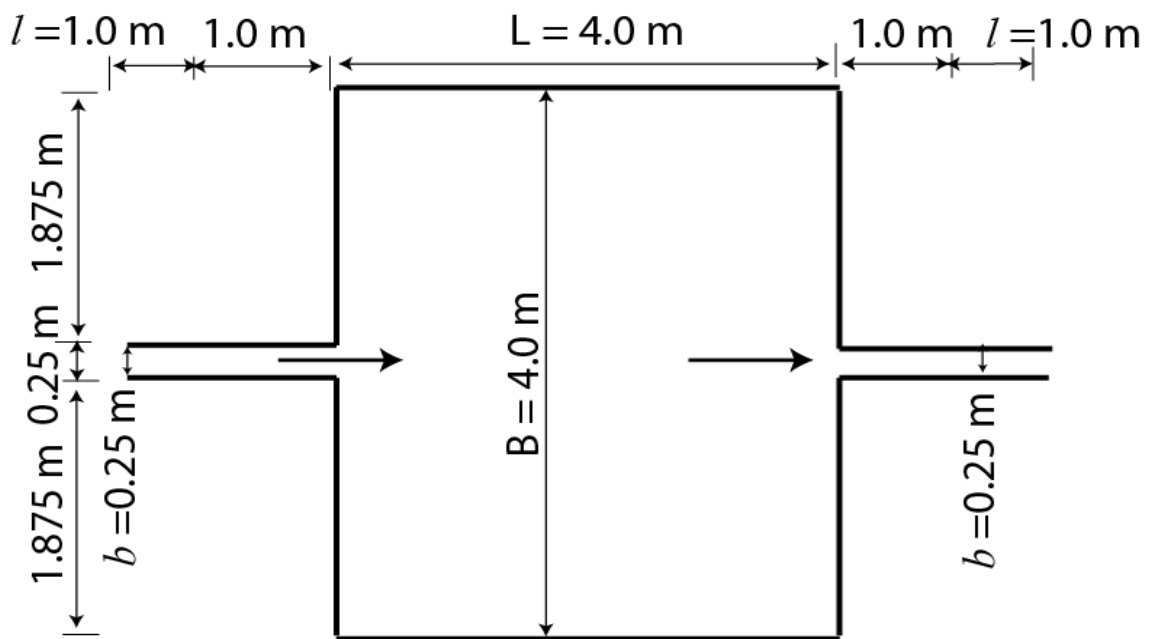


Figure A11.6: Contours of deposition pattern after the first period run after 1.5 hour

A12 Results of rectangular geometry Test12



A12.1 Surface velocity obtained by (LSPIV) measurements with clear water for Test12 (Square geometry)

Results of flow field with the velocity magnitude and streamlines obtained for the following flow characteristic:

- Discharge $Q = 7.0$ [l/s]
- Water depth $h = 0.2$ [m]
- Froude Number $F_r = 0.1$
- Reynolds number $Re = 28000$

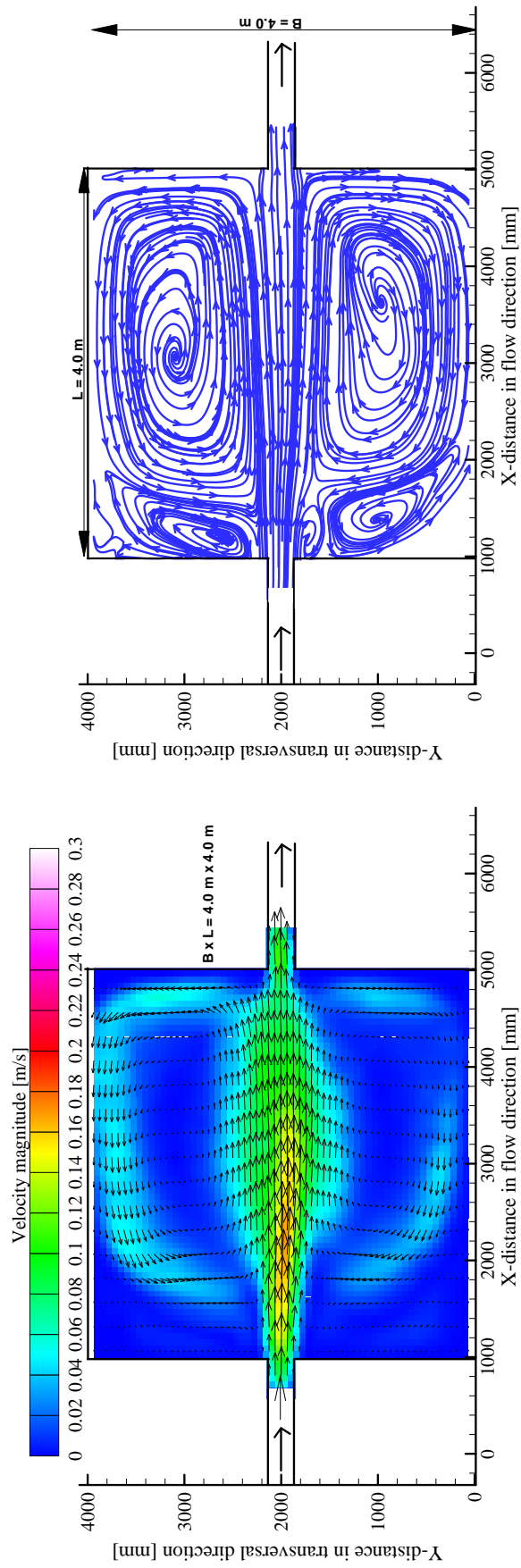
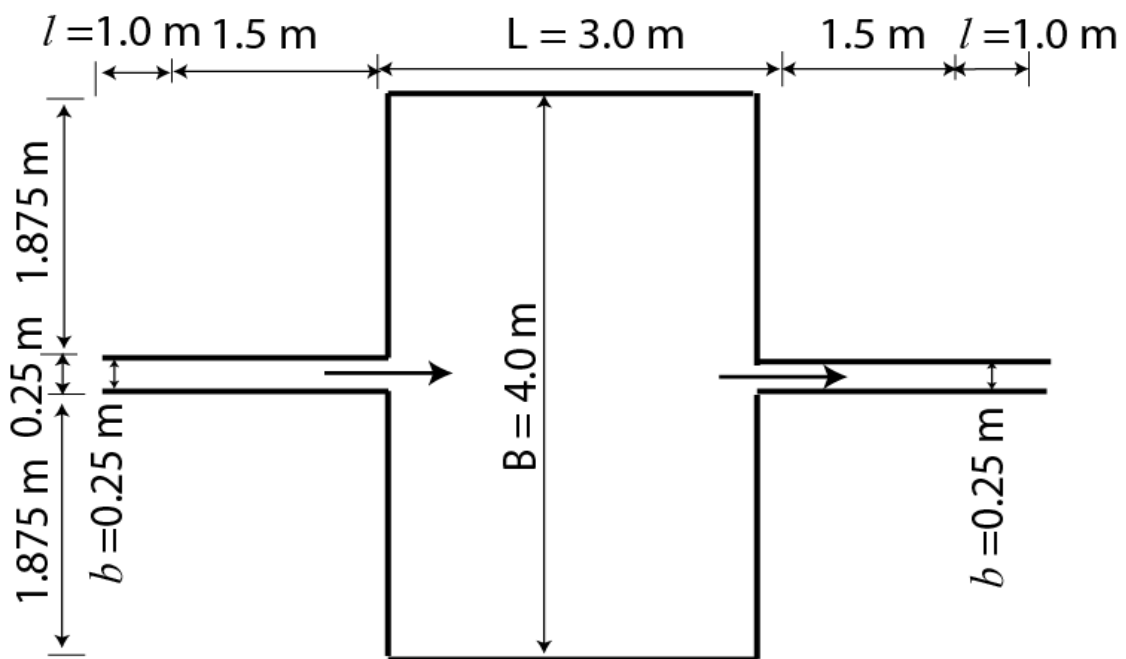


Figure A12.1: Time average flow pattern with velocity vectors (left); streamlines (right) with clear water after stable state for the square geometry (Test12)

A13 Results of rectangular geometry Test13



A13.1 Surface velocity obtained by (LSPIV) measurements

Results of flow field with the velocity magnitude and streamlines obtained for the following flow and sediment characteristic:

- Discharge $Q = 7.0$ [l/s]
- Water depth $h = 0.2$ [m]
- Froude Number $F_r = 0.1$
- Reynolds number $Re = 28000$
- Sediment diameter $d_{50} = 50$ [μ]
- Sediment density $\rho = 1500$ [kg/m³]
- Suspended sediment concentration $C = 3.0$ [g/l]

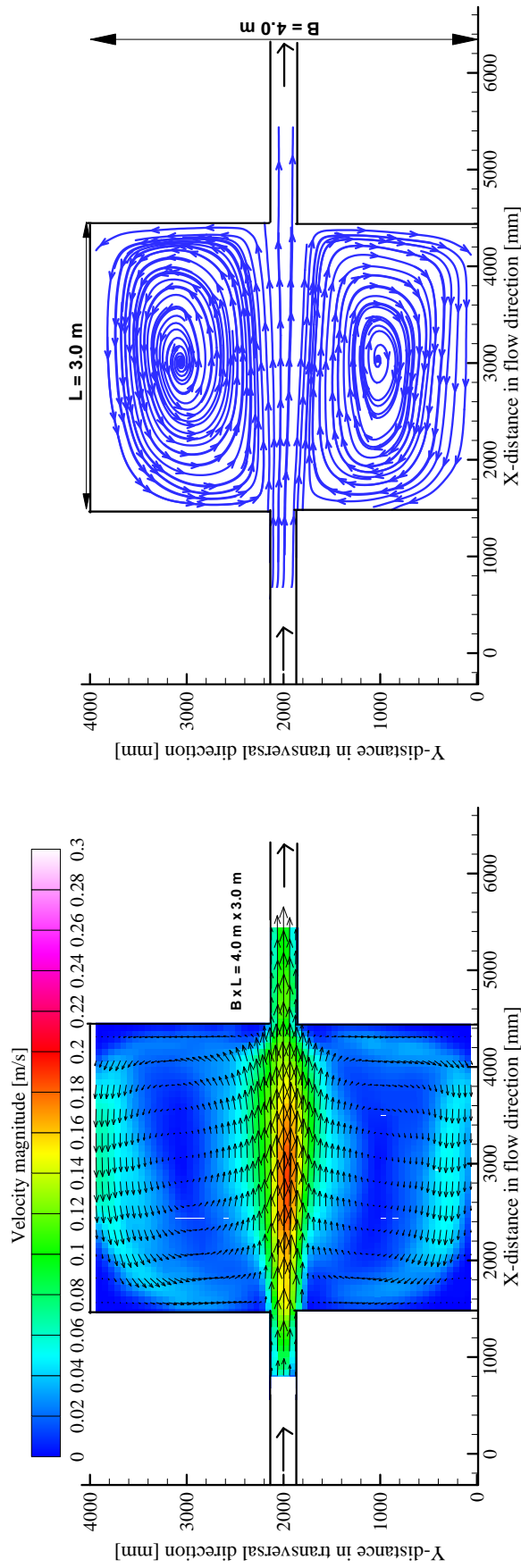


Figure A13.1: Time average flow pattern with velocity vectors (left); streamlines (right) with clear water after stable state

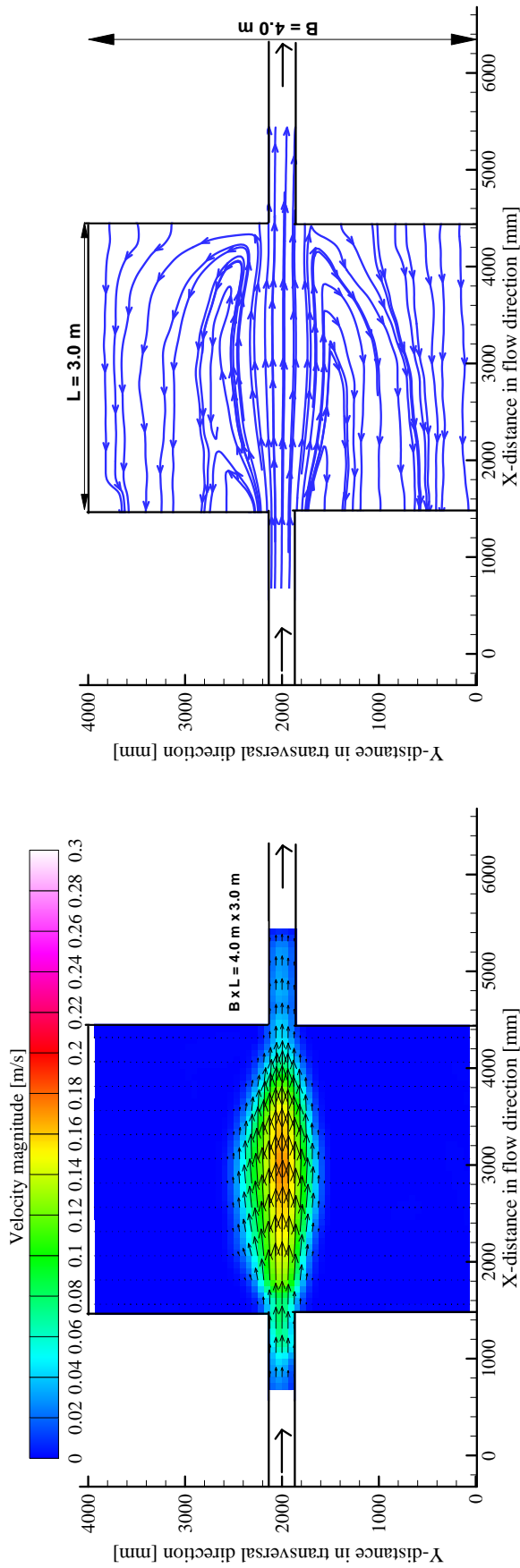


Figure A13.2: Time average flow pattern (left); streamlines (right) after 60 minutes of the third period with sediments

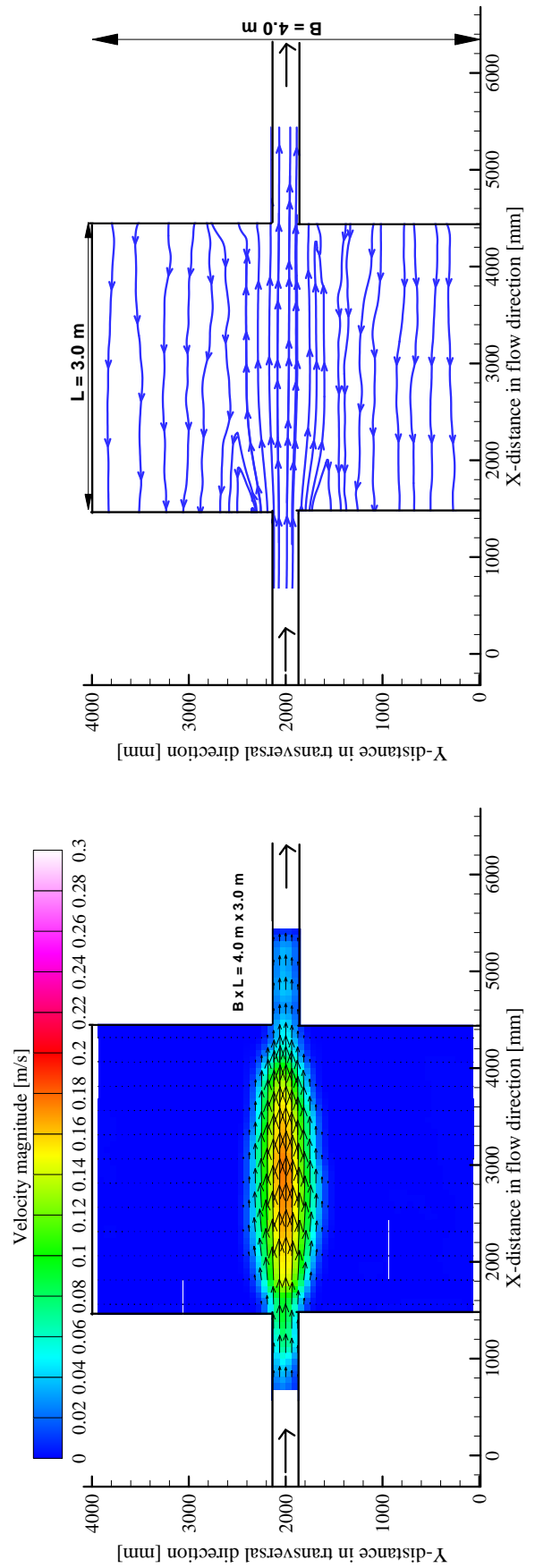


Figure A13.3: Time average flow pattern (left); streamlines (right) after 90 minutes of the third period with sediments

A13.2 Measurements of suspended sediment concentration obtained by turbiditymeter

Results of sediment concentration obtained for the following flow and sediment characteristic:

- Discharge $Q = 7.0$ [l/s]
- Water depth $h = 0.2$ [m]
- Froude Number $F_r = 0.1$
- Reynolds number $Re = 28000$
- Sediment diameter $d_{50} = 50$ [μ]
- Sediment density $\rho = 1500$ [kg/m³]
- Suspended sediment concentration $C = 3.0$ [g/l]

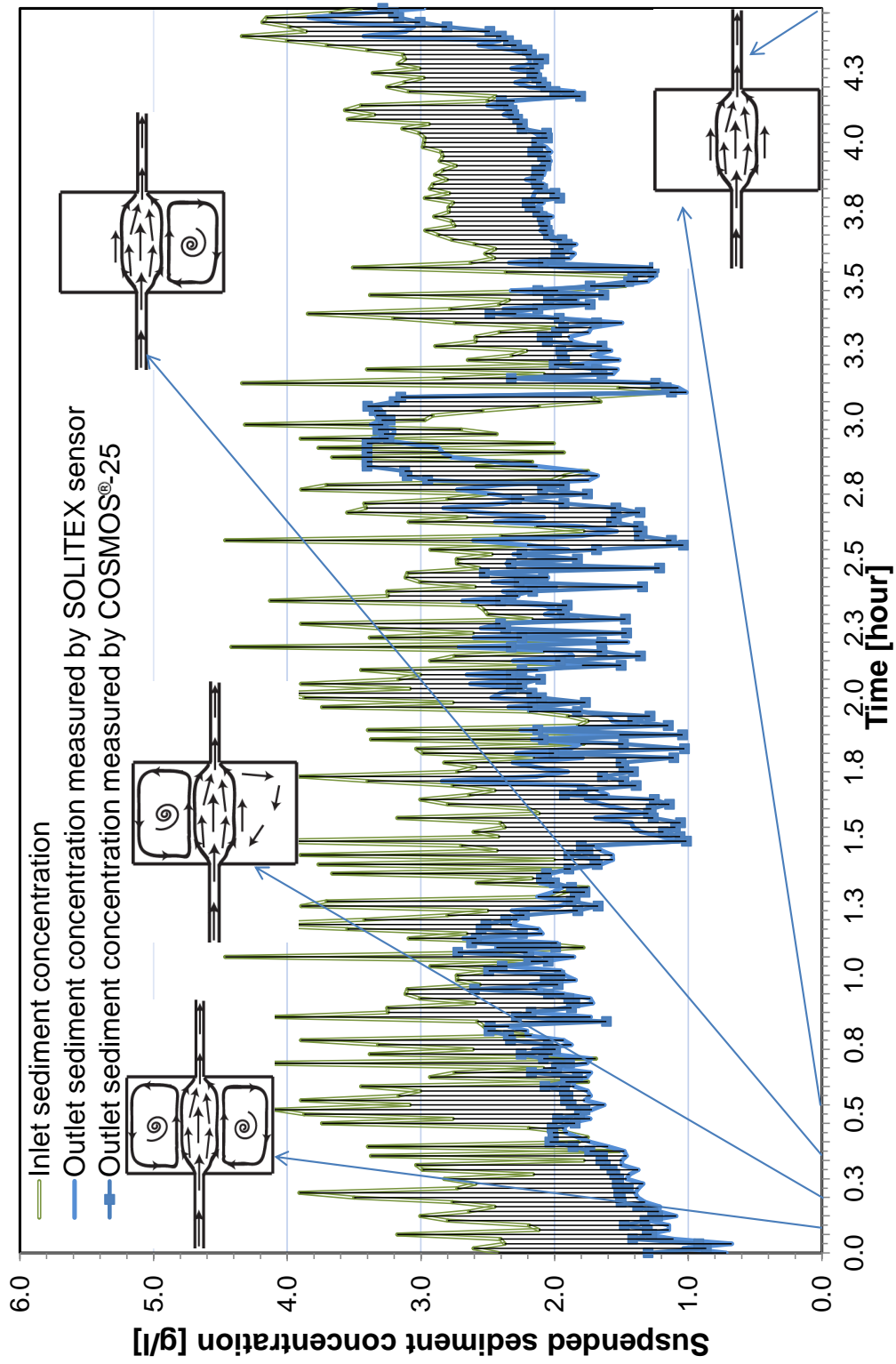


Figure A13.4: Inflow and released suspended concentration of sediments from the reservoir during the first, second and third period of 4.5 hours, measured every minute

A13.3 Measurements of bed thickness deposition obtained by Mini Echo Sounder

Results of morphological evolution obtained for the following flow and sediment characteristic:

- Discharge $Q = 7.0$ [l/s]
- Water depth $h = 0.2$ [m]
- Froude Number $F_r = 0.1$
- Reynolds number $Re = 28000$
- Sediment diameter $d_{50} = 50$ [μ]
- Sediment density $\rho = 1500$ [kg/m^3]
- Suspended sediment concentration $C = 3.0$ [g/l]

A13.3.1 Depositions contours

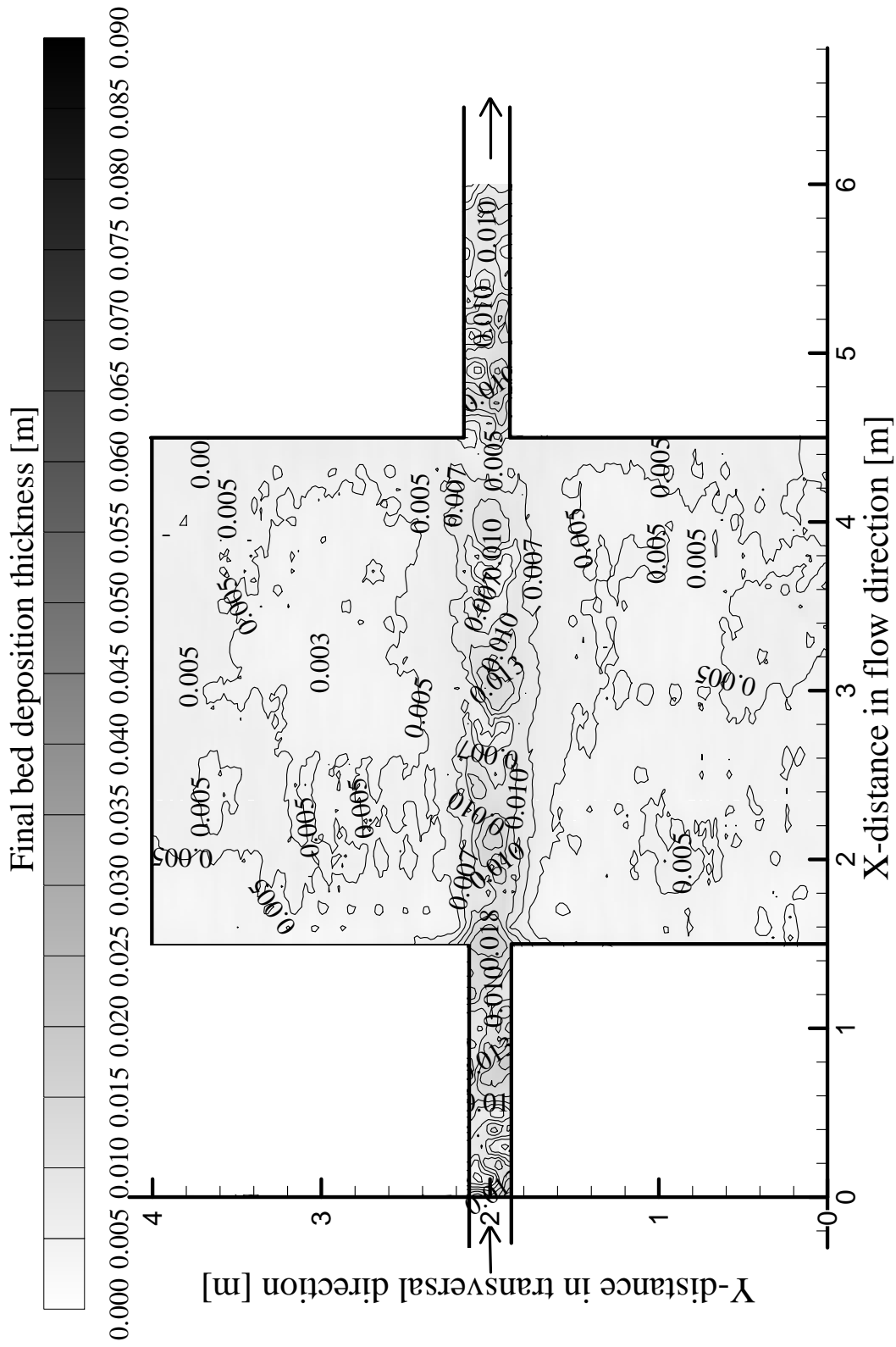


Figure A13.5: Contours of deposition pattern after the first period run after 1.5 hour

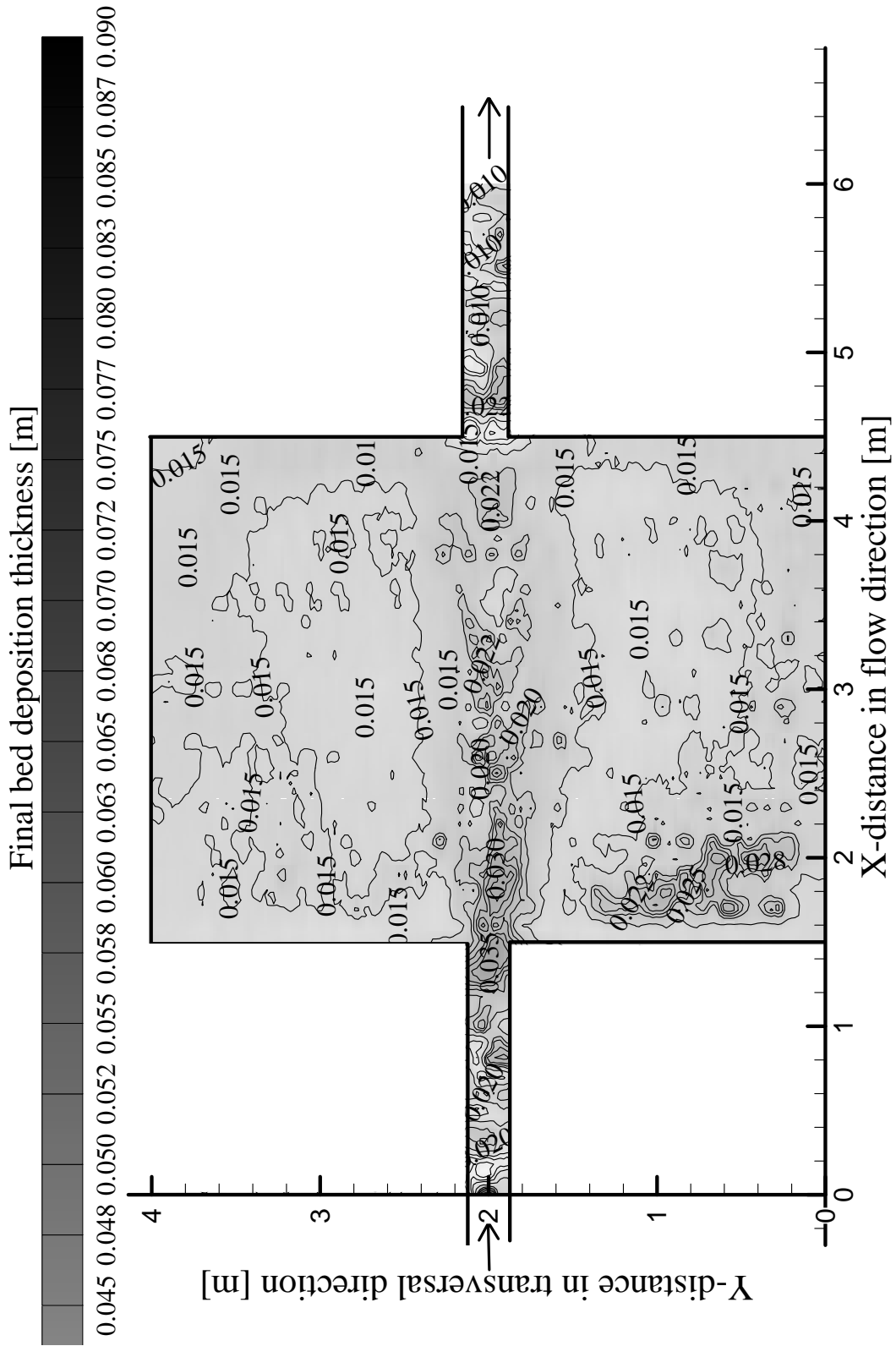
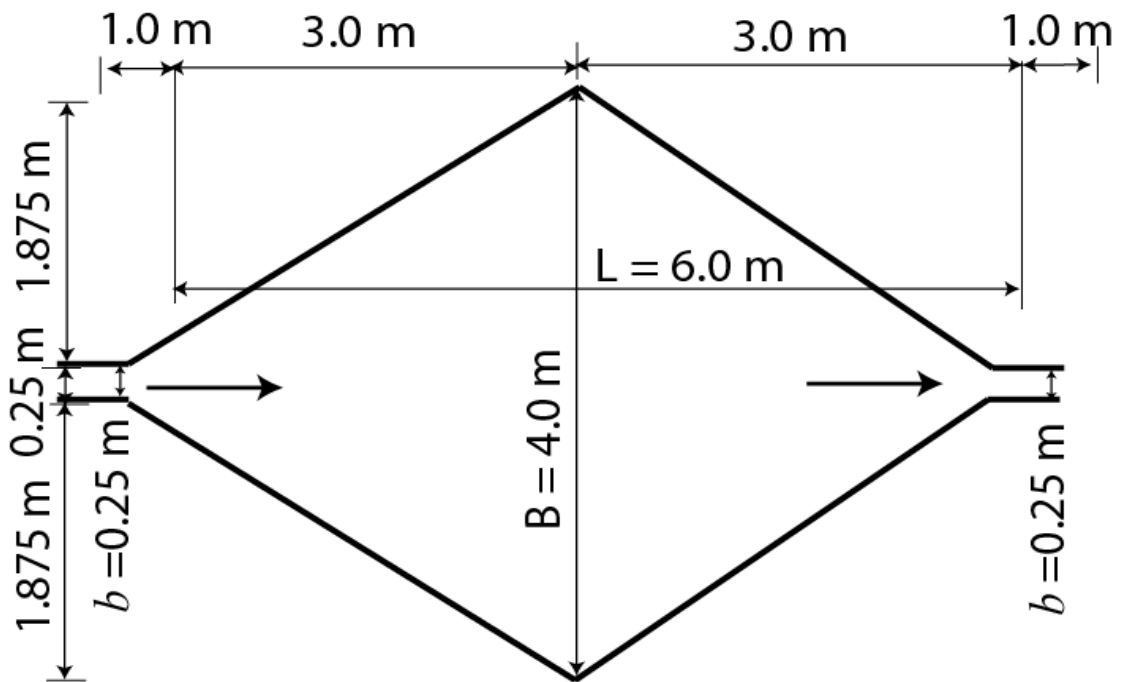


Figure A13.6: Contours of deposition pattern after the second period run after 3.0 hour

A14 Results of rectangular geometry Test14



A14.1 Surface velocity obtained by (LSPIV) measurements

Results of flow field with the velocity magnitude and streamlines obtained for the following flow and sediment characteristic:

- Discharge $Q = 7.0$ [l/s]
- Water depth $h = 0.2$ [m]
- Froude Number $F_r = 0.1$
- Reynolds number $Re = 28000$
- Sediment diameter $d_{50} = 50$ [μ]
- Sediment density $\rho = 1500$ [kg/m³]
- Suspended sediment concentration $C = 3.0$ [g/l]

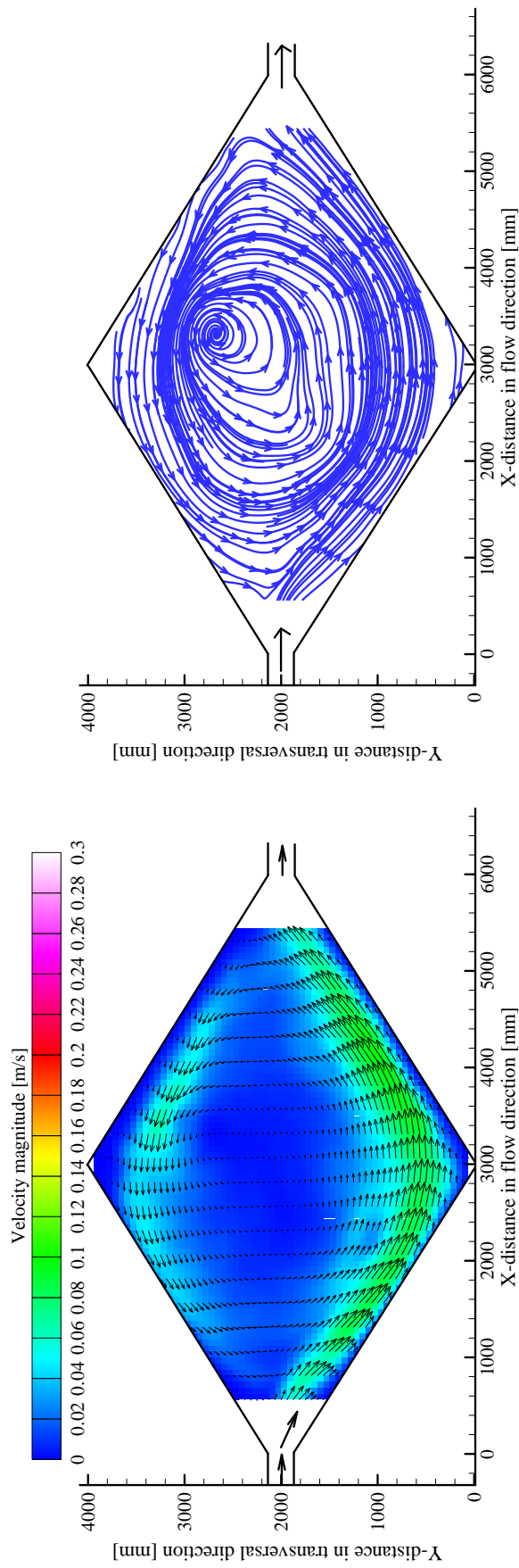


Figure A14.1: Time average flow pattern with velocity vectors (left); streamlines (right) with clear water after stable state

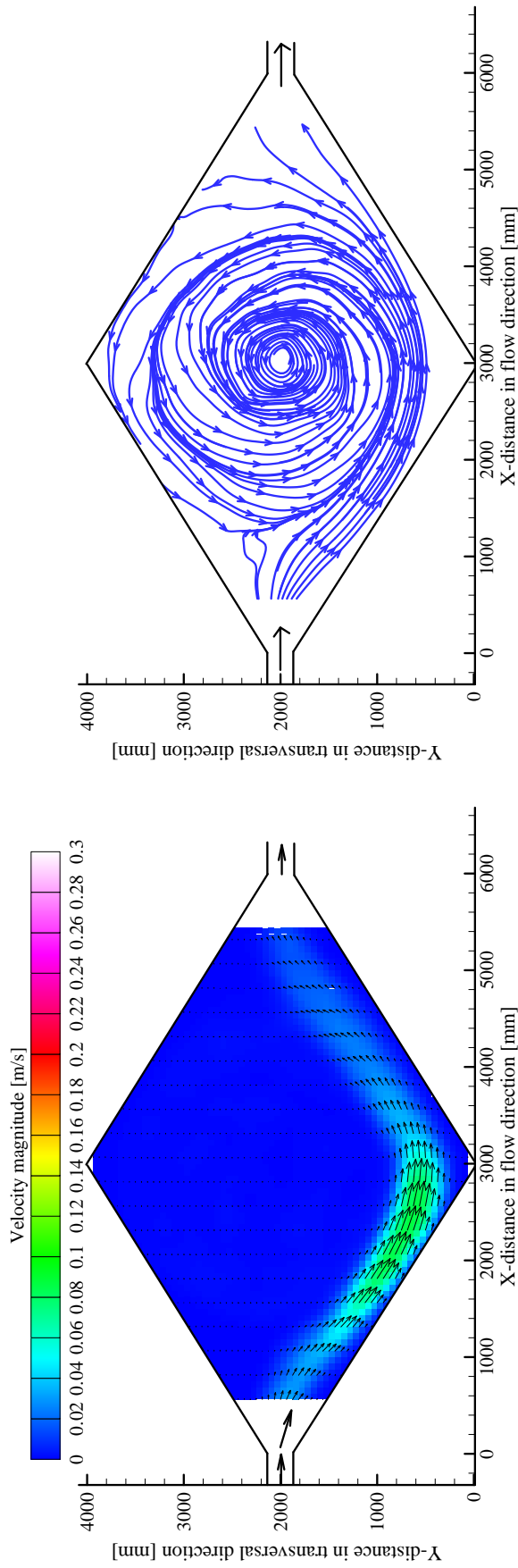


Figure A14.2: Time average flow pattern (left); streamlines (right) after 120 minutes of the fourth period with sediments

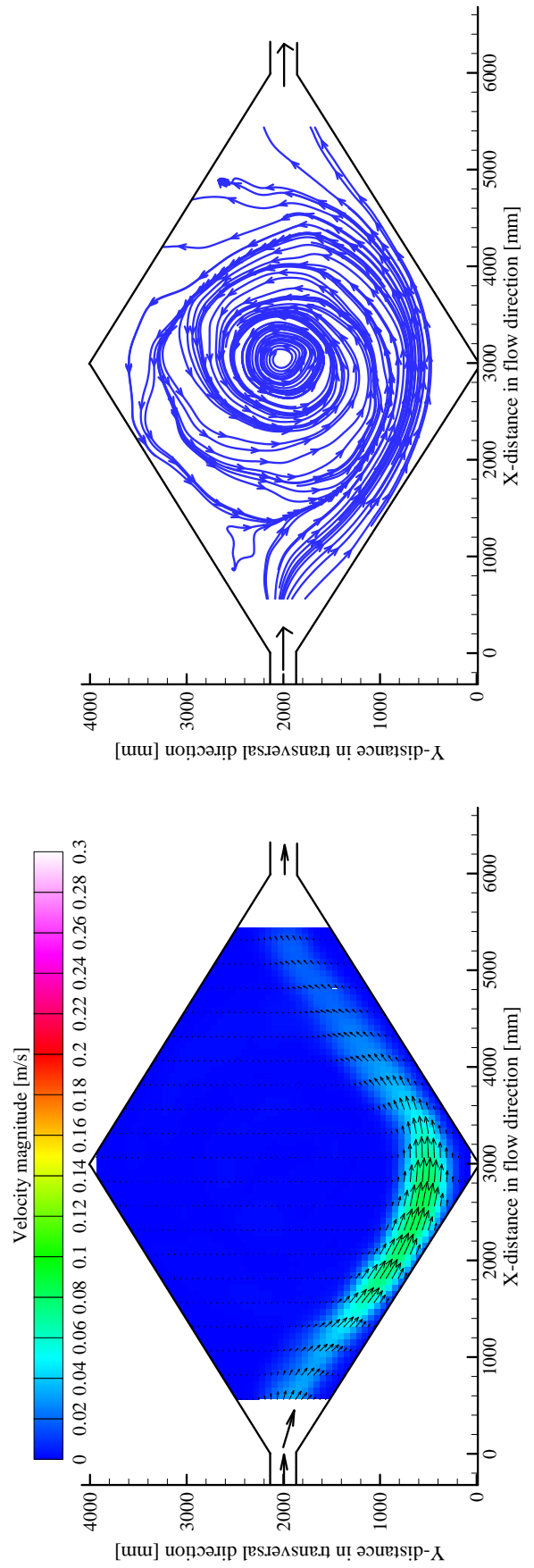


Figure A14.3: Time average flow pattern (left); streamlines (right) after 150 minutes of the fourth period with sediments

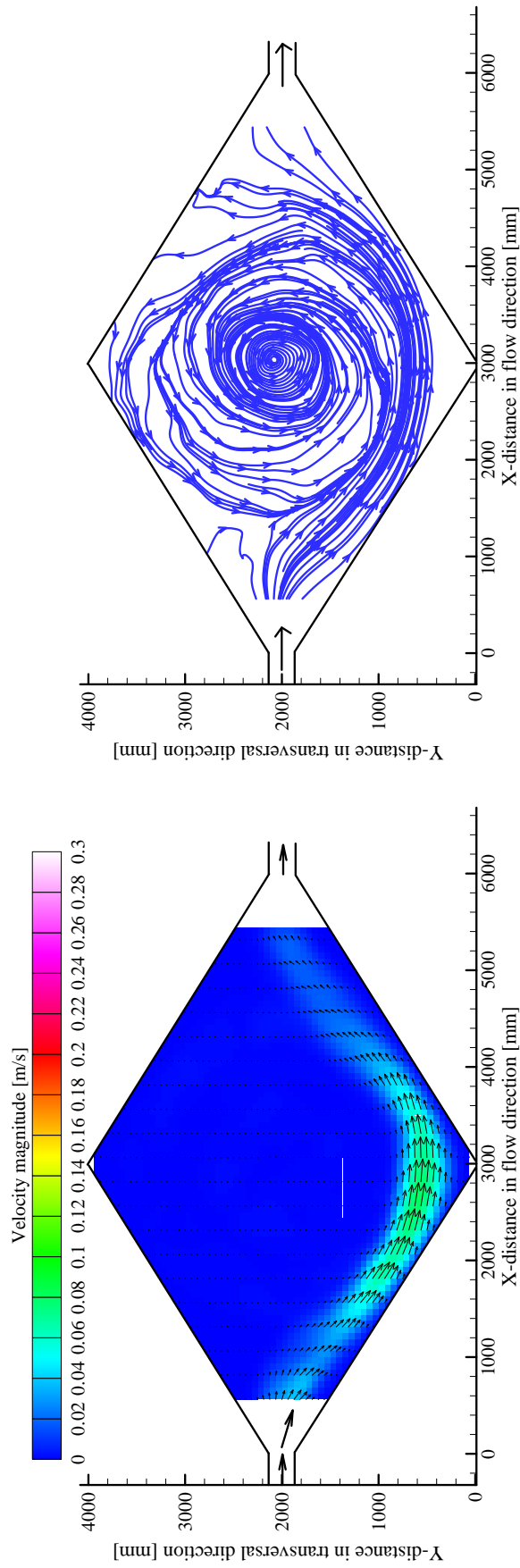


Figure A14.4: Time average flow pattern (left); streamlines (right) after 180 minutes of the fourth period with sediments

A14.2 Two days flushing with clear water over the final bed deposition of the third period (4.5 hours)

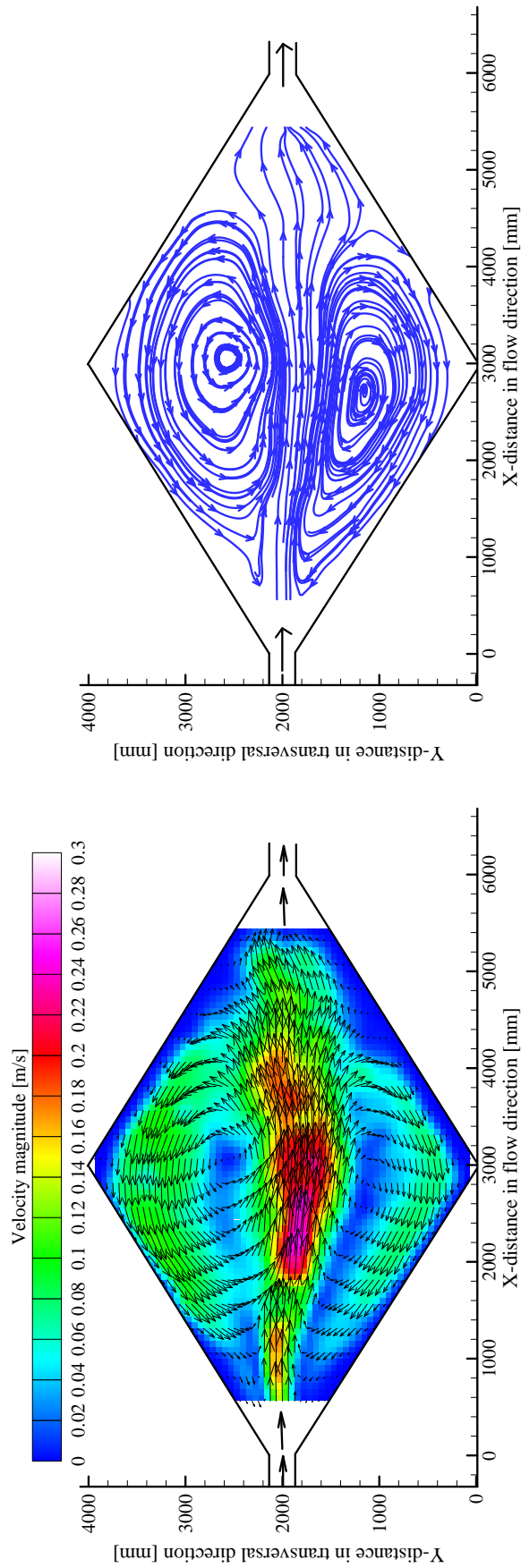


Figure A14.5: Time average flow pattern (left); streamlines (right) of the drawdown flushing with water depth $h = 10\text{cm}$

A14.3 Measurements of suspended sediment concentration obtained by turbiditymeter

Results of sediment concentration obtained for the following flow and sediment characteristic:

- Discharge $Q = 7.0$ [l/s]
- Water depth $h = 0.2$ [m]
- Froude Number $F_r = 0.1$
- Reynolds number $Re = 28000$
- Sediment diameter $d_{50} = 50$ [μ]
- Sediment density $\rho = 1500$ [kg/m^3]
- Suspended sediment concentration $C = 3.0$ [g/l]

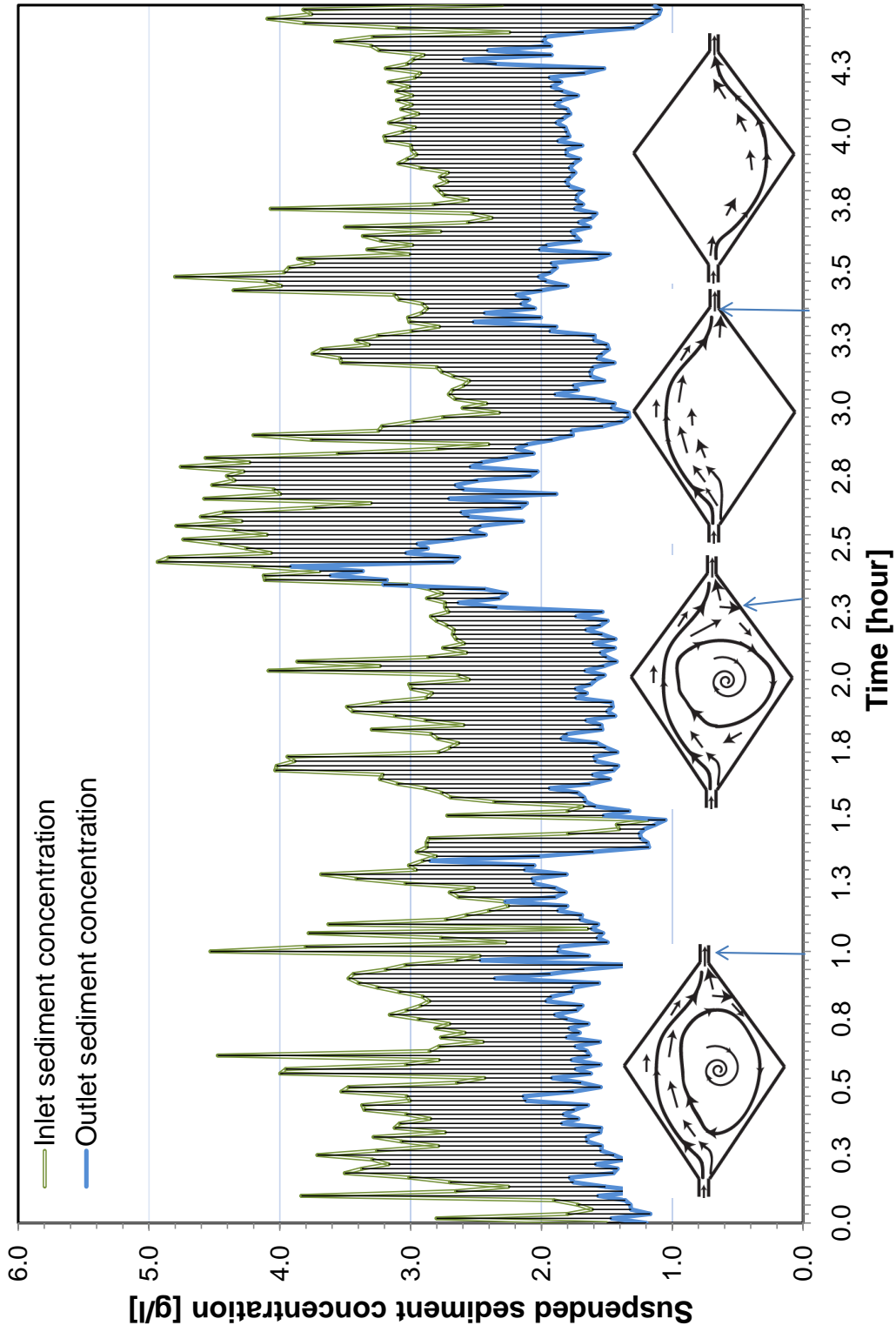


Figure A14.6: Inflow and released suspended concentration of sediments from the reservoir during the first, second and third period of 4.5 hours, measured every minute

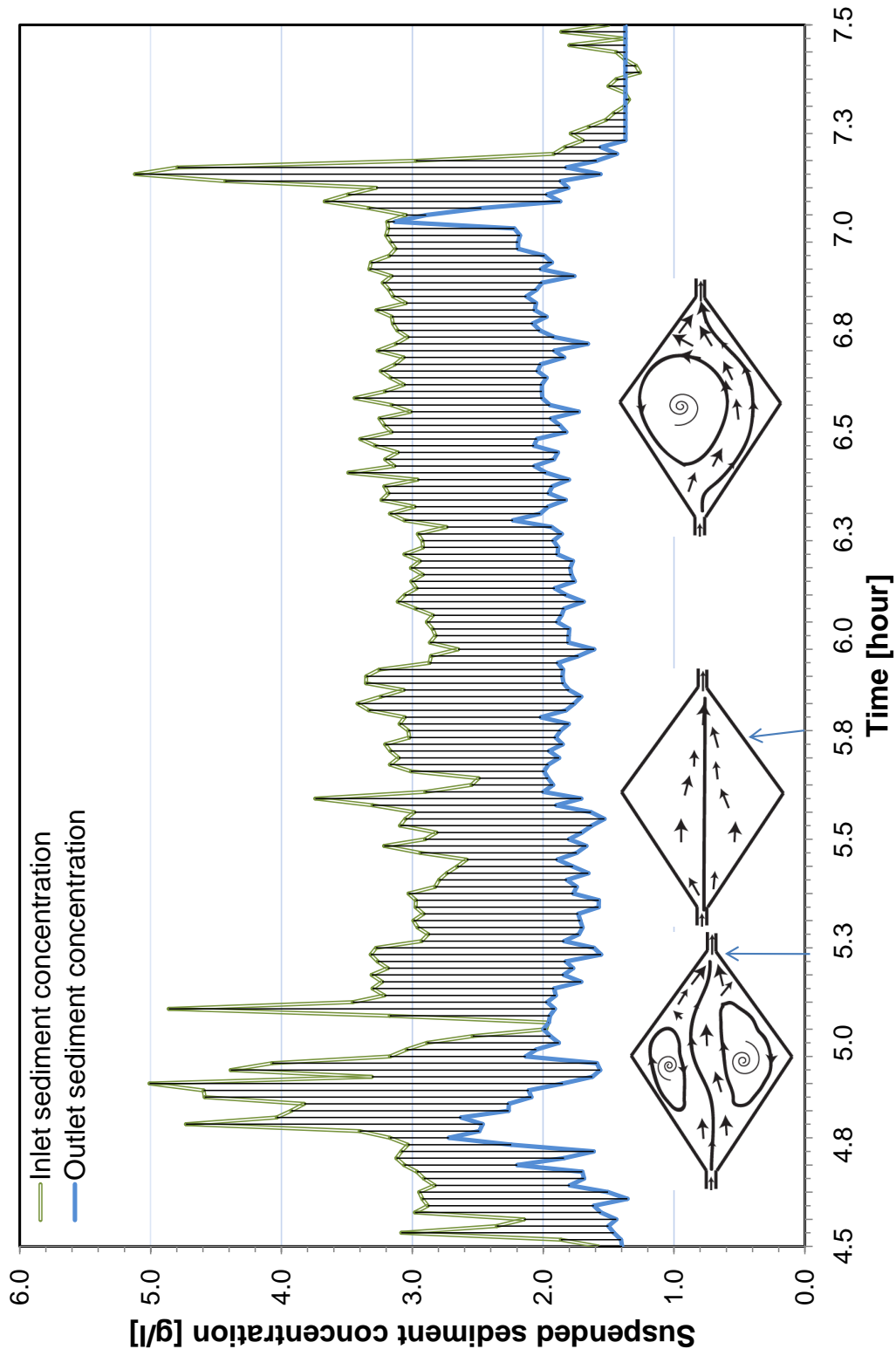


Figure A14.7: Inflow and released suspended concentration of sediments from the reservoir during the fourth period of 3.0hours, measured every minute

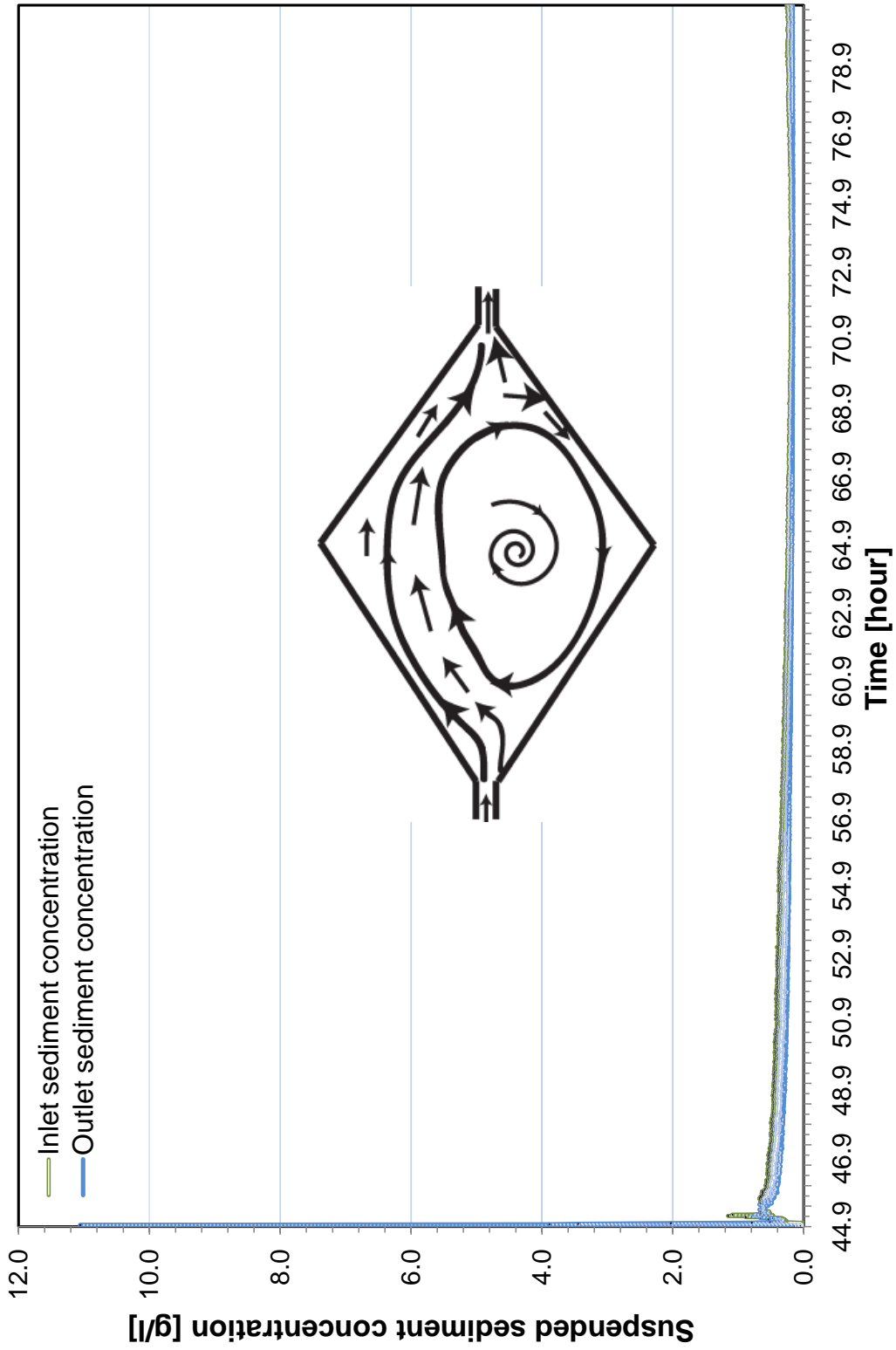


Figure A14.8: Inflow and released suspended concentration of sediments from the reservoir during the flushing period of 48hours, measured every minute

A14.4 Measurements of bed thickness deposition obtained by Mini Echo Sounder

Results of morphological evolution obtained for the following flow and sediment characteristic:

- Discharge $Q = 7.0$ [l/s]
- Water depth $h = 0.2$ [m]
- Froude Number $F_r = 0.1$
- Reynolds number $Re = 28000$
- Sediment diameter $d_{50} = 50$ [μ]
- Sediment density $\rho = 1500$ [kg/m^3]
- Suspended sediment concentration $C = 3.0$ [g/l]

A14.4.1 Depositions contours

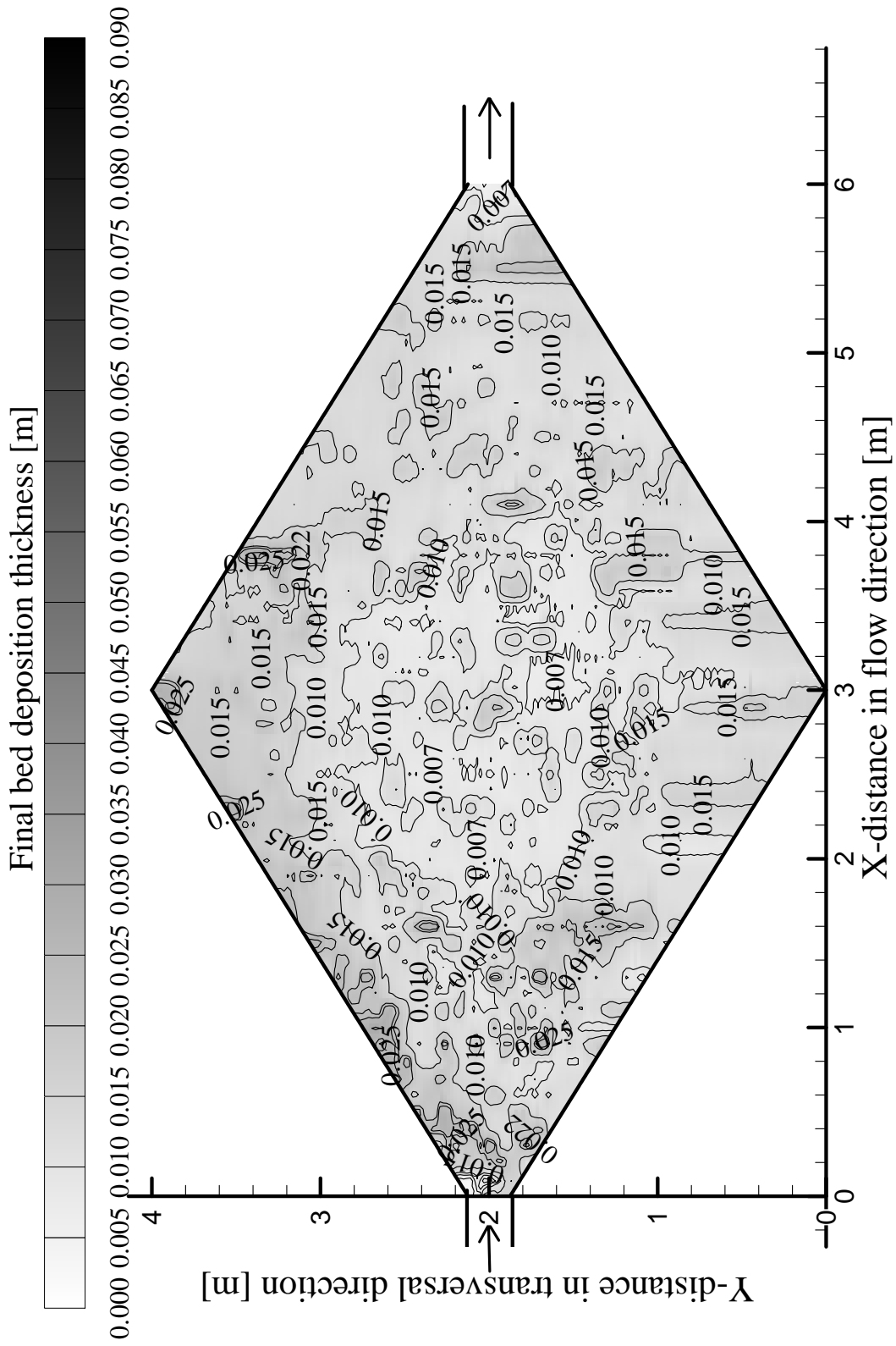


Figure A14.9: Contours of deposition pattern after the first period run after 1.5 hour

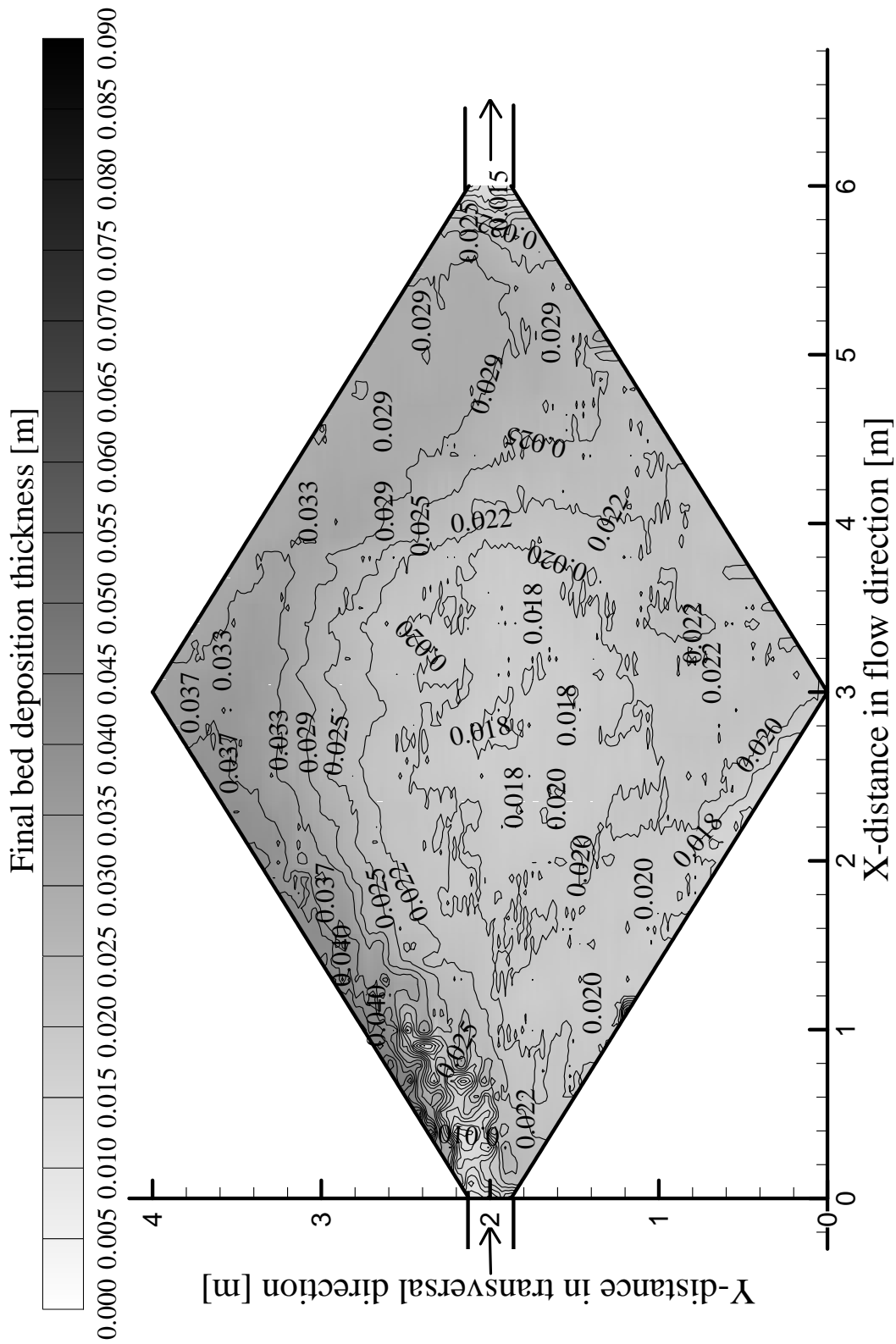


Figure A14.10: Contours of deposition pattern after the second period run after 3.0 hour

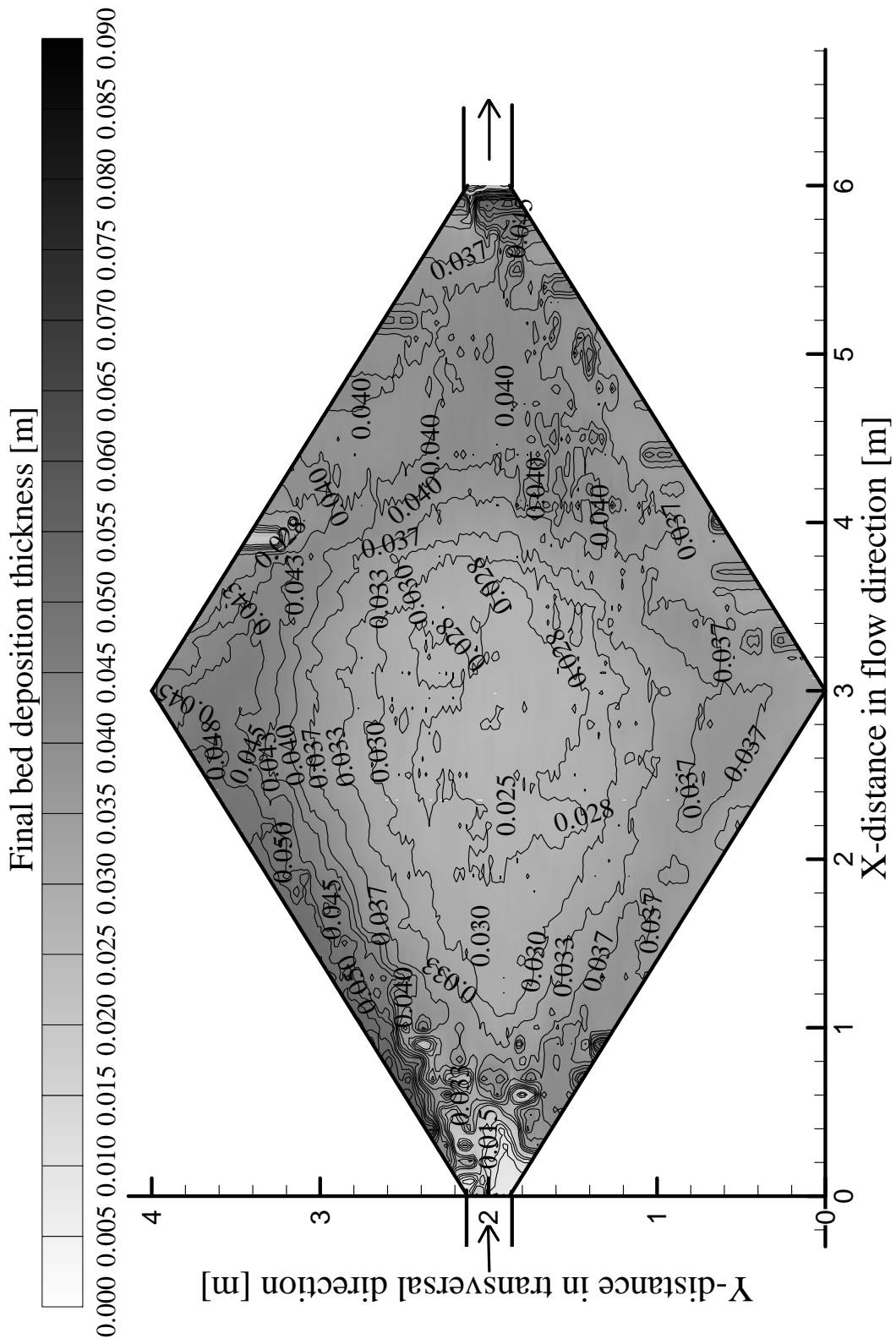


Figure A14.11: Contours of deposition pattern after the third period run after 4.5 hour

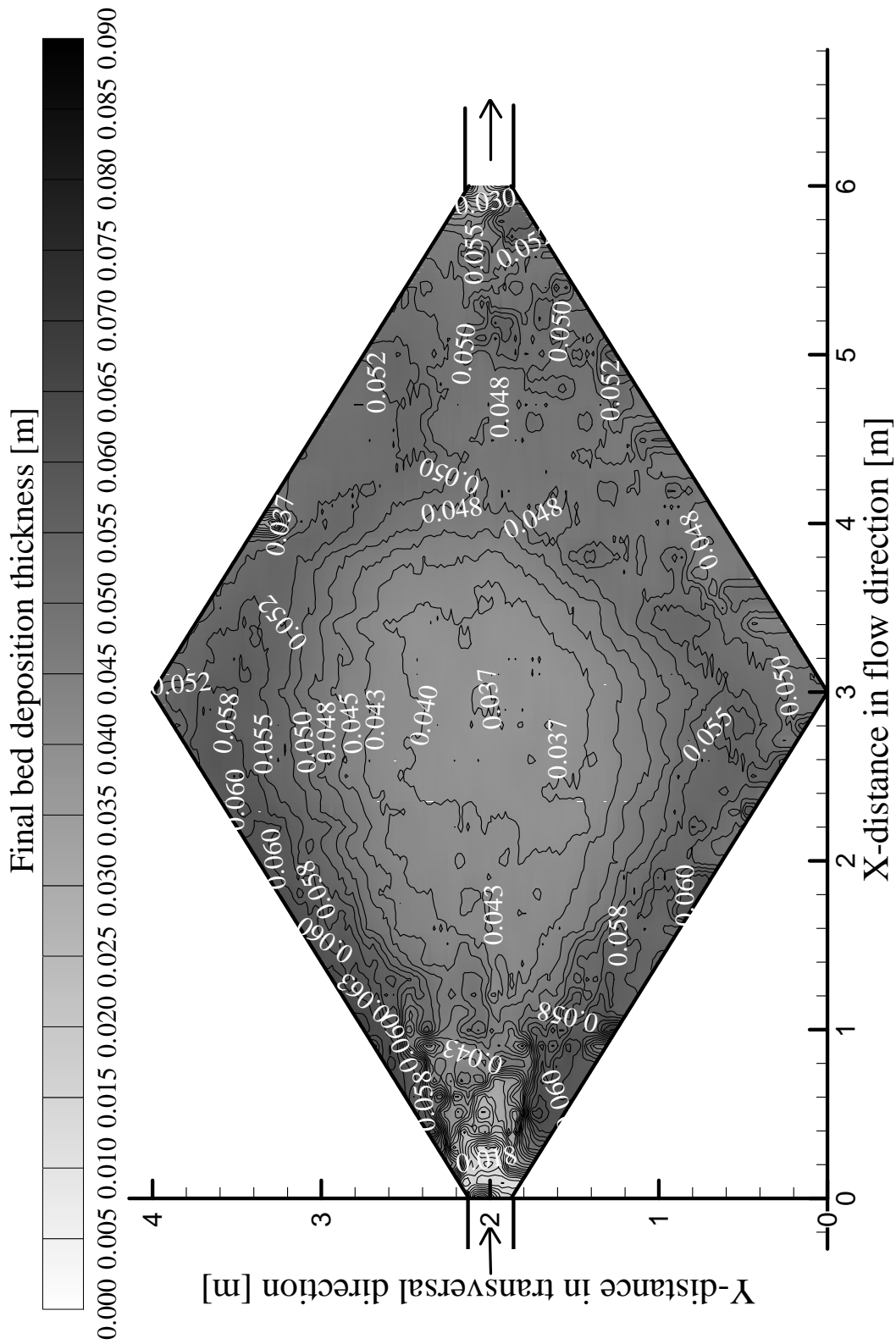


Figure A14.12: Contours of deposition pattern after the fourth period run after 7.5 hour

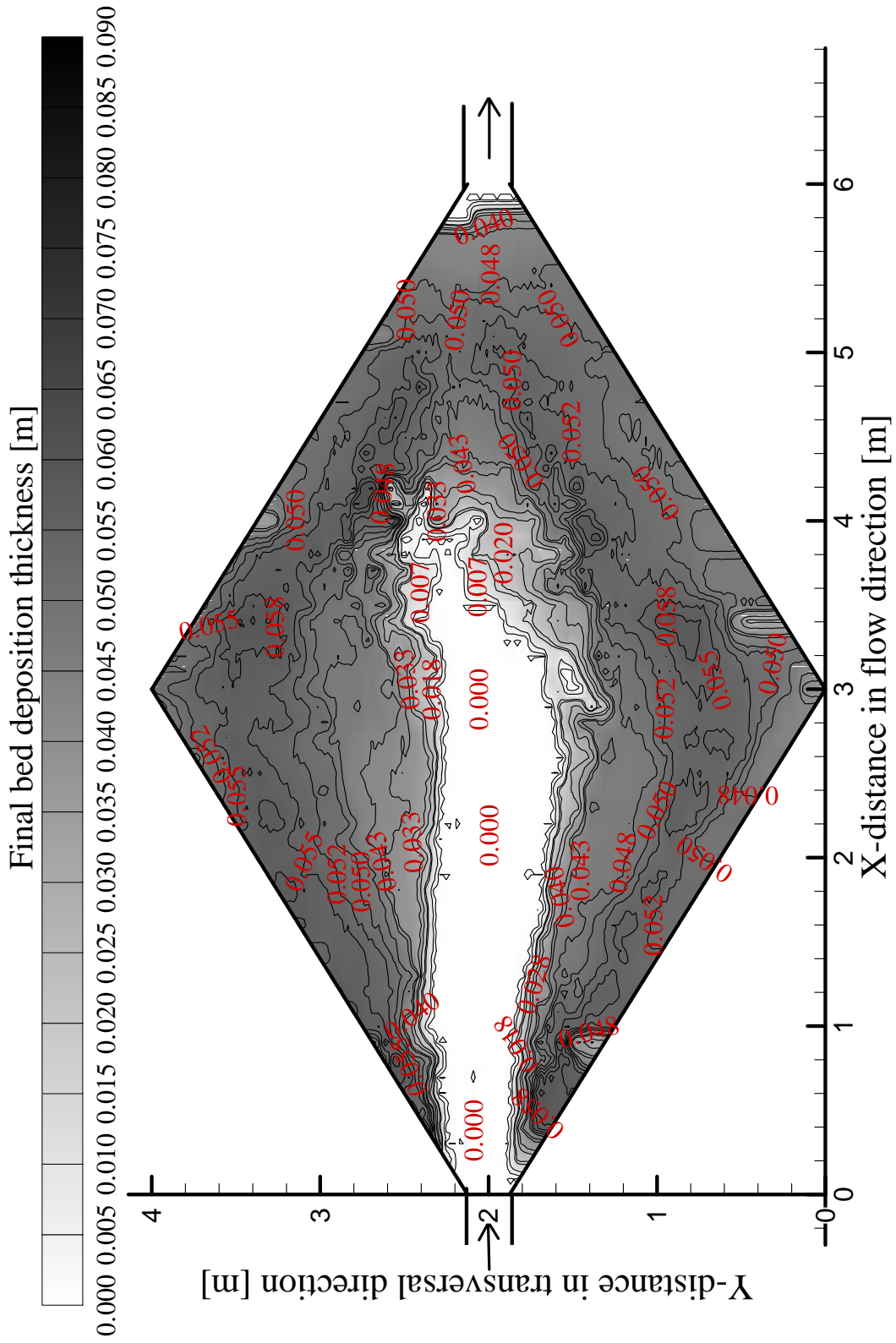


Figure A14.13: Contours of deposition pattern for the drawdown flushing period run after 48 hour

A14.4.2 Bed thickness cross and longitudinal sections

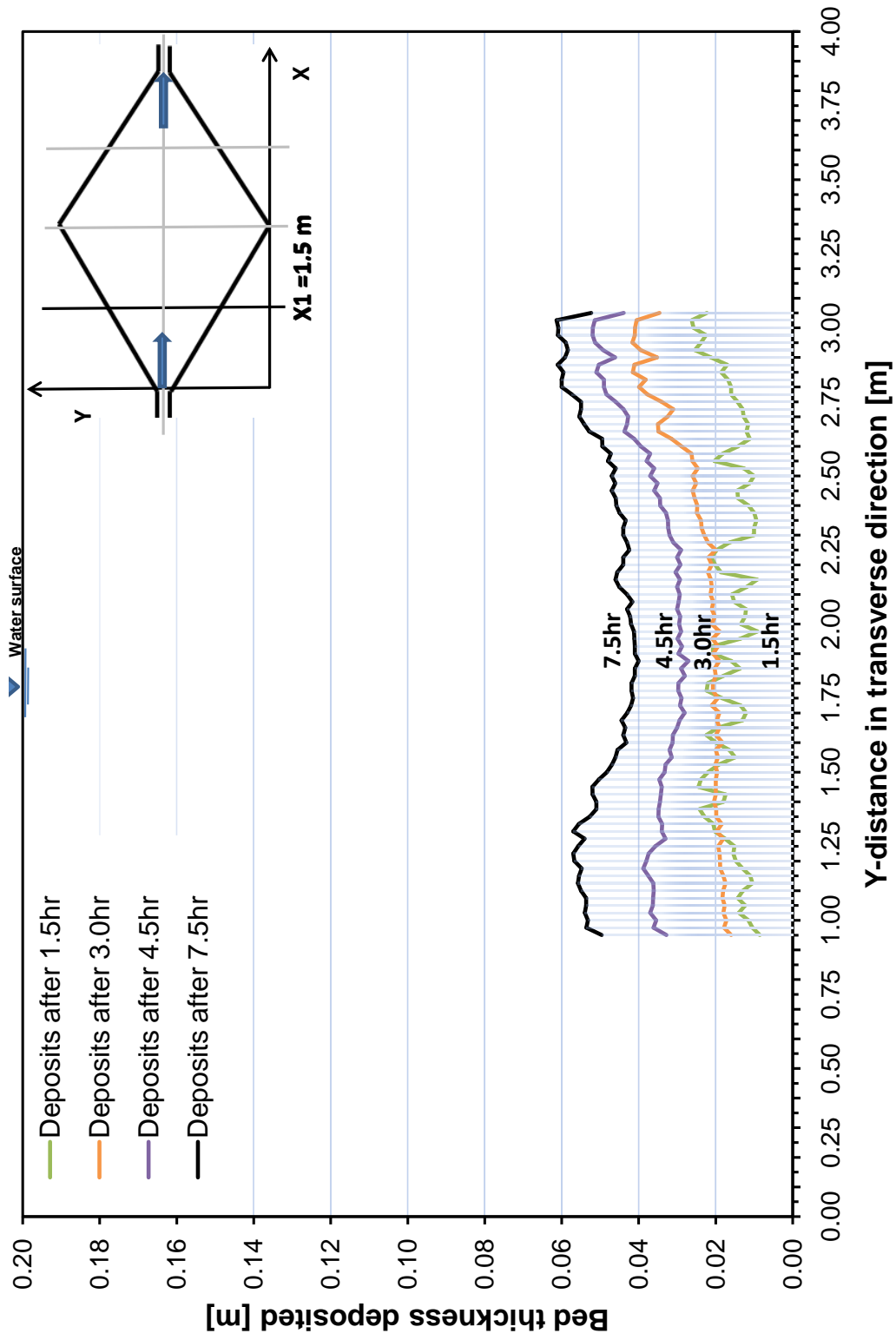


Figure A14.14: Evolution of sediment deposits for four periods runs at cross section $X_1 = 1.5m$ from the entrance

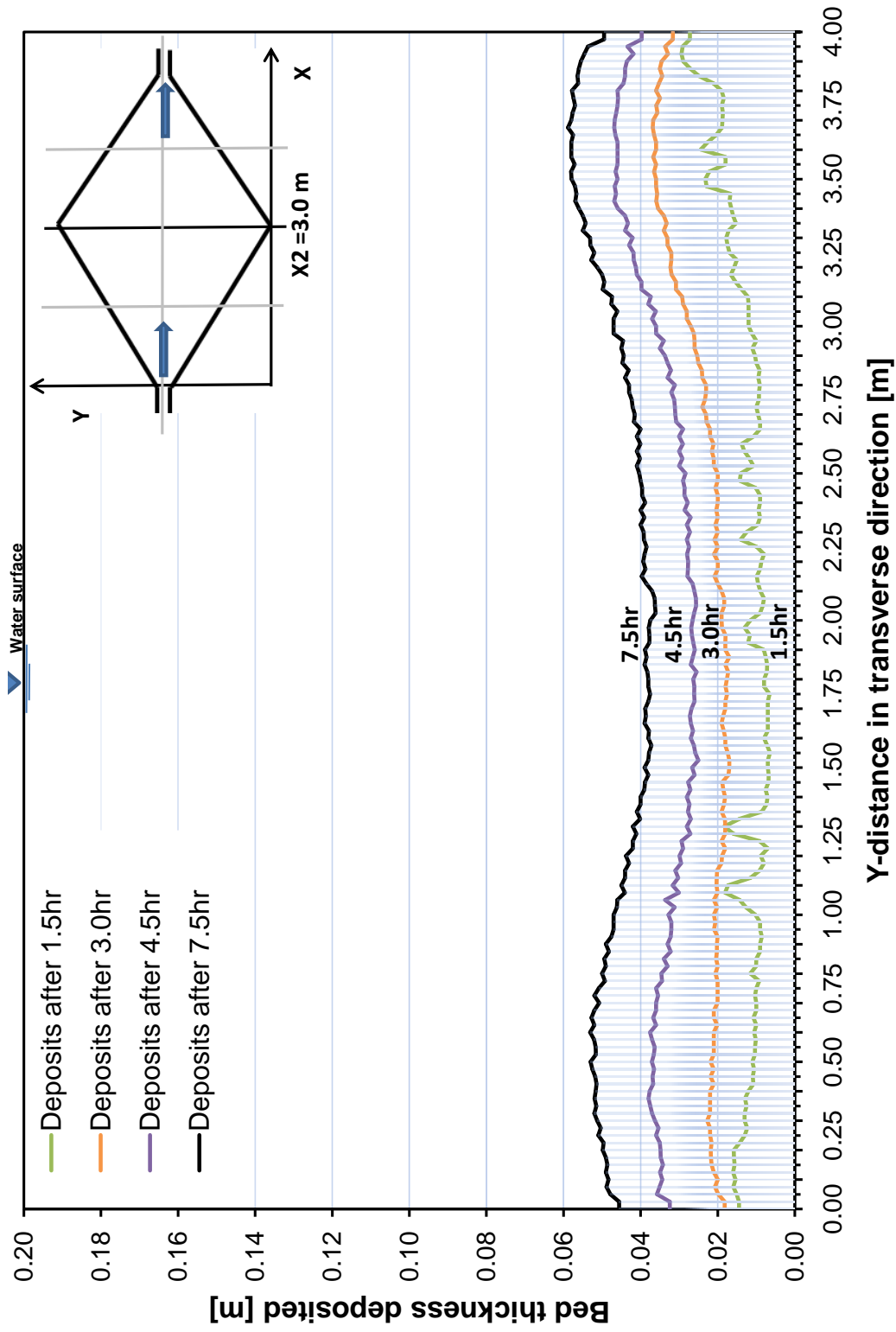


Figure A14.15: Evolution of sediment deposits for four periods runs at cross section $X_2 = 3.0m$ from the entrance

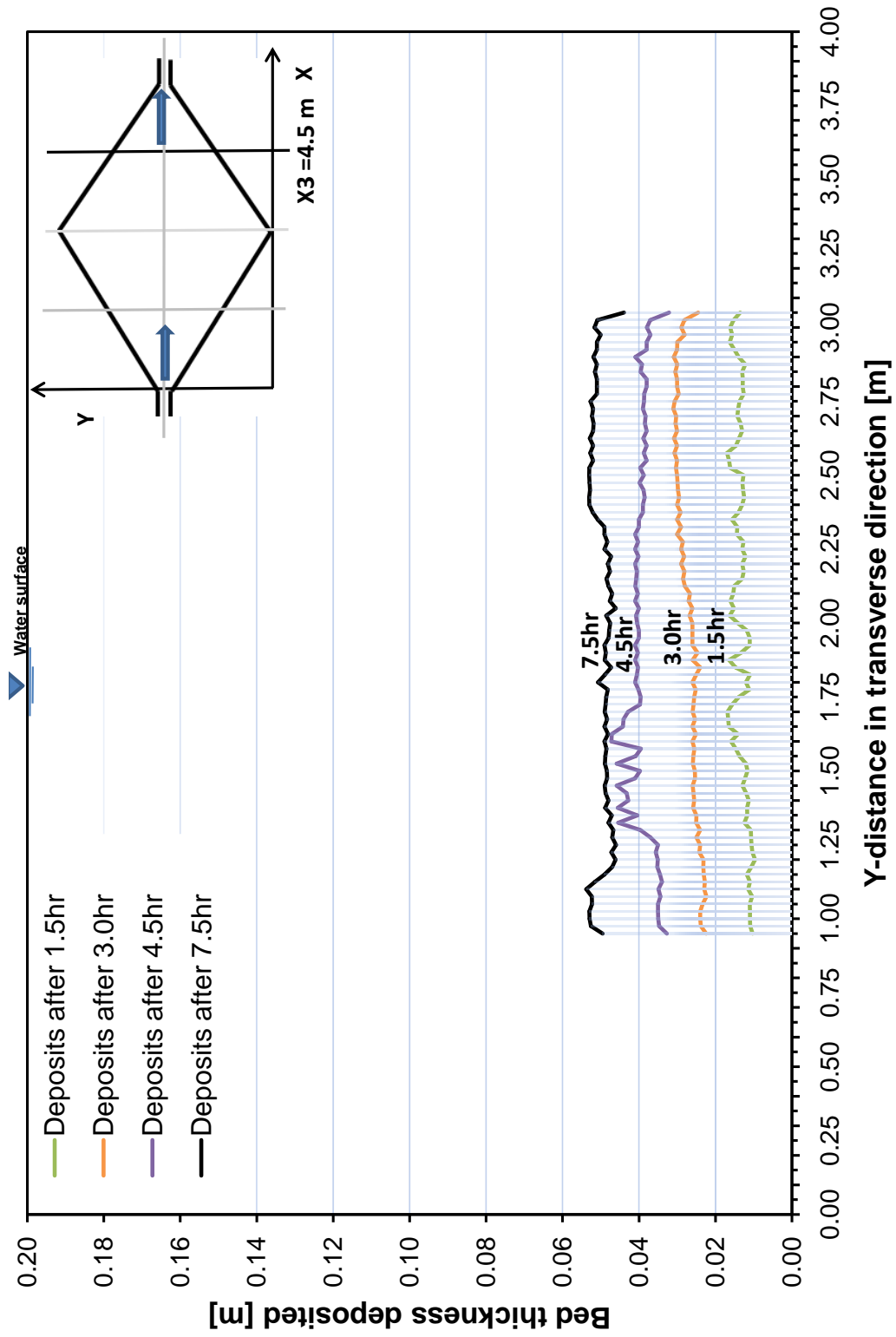


Figure A14.16: Evolution of sediment deposits for four periods runs at cross section $X_3 = 4.5m$ from the entrance

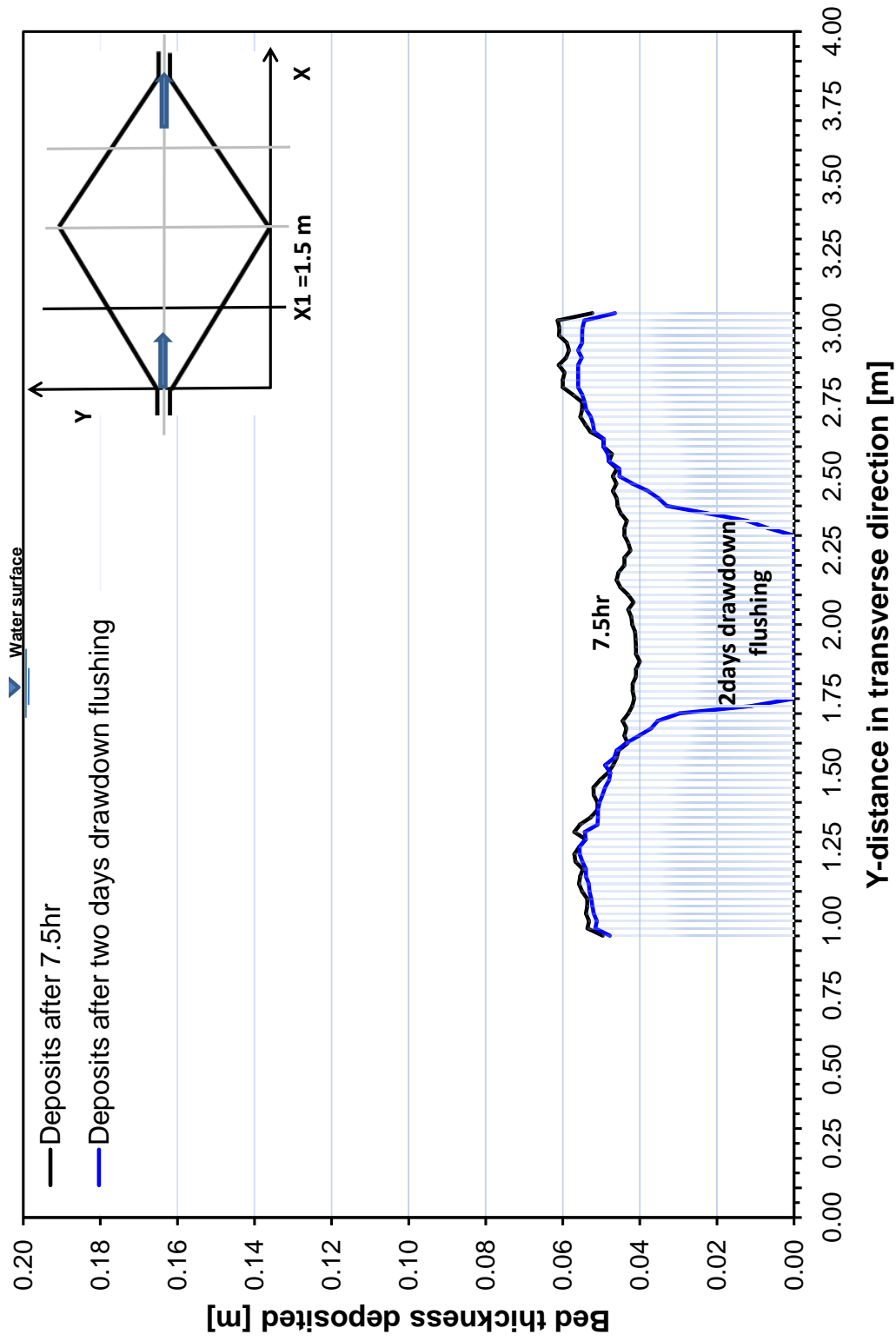


Figure A14.17: Sediment deposits comparison for fourth and flushing periods run at cross section $X_1 = 1.5\text{ m}$ from the entrance

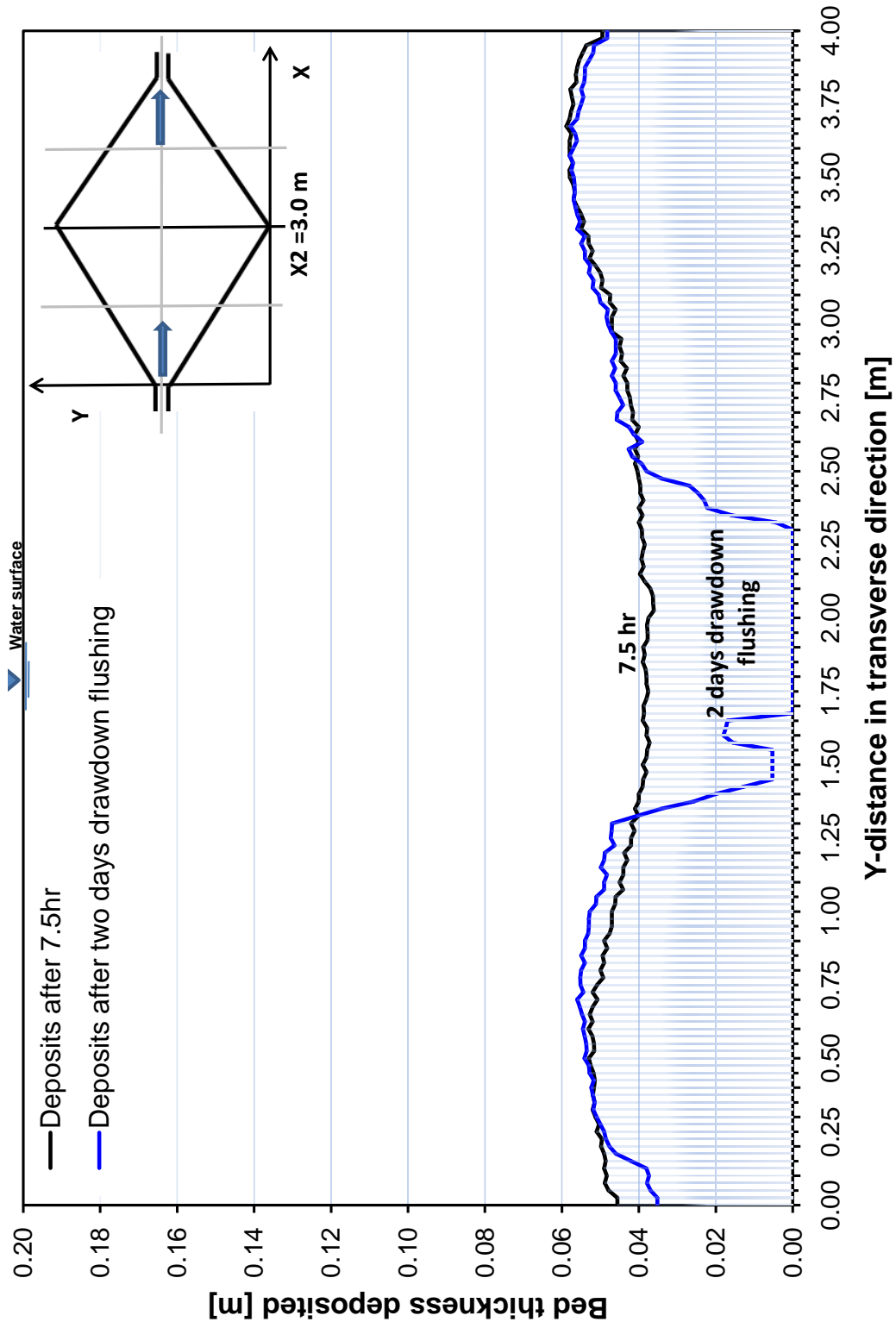


Figure A14.18: Sediment deposits comparison for fourth and flushing periods run at cross section $X_2 = 3.0m$ from the entrance

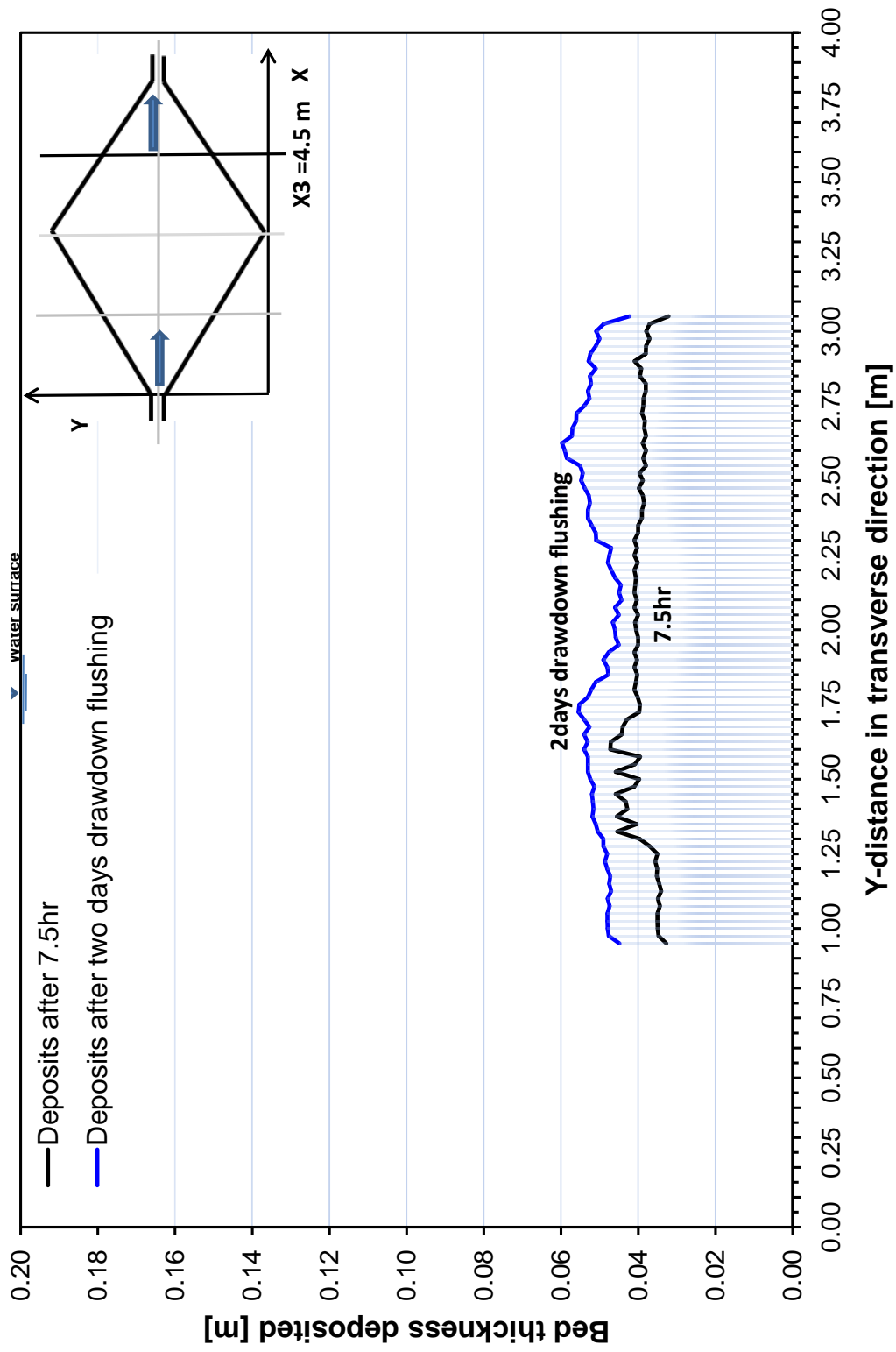


Figure A14.19: Sediment deposits comparison for fourth and flushing periods run at cross section $X_3 = 4.5m$ from the entrance

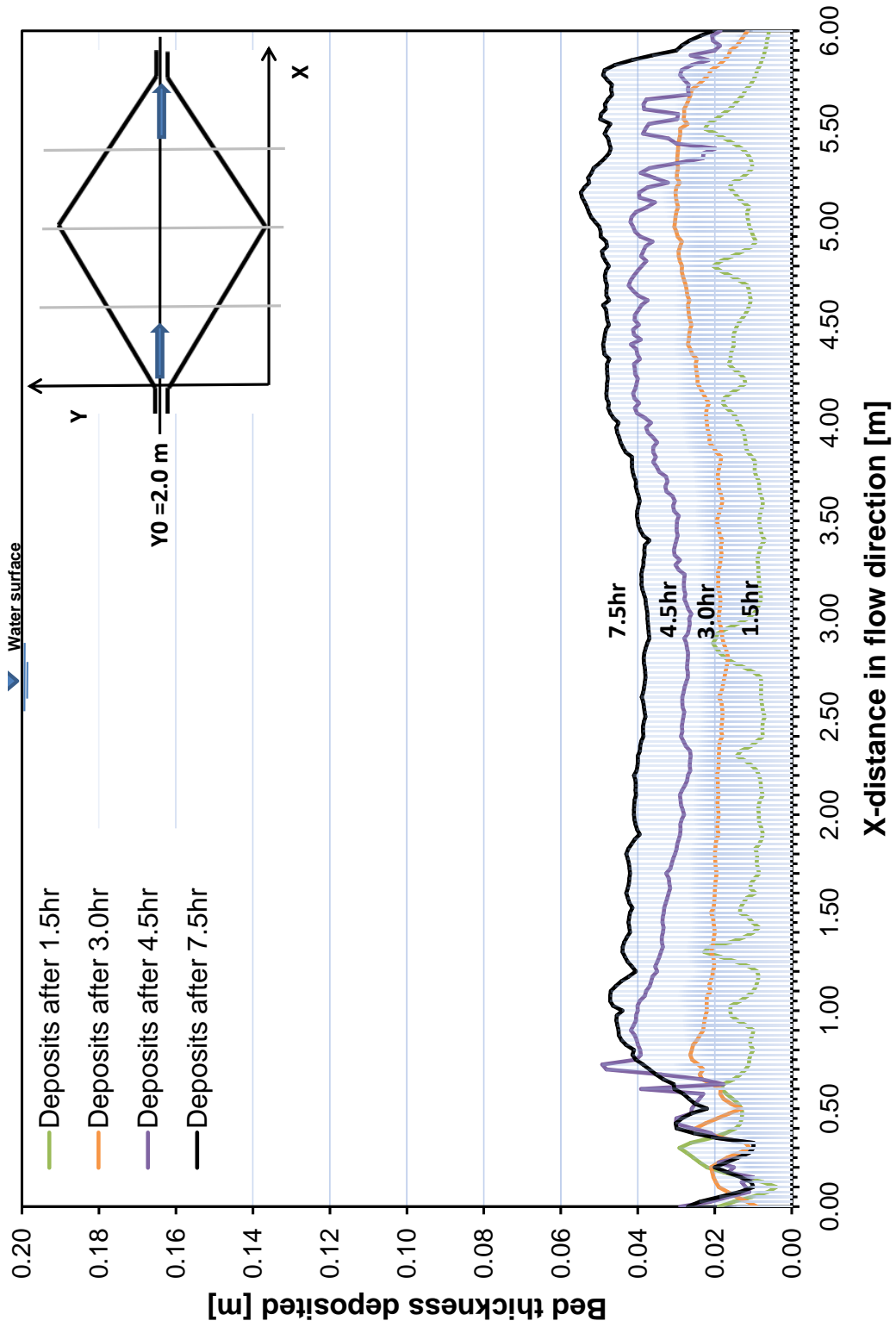
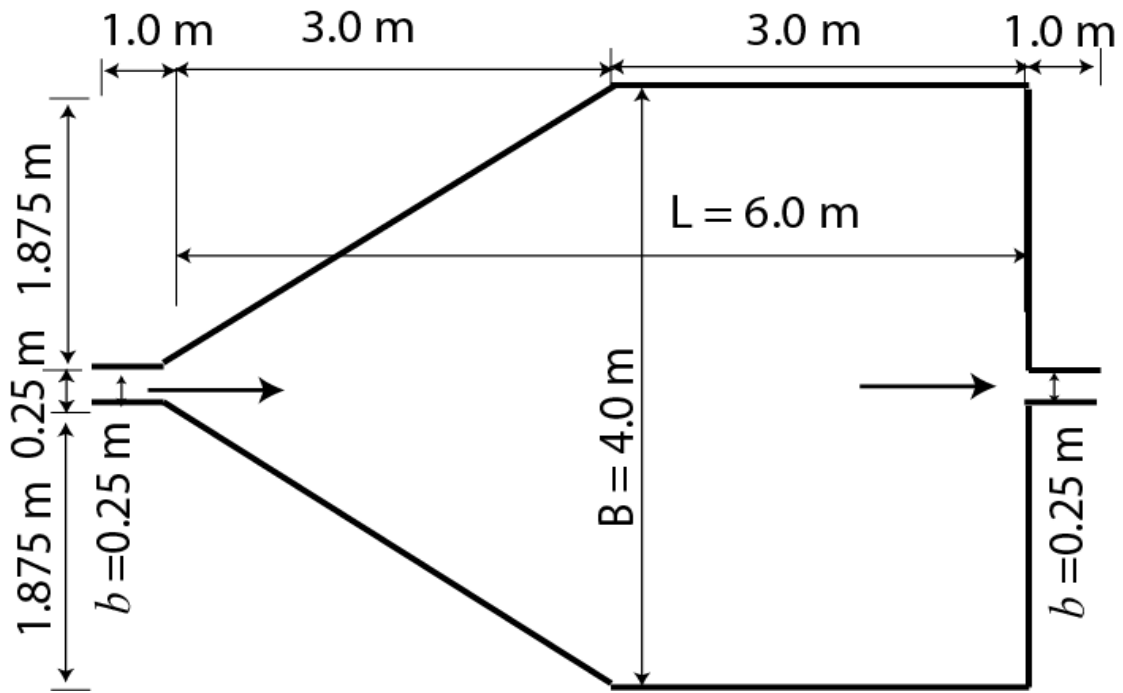


Figure A14.20: Evolution of sediment deposits for four periods runs at centerline longitudinal section $Y = 2.0\text{m}$

A15 Results of rectangular geometry Test15



A15.1 Surface velocity obtained by (LSPIV) measurements with clear water for Test15 (Square geometry)

Results of flow field with the velocity magnitude and streamlines obtained for the following flow characteristic:

- Discharge $Q = 7.0$ [l/s]
- Water depth $h = 0.2$ [m]
- Froude Number $F_r = 0.1$
- Reynolds number $Re = 28000$

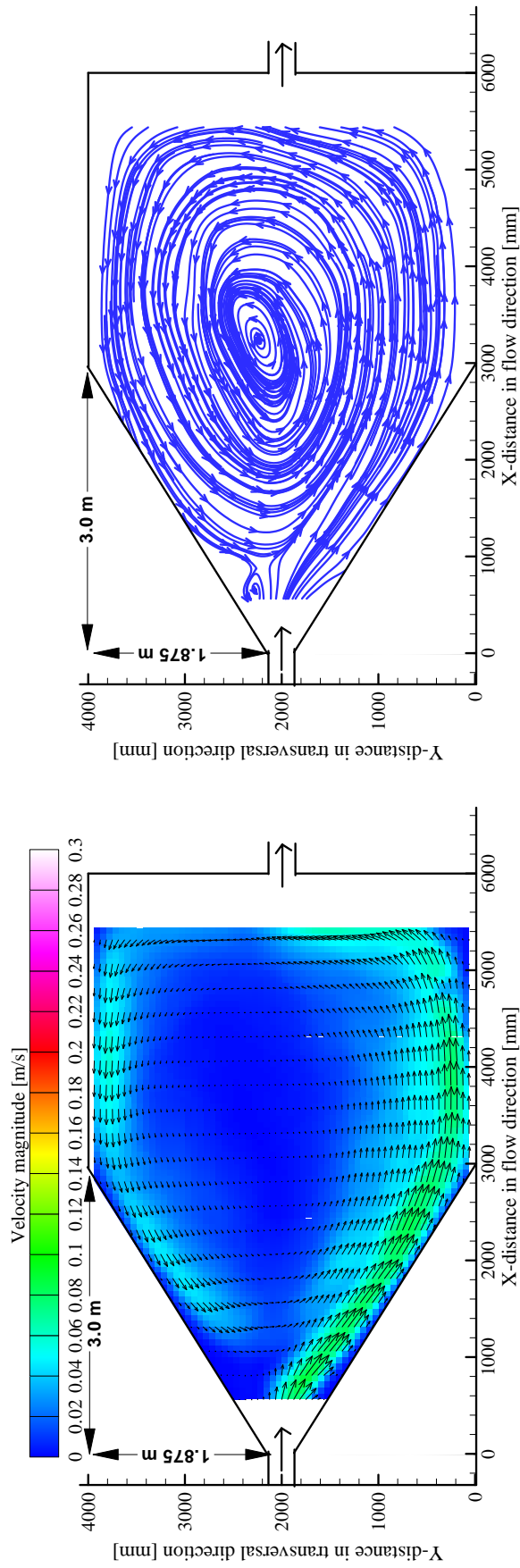
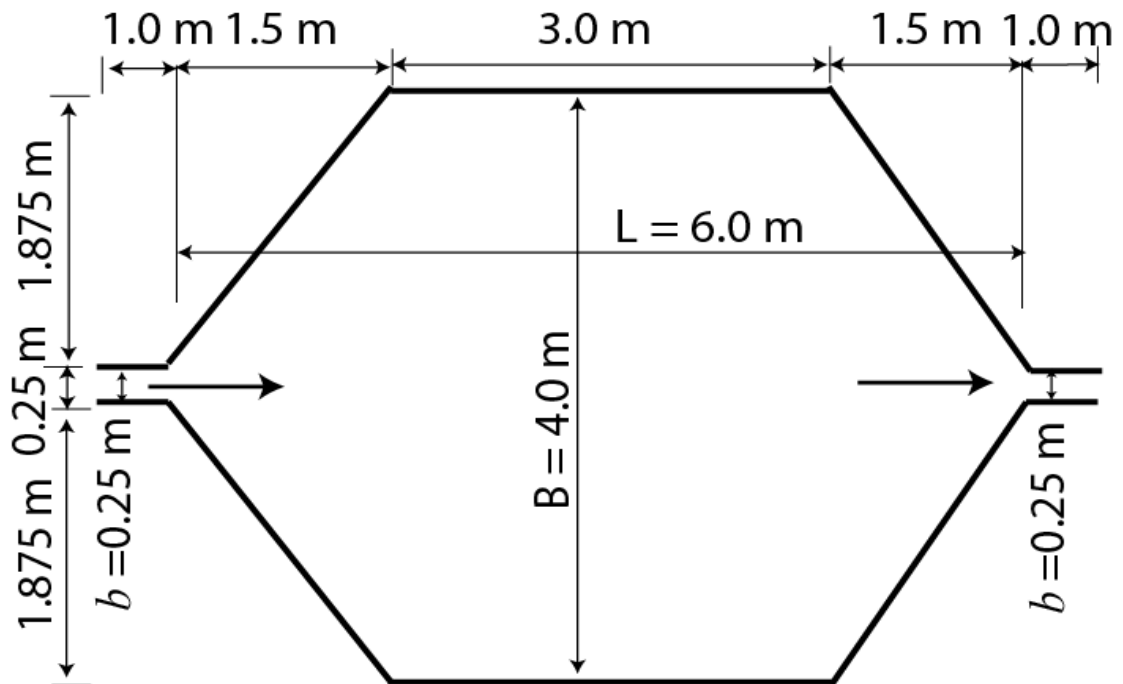


Figure A15.1: Time average flow pattern with velocity vectors (left); streamlines (right) with clear water after stable state for the square geometry (Test15)

A16 Results of rectangular geometry Test16



A16.1 Surface velocity obtained by (LSPIV) measurements

Results of flow field with the velocity magnitude and streamlines obtained for the following flow and sediment characteristic:

- Discharge $Q = 7.0 [l/s]$
- Water depth $h = 0.2 [m]$
- Froude Number $F_r = 0.1$
- Reynolds number $Re = 28000$
- Sediment diameter $d_{50} = 50 [\mu]$
- Sediment density $\rho = 1500 [kg/m^3]$
- Suspended sediment concentration $C = 3.0 [g/l]$

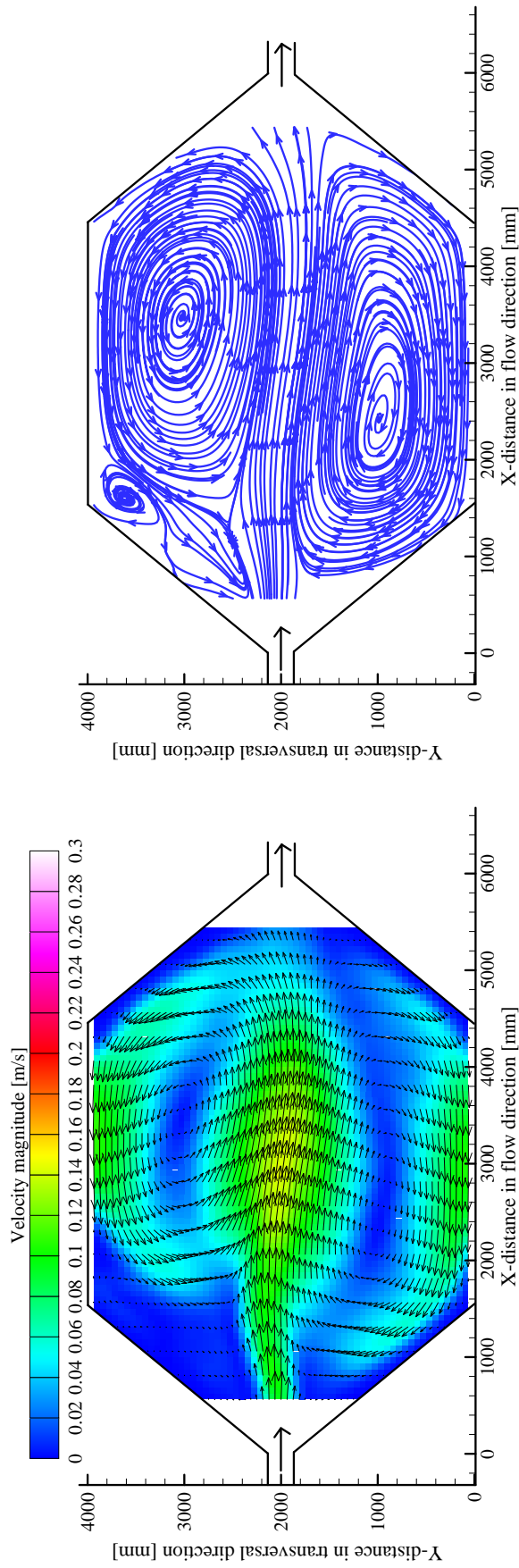


Figure A16.1: Time average flow pattern with velocity vectors (left); streamlines (right) with clear water after stable state

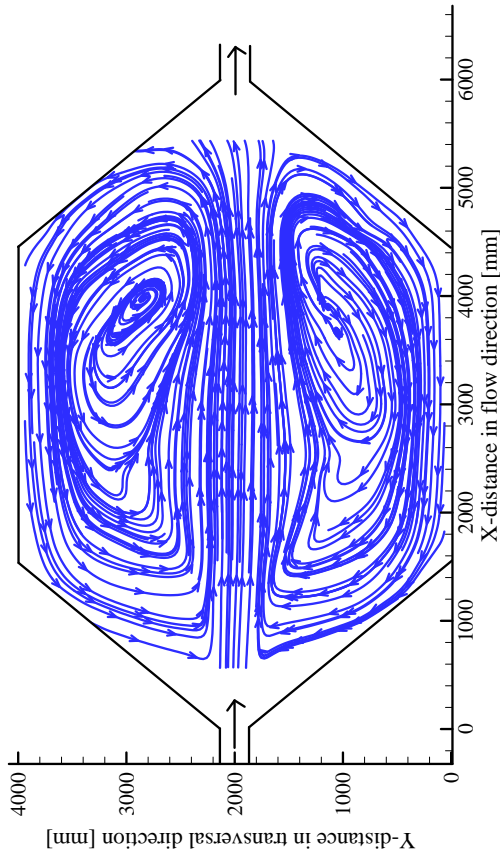
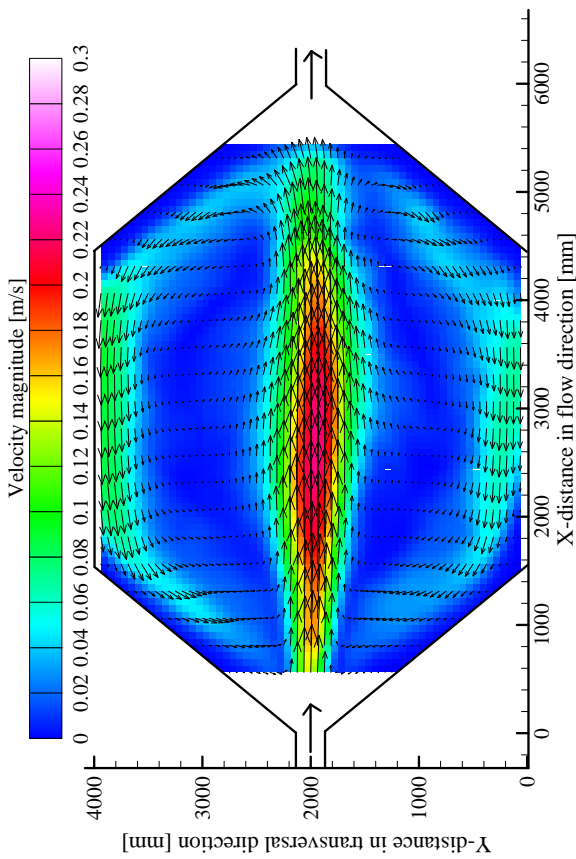


Figure A16.2: Time average flow pattern (left); streamlines (right) after 210 minutes of the fourth period with sediments

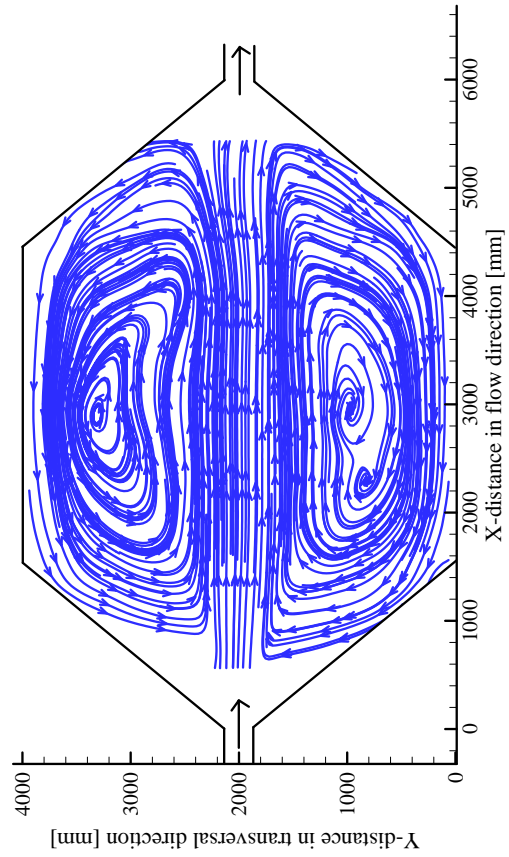
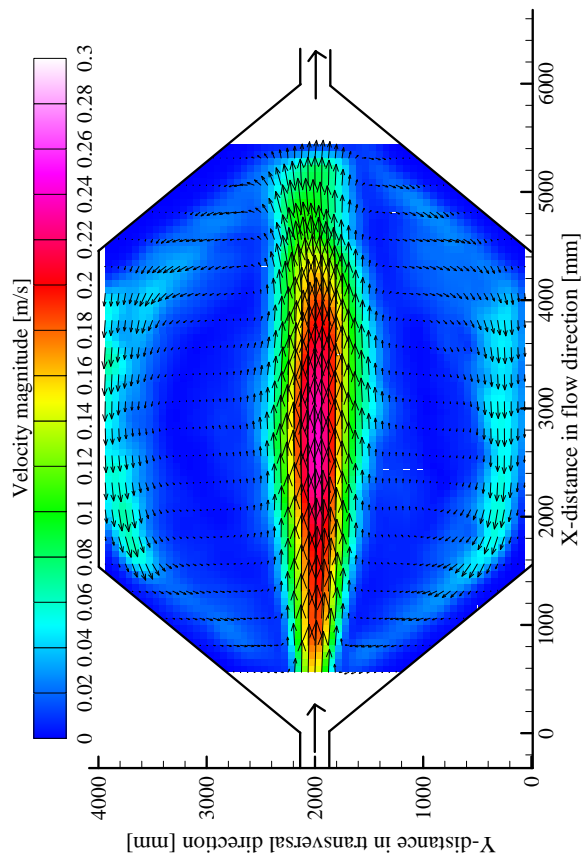


Figure A16.3: Time average flow pattern (left); streamlines (right) after 240 minutes of the fourth period with sediments

A16.2 Two days flushing with clear water over the final bed deposition of the third period (4.5 hours)

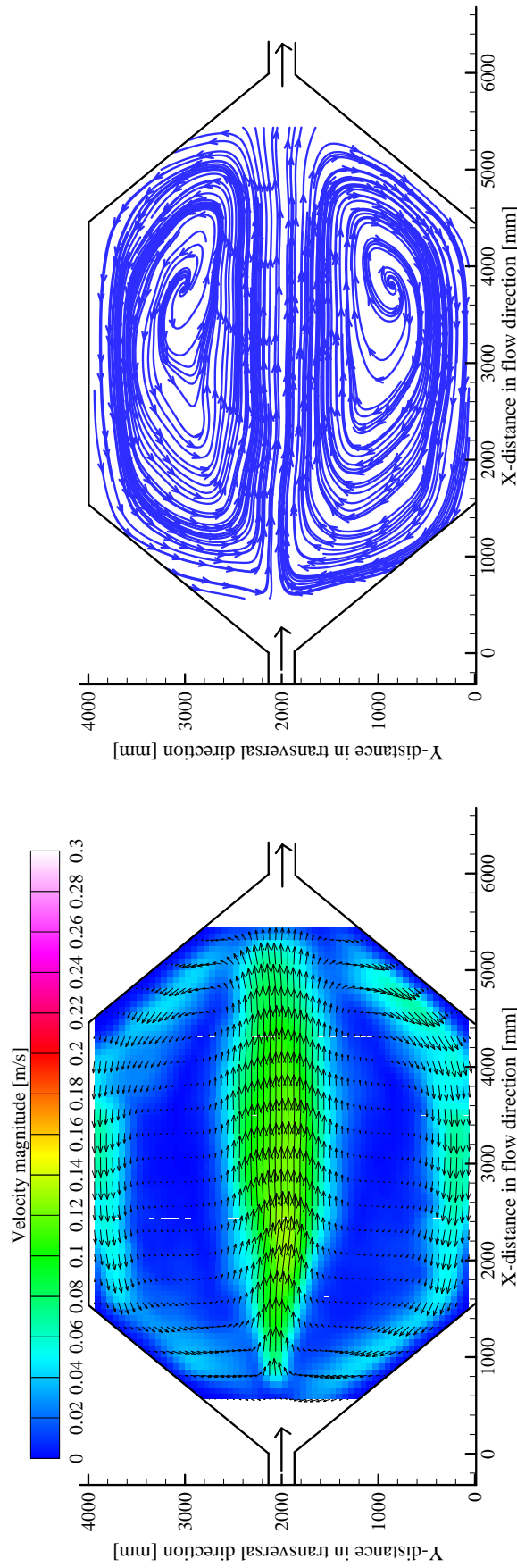


Figure A16.4: Time average flow pattern (left); streamlines (right) of the free flow flushing with water depth $h = 20\text{cm}$

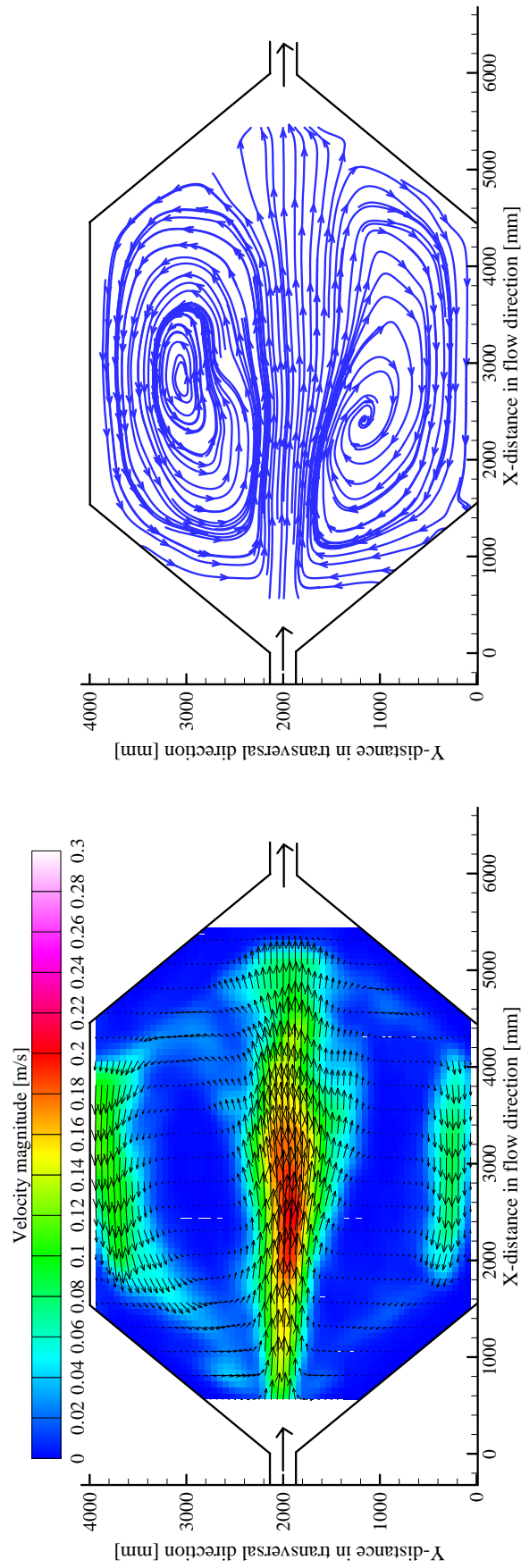


Figure A16.5: Time average flow pattern (left); streamlines (right) of the drawdown flushing with water depth $h = 10\text{cm}$

A16.3 Measurements of suspended sediment concentration obtained by turbiditymeter

Results of sediment concentration obtained for the following flow and sediment characteristic:

- Discharge $Q = 7.0$ [l/s]
- Water depth $h = 0.2$ [m]
- Froude Number $F_r = 0.1$
- Reynolds number $Re = 28000$
- Sediment diameter $d_{50} = 50$ [μ]
- Sediment density $\rho = 1500$ [kg/m³]
- Suspended sediment concentration $C = 3.0$ [g/l]

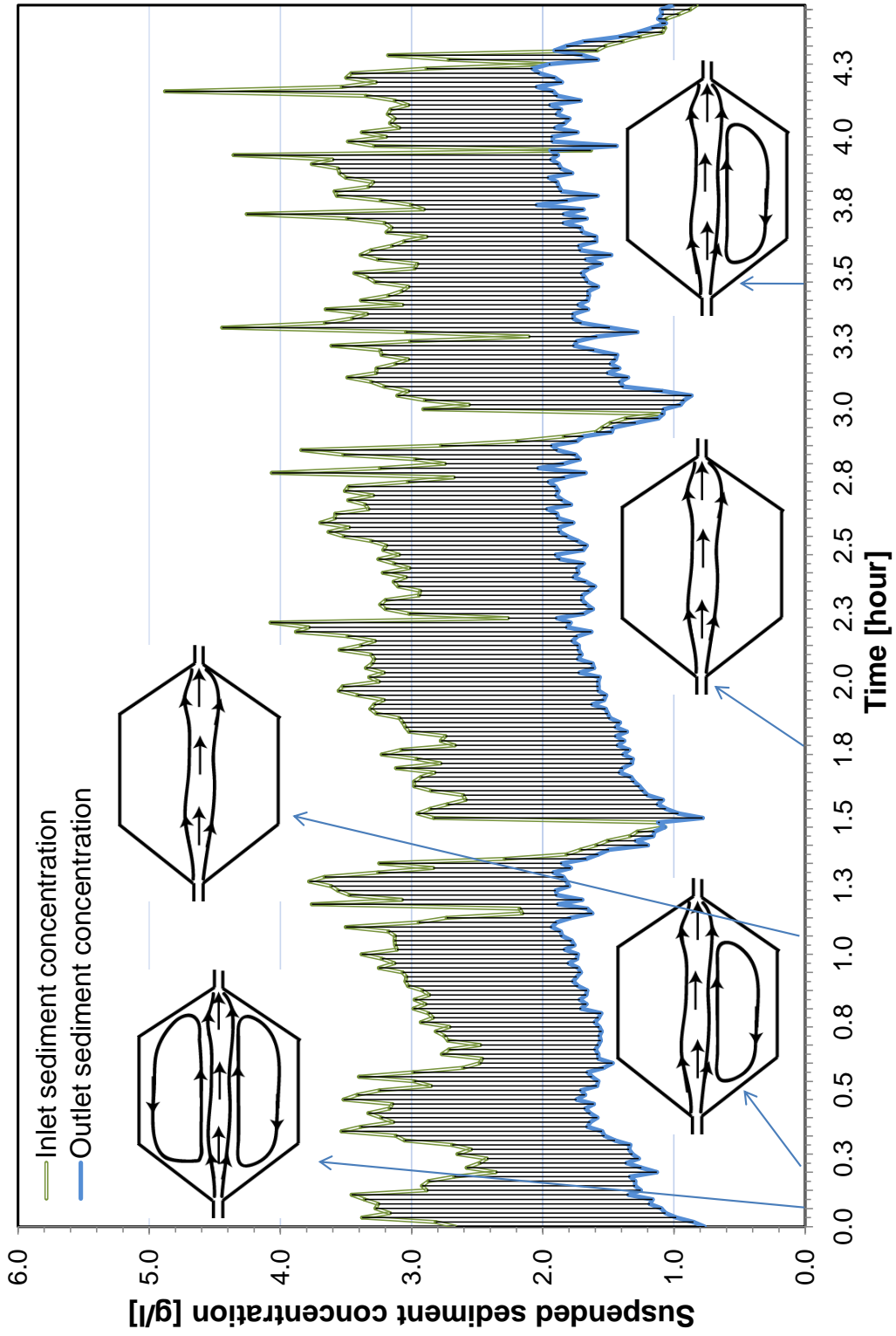


Figure A16.6: Inflow and released suspended concentration of sediments from the reservoir during the first, second and third period of 4.5 hours, measured every minute

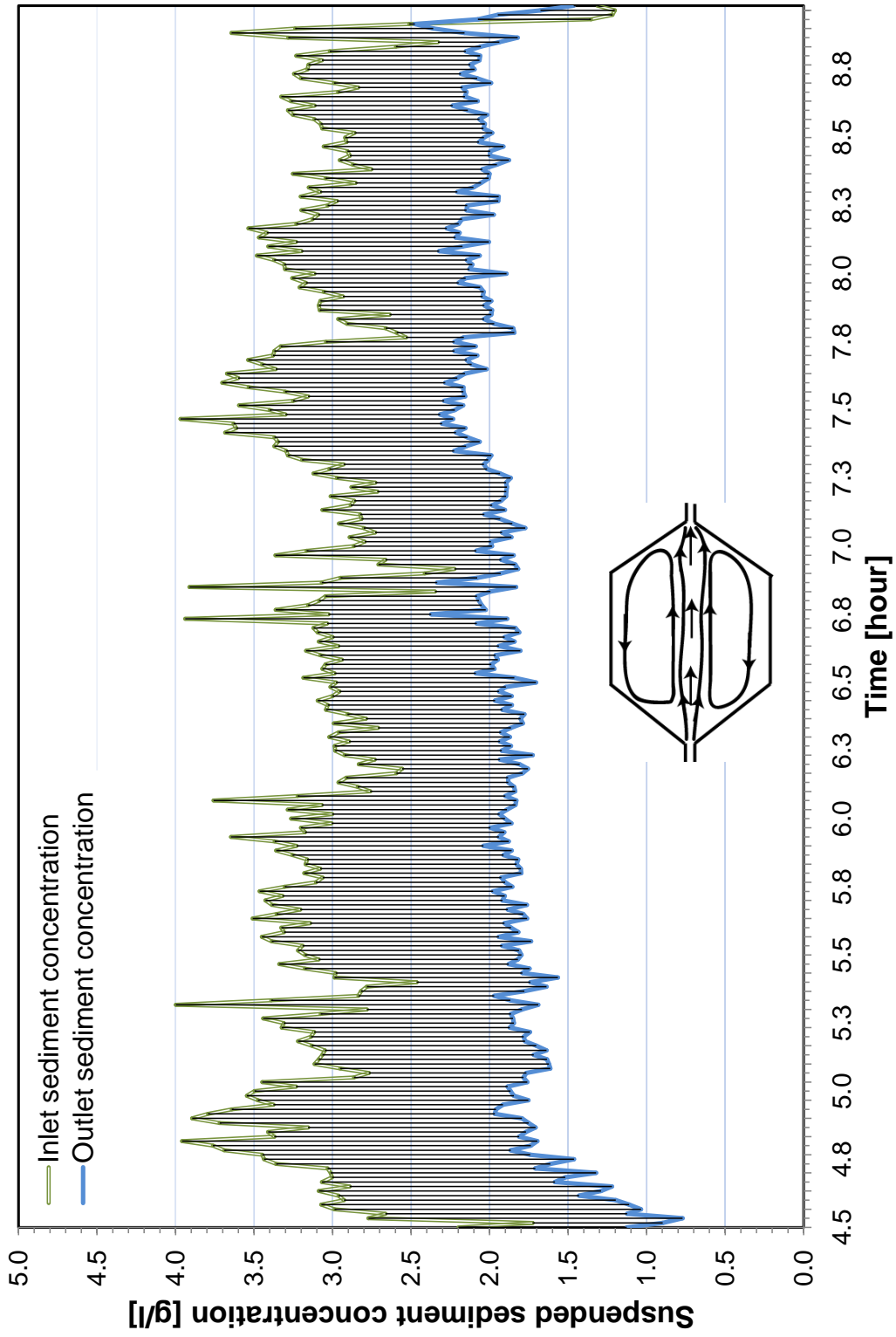


Figure A16.7: Inflow and released suspended concentration of sediments from the reservoir during the fourth period of 4.5hours, measured every minute

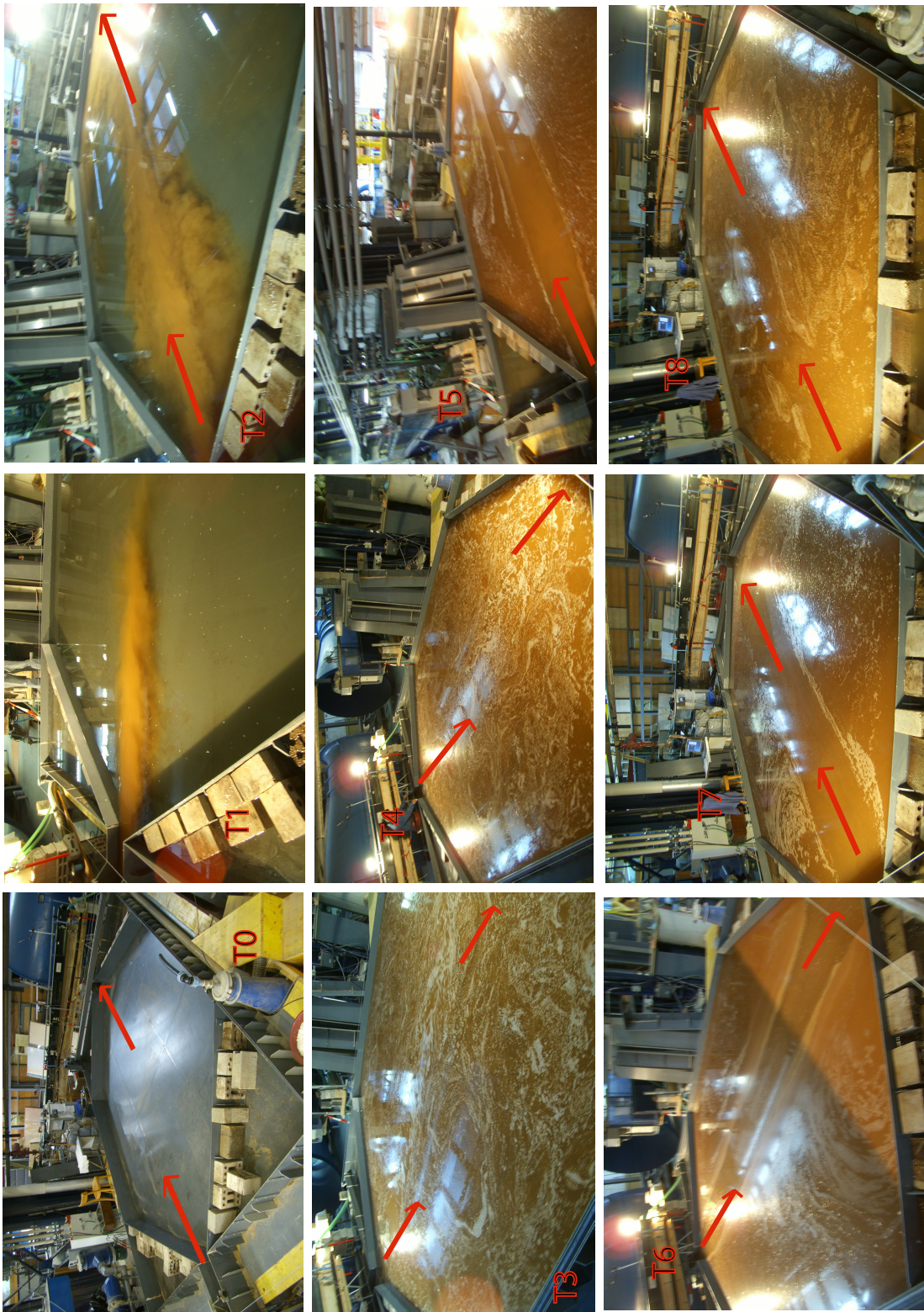


Figure A16.8: Test phases, measurement and procedures pictures during four runs

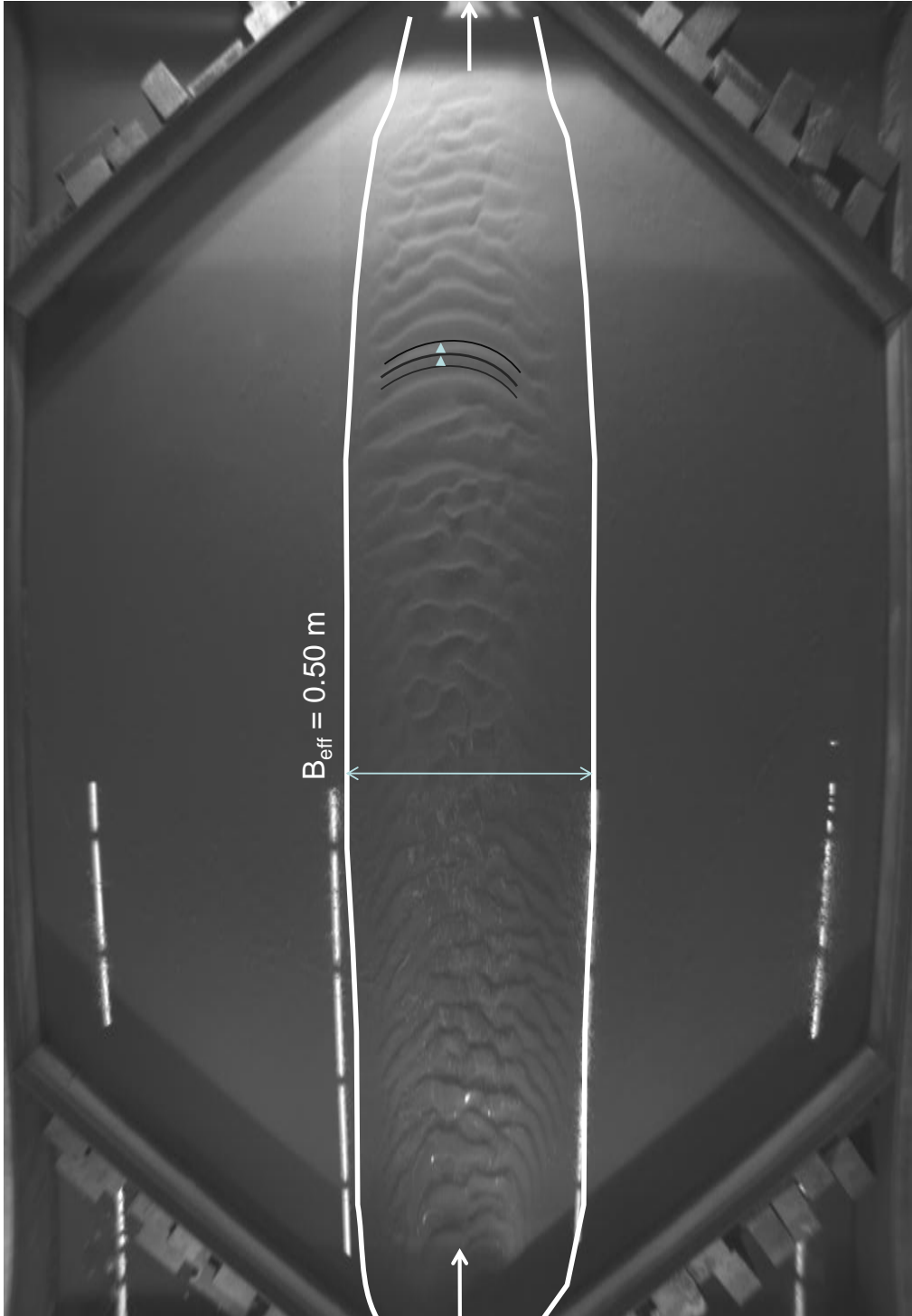


Figure A16.9: Plan view of the final bed depositions features after the fourth period 9.0 hour



Figure A16.10: Downstream looking of final deposition with ripple formations details after 9.0 hour

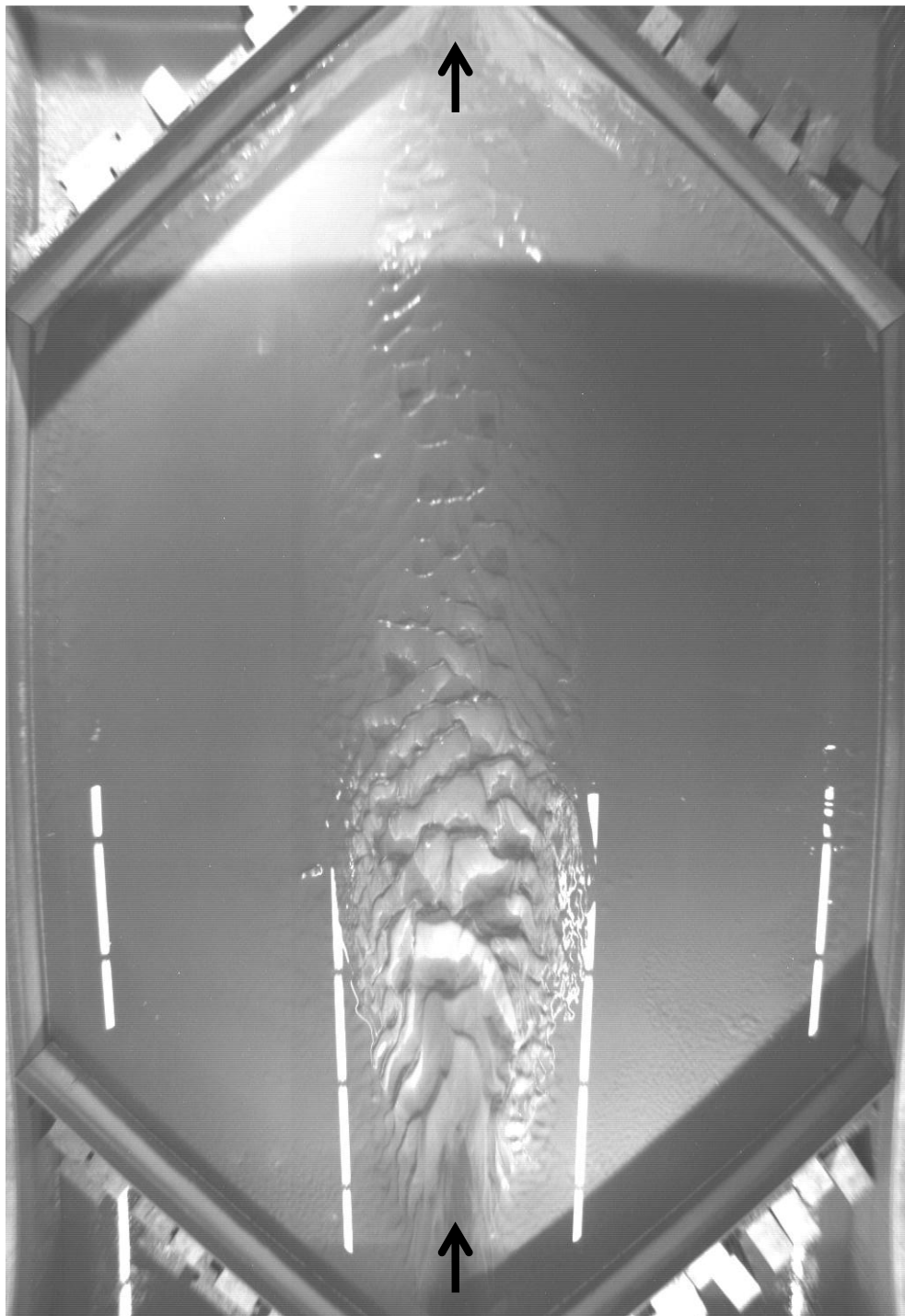


Figure A16.11: Plan view of the final bed depositions features after the 48 hour of free flow flushing

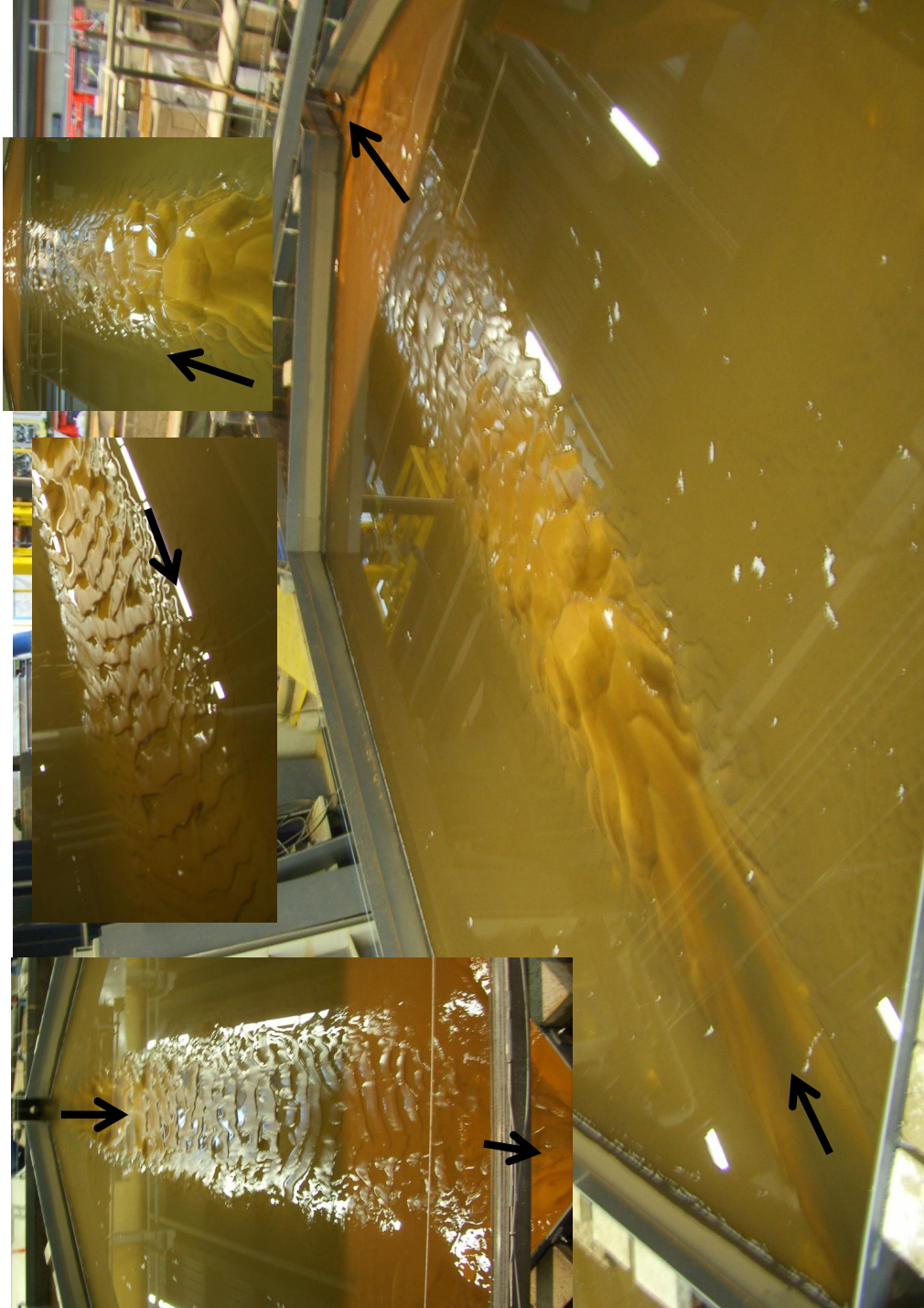


Figure A16.12: Downstream looking of final deposition with ripple formations details after 48 hour of free flow flushing

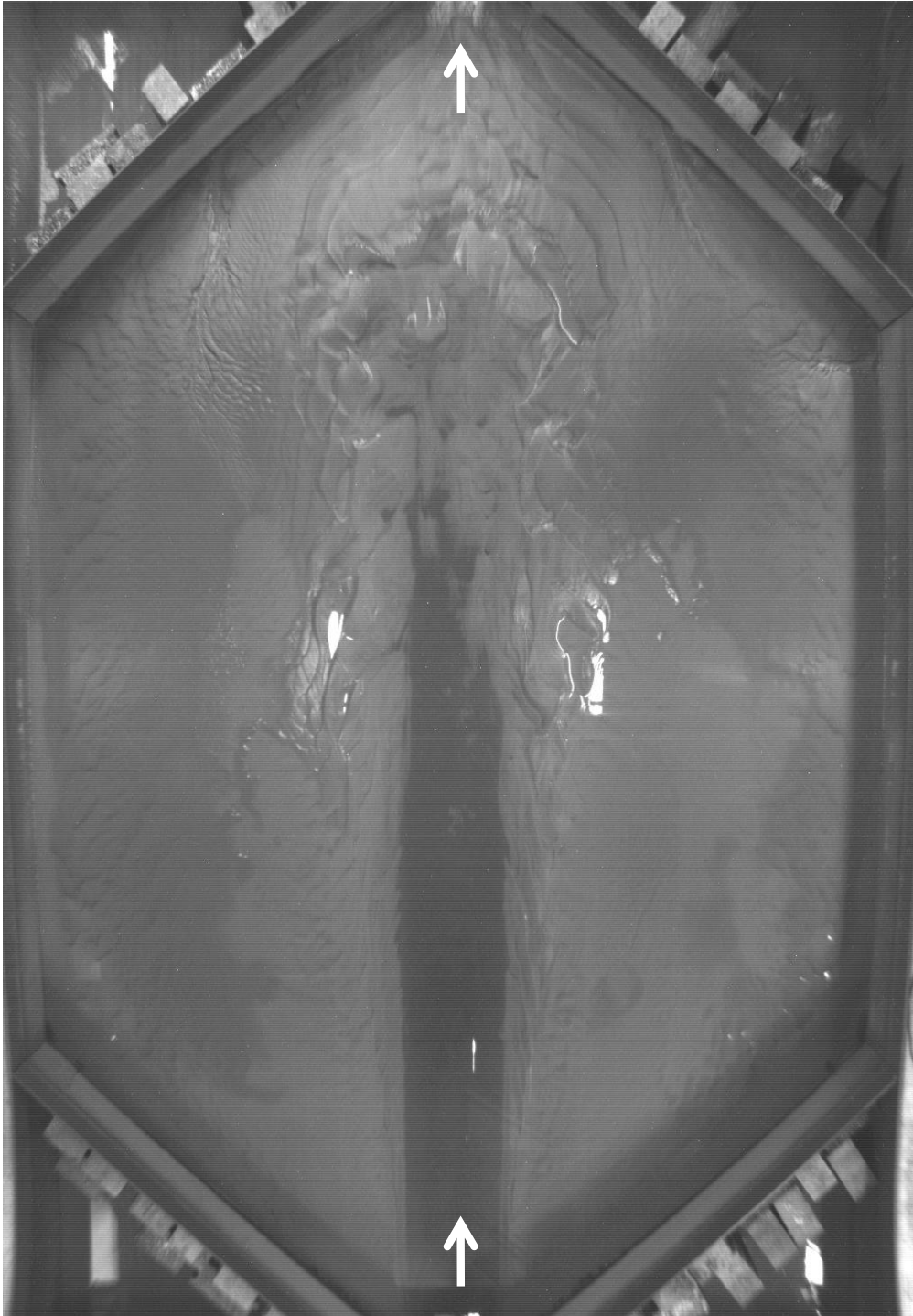


Figure A16.13: Plan view of the final bed depositions features after 48 hour of drawdown flushing

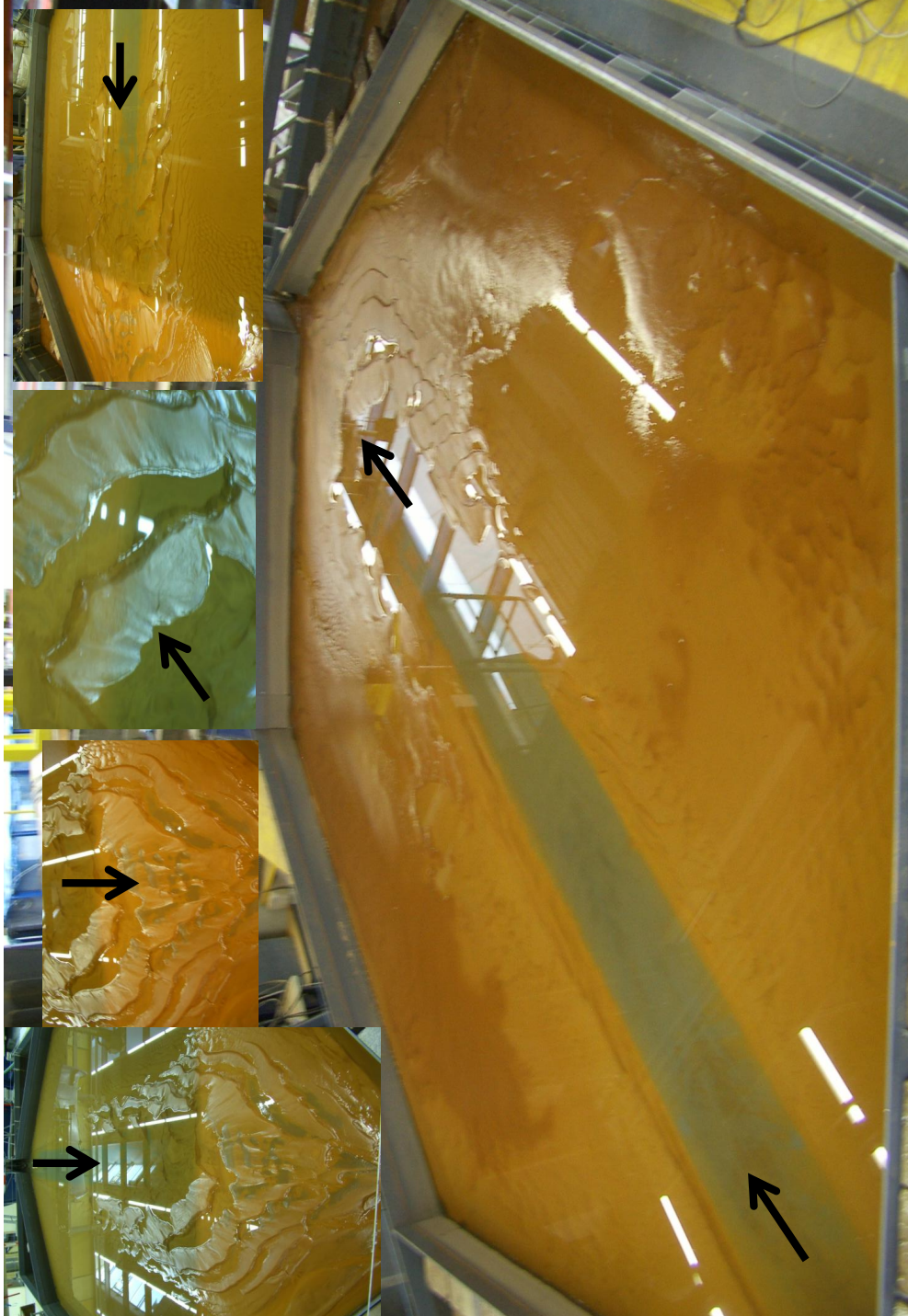


Figure A16.14: Downstream looking of final deposition with ripple formations details after 48 hour of drawdown flushing

**A17 Results of prismatic channel without enlargement
zones geometry Test17**

A17.1 Surface velocity obtained by (LSPIV) measurements with clear water for Test17 (Square geometry)

Results of flow field with the velocity magnitude and streamlines obtained for the following flow characteristic:

- Discharge $Q = 7.0$ [l/s]
- Water depth $h = 0.2$ [m]
- Froude Number $F_r = 0.1$
- Reynolds number $Re = 28000$

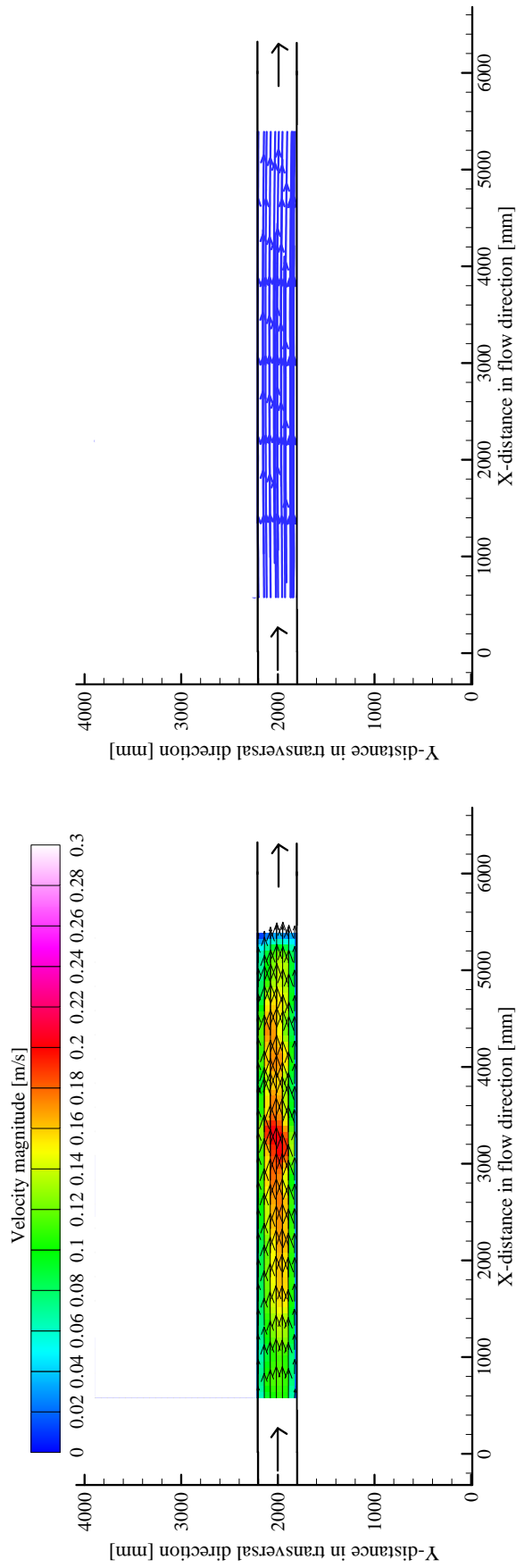


Figure A17.1: Time average flow pattern with velocity vectors (left); streamlines (right) with clear water after stable state for the square geometry (Test17)

Recommendations for LSPIV applications

The previous described LSPIV system has been implemented for five hydraulic engineering applications covering surfaces from 4 m^2 to 100 m^2 .

These applications are: sediment processes between groyne field experiments , approach flow in spillways and dams, a model river confluence, oil spill with rigid and flexible barriers and prototype model of river junctions.

LSPIV system consists of six elements:

1. Camera
2. Tracer particles
3. Tracer distributor
4. Illumination system
5. Computer for acquisition and treatment
6. Software for recording the images and another one for postprocessing and treatment of the images

Recommendations for the special problems encountered in each of these experiments, as well as the selection and adjustments of the parameters to properly solve them, are explained as the following:

- a) Depending on the flow velocity a suitable camera characteristic has to be chosen and record images of the flow at a suitable rate with an adequate image resolution. The sampling frequency of the recorded images (frame per second FPS) has a significant influence on the accuracy of the LSPIV velocity estimates. The optimum FPS and flow velocity relationship was established based on several experiments with various FPS of 4.0, 6, 7, 8, 10, 12, 15, 24 FPS. Moreover, four experiments series were conducted with

different exposure time and fixed FPS. Eight FPS is an optimum sampling frequency and the high error occurring for smallest FPS. A grid of known spacing has to be placed close to the water surface at the start of each experimental run in order to relate image coordinates to physical real world coordinates. There are several types of the camera can be use e.g. CMOS camera (SMX 155, or SMX 150) with USB2.0 interface or Sencam Camera, with CCD sensor with monochrome of 12 or 8 bits or a digital video camera recorder as Sony, (DCRTRV900) and etc.

- b) A difficult part of the experimental setup is the choice of proper tracer particles. The particles have to fit different requirements to be applicable. Choosing the tracer particles characteristics according to the application types. The LSPIV accuracy depends on the ability of the particles to follow the flow fluctuations. When a particle is placed inside the flow or when the flow has a velocity oscillation, a time lag is verified until the particle velocity is equal to the flow velocity. Therefore, fluid mechanical properties of the particles have to be checked in order to avoid large discrepancies between fluid and particle motion. The evaluation of the tracers' ability to follow the flow streamlines without excessive slip is also performed by determining the settling velocity of the particle under gravity. Seed a well-illuminated region of the flow field of interest with particles that accurately trace, but do not significantly interfere, with the flow. The contrast between the seeding particles and the water has to be adjust by several methods: by painting the model floor and walls with different color than the seeding particle one (if particles are white so a black painting has to be use or vice versa) or placing white or black paper sheets under the glass flume floor.
- c) A homogeneous distribution of particles within the measuring field is important for good results in terms of a closed velocity vector field. A tracer distributor which is able to seed the water surface homogeneously with particles, at a rate that depends on the ambient flow velocity has to be develop. The distributor has to be located near the water surface in order to avoid surface waves from falling particles. The particles have to recollected at the end of the flow section and reused, as the number of particles which is needed for such an experiment is quite high.
- d) The component of illumination proved to be the most crucial in order to get high-quality data. The spots have to placed around or on top of the camera to get a homogenous light intensity distribution over the entire area, otherwise the reflections and shadows will show different characteristics on either side. Furthermore the amount of achievable data would differ, because unequal amounts of reflections would be recorded on either side. Sometimes the natural light could be enough.
- e) The appropriate choice of the computer is helping capturing process of images and not loosing any recorded images and have all in a good sequences. The PC has to equipped

at least with 1 GB RAM to store the images before shifting them to the hard disk. Therefore, the RAM is the limiting factor for the length of a time series.

- f) Choice of the type of software is important. Special software for PIV analyze the recorded images using statistical means to estimate the displacement of flow tracers between images and estimate velocities over the entire imaged area. Two type of software are exists: Free code programmes e.g. MatPIV, PIVMat, mpiv, URAPIV, DigiFlow, PIV Sleuth and etc. and the commercial PIV package e.g. FlowManager (Dantec dynamics), DaVis (LaVisions) software and etc.

Curriculum Vitae

SAMEH KANTOUSH

**Ecole Polytechnique Fédéral de Lausanne,
EPFL ENAC LCH, Station 18, CH 1015 Lausanne,
Switzerland**



Email sameh.kantoush@epfl.ch , kantoush@yahoo.com

Web <http://lchwww.epfl.ch>

Work Phone: +41 21 693 59 33

Mobile Phone: +41 76 407 92 79

Fax: +41 21 693 22 64

PROFESSIONAL PROFILE

Extensive research and teaching experience in Reservoir Sedimentation, Hydraulic Constructions, Sediment transport; Fluid Mechanics; Physical and Numerical Modeling; River Mechanics; Hydrology; Water Resources Engineering. Broad laboratory and field practice. Major research interests and working experience include:

- Various aspects of river mechanics and fluvial sediment transport

Curriculum Vitae

- Reservoir sedimentation and investigations of the shape factor effect on the reservoir trap efficiency and the interaction between deposits and flow patterns
 - Particle Image Velocimetry techniques (DANTEC software FlowManager)
 - Physical modeling in laboratory and prototype
 - Hydraulic instrumentations (Velocity measurements (UVP, PIV), Turbidity meter, Bathymetry measurements (MiniEcho Sounder), Pressure measurements, Visualizations)
 - Hydraulic structures (dame spillway and approaching basins of the dam)
 - Numerical simulations for 1D, 2D & 3D modeling (CCHE2D, Flow-3D, Dupiro, Node-Branch model)
-

EDUCATION

- **Ph.D. Candidate, Swiss Federal Institute of Technology (EPFL)**, Laboratory of Hydraulic Constructions (LCH), Lausanne, Switzerland , November 2003 till Present,
Advisor: Prof. Dr. Anton Schleiss (anton.schleiss@epfl.ch).
Dissertation: Influence of geometry of shallow reservoirs on flow pattern and sedimentation processes by suspended sediments
 - **M. Sc. in Civil engineering, Saga University**, Faculty of Engineering, Civil Engineering Department, Saga shi, Japan, September 2001 to October 2003,
Advisor: Prof. Dr. Kunitoshi Watanabe (watak@cc.saga-u.ac.jp).
Dissertation: Modeling for water management and flood prevention for the channel networks in the Nile delta of Egypt
 - **B. Sc. in Civil Engineering, Alexandria University**, Faculty of Engineering, Civil Engineering Department, Alexandria, Egypt, September 1992 to June 1997.
-

ACADEMIC POSITIONS

- Research Assistant & **PhD Student**, *Swiss Federal Institute at Lausanne, Switzerland. From 11/2003 till present*
- Research Assistant & **MSc. Student**, *Saga University, Faculty of Engineering, Japan, From 9/2001 To 10/2003.*

- Research Assistant & **Part-time MSc. Student**, *Alexandria University, Egypt, From 7/1998 To 10/2000.*

 - **Instructor**, *Alexandria University, Egypt, From 7/1999 To 7/2001.*
-

AWARDS & SCHOLARSHIPS

- Asahi Ryunetsu Student Paper Award for outstanding paper entitled, Flow field investigation in a rectangular shallow reservoir using UVP, LSPIV and numerical model. 5th International Symposium on Ultrasonic Doppler Methods for Fluid Mechanics and Fluid Engineering, ETH Zurich, Switzerland, from 12.09.2006 to 14.09.2006.
 - Doctoral school scholarship, Swiss Federal institute of technology May 2003 (competition rate: 1/14).
 - Japan Society of Civil Engineering (ISCE) prize for the excellent presentation, 2002. item Japanese Government (MONBU-KAGAKU-SHO) Scholarship for Master study in civil Engineering, two years (2001 to 2003).
 - Prof. Dr. Mounir KNSOH prize for the excellent student in Hydraulics, Alexandria University prize, 1997.
-

PERSONAL

- Born January 3, 1974 in Behira, Egypt. Egyptian citizen. Swiss residences permit B. Married.

Languages

- Arabic native speaking, Good in English, Good working knowledge of French, Poor in Japanese.
-

RESEARCH EXPERIENCE

Research Assistant & PhD student, EPFL, LCH, Switzerland.

11/2003 till

- Evaluation and comparison of different computer programs (both commercial and academic codes) for sediment transport models.
- Developing and designing physical model for a large shallow reservoir with reference to the characteristics of the Rhone River upstream of Lake Geneva.
- Constructing a complete system of Large Scale Particle Image Velocimetry (LSPIV) of different shaped shallow reservoirs and other several applications measured such as in groyne field experiments, prototype model of river junctions and approach flow in spillways and dams and oil spill investigations.
- Physical model tests to improve the hydraulic performance of the existing sewer system at La Paz in the western part of Bolivia.
- Particle image velocimetry measurements for many engineering applications at LCH.

present

<p>MSc. Student, <i>Saga University, Faculty of Engineering, Japan</i></p> <ul style="list-style-type: none"> • Simulating the drain flow in unsteady state by using NODE-Branch modeling system. • Modeling for water management and flood prevention for the channel networks in the Nile Delta by using 1-D numerical simulations. • Numerical simulation of the flow in the tree type channel network in the Delta of the Nile river. • Modifying the NODE-Branch program to be suitable for the networks in the Nile Delta. • IHP training course in Asia and Pacific Region on precipitation and water resources which held from 23 February to 8 March, 2003 by the hydrospheric Atmospheric Research Center, Nagoya University, Kyoto University. 	<p>9/2001 to 10/2003</p>
<p>Part time MSc. Student, Alexandria University, Faculty of Engineering, Alexandria, Egypt</p> <ul style="list-style-type: none"> • Ground water modeling by using numerical simulation of program SWITCHA. • Postgraduate courses Water resource, Stability of embankments, Finite element method in fluid Flow, Advanced hydraulic measurements and modeling, Computer programming for irrigation and hydraulics design. 	<p>9/1998 to 10/2000</p>
<p>TEACHING EXPERIENCE</p>	
<p>Teaching assistant, EPFL, LCH, Switzerland.</p> <ul style="list-style-type: none"> • Co-supervised two graduation projects. • Supervised 12 semester projects. 	<p>11/2003 till present</p>

Curriculum Vitae

<p>Tutor, Saga University, Faculty of Engineering, Japan</p> <ul style="list-style-type: none">• Fluid mechanics and laboratory instructor	9/2001 to 10/2003
<p>Instructor, Alexandria University, Faculty of Engineering, Alexandria, Egypt</p> <p>Instructor, Arab Academy For Science & Technology-Faculty of engineering-Building & construction department, Alexandria, Egypt</p> <ul style="list-style-type: none">• Teaching and preparing assignments, their solutions, and marking them for undergraduate courses in Water resources, Fluid Mechanics, Irrigation, Hydraulics and Surveying.	7/1999 to 7/2001
<p>INDUSTRIAL EXPERIENCE</p> <p>PhD student, <i>EPFL, LCH, Switzerland.</i></p> <ul style="list-style-type: none">• PIV measurements for a prototype multi purpose modeling of the Rhone River in the region of Visp (Switzerland).• Measurements and analysis of approaching field velocities with PIV in the spillways of the Saint Marc dam, owned by EDF France, for different spillway operations with and without PK Weir.• Constructing a complete system of Large Scale Particle Image Velocimetry (LSPIV) (illumination, seeding, a digital camera, and pre-processing of the recorded images for surface velocity measurements of different shaped shallow reservoirs and other several applications measured such as in groyne field experiments, prototype model of river junctions and approach flow in spillways and dams and oil spill investigations.• Upstream velocity field measurements using PIV for high return period floods (Q10,000 and PMF) Shahryar dam is currently under construction on the Qezel Owzan River (East Azerbaijan Province) in northwest Iran.	11/2003 till present

<p>Design and Site Engineer, <i>Consulting office in Alexandria (EKR), (The leading consulting office in Egypt), Part time Egypt.</i></p> <ul style="list-style-type: none"> • Design and site works for several bridges and multistory buildings. • A part in several projects for structural analysis and working details of reinforced concrete structural water tanks and steel structural. • Design several of several villas around Alexandria and Cairo. • Preparing the documents for tenders. 	<p>11/1997 to 10/1999</p>
<p>Site Engineer, <i>EL-Saraya Company For Construction and Design, Alexandria, Egypt.</i></p> <ul style="list-style-type: none"> • Responsible for surveying working, aligning structural axes, foundation construction and Dewatering using well Point system and all related work for the construction of the R.C. structural. 	<p>5/1998 to 7/2001</p>

PUBLICATIONS

Journal

1. Nagy, H., **KANTOUSH**, S. A., and K. Watanabe (2003), Modeling Simulation for flood routing and tidal propagation in coastal drains. Alexandria Engineering Journal, VOL. 42, No.6, 715-722.
2. **KANTOUSH**, S. A., H. Nagy and K. Watanabe (2004), Modeling for flood prevention for the coastal area of Nile Delta in Egypt. Journal of Hydraulic Engineering, JSCE, VOL. 48, 637-642.
3. **KANTOUSH**, S. A., G. De Cesare, J.L. Boillat and A. J. Schleiss, (2007). Flow Field Investigation in a Rectangular Shallow Reservoir using UVP, LSPIV and numerical modeling. Journal of Flow Measurement and Instrumentation.
4. H. Moukhliiss, **KANTOUSH**, S. A., A. J. Schleiss and G. De Cesare (2007). Et si les crues de l'Arve rejoignaient le Léman? Etude de faisabilité de la dérivation des crues de l'Arve

- pour améliorer le rendement de la centrale du Seujet et décharger la retenue de Verbois. Journal Archives des Sciences.
5. **KANTOUSH**, S. A., Bollaert, E., Boillat, J.L., and Schleiss, A., (2008). Experimental and numerical modeling of sedimentation in rectangular shallow reservoirs: a first comparison. International Journal of Sediment Research (Accepted and revised version was submitted)
 6. B. J. Dewals, **KANTOUSH**, S. A., S. Erpicum, M. Piroton and A. Schleiss, (2008), Analysis of flow instabilities in Shallow rectangular basins, Journal Environmental Fluid Mechanics.
 7. **KANTOUSH**, S. A and A. J. Schleiss, Large scale PIV measurements at the surface of different shallow reservoir geometries, Journal of Visualization (In revision)

Conferences

1. **KANTOUSH**, S. A., A. J. Schleiss and H. Balzerek, (2007). Evaluation of MiniEcho Sounder measurements to estimate sediment thickness in shallow reservoirs. Hydraulic Measurements & Experimental Methods Conference (HMEM 2007), (EWRI of ASCE) and (IAHR), Lake Placid, NY, USA.
2. **KANTOUSH**, S. A., J.L. Boillat and A. J. Schleiss, (2007). Economical large scale PIV measurements at the surface of different shallow reservoir geometries. Hydraulic Measurements & Experimental Methods Conference (HMEM 2007), (EWRI of ASCE) & (IAHR), Lake Placid, NY, USA.
3. A. Amini, **KANTOUSH**, S. A., B. Rosier, M. Geiges, and A. J. Schleiss, (2007). Large reservoirs and greenhouse gas emissions-A network thinking analysis. 14th German Dam Symposium and the 7th ICOLD European Club Dam Symposium, Munich, Germany.
4. **KANTOUSH**, S. A., J.L. Boillat and A. J. Schleiss, (2007). Evolution of sediment deposition and flow patterns in a rectangular shallow reservoir under suspended sediment load, 5th IAHR symposium on river, coastal and estuarine morphodynamics , 2007, University of Twente, The Netherlands.

5. **KANTOUSH**, S. A. and A. J. Schleiss, (2007). Evolution of sediment deposition and flow patterns in shallow reservoir: experimental study. 10th International Symposium on River Sedimentation, Moscow, Russia.
6. **KANTOUSH**, S. A., Symmetric or asymmetric flow patterns in shallow rectangular basins with sediment transport (2007) 32nd Congress of IAHR, John F. Kennedy student competition, 1-6 July, 2007, Venice, Italy.
7. **KANTOUSH**, S. A., E. Bollaert and A. J. Schleiss, (2007). Influence of the width of a rectangular shallow reservoir on sedimentation behavior and trap efficiency, 32nd Congress of IAHR, Special session of reservoir sedimentation, 1-6 July, 2007, Venice, Italy.
8. M. Leite Ribeiro, J.-L. Boillat, **KANTOUSH**, S. A., C. Albalat, F. Laugier and A. Lochu, (2007). Rehabilitation of St-Marc dam Model studies of spillways. Hydro2007, Granada, Spain.
9. H. Moukhliiss, G. De Cesare, **KANTOUSH**, S. A. and A. J. Schleiss (2006). Et si les crues de l'Arve rejoignaient le Léman? Congres Du Rhône, 15-16 Juin, Genève, Switzerland.
10. **KANTOUSH**, S. A., Bollaert, E., Boillat, J.L., and Schleiss, A., (2005). Suspended Load Transport in Shallow Reservoirs. Final Proc. XXXI IAHR Congress. Korea Water Resources Association, Seoul, South Korea, 1787-1799.
11. **KANTOUSH**, S. A., Bollaert, E.F.R., Boillat, J.-L., Schleiss, A.J. (2005). Sedimentation Processes in Shallow reservoirs with different geometries. Proc. of 8th International Conference on Fluvial Sedimentology, Delft, The Netherlands.
12. **KANTOUSH**, S. A., Bollaert, E.F.R., Boillat, J.-L., Schleiss, A.J. (2006). Sedimentation processes in shallow reservoirs comparison of numerical and experimental simulations. Proc. of 7th International Conference on HydroScience and Engineering, September, Philadelphia, USA.
13. **KANTOUSH**, S. A., Bollaert, E.F.R., Boillat, J.L., Schleiss, A.J., Uijttewaal, W.S.J., (2006). Experimental study of suspended sediment transport and deposition in a rectangular shallow reservoir. IAHR Proc. of the International Conference on Fluvial Hydraulics,

- Lisbon, Portugal, Taylor & Francis Group, London, ISBN 0-415-40815-6 ,pp.15623-1631.
14. **KANTOUSH**, S. A., Bollaert, E.F.R., Boillat, J.L., Schleiss, A.J., (2006). Experimentelle Studie von Schwebstofftransport und absetzung in einem rechteckigen Flachwasserbecken. Proc. Symposium Graz, 27-30 september 2006, Schriftenreihe zur wasserwirtschaft, Technische Universität Graz, ISBN 3-902465-50-6, 46/2, pp. 136-150.
 15. **KANTOUSH**, S. A., Bollaert, E., Boillat, J.L., and Schleiss, A.J., (2006). Physical Processes of the Suspended Sediment Deposition and Sediment Transport in Shallow Reservoirs. Abstract, 17th International Sedimentological Congress, Fukuoka Japan, O-138.
 16. **KANTOUSH**, S. A., Erik Bollaert, Giovanni De Cesare, Jean-louis Boillat and Anton Schleiss, (2006). Flow Investigation in a Rectangular Shallow Reservoir Using UVP, LSPIV and Numerical model. Proceeding of the 5th International Symposium on Ultrasonic Doppler Methods for Fluid Mechanics and Fluid Engineering. ETH Zurich, Switzerland, ISBN 3-905609-29-0, pp. 129-133.
 17. **KANTOUSH**, A. J. Schleiss, H.M. Nagy, K. Watanabe; (2004) Numerical Investigation of the Flooding Problem for the Costal Drainage System in Egypt, ISLT Proc., Thailand, pp. 4461-466.
 18. **KANTOUSH**, S. A. and K.Watanabe, (2003). Evaluation of the Shallow Lake Effect on the Drainage System in the Delta Area of Egypt. Japan Society for Civil Engineering, Kita Kyusho, Japan.
 19. **KANTOUSH**, S. A., H.M. Nagy and K. Watanabe, (2004). Modeling for flood prevention for the coastal area of the Nile Delta in Egypt, Annual conference of Japan society for civil engineering, 16-18 March 2004, Kumamoto University, Kumamoto, Japan.
 20. **KANTOUSH**, S. A., H.M. Nagy and K. Watanabe, (2003). A modeling System for Design and Operation of Dendritic Channel Networks in Nile Delta of Egypt. XXXth IAHR Congress, Thessaloniki, Greece.
 21. **KANTOUSH**, S. A., H. M. Nagy and K. Watanabe, (2003). Evaluation of the Drainage Management by Hydraulic Modeling in the Coastal Area of Egypt. XXXth IAHR Congress,

Thessaloniki, Greece.

22. **KANTOUSH**, S. A. and K. Watanabe, (2002). Improvement Strategy of Irrigation System in Nile Delta of Egypt. Japan Society of Civil Engineering conferences JSCE, Saga, Japan.
23. **KANTOUSH**, S. A., H.M. Nagy and K. Watanabe, (2002). Numerical Analysis for Tree Type Channel Network in Delta of the Nile River. International Symposium on Lowland Technology, ISLT Proc., Saga, Japan.
24. **KANTOUSH**, S. A., H. M. Nagy and K. Watanabe (2002) Calibration of Dynamic Unsteady Flow Model for Flood Routing in Drainage Networks. Role of Engineering towards Better Environment conference, Alexandria University, Fac. of Engineering, Alexandria, Egypt.

Reports and thesis

1. **KANTOUSH**, Modeling for Water Management and Flood Prevention for the Channel Network in the Nile Delta of Egypt, MSc. Thesis, Department of Civil Engineering, Saga University, Saga, Japan, August 2003.
2. **KANTOUSH**, S. A., Influence of reservoir geometry on the process of sedimentation in shallow reservoirs by suspended sediment load. Research plan report for Doctoral school ENAC, Swiss Federal Institute of Technology EPFL, Laboratory of hydraulic constructions LCH, Lausanne, Switzerland, October, 2004.
3. **KANTOUSH**, S. A., Jean-Louis Boillat. Physical model tests for La Paz sewer system (La Paz, Bolivia). Experimental rapport, Swiss Federal Institute of Technology, Laboratory of hydraulic constructions LCH, Rapport No 9/04, Lausanne, 29 July, 2004.
4. **KANTOUSH**, S. A., Influence of reservoir geometry on the process of sedimentation in shallow reservoirs by suspended sediment load. Three Annual thesis reports for doctoral school ENAC, Swiss Federal Institute of Technology EPFL, Lausanne, Switzerland, December 2004, 2005 and 2006.

5. **KANTOUSH**, S. A., Influence of reservoir geometry on the process of sedimentation in shallow reservoirs by suspended sediment load. Three Annual reports for Research Projects Rhone-Thur, 2004, 2005 and 2006.

PROFESSIONAL SERVICES

- Journal of Environmental Fluid Mechanics, EFMC.
- 7th International Conference on Hydrosience and Engineering (ICHE-2006), Philadelphia, USA, September 10 to 13, 2006.

Reviewer of technical Papers

- **Session organizer**, IAHR International Conference on Fluvial Hydraulics, Lisbon, Portugal.
- **Session organizer**, International Symposium on Lowland Technology, ISLT, Saga, Japan.

Scientific advisory committee for conferences

- Session organizer, IAHR International Conference on Fluvial Hydraulics, Lisbon, Portugal.
- Member, 4th International Conference on Role of Engineering towards Better Environment, 2002, Alexandria, Egypt.
- Session organizer, International Symposium on Lowland Technology, ISLT, Saga, Japan.
- Member of the Syndicate of Engineers, Egypt, (1997- present)

Technical membership

- Member of American Society of Civil Engineering (ASCE) (Student membership)
- Member of Japan Society of Civil Engineering (JSCE) (Student membership).
- Member of International Association of Hydraulics Research (IAHR).
- Member of the Syndicate of Engineers, Egypt, (1997- present)